DESIGN OF A PERMANENT MAGNET AXIAL FLUX HIGH-SPEED GENERATOR

TAREQ SADEQ FAWZI EL-HASAN

A thesis submitted in partial fulfilment of the requirements of the University of Hertfordshire for the degree of Doctor of Philosophy

The program of research was carried out in the Department of Aerospace, Automotive and Mechanical Engineering, University of Hertfordshire

In collaboration with

King Abdullah II Design & Development Bureau (KADDB) and Jordan Armed Forces

November 2002

THESIS CONTAINS

VIDEO CD DVD TAPE CASSETTE

ABSTRACT

Electrical generating sets powered by gas turbines are required for many applications, in particular for emergency situations due to their critical attributes; high reliability, lightweight, small size, multi-fuel capabilities, low maintenance, low noise and low gas emissions.

This research contends that a permanent magnet axial flux (*PMAF*) high-speed generator with a small gas turbine engine offers advantages over the radial flux permanent magnet generators. Higher power densities can be achieved with the axial flux configuration when compared to their counter parts of the radial flux machines of similar output power. The attributes of the *PMAF* machines were certainly appealing; lightweight, small size, high efficiency and ease of construction.

In this research, a design approach for the *PMAF* high-speed generator which accounts for the mechanical and electrical aspects was provided. The machine's key components such as retainment ring was carefully designed and the materials utilised in their structures were appropriately selected to insure high mechanical integrity, ease of construction and low manufacturing cost. The generator's principle dimensions were determined from a theoretical model which was derived from the machine's main design parameters. This theoretical model was then correlated by some empirical coefficients determined through the manipulation of the experimentally validated finite element (*FE*) results. The analytical results have shown that with the appropriate design considerations, *PMAF* high-speed generators can be designed with high power densities in the range of 6 – 8 kW/kg and high efficiencies ideally in the range of 94 – 96 %. The mechanical integrity and the steady state electrical performance of the machine were analysed using three-dimensional (*3D*) *FE* models. More in this research, a parametric study was carried out on the most influential parameters of the machine to improve its electrical performance through minimise rotor and stator eddy current losses. In addition, the total harmonic distortion in the output waveform was minimised through the appropriate and careful design of the magnet shape and

topology with the aid of ***3D*** electromagnetic ***FE*** analysis. Furthermore, using ***FE*** it was possible to design, optimise and analyse the rotor back-iron disc through the selection of best material, shape and size for use in the ***PMAF*** high-speed generator. A prototype of the ***PMAF*** high-speed generator was constructed and tested preliminary at low speed for the purpose of the evaluation of the electrical performance of the machine. Experimental results have shown that the machine was capable to meet the design requirements. For the mechanical integrity of the machine, the rotors were safely tested on a cold run test rig at the speed of 47,000 rpm. This thesis describes also the trends and the technical details in the manufacturing, construction and experimental setup for the ***PMAF*** high-speed generator.

ACKNOWLEDGEMENTS

I would like to express my sincere thanks to my supervisors Prof. F. S. Bhinder and Dr. Patrick C. K. Luk for their help, guidance, support and encouragement throughout the research.

I would like to thank Dr. John Davis for his valuable comments on the Thesis and all members of the department who have provided help during the project. Special thanks go to the Assistant Technical Manager in the Department of Manufacturing Systems Engineering, Mr. P. Luker for his technical support during the manufacturing process in this project. Thanks go as well to the members of staff in Science & Technology Research Centre for their help, warmth and friendliness.

I would like to thank Prof. M. El-Zayyat, Prof. M. Hammad, Prof. M. Z. Khader and Dr. O. Abu-Zaid at the University of Jordan for their encouragements and their constructive help through the project.

I would like to express my thanks to the Jordan Armed Forces and King Abdullah II Design & Development Bureau for their financial support to do this research, in particular thanks go to Col. Ghazi Khdairi for his guidance as an Industrial Montour throughout the project.

Finally, I am most grateful to my family for their support, encouragement, and patience through this study. In particular, I would like to thank my wife for her endless support and patience and I dedicate her this thesis.

CONTENTS

Paper 3. P. C. Luk and El-Hasan T. S. "Back iron design for high speed PM axial flux generators". *INTERMAG2003 Conference proceedings*. Digest No. 201, Boston, USA. April 2003.

Paper 4. El-Hasan T. S. and P. C. Luk "Magnet topology optimisation to reduce harmonics in high-speed axial flux generators". *INTERMAG2003 Conference proceedings*. Digest No. 886, Boston, USA. April 2003.

Paper 5. El-Hasan T. S. and P. C. Luk "Three-Dimentional FE analysis of disc type high-speed PM generators". *INTERMAG2003 Conference proceedings*. Digest No. 1235, Boston, USA. April 2003.

APPENDIX D: ANSYS FILES & SIMULATION RESULTS ON CD-ROM

- 2D STRESS ANALYSIS OF THE *PMAF* ROTOR
- 2D ELECTROMAGNETIC ANALYSIS
- 3D STRESS ANALYSIS OF THE *PMAF* ROTOR
- 3D MAGNETOSTATIC ANALYSIS
- 3D HARMONIC ANALYSIS

NOMENCLATURE

$\{a\}$	Nodal displacement vector, m
A_b	Total bundle area, m^2
A_{bi}	Surface area of the back-iron disc, m^2
A_c	Cross sectional area of the copper conductor, m^2
A_{Cls}	Total axial clearance between the rotor and stator surface, m
A_g	Area of air gap, m^2
A_m	Area of permanent magnet, m^2
A_{mg}	Air gap/magnet interface area, m^2
A_p	Area of the virtual path, m^2
A_R	Circumferential area of the inner surface of the ring, m^2
A_{std}	Cross sectional area of strand, m^2
A_t	Area enclosed by a single turn in a coil winding, m^2
A_{2n-1}	Amplitude of harmonic coefficient of the flux, Web
A	Magnetic vector potential
b	Magnet radius, m
B	Air gap flux density, T
B_{ave}	Average flux density, T
B_i	Flux density in the gap between the back-iron and magnet rotor , T
B_m	Flux density in the magnet, T
B_p	Peak flux density in the air gap, T
B_r	Residual flux density in the permanent magnet, T
B_s	Saturation level of flux density, T
B_u	Attainable flux density at the surface of the magnet, T
B	Magnetic flux density vector
BHD	Belt harmonic distortion
C_B	Average flux density to air gap flux density ratio

C_l	Coil mean length, m
C_p	Specific heat capacity of the air, $J/kg \cdot K$
C_R	Contact radius, m
C_{2n-1}	Harmonic sine coefficient of the flux, Web
d_b	Bundle diameter, m
d_m	Magnet diameter, m
d_s	Space between semicircular magnets, m
d_{shaft}	Shaft diameter, m
d_{std}	Strand diameter, m
$[D]$	Elasticity matrix, MPa
D_{2n-1}	Harmonic cosine coefficient of the flux, Web
$e(t)$	Air gap induced voltage, V
E	Young's modulus of elasticity, GPa
E_{NL}	No-load induced voltage, V
E_1	Air gap induced voltage at a certain load current, V
f_e	Electrical frequency, Hz
f_f	Filling factor for the stranded wire
F_m	Force from magnets on the retainment ring due to rotation, N
F_x	Magnetic force exerted on the back-iron disc from the magnet rotor, N
$\{F\}$	Overall external force vector, N
G	Shear modulus of elasticity, GPa
H_c	Permanent magnet coercivity, kA/m
H_m	Flux intensity in the magnet in a magnetic circuit, kA/m
H	Magnetic field intensity vector
I_L	Load current, A
J_c	Conductor current density, Amp/m^2
J	Total current density vector
k_{ax}	Winding axial backing factor
k_{Br}	Magnet leakage coefficient

k_g	Air gap length coefficient
k_{mr}	Magnet inner radius to outer radius ratio
k_p	Pole leakage factor
k_R	Winding radial backing factor
k_{size}	Coil size coefficient
K_b	Combined shock and fatigue factor applied for bending moment
K_N	Contact element normal stiffness
K_S	Contact element sticking stiffness
K_t	Combined shock and fatigue factor applied to torsional moment
$[K]$	Element stiffness
l_g	Air gap length, m
l_i	Axial thickness of the back-iron disc, m
l_{mg}	Total magnet air gap length, m
l_m	Magnet axial length, m
L_L	Leakage inductance, H
L_M	Magnetising inductance, H
L_{shaft}	Shaft length, m
L_{Tw}	Total winding length, m
$\dot{m}$	Air mass flow rate, kg/sec
M_b	Bending loads due to weights of components, N.m,
M_{depth}	Magnet depth, m
n	Numeric counter
N_o	Operating speed, rpm
N_c	Number of coils per phase in the stator windings
N_{CT}	Total number of turns per coil
N_l	Number of layers per coil
N_m	Mechanical design speed, rpm
N_r	Number of rotors

N_s	Number of stator stages
N_{std}	Number of strands per bundle
N_t	Number of turns per layer per coil
p	Number of poles per rotor
ph	Number of phases
pp_{arc}	Pole pitch arc, m
P_c	Stator copper losses, W
P_{cont}	Contact pressure due to interference fit, MPa
P_{eu}	Eddy current losses per unit length of the stranded conductor, W
P_{in}	Input power, W
P_{loss}	Total losses in the generator, W
P_m	Magnetic pressure exerted on the back-iron disc, MPa
P_o	Output power ,W
P_{Re}	Rotor eddy current losses, W
P_{Se}	Stator eddy current losses, W
P_w	Windage losses, W
Pr_i	Pressure, MPa
R_{AC}	Winding effective resistance, Ω
R_c	Radius of the contact surface, m
R_{ci}	Inner radius of the virtual path of the coil, m
R_{co}	Outer radius of the virtual path of the coil, m
R_{cut}	Cutting radius for the back-iron disc, m
R_{Cls}	Total radial clearance, m
R_{ho}	Hub outer radius, m
R_{hi}	Hub inner radius, m
R_{ii}	Inner radius of the back-iron disc, m
R_{inner}	Rotor inner radius, m
R_{io}	Outer radius of the back-iron disc, m

R_{mi}	Magnet inner radius, m
R_{mo}	Magnet outer radius, m
R_{outer}	Rotor outer radius, m
R_{Ro}	Retainment ring outer radius, m
R_{Ri}	Retainment ring inner radius, m
R_{sc}	DC Stator winding resistance, Ω
R_{eq}	Equivalent reluctance, A. turn/Web
S_f	Stress safety factor
S_s	Maximum allowable stress, MPa
t	Time, sec
T_d	Design temperature, °C
T_{shaft}	Torque applied to the shaft, N.m
THD	Total harmonic distortion
V_{pk}	Peak induced voltage, V
V_t	Terminal voltage, V
VR	Voltage regulation, %
W	Stored energy, Joule
W_{ax}	Winding axial thickness, m
W_{ie}	Inner end winding thickness, m
W_{oe}	Outer end winding thickness, m
W_{SC}	Winding circumferential span, m
X_L	Leakage reactance, Ω
X_M	Magnetising reactance, Ω
X_s	Synchronous reactance, Ω
α_T	Thermal expansion coefficient, K^{-1}
$\overline{\alpha}_c$	Temperature coefficient for copper, deg^{-1}
β_{2n-1}	Phase angle for the harmonics in the flux waveform, Deg
δ	Interference fit value, m

δ_L	External load angle, Deg
δ_i	Internal load angle, Deg
$\{\varepsilon\}$	Total strain vector
θ	Angular position, Deg
θ_m	Angular span of the magnet, Deg
θ_s	Angular space between adjacent magnets, Deg
θ_{twist}	Mechanical angle of twist for the shaft, deg
θ_1	Pole pitch angle, Deg
θ_2	Half pole pitch angle, Deg
ϕ	Flux enclosed by the coil, Web
μ_{air}	Coefficient of viscosity of the air, kg/m.s
μ_m	Magnet permeability,
μ_r	Relative permeability
μ_o	Free space relative permeability, H/m
ν	Poissons ratio
ΔT	Temperature difference, $^{\circ}C$
η	Generator efficiency, %
ω_e	Electrical angular frequency, rad/sec
ρ_{air}	Density of air, kg/m^3
ρ_m	Mass density, kg/m^3
ρ_c	Copper resistivity,
σ_r	Radial stress, MPa
σ_d	Design strength, MPa
σ_{Ty}	Yield tensile strength, MPa
$\sigma_{\theta pressure}$	Hoop stress due to pressure, MPa
$\sigma_{\theta rotation}$	Hoop stress due to rotation, MPa
$\sigma_{\theta T}$	Total hoop stresses, MPa
$\{\sigma\}$	Stress vector, MPa
ψ_i	Angle of internal power factor, Deg

CHAPTER 1

INTRODUCTION

1.1 BACKGROUND

Electric generating sets powered by small gas turbines are needed in a wide range of applications. They are strong competitors to the conventional generating sets powered by diesel engines because of their critical attributes; high reliability, lightweight, small size, multi-fuel, low maintenance, low noise, low vibration and low emissions [1,2,3,4]. Such generating sets can be employed for maintaining power electricity in emergency situations and disasters such as earthquakes, floods, tornados or war, and they can be used to provide necessary lighting for evacuation, power for communication systems and the maintenance of water supplies and power for the operation of elevators for use either by firefighters or rescue crews. In hospitals and other health care facilities, the continuous supply of electrical power is critical for maintaining the health of patients such as those on life support systems or those in surgery where a loss of power could prove life threatening.

The keys to substantial market penetration for gas turbine-powered generating sets lies in having adequate range and power with reasonable prices in the eyes of the user. Such sets can be also used in applications in which connection to the utility grid is not possible, such as hybrid electric vehicles (*HEV*), or in remote locations where utility service is not available, such as military field exercises. In addition to these applications, gas turbine-powered generating sets can be also utilised in many business and industries where it is necessary to maintain operations and protect equipment in the event of a utility failure and also to provide additional electric power in times of peak demand without increasing the facility electric bill.

However, gas turbine-powered generating sets have two major problems which have held up their development. The first problem is related to the availability and cost

of gas turbine engines since they contain some of the key components which are conventionally considered to be the province of aerospace technology with high manufacturing costs [5,6,7]. By improving their performances, and their production processes, and with the utilisation of less expensive material, gas turbine engines can be produced with competitive prices and can find their ways to the markets.

The second problem is associated with the electrical generator itself. Gas turbine engine is designed to operate at high rotational speeds in the range of 30,000 – 100,000 rpm for optimum efficiency. Hence any electric generator coupled directly to the gas turbine engine must have the capability to withstand the high centrifugal forces developed due to the high rotational speed. In an initial review of possible generators for the gas turbine-powered generating sets, it was found that such generators do not exist commercially. At the earliest stages of the developments of such generating sets, high-speed induction and reluctance generators were used for aerospace and military applications [6,7,8]. However, such generators were relatively heavy, inefficient, too expensive and required special cooling techniques.

1.2 PROBLEM IDENTIFICATION

In the last decade, several direct drive turboalternators were built with their conventional field wound rotors were replaced by the state of the art of rare earth permanent magnet materials. The majority of these alternators were of cylindrical (radial flux) type configuration [9,10,11,12]. In this type of machines, the magnets are mounted on the rotor surface and surrounded by carbon-fibre sleeve to insure magnet retention at high rotational speed. However, the introduction of the retainment sleeve resulted in an increase of the effective air gap length. Moreover, the stator of the high speed *PM* cylindrical generator is identical to the stator of a conventional one in which the iron core consists of thin laminated sheets. This in turn has lead into less exploitation of the machine's volume and detracted from its performance and power to weight ratio. Alternatively, other types of high speed *PM* alternators also were proposed and these were of disc type (axial flux) configuration. The attributes of the *PM* axial flux machines were certainly appealing; lightweight, small size, high efficiency and ease of construction.

As far as the author is aware, two research activities were involved in the development of high-speed permanent magnet disc type machines [13,14]. However, the body of the work was focused on the mechanical design aspect with a little attention is paid towards the electromagnetic design. Moreover, the design data and technical information for such types of machines are scarce. Nevertheless, axial flux machines of low speed/low output power were used extensively in many applications and were reported in a number of papers that were of great importance for assisting in the design of high-speed generators [15,16,17]. From the review on these machines, it was found that, axial flux machines have higher power densities when compared to their counterparts of radial flux machines of similar output power and with appropriate design consideration can be designed at high efficiency.

The research work described in this thesis contends that the use of a permanent-magnet axial-flux high-speed electrical generator in conjunction with a small gas turbine engine offers a number of significant advantages over radial flux or any other types of generators for use in an emergency power generation system. These advantages centre on system reliability, ultimate power density, compactness and a high level of efficiency.

However, a number of design challenges arise as a consequence of the high-speed operation of the generator. First, the mechanical integrity of the rotor becomes an issue. Keeping the rotor radius small enough should guarantee operation below critical speed, but the volume of permanent magnet required to produce a certain power and the size of the air gap required to accommodate the windings for a certain electrical loading are highly affected by the rotor radius. The introduction of a retainment ring (such as Maraging G125) will ensure magnet retention. This result in an increase of the rotor radius hence an increase in the windage losses of the machine. Another design issue occurring at high speeds is that of increased rotor losses arise because the rotor is exposed to a time varying magnetic fields from the spatial harmonics of the stator currents. The eddy current losses are proportional to the square of the magnetic field amplitude, the square of the frequency and inversely proportional to the rotor materials resistivities. As a result, ensuring low levels of rotor loss amounts to making rotor surface have relatively low surface conductivity and producing stator currents that are sinusoidal, which could be achieved through careful design and proper

material selection. Furthermore, the stator eddy current loses and copper losses can be dominant losses if several precautions are not considered in the design. By using Litz wire construction and by insuring a sinusoidal flux density distribution in the air gap through magnet topology optimisation, eddy current losses can be minimised and a successful design can be obtained.

In order to analyse the mechanical stresses in the rotor and accurately evaluate the losses in the machine, a rigor analysis using finite element method (***FEM***) should be performed. The permanent magnet axial flux (***PMAF***) machine by its nature has a three-dimensional (***3D***) pattern. The magnetic flux path and its corresponding spatial flux distribution are truly ***3D*** in their nature and are at variance with the usual conventional or radial flux ***PM*** machines. This unusual ***3D*** flux patterns in the ***PMAF*** machines is largely caused and shaped by the nature of the magnetic circuit geometry of the rotor, the location and the shape of the stator winding coils. Any attempts to simplify the machine into a two-dimensional (***2D***) ***FE*** model will give inaccurate results. Moreover, for this particular machine configuration, the magnetic losses, inductances and harmonics are not possible to be evaluated by the ***2D FE*** model. For the stress analysis of the rotor, the simulation of the influence of interference fit between the rotor parts in the ***3D FE*** model is an essential task to be performed in order to get accurate results.

The design of the ***PMAF*** high-speed generator is a challenging task and requires multidisciplinary knowledge. It is believed that the technology in the development of such machine is immature. Hence, the need for further research to overcome all the difficulties associated with design of ***PMAF*** generators for high-speed applications continues to exist.

1.3 AIM AND OBJECTIVES OF THE RESEARCH

The main aim of the research described in the following Chapters is to provide a design methodology for a permanent magnet axial-flux high-speed generator directly coupled to a gas turbine engine for use as an emergency generating set. Taking into account all mechanical and electromagnetic conflicting design requirements such as

design of shaft, rotor, magnet and stator, the method will include a selection process for the best among several possible successful designs.

This goal can be accomplished through the achievement of several objectives in this research. First, a comprehensive literature review on the available machines and on some aspects related to the design and analysis of several proposed electric machines will be carried out. Then a mathematical model of the ***PMAF*** generator will be developed and analysed based on the principle dimensions of the machine. Next, a basic ***FE*** model for a particular design will be developed and the results obtained will be verified by comparing the results of the ***FE*** model to the experimental data obtained from a particular ***PMAF*** prototype. These results will be used as feedback process to define a set of empirical coefficients that will be used to calibrate the developed mathematical models. Finally, the calibrated model will be used to simulate and evaluate several possible designs resulted from the variation in some of the design parameters such as number of poles and number of stator turns. The results of the simulations will be used for the selection of the best design of the ***PMAF*** high-speed generator based on the following order of priority; power density, size and efficiency.

The back-iron disc is another key component in the machine which will be designed and analysed carefully in order to achieve machine's ultimate compactness and lightness without detracting from its electrical performance. Later, a ***3D FE*** models will be developed for both mechanical stress analysis as well as for the electromagnetic analysis for accurate prediction of the performance of the machine. These models will be helpful in minimising machines electrical losses such as eddy current losses by optimising the magnet shape and topology. A prototype of the PMAF machine will be constructed and tested experimentally in order to obtain the design data for such machine for the evaluation and the assessment of the proposed integrated design methodology.

CHAPTER 2

LITERATURE REVIEW

2.1 INTRODUCTION

A considerable research has been carried out worldwide in the development of permanent magnet machines due to the advantages offered by this technology. New machines are being developed with higher power density and efficiency and at the same time, work is continuing towards the improvement of exciting machines. In this Chapter, a brief of the work carried out in the recent past on development, construction and analysis of permanent magnet machines for use as generators for high-speed applications is presented.

2.2 CONVENTIONAL HIGH-SPEED GENERATORS

2.2.1 High-speed induction generators

The induction machine is one of the simplest electrical machines and it has been used in many applications for more than a century. The rotor of such a machine is simple, robust and rigid and is suitable to withstand high stresses when used in high-speed applications. These types of machines are mostly used in the motoring operating mode however, they can be used in the generator operating mode [5,6,7,18,19].

In the 1960's, **Cohen et al** [5] in collaboration with *NASA*, have developed an induction high-speed generator for aerospace applications mainly to supply electrical power for extended space missions. The machine, which is a 12 kW alternator, has four-pole brushless solid rotor running at speed of 12000 rpm directly coupled to a two-stage axial flow gas turbine engine. The rotor pole tips are laminated. The stator consists of stacks of laminations and the power coils for the three phases are mounted

in axial slots on the inside diameter of the stator. The stator stacks are shrunk-fit into the stator steel frame. The steel frame provides a conduction path for magnetic flux, structural support, and contains liquid cooling provisions. An efficiency of 91 % has been quoted for the alternator having radial and axial dimensions of 220 mm (stator core OD) and 156 mm respectively. The total machine mass being 212 kg makes the power to weight ratio relatively low and this is expected since the machine's operating speed is still far away from the nominal operating speed of the gas turbines. Also the efficiency of the generator will be reduced drastically when operating such machines at higher speeds in excess of 50,000 rpm.

Rodgers [7] has presented a 10 kW gas turbine driven turboalternator at a speed of 100,000 rpm developed for the U.S army. The alternator design selected is a two pole machine which is similar to that presented by **Demerdash** [20]. The tested efficiency of the generator is 80 %.

In addition to their low power to weight ratio, the induction machines have the following disadvantages when used in the generator mode of operation:

- It consumes reactive power and always operates with a lagging power factor unless capacitors are connected to the terminals.
- Both magnitude and frequency of the output voltage and current are load dependent.
- Its principle of operation depends on the residual flux in the rotor which in turn gives rise to the possibility of the rotor becoming totally demagnetised.
- Relatively low efficiency.
- Requires considerable stator back-iron length to reduce saturation.
- Requires efficient cooling.
- Requires laminated rotor and stator structures.

2.2.2 High-speed reluctance generators

The reluctance machine offers another option for providing motor or generator modes of operation for high-speed applications. It has the advantages of being brushless, robust, simple, of low cost and maintenance-free. With appropriate design

consideration, such a machine can be built with higher power to weight ratio [21] when compared to other conventional machines. Moreover, its frequency is determined only by the prime mover speed, rather than by both load and the prime mover speed as in an induction generator.

Ferreira et al [8], have reported a 30 kW three-phase reluctance machine with six stator poles and four rotor poles directly coupled to an aircraft 1400 hp gas turbine engine. The machine operates in both start mode and in generate mode of operation covering a speed range from 27,000 rpm to 46,850 rpm. Both rotor and stator are made of vanadium iron cobalt laminations having 0.15 mm thickness to keep iron losses to a minimum. The stator windings consist of Litz conductors, to minimise the eddy current losses. The machine has an overall length of 113 mm and outer diameter of 159 mm and electromagnetic weight of 7.71 kg. The tested efficiency of the machine is close to 87 %.

Despite the advantages offered by such types of machines over the induction machines, a high-speed reluctance generator would have the following disadvantages:

- High ripple torque due to the saliency of the rotor poles which in turn may cause noise and vibration if mechanical tolerances are not held to close limits.
- Power factor is always less than unity.
- In addition, the construction of these machines especially the stator, will be very similar to that of induction machines and therefore, it will have similar structural disadvantages associated with lamination and considerable back-iron length.

2.3 PERMANENT MAGNET GENERATORS

Permanent magnet machines and in particular generators were the first types of electrical machines to be developed. During the early stages of their use, three problems held up their development, and because of these problems they have been regarded as unreliable. The first problem was the poor magnetisation characteristic of permanent magnet materials available at that time. The second was related to the manufacture of permanent magnets since there was limited experience in developing

alloys with acceptable characteristics and in shaping magnets that could be built into a machine. The third problem was the lack in design experience and methods to help in the optimal utilisation of the magnets in electrical machines. In the mean time, conventional DC and AC types of machines offered an effective solution to industrial problems and therefore it was little incentive to replace them with alternative types of machine.

It was not until the mid-sixties when new types of permanent magnet materials emerged on the scene and their considerably improved properties renewed interest in the development of permanent magnet machines. The powerful rare earth magnets such as samarium-cobalt (***SmCo***) and neodymium-iron-boron (***NdFeB***), satisfied the stringent requirements and eliminated the risk of demagnetisation under severe operating conditions. The properties and classification of the new permanent magnet materials in terms of the required characteristics to fulfil the design objectives of *PM* generators are briefly described, before reviewing the development of different types of permanent magnet generators.

2.3.1 Permanent magnet materials

Permanent magnet materials are used in a vast number of applications ranging from fractional wattage devices to large scale applications using hundreds of kilowatts of power [22,23]. The range of permanent magnet materials now available includes metallic materials such as "Alinco's", ferrite such as "ceramic" and rare earth magnets such as "NdFeB" and "SmCo". The use of these new materials in electrical generators is resulting in significant improvements in performance and power density.

The design process of electric devices utilising permanent magnet materials have been presented in many publications [24,25,26,27]. The selection of a particular type of permanent magnet for a certain application depends on many factors and the most important are the magnetic properties, the physical properties, the cost and availability. Initial review on the available permanent magnet materials have shown that the rare earth permanent magnets are highly suitable for use in electric machines for many applications for the following reasons:

- High magnet residual flux density, B_r.
- High magnetic coercive force H_c.
- High magnetic energy product, $(B_m H_m)_{\max}$. Hence machines with higher power/weight ratio can be developed.
- Rare earth magnets possess linear demagnetisation curves which can be simply modelled in any magnetic circuit.

However, the reversible magnetisation characteristic of the ***PM*** is limited by its maximum operating temperature which is normally $120°C$ for ***NdFeB*** and $250°C$ for ***SmCo***. Temperatures exceeding these limits will cause progressive, irreversible demagnetisation until at the Curie temperature the magnetisation drops to zero. If the magnets are then exposed to temperatures above the Curie temperature for a long time then the magnetism cannot be recovered by any means due to metallurgical changes in the material.

The ***NdFeB*** offers 30 – 40 % higher energy levels than ***SmCo*** alloys and is considerably lower in cost. Hence it would seem to be ideal for use in many electric machines and in particular in high-speed generators. However, ***NdFeB*** is a brittle material and its tensile strength is very low. Hence, special design techniques are required to ensure the mechanical integrity of the magnets when they are used in the rotors of high-speed generators.

2.3.2 Evolution of permanent magnet generators

The availability of new powerful rare earth magnets during the last two decades has resulted in the development of several types of permanent magnet generator for a wide spectrum of applications [15,16,17,28,29,30]. Furthermore, the increasing demand for generators having a high power to weight ratio and with high efficiency has encouraged the development of new permanent magnet generators to meet specific requirements. In addition, the introduction of the new techniques to improve the mechanical design plus parallel developments in the fields of power electronics, microprocessor control and the efficient design and analysis methods have made it possible to design and develop permanent magnet generators for high-speed

applications. These generators can be classified into two main categories based on the direction of the magnetic flux. These are; permanent magnet radial flux (***PMRF***) high-speed generators and permanent-magnet axial flux ***(PMAF)*** high-speed generators, and they are described briefly hereafter.

2.4 *PMRF* HIGH-SPEED GENERATOR

The permanent magnet radial flux generator has a stator identical to the stator of a conventional machine. The rotor of such a machine can have surface-mount magnets or buried magnets configurations. A number of permanent magnet radial flux generators designed for low speed applications are described in a number of papers [31,32,33,34]. For high-speed applications, the rotor of such machines is wrapped with special fibre sleeve or sometimes with non-magnetic conductive "can" to restrain the magnets at high speeds with minimised eddy current losses in the PM.

ABB have developed a high speed cylindrical (radial flux) ***PM*** generator derived from ***HSG100*** generator design in [9]. The machine is designed for use in the combined heat and power plant units (***CHP***) to produce an electrical output power in the range of 70 – 100 kW. The generator is directly driven by a gas turbine running at speed of 70,000 rpm. The stator core consists of thin laminations of low-loss electrical steel and the winding is made with Litz wire to reduce stator eddy current losses. Water-cooling is used to keep the temperature low in the winding. The rotor consists of a magnetic steel body with surface-mounted (four pole) ***NdFeB PM***. A carbon-fiber bandage holds the magnets firmly in place at the design speed. The rotor radius is selected according to mechanical design criteria, and is a trade-off between an optimum bending stiffness and the largest magnet thickness that can be retained by reasonably thin bandage. Using the rotor radius as a basis, the stator core radius and the axial length are determined in an iterative process. The rotor faces a major problem that the carbon-fiber bandage acts as a thermal insulator hence high possibility for ***PM*** demagnetisation due to excessive temperature.

Similar types of radial flux machines of different power ranges and different speeds have been presented in a number of publications [10,11,12,35]. Although ***PM*** radial

flux high-speed generators have high efficiencies and high power densities compared to their counterparts of induction and reluctance generators, they have the following drawbacks:

- They have considerable rotor axial length with more potential for damaging vibration.
- A considerable mass of back-iron is required for the stator to prevent saturation.
- Laminated stator structure is required to reduce core losses, thus increasing cost and manufacturing complexity.
- The stationary ferromagnetic core induces iron losses.
- A conductive shield is required to surround the PM in the rotor to prevent eddy current circulation in the magnets [36,37,38]. Hence adding more complexity to the structure.
- The effective air gap length is affected by the thickness of the carbon-fibre sleeve which surrounds the magnets. Further increase in the thickness will require larger air gap hence reducing the magnetic flux density in the air gap for a particular *PM* size.
- Carbon-fibre and composite materials retainment sleeves are expensive and require a complicated manufacturing process. In addition, the assembling of the sleeve on the rotor requires special arrangements and mechanical setup.
- The carbon-fibre sleeve acts as a thermal insulator which prevents heat removal from the rotor.

2.5 *PMAF* HIGH SPEED MACHINES

The history of electrical machines shows that the earliest generators were of the axial-field type [29]. The Faraday disc generator, which was invented 1832, was based on the axial configuration. Axial flux generator has its air gap flux directed axially and the conductors positioned radially. A description of the evolution, classification, main configuration and the applications of a numerous axial flux permanent magnet machines can be found in [30] which shows suitability of such machines for many applications. However, in the literature, few of these machines have been addressed for

high-speed applications [13,14,40,41]. A review on some of the ***PMAF*** high-speed generators is given hereafter.

In 1991, **Pullen** [13], designed and developed a small gas turbine and high speed generator. The generator is directly driven by inward flow gas turbine engine (***IFR***) which provides 50 kW at speed of 100,000 rpm as an ultimate goal. Much of the work is focused on the mechanical design with a little attention is paid to the electromagnetic design and analysis of the machine. He has investigated several alternatives of geometry and configuration for the proposed axial flux generator and have sited the reasons for the selection of disc type. The rotor which has a disc type configuration, uses a carbon fibre material as a retainment shell for magnet retention at the design speed. The thickness of this shell is optimised based on the minimum attainable hoop stresses for a certain rotor diameter. A ***2D*** finite element stress analysis is performed on the rotor to verify its mechanical integrity. Final magnet shape is selected based on the ease of manufacturing and optimal suggested shape of the windings. The effect of the magnet shape on the performance of the machine was not considered. The effect of design parameters such as magnet principal dimensions, number of poles, number of turns and number of stator and rotor stages, on the performance and characteristics of the machine have not been considered. The stator has an ironless core with the three-phase windings are all placed in one stack per stator stage and encapsulated by epoxy resin. Ironless stator has lower inductances hence lower armature reaction and voltage regulation. The windings are lap "wave" type and constructed from fine strands. The author has ignored stator eddy current losses however he has evaluated the windage losses in the machine and verified the results experimentally. He also mentioned the rotor eddy losses could be problematic and it requires thorough investigations. Manufacturing of the stator process has been described for alternative winding types. Assembling the rotor and manufacturing process for the carbon fiber shell also have been described. Shaft and component vibration analysis has been performed and the critical speeds have been predicted using PAFEC graphics package. Prototypes of the alternator have been successfully tested (up to 70000 rpm compared to the target of 100000 rpm) on the high-speed rigs, designed and commissioned specifically for this task. Heating losses and stator cooling have been justified and different methods for forced cooling are suggested. Finally, the performance data of the machine is not available. In another paper for the same author

[40], three units of 10, 30 and 50 kW are developed tested at the speed of 60000 rpm and an efficiency of 95 % is quoted at full load currents.

Sahin et al [14], have reported a 30 kW axial flux permanent magnet machine mounted inside a flywheel used for the transient energy storage in an *HEV*. The machine which runs at speed of 16000 rpm, has its permanent magnets placed on the rotor which is an integral part of the flywheel, and the stators are fixed to the housing. In the paper, the design aspects for the machine are given. Analysis of the losses and thermal behaviour of the machine is included. Mechanical constraints and the aspects of manufacturing are summarised. The machine test bench is described and the measurements of losses are shown. Machine measured efficiency is 91.47 % whereas the predicted one is close to 95 %. Author detected the discrepancy is due to the unpredictable hysteresis loss are appearing in the stator cores.

Much of the work carried out on the design and development of such machines was focused on the mechanical aspects with a little attention paid towards the electromagnetic design and analysis of such machines. Moreover the design data and technical information for such types of machines are still scarce and further work is still required.

2.6 TREND FOR THE DESIGN AND ANALYSIS OF *PMAF* HIGH-SPEED GENERATORS

As it was found from the literature that the detailed technical information, design data and performance analysis for the high speed *PM* axial flux machines are sparse and those are published are focused on the mechanical design with a little attention is paid towards the electromagnetic design and analysis. Therefore, main issues related to the design and analysis of the axial flux machines and other types of machines have been reviewed.

2.6.1 Design aspects

The design aspects for the axial flux machines can be found in a number of papers [15,16,17]. In most of these publications, the output power equations for each type of machine are used for the design purposes. The rotor is optimised by the magnet inner radius to outer radius ratio which is 0.577 [15]. However it was argued in some other publication [42], that there should be no fixed value for this ratio since it is a function of rotor geometry, number of poles, material used and the objective of optimisation.

2.6.2 FE electromagnetic analysis and performance evaluation

In the *PMAF* machine, the magnetic flux path and its corresponding spatial flux distribution are truly *3D* in their nature and are at variance with the usual conventional or radial flux *PM* machines. This unusual *3D* flux patterns in the *PMAF* machines is largely caused and shaped by the nature of the magnetic circuit geometry of the rotor, the location and the shape of the stator winding coils. Information concerning electromagnetic modelling of the *PMAF* machines is spars. Attempts have been reported in some publications for modelling such machines using *2D* simplified *FE* models [39,43,44]. In some other publications the evaluation of magnetic losses [45,46,47], accurate prediction of inductances [48] and harmonic analysis and their effect on the stator eddy current losses [49], were performed using *FE* electromagnetic models for *PM* cylindrical machines and can be of use for analysis of the *PMAF* generator. Further details concerning the *FE* analysis will be discussed in Chapter Four.

2.6.3 *FE* stress analysis

The rotor is the most crucial part in the machine and extra care should be taken when designing such a rotors for high-speed applications. The accurate analysis of rotor for its mechanical integrity requires the utilisation of *FEM*. Pullen [13], have used a *2D* planar model but without modelling the interference fit between the magnet and the carbon-fibre shell. The planar model does not consider the deformation hence, stresses in the axial direction. In another related subject, **Wei** [50] have used a

simplified *2D* axisymmetric model for two compound cylinders with the interference fit is taken into account. A *3D* model with the influence of interference fit would be more realistic and would give more accurate results.

2.7 MAIN OBSERVATIONS

The following main observations are found through the literature review on different types of electric machines:

A) The *PM* axial flux machines are strong competitors to radial flux machines in many applications. Compared with the radial flux machines, when designed for high-speed applications, the axial flux machines have the following potential advantages:

- Compact configuration with short axial length. Machines with a large number of poles can be constructed.
- For the same output power, a higher power density can be achieved in comparison with the radial flux generator.
- Metallic, either magnetic or non-magnetic, materials can be used as retainment rings for the rotor.
- The thickness of the retainment ring does not affect the effective air gap length since it is not placed across the air gap.
- The stator can be a slotless/ironless structure thus reducing stator core losses and thus giving better efficiency and reducing the total weight of the machine.
- The flux path is completed through the back-iron discs which are rotating with the rotors thus eliminating iron losses.
- Better cooling is achieved since the windings have open structure and are exposed to the air circulating around the stator.
- Axial flux machines can be constructed on a modular design basis. Hence, the output power of the machine can be increased by using a larger number of stator and rotor stages.

B) Published literature on the design and development of the *PM* axial flux high-speed generator is still scarce and further work is required to overcome all problems associated with the design of such machines.

C) Among the axial flux ***PM*** machines, the disc type rotor with ironless stator design is a strong competitor to any other configuration for high-speed applications.

D) The axial flux machine has unusual ***3D*** magnetic flux patterns and its performance analysis requires a ***3D FE*** modelling.

E) It is argued that the rotor of the axial flux machine can be optimised based on a fixed value for the ratio of magnet inner radius to magnet outer radius.

F) Accurate stress prediction in the complex shapes of the rotor parts of the axial flux machine requires a ***3D*** finite element modelling taking into account the influence of interference fit between all rotor parts.

From these main observations concerning the ***PM*** generators and in particular for the ***PMAF*** high-speed generator, the main objectives of the project are justified.

CHAPTER 3

DESIGN METHODOLOGY, MODELLING & THEORETICAL ANALYSIS

3.1 INTRODUCTION

The earliest electrical machine was axial flux machine. Nowadays, the emergence of powerful rare earth magnets such as *NdFeB* has made it possible for such machines to be constructed with high power/weight ratios, high efficiency and high degree of reliability. However the design of such machines for high-speed applications involves many technical challenges. Before setting the design procedures for the *PMAF* high-speed generators, the description the machine and of the key components is presented in the following section.

3.2 DESCRIPTION OF KEY COMPONENTS OF THE *PMAF*

In contrast to the radial flux (cylindrical) machines, The *PMAF* generators have their air gap flux in the axial direction whereas the windings are directed in the radial direction. These windings enclose a part of the magnetic filed produced by the *PM* in the rotor. Hence, whenever there is a relative motion between the magnetic field and the coils, a voltage is generated across the coil ends. If the generated voltage is applied across an electrical load, a current can be drawn from the stator. Typically the construction of the *AF* generators takes two forms; a multi-pole *PM* rotor disc rotating between two stator windings, or a disc type stator winding being inserted between two *PM* rotor discs. The latter form is considered more convenient for high-speed applications since the back iron discs are rotating with the *PM* disc hence eddy currents and hysteresis losses in the back-iron discs are eliminated. Whereas the first form have two stationary iron discs at the backside of each stator disc hence subjected

to a time varying flux density which in turn produces core losses in the back-iron discs. The configuration also facilitates multistage (modular) and multiphase arrangement by adding numbers of magnet rotors and stator discs. A ***3D*** exploded view of a modular design configuration of the ***PMAF*** generators, which was found in the literature, is shown in Figure 3.1. This forms the basis for the design methodology which will be developed in the following Chapters.

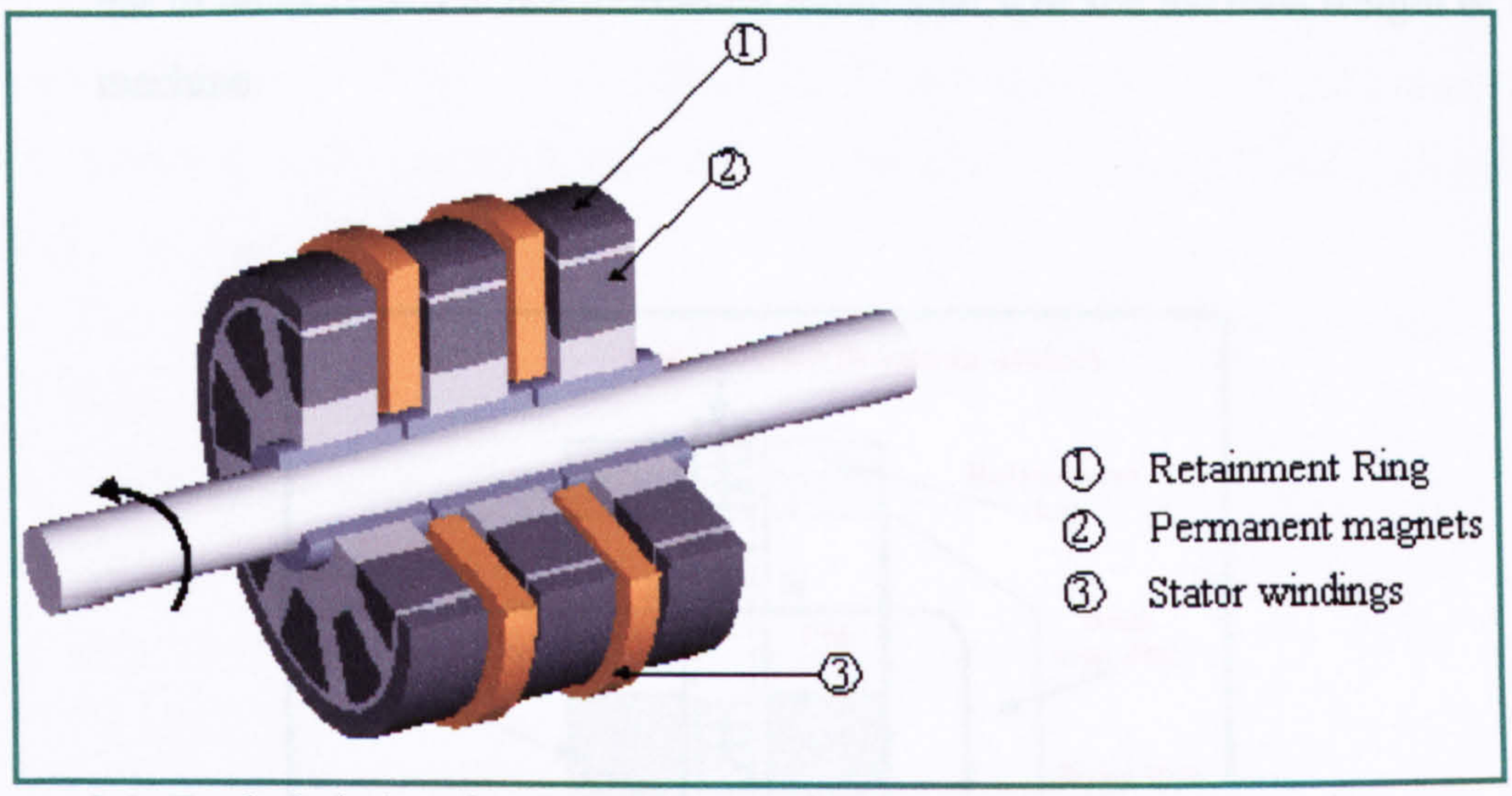

Figure 3.1 Exploded view for the permanent magnet axial flux high speed generator

To design a ***PMAF*** generator for high-speed applications, some essential arrangements should be considered in the design and construction of such machines to satisfy electromechanical design requirements. In order to describe the arrangements for the proposed ***PMAF*** high-speed generator, a cross sectional view of the machine is depicted in Figure 3.2. These arrangements are described briefly as follows:

3.2.1 Ironless stator core

From the literature, most of the proposed ***PMAF*** generators have used ironed, either slotted or slotless, core in their stators [15,16]. Although this will have the obvious advantage of increasing the flux density levels, hence high voltages can be induced, the iron structure have the following disadvantages for high speed applications:

- The iron core is subjected to a time varying flux density hence causing significance iron losses due to the high rotational speed. Therefore this calls

for using thin insulated laminated sheets instead of solid ironed core to reduce core losses, thus increasing the manufacturing cost and complexity.

- The machine will have relatively high saliency torque due to the standstill attraction between the ***PM*** and the iron core.
- Slotted iron core produces ripples in the induced voltage.
- The iron core reserve extra space in the air gap between the two magnet rotor discs, hence less space is left for the windings. Otherwise the air gap length has to be increased hence increasing the overall size and the total weight of the machine.

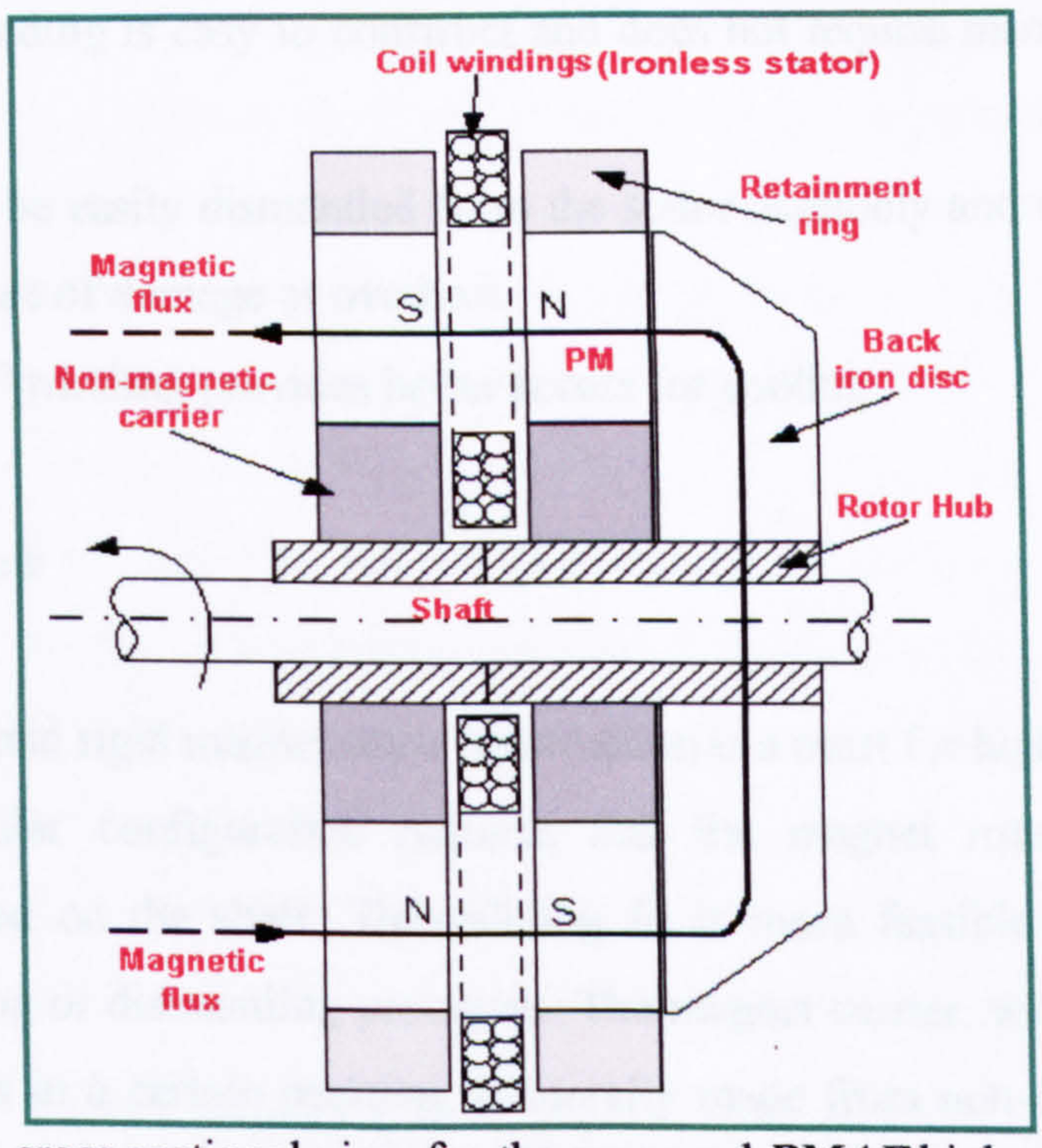

Figure 3.2 A cross sectional view for the proposed ***PMAF*** high speed generator

Hence a decision was made at the earliest stage of the design of the generator to use an ironless stator core due to the problems associated with the iron core stator. However the following design precautions must be considered when adopting ironless stator core:

- Fine stranded insulted, twisted or braided, wires such as Litz wire are necessary to minimise the conductor eddy current losses in the stator since they will be directly exposed to a time varying magnetic flux density in the air gap.

- A self-supported rigid stator construction should be maintained using epoxy resins and some non-magnetic reinforcing materials.
- Due to the absence of the iron core, cooling by conduction is not possible, hence the coils of the stator should be arranged in a way so that maximum surface area of the conductors are exposed to the forced ventilation.

There are two forms of winding that can be used for the ironless stators these are; "coil" winding type and "wave" (lap) winding type. The description and the features offered by each type can be found in [51]. It was found that "coil" winding is more suitable for the proposed machine for the prescribed application due to the following reasons:

- "Coil" winding is easy to construct and does not require many accessories for forming.
- Coils can be easily dismantled from the stator assembly and replaced by other coils in case of damage or overheat.
- The "coil" winding provides better access for cooling.

3.2.2 Rotor hub

A robust and rigid magnet rotor construction is a must for high operating speed. Moreover, modular configuration requires that the magnet rotor should not be permanently fixed on the shaft. Thus sliding fit is more feasible to allow for any further assembling or dismantling processes. The magnet carrier, which is designed to hold the magnets in a certain position, is literally made from non-magnetic material. However this material is not suitable to withstand the high stresses resulted from the mechanical interaction between the magnet rotor disc and the shaft. This in turn has called for the inclusion of a solid, rigid and high strength mechanical part (rotor hub) as a connection between the magnet rotor and the shaft. This part is designed to be shrunk fit at the bore of the magnet rotor disc to prevent slippage of the magnet rotor at high operating speeds. Also, the rotor hub is designed to be coupled with other rotor hubs on the same shaft through mechanical splines which are machined face to face on the rotor hub. The dimensions of the rotor hub are determined based on the knowledge of other parts dimensions such as the magnet axial length, back iron thickness and the

air gap axial length. The detailed description on the construction of this part can be found in ***Appendix A*** whereas the detailed drawings can be found in the ***AutoCAD*** drawings in ***Appendix B***.

3.2.3 Segmented PM

To produce a time varying magnetic field, the ***PM*** in the rotor should have alternate polarity of minimum two poles. A one-piece annular magnet having alternate polarity is possible to be produced and is easy to manufacture with the required dimensions. However, a segmented magnet poles in particular shapes were found to be more suitable for the construction of the high-speed generator due to the following reasons:

- The ***PM*** is a brittle material and it has a very low tensile strength but it can withstand high compressive stresses. Thus a one-piece annular magnet will be subjected to high tensile stresses when rotating at high rotational speeds. Whereas individual segmented magnets can be secured in their places without exceeding their design tensile strength.
- Annular ***PM*** cannot be assembled via shrink fit on the rotor hub since any attempts to expand it by any means would cause high tensile stresses to the ***PM***. Thus, it will not be possible to lock the annular magnet on the rotor hub to prevent slippage at high operating speed.
- A small gap or spaces between the alternate polarities on the same rotor should be left to reduce the magnetic leakage and this can only be achieved by having segmented ***PM***.
- The spaces between the alternate polarities at the annular magnet surface are considered as dead zones, which are not beneficial for the magnetic flux. In addition, these inevitable dead zones add more weight to the ***PM*** hence increasing the total weight of the generator.
- With segmented ***PM***, it is possible to manufacture the magnets in particular shapes, thus allowing for the adjustment of the quality of the induced voltage and the performance of the generator by selecting proper magnet shapes and topologies.

3.2.4 High strength retainment ring

In most of the *PMAF* machines found in the literature, the operating speed was very low (< 3000 rpm). Hence it was possible for the designer of such machines to fix the magnets on the rotor surfaces by using some special adhesive materials. With the most recent advancement on the available glues, they can however withstand a tensile strength up to 35 MPa, which is still far below the expected stresses developed on the magnet surfaces due to the high centrifugal forces at the design speed. In addition to the high centrifugal forces exerted on the magnets, the machine with its permanent magnets represents a magnetic system, which creates magnetic related forces. The major magnetic forces which should be considered for the axial-flux generators are the axial attractive forces between the opposite permanent magnets on the opposite rotors. With such high combined forces acting on a magnet, it is not possible to protect them by means of glue or any adhesive materials.

In the literature, some of the mechanical techniques have been suggested based on using a "T" shape disc or flywheel disc where permanent magnets were glued underneath the "T" edges of the disc [14]. However the "T" edges were highly stressed although the rotors were designed for operating speeds in the range of (16000 – 24000 rpm). Hence this type of construction would not be possible for higher rotational speeds. Another alternative construction was the use of high strength rings to retain the permanent magnets [13] similar to those wrapping sleeves that have been proposed for *PM* cylindrical (radial flux) machines [36,37]. Using wrapping sleeves or retainment rings was found to be more suitable than the previous technique to retain the magnets in their positions at high rotational speeds. It is worth mentioning that these retainment rings could be made from composite material such as carbon fibre or fibre glass or could be made from high strength special metal alloys. In this research, a high strength steel alloy will be used as a retainment ring for reasons that will be described later in this Chapter.

3.3 DESIGN METHODOLOGY

The design of the *PMAF* generator is a complicated process due to the many design variables that affect the performance and geometrical characteristics of the machine. However, the design process can be simplified by reducing the number of the unknown variables which can be done by synthesising some of the variables at the beginning of the design process. The first step in the design procedure is to set the design requirements that should be achieved at the end of the design of the machine.

3.3.1 Design requirements

Although the proposed design methodology can be adopted for several machines ratings, in this thesis, the following requirements should be achieved:

- Output power, P_o = 16.7 kW at the operating speed , N_o = 50000 rpm
- Phase-line terminal output voltage, V_t = 220 Volt
- Maximum current per phase, I_L =75 Amp
- Number of phases, ph = 1
- Electrical frequency, f_e = 3333 Hz

3.3.2 Shaft design and bearings selection

At the earliest stage of the design, it was required that the type of the shaft (solid or hollow) and its outside diameter are determined so that the dimensions of other mechanical parts can be calculated consequently. The generator shaft should be designed to transmit power from the gas turbine through a mechanical flexible coupling or magnetic coupling without suffering any problems. Hence to achieve a safe shaft design for a certain material and certain design inputs, the minimum shaft diameter and the maximum permissible angle of twist should be calculated. But first the following loads are considered for the gas turbine driven generator:

- Torsional loads which transmitted to the shaft through the couplings from the gas turbine engine. The torque, T_{shaft}, N.m, applied to the shaft can be calculated as:

$$T_{shaft} = \frac{P_{in}}{\omega_m} \tag{3.1}$$

where P_{in} is the power input from the turbine and ω_m is the mechanical angular velocity in rad/sec.

- Bending loads: In this case there is no pulleys on the shaft and the only bending loads applied are due to the vertical loads from the weights of different parts supported on the shafts such as the weight of the shaft itself, rotors, fans, etc. for simplicity, we shall neglect the weight of the shaft and consider the loads of the rotors on the shaft as concentric loads.
- Axial loads which can be neglected in the calculations. The different loads on the shaft can be shown in Figure 3.3.

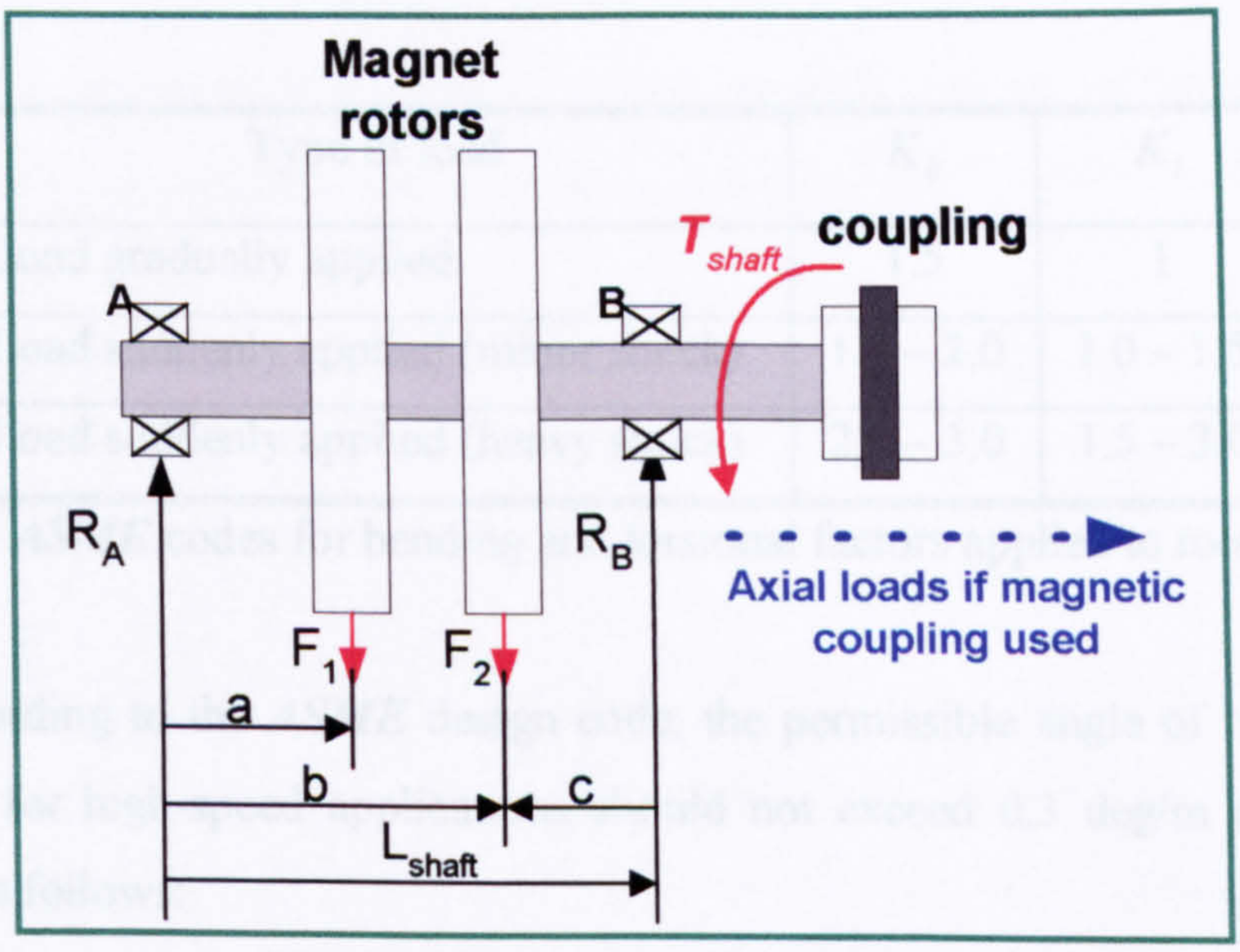

Figure 3.3 Different loadings on the generator shaft

Although hollow shaft has less weight and less moment of inertia compared to the solid shaft, the later is found to be more rigid, thus it can withstand various bending loads existed on the shaft. The ***ASME*** code equation for the solid shaft having no axial loading can be expressed as follows [52]:

$$d_{shaft} = \left\{ \frac{16}{\pi S_s} \left[\left(T_{shaft} K_t \right)^2 + \left(M_b K_b \right)^2 \right]^{1/2} \right\}^{1/3} \tag{3.2}$$

where M_b is the bending loads due to weights of components, N.m, S_s is the maximum allowable stress in MPa which can be calculated as follows:

$$S_s = 0.18\sigma_U \tag{3.3}$$

where σ_U is the ultimate tensile strength for the material selected for the shaft in MPa. K_b is the combined shock and fatigue factor applied for bending moment and K_t is the combined shock and fatigue factor applied to torsional moment. The values of K_b and K_t for rotating shafts are determined from the ***ASME*** codes which can be found in Table 3.1 [52].

Type of load	K_b	K_t
Load gradually applied	1.5	1
Load suddenly applied (minor shock)	1.5 – 2.0	1.0 – 1.5
Load suddenly applied (heavy shock)	2.0 – 3.0	1.5 – 3.0

Table 3.1 ***ASME*** codes for bending and torsional factors applied to rotating shafts

According to the ***ASME*** design code, the permissible angle of twist for solid shafts used for high-speed applications should not exceed 0.3 deg/m and it can be calculated as follows:

$$\theta_{twist} = \frac{584 T_{shaft} L_{shaft}}{G d_{shaft}^4} \tag{3.4}$$

where L_{shaft} is the shaft length and G is the shear modulus of elasticity, GPa.

To perform the design calculations we shall consider the simple case of the generator, which was shown in Figure 3.3 since we do not know yet the geometrical dimensions, weight and locations of the components on the shaft. Preliminarily, two

magnet rotor discs are proposed with their design input are listed in Table 3.2. The physical and mechanical properties of the material used for the shaft, EN24T steel, are given in Table 3.3.

P_{in} kW	N_o krpm	K_b -	K_t -	F_1 N	F_2 N	L_{shaft} mm	a mm	b mm	c mm
50	50	3	3	25	25	15	5	5	5

Table 3.2 Design input for shaft design calculations

ρ_m kg/m^3	σ_U MPa	E MPa	G MPa	ν
7800	700	200	87	0.29

Table 3.3 Specifications of shaft material, EN24T steel

Hence, the bending moments M_b on the shaft can be calculated using the following equations derived from the equilibrium state:

$$R_A = \frac{F_1(L_{shaft} - a) + F_2 c}{L_{shaft}} \tag{3.5}$$

$$R_B = \frac{F_1 a + F_2 b}{L_{shaft}} \tag{3.6}$$

$$M_{b1} = R_A a \tag{3.7}$$

$$M_{b2} = R_A b - F_1(b - a) \tag{3.8}$$

or

$$M_{b2} = R_B c \tag{3.9}$$

where M_{b1} and M_{b2} are the bending moments at the left and right rotors respectively, hence the total bending moments can be determined as $M_b = M_{b1} + M_{b2}$.

The results obtained from the calculations are summarised in Table 3.4.

T_{shaft} N.m	S_s MPa	M_b N.m	d_{shaft} mm	θ_{twist} Deg.
9.55	126	1.25	10.5	0.791

Table 3.4 Initial results obtained form the shaft design calculations

It is shown from Table 3.4 that the permissible angle of twist has exceeded the limit of 0.3 Deg/m, based on the value of 10.5 mm for the initial shaft diameter. Hence the shaft diameter should be slightly modified and this time it can be calculated from Equation 3.4 by setting $\theta_{twist} = 0.3$ Deg/m. Accordingly, the minimum diameter was found to be $d_{shaft} = 13.3$ mm. The nearest standard size for the shaft is 13.5 mm.

However, when considering the bearings for the shaft, it is important that the shaft diameter should meet the standard dimensions of the available bearings. In contrast, if the shaft final diameter is set without paying attention to the bearing size, then further machining might be required on the shaft either by making a shoulder or inserting a sleeve so that the selected bearing can fit at its place on the shaft. A simple and uniform solid shaft is much easier to machine and would require less manufacturing cost.

The spindle bearings, which are angular contact ceramic high precession ball bearings, are found to be the most suitable bearings for high-speed application. The ***FAG-Barden*** Corporation offered a wide range of different types of bearings for better selection [53]. The inner diameter of the bearings comes in 10 mm, 12 mm and 15 mm. The calculated shaft diameter was found to be 13.5 mm. Hence the bearing type ***HCS7002C.TP4S.UM*** of 15 mm inner diameter was selected and the shaft size was again adjusted to meet the bearing dimensions hence a final value of 15 mm was set for the shaft diameter.

In fact, the shaft design procedure requires an iterative process to synthesise the final dimensions of the shaft. This process is described in the flowchart depicted in Figure 3.4.

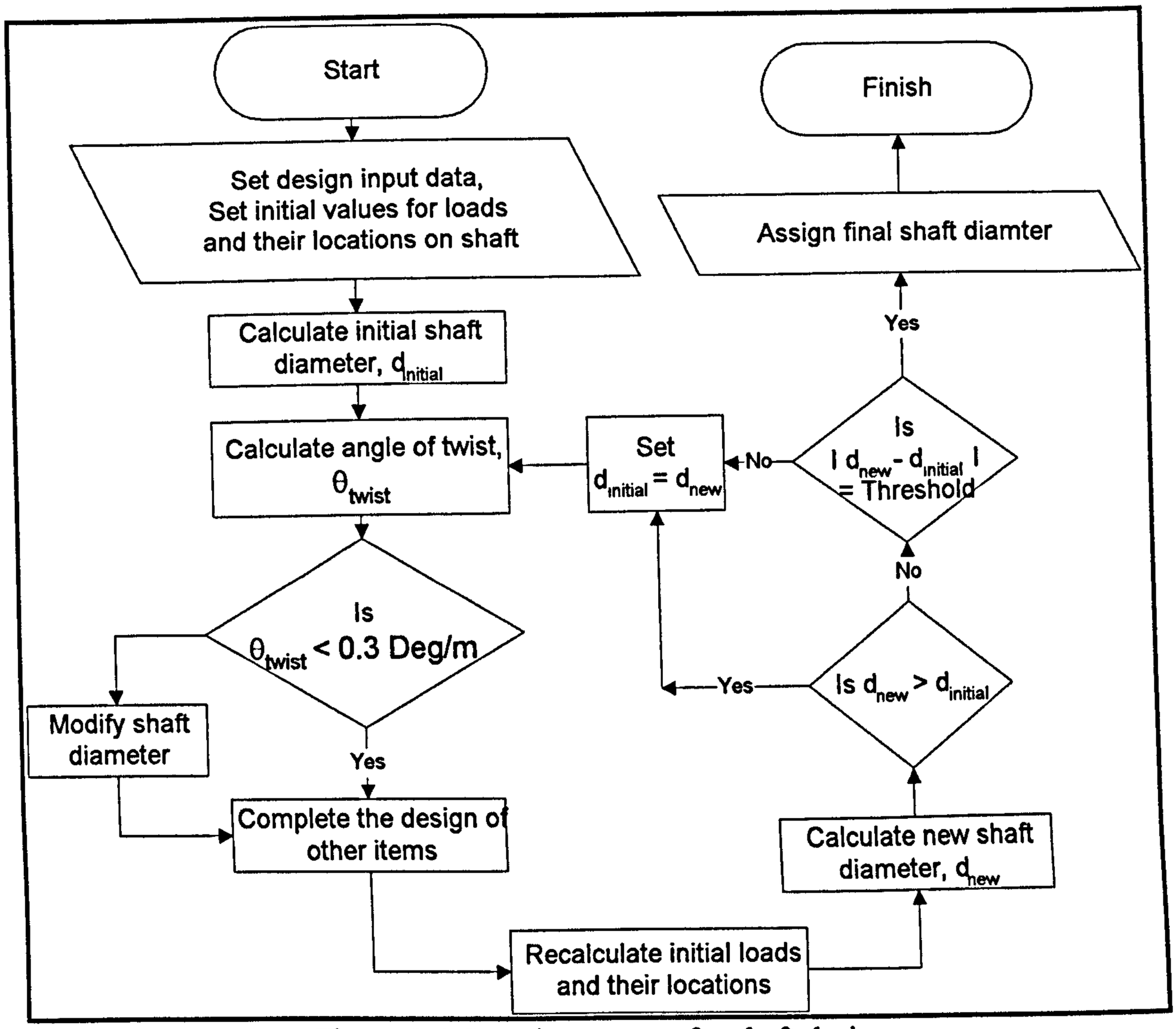

Figure 3.4 Iterative process for shaft design

3.3.3 Winding design

As mentioned earlier in this Chapter that stator structure will have ironless core. The stator windings which are of "coil" type, consist of number of coils, N_c, which are connected together in series to form one single phase winding. The coil itself consists of number of turns, N_t. Each turn is formed from a bundle of fine stranded insulated wires of certain diameter, d_{std}. Based on the knowledge of the overall bundle diameter, d_b, other design variables can be determined consequently. The design procedure of the stator windings can be summarised as follows:

3.3.3.1 Determination of the conductor size

To calculate the area of the required copper, A_c, the current density, J_c, is specified based on standard codes for electric insulated wires. Normally values in the range (10 – 15 Amp/mm^2) are used in most of electrical machines. However, higher values of J_c (up to 25 Amp/mm^2) can be specified when using the proper type of insulated wires, but with sufficient cooling to remove all the excessive heat in the windings. In this work, $J_c = 25$ Amp/mm^2, was specified in the design calculations. Hence A_c can be calculated as follows:

$$A_c = \frac{I_L}{J_c} \tag{3.10}$$

The maximum required current in the stator winding is 75 Amp, thus $A_c = 3.00 \times 10^{-6}$ Amp/m^2.

3.3.3.2 Determination of number of strands and strand diameter

The total area of the solid conductor found from the previous calculation is divided into a number of fine insulated strands to reduce stator eddy current losses. The angular mechanical speed, ω_m, number of poles, p, and the diameter of the strand, d_{std}, are the determinant factors which affect the eddy current losses in the conductors for a certain air gap peak flux density, B_p. Hence eddy current losses, P_{Se} per unit conductor volume can be expressed as follows [16]:

$$P_{Se} = \frac{B_p^2 (\omega_m p/2)^2 d_{std}^2}{32 \rho_c} \tag{3.11}$$

where ρ_c is the resistivity of the copper which can be calculated as:

$$\rho_c = \rho_\circ [1 + \overline{\alpha}_c (T_d - T_\circ)] \tag{3.12}$$

where $\rho_o = 1.56\times10^{-8}\ \Omega\cdot m$ is the copper resistivity at temperature $T_o = 0°C$ and $\overline{\alpha}_c = 4.3\times10^{-3}\deg^{-1}$ is the temperature coefficient for the copper conductor. Hence, $\rho_{c(25)} = 1.727\times10^{-8}\ \Omega\cdot m$ calculated at room temperature, $T_d = 25°C$

The selected wire is a high class insulated with modified polyester resin. It is a solderable wire (at $450°C$) that has a two part insulation system in which the ester-imide base coat is overcoated with nylon which improves the solvent resistance and windability [54]. Although this type of wire can withstand a temperature of $180°C$, a maximum design temperature, $T_d = 110°C$ was specified for the stator windings since the maximum operating temperature for the ***NdFeB PM*** is limited to $125°C$.

As can be seen from Equation 3.11 that the smaller the diameter of the wire, the less will be the eddy current losses. Thus using the finest available wire will be beneficial for the design in terms of minimising stator eddy current losses. However, dividing the solid conductor into fine insulated strands reduces the total copper area available for a certain bundle size due to the worse filling factor, f_f, associated with the round cross sectional wires which is found in the literature normally in the range from 0.55 to 0.65 [44]. Thus, increasing the total copper losses, P_c, in the stator which can be calculated as follows:

$$P_c = I_L^2 R_{sc} \tag{3.13}$$

where R_{sc} is the resistance of the conductor which is found at T_d. Hence, if the conductor total length, L_{Tw}, and the area of copper conductor are known, the resistance can be calculated by applying the following Equation:

$$R_{sc} = \frac{\rho_c L_{Tw}}{A_c} \tag{3.14}$$

where $\rho_c = 2.297\times10^{-8}\ \Omega\cdot m$ this time is calculated at temperature $T_d = 110$.

A good quality construction of a stranded bundle requires a proper combination between the number of strands, N_{std}, and the diameter of the strand, d_{std} to achieve high filing factors like those specified for Litz wire.

Before proceeding in the design calculations, it was required to determine the filling factor that will be used through calculations by actual construction of bundles of different sizes (2.2 2.3 and 2.4 mm). Each bundle was filled with maximum allowable number of strands of certain size at a time. Three different sizes of strands have been tried (0.1, 0.2 and 0.3 mm) for each bundle which makes the total number of bundles constructed for the test is nine bundles. The procedure for constructing these bundles is described later in ***Appendix A***. Thus, once the maximum number of strands for each bundle size is known, the filling factor for each bundle of area A_b can be calculated using Equation 3.15 presented below. The results of filling factor are presented graphically in Figure 3.5:

$$f_f = \frac{A_{std} N_{std}}{A_b} \tag{3.15}$$

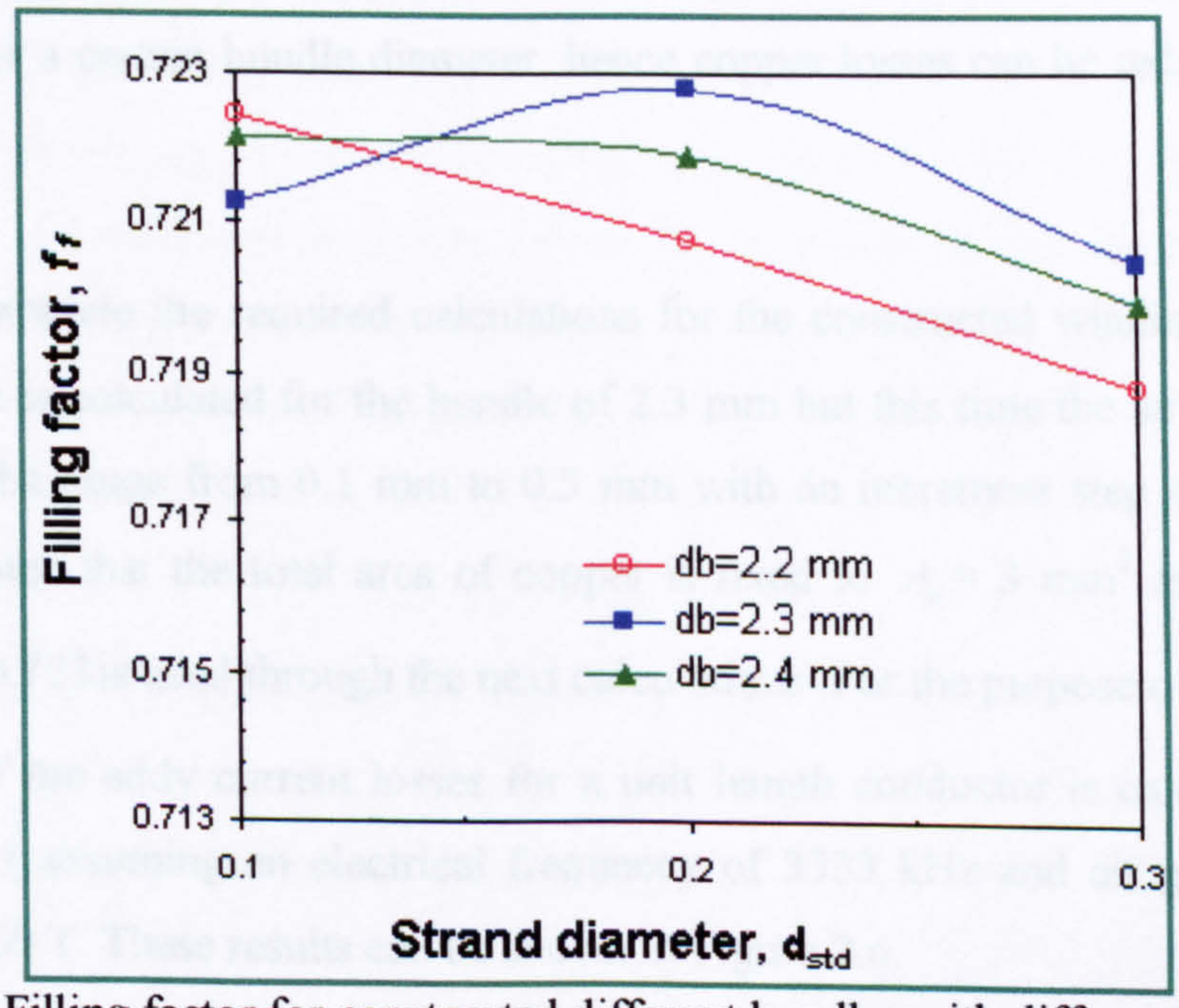

Figure 3.5 Filling factor for constructed different bundles with different strand sizes

It can be seen that the results are close to each other, however a local maximum filling factor ($f_f = 0.723$) can be found for a combination of 96 strands of 0.2 mm diameter which forms an overall bundle diameter of 2.3 mm.

These results were compared to the data obtained for a commercial Litz wire of 11/32 AWG provided by Wire Tronic Inc. [54] which has an equivalent bundle diameter and strand diameter similar to the constructed winding. The summary of the comparison between the constructed windings and the commercial Litz wire is found in Table 3.5.

Type of wire	d_b mm	d_{std} mm	N_{std}	f_f	A_c mm^2	P_c / unit length W/m
Constructed	2.3	0.2	96	0.723	3.00	43
Litz (11/32)AWG	2.3	0.2	115	0.869	3.61	36

Table 3.5 Comparison between the constructed wire and commercial Litz wire

It can be seen from the above Table that the filling factor for the commercial Litz wire is higher than that for the constructed wire, thus more copper can be maintained for a certain bundle diameter, hence copper losses can be reduced by 16.2 %.

To complete the required calculations for the constructed windings, the eddy current losses is calculated for the bundle of 2.3 mm but this time the strand diameter is varied in the range from 0.1 mm to 0.5 mm with an increment step of 0.1 mm. It should be noted that the total area of copper is fixed to $A_c = 3$ mm^2 and the filling factor $f_f = 0.723$ is used through the next calculations. For the purpose of comparison, the results of the eddy current losses for a unit length conductor is calculated using Equation 3.11 assuming an electrical frequency of 3333 kHz and air gap peak flux density of 0.60 T. These results can be shown in Figure 3.6.

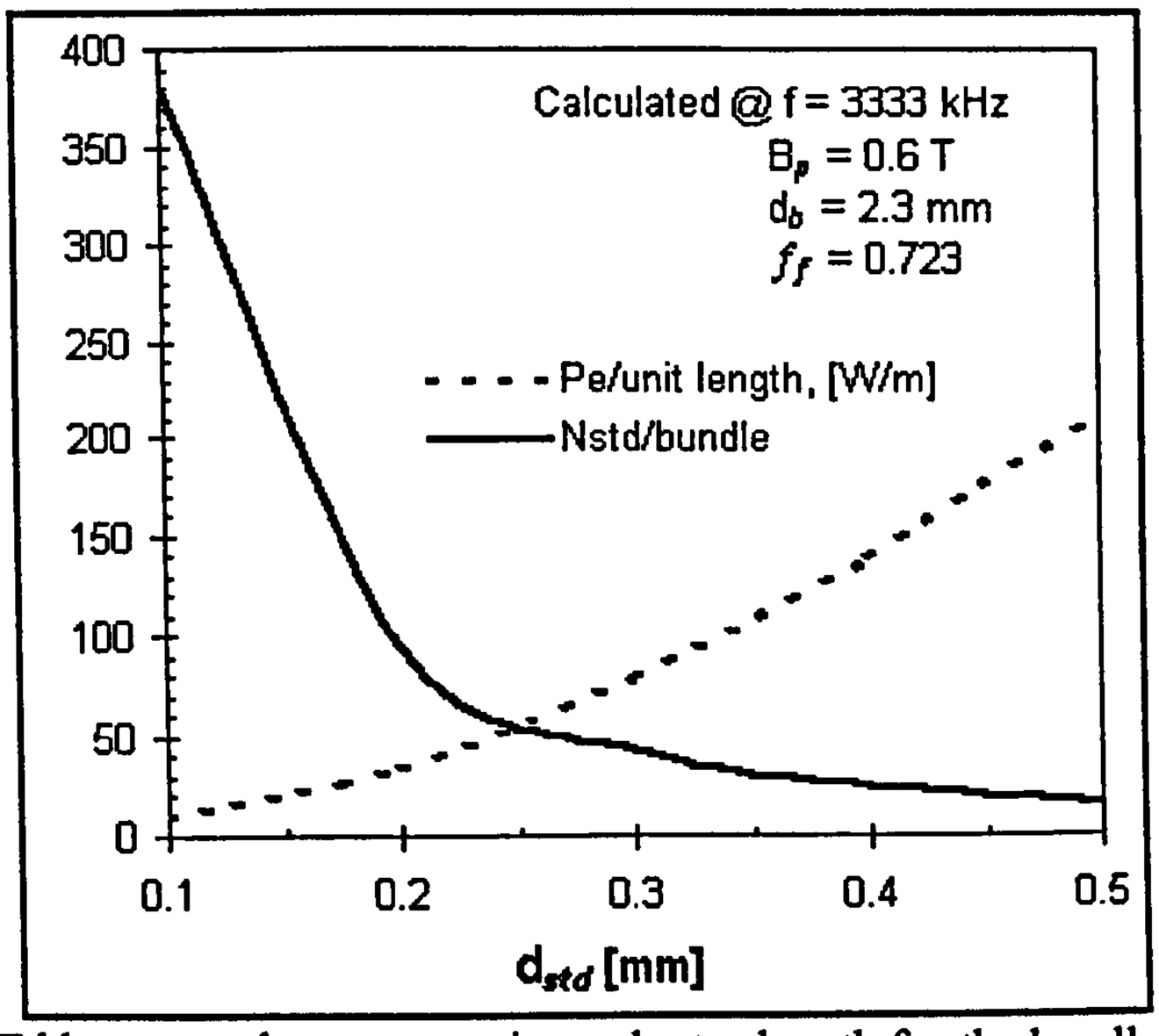

Figure 3.7 Eddy current losses per unit conductor length for the bundle of 2.3 mm and different strand diameter

It can be seen from the above Figure that the eddy current losses are drastically reduced when using smaller strand diameters. However, higher number of strands is required to fill the area of the bundle to achieve a fixed copper area. Moreover, practically, constructing a bundle which consists of a high number of very fine strands, requires a special machines and tools. Hence, it was decided to construct and use the bundle of 2.3 mm with 96 strands of 0.2 mm diameter in the design of the ***PMAF*** high-speed generator through this work. The eddy current predicted per unit conductor length of this bundle is 35 Watt. However, this losses is calculated for the resistivity at room temperature, i.e. $\rho_{c(25)} = 1.727 \times 10^{-8}\ \Omega \cdot m$. Hence, as the temperature of the conductor increases, the eddy current loss in the stator decreases.

3.3.4 Synthesising the design variables

It is important at this stage to identify the design variables, their reasonable ranges and their influence on the design. By doing this, the number of unknown variables can be reduced, the range for each variable can be defined and its bandwidth

can also be narrowed. To investigate their influence on the design we shall put the output power equations as a function of the main design variables for the stator and rotor, which can be defined as follows:

$$P_o = f(N_m, d_b, N_s, N_t, l_g, R_{mi}, p, R_{mo}, B_g, l_m) \tag{3.16}$$

This equation has considered the main design parameters for the generator. However, some of these parameters are themselves dependent variables. Thus any change in one of these parameters would imply changing the other parametrs. For instance, if the number of turns is to be increased, then there are at least two major variables should change consequently to allow for the space required for the extra number of turns. The first choice would be by increasing the magnet inner radius, R_{mi}, thus increasing outer radius as well. The second choice would be by increasing the axial air gap length l_g hence increasing the magnet length to compensate for the loss in the air gap flux density. Accordingly, any of the options will cause a change in the whole structure and geometry, hence performance of the generator. In general, assuming reasonable values for some of the design variables would help and accelerate the design process, but this requires a design experience. To do so, the limitations on each design variable are considered hereafter.

3.3.4.1 Number of stator stages

As was mentioned before, that one of the advantages of the *PMAF* configuration, that it can be designed based on a modular basis i.e. number of stators and rotors on the same shaft. The minimum requirement for a single stage is two magnet rotors and one single stator in between. Thus, the number of rotors will always be $N_r = N_s + 1$. For any number of stators, they can be connected at the terminal either in series or parallel to provide the specified outputs. In a specific design case the stator stages can be also connected in Y or Δ connection to form a multiphase generator. Although more than one phase can be built in the same stator stage, for the three phase generator design, it was decided to construct each phase in a separate stator stage for two main reasons:

- To prevent mutual effect between the three different phases.

- To overcome the unbalance situation that might be caused by the unsymmetrical distribution of the stator coils in the air gap with respect to the magnet surface. The stator coils that are close to the magnet surface will receive greater flux densities compared to the coils which are placed in the middle of the air gap.

Hence for the design of three-phase 50-kVA generator, each phase is built into three separate stages where each stage is capable to produce a maximum power of 16.7 kVA. In this work, a prototype of only one single stator stage (one module) capable of producing 16.7 kVA is designed, constructed and tested. The remaining stages can be constructed once the prototype is evaluated. Therefore, N_s variable is set to one through the next calculations.

Vibration and critical speeds limit the increase of number of stator stages. Increasing the number of the stator stages will increase the overall length of the machine hence making the structure more critical for vibrations. The shorter the length, the more robust and rigid machine can be achieved.

3.3.4.2 Number of turns and layers per coil

Ideally, each turn of the stator coil should enclose the maximum flux coming from the magnet so that the maximum ***emf*** can be produced. The maximum area enclosed by a single turn can be maintained if the turn spans the same area of the pole pitch on the rotor. This can be possible if the conductor thickness is neglected i.e. a thin wire is assumed to follow the shape of the path shown in Figure 3.8. However, practically it is not possible to put all the turns of a certain coil at the same place due to the thickness of the conductor. Thus if a coil has a number of turns N_t, only one turn will approximately span the same area of the pole pitch whereas the remaining turns will be formed in a concentric shape having smaller areas. Hence the final shape of the coil will have an oval shape instead of the semi trapezoidal shape as shown in Figure 3.9.

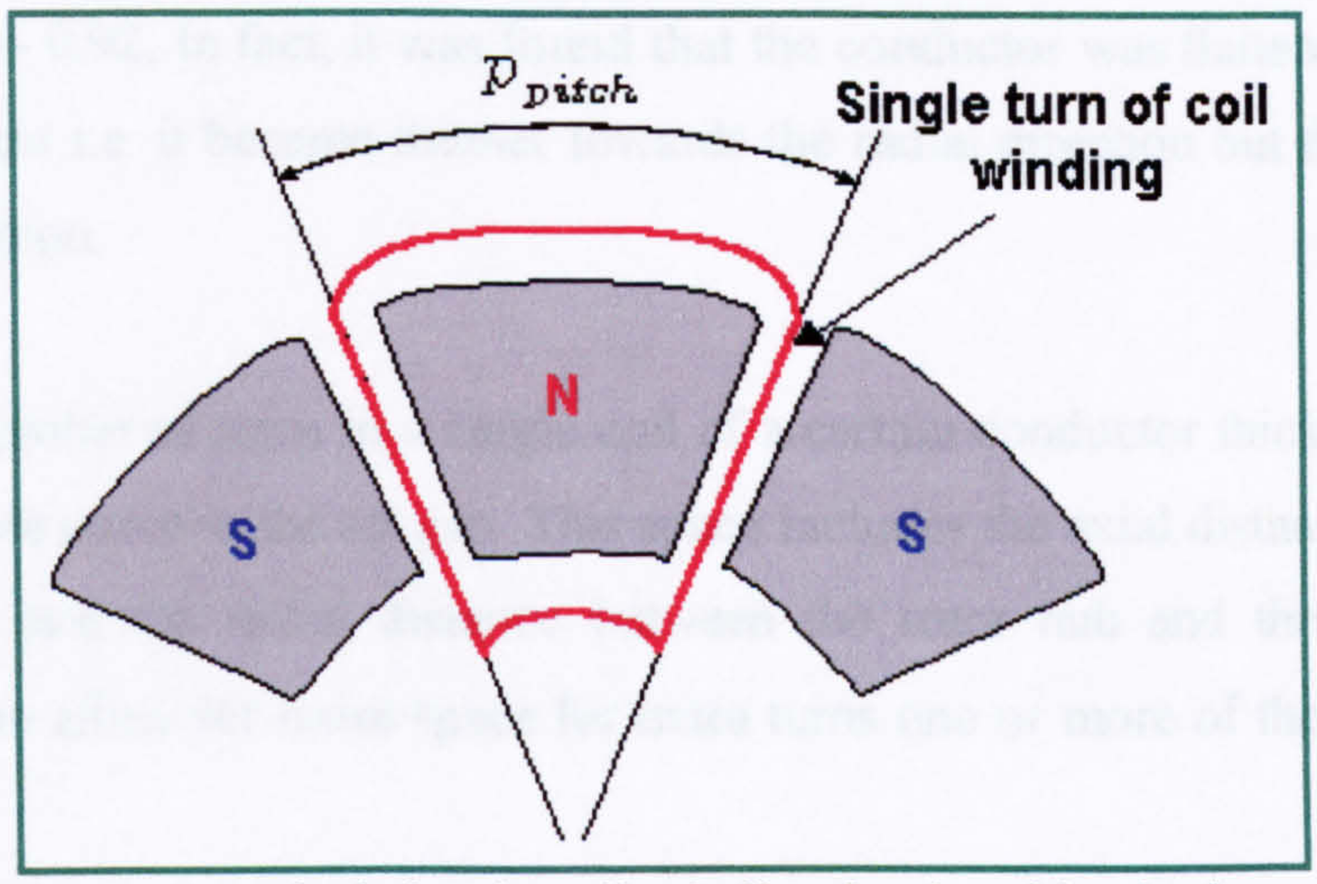

Figure 3.8 Ideal simple coil winding having thin single turn

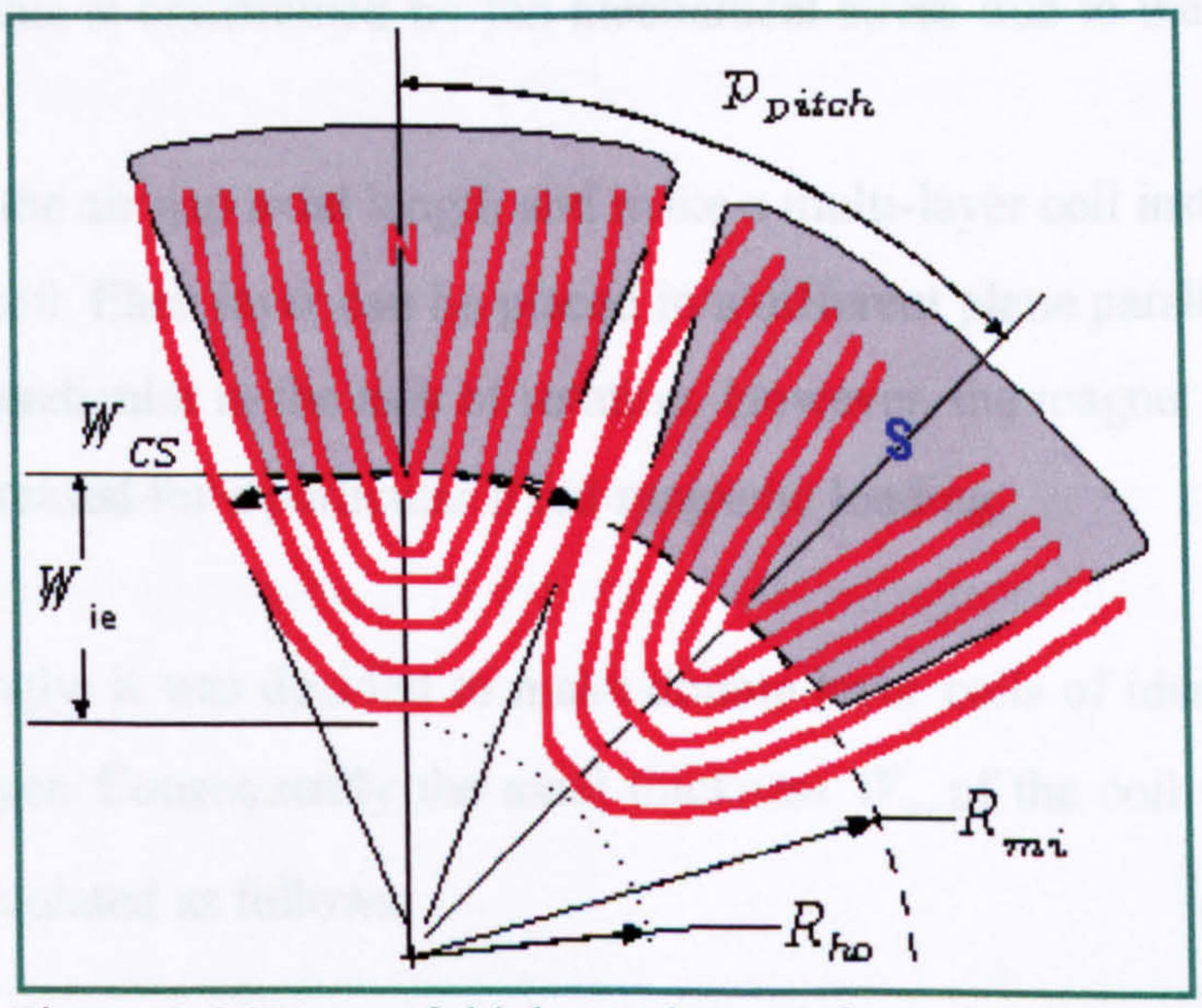

Figure 3.9 Turns of thick conductors for coil windings

Another issue associated with the increased number of turns of the coil with a certain conductor thickness can be seen from Figure 3.9. The width of the inner end winding, W_{ie}, is relatively large protruding radially towards the rotor hub. This inner end winding can be calculated as follows:

$$W_{ie} = N_t d_b k_R \tag{3.17}$$

where k_R is the winding radial backing factor and it was found experimentally in the range of 0.90 – 0.92. In fact, it was found that the conductor was flattened through the winding process i.e. it became thinner towards the radial direction but thicker towards the axial direction.

The number of turns in a single coil of a certain conductor thickness is limited by the available space in the air gap. This space includes the axial distance between the magnet discs and the radial distance between the rotor hub and the magnet inner radius. Thus to allow for more space for extra turns one or more of the following can be done:

- Increase the magnet inner radius which consequently requires an increase in the magnet outer radius to keep the same magnetic loading. However, The magnet outer radius is constrained by the mechanical stress due to the high rotational speed.
- Increase the air gap axial length and make a multi-layer coil instead of a single-layered coil. Each layer can be placed in a different plane parallel to each other and perpendicular to the axis of rotation. However, the magnet axial length has to be increased for a particular fixed magnetic loading.

Accordingly, it was decided to make double layer coils of identical number of turns in each layer. Consequently the axial thickness W_{ax} of the coil will be enlarged and it can be calculated as follows:

$$W_{ax} = N_l d_b k_{ax} \tag{3.18}$$

where N_l is the number of layer per coil and k_{ax} is the winding axial backing factor and it is found practically in the range of 1.70 – 1.74.

In this work, a value of 1.74 was considered for k_{ax}, hence the winding axial thickness was found to be 8.0 mm. Finally, the range for the number of turns per layer per coil is defined as $N_t = [1-8]$ turns. Hence, for the rest of design calculations in this Chapter, the following design variables are defined as follows:

- $N_l = 2$ layers/coil and
- $N_t = [1,2,3,4,5,6,7,8]$ turns/layer/coil.
- $W_{ax} = 8.0\,\text{mm}$.

3.3.4.3 Air gap length

The air gap length is defined by the winding axial thickness and the clearance on both sides between the windings and the rotating magnet rotor. Hence, it can be found as follows:

$$l_g = W_{ax} + A_{Cls} \tag{3.20}$$

where A_{Cls} is the total axial clearance between the stator and the magnet discs.

A clearance of 1.0 mm was given on both sides of the stator which should be sufficient to prevent any rubbing between the magnet discs and the stator windings during the rotation. Hence, the axial air gap length was found to be 10.0 mm. This air gap length will be used throughout the remaining design calculations.

3.3.4.4 Magnet inner radius

This design parameter is determined based on the determination of previous design parameters. More precisely it is limited from the inside by the inner end winding. Thus for the predefined range of N_t, the magnet inner radius, R_{mi}, can be calculated as follows:

$$R_{mi} = W_{ie} + R_{Cls} \tag{3.21}$$

where R_{Cls} is the radial clearance between the inner end winding and the rotor hub outer radius. Normally, 1.0 mm should be an acceptable clearance for the end windings.

3.3.4.5 Number of poles

Higher number of poles allows designing a more compact machine by reducing the number of turns or ***PM*** volume required to produce a certain output power in the generator. Since the magnet inner radius is determined by the number of turns per coil, the maximum number of poles also is constrained by the number of turns utilised per coil. If for a proposed design, the pole pitch arc at the calculated magnet inner radius less than the winding circumferential span, then the proposed design cannot accept the specified number of poles. The pole pitch arc at the magnet inner radius of the machine is calculated by:

$$pp_{arc} = \frac{2\pi}{p} R_{mi} \tag{3.22}$$

and the winding circumferential span is calculated by:

$$W_{SC} = 2N_t d_b k_R \tag{3.23}$$

The results for the maximum allowable number of poles for the specified range of number of turns and for the corresponding magnet inner radii are summarised in Table 3.6.

N_t	1	2	3	4	5	6	7	8
Corresponding R_{mi}	18	20	22	24	27	29	31	33
Max. p	26	14	10	8	8	6	6	6

Table 3.6 Maximum allowable number of poles for the range of number of turns

3.3.4.6 Magnet outer radius

The ratio of magnet inner radius to its outer radius, k_{mr}, is a major design parameter which has a significant effect on the characteristics of the machine. More precisely, the magnet outer radius diameter has a strong effect on the power density,

mechanical integrity and generator performance where windage losses are greatly affected by the outer diameter of the rotor. It was found from design optimisation studies related to ***PMAF*** machines, mainly addressed for low speed applications, that attempts have been made to define an optimum value for the ratio k_{mr}. In some papers, a numerical value of $k_{mr} = 1/\sqrt{3}$ has been reported as an optimum value for a given magnetic and electric loadings of the machine [15]. However, it was argued in some other papers [42], that this ratio cannot be reduced into a simple numeric value since it depends upon the optimisation goal, rated power, number of poles, materials and machine topology.

Hence for the current design process, two approaches are adopted for determining the magnet outer radius, these are:

- Using an optimum numerical value of k_{mr}, where magnet outer radius can be calculated as:

$$R_{mo} = \frac{R_{mi}}{k_{mr}} \tag{3.24}$$

- Determine the magnet outer radius required to produce a certain output voltage by assuming a certain air gap magnetic flux density.

Both approaches will be described in details in the next section.

3.4 MODELLING THE *PMAF* GENERATOR

Once the main design parameters are defined and synthesised, it is possible to develop a mathematical model based on the combination of these design parameters. Using such a mathematical model, the electrical performances and characteristics of different designs can be predicted and compared to each other in order to select the best machine design that provides highest power density while ensuring that high efficiency is maintained. A simplified ***2D*** drawing of the proposed ***PMAF*** generator is depicted in Figure 3.10. This Figure is used as an illustration when developing the mathematical model of the machine as described in the following sections.

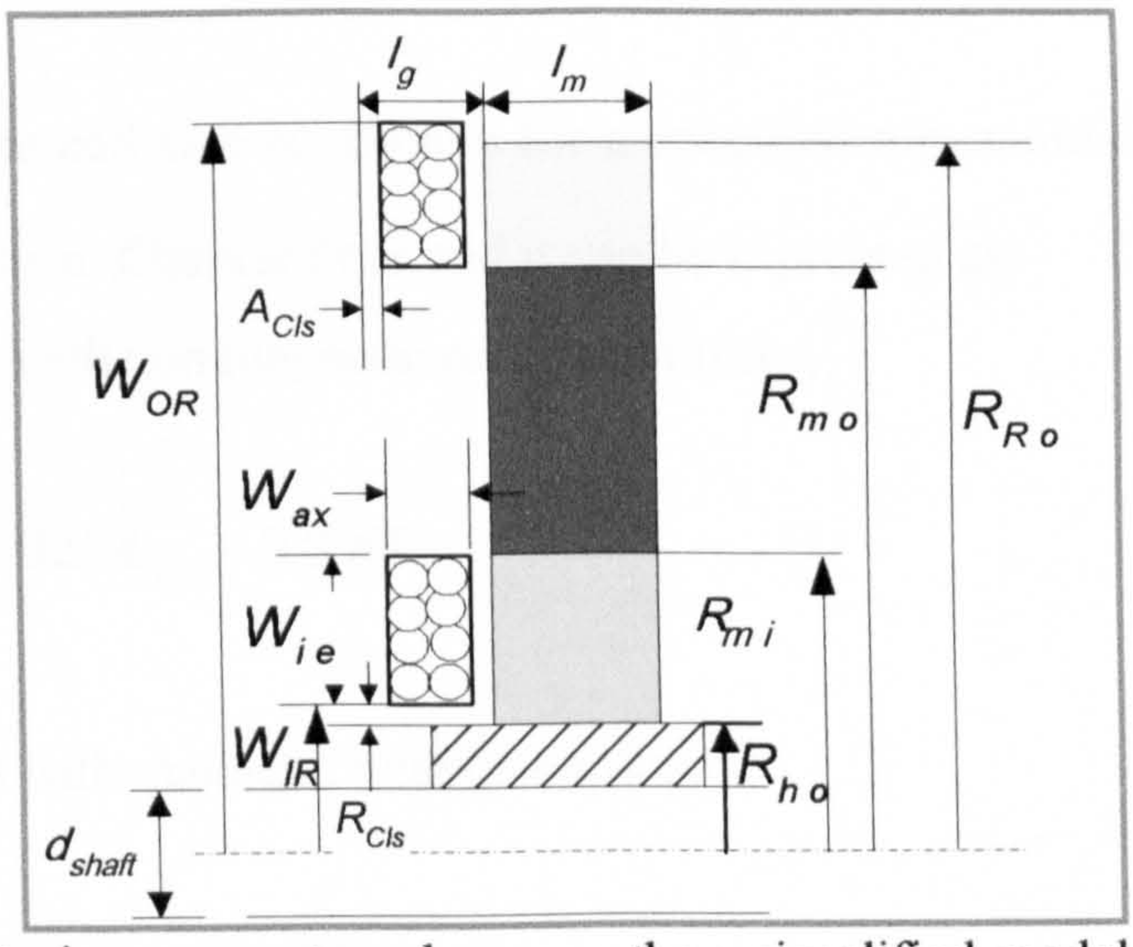

Figure 3.10 Design parameters shown on the a simplified model of the generator

3.4.1 Induced voltage equation

The voltage developed by an ideal single turn similar to that was shown in Figure 3.8, can be described by Equation 3.25 where E_{NL} is the induced no-load voltage.

$$E_{NL}(t) = -\frac{d\phi(t)}{dt} \tag{3.25}$$

where $\phi(t)$ is the instantaneous flux passing through the turn. However, in reality the coil of interest has concentric turns where the inner turns have smaller areas. Thus, assuming a sinusoidal flux density distribution in the angular direction, the flux passing through each separate turn can be expressed as follows:

$$\phi(t)_{(n)} = \phi_{p(n)} \sin(\omega_e t) \tag{3.26}$$

where n is the index number representing the turn number and ϕ_p is the peak flux passing through that turn and it can be calculated as follows:

$$\phi_{p(n)} = k_{size(n)} A_{t(n)} B_g \tag{3.27}$$

where $k_{size(n)}$ is the coil size coefficient for a specified turn number n which is found from the ***FE*** results in Chapter Four and it can be expressed as:

- For rotors with non magnetic retainment rings;

$$k_{size(n)} = -325 A_{t(n)} + 0.8098 \tag{3.28}$$

- For rotors with magnetic retainment rings;

$$k_{size(n)} = -338 A_{t(n)} + 0.7782 \tag{3.29}$$

Hence for a coil having N_t number of turns per layer, the total flux passing through these turns will be:

$$\phi_T(t) = \sin(\omega_e t) \sum_{n=1}^{N_t} \phi_{p(n)} \tag{3.30}$$

Thus, by differentiating Equation 3.30 with respect to time, the peak induced no-load voltage in one single coil having N_l number of layers can be found as:

$$e_{peak} = \omega_e N_l B_g \sum_{n=1}^{N_t} k_{size(n)} A_{t(n)} \tag{3.31}$$

where ω_e is the electrical frequency which can be determined as:

$$\omega_e = \frac{2\pi N_m P}{120} \tag{3.32}$$

Thus for N_s number of stator stages with each stator stage having number of coils equal to number of poles p, the total rms no-load voltage can be expressed as follows:

$$E_{(NL)rms} = \frac{2\pi N_m N_s p^2 N_l B_g}{120\sqrt{2}} \sum_{n=1}^{N_t} k_{size(n)} A_{t(n)} \tag{3.33}$$

The area of each turn per layer in the coil can also be defined in terms of the design parameters, thus:

$$A_{t(n)} = \left[\frac{\pi}{p} - \frac{((N_t - n)+1)d_b k_R + d_b k_R}{R_{mi}}\right]\left[R_{mo}^2 - R_{mi}^2 + n d_b k_R (R_{mo} + R_{mi})\right] \tag{3.34}$$

With the magnet outer radius is determined by Equation 3.24, the flux density in the air gap, B_g, which is required to produce a certain output voltage, $E_{(NL)rms}$, can be determined from Equation 3.33 as follows:

$$B_g = \frac{120\sqrt{2}E_{(NL)rms}}{2\pi N_m N_s p^2 N_l \sum_{n=1}^{N_t} k_{size(n)} A_{t(n)}} \tag{3.35}$$

Hence, the magnet axial thickness required to produce that magnetic flux can be determined as described in the following Section.

3.4.2 Magnetic modelling

The *PM* used for the current design is a sintered ***NdFeB PM*** which has high remanence B_r in excess of 1 T and coercivity H_c approaching 1 kA/mm. It has a linear demagnetisation characteristics, with recoil permeability μ_r approximately equal to unity. This has simplified the analysis of the magnetic assembly of the proposed rotor. Thus for any structure having *PM*, iron core and air gap, the total

magnetomotive force (***mmf***) can be found from Ampere's circuital law which can be expressed as follows:

$$\oint \vec{H} \cdot d\vec{l} = H_m l_m + H_{iron} l_{iron} + H_g l_g = 0 \tag{3.36}$$

The integral is equal to zero because no current is enclosed. Assuming there is no saturation in the iron core, its reluctance and its ***mmf*** may safely be ignored. The ***B-H*** characteristic curve for the ***NdFeB PM*** can be modelled by the relation:

$$B_m = B_r + \mu_r \mu_o H_m \tag{3.37}$$

where B_m and H_m are the flux density and flux intensity in the ***PM*** respectively. Thus, the magnetic flux ϕ can be found as,

$$\phi = B_m A_m = B_g A_g \tag{3.38}$$

Substituting Equation 3.37 into Equation 3.36 gives:

$$\frac{B_m - B_r}{\mu_r \mu_o} l_m + \frac{B_g}{\mu_o} l_g = 0 \tag{3.39}$$

Substituting for B_m from Equation 3.38 into Equation 3.39 and rearrange for B_g gives:

$$B_g = \frac{B_r}{\left(\frac{A_g}{A_m} + \mu_r \frac{l_g}{l_m}\right)} \tag{3.40}$$

where A_m is the surface area of the ***PM***, A_g is the area of the air gap physically crossed by the flux. For axial flux permanent machine, $A_g = A_m$, thus Equation 3.40 can be reduced as follows:

$$B_g = \frac{l_m}{l_m + l_g} B_r \tag{3.41}$$

However, Equation 3.41 in its plain form, dose not account for the leakage and ***mmf*** losses in the magnetic assembly. These losses are difficult to calculate accurately since they depend on machine geometry, number of poles and air gap length as shown in Figure 3.11.

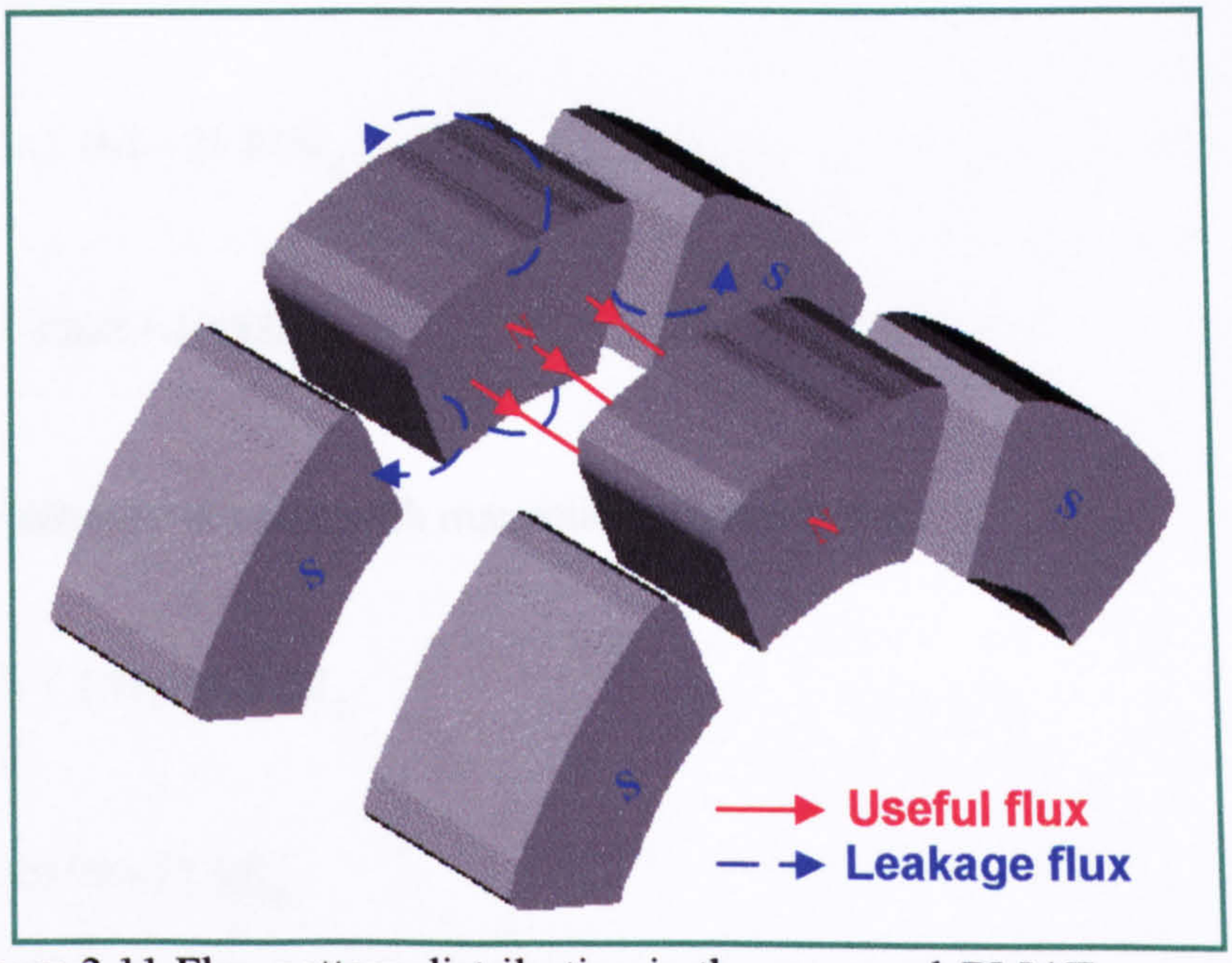

Figure 3.11 Flux pattern distribution in the proposed ***PMAF*** generator

However, it was possible to determine empirical coefficients that account for the leakage for certain geometries by validated ***FE*** results in Chapter Four. Hence Equation 3.41 can be slightly modified as follows:

$$B_g = \frac{k_p l_m}{l_m + k_g l_g} k_{Br} B_r \tag{3.42}$$

Accordingly, the magnet axial length can be found by rearranging the above equation as follows:

$$l_m = \frac{k_g B_g}{(k_p k_{Br} B_r - B_g)} l_g \tag{3.43}$$

where k_p is the pole leakage factor which can be gives as:

$$k_p = 1 - \frac{p}{360} \tag{3.44}$$

As for the magnet leakage coefficient, k_{Br}, and the air gap length coefficient, k_g, they can be expressed as follows:

- For magnet rotor disc with nonmagnetic retainment ring,

$$k_{Br} = 1.161 - 21.816 l_g \tag{3.45}$$

$$k_g = 1.028 + 10.33 l_g \tag{3.46}$$

- For magnet rotor disc with magnetic retainment ring,

$$k_{Br} = 1.164 - 26.312 l_g \tag{3.47}$$

$$k_g = 0.99 + 17.33 l_g \tag{3.48}$$

More details regarding the determination of these empirical coefficients can be found in Chapter Four. Hence, by using the above equations it was possible to predict accurately the flux density in the air gap for several possible designs. Thus the design calculations of the machine can be performed using one of the following approaches:

- Given the magnet outer radius, R_{mo}, determined by Equation 3.24, for a certain required output voltage of the machine, B_g can be determined from Equation 3.35. Hence l_m can be found by Equation 3.43.
- For unknown magnet outer radius, R_{mo}, chose a design value for the air gap flux density from the *B-H* curve of the selected *PM* material. Normally, a working point is selected where maximum energy $(B_m H_m)_{max}$ product can be maintained from the magnet. Then calculate the required magnet axial length to produce such an air gap flux density using Equation 3.43. Substitute the value

of B_g in Equation 3.33 and solve the equation iteratively to determine the magnet outer radius which satisfies the required induced voltage.

To check the accuracy of the analytical solutions, B_g is obtained from ***FEM*** for a particular rotor design having magnet axial length of 17 mm and the axial air gap distance is varied over the range from 8 to 16 mm with an increment step of 2 mm for both magnetic and nonmagnetic retainment rings. Results obtained from both solutions are presented graphically in Figure 3.12. A good agreement between the results can be seen. The graph also shows that the flux density in the air gap is reduced when magnetic material is used as a retainment ring. This can be referred to the increased leakage flux since the magnetic ring has a relatively low reluctance compared to the reluctance of air. The details of the ***FE*** magnetic analysis can be found in Chapter Four.

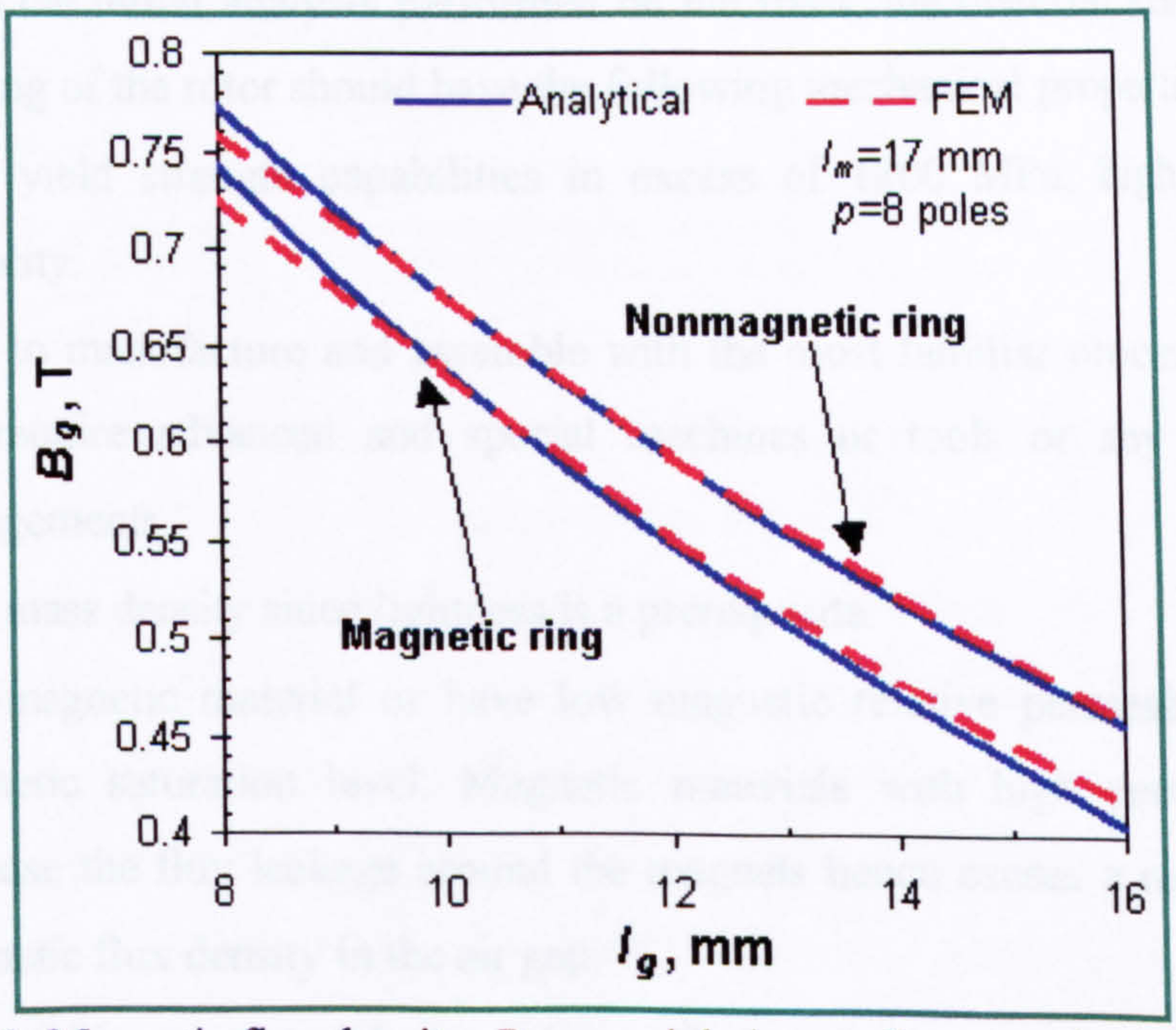

Figure 3.12 Magnetic flux density B_g vs. axial air gap distance obtained from both analytical and ***FEM*** solutions for magnetic and non magnetic ring rotors

With all geometrical design parameters of the machine are known, it can be possible now to perform mechanical analysis and to predict the performance of the machine as described in the following sections.

3.5 ROTOR MECHANICAL ANALYSIS

To insure the mechanical integrity of the proposed design of the ***PMAF*** generator, a stress analysis is performed on the rotor of the machine at the design speed in excess of 50,000 rpm. For safe designs, it is required to keep the tensile stress levels in the magnet and in the retainment ring well below their design strengths. In addition, the rotor fails if a separation occurs between any of the rotor parts while rotating at the design speed. Thus any possible designs that fail in the mechanical tests will not be used in further electromagnetic and performance analysis. The first step in the mechanical analysis is to study some of the available materials for use as a retainment ring for the rotor and select one that will satisfy the design requirements.

3.5.1 Material selection for the retainment ring

From the initial analysis performed on the rotor, the material selected for the retainment ring of the rotor should have the following mechanical properties:

- High yield strength capabilities in excess of 1800 MPa, high modulus of elasticity.
- Easy to manufacture and assemble with the most familiar processes and does not require advanced and special machines or tools or any sophisticated arrangements.
- Low mass density since lightness is a prerequisite.
- Non-magnetic material or have low magnetic relative permeability and low magnetic saturation level. Magnetic materials with high permeability will increase the flux leakage around the magnets hence causes a reduction in the magnetic flux density in the air gap.
- Reasonable raw material cost and manufacturing cost.

An extensive survey has been carried out on some of the high strength materials to investigate their suitability for prescribed application. Table 3.7 shows these materials and the properties that are investigated through the survey.

Material	σ_{Ty} MPa	E GPa	Manufacturing & Assembling	ρ_m kg	Magnetic properties	Cost
Titanium alloys	750	110	• Machineable • Nonhazardous	4500	Nonmagnetic	Expensive
17-4PH-925 steel	1300	210	• Machineable • Nonhazardous • Requires heat treatment	7800	Magnetic	Low cost
Beryllium copper	1100	200	• Health Hazardous • Requires high safety precautions	7500	Nonmagnetic	Expensive
Maraging G125	1950	195	• Machineable • Nonhazardous • Requires heat treatment	7900	Magnetic	moderate
Carbon fibre	2500	160	• Non machineable • Complicated structure • Nonhazardous • Requires special manufacturing & assembling tools & fixtures	1650	Nonmagnetic	expensive

Table 3.7 Investigation on some of the materials that can used as retainment rings

It can be seen from the above Table that among the available materials, only Carbon fibre and Maraging G125 are capable to withstand high stresses. As far as the author is aware of that, among the nonmagnetic materials, only the composite materials such as Carbon Fibre can withstand high stresses. None of the nonmagnetic metals could have such high strength capabilities. Carbon fibre is a light material; hence it would be an ideal choice for ultimate generator electromagnetic performances. However, using this material in the form of circular rings would have the following disadvantages:

- The manufacturing process for such material is a complicated process and requires special tools and advanced techniques which increase the over all production cost of the generator [13,55].
- The assembling process of carbon fibre ring on the magnet rotor requires a special hydraulic expansion jig or vessel which has to be manufactured

specially for this purpose. Assembling via heat shrink fit is not possible since excessive heat damages the resin between the carbon fibre layers [50].

Hence, it was decided to use Maraging G125 as a material for the retainment ring. The manufacturing and assembling processes for the retainment rings can be found in ***Appendix A***.

Once the type of the material has been selected, it is possible to determine the minimum radial thickness of the ring and the amount of interference fit required to prevent separation between the magnet and ring at the design speed.

3.5.2 Determination of minimum radial thickness of the retainment ring

To perform the stress analysis on the magnet rotor discs, the rotor which was presented previously in Figure 3.10 is considered for the calculations. For the initial stress calculations in this Chapter, the proposed geometry of the rotor is simplified by assuming that the magnets are continuous annular ***PM***. The rotor hub and the magnet carrier are not considered in this analysis since the most critical parts in the structure are the ***PM*** and the retainment ring that supposed to withstand all the centrifugal forces developed due to high rotational speed. Hence the ***PM*** and the ring are represented by two concentric discs as shown in Figure 3.13.

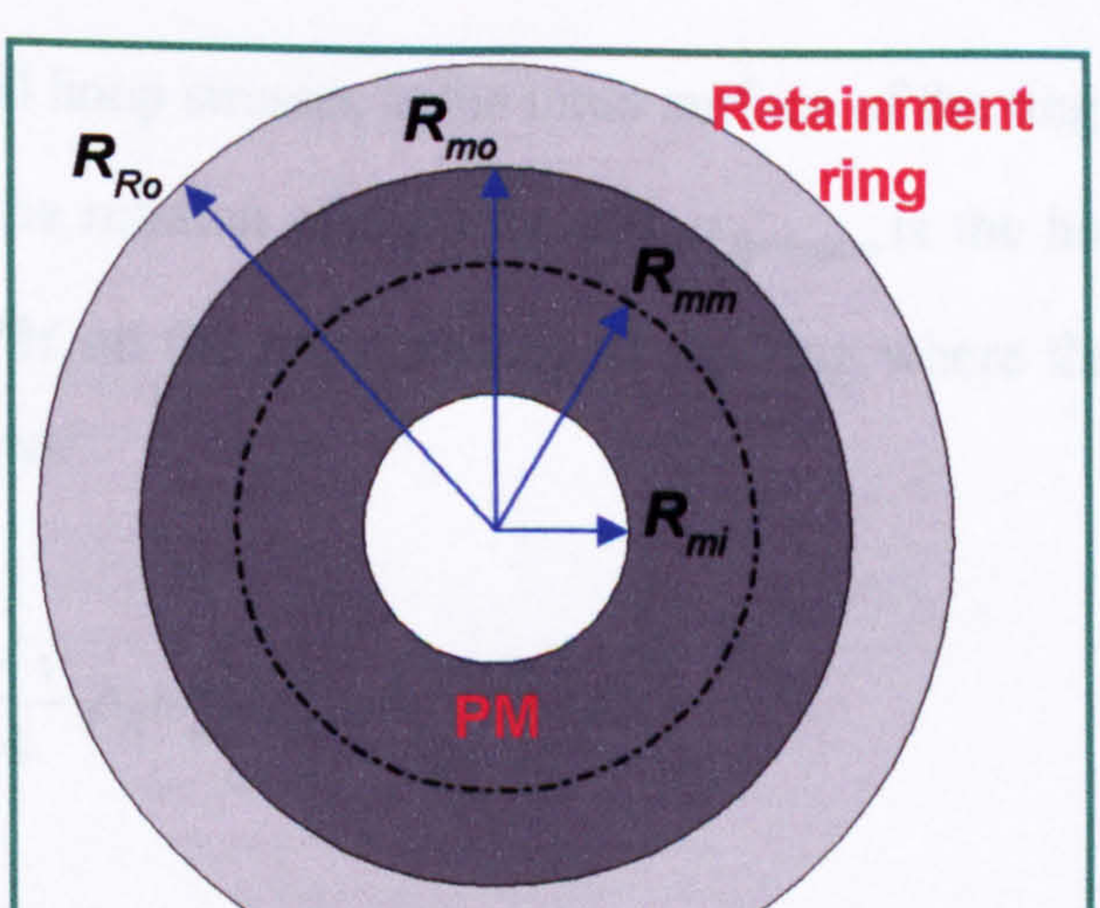

Figure 3.13 PM & retainment ring presented by concentric discs for stress analysis

The inner disc represents the magnet where its dimensions are determined from the electromagnetic design calculations that was performed in the previous sections and the outer disc represents the retainment ring. It is required to determine the minimum outer radius R_{Ro} of the ring that keeps the hoop stresses in the ring below the specified design strength while it is rotating at the design speed. Normally, a design speed is considered in excess of 5 % higher than the operating speed which is specified for electrical output. This gives an adequate margin for the rotor to run safely if an inevitable over speed occurs during operation.

The maximum hoop stress is found at the inner surface of the retainment ring. The hoop stress at the inner surface of the ring is developed due to the following loads:

- Centrifugal forces due to the rotation of the ring itself.
- Inner pressure which is developed due to the centrifugal forces coming from the *PM*

The above statements are valid as long as there is a contact between the PM and the retainment ring . Hence the total stresses at the inner surface of the ring can be found from Lame solution for thick-walled cylinder under pressure [56,57] and it is given as:

$$\sigma_{\theta T} = \sigma_{\theta rotation} + \sigma_{\theta pressure} \tag{3.49}$$

where $\sigma_{\theta T}$ is the total hoop stresses at the inner surface of the ring MPa, $\sigma_{\theta rotation}$ is the hoop stress due to the rotation of the ring and $\sigma_{\theta pressure}$ is the hoop stress due to the pressure from the *PM* on the inner surface of the ring where they can be expressed respectively as follows:

$$\sigma_{\theta rotation} = \frac{3+\nu}{4}\rho_R \omega_m^2 \left[R_{Ro}^2 + \left(\frac{1-\nu}{3+\nu}\right) R_{Ri}^2 \right] \tag{3.50}$$

$$\sigma_{\theta pressure} = \mathrm{Pr}_i \frac{\left(R_{Ro}^2 + R_{Ri}^2\right)}{\left(R_{Ro}^2 - R_{Ri}^2\right)} \tag{3.51}$$

where ν is the Poissons ratio for the ring, R_{Ri} is the ring inner radius and it is equal to the magnet outer radius R_{mo} and Pr_i is the pressure developed at the ring inner radius from the ***PM*** and it can be calculated as:

$$\mathrm{Pr}_i = \frac{F_m}{A_R} \tag{3.52}$$

where $A_R = 2\pi R_{mo} l_m$ is the circumferential area of the inner surface of the ring and F_m is the total force exerted by the ***PM*** and is given by:

$$F_m = 0.5\ \pi \rho_m l_m \omega_m^2 \left(R_{mo}^2 - R_{mi}^2\right)\left(R_{mo} + R_{mi}\right) \tag{3.53}$$

Substituting Equations 3.50 and 3.51 into Equation 3.49 gives:

$$\sigma_{\theta T} = \frac{3+\nu}{4}\rho_m \omega_m^2 \left[R_{Ro}^2 + \left(\frac{1-\nu}{3+\nu}\right)R_{Ri}^2\right] + \mathrm{Pr}_i \frac{\left(R_{Ro}^2 + R_{Ri}^2\right)}{\left(R_{Ro}^2 - R_{Ri}^2\right)} \tag{3.54}$$

The above Equation can be solved iteratively to find R_{Ro} for a given value of $\sigma_{\theta T}$. However, the exact solution can be found by formulating the above equation in the following form:

$$R_{Ro}^4 + BR_{Ro}^2 + C = 0 \tag{3.55}$$

where B and C are coefficients and given as follows:

$$B = \frac{\left(\mathrm{Pr}_i - \sigma_{\theta T} - 0.825\rho_{Ring}\omega_m^2 R_{mo}^2 + 0.175\rho_{Ring}\omega_m^2 R_{mo}^2\right)}{\left(0.825\rho_{Ring}\omega_m^2\right)} \tag{3.56}$$

$$C = \frac{\left(\mathrm{Pr}_i + \sigma_{\theta T} - 0.175\rho_{Ring}\omega_m^2 R_{mo}^2\right)R_{mo}^2}{\left(0.825\rho_{Ring}\omega_m^2\right)} \tag{3.57}$$

thus,

$$\left(R_{Ro}^2 - m\right)\left(R_{Ro}^2 - n\right) = 0 \tag{3.58}$$

where,

$$(-m)(-n) = C$$

$$(-m) + (-n) = B$$

from which,

$$m^2 + Bm + C = 0 \tag{3.59}$$

and

$$m_{1,2} = \frac{-B \pm \sqrt{B^2 - 4C}}{2C} \tag{3.60}$$

Once the outer radius of the ring is determined, it is possible to calculate the amount of interference required to prevent the separation between the magnet and ring at the design speed. Hence, the radial and hoop stresses in the rotor can be determined. This can be described in the following section.

3.5.3 Calculation of the interference fit

The two concentric discs which represent the *PM* and the retainment ring are assembled via shrink fit process with a specified amount of interference fit. Interference fit is performed by machining the retainment ring having an inside diameter slightly less than needed to fit over the *PM* disc. By heating the ring to a specified temperature (sometimes cooling is necessary for the inner part) the ring expands and slip over the *PM* disc. After cooling to a uniform temperature, a contact pressure P_{cont} is developed between the ring and the *PM* disc, which causes the inner and outer discs to be in compression and tension, respectively, in the hoop direction.

Stresses produced by P_{cont} can be regarded as residual stresses, as they are present before the rotation of the rotor.

To prevent the separation between the two discs while rotating at the design speed, this residual contact pressure should be sufficient to keep the magnets and all other parts below the retainment ring under negative pressure. Only the ring in this case will be exposed to a positive pressure. Thus, making $P_{cont} = \mathrm{Pr}_i$, and the total interference fit δ required to develop that pressure is calculated as follows:

$$\delta = \frac{2R_c^3 P_{cont}(R_{Ro}^2 - R_{mi}^2)}{E(R_{Ro}^2 - R_c^2)(R_c^2 - R_{mi}^2)} \tag{3.61}$$

where R_c is the radius at the contact surface i.e. $R_c = R_{Ri} = R_{mo}$.

Hence to assemble the retainment ring via shrink fit process, the temperature difference to allow for the ring to slip over the magnet is calculated as follows:

$$\Delta T = \frac{\delta}{R_c \alpha_T} \tag{3.62}$$

where ΔT in $^{\circ}C$ is the temperature difference required to perform the shrink fit and α_T in K^{-1} is the thermal expansion coefficient for the assembled materials

When the rotor parts (ring and *PM*) are assembled and the rotor starts rotating, additional stresses are developed on the rotating parts and these stresses are superposed to the residual stresses. This is valid as long as there is no separation occur between the rotor parts during the rotation. The radial and hoop stresses due to rotation are calculated as if only one disc is rotating with R_{mi} and R_{Ro} are its inner and outer radii respectively. Hence, the total radial and hoop (due to residual and rotation) stresses distribution at any point on the *PM* and retainment ring can be calculated as follows:

- Total radial stresses and hoop stresses in the retainment ring are given respectively as:

$$\sigma_{rT_{Ring}} = \frac{P_{cont}R_c^2}{(R_{Ro}^2 - R_c^2)}\left(1 - \frac{R_{Ro}^2}{r^2}\right) + \frac{(3+\nu)}{8}\rho_m\omega_m^2\left(R_{Ro}^2 + R_{mi}^2 - \frac{R_{Ro}^2R_{mi}^2}{r^2} - r^2\right) \quad (3.63)$$

$$\sigma_{\theta T_{Ring}} = \frac{P_{cont}R_c^2}{(R_{Ro}^2 - R_c^2)}\left(1 + \frac{R_{Ro}^2}{r^2}\right) + \frac{(3+\nu)}{8}\rho_m\omega_m^2\left(R_{Ro}^2 + R_{mi}^2 + \frac{R_{Ro}^2R_{mi}^2}{r^2} - \frac{(1+3\nu)}{(3+\nu)}r^2\right) \quad (3.64)$$

- Total radial stresses and hoop stresses in the ***PM*** disc are calculated respectively by:

$$\sigma_{rT_M} = \frac{-P_{cont}R_c^2}{(R_c^2 - R_{mi}^2)}\left(1 - \frac{R_{mi}^2}{r^2}\right) + \frac{(3+\nu)}{8}\rho_m\omega_m^2\left(R_{Ro}^2 + R_{mi}^2 - \frac{R_{Ro}^2R_{mi}^2}{r^2} - r^2\right) \quad (3.65)$$

$$\sigma_{\theta T_M} = \frac{-P_{cont}R_c^2}{(R_c^2 - R_{mi}^2)}\left(1 + \frac{R_{mi}^2}{r^2}\right) + \frac{(3+\nu)}{8}\rho_m\omega_m^2\left(R_{Ro}^2 + R_{mi}^2 + \frac{R_{Ro}^2R_{mi}^2}{r^2} - \frac{(1+3\nu)}{(3+\nu)}r^2\right) \quad (3.66)$$

It should be noticed that all the above-mentioned Equations are based on Lams solutions for compound cylinders which can be found in details in [56]. In all equations, it is assumed that both inner and outer disc have the same mass density, ρ_m (kg/m^3), modulus of elasticity, E (GPa) and Poissons ratio.

3.5.4 Rotor stress distribution

The stress distribution in the *PM* and retainment ring at the design speed, is calculated using Equations 3.63 – 3.66. The design data used in the calculations for a particular rotor design are given in Table 3.8.

R_{Ro} mm	R_c mm	R_{RI} mm	ρ_m kg/m3	E GPa	ν -	ω_m rad/sec	P_{cont} MPa	δ mm
55	47	27	7850	210	0.3	5500	138	0.260

Table 3.8 Design data given for a particular rotor design for the calculation of radial and hoop stress

where P_{cont} and δ are calculated using Equations 3.52 and 3.61 respectively.

The radial stress distribution in the retainment ring and *PM* disc are presented graphically in Figure 3.14 and the hoop stress distribution for both parts are shown in Figure 3.15.

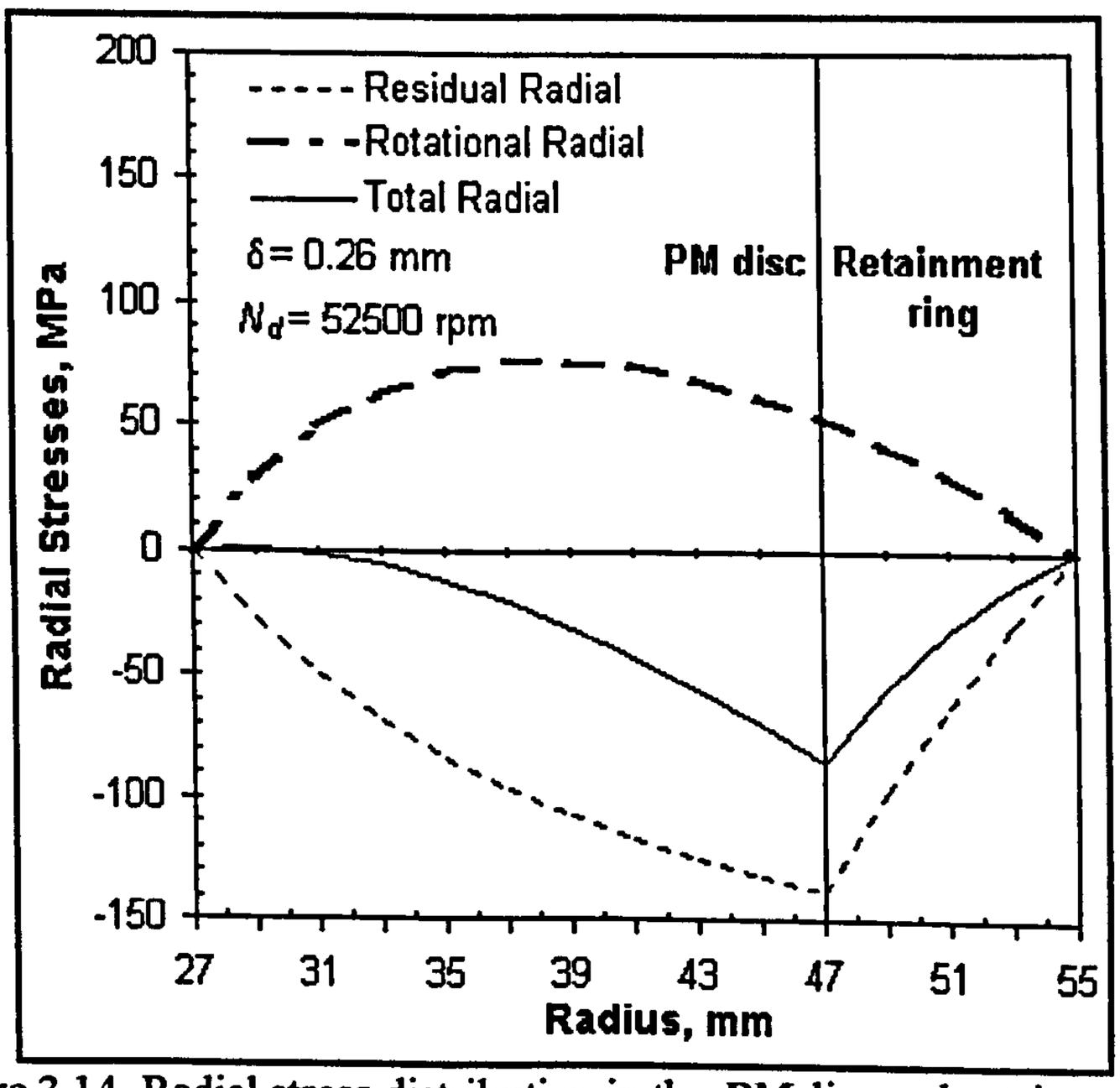

Figure 3.14 Radial stress distribution in the *PM* disc and retainment ring

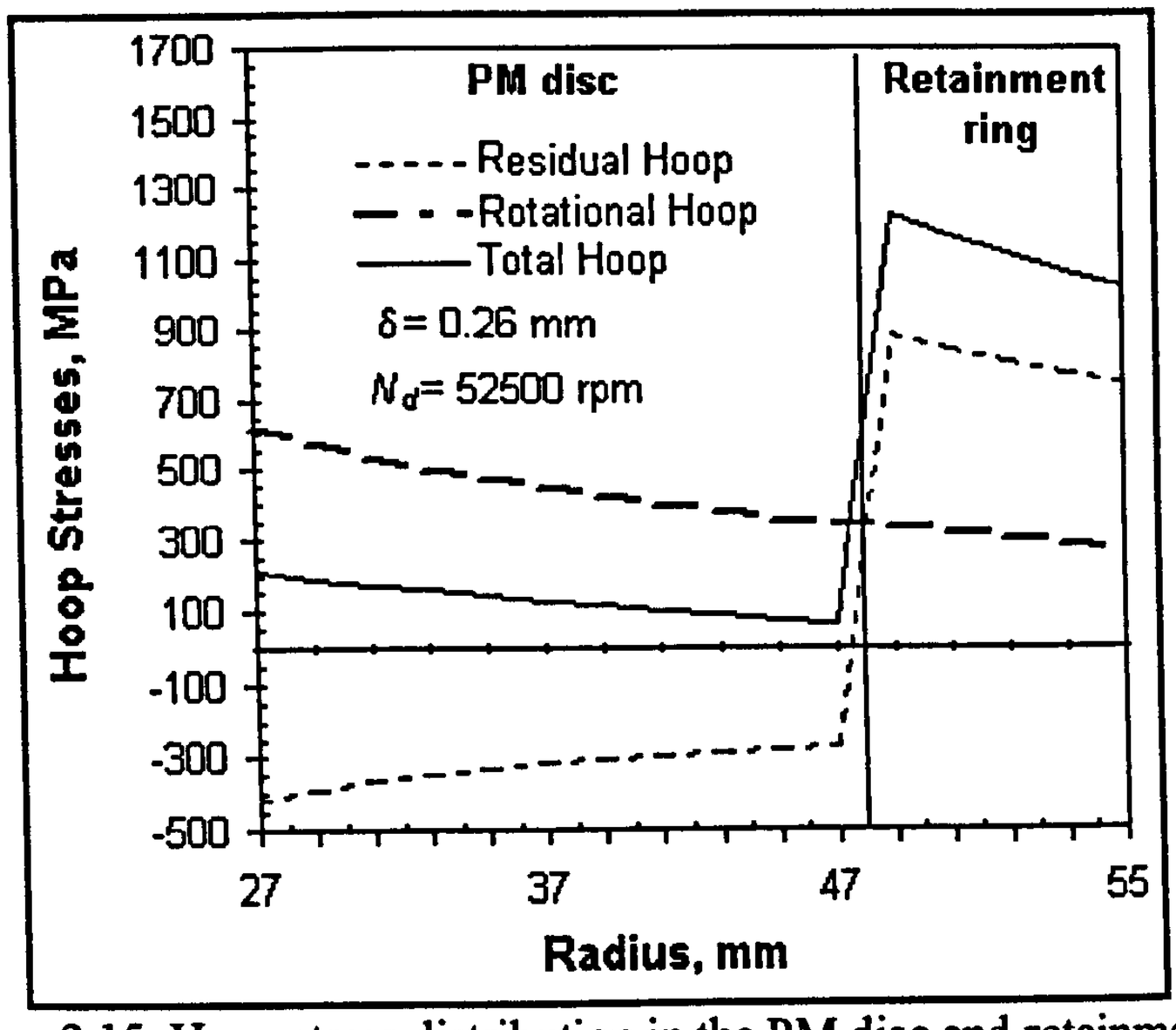

Figure 3.15 Hoop stress distribution in the PM disc and retainment ring

These analytical results can be used to check for mechanical integrity of the rotor, with the following criterion should be considered:

- Hoop stresses at the inner radius of the retainment ring at the specified design speed should be below the specified design strength, σ_d which is given as $\sigma_d = \sigma_y / S_f$, where σ_y is the yield strength of the retainment ring material and S_f is the safety factor. For the rest of this work, a design strength value of 1333 is considered for the Maraging G125 retainment ring, based on safety factor $S_f = 1.5$.
- According to the manufacturer data [58], ***PM*** should always be in compression state since it can only withstand high compressive stresses (in excess of 1500 MPa) and very low tensile stresses (below 100 MPa). Preliminary results for the hoop stresses at the inner radius of the ***PM*** examined at the design speed are found in excess of 209 MPa where it could damage the magnet disc. However this problem can be solved by, using segmented ***PM*** in the rotor structure instead of having continuous annular ***PM***.

- Negative radial stresses at the surface of contact between the ***PM*** and the ring, indicate that a continuous contact is maintained at the design speed.

Finally, it is worth mentioning that for the stress analysis of the real structure of the ***PM*** rotor, a ***FE*** model is found to be more convenient due to the following reasons:

- The analytical solution is based on a simplified model of uniform homogeneous concentric discs having similar mechanical and physical properties. The real ***PM*** rotor disc contains four different materials and they all should be considered in the analysis.
- The analytical solution assumes that there is no axial deformation hence no stresses in the axial direction.
- The actual geometry of the magnet rotor disc is much complicated especially when using segmented PM with different shapes which requires a ***3D FE*** models.

3.6 STEADY STATE PERFORMANCE ANALYSIS

The steady state performance of the ***PM*** generator is conveniently explained by the energy conversion process that takes place in the machine, which is achieved by the linkage of both the stator and rotor magnetic fields. Machine electrical parameters such as leakage and magnetising inductances are highly affected by the distribution of the magnetic field in the machine. Therefore the performance prediction depends critically on accurate computation of such electrical parameters. Electrical machine can be modelled typically using one of two methods. The first method involves the generalised electrical machine theory, from which an equivalent circuit can be constructed. The second method involves numerical calculations such as ***FEM*** from which the field distribution can be obtained.

Although ***FEM*** allows accurate determination of machine parameters including inductances through magnetic field solutions, they require a lot of effort especially when the geometry of the machine is complex. At the earlier stages of the design process, it is recommended that machine performance can be predicted with sufficient accuracy using analytical models. Hence, several proposed designs can be quickly evaluated then those with acceptable performances can be then analysed accurately using ***FEM*** techniques once they are selected. In this section, an equivalent circuit is constructed based on lumped parameters from which the performance of several ***PMAF*** high-speed generators are examined. Later, in the next Chapter, a ***FE*** analysis is performed on a particular proposed machine designs from which performance is predicted and compared to the results obtained from the analytical approach adopted in this section.

3.6.1 Equivalent circuit

In an equivalent circuit, the machine is represented by lumped parameters such as inductances and resistances derived based on simplifying assumptions. These assumptions generally include linear magnetic material and simplified stator/rotor geometry. Several methods of representing the equivalent circuit for conventional synchronous generators are available [18,59]. Permanent magnet generators have the

same parameters of field excited generators for the air gap and the stator, but the rotor is slightly different because of the presence of the magnets, which are regarded as a fixed field excitation source. The equivalent circuit for the proposed ***PMAF*** generator is presented in Figure 3.16-a). Whereas the generator phasor diagram at pure resistive load i.e. unity power factor is shown in figure 3.16-b).

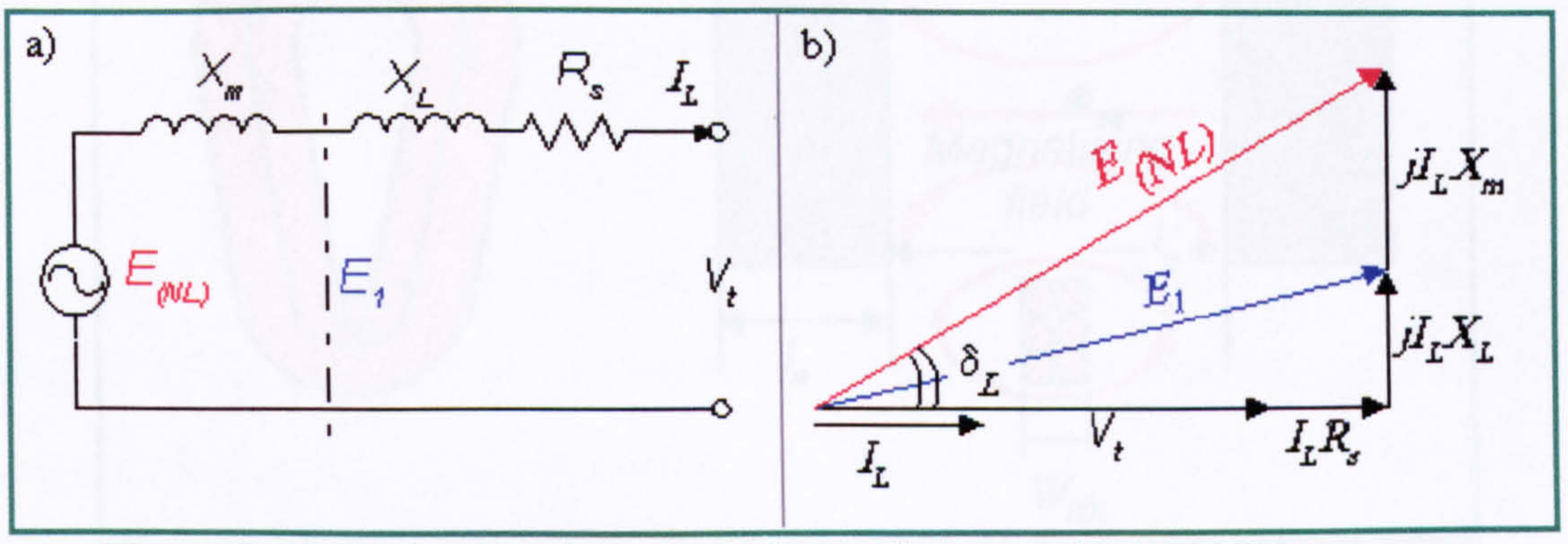

Figure 3.16 Equivalent circuit and phasor diagram of the ***AFPM*** generator at unity power factor

3.6.2 Synchronous reactance

When a current I_L is drawn in the stator windings, a flux ϕ_a is produced. Part of it, ϕ_L known as the leakage flux, links with the stator windings only and does not link with the flux from the ***PM***. A major part, ϕ_M, known as the magnetising flux, is established on the air gap and links with the main flux produced by the ***PM***. Accordingly, the synchronous reactance, X_s, can be calculated as follows:

$$X_s = X_L + X_M \tag{3.67}$$

where X_L and X_M are the leakage and magnetising reactances and they are calculated as follows:

$$X_L = \omega_e L_L \tag{3.68}$$

$$X_M = \omega_e L_M \tag{3.69}$$

where L_L and L_M are the leakage and magnetising inductances respectively and they can be calculated from the coil geometry which as shown in Figure 3.17.

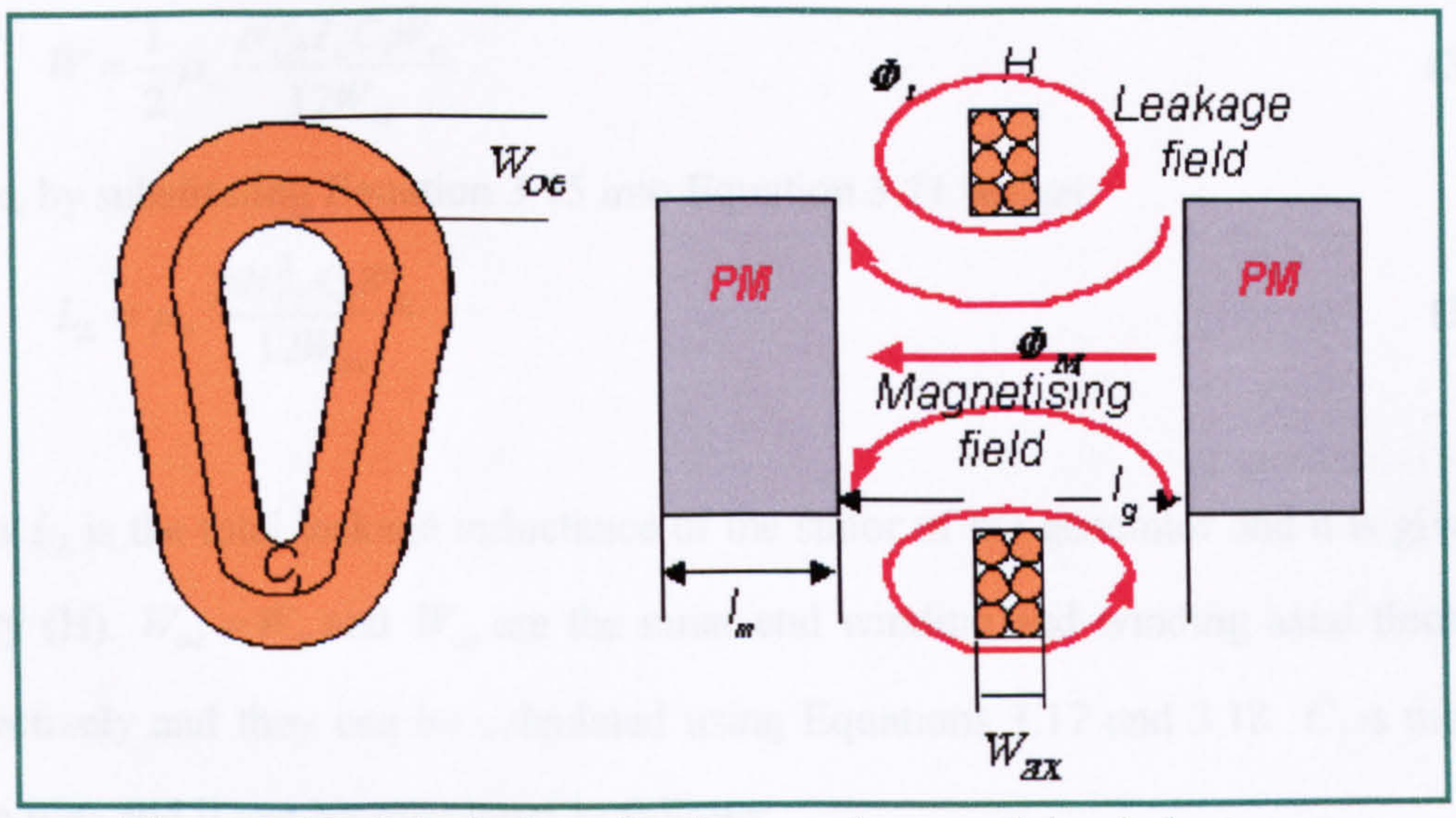

Figure 3.17 Calculation of leakage and magnetising inductances

3.6.2.1 Leakage inductance

The coil proposed for the current design has its dimensions determined from the calculations performed in the previous sections. Hence for the coil having a total number of turns $N_{CT} = N_t N_l$, if the energy stored in the magnetic field linking the coil can be determined, the value of the leakage inductance for a total number of coils equal to the number of poles, p, can be found as follows:

$$W = \int \frac{1}{2} \mu_o H^2 d(vol) \tag{3.70}$$

where, vol is the volume of the coil, from which:

$$L_L = p \frac{2W}{I_L^2} \tag{3.71}$$

$$2HW_{ax} = N_{CT} I_L \frac{x}{W_{ie}} \tag{3.72}$$

$$H = \frac{N_{CT} x}{2W_{ax} W_{ie}} \tag{3.73}$$

$$W = \frac{1}{2}\mu_o \frac{N_{CT}^2 I_L^2 C_l}{4W_{ax}W_{ie}^2} \int_0^{W_{ie}} x^2 dx \tag{3.74}$$

$$W = \frac{1}{2}\mu_o \frac{N_{CT}^2 I_L^2 C_l W_{ie}}{12W_{ax}} \tag{3.75}$$

hence, by substituting Equation 3.75 into Equation 3.71 we get:

$$L_L = \mu_o \frac{pN_{CT}^2 C_l W_{ie}}{12W_{ax}} \tag{3.76}$$

where L_L is the total leakage inductance of the stator of the generator and it is given in Henry (H). $W_{oe} = W_{ie}$ and W_{ax} are the inner end winding and winding axial thickness respectively and they can be calculated using Equations 3.17 and 3.18. C_l is the coil mean path and it can be calculated as follows:

$$C_l = \frac{2\pi}{p}\left[\left(R_{mo} + \frac{W_{ie}}{2}\right) + \left(R_{mi} - \frac{W_{ie}}{2}\right)\right] + 2\left(R_{mo} - R_{mi} + W_{ie}\right) \tag{3.77}$$

hence;

$$C_l = 2R_{mo}\left(\frac{\pi}{p} + 1\right) + 2R_{mi}\left(\frac{\pi}{p} - 1\right) + 2W_{ie} \tag{3.78}$$

3.6.2.2 Magnetising inductance

Magnetising inductance can be calculated based on the determination of the reluctance of the magnetising path through the air gap and permanent magnet [60]. Thus;

$$L_M = \frac{pN_{CT}^2}{R_{eq}} \tag{3.79}$$

where R_{eq} is total reluctance of the path of the magnetising flux and can be calculated as:

$$R_{eq} = \frac{l_{mg}}{\mu_o A_{mg}} \tag{3.80}$$

$$l_{mg} = 2l_m + l_g \tag{3.81}$$

$$A_{mg} = \pi \frac{\left(R_{outer}^2 - R_{inner}^2\right)}{p} \tag{3.82}$$

where l_{mg} is the total magnet air gap length, A_{mg} is the air gap/magnet interface area, R_{outer} and R_{inner} are the rotor outer and inner radii respectively.

3.6.3 Voltage regulation, *VR*

The voltage regulation of the ***PMAF*** generator can be determined from the following Equation:

$$\% \ VR = \frac{E_{NL} - V_t}{E_{NL}} \times 100 \tag{3.83}$$

where V_t is the terminal voltage calculated at full load current and it can be found as follows:

$$V_t = \left[E_{(NL)}^2 - (I_L X_s)^2\right]^{1/2} - (I_L R_{sc}) \tag{3.84}$$

where R_{sc} is the resistance of the stator windings calculated from Equation 3.14 at temperature of $110°C$. It should be noted that only the DC resistance is considered in the calculations and skin effect in the conductor is neglected since it is constructed from fine stranded wires. The total winding length, L_{Tw}, used for the resistance calculations is determined using Equation 3.78, where:

$$L_{Tw} = N_l N_t p C_l \tag{3.85}$$

3.6.4 Efficiency calculations

The efficiency, η, of the ***PMAF*** high-speed generator can be calculated as follows:

$$\% \ \eta = \frac{P_o}{P_{in}} \times 100 \tag{3.86}$$

where P_o and P_{in} is the electrical output power and total input power respectively and they can be found as follows:

$$P_o = V_t I_L \tag{3.87}$$

$$P_{in} = P_o + P_c + P_{Se} + P_w + P_{\mathrm{Re}} \tag{3.88}$$

where

P_c = stator copper losses, W, calculated using Equation 3.13

P_{Se} = stator eddy current losses, W, calculated using Equation 3.11

P_w = windage losses, W

P_{Re} = rotor eddy current losses, W

where the total conductor length, L_{edd}, used for the stator eddy current losses is calculated as follows:

$$L_{edd} = 2N_t N_l (R_{mo} - R_{mi}) \tag{3.89}$$

For the efficiency calculations in this Chapter, only the first three types of losses will be considered. Accurate prediction of the rotor eddy current losses requires ***FEM*** which will be considered in Chapter Four. As for rotor windage losses, it can be calculated using one of the empirical formulae which has been presented in a number of papers [61, 62] for the evaluation of windage losses for rotating masses. These formulas are theoretical functions approximated to practical results. **James et al** [10]

have predicted the windage losses in a small high-speed alternator using one of the most common formulae which can be expressed as follows:

$$P_w = N_R 0.0311 \rho_{air}^{4/5} \omega_m^{14/5} R_{Ro}^{23/5} \mu_{air}^{1/5} \tag{3.90}$$

where:

N_R = Number of rotating discs

ρ_{air} = density of the surrounding air, 1.18 kg/m^3

μ_{air} = coefficient of viscosity of the air, 1.98×10^{-5} kg/m.s

Hence in this work, the windage losses in the ***PMAF*** high-speed generator is calculated using the formula presented in Equation 3.90.

Once the losses in the machine are evaluated, the amount of air mass flow required to cool the generator can be calculated as follows [63]:

$$\dot{m} = \frac{P_{loss}}{C_p \Delta T_{gen}} \tag{3.91}$$

where $\dot{m}$ is the air mass flow rate, kg/sec, P_{loss} is the total losses in the generator, W, $C_p = 1004.7$ in $J/kg\cdot K$ is the specific heat capacity of the air at $25°C$ and ΔT_{gen} is the temperature rise in the generator. This value of mass of flow is helpful in the design or selection of an integral fan which can be mounted on the same shaft of the generator. A suitable cooling fan can be used for this application is the centrifugal fan. The design of the centrifugal fan is beyond the scope of this thesis.

3.7 SIMULATION

In this section, the model developed for the ***PMAF*** high-speed generator was explored and applied to several possible designs. With the known data for some of the design parameters which are given in Table 3.9, it was possible to perform the simulation in two different approaches which are described in the following Sections.

R_{hi}, mm	R_{ho}, mm	d_b, mm	d_{std}, mm	N_{std}, No of strands	N_l, No of layers	l_g, mm	E_{NL} Volt	I_L, Amp	N_m, rpm
7.5	15	2.3	0.2	96	2	10	220	75	50000

Table 3.10 Major design data used for the simulation of the model developed for the ***PMAF*** high-speed generator

3.7.1 First approach

In this approach, the air gap flux density, B_g, is calculated where magnet outer radius, R_{mo} is given from Equation 3.24. Hence several designs of different characteristics and performances can be obtained through the exploitation of all possible design variables. However, those designs, which have poor mechanical structure, insufficient space for the windings and those which require extreme air gap flux density in excess of 1.1 T are eliminated and only those feasible designs for different number of turns and number of poles are presented in Table 3.10. Finally the power density of a machine plays a vital role in the selecting any of the proposed designs having such high performances. Although designs **A1** & **B1** have the highest efficiencies, their power densities are very low compared to design **D1** which has the highest power density and a good efficiency. Hence this design is adopted and will be used in the ***FEA*** in the following Chapter. A prototype of this design is built and tested and the experimental results obtained can be found in Chapter Seven.

3.7.2 Second approach

In contrast to the first approach, in this approach a specified value of flux density, B_g, is inputted into the model. Normally a working point at the maximum energy of the magnet or slightly greater values are selected to keep the operating point of the magnets on the reversible line and to avoid magnet demagnetisations. For ***NdFeB*** grade ***N38H*** having $B_r = 1.22$ T, a flux density of 0.63 is considered for the calculation. Several designs with the possible combinations of the number of turns and number of poles were taken into account. The magnet outer radius is found for each

possible design to satisfy electrical output. Again all designs which have poor mechanical structure and insufficient space for the windings are eliminated. In addition, designs which do not satisfy electrical requirements are not considered and only the accepted designs are presented in Table 3.11. A comparison between these designs based on the power density and efficiency of the generators are shown in Figures 3.18 and 3.19 respectively. Two more designs (**D2** & **H2**) were found to have high power density and high efficiency through using this approach.

Proposed design	**A1**	**B1**	**C1**	**D1**	**E1**
N_t, turns	**3**	**4**	**5**	**5**	**6**
p, poles	**10**	**8**	**6**	**8**	**6**
R_{mi}, mm	22	24	27	27	29
R_{mo}, mm	38	42	47	47	50
R_{Ro}, mm	41	47	55	55	62
l_m, mm	241.5	47.4	45.12	17	23.3
L_{Tw}, m	5.61	7.6	9.44	10.83	12.26
Rotor weight, kg	17.37	4.53	5.9	2.25	3.93
Stator weight, kg	0.12	0.16	0.2	0.23	0.26
Total weight, kg	17.49	4.69	6.1	2.48	4.19
δ, mm	0.247	0.24	0.26	0.26	0.249
Max $\sigma_{\theta T}$, MPa	1371	1232	1227	1227	1178
R_{sc}, Ω	0.0429	0.0583	0.0723	0.0829	0.0939
L_L, μH	2.46	5.94	11.51	13.2	21.54
L_M, μH	0.42	4.78	11.03	25.12	36.3
B_g, T	1.019	0.862	0.86	0.637	0.721
V_t, Volt	216.7	215	212.9	205.4	202.12
f_e, Hz	4166.6	3333.3	2500	3333.3	2500
P_{Se}, W	298.34	164.1	95.35	124.61	84.62
P_c, W	241.7	327.8	406.82	466.6	528.5
P_w, W	87.6	164.23	338.44	338.45	587.25
P_o, W	16252.7	16123.67	15972.52	15403.46	15159.6
% VR	1.5	2.28	3.19	6.64	8.12
% η	96.28	96.1	95.00	94.31	92.66
Power density, kW/kg	0.929	3.437	2.618	6.211	3.618

Table 3.10 Successful possible designs determined by first approach

Proposed design	**A2**	**B2**	**C2**	**D2**	**E2**	**F2**
N_t, turn	**1**	**1**	**1**	**1**	**1**	**1**
p, poles	**16**	**18**	**20**	**22**	**24**	**26**
R_{mi}, mm	18	18	18	18	18	18
R_{mo}, mm	56.2	51.25	47.75	45	43	41.25
R_{Ro}, mm	72.2	62	56	52	49	46.25
l_m, mm	18	18.27	18.55	18.845	19.13	19.44
Total weight, kg	4.6	3.47	2.88	2.52	2.27	2.03
ΔT_{shrink}, $^{\circ}C$	510.8	518.4	542	510	507	520
δ, mm	0.316	0.292	0.284	0.252	0.239	0.236
Max $\sigma_{\theta T}$, MPa	1323	1270	1290	1208	1191	1215
R_{sc}, Ω	0.03	0.0297	0.0293	0.0291	0.0291	0.0294
L_L, μH	0.2	0.189	0.186	0.185	0.186	0.187
L_M, μH	1.71	1.23	0.975	0.82	0.711	0.61
V_t	217.6	217.7	217.75	217.7	217.7	217.75
E_{NL}	219.55	220.79	220.88	219.96	221.2	221.3
P_{Se}, W	381.25	471.88	579.16	699.6	841	994.4
P_c, W	171.9	167	165	164	164.78	165.4
P_w, W	1187	587	367.7	261.5	199	148.7
P_o, W	16321	16328	16331	16332	16332	16331.7
% VR	1.07	1.03	1.02	1.01	1.01	1.02
% η	90.36	93.01	93.625	93.55	93.13	92.58
Power density, kW/kg	3.54	4.70	5.67	6.48	7.19	8.04

Table 3.11 Successful possible designs determined by second approach

Proposed design	G2	H2	I2	J2	K2	L2	M2
N_t = 1 turn	**2**	**2**	**3**	**4**	**5**	**7**	**8**
p , poles	**12**	**14**	**10**	**8**	**8**	**6**	**6**
R_{mi} , mm	20	20	22	24	27	31	33
R_{mo} , mm	51.25	46.75	49.5	52	47	52.75	47.5
R_{Ro} , mm	62.25	55	60	64	55	66	55
l_m , mm	17.48	17.74	17.23	16.99	16.99	16.76	16.76
Total weight, kg	3.33	2.66	3	3.43	2.48	3.52	2.36
ΔT_{shrink} , $^{\circ}C$	522	513.6	509	513.2	502.6	495	517.4
δ , mm	0.294	0.263	0.277	0.293	0.295	0.287	0.27
Max $\sigma_{\theta T}$, MPa	1284	1228	1250	1291.5	1227	1298	1269
R_{sc} , Ω	0.0452	0.0447	0.0587	0.0737	0.0829	0.117	0.1228
L_L , μH	1.15	1.14	3.36	7.52	13.2	36.65	50
L_M , μH	5.08	3.88	10.78	22.22	25.12	73.4	65
V_t	216.1	216.2	213.8	209.4	205.4	168.9	164
E_{NL}	220.65	221.16	220.55	220.3	219.98	219.77	219.53
P_{Se} , W	262.8	357.2	200.76	139.54	124.59	80.027	60.97
P_c , W	254	251.7	330.4	415	466.6	660.6	690.8
P_w , W	587	338.4	505	679.5	338.4	783	338
P_o , W	16209	16215	16037	15708.4	15403.3	12667.4	12304.4
% VR	1.76	1.72	2.8	4.79	6.64	23.2	25.4
% η	93.62	94.47	93.93	92.71	94.3	89.26	91.86
Power density, kW/kg	4.86	6.09	5.34	4.57	6.21	3.59	5.21

Continued Table 3.11

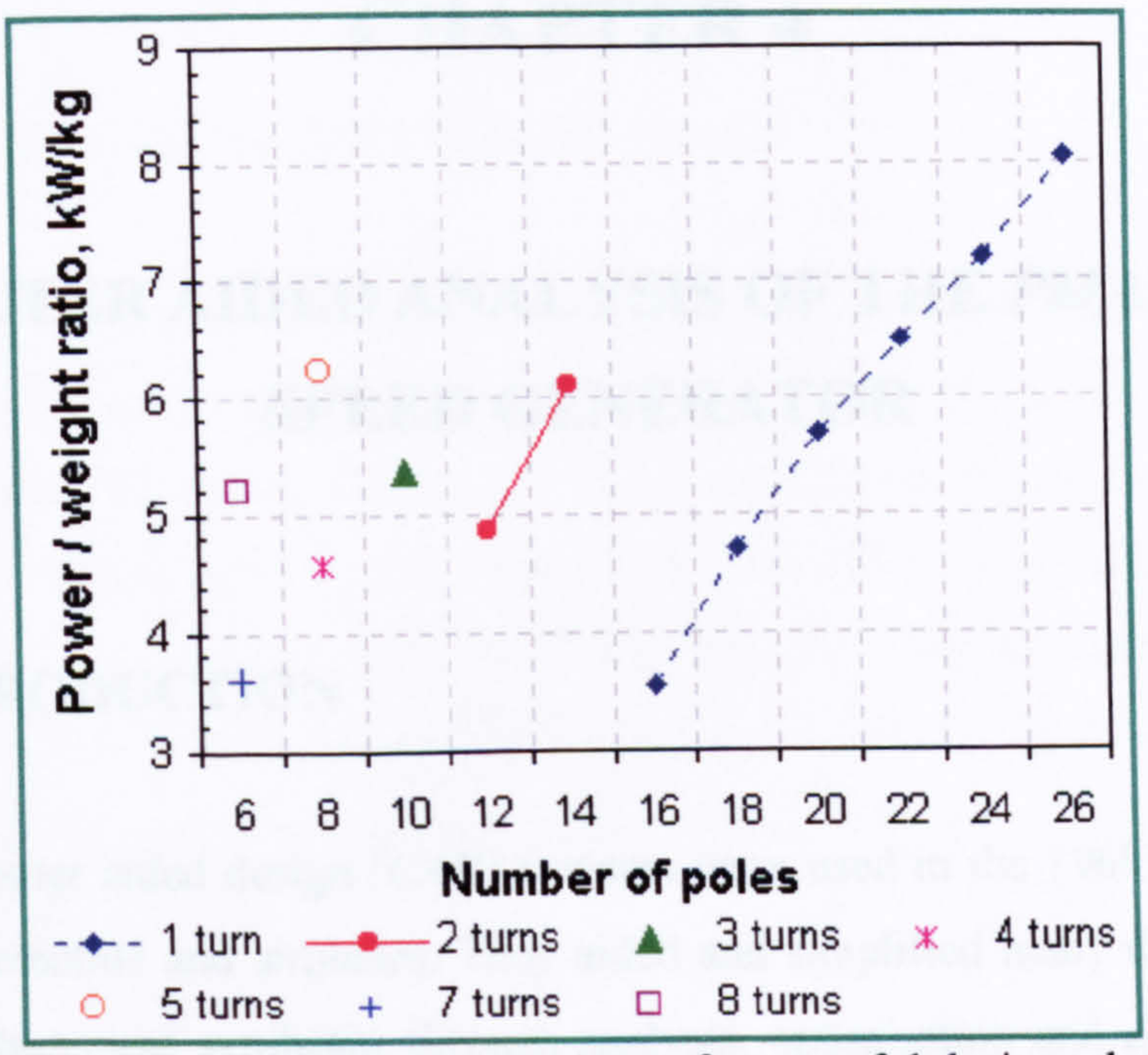

Figure 3.18 Power density comparison of successful designs determined via second approach

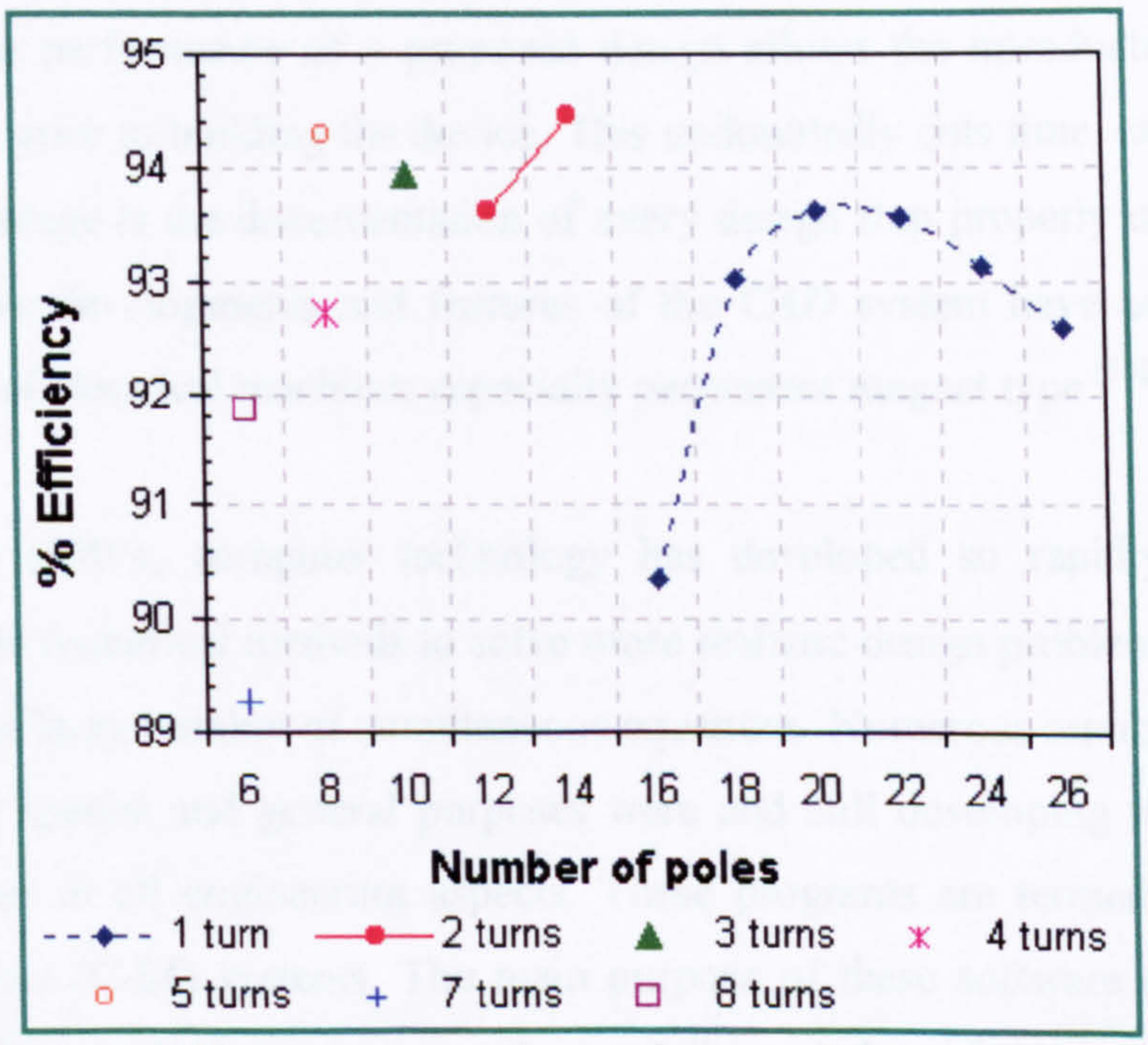

Figure 3.19 Efficiency comparisons of successful designs determined via second approach.

CHAPTER 4

COMPUTER AIDED ANALYSIS OF THE *PMAF* HIGH-SPEED GENERATOR

4.1 INTRODUCTION

Computer aided design (*CAD*) systems were used in the 1960's in the design phase of automobile and airplanes. They aided and simplified many design processes from conceptions and synthesis, through analysis, optimisation and drafting, through building and testing of prototypes [64]. *CAD* systems provide a computer-human interaction which enables the designer to obtain the performance and characteristics for a model under consideration, and optimise the model by mathematical tools. Simulating the performance of a proposed design allows the introduction of design modifications prior to building the device. This undoubtedly cuts time, effort and cost. Another advantage is the documentation of every design step properly using database systems. These developments and features of the *CAD* system have accelerated the development of electrical machines especially permanent magnet type [65].

Since 1970's, computer technology has developed so rapidly, it made it possible to use numerical methods to solve more realistic design problems that involve the solution of large number of simultaneous equations. Numerous number of software programs for special and general purposes were and still developing to assist in the design process in all engineering aspects. These programs are termed as Computer Aided Analysis (*CAA*) systems. The main purpose of these software packages is to analyse models under certain operating conditions, through solving the related modelling equations. Nowadays, computer aided drafting, analysis, and optimisation are essential building bricks of any commercial general purpose package in the market

[66] in which its structure is based on the implementation of the Finite Element method (*FEM*).

4.2 THE FINITE ELEMENT METHOD

In the 1960's, structural and mechanical engineers were involved in developing and using a new numerical method for solving the Partial Differential Equations (*PDE*) in the mechanical and structural systems, called finite element method [67]. This method then adopted by electrical engineers to solve electromagnetic problems for simple electric devices. Later it has been used to predict flux distribution in different electrical machines [68]. Hence, this method has enhanced the capability of analysing complex structures and complicated machines which was impossible to perform by ordinary methods.

The finite element method is a direct numerical computational method which provides an approximation to large number of complicated engineering and physical problems, which can be described by *PDE*. This method derives its name from the basic concept of the method that involves the subdivision of the domain under consideration into a number of small regions called elements. The elements can have different shapes and they can be put together to model any irregular shapes and complex objects composed of different materials and have mixed boundary conditions. The elements are joined by ensuring the boundaries of each element are compatible with those of its neighbours and with the overall boundary conditions of the model. After setting up the differential equations for the elements and applying load and boundary conditions, the global matrix equation can be solved at the nodes. This method is regarded currently as the computational base of many *CAD* systems and it is capable to solve many design problems associated with several fields such as structural, electromagnetic, thermal and fluid dynamics problems.

Nowadays, general or special purpose commercial *FEM* packages are highly developed and they are available for educational purposes for research and for industry. In this project, a *FE* package called *ANSYS* version 5.4, which was licensed to Aerospace Civil and Mechanical Department (*ACME*) of University of

Hertfordshire, is used to perform the required structural and electromagnetic analysis for the proposed design of the ***PMAF*** high-speed generator. This version has a limitation on the node number. Nevertheless, through this work, it was possible to build different ***FE*** models with relatively reliable results obtained without significant loss of accuracy.

4.3 OVERVIEW OF *ANSYS* FE SOFTWARE

ANSYS, is a general purpose ***FE*** software package developed by ***ANSYS Inc.***, is a powerful tool, and extensively used in this Chapter. With high computing capability, ***ANSYS*** can deal with three-dimensional structural problems or complicated models quite well. In addition, it has the ability to quantify design parameters and visualise electromagnetic fields, which helps to understand performance variations and to obtain reliable and accurate characterisation data.

There are three major parts involved in the analysis of any ***FE*** model when using ***ANSYS*** [69] these are:

- Describing the model and defining the problem.
- Solving the problem.
- Viewing the result of the analysis.

The first part consists of creation of the model and definition of the problem. Usually, this part consumes most of the users time since it involves building the geometry, applying loads and boundary conditions, and creating the finite element model. It is worth mentioning that ***FE*** models, can be build using ***ANSYS*** Parametric Design Language (***APDL***) in which the model is built in terms of parameters, which in turn allows to make design changes easily and conveniently. ***APDL*** also encompasses a wide range of other features such as repeating a command, macros, branching, loops, and vector and matrix operations. This can be done in a batch file (normally text file) where all the commands are written in the file and then the file can be executed directly.

Later, the solution part offers users two options for running automatic analysis mode or manual analysis mode. In general, automatic mode is suitable for most of the analysis but if special options are required for a certain analysis, then manual analysis can be set. However, this requires that the users should have adequate experience in dealing with all options available in the solution interface.

Finally, the results can be viewed after the solver has finished the calculations. Hence results can be evaluated and design modifications can be made based on information gleaned from the analysis. In general, whether the ***FE*** analysis is addressed for structural or electromagnetic analysis, the flowchart depicted in Figure 4.1 describes the algorithm for performing general ***FE*** analysis used through this work.

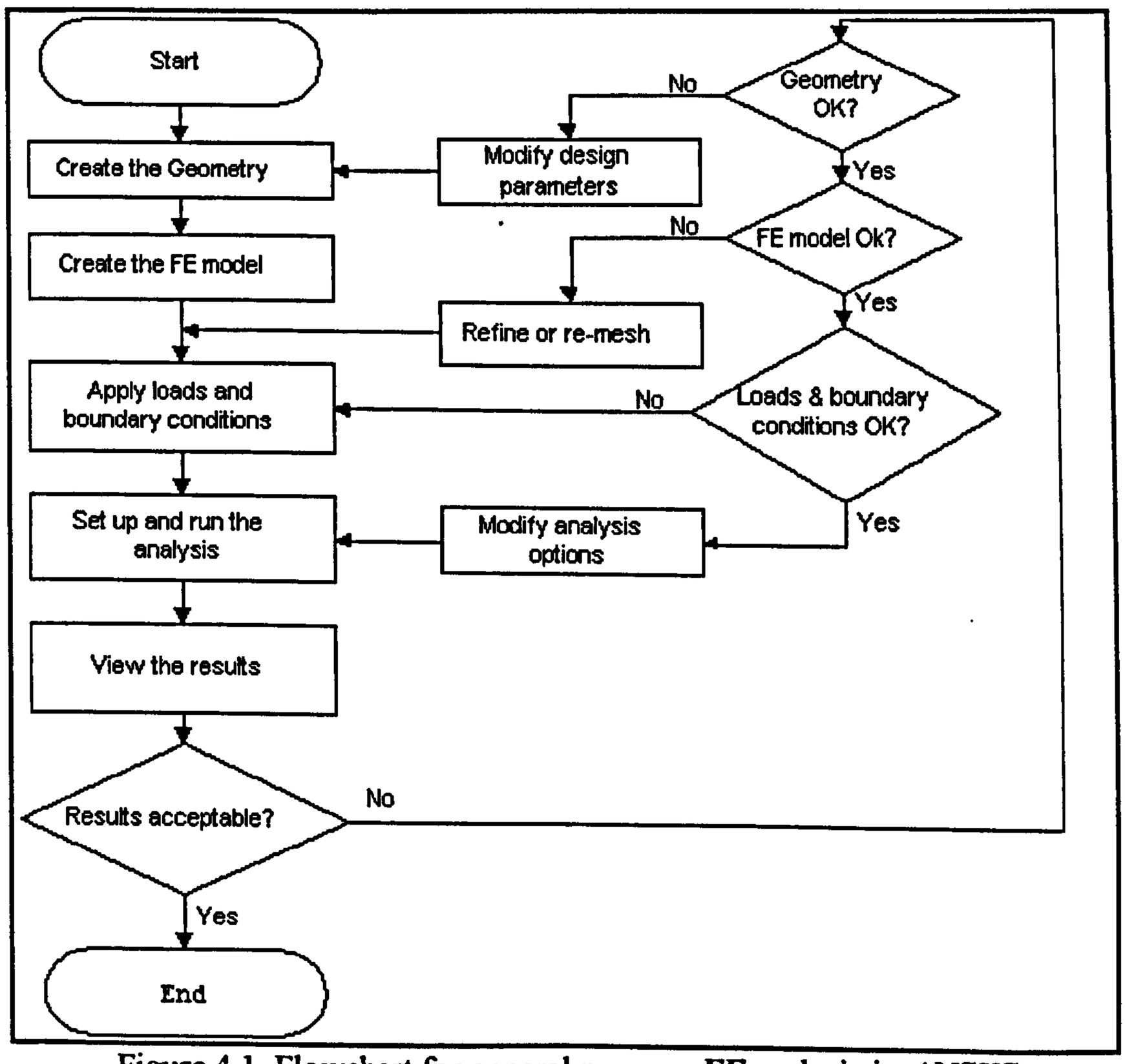

Figure 4.1 Flowchart for general purpose ***FE*** analysis in ***ANSYS***

4.4 FE STRESS ANALYSIS OF THE ROTOR DISC

The design of the rotor of the ***PMAF*** high-speed generator is the most crucial part of the machine. Hence a reasonable attention is paid towards ensuring the mechanical integrity of the rotor. For stress analysis, the rotor is treated as any structural problem which is under static loadings, hence the governing equations which describe the ***FE*** are presented hereafter.

4.4.1 Theory and general considerations for FE stress analysis

For linear materials involved in any mechanical structure, the stress strain relationship in each element can be described as follows:

$$\{\sigma\}=[D]\{\varepsilon\} \tag{4.1}$$

where:

$\{\sigma\}$ = stress vector $\begin{bmatrix}\sigma_x & \sigma_y & \sigma_z & \sigma_{xy} & \sigma_{yz} & \sigma_{xz}\end{bmatrix}^T$

$[D]$ = elasticity matrix

$\{\varepsilon\}$ = total strain vector $\begin{bmatrix}\varepsilon_x & \varepsilon_y & \varepsilon_z & \varepsilon_{xy} & \varepsilon_{yz} & \varepsilon_{xz}\end{bmatrix}^T$

Also the strain can be described as:

$$\{\varepsilon\}=[B]\{a\} \tag{4.2}$$

where $[B]$is the shape function which describes the geometry and variable change over each element and $\{a\}$is the nodal displacement vector at each node of the element. At equilibrium state, the following formulation can be achieved:

$$\{F\}=[K]\{a\} \tag{4.3}$$

where $\{F\}$is the overall external force vector and $[K]$is the element stiffness which can be found as:

$$[K]= \int [B]^T [D] [B] \, d(vol) \tag{4.4}$$

For the overall domain, the global stiffness matrix can be determined from the summation of the overall element stiffness matrixes, thus Equation 4.4 can be generalised for the whole elements as follows:

$$\{F\}=[K]^g \{a\}^g \tag{4.5}$$

where

$$[K]^g = \sum_g [K] \tag{4.6}$$

The summation of element stiffnesses is performed over the elements which share a particular nodal point.

These equations are common for structural finite element method [69]. The analytical solutions that have been presented in Chapter Three can be used to solve these problems but mainly with many simplifying assumptions. Hence they are unable to solve complex structural geometry with different materials. Thus, ***FE*** solution overcomes the problems encountered with the analytical solutions and can be ideal for solving complex structural problems. However, when performing ***FE*** analysis, the following general guidelines should be considered:

- The results obtained from the ***FE*** analysis should always be examined closely for discrepancies or checked against other solutions.
- A compromised mesh density should be maintained for the model for good accuracy and acceptable time. Normally it is preferred to start with coarse meshing and then refine gradually till there is no significant change in the obtained results.
- A good mesh should contain smaller elements at the area of interest and in the region where rapid variation on the geometry is found.
- Inaccurate representation of the actual loads or boundary conditions leads to inaccurate results even if a good mesh is used.

- Rigid body motion of the model should be prevented by means of displacement restrain in certain directions. More detailed guidelines for ***FE*** modelling can be found in [69].

4.4.2 Initial stress analysis of the *PM* rotor using *2D FE* model

The ***PM*** rotor which has been described in Chapter Three, has only considered the ***PM*** and the retainment ring for stress analysis since they are the most critical parts in the rotor. In addition, the analytical stress analysis was based on the assumption that there is no deformation hence no stresses in the axial direction of the rotor and both ***PM*** and retainment ring have the same mechanical and physical properties. In contrast, the rotor consists of four different layers each layer presents a different material with different mechanical and physical properties. Moreover, the permanent magnet in the final rotor design is segmented into a number of magnets called poles with several proposed shapes, which in turn adds more complexity to the rotor structure. This has called for the utilisation of the ***FEM*** for the stress analysis of the rotor of the ***PMAF*** high-speed generator.

In fact, the ideal ***FE*** modelling for the proposed design of the rotor would be a ***3D*** model. However, ***3D*** model requires considerable effort and is time consuming especially at the earlier stage of the design where parametric analysis is required to investigate the mechanical integrity of several proposed designs. Moreover, ***3D*** model requires large number of nodes, hence inevitable coarse meshing will be forced due to the limitation on the number of nodes available for the current software package. In response to this problem, it was decided to perform the initial stress analysis, investigations and parametric analysis for mechanical integrity of the rotor using ***2D FE*** modelling. Once the final geometry with its final design data is determined, a ***3D*** model then can be used for obtaining the final results of the rotor.

One of the methods could be used for modelling the current rotor in two-dimensional modelling is the planar form [13]. The planar form allows for modelling of the whole rotor including segmented magnets. However, such a model lacks some of the accuracy since it assumes that there is no deformation in the axial direction of the

rotor hence neglects the axial stresses. Moreover, in this type of modelling, in order to prevent rigid body motion, spring elements should be introduced between the nodes at the inner surface of the rotor and a single constrained node placed at the centre of rotation. Thus, adding another source of uncertainty to the results since the results will be affected by the specified values of stifnesses for these springs.

Accordingly, the alternative option is to use the ***2D*** axisymmetric ***FE*** modelling for the analysis of the simplified rotor. In this analysis, annulus ***PM*** disc is inevitably assumed and only half of the rotor is modelled in the $x-y$ plane. Although the simplified rotor has four different concentric layers, the first axisymmetric ***FE*** model was performed for only two layers that represent the ***PM*** and the retainment ring. This was required in order to check the validity of the ***FE*** model against the analytical solution that was performed on similar layers in Chapter Three. Then all layers were considered and a parametric analysis is carried out to investigate the influence of some design parameters on the mechanical integrity of the rotor. First, the ***ANSYS*** program structure written for the axisymmetric ***FE*** model is described hereafter.

4.4.2.1 ANSYS program structure for the axisymmetric *FE* stress model

For this analysis, the ***ANSYS*** package was operated in the batch mode in which all commands are written in text file using ***APDL*** to allow for any changes required on the ***FE*** model and alteration of the design parameters. The file is read and executed automatically into the ***ANSYS*** processor and the output results are written to an output file where results of interest are viewed graphically in the ***ANSYS*** general postprocessor. This method is contrast to using the Graphical User Interface (***GUI***) to enter and analyse the model.

The ***ANSYS*** environment is divided into several subsections. The begin stage (***/BEGIN***) is used to define the main parameters of the rotor disc. In the pre-processor stage (***/PREP7***), the model of the simplified rotor is developed, material properties are defined and assigned, areas are meshed and loads and boundary conditions are applied. In the solution processor (***/SOLU***) the finite element solutions are generated. Finally,

in the postprocessor stage (***/POST1***), the outputs are generated and results obtained are stored and visualised.

For this type of analysis, The ***ANSYS PLANE42*** element type is selected. The ***PLANE42*** element is defined by four nodes having two degrees of freedom at each node that are translation in the nodal x and in the y directions. Since the simplified rotor of retainment ring and ***PM*** discs is assumed symmetric about the centreline of the shaft, it is only necessary to model half of the geometry in ***ANSYS***. Hence, the parameter option for the defined element is set as axisymmetric elements.

In reality, the retainment ring is assembled on the permanent magnet disc via shrink fit. To simulate the interference fit between retainment ring and the ***PM*** disc, a point-to-point contact element known in ***ANSYS*** as ***CONTAC52*** was introduced between the two surfaces of contact. The amount of interference fit required is inputted in the pre-processor stage as one of the real constants defined by ***ANSYS*** for this type of elements. Other real constants such as normal, K_N, and sticking, K_S, stiffnesses are also defined and their values were also inputted at that stage. In general, random values for these stiffnesses can be chosen. High stiffness values are recommended to accelerate the convergence rate; however, too high stiffness values could sometimes result in a non-converged solution. As a general rule, the normal stiffness, K_N, can be estimated by the following calculations:

$$K_N = C_R E \tag{4.7}$$

where C_R is the contact radius and E is the material Young's Modulus of elasticity and the sticking stiffness, K_S, can be found as:

$$K_S = K_N/100 \tag{4.8}$$

However, in some cases it is useful to change K_N values between the load steps in order to obtain an accurate converged solution.

Once the element types are defined, all the relevant properties for the material used in the model are specified. For this application, the required properties are mass density ρ_m, Young's modulus of elasticity E, Poisson's ratio ν and friction coefficient μ_u.

Next, the different regions of the model are defined and materials are assigned to each region. In the axisymmetric models all specified regions are presented by areas. In this particular analysis, rectangular area represented the retainment ring and the ***PM*** disc since they have uniform rectangular cross-sections. These rectangles are specified by supplying their x and y coordinates. Figure 4.2-a) shows the ***ANSYS*** axisymmetric model for the geometry of the ***PM*** disc and retainment ring. The design data and material properties for the ***PM*** and the retainment ring are found in Table 3.8 in Chapter Three.

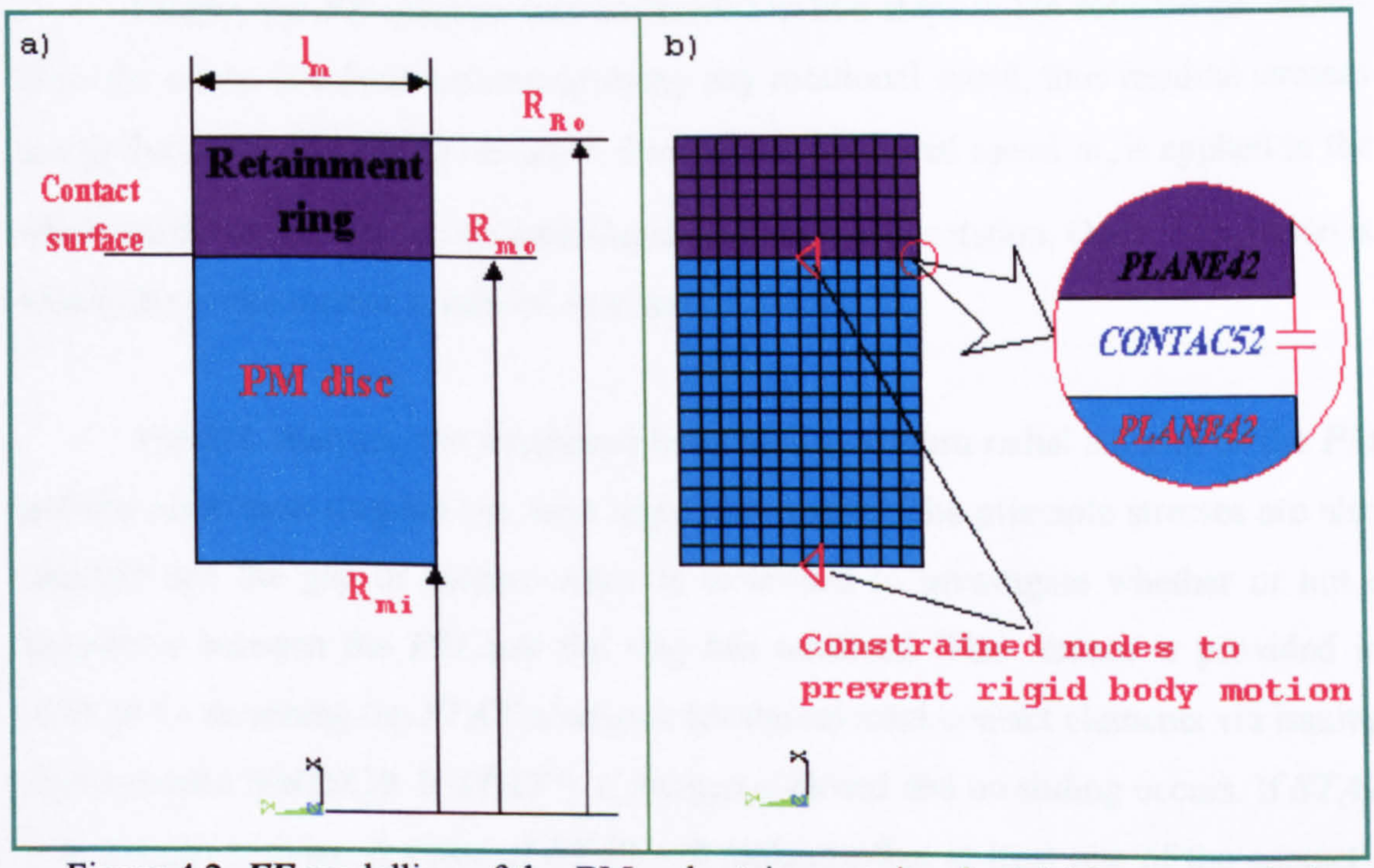

Figure 4.2 ***FE*** modelling of the ***PM*** and retainment ring for initial stress analysis.
a) creating geometry b) meshing and applying boundary conditions

With all of the areas defined and given material properties, the model can now be meshed. Meshing of the model involves dividing each area into the small elements which will be used for the finite element solution. The ***ANSYS*** processor provides an automated method for meshing the model in which software chooses the meshing

parameters. However, in this analysis, the meshing was controlled manually where quadrilateral mapped meshing is performed by setting an appropriate number of divisions for the lines enclosing the rectangular areas. The adopted meshing for the model can be seen in Figure 4.2-b). When meshing the separated regions it is necessary to ensure that the mating nodes are lined up at the surface where they supposed to meet. This is required since contact elements are created separately after meshing, where each element is connecting two opposite nodes together.

Once the elements are created, boundary conditions and loads must be applied to the model. For this analysis, the ***PM*** and the ring are allowed to rotate about y-axis, and rigid body motion for the whole model is prevented by constraining one node at each separate area i.e. at $x = R_{mi}$ and $y = 0$ for the ***PM*** and $x = R_{Ri}$, $y = 0$ for the retainment ring as can be seen in Figure 4.2-b).

Finally, the ***FE*** solution was performed in two steps in the solution processor. First, the model is solved without applying any rotational speed, thus residual stresses due to the shrink fit alone is obtained. Second, the rotational speed ω_y is applied to the whole model to account for the centrifugal stresses due to rotation. Once the solution is found, the postprocessor is utilised to examine the results.

For this analysis, the maximum hoop and maximum radial stresses in the ***PM*** and the retainment ring are the most important results. The principle stresses are also checked and the gap or contact status is examined to investigate whether or not a separation between the ***PM*** and the ring has occurred. This feature is provided in ***ANSYS*** by screening the ***STAT*** condition for the selected contact elements via issuing the command ***NMISC,9***. If ***STAT*** = 1, the gap is closed and no sliding occurs. If ***STAT*** = 3, the gap is open. A value of ***STAT*** = 2 indicates that at least one of the contact's nodes is sliding relative to the other. Another simple method of determining the contact status is to check the values of radial stresses at all nodes on the surfaces of contact between the ***PM*** disc and ring. A negative radial stress value indicates the availability of contact and no separation is occurring at the design rotational speed. The detailed code written for the ***FE*** **2D** axisymmetric analysis can be found in ***Appendix D***.

4.4.2.2 Validation of the axisymmetric *FE* stress model

For the validation process of the adopted axisymmetric ***FE*** model, the results obtained are compared to the results obtained from the analytical solution performed on similar structure. The computed results of interest are the maximum radial and hoop stresses and the status of contact between the magnet and the ring. The comparison between the results obtained from both solutions are summarised in Table 4.1. More detailed results concerning radial and hoop stress distribution in the model obtained from both models are presented graphically in Figures 4.3 and 4.4. As it can be seen from the results obtained that a good agreement between the analytical and ***FE*** model is achieved, thus further analysis and investigations on the rotor structure is performed with great confidence using the adopted ***FE*** model.

Stresses		PM disc		Retainment ring	
		$R_{mi} = 27$ mm	$R_{mo} = 47$ mm	$R_{Ri} = 47$ mm	$R_{Ro} = 55$ mm
Radial [MPa]	Analytical	0	-84.77	-84.77	0
	FEM	-3.97	-77.17	-77.17	8.75
Hoop [MPa]	Analytical	209.98	66.33	1228.21	1017.48
	FEM	210.00	70.27	1232.5	1019.3

Table 4.1 Comparison of stress results obtained by analytical and ***FE*** solutions for the simplified ***PM*** rotor

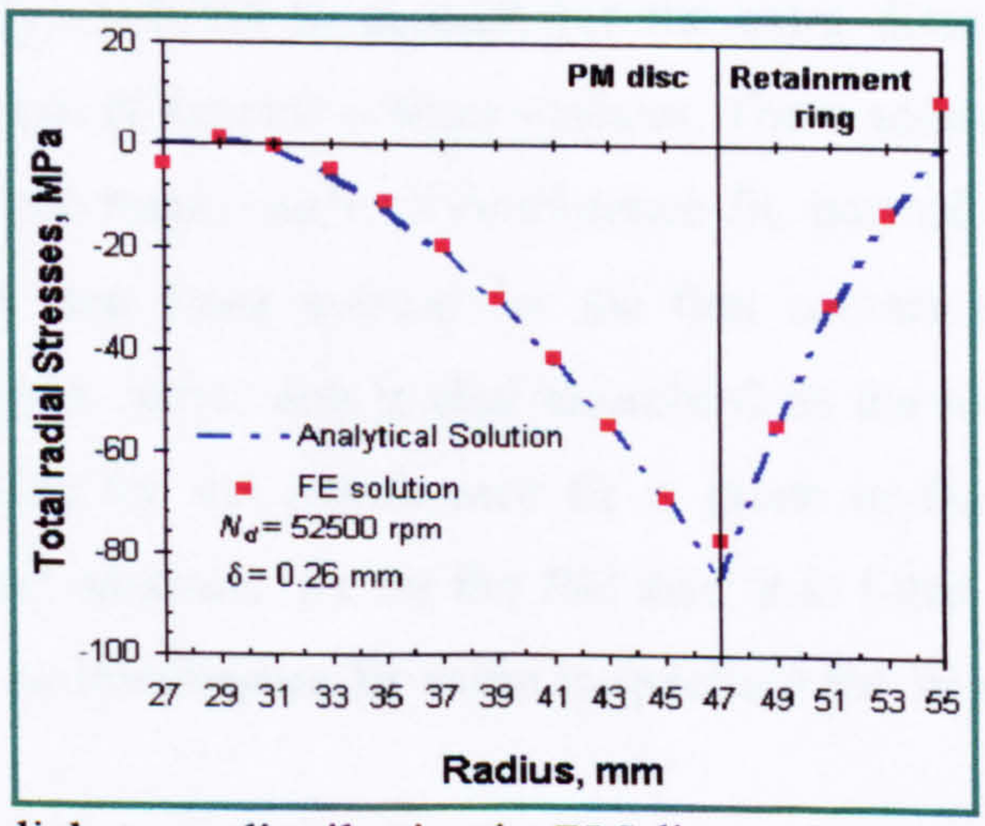

Figure 4.3 Total radial stress distribution in ***PM*** disc and retainment ring obtained by ***2D*** axisymmetric ***FE*** model and analytical solution

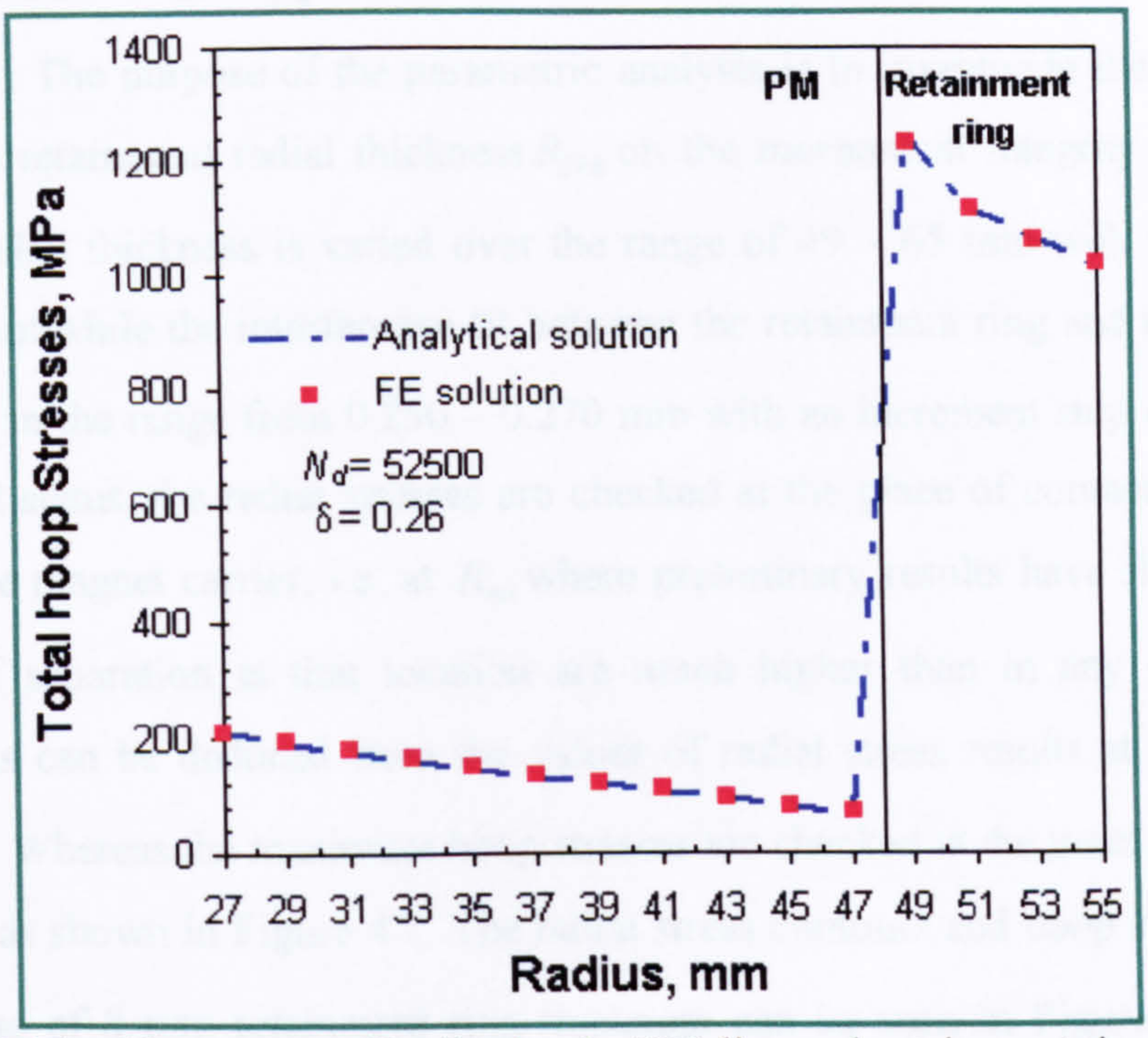

Figure 4.4 Total hoop stress distribution in ***PM*** disc and retainment ring obtained by ***2D*** axisymmetric ***FE*** model and analytical solution

4.4.2.3 Parametric analysis

The next analysis is performed for the simplified rotor taking into account the four different materials assembled on the rotor which are presented by four concentric discs as shown in Figure 4.5. The same code which was written for the previous analysis was slightly modified to account for the extra discs. Also, more contact elements are introduced at the new contact surfaces. These additional contact elements have their own real constants such as interference fit, normal and sticking stiffness values are different than those defined for the first contact element. It should be noticed that the magnet carrier disc is also assembled on the rotor hub via shrink fit, thus a specified value for the interference fit is given in the real constant of the corresponding contact elements. As for the ***PM*** disc, it is fitted on the magnet carrier by sliding fit, thus no interference fit value is specified for its corresponding contact element.

The analysis is performed for the rotor having the design data given in Table 4.2 and the mechanical properties for the materials used in the analysis are given in

Table 4.3 where ν and μ_u are the material Poisson's ratio and friction coefficient respectively. The purpose of the parametric analysis is to investigate the influence of varying the retainment radial thickness R_{Thk} on the mechanical integrity of the rotor. The ring radial thickness is varied over the range of 49 – 65 mm with an increment step of 2 mm while the interference fit between the retainment ring and the ***PM*** δ_3 is also varied in the range from 0.250 – 0.270 mm with an increment step of 0.010 mm. For contact status, the radial stresses are checked at the place of contact between the ***PM*** and the magnet carrier, i.e. at R_{mi} where preliminary results have shown that the chances of separation at that location are much higher than in any other contact locations as can be deduced from the values of radial stress results at R_{mi} shown in Figure 4.6. Whereas the maximum hoop stresses are checked at the inner surface of the ring, R_{Ri}, as shown in Figure 4.7. The radial stress contours and hoop stress contours for the case of 8 mm retainment ring thickness can be seen in Figures 4.8 and 4.9 respectively.

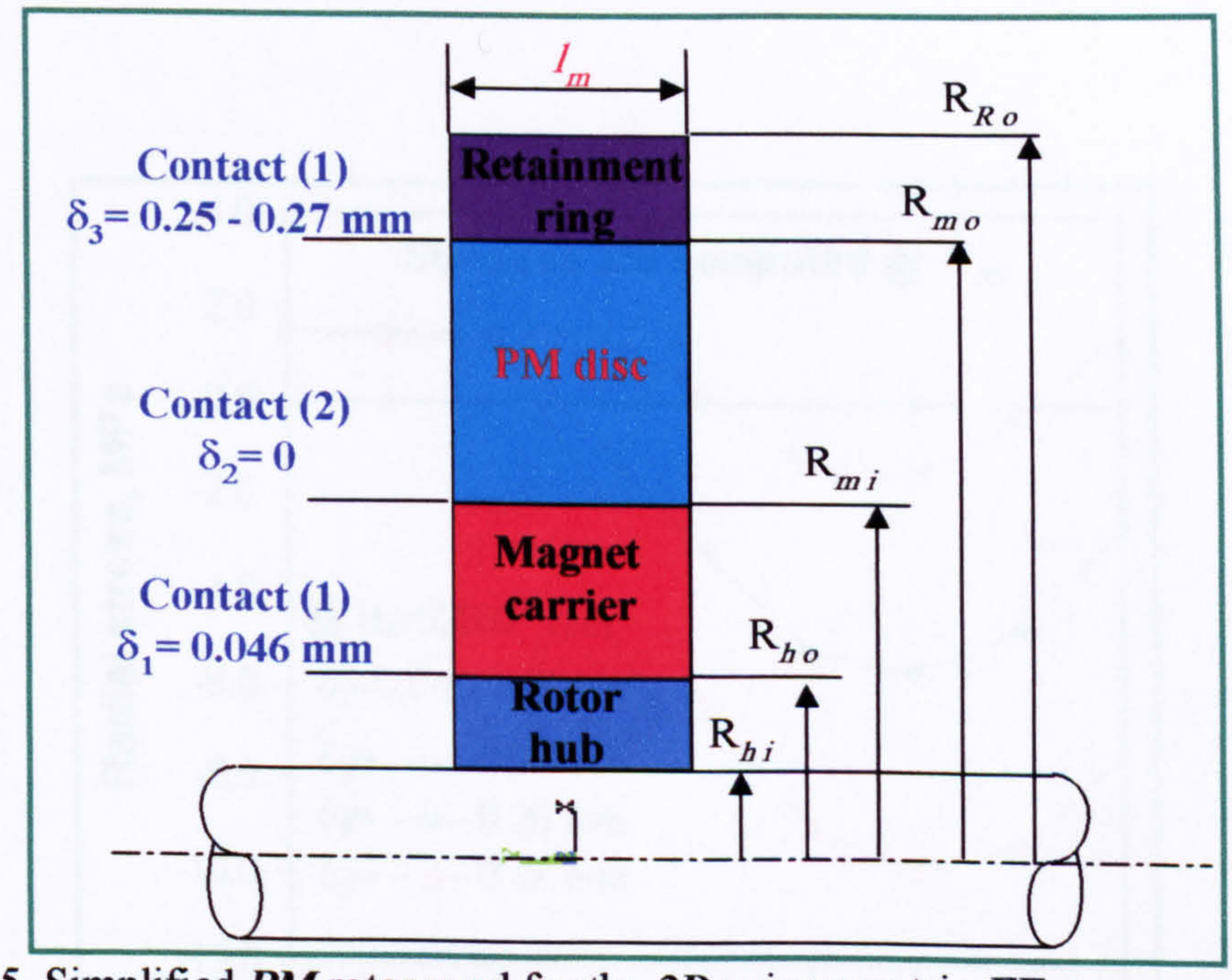

Figure 4.5 Simplified ***PM*** rotor used for the ***2D*** axisymmetric ***FE*** stress analysis

R_{hi} mm	R_{ho} mm	R_{mi} mm	R_{mo} mm	R_{Thk} mm	δ_1 mm	δ_2 mm	δ_3 mm	l_m mm	N_d mm
7.0	14.0	27.0	47.0	2 – 18	0.046	-	0.250 – 0.270	17.0	52500

Table 4.2 Design data used for the parametric analysis performed by ***2D FEM***

Material	Type	ρ_m kg/m^3	E GPa	ν	μ_u
Rotor hub	17/4 PH steel	7800	210	0.3	0.4
Magnet carrier	Alumec 79	2750	71	0.29	0.4
PM	Sintered NdFeB	7500	160	0.3	0.4
Retainment ring	Maraging G125	7800	200	0.3	0.4

Table 4.3 Mechanical properties for the material used in the ***FE*** model of the ***PM*** rotor

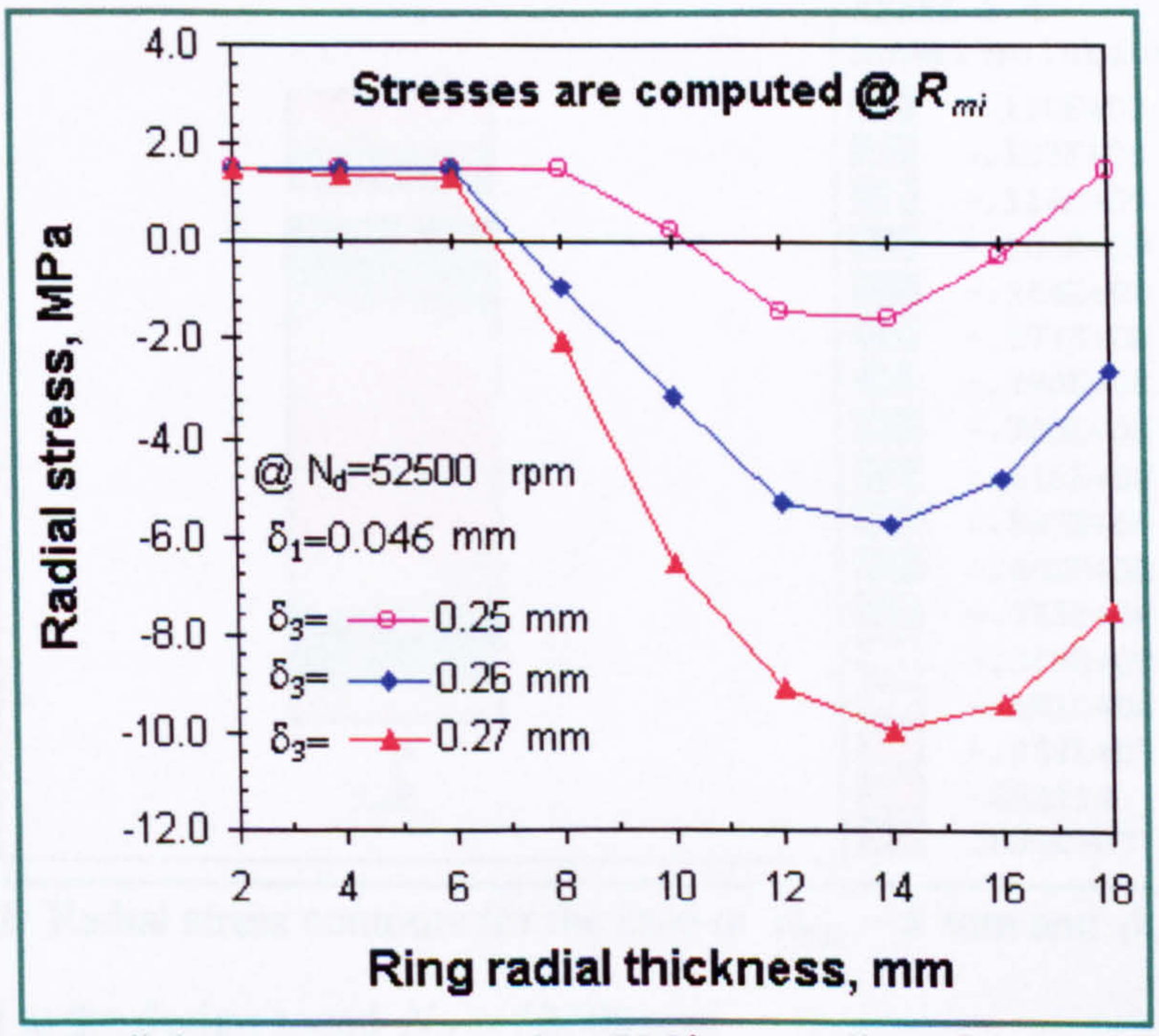

Figure 4.6 Radial stresses computed at ***PM*** inner radius of the rotor at different retainment ring thicknesses and different interference fits

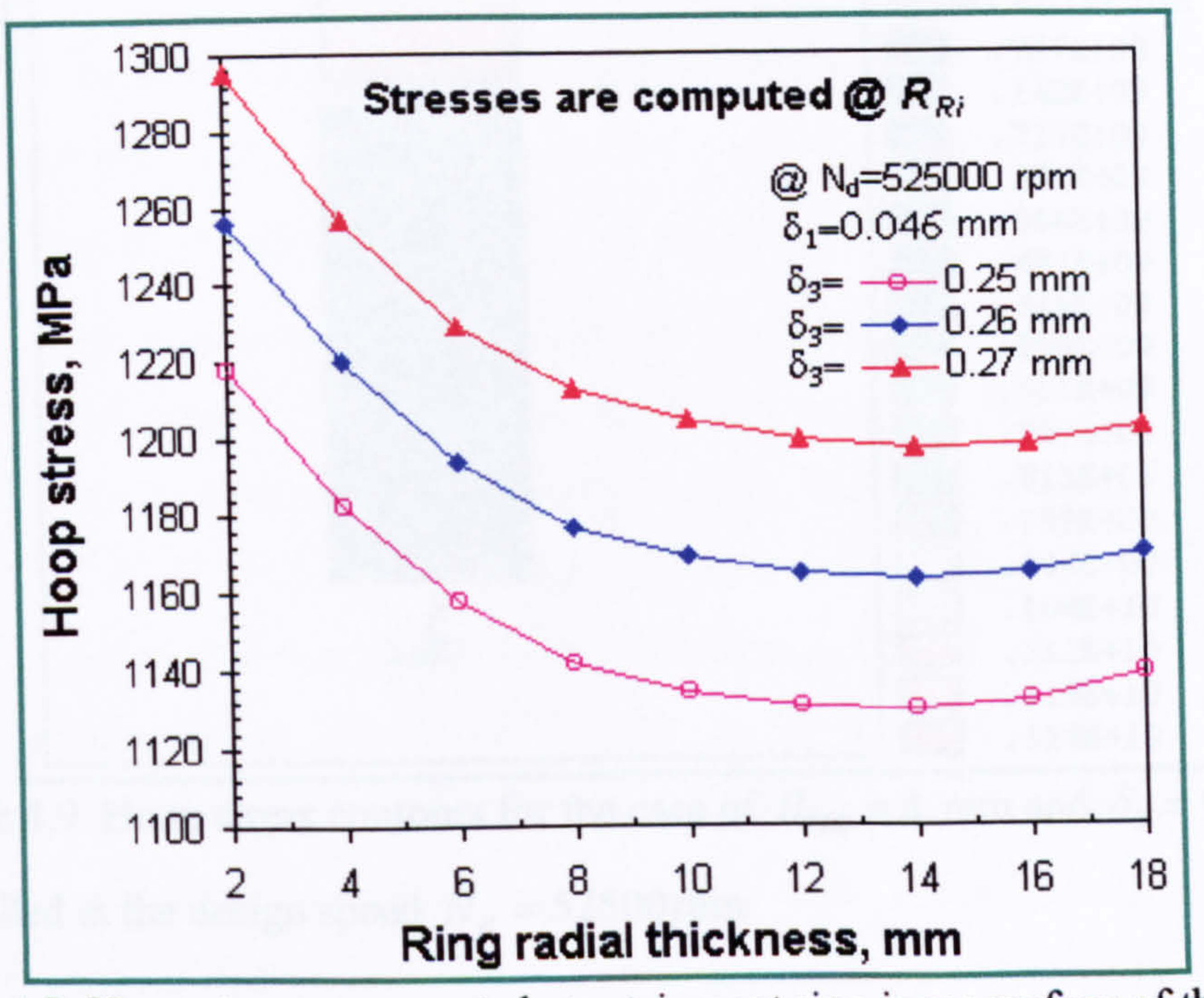

Figure 4.7 Hoop stresses computed at retainment ring inner surface of the rotor at different retainment ring thicknesses and different interference fit

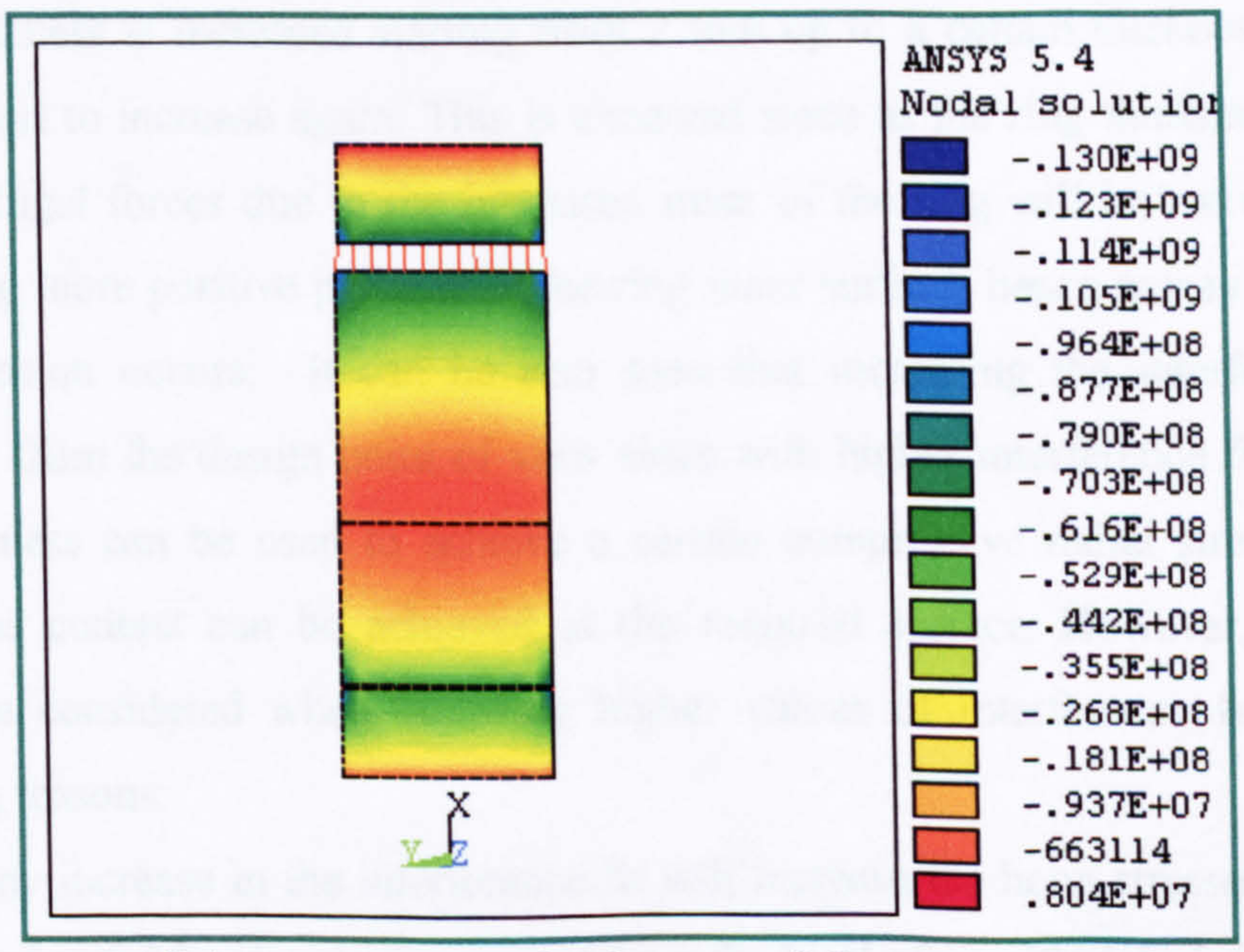

Figure 4.8 Radial stress contours for the case of $R_{Thk} = 8$ mm and $\delta_3 = 0.26\,\text{mm}$ modelled at the design speed $N_d = 52500\,\text{rpm}$

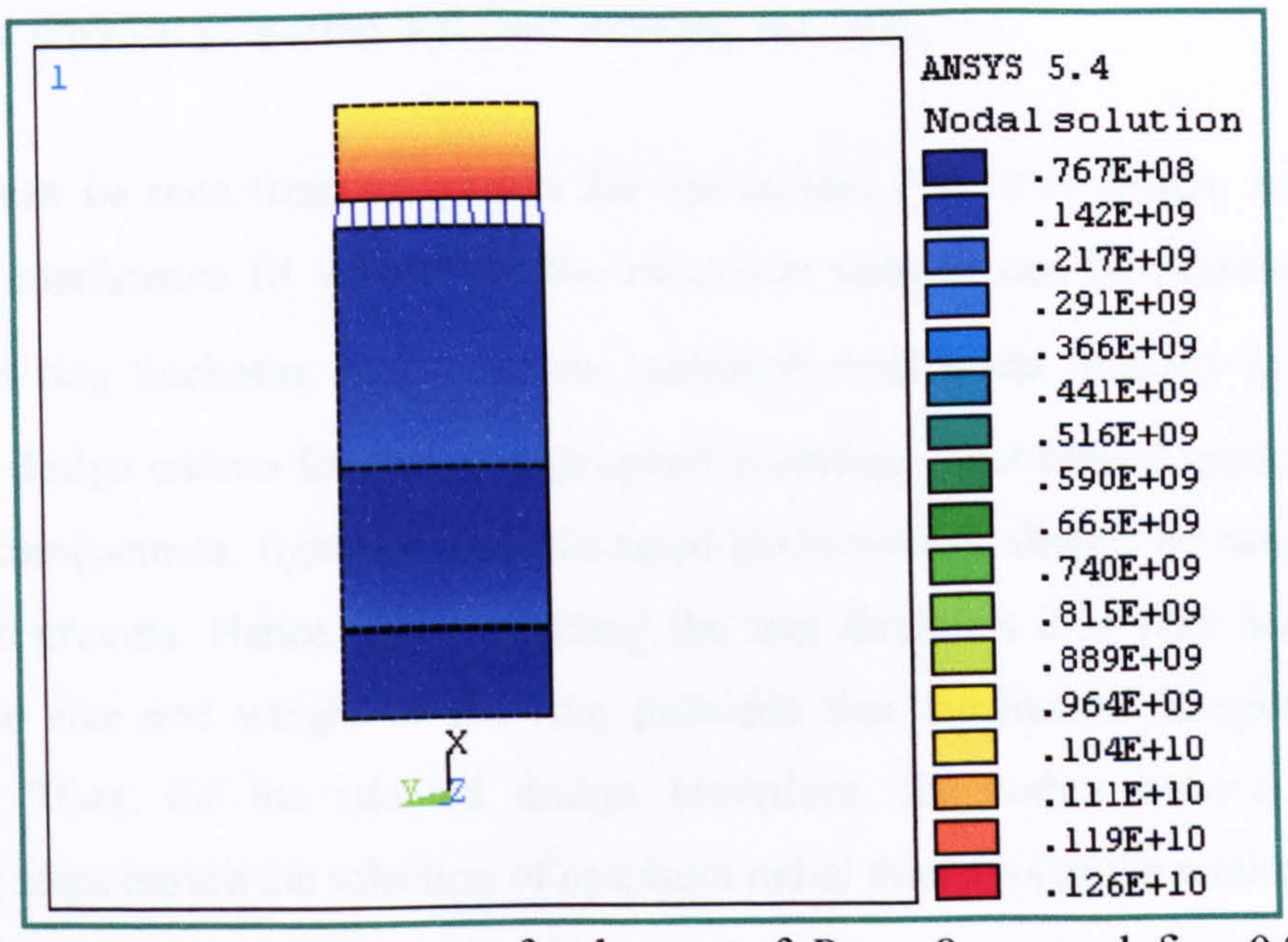

Figure 4.9 Hoop stress contours for the case of $R_{Thk} = 8$ mm and $\delta_3 = 0.26\,\text{mm}$ modelled at the design speed $N_d = 52500\,\text{rpm}$

It can be seen from the results that for a particular ***PM*** rotor, there is an optimum thickness for the retainment ring where hoop and radial stresses can be reduced to their minimum values. The stresses are decreased as the retainment ring radial thickness is increased starting from 2 mm up to a certain thickness where the stresses start to increase again. This is expected since as the ring thickness increases, the centrifugal forces due to the increased mass of the ring will be increased. Thus, developing more positive pressure at the ring inner surface, hence more radial growth and expansion occurs. It can be also seen that increasing the interference fit is beneficial from the design point of view since with higher interference fit, rings with less thickness can be used to achieve a certain compressive radial stress. Hence, a continuous contact can be achieved at the required surface. However, precautions should be considered when choosing higher values of interference fit due to the following reasons:

- Any increase in the interference fit will increase the hoop stresses at the inner surface of the ring, hence approaching the level of specified design strength.
- High interference fit values requires higher temperature difference to allow for the required expansion for the assembling of the matting parts. The limitation of the temperature on the retainment rings and on the permanent magnets does

not allow for excessive temperature since it will deteriorate their mechanical and physical properties and their ultimate strengths.

It can be seen from the graphs for the current *PM* rotor design, and for the specified interference fit values δ_3, the minimum stresses can be achieved with a retainment ring thickness $R_{Thk} = 14\,\text{mm}$. Although mechanical integrity is the most important design criteria for such a high-speed machines, other related aspects such as ultimate compactness, lightness and increased performances should be considered in the design process. Hence, when selecting the ring thickness it is very important to reduce the size and weight of the ring provided that mechanical integrity can be achieved. Thus, for the adopted design procedure, the author believes that the following steps ensure the selection of optimum radial thickness of the retainment ring:

- Start with the highest interference fit values. If the temperature required for the expansion for the specified interference fit value exceeds the limits for any of the specified materials then the next lower value of the interference fit is selected. For the current design, according to the manufacturer recommendation and based on the heat treatment process of the ring, the maximum allowable temperature on the ring after heat treatment should not exceed $350°C$. The minimum temperature required, ΔT, for the expansion for each specified interference fit value is calculated by Equation 3.62 in Chapter Three. The results are obtained for thermal expansion coefficients of $\alpha_T = 11\times10^{-6}\ K^{-1}$ for the ring and with an additional temperature of 50 $°C$ is considered to account for the temperature decay during assembling process. The results obtained are presented in Table 4.4.

δ_3, [mm]	$R_c = 47\,\text{mm},\ \alpha_T = 11\times10^{-6}\ K^{-1}$		
	ΔT, [$°C$]	T_{mag}, [$°C$]	T_{Ring}, [$°C$]
0.250	484	-190	344
0.260	503	-190	363
0.270	523	-190	383

Table 4.4 Minimum temperatures required for the expansion of the retainment ring

Where T_{mag} is the maximum cooling temperature can be maintained for the PM disc using liquid nitrogen and T_{ring} is the minimum heating temperature required for the ring expansion and it is calculated as follows:

$$T_{ring} = \Delta T - \left|T_{mag}\right| + 50 \tag{4.9}$$

It can be seen from Table 4.4 that the interference fit $\delta_3 = 0.270\,\text{mm}$ requires high temperature for expansion, hence it was excluded from the selection process due to the temperature limitations. Therefore, the interference fit of 0.260 mm is selected for the current design.

- Once the proper value of interference fit is set, a minimum radial thickness of the ring is selected provided that the maximum hoop stresses are not exceeding the specified design strength for each specified material. It can be seen from Figure 4.7 that the predicted hoop stresses even at the lowest values of ring thickness are still bellow the specified design strength $\sigma_d = 1333\,\text{MPa}$ for the retainment ring.
- For any particular selected thickness of the ring, the contact status at each surface of contact, in particular the contact at the surface between the magnet carrier and the *PM* itself is checked. This can be simply done by viewing the radial stress results at the place of interest. Negative radial stress indicates a continuous contact is maintained at the design speed. From Figure 4.6, it can be seen that for the selected value of interference fit, a minimum radial thickness of 8.00 mm is required for the retainment ring to achieve a continuous contact at the surface between the magnet carrier and the *PM* disc.

By adopting such processes in determining the retainment ring thickness, not only the mechanical integrity of the rotor is insured, but also other design aspects such as compactness and increased performance have been considered. The final step in the structural *FE* analysis is to perform a *3D FE* modelling for the final design of the rotor to account for the unsymmetrical and non-homogeneous structure due to the segmented *PM* topology. Hence results of the *2D* axisymmetric *FE* model can also be

compared to those obtained from the *3D* model which is described in the following section.

4.4.3 Three-dimensional FE stress analysis of the final rotor

The final design of the rotor has its basic geometry similar to the one which was presented in the *2D* model except that the *PM* is not in the form of annulus disc. In contrast the rotor consists of eight magnets of interchanged polarities having semicircular shapes which were selected at that stage based on the ease of manufacturing. These magnets are held in their positions by the magnet carrier as shown in the sectional view of the rotor in Figure 4.10. As for the detailed dimension of the rotor, they can be found in the *AutoCAD* drawings in *Appendix B*.

The process of performing the *3D* stress analysis is similar to that which have been described for the *2D* analysis except *SOLID45* is used for the *3D* modelling. This element is defined by eight nodes having three degrees of freedom at each node, these are; translation in the nodal x, y, and z directions. The same contact element (*CONTAC52*) is used for defining all contact surfaces. For this analysis, only 1/8 of the full geometry is modelled. The model is constrained at specified nodes to prevent rigid body motion in the z-direction. *ANSYS* software provides two methods for applying symmetry boundary conditions at the surfaces of symmetry. The first method is automatically done through the *GUI*, either in the pre-processor stage or in the solution processor stage, simply by applying the symmetry condition on the picked surfaces that represent the planes of symmetry. The second method is done manually by picking the nodes at the specified surfaces and rotate these nodes in the cylindrical coordinates, then constrain these nodes in the hoop direction and allow them to move only in the radial direction. The modelled section of the rotor and its related hoop stress contours are shown in Figure 4.11-a) and 4.11-b) respectively. Other results can be shown for the full rotor by invoking the symmetric expansion option in the plot control menu. These results can be shown in Figures 4.12 and 4.13.

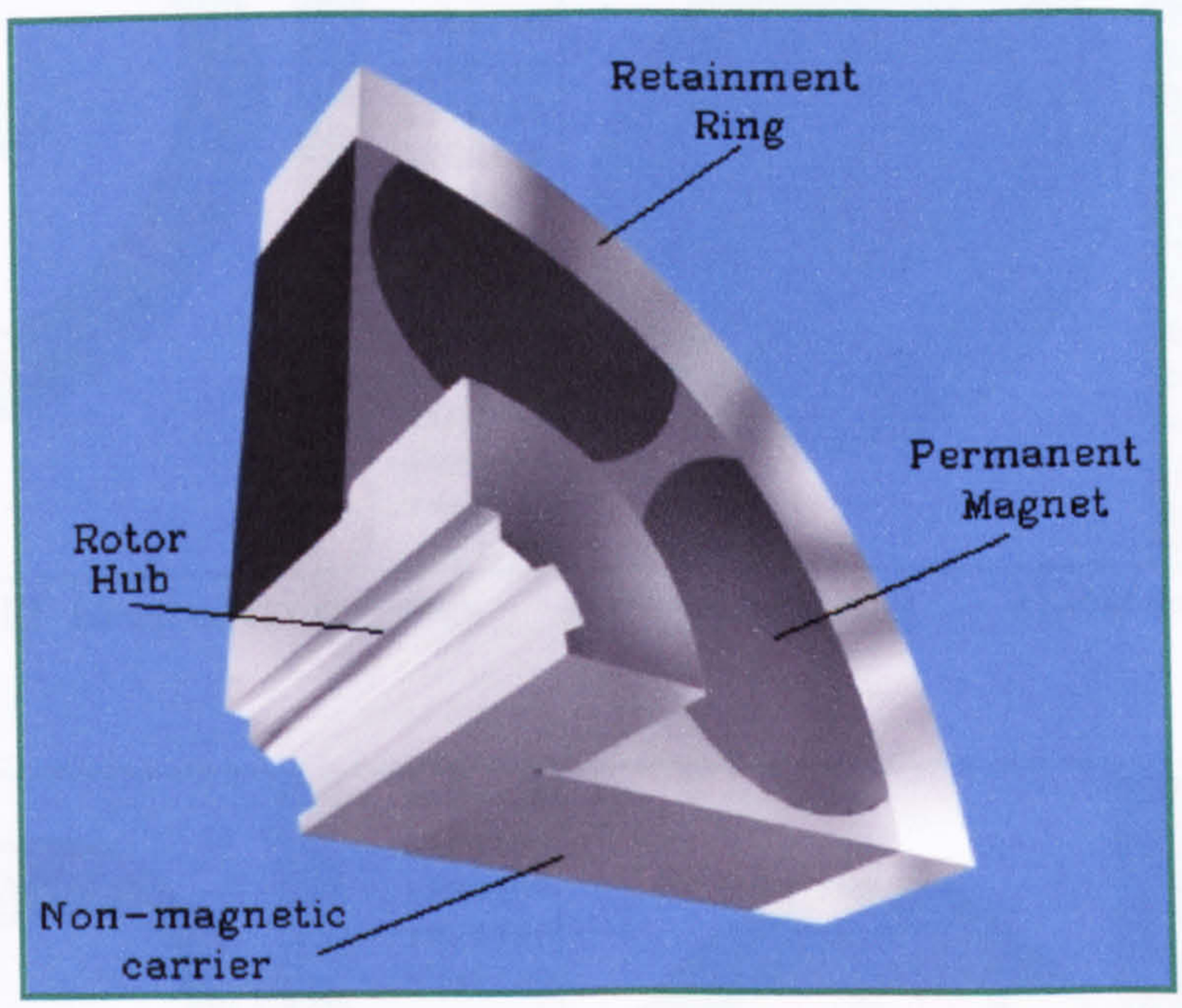

Figure 4.10 Sectional view for the proposed final design of the rotor

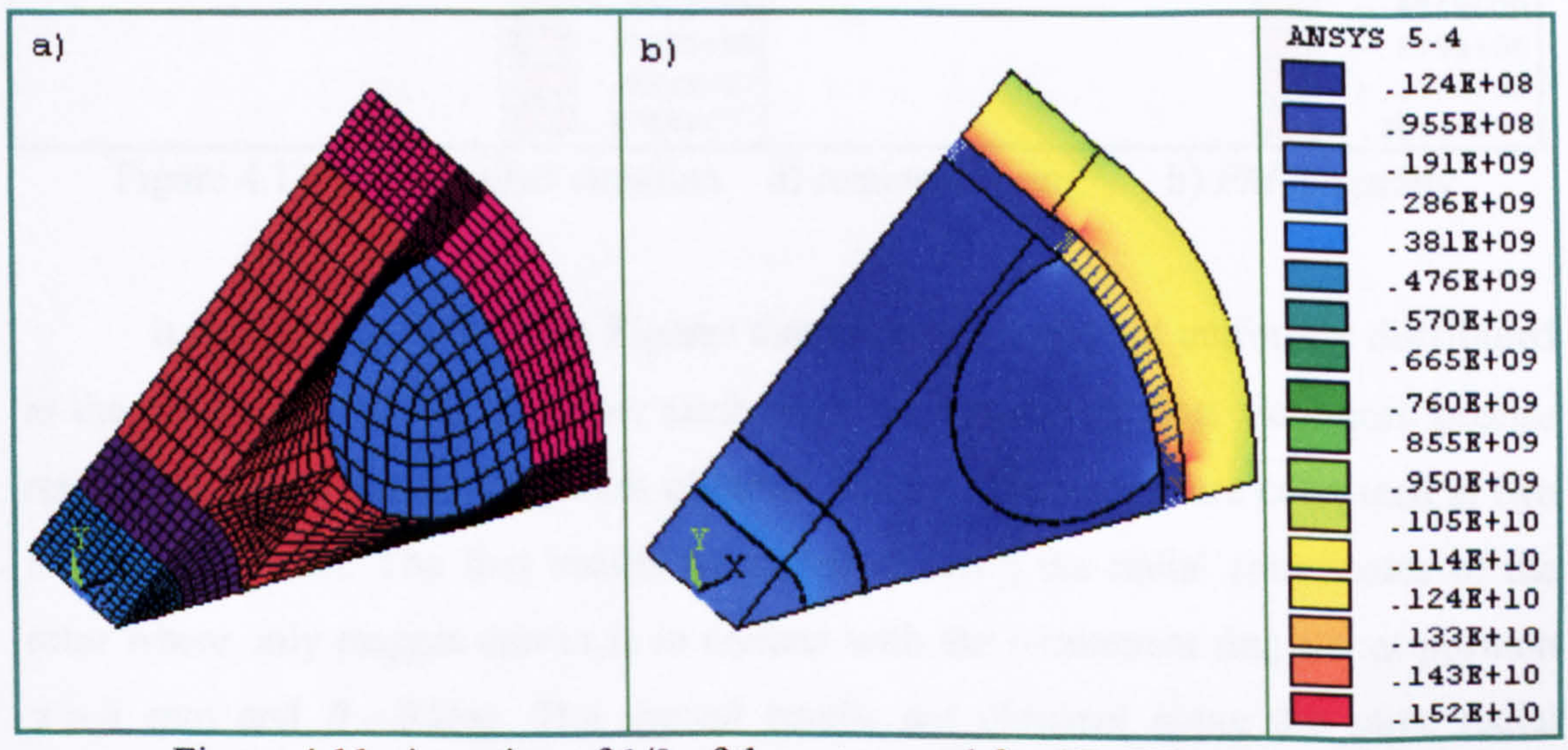

Figure 4.11 A section of 1/8 of the rotor used for ***3D FE*** stress model

a) meshing the model b) hoop stress contours

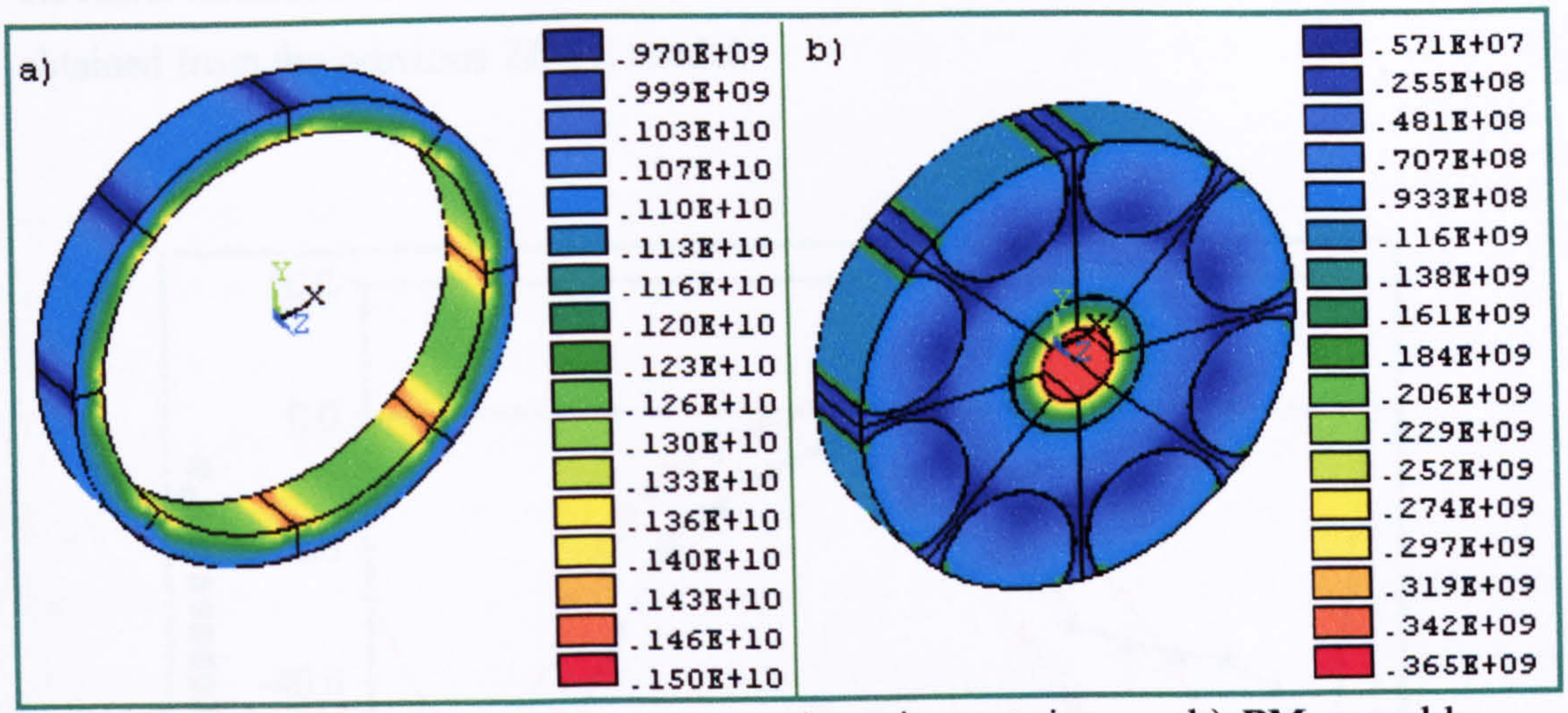

Figure 4.12 Hoop stress contours a) retainment ring b) ***PM*** assembly

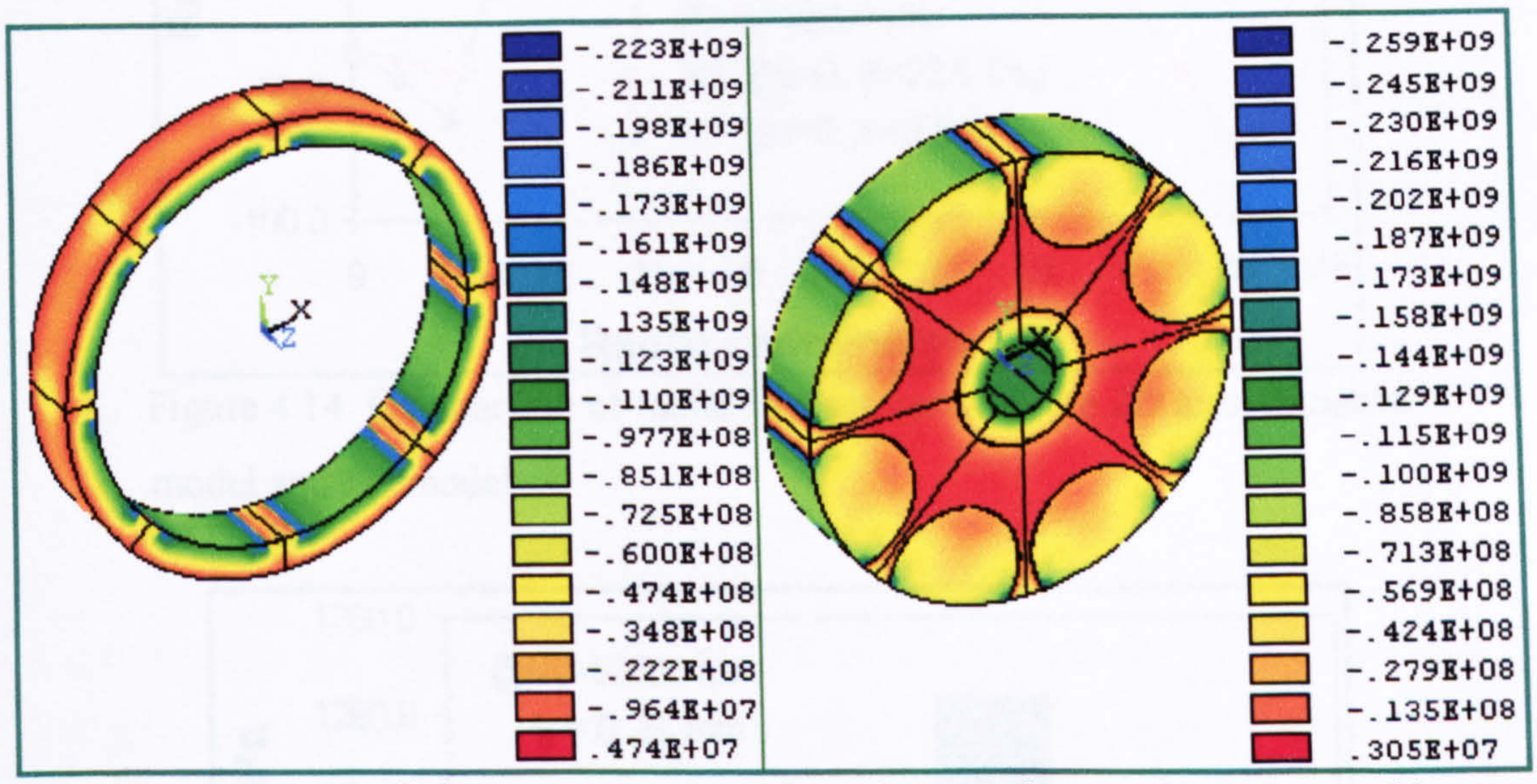

Figure 4.13 Radial stress contours a) retainment ring b) ***PM*** assembly

It can be seen from these Figures that the stresses are not uniformly distributed in the rotor especially at the inner surface of the retainment ring. For more precise results, the radial and hoop stresses obtained from the ***3D*** model are computed at two different positions. The first results are obtained along the radial coordinates of the rotor where only magnet carrier is in contact with the retainment ring i.e. at position $z = 0$ mm and $\theta = 0$ Deg. The second results are obtained along the same radial coordinates but with the angular coordinates is shifted at the centre of the ***PM*** i.e. $z = 0$ and $\theta = 22.5$ Deg. At this position, the ***PM*** is in contact with the retainment ring. The results obtained are presented graphically in Figure 4.14 and Figure 4.15 where

the radial stresses and maximum hoop stresses are compared respectively to the results obtained from the previous ***2D*** FE model.

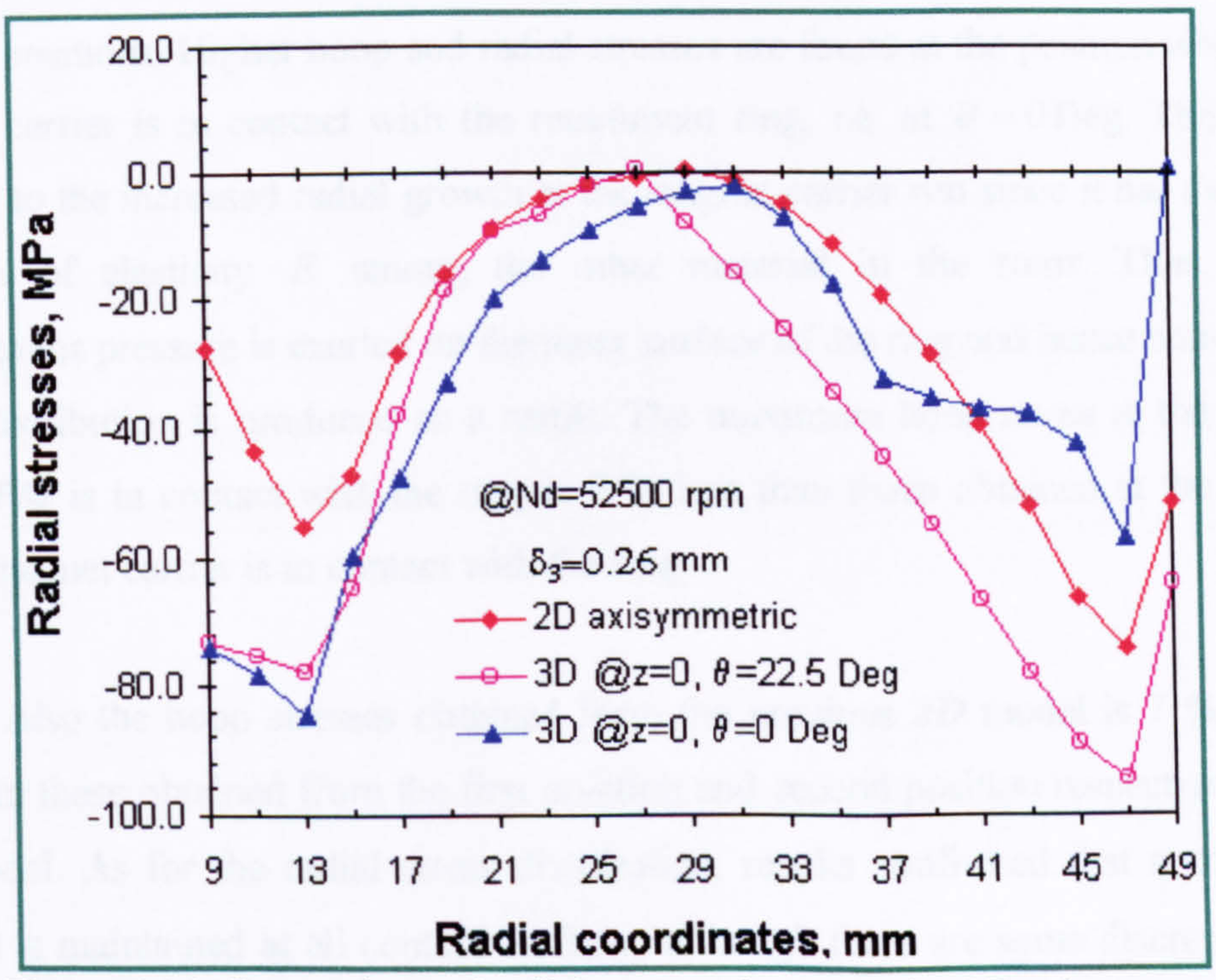

Figure 4.14 Comparison of radial stresses between the ***2D*** axisymmetric model and ***3D*** model

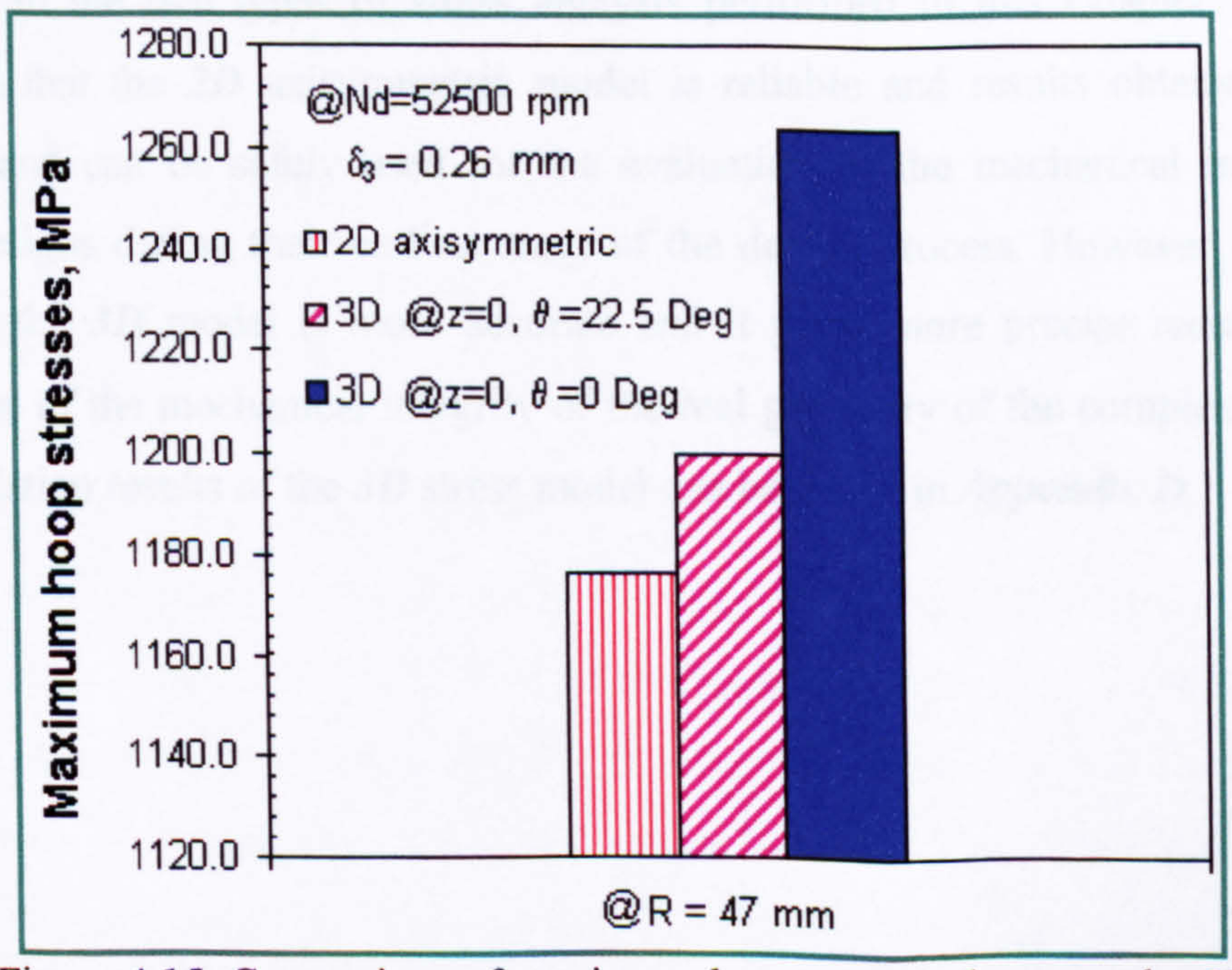

Figure 4.15 Comparison of maximum hoop stresses between the ***2D*** axisymmetric model and ***3D*** model

Both Figures show that there are some discrepancies between the results obtained from the ***2D*** and these obtained from the ***3D*** model. Also, in the same ***3D*** model the results vary according to the place where they are calculated. This is expected since there are two different materials in contact with the ring at different angular positions. Higher hoop and radial stresses are found at the position where only magnet carrier is in contact with the retainment ring, i.e. at $\theta = 0\,\text{Deg}$. This can be referred to the increased radial growth at the magnet carrier rim since it has the lowest modulus of elasticity E among the other material in the rotor. Thus, a non-homogenous pressure is exerted on the inner surface of the ring and hence non-uniform stress distribution is produced as a result. The maximum hoop stress at the position where ***PM*** is in contact with the ring is 5 % less than those obtained at the position where magnet carrier is in contact with the ring.

Also the hoop stresses obtained form the previous ***2D*** model is 7 % and 2% less than these obtained from the first position and second position respectively in the ***3D*** model. As for the radial stress distribution, results confirmed that a continuous contact is maintained at all contact surfaces, although there are some discrepancies in the negative radial stresses due to the non-homogenous geometry.

From the two types of stress analysis performed in this Chapter, it can be concluded that the ***2D*** axisymmetric model is reliable and results obtained can be accepted and can be safely used for the evaluation of the mechanical integrity of several designs during their earliest stage of the design process. However, it is quite clear that the ***3D*** model is more accurate and it gives more precise results for the assessment of the mechanical integrity of the real geometry of the complex structure. The simulation results of the ***3D*** stress model can be found in ***Appendix D***.

4.5 ELECTROMAGNETIC *FEA* OF THE PMAF HIGH-SPEED GENERATOR

With the increased interest in the demand in using ***PM*** machines for different applications, accurate modelling and analysis methods become essential in order to design machines that operate with high power density, high efficiency, high degree of reliability and minimum design and construction costs. The steady state performance of the ***PM*** machines is conveniently explained by the energy conversion process that takes place in electrical machines, which is achieved by linkage of both the stator and the rotor magnetic fields. Therefore the performance prediction depends critically on the accurate computation of the magnetic field distribution in different parts of the machine.

Although a number of special methods for the analysis of ***PM*** machines have been implemented using analytical models [28,32,41,42,70], these analytical models are not always applicable especially in the case of complex machines geometries and for small high-speed machines. Moreover these models are mostly presented in terms of special factors that are affected by the shape and geometrical dimensions of the machine. Therefore the suitable alternative to overcome this difficulty in modelling and analysis of such machines is to use ***FEM***.

FEM shows superiority in providing the required information which later can be used in the ***CAD*** systems. ***FEM*** has been used extensively for modelling electrical machines and to predict their performances [71]. Most of the work has been published in the literature is focused on modelling radial flux machines where a ***2D FE*** model was found satisfactory for such machines [72,73,74]. Few have been published on the modelling and simulation of axial flux or disc type machines [75,76]. However, these ***2D*** models were based on many simplified assumptions and geometries. In addition, some important factors such as end windings and the leakage flux due to the interchanged ***PM*** polarities in the rotor were not considered. In fact axial flux machines do not have a complete symmetrical nature and they are away from being simplified into ***2D*** models. Therefore a ***3D FE*** model was found necessary to evaluate the performance of such machines although a ***2D*** magnetostatic model was used at the preliminary stages

of the design to assist for the evaluation of the effect of type of retainment ring and its radial thickness on the magnetic flux in the air gap.

In this work, the ***ANSYS*** software package is used to perform the electromagnetic analysis for the proposed design of the ***PMAF*** high-speed generator. The postprocessor of the software provides the user with interactive computation and graphics visualisation for the purpose of predicting the synchronous performance of the machines. The software provides the flux plots for different parts of the machine, air gap flux density distribution, thus with the aid of special purpose macros it is possible to view the induced voltage and the harmonics contents in the output waveform. In addition, parameters such as resistance of the windings, inductance, eddy currents and power losses can be computed through the model. In this section, the methods used to evaluate the ***PMAF*** generator performance and parameters mainly using ***3D FE*** magnetostatic models are discussed. At the beginning, the ***2D FE*** model is described and implemented for the purpose of parametric analysis which will be shown in details hereafter. However, the theory for the general magnetostatic ***FE*** formulation is given first in the following subsection.

4.5.1 Theory of the magnetostatic FE analysis

Magnetostatic analysis is governed by the following subset of Maxwell's equation [6,11,25]:

$$\nabla \bullet \mathbf{B} = 0 \tag{4.10}$$

$$\nabla \times \mathbf{H} = \mathbf{J} \tag{4.11}$$

where

$\mathbf{B}$ = magnetic flux density vector

$\mathbf{H}$ = magnetic field intensity vector

$\mathbf{J}$ = total current density vector

The above Maxwell's field equations are supplemented by constitutive relation that describes the behaviour of the electromagnetic materials. For problems

considering saturable materials without permanent magnets, the constitutive relation for the magnetic field is given as:

$$\mathbf{B} = \mu\mathbf{H} \tag{4.12}$$

where μ is the magnetic permeability of the material. When permanent magnets are considered, the constitutive relation becomes:

$$\mathbf{B} = \mu\mathbf{H} + \mu_o\mathbf{M}_o \tag{4.13}$$

where $\mathbf{M}_o$ is the remanent intrinsic magnetisation vector. Subsequently, the magnetic vector potential is introduced as:

$$\mathbf{B} = \nabla \times \mathbf{A} \tag{4.14}$$

Use of the magnetic vector potential, $\mathbf{A}$, from Equation 4.14 along with the constitutive Equation given in 4.12, allows Equations 4.10 and 4.11 to be written in terms of magnetic vector potential as:

$$\nabla \bullet \nabla \times \mathbf{A} = 0 \tag{4.15}$$

$$\nabla \times \nabla \times \mathbf{A} = \mu\mathbf{J} \tag{4.16}$$

Furthermore, the Coulomb gauge can be defined as:

$$\nabla \bullet \mathbf{A} = 0 \tag{4.17}$$

With coupling of the Coulomb gage to the vector identity $\nabla \times \nabla \times \mathbf{A} = \nabla(\nabla \bullet \mathbf{A}) - \nabla^2\mathbf{A}$, Equation 4.16 can be expressed in a more manageable form as:

$$\nabla^2\mathbf{A} = -\mu\mathbf{J} \tag{4.18}$$

The above ***PDEs*** are solved first by discretising these Equations in their space dimensions. The discretisation is performed locally over small regions of simple but arbitrary shape. The results in matrix equations relate the input current density vector, **J**, at specified nodes of the elements to the output vector potential **A** at the same nodes. To solve the equations over large regions, the matrix equations for these small-sub-regions can be summed node by node. Then the results for global matrix Equations are obtained.

4.5.2 Magnetostatic analysis of the *PMAF* generator using *2D FE* model

The geometry of the ***PMAF*** generator is complex and at the advanced stage of the design, the accurate prediction of the generator's parameters and performances requires a ***3D FE*** solution to represent the fields properly and also to account for the leakage and fringing effects between the adjacent magnets. However, at the earliest stage of the design process of the rotor of the ***PMAF*** high-speed generator, it is more convenient to adopt an appropriate ***2D FE*** approximated model where several models with a range of dimensions of the retainment ring and made of different materials can be evaluated within minimum time of computation with accepted accuracy.

The significance of this model that it accounts for the non-linearity and saturation effect if magnetic materials are used for the retainment ring and can be quickly built with a negligible computation time when compared to a ***3D*** model. Also, in order to complete the magnetic circuit in the ***AFPM*** generator, another magnetic material is used for the rotor-back iron disc. For this analysis the back-iron disc was given a fixed shape having an arbitrary axial thickness of 20 mm and outer radius similar to the outer radius of the ***PM***. It is worth mentioning that this ***2D*** model will be also used for the design and analysis of the back-iron disc which will be discussed more in details in the following Chapter.

4.5.2.1 *2D* magnetostatic program structure

The program written for the ***2D*** magnetostatic analysis is similar in its main structure to that which was built for the ***FE*** stress analysis (***Appendix D***). The program also uses the ***APDL*** for the parametric analysis. The main difference in this program that the type of elements used is ***PLANE53*** which is special for magnetostatic analysis and the planar option is chosen instead of axisymmetric. The axisymmetric model does not simulate the real magnetic model since in this case the permanent magnets would be presented as continuous annulus shape of one single polarity whereas in reality there are eight poles of interchanged polarities. Hence the behaviour of the flux lines would be totally different. The appropriate model alternative to the ***3D*** model is the ***2D FE*** planar model which is found convenient for analysis of the simplified model of the generator. The planar model is represented by a cross sectional cut made by the x-y plane in the ***PMAF*** generator and a unit depth is assumed in the z-axis. The ***3D*** model and the two alternative ***2D*** models are depicted in Figures 4.16 and 4.17 respectively.

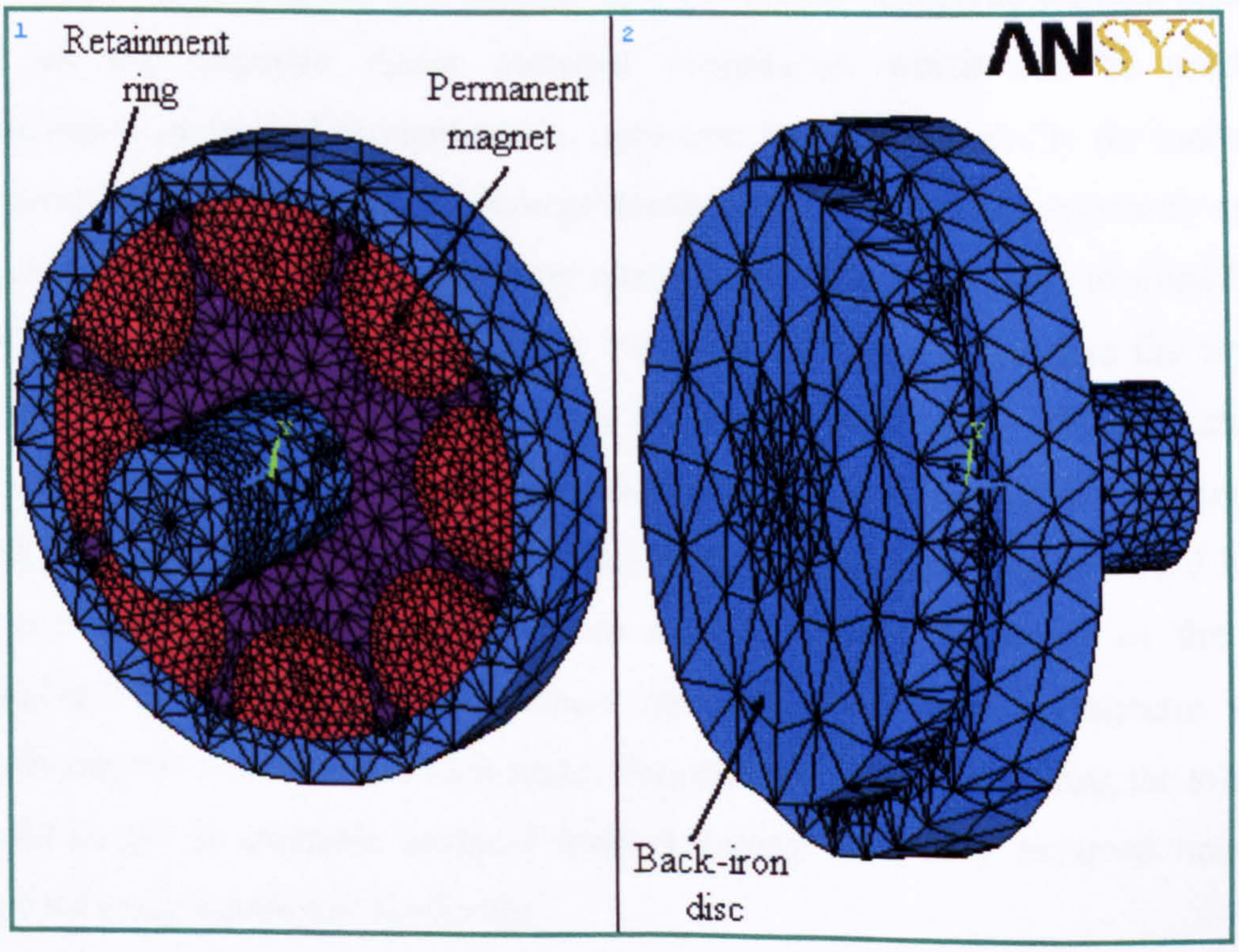

Figure 4.16 ***3D*** model for one magnet rotor disc and back-iron disc proposed for the ***PMAF*** high-speed generator

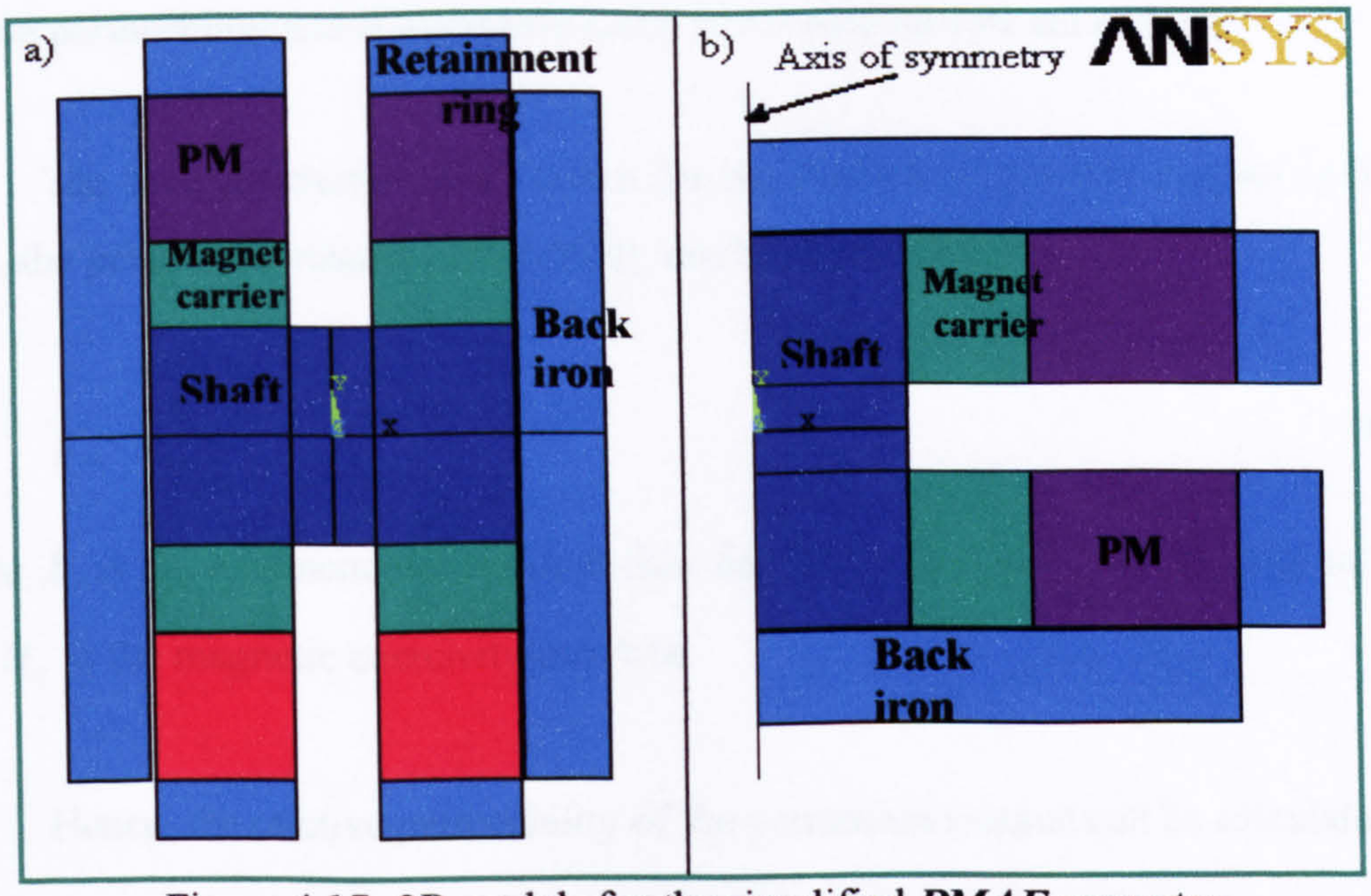

Figure 4.17 *2D* models for the simplified ***PMAF*** generator

a) planar model b) axisymmetric model

The ***ANSYS*** element (***PLANE53***) is a ***2D 8-Node*** magnetic element and it is based on the magnetic vector potential formulation which can be used for magnetostatic analysis. The element has nonlinear magnetic capability for modelling ***B-H*** curves or permanent magnet demagnetisation curves. Although symmetry can be used so that only quarter of the geometry needs to be modelled in order to simplify the model and reduce the time required for the analysis, it was found that the time of computation for the full model was not increased significantly. Hence, the full geometry was modelled to avoid any complication associated with applying the boundary conditions. In addition, the exterior of the full model was enclosed by ***2D*** infinite boundary elements (***INFIN9***) to model an open boundary of the two-dimensional planar model. This element has two nodes with a magnetic vector potential degree of freedom at each node. This element allows modelling the effect of far-field decay in magnetic analysis without having to specify assumed boundary conditions at the exterior of the model.

Once the ***ANSYS*** element type is specified, the material properties for all of the materials used in the model are specified. In particular, the ***B-H*** curve for the material used for the rotor retainment ring and the back-iron are provided to ***ANSYS***. Also, the

relative permeability for the Alumec magnet carrier and air are given. Finally the relative permeability and the coercive force of the ***NdFeB PM*** are entered.

The demagnetisation ***B-H*** curve for the ***NdFeB*** permanent magnet is linear. Thus, the permanent magnet permeability can be defined as:

$$\mu_m = \frac{B_r}{H_c} \tag{4.19}$$

where B_r is the remanence or residual flux density in the permanent magnet in Tesla and H_c is the magnetic coercivity in kA/m.

Hence, the relative permeability of the permanent magnet can be calculated as:

$$\mu_r = \frac{\mu_m}{\mu_0} \tag{4.20}$$

With all regions defined in terms of geometry and material properties, the model can now be meshed. Although ***ANSYS*** provides automatic meshing, here quadrilateral mapped meshing was used to ensure fine meshing in the areas representing the air gap between the magnet rotor discs and also to keep a fixed meshing density during any subsequent change in the retainment ring radial thickness so that alike model can be compared to each other. The exterior lines of the whole model which represent the lower order infinite element, ***INFIN9***, is divided and meshed first then the areas represented by ***PLANE53*** for the rest of the model are meshed subsequently so that the higher order plane elements will appropriately drop their midside nodes during meshing.

Once all of the elements are created, boundary conditions must be applied to the model before performing the solution. For this particular analysis, no boundary conditions needed to be applied since the infinite boundary elements ***INFIN9*** enclose the full model.

Once the solution is found, the postprocessor is utilised to examine the results. For this analysis, the useful flux crossing the air gap is the most important result. Hence, the flux is calculated along a predefined path, which is represented by a vertical straight line in the ***2D*** planar model. This line is placed in the middle of the air gap i.e. at $x = 0$ and extended from the shaft outer edge i.e. $y = 15\,\text{mm}$ to the surrounding air outer edge i.e. $y = 70\,\text{mm}$. Then flux is calculated by invoking the ***ANSYS*** command macro ***FLUXV*** along that defined path. This path can be shown in the ***2D*** meshed planar model depicted in Figure 4.18 and the written code for this model can be found in ***Appendix D***.

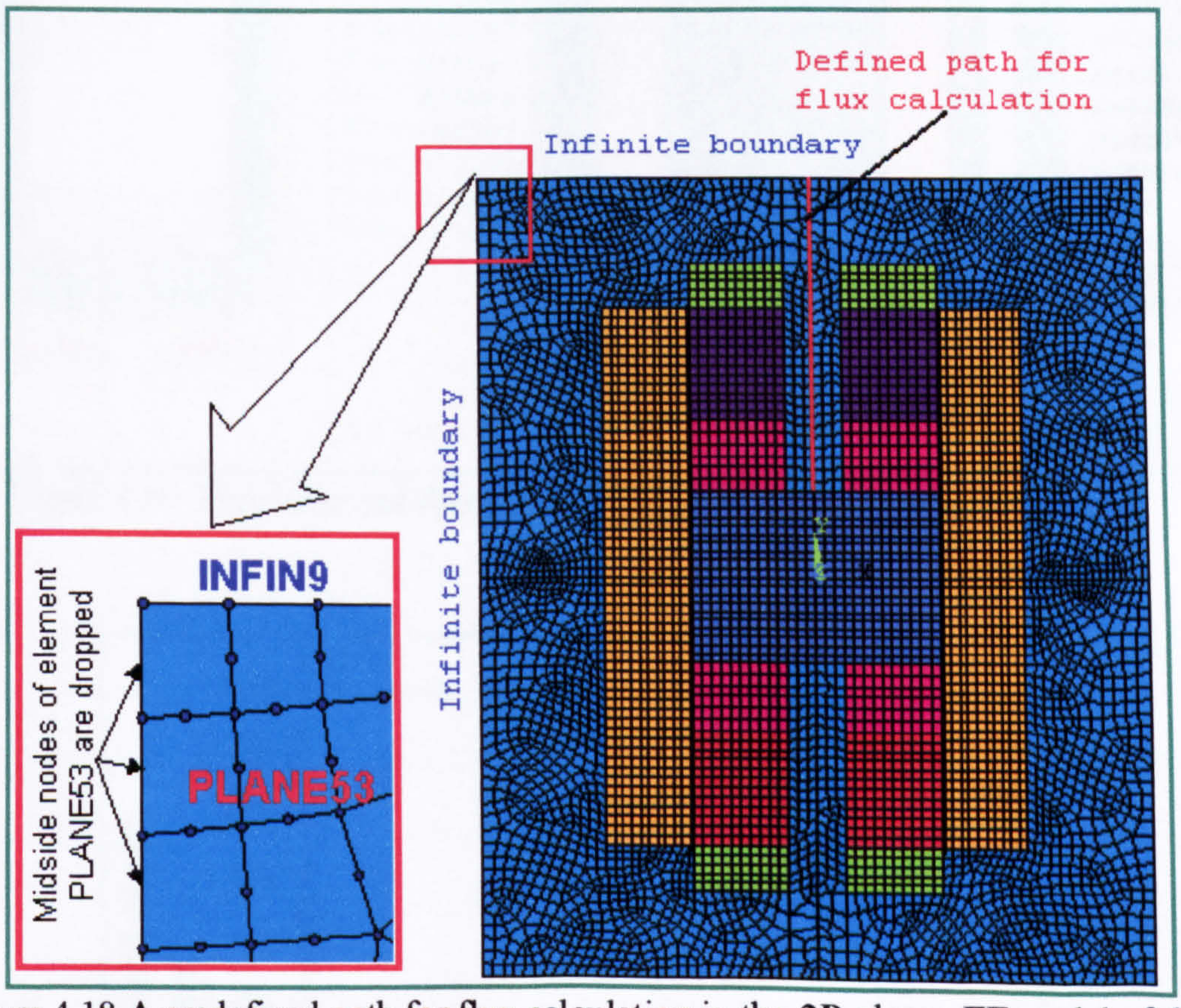

Figure 4.18 A predefined path for flux calculation in the ***2D*** planar ***FE*** model of the ***PMAF*** high-speed generator

4.5.2.2 Effect of radial thickness of the retainment ring on the magnetic flux

The retainment ring radial thickness is varied in the range of 2 – 18 mm with an increment step of 2 mm while all other design parameters are fixed. The first analysis

is performed using the Maraging G125 material for the retainment ring. The flux lines and flux density distribution obtained from the nonlinear solution for one particular case of the model are shown in Figure 4.19. Whereas the results obtained from the parametric analysis for varying the retainment ring radial thickness is presented graphically in Figure 4.20.

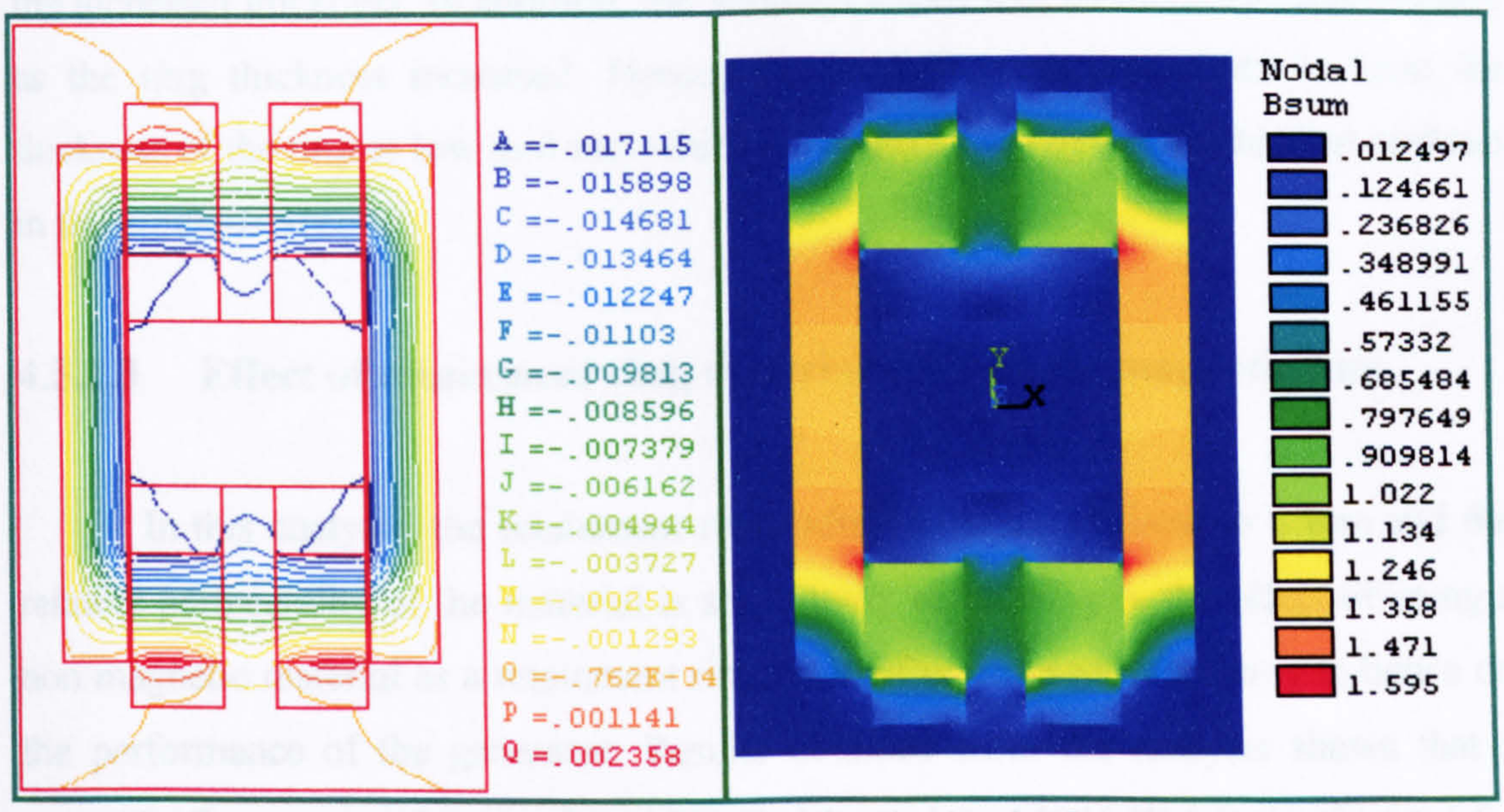

Figure 4.19 Flux lines and flux density distribution in the ***PMAF 2D*** model

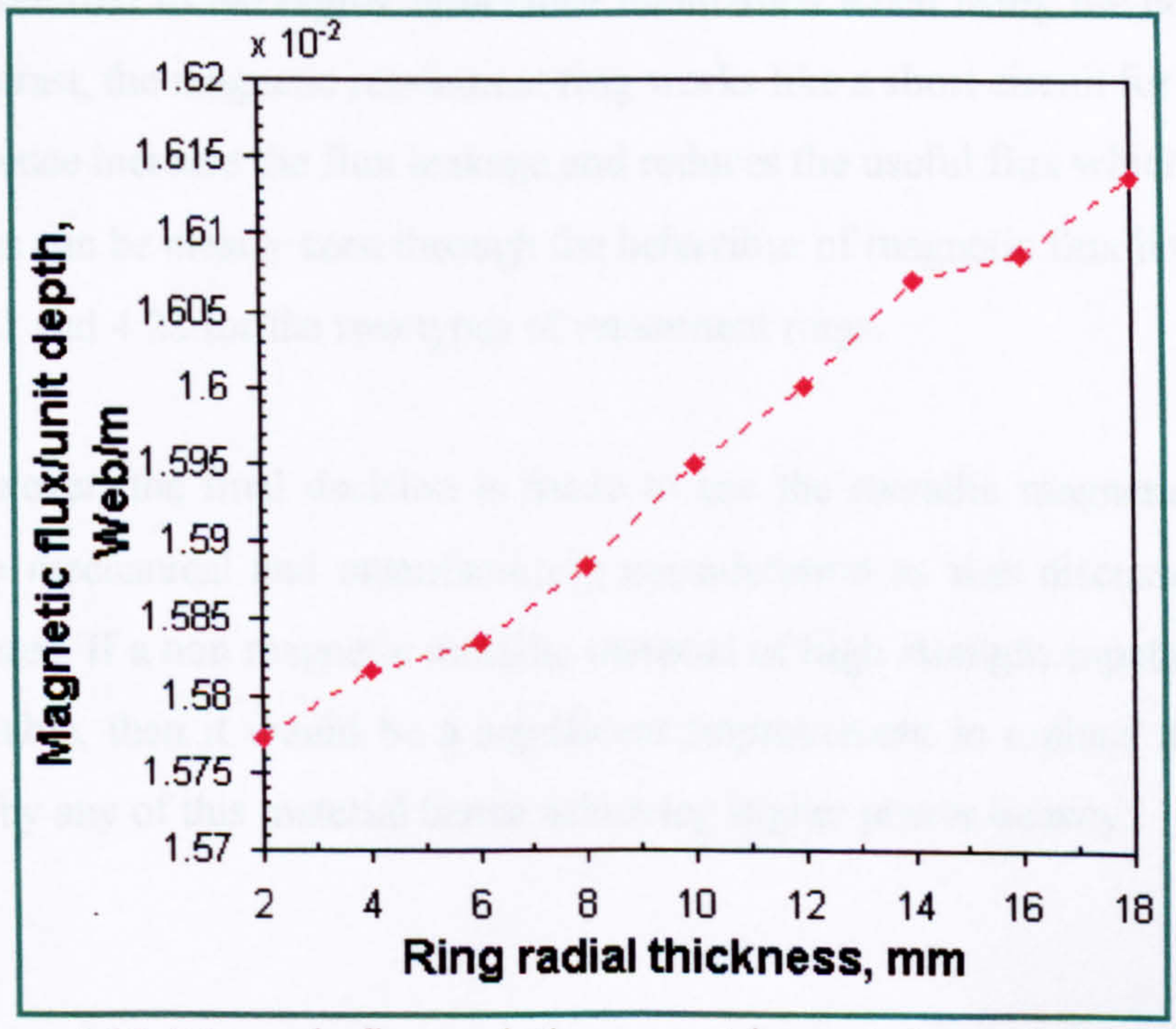

Figure 4.20 Magnetic flux variation vs. retainment ring radial thickness

It can be seen from the above Figure that the magnetic flux level crossing the air gap increases as the radial thickness of the ring increased. This can be referred to the fact that some of the flux lines tends to link with the useful flux as the path through the ring becomes relatively longer than the path through the air gap i.e. increased reluctance through the ring. However, this improvement in the flux level hence generator performance is marginal (< 2.5 %) when compared to the mass added due to the increased thickness. In addition, the windage losses will be increased significantly as the ring thickness increased. Hence, the final decision was made to keep the thickness of the ring as low as 8 mm which was determined by the mechanical analysis in the previous Section.

4.5.2.3 Effect of retainment ring material type on the magnetic flux

In this analysis, the retainment ring radial thickness is fixed to 8 mm and the relative permeability of the material is set to unity to investigate the effect of using a non magnetic material as a retainment ring on the flux linkage in the air gap hence on the performance of the generator. Results obtained from the analysis shows that a magnetic flux per unit length of 0.01750 Web/m and 0.015885 Web/m is obtained for the non magnetic ring and Maraging ring respectively. This improvement of 10 % in the flux is referred to the higher reluctance maintained when using the non magnetic ring. In contrast, the magnetic retainment ring works like a short circuit for some of the flux lines hence increase the flux leakage and reduces the useful flux which crosses the air gap. This can be clearly seen through the behaviour of magnetic flux lines shown in Figures 4.21 and 4.22 for the two types of retainment rings.

However, the final decision is made to use the metallic magnetic retainment ring due to mechanical and manufacturing consideration as was discussed earlier in Chapter Three. If a non magnetic metallic material of high strength capabilities can be made available, then it would be a significant improvement to replace the Maraging G125 ring by any of this material hence achieving higher power density.

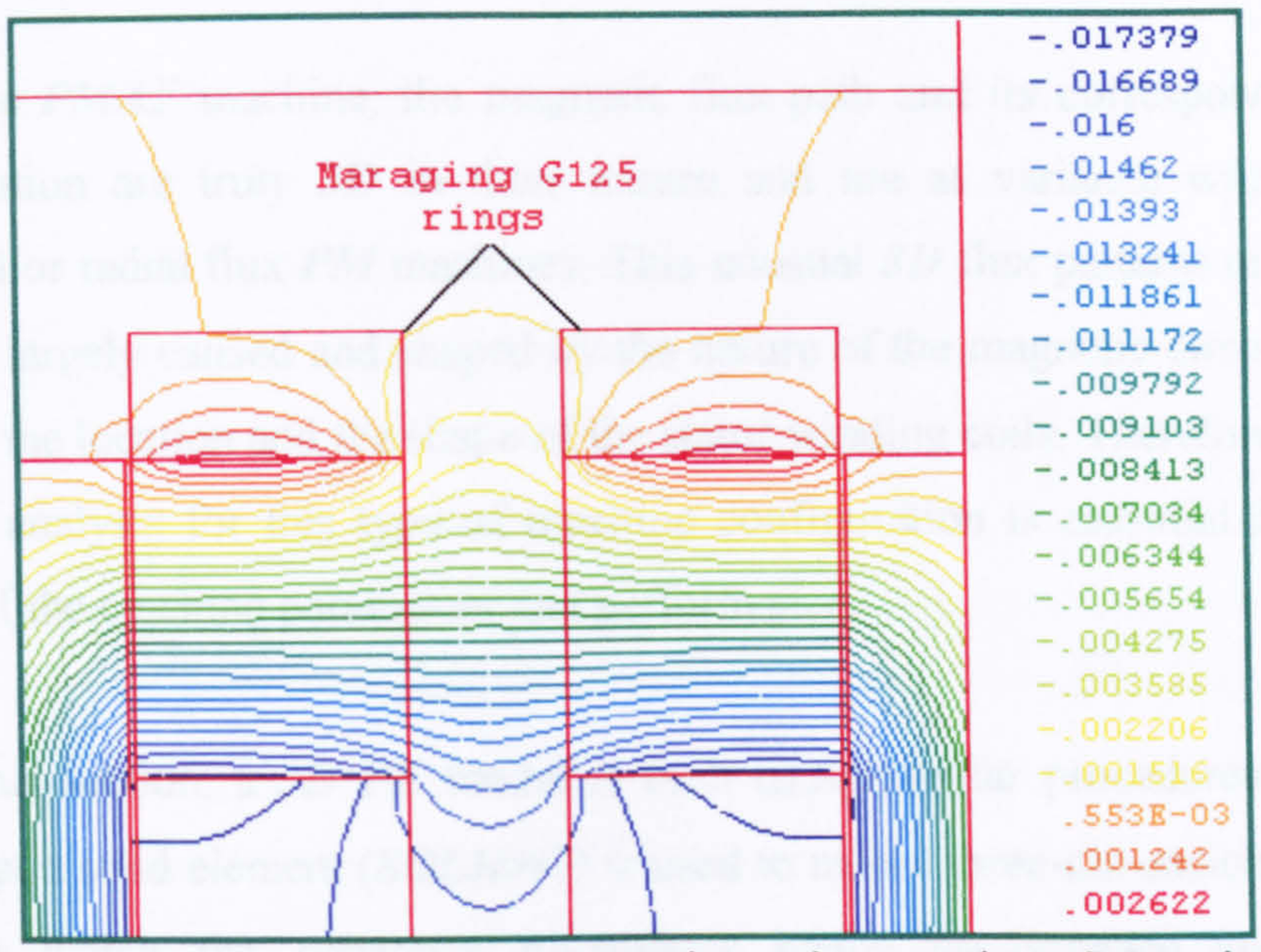

Figure 4.21 Flux lines when using magnetic retainment rings (Maraging G125)

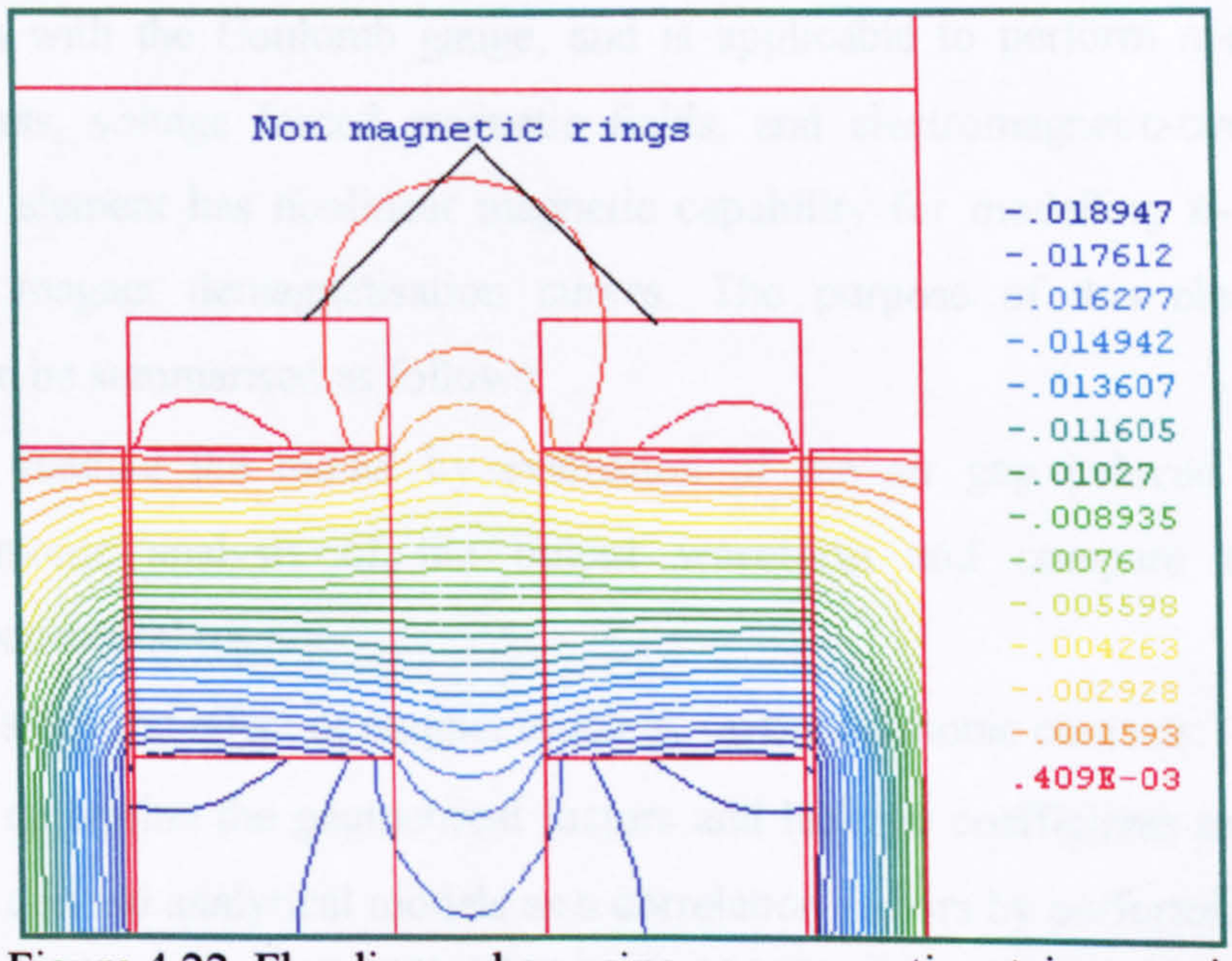

Figure 4.22 Flux lines when using non magnetic retainment ring

4.5.3 3D Electromagnetic analysis of the *PMAF* high-speed generator

In the ***PMAF*** machine, the magnetic flux path and its corresponding spatial flux distribution are truly ***3D*** in their nature and are at variance with the usual conventional or radial flux ***PM*** machines. This unusual ***3D*** flux patterns in the ***PMAF*** machines is largely caused and shaped by the nature of the magnetic circuit geometry of the rotor, the location and the shape of the stator winding coils. Therefore, the use of the ***3D FE*** analysis for this type of machine configuration is essential for accurate prediction of the machine parameters and performance.

In this section, a ***3D FE*** model is built using similar procedures for the ***2D*** model except a solid element (***SOLID97***) is used to model three-dimensional magnetic fields from which the generator parameters hence performance are evaluated (***Appendix D***). The element is defined by eight nodes, and has up to five degrees of freedom (***DOFs***) per node out of six defined ***DOFs***, i.e., the magnetic vector potential (***AX, AY,AZ***), the electric scalar potential (***VOLT***), the electric current (***CURR***), and the electromotive force (***EMF***). ***SOLID97*** is based on the magnetic vector potential formulation with the Coulomb gauge, and is applicable to perform magnetostatics, eddy currents, voltage forced magnetic fields, and electromagnetic-circuit coupled fields. The element has nonlinear magnetic capability for modelling ***B-H*** curves or permanent magnet demagnetisation curves. The purpose of this electromagnetic analysis can be summarised as follows:

- To validate the model by evaluation of the air gap induced voltage and harmonic analysis of the output waveform and compare them to the experimental results.
- To study the effect of magnet topology on the harmonic contents.
- To determine the geometrical factors and leakage coefficients to use them in the derived analytical models as a correlation factors by performing parametric analysis.
- To compute the generator synchronous reactance.
- To evaluate rotor magnetic losses and the generator performance.

4.5.3.1 Validation of the 3D FE magnetostatic model

The usefulness of any developed ***FE*** model and simulation can be determined by the accuracy with which they represent the actual system. To determine the usefulness of the ***3D FE*** magnetostatic models developed for the ***PMAF*** high-speed generator, the results of the models must be validated against known data.

To validate the simulations, the ***FE*** model was applied to the constructed preliminary prototype of the ***PMAF*** generator. This prototype has its main design parameters obtained from the previous analysis in Chapter Three. The most important parameters such as magnet inner and outer radii, types of material used and retainment ring radial thickness have already been determined. However, since the ***PM*** has to be segmented, a choice has to be made to use a convenient shape of the magnet out of the two possible shapes (semi circular and semi trapezoidal) to satisfy magnetic, mechanical and manufacturing requirements. Figure 4.23 shows the two possible ***PM*** shapes for the proposed rotor design.

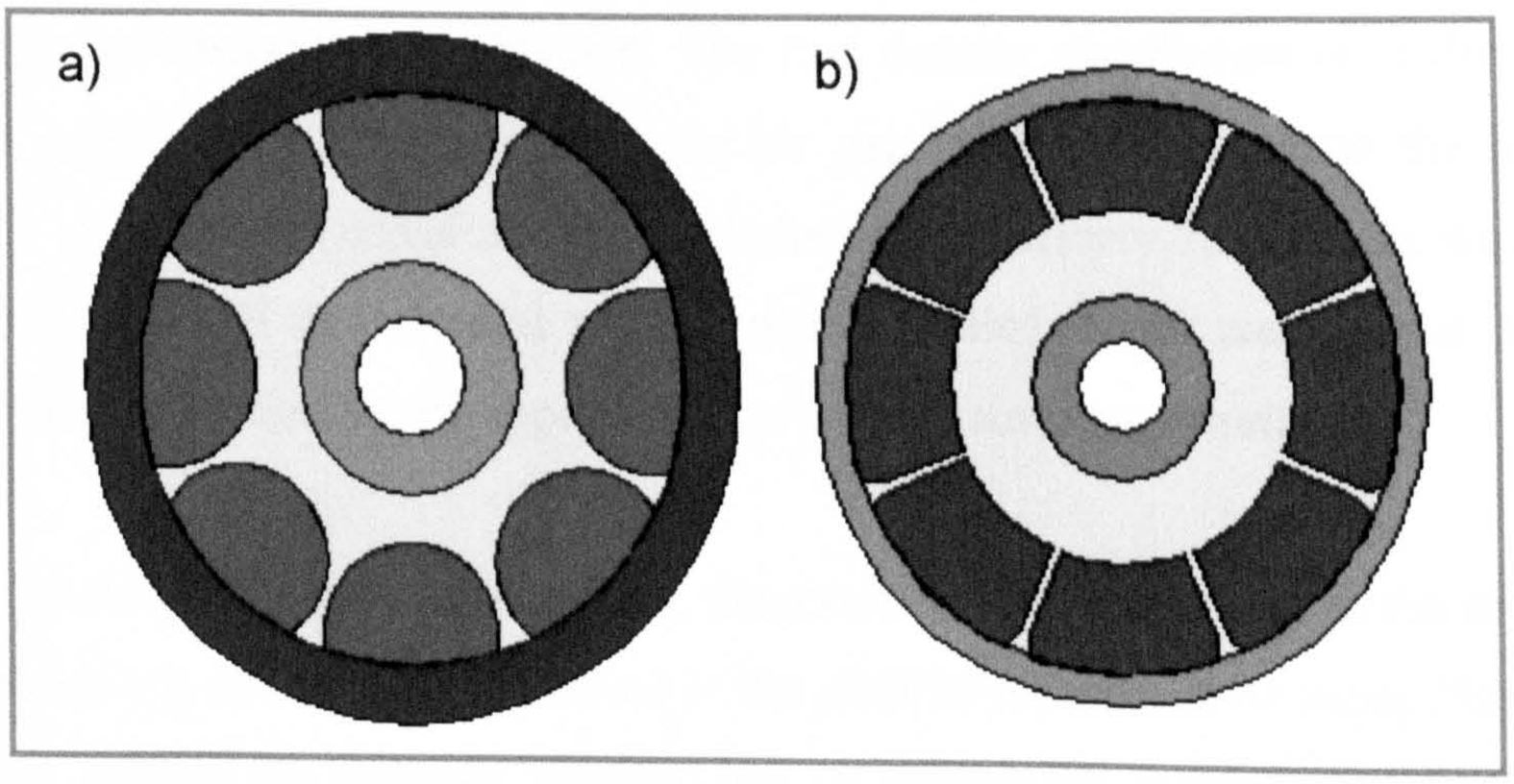

Figure 4.23 Possible ***PM*** shapes for the ***PMAF*** high-speed rotor
a) semicircular b) semi trapezoidal

In fact, at the earlier stage of the design and prior to performing this analysis, there was no precise knowledge of how could the shape of the magnet or the distance between the adjacent magnets on the same disc affect the performance of the generator. Accordingly, the ***PM*** manufacturer and the workshop that has been given

the task were consulted in order to select a feasible shape and dimensions for the ***PM*** to fit into the proposed design of the rotor. It was found that circular shape or disc permanent magnets are readily available at the manufacturer stocks and they are available in different standard diameters. Hence adjusting one of these magnets into the rotor would reduce the manufacturing cost of the prototype despite that these circular disc magnets require machining and grinding after assembling them into the rotor. In addition, the circular holes at the peripheral of the magnet carrier for the semicircular permanent magnets can be made by ordinary milling machine whereas the semi trapezoidal or any other shapes would require a ***CNC*** machine which in turn increases the manufacturing cost of the prototype. In respond to these limitations, the semicircular ***PM*** shape of diameter, $d_m = 29$ mm was selected for the proposed prototype based on the ease of manufacturing, availability and cost reduction. Thus, the manufactured prototype has the final geometry which has been shown earlier in Figure 4.10. Full description regarding the manufacturing and assembling of the prototype can be found in ***Appendix A***.

Hence, this prototype was modelled using the ***3D FE*** magnetostatic model and the results of interest were obtained. The flux density distribution is of the primary interest where other results such as the air gap induced voltage and the harmonic contents in the output waveform can be deduced. To perform the analysis, a quarter of the rotor with half of the axial air gap was modelled in ***3D*** and manual boundary conditions are applied on the appropriate surfaces to simulate symmetry.

Once the solution is performed, the results of the flux density in the air gap and its components can be directly viewed in the ***ANSYS*** postprocessor menu. However, in order to predict the induced voltage and to analyse the harmonics in the output waveform, special techniques are required. It is worth mentioning that in contrast to time stepping techniques which require the incremental rotation of the rotor [77,78,79], in this analysis the results are obtained from one common solution where no incremental rotation of the rotor is performed. Instead, the results are obtained simply by defining a virtual path which simulates a single turn of thin wire in the stator coils. This path which is placed in a plane at the centre of the air gap and normal to the axis of rotation, is rotated to trace the flux at each particular position. Figure 4.24-a) shows the

modelled part of the generator with the virtual path defined at a particular position whereas the flux density contours obtained from the model is shown in Figure 4.24-b)

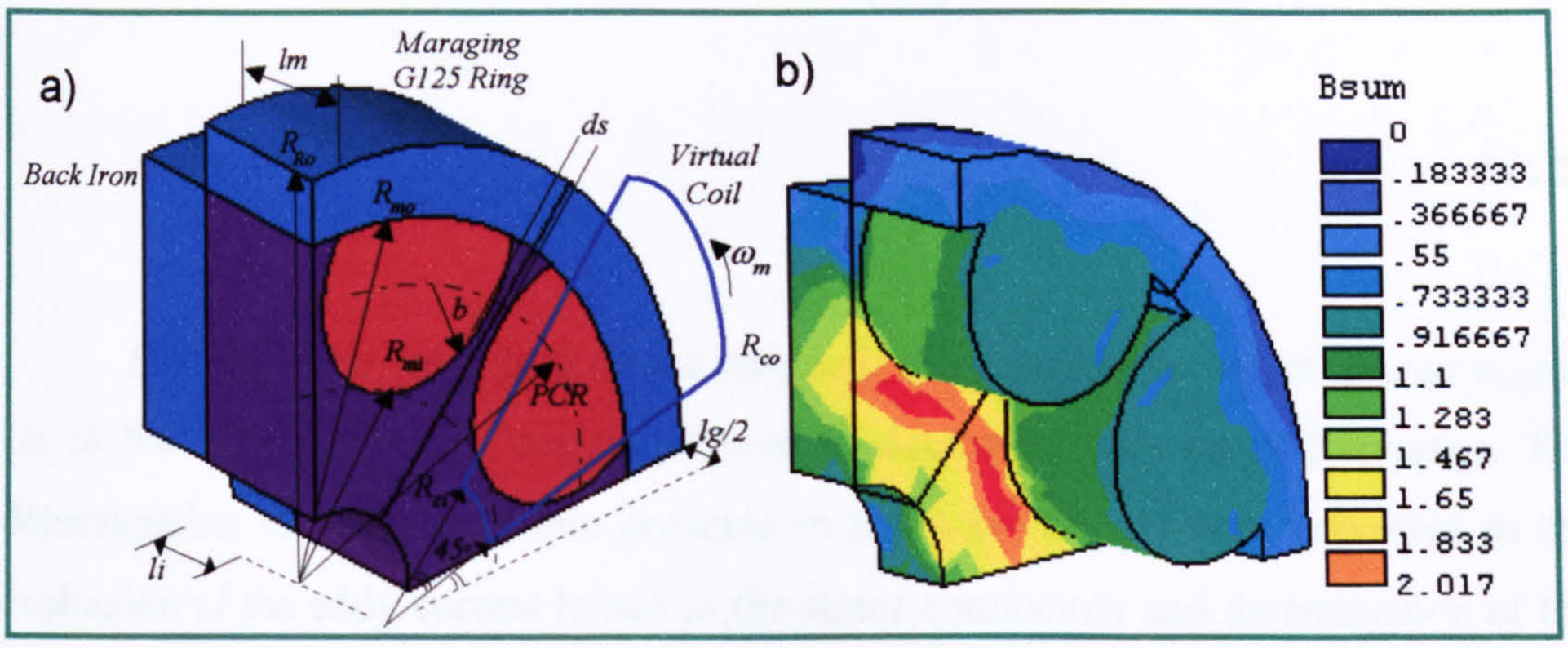

Figure 4.24 Part of the ***PMAF*** generator modelled by magnetostatic ***3D FE***

a) details of the model b) magnetic flux density in the model

For this analysis, the defined path has an angular span equals to the pole pitch i.e. $45°$ whereas the inner and outer radii of the coils are defined as $R_{ci} = 18$ mm and $R_{co} = 66\,\text{mm}$ respectively.

Then, the flux enclosed by the defined path is Fourier analysed as a function of time, t, to determine the various harmonics in the flux waveform. Even harmonics are not considered in the analysis since they were negligible [85] and only the fundamental and odd harmonics are considered as follows [49,].

$$\phi(t) = \sum_{n=1}^{\infty} \left\{ -A_{2n-1} \cos[(2n-1)\omega_e t - \beta_{2n-1}] \right\} \tag{4.21}$$

where n = numeric counter

$2n-1$ = harmonic order

A_{2n-1} = $\sqrt{C_{2n-1}^2 + D_{2n-1}^2}$,

C_{2n-1} = harmonic sine coefficient of the Fourier series,

D_{2n-1} = harmonic cosine coefficient of the Fourier series,

β_{2n-1} = $\tan^{-1}\left(\frac{C_{2n-1}}{D_{2n-1}}\right)$, is the phase angle for the $(2n-1)$ harmonic

Accordingly, for a given number of turns represented by the defined path, number of poles and specified rotational speed, the induced voltage, $e(t)$, due to the flux change in the defined path can be determined by:

$$e(t) = -N_t p \frac{d\phi(t)}{dt} \tag{4.22}$$

Similarly, the waveform of the magnetic flux density in the conductor region i.e. in the air gap can be Fourier analysed to determine its various harmonics. The determination of these harmonic contents in the waveform is very important in the evaluation of the eddy current losses in the stator conductors and determination of the magnet working point after assembly. In this analysis, the magnet flux density was traced in the angular direction i.e. one pole pitch, at a constant radial position equals to the pitch circle radius ($PCR = 36\,\text{mm}$). A *3D* flux density distribution in the air gap for the *PMAF* generator determined by *FEM* is shown in Figure 4.25.

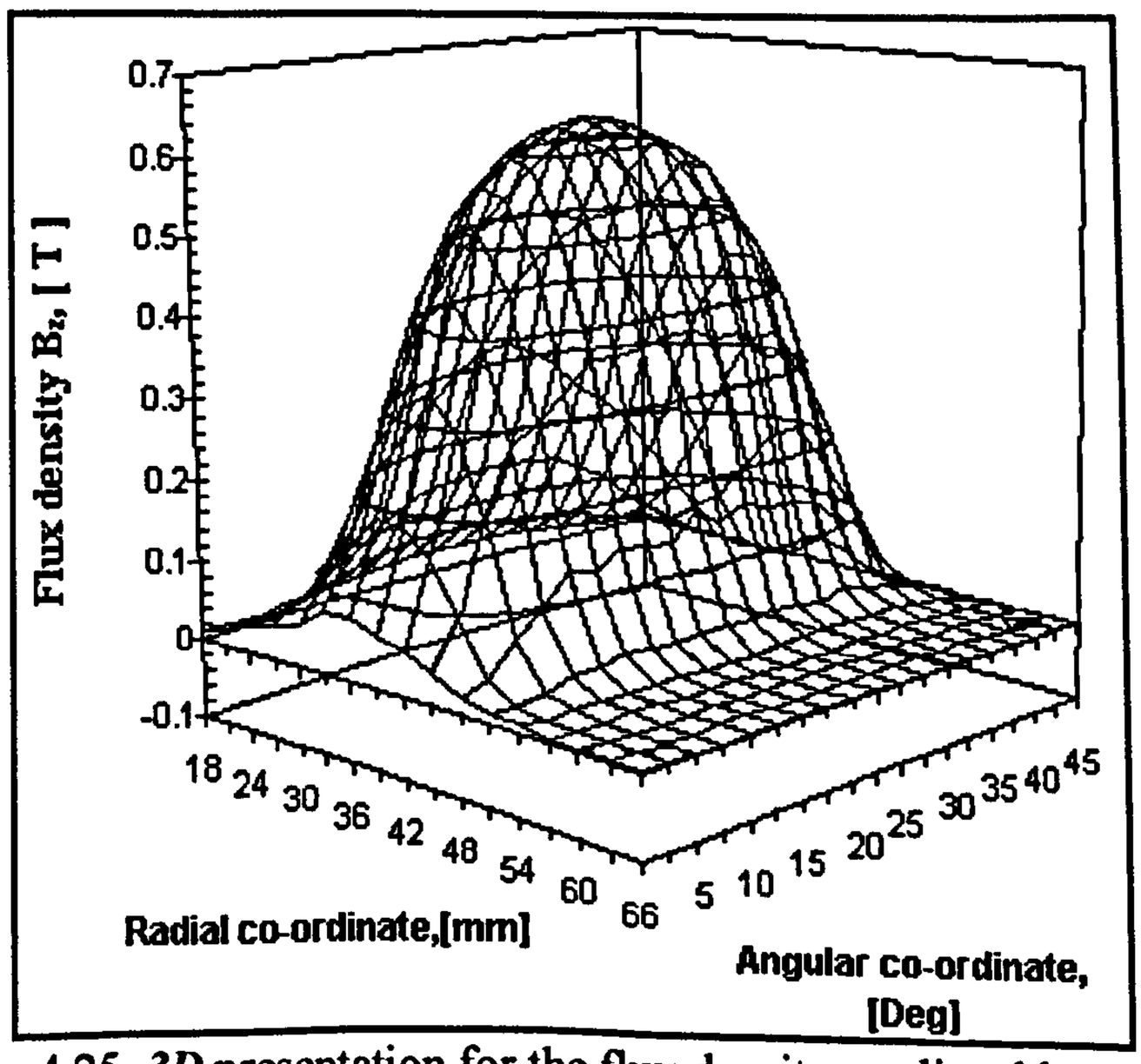

Figure 4.25 *3D* presentation for the flux density predicted by *FE* for the *PMAF* prototype having 10 mm air gap length

The results of the *FE* model was then compared with the experimental data obtained from the actual machine. The following Figures illustrate the results of the

FE models compared to the experimental data. The experimental setup and procedures of measurements are described in details in Chapter Seven.

Figures 4.26 – 4.28 show the results obtained from the ***FE*** simulation compared with the measured normal component of the flux density at different positions of the prototype which has an axial air gap length $l_g = 10\,\text{mm}$. Figures 4.29 and 4.30 shows the modelled and measured induced voltage and harmonic analysis respectively for the same prototype at the speed of 1830 rpm. These Figures confirms the validity of the ***3D FE*** model where a good agreement between the ***FE*** results and the measured values is achieved hence. Hence, the ***FE*** models can now be used with great confidence for further analysis which will be described hereafter.

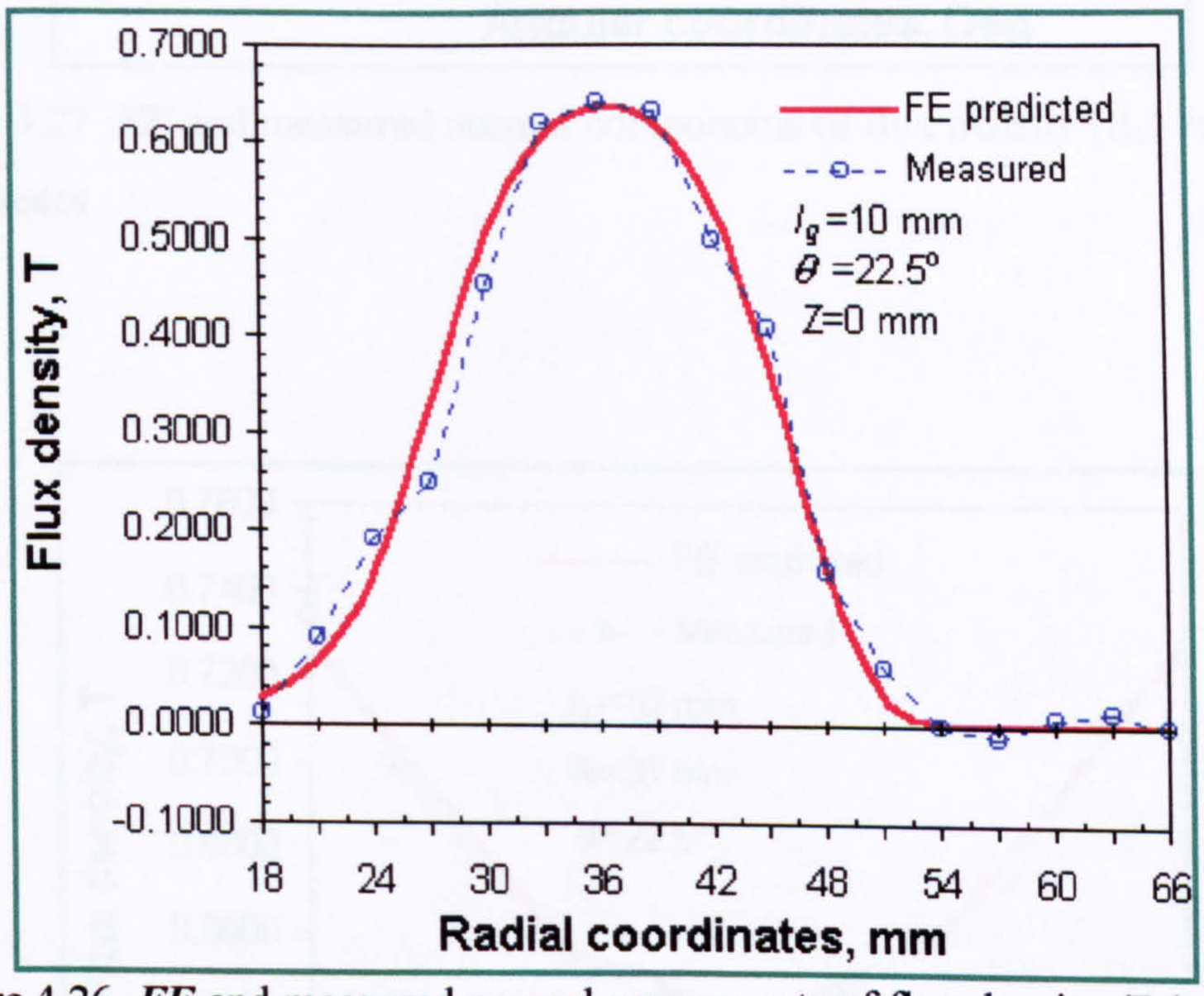

Figure 4.26 ***FE*** and measured normal components of flux density (B_z) vs. radial coordinates

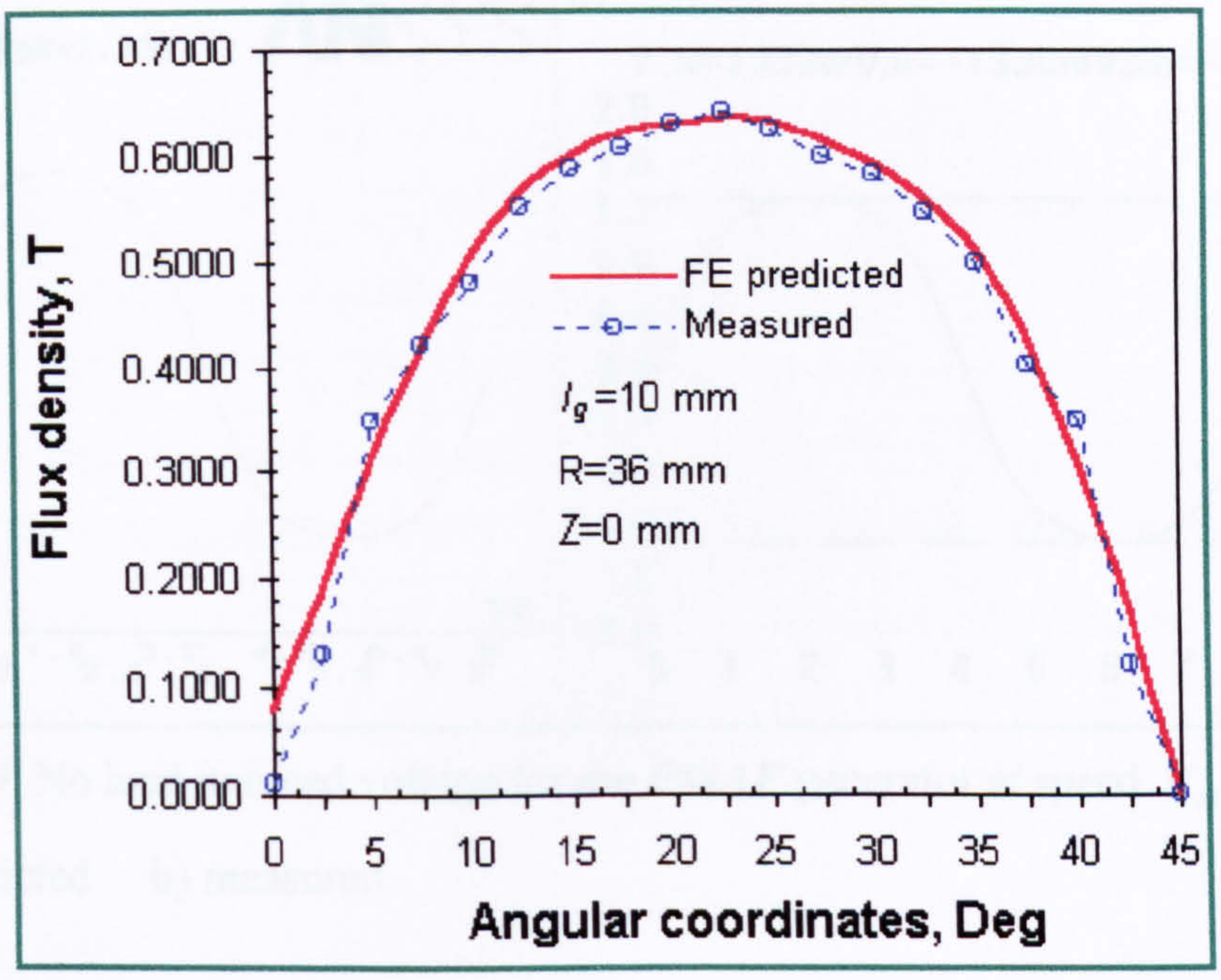

Figure 4.27 ***FE*** and measured normal components of flux density (B_z) vs. angular coordinates

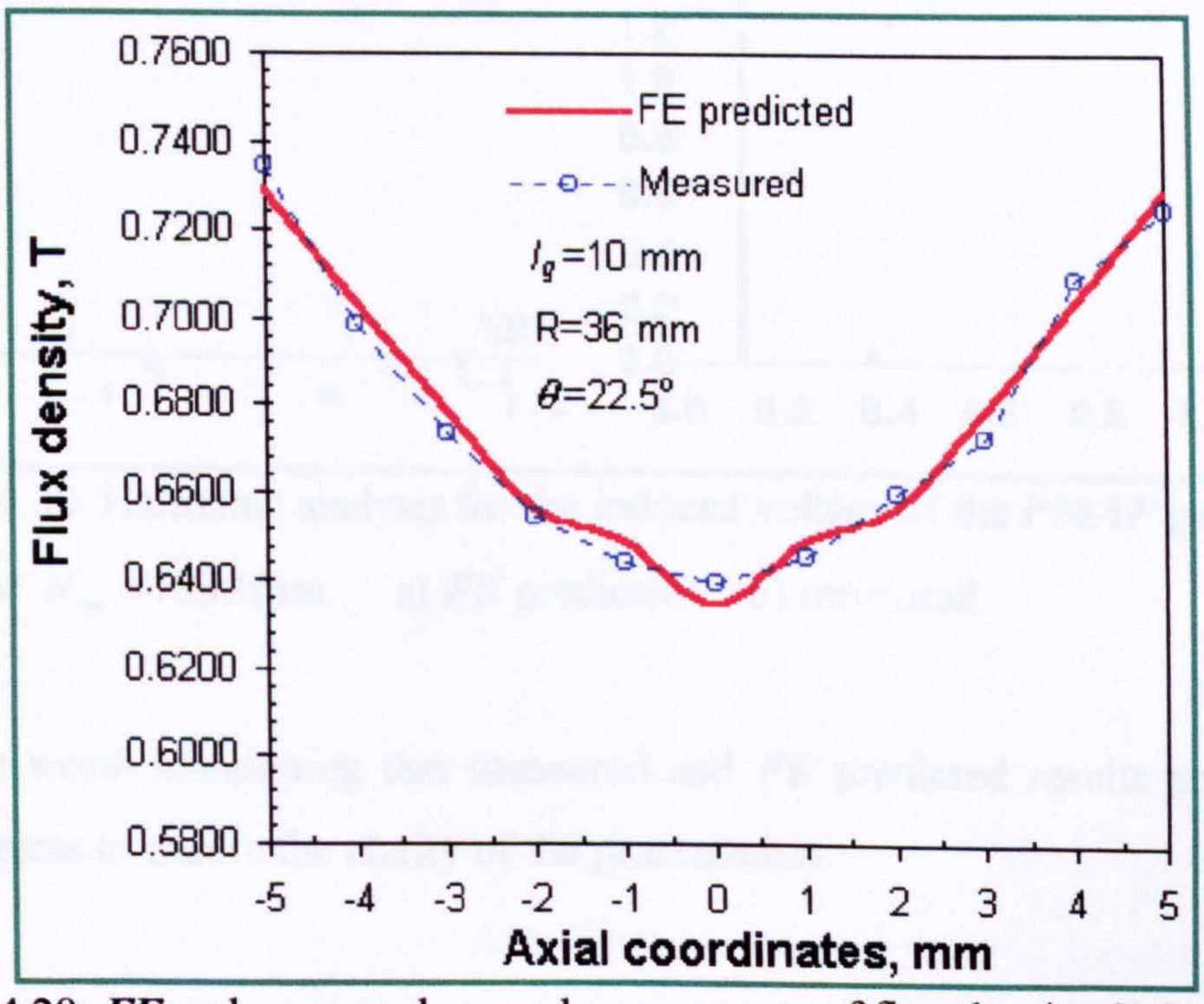

Figure 4.28 ***FE*** and measured normal components of flux density (B_z) vs. axial coordinates

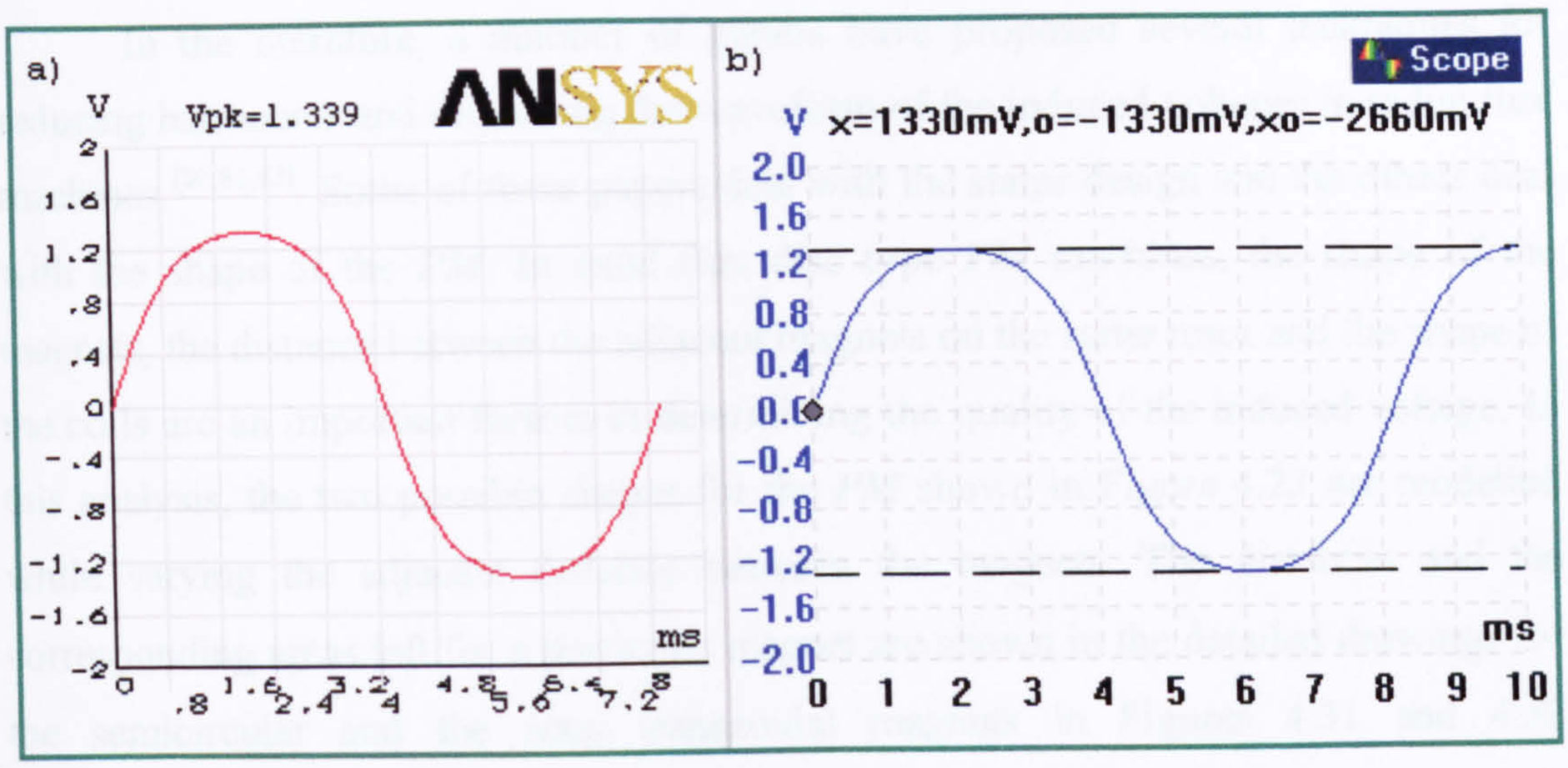

Figure 4.29 No load induced voltage for the ***PMAF*** generator at speed $N_m = 1830\,\text{rpm}$

a) ***FE*** predicted b) measured

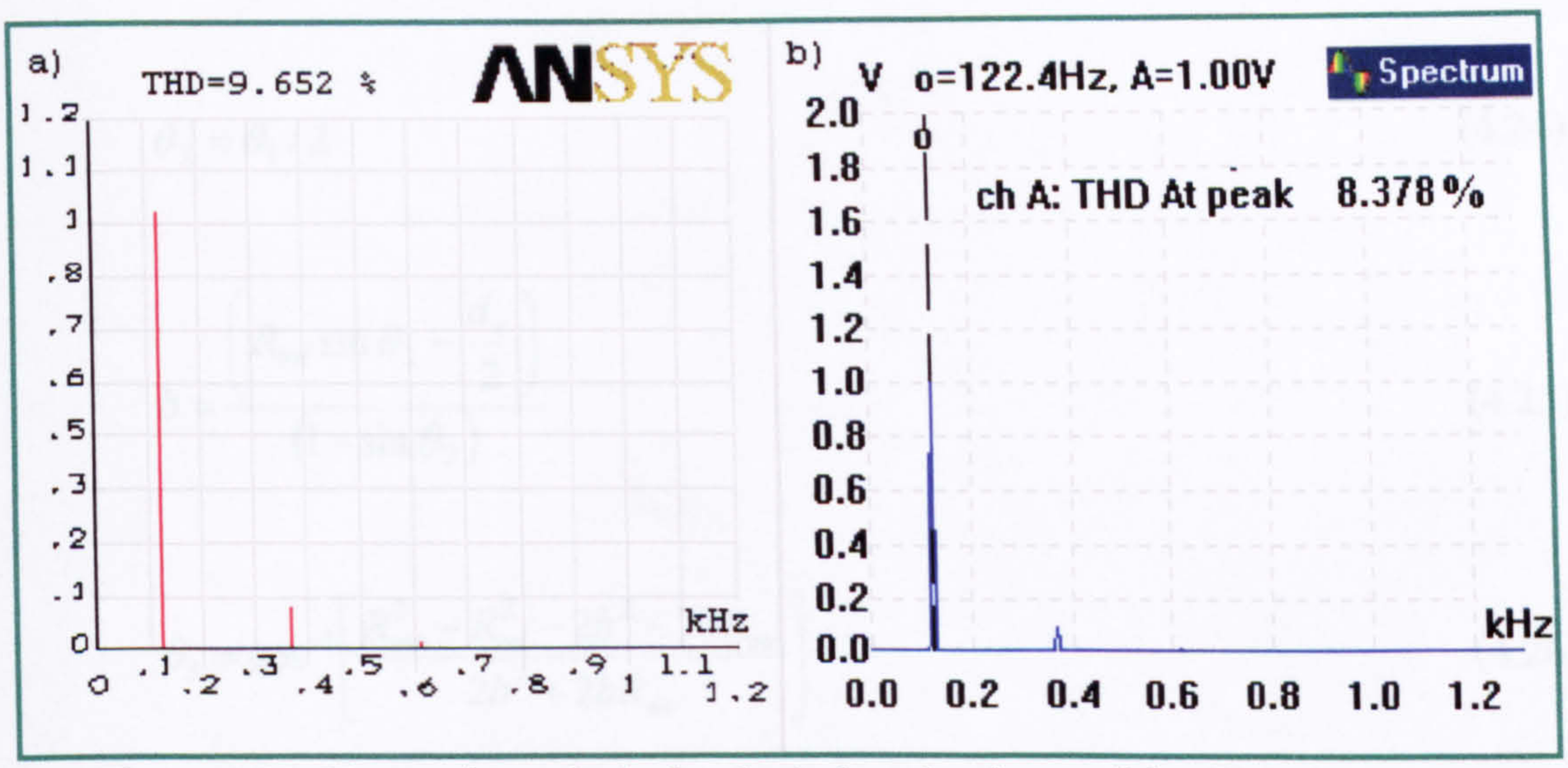

Figure 4.30 Harmonic analysis for the induced voltage of the ***PMAF*** generator at speed $N_m = 1830\,\text{rpm}$. a) ***FE*** predicted b) measured

It is worth mentioning that measured and ***FE*** predicted results are shown in separate figures to ensure the clarity of the presentation.

4.5.3.2 Effect of magnet topology on the induced voltage harmonics

In the literature, a number of papers have proposed several techniques for reducing harmonics and improving the waveform of the induced voltages in radial flux machines [80,81,82]. Some of these papers deal with the stator design and the others deal with the shape of the ***PM***. In axial flux disc type ***PM*** machines, the shape of the magnets, the distance between the adjacent magnets on the same rotor and the shape of the coils are an important factors in determining the quality of the induced voltage. In this analysis, the two possible shapes for the ***PM*** shown in Figure 4.23 are modelled while varying the adjacent distance between the magnets. The distances and the corresponding areas left for a particular magnet are shown in the detailed drawings for the semicircular and the semi trapezoidal magnets in Figures 4.31 and 4.32 respectively. The related geometrical equations are derived as follows:

$$\theta_1 = \frac{360}{p} \tag{4.23}$$

$$\theta_2 = \theta_1 / 2 \tag{4.24}$$

$$b = \frac{\left(R_{mi}\sin\theta_2 - \frac{d_s}{2}\right)}{(1-\sin\theta_2)} \tag{4.25}$$

$$\theta_3 = \cos^{-1}\left[\frac{R_{mo}^2 - R_{mi}^2 - 2b^2 - 2bR_{mi}}{2b^2 + 2bR_{mi}}\right] \tag{4.26}$$

$$A_m = \pi b^2 - \left(b^2\frac{\pi\theta_3}{180} - b^2\sin\theta_3\cos\theta_3\right) + \left(R_{mo}^2\frac{\pi\theta_4}{180} - R_{mo}^2\sin\theta_4\cos\theta_4\right) \tag{4.27}$$

$$\theta_m = \frac{2A_m}{R_{mo}^2 - R_{mi}^2} \tag{4.28}$$

$$\theta_s = \theta_1 - \theta_m \tag{4.29}$$

where all angles in the above equations are in degrees.

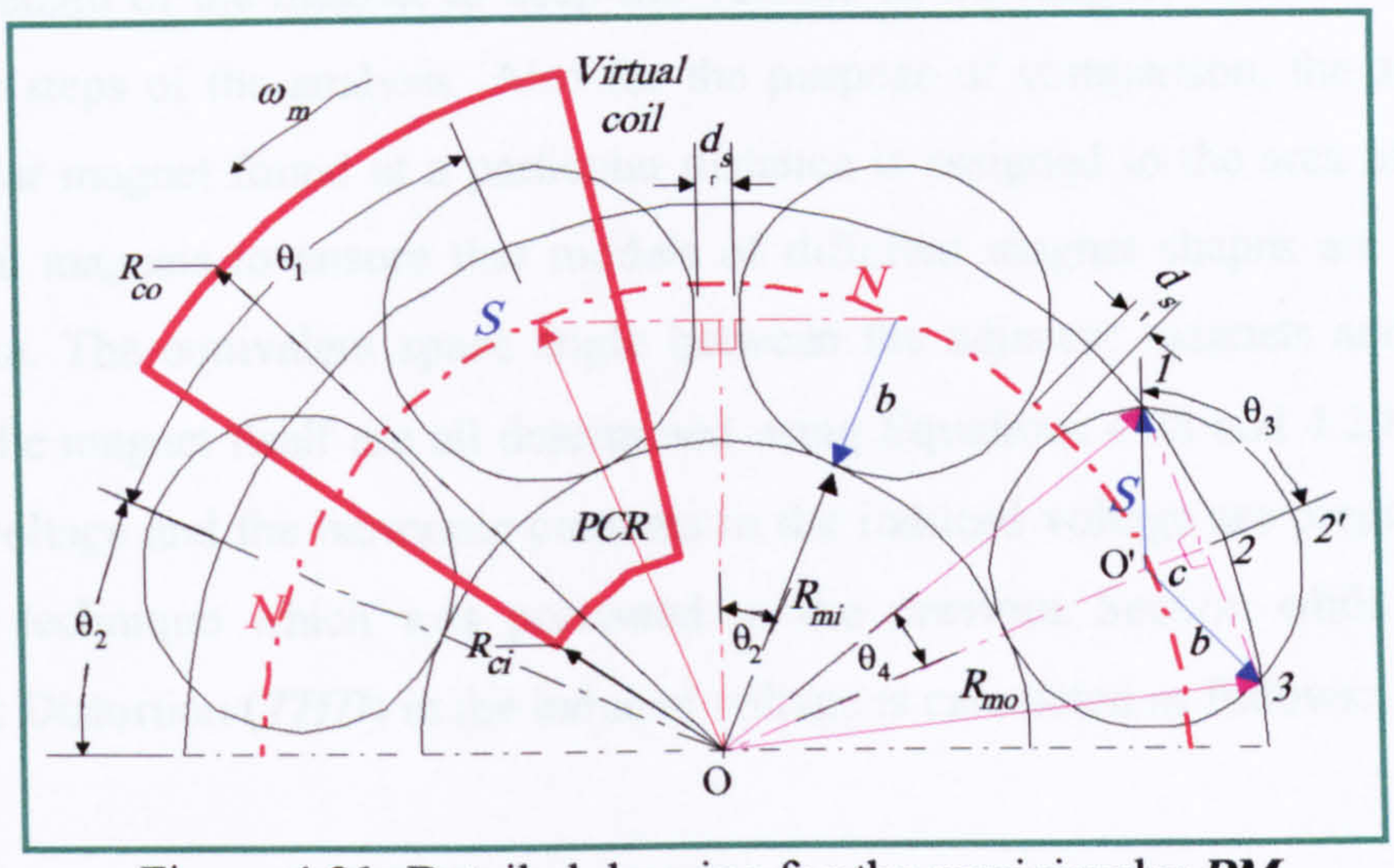

Figure 4.31 Detailed drawing for the semicircular ***PM***

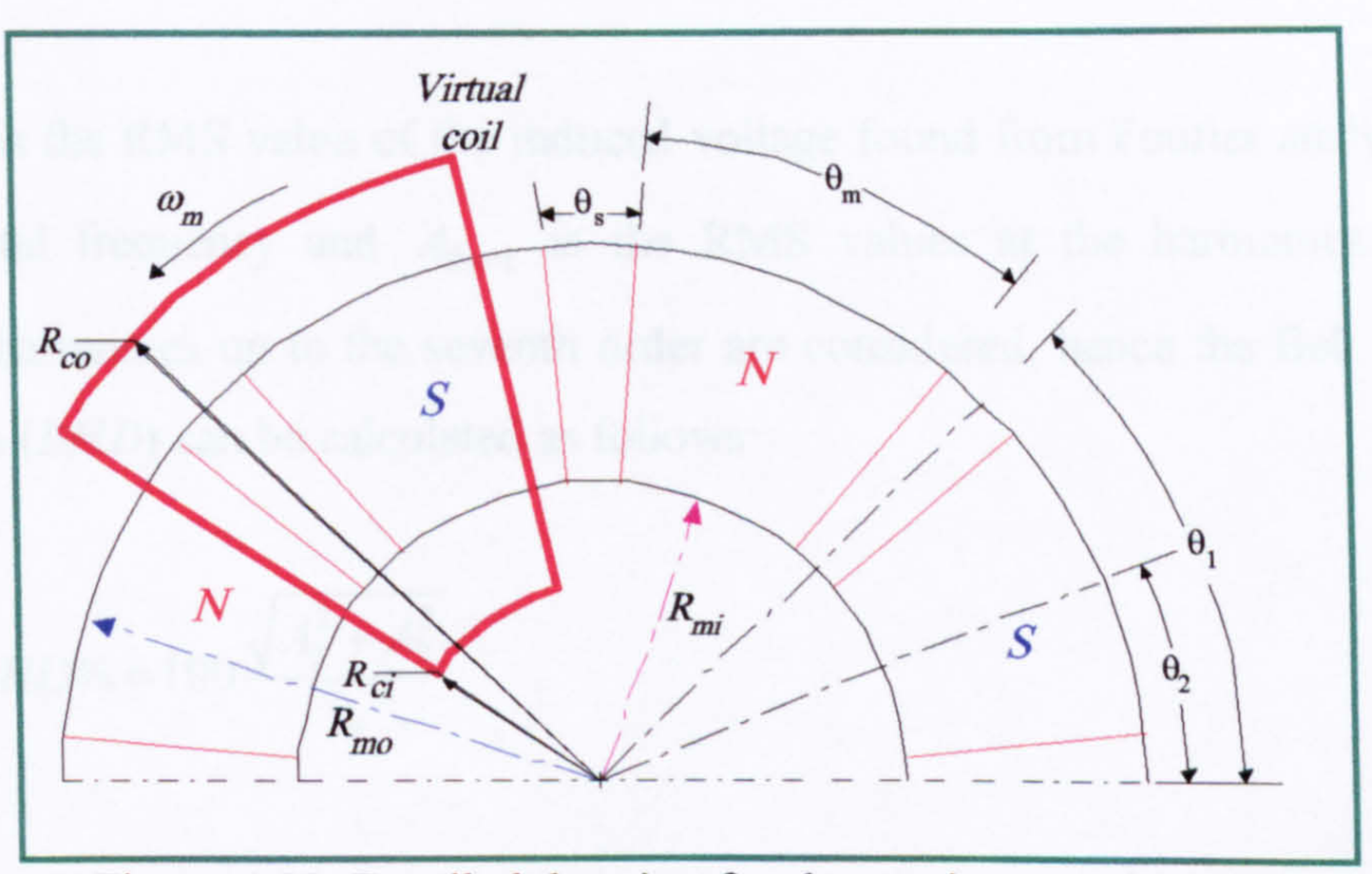

Figure 4.32 Detailed drawing for the semi trapezoidal ***PM***

To start the analysis, the semicircular ***PM*** shape is selected first, with the distance between the adjacent magnets, d_s, is varied over the range from 1 mm to 8 mm with an increment step of 1 mm. For that distance the magnet radius, b, hence

area, A_m required to fit it in the available space in the rotor is determined using Equations 4.25 and 4.27 respectively. Since the magnet inner radius, R_{mi}, and the magnet outer radius, R_{mo}, are fixed for a particular rotor design, any reduction in the magnet surface area due to the increased adjacent distance is substituted by increasing the axial length of the magnet to keep the volume of the magnet constant during the successive steps of the analysis. Also for the purpose of comparison, the area of the semicircular magnet found at a particular distance is assigned to the area of the semi trapezoidal magnets to ensure that models of different magnet shapes are compared like to like. The equivalent space angle between the adjacent magnets and the span angle of the magnet itself are all determined using Equations 4.28 and 4.29. Then the induced voltage and the harmonic contents in the induced voltage are predicted using the same technique which was presented in the previous Section while the Total Harmonic Distortion (***THD***) in the induced voltage is calculated as follows:

$$THD\% = 100\frac{\sqrt{\sum_{n=2}^{\infty} A_{2n-1}^2}}{A_1} \tag{4.30}$$

where A_1 is the RMS value of the induced voltage found from Fourier analysis at the fundamental frequency and A_{2n-1} is the RMS values at the harmonics. For this analysis, harmonics up to the seventh order are considered, hence the Belt Harmonic Distortion (***BHD***) can be calculated as follows:

$$BHD\% = 100\frac{\sqrt{A_5^2 + A_7^2}}{A_1} \tag{4.31}$$

The breakdown of the harmonics in the induced voltage and the peak induced voltages are presented in Table 4.5 and 4.6 for the semi trapezoidal and semicircular ***PM*** respectively. The geometrical variation in the rotor due to the corresponding variation in the distance between the adjacent magnets, d_s, is presented in Table 4.7. The harmonic analyses are presented graphically in Figures 4.33 – 4.35 for the purpose of comparison between the possible shapes of ***PM*** as the distance between the magnets

is increased. It is worth mentioning that harmonics above the 7th order and even harmonics are not considered in the comparison since they were found to be almost negligible [ ].

d_s mm	Fundamental V, RMS	3rd V, RMS	5th V, RMS	7th V, RMS	% BHD	% THD	*Vpk* V
1	1.08201	0.1228	0.01394	0.00218	1.304	11.424	1.3743
2	1.07634	0.1085	0.00697	0.00343	0.721	10.106	1.3833
3	1.05886	0.0890	0.00132	0.00818	0.782	8.441	1.3813
4	1.03916	0.0692	0.01332	0.00724	1.459	6.817	1.3601
5	1.01329	0.0422	0.02216	0.00673	2.285	4.750	1.3512
6	0.98508	0.00533	0.03223	0.00576	3.323	3.367	1.3500
7	0.92591	0.0329	0.03653	0.00520	3.985	5.339	1.3125
8	0.86342	0.0756	0.0385	0.00341	4.484	9.837	1.2681

Table 4.5 Harmonic analysis for semi trapezoidal *PM*

d_s mm	Fundamental V, RMS	3rd V, RMS	5th V, RMS	7th V, RMS	% BHD	% THD	Vpk V
1	1.03601	0.11698	0.02510	0.005196	2.474	11.559	1.3278
2	1.02530	0.1115	0.01703	0.00562	1.749	11.0146	1.328
3	1.0127	0.09506	0.00967	0.006328	1.141	9.4558	1.3396
4	0.9955	0.07314	0.000845	0.00695	0.703	7.3806	1.3154
5	0.9810	0.05340	0.01305	0.00518	1.431	5.628	1.3062
6	0.9505	0.02073	0.02188	0.001926	2.311	3.1775	1.2866
7	0.9075	0.01561	0.02573	0.00126	2.838	3.3191	1.267
8	0.86311	0.03487	0.02537	0.00109	2.942	4.9977	1.2322

Table 4.6 Harmonic analysis for semi circular *PM*

d_s, mm	1	2	3	4	5	6	7	8
θ_s°	6.363	7.726	9.20	10.813	12.59	14.57	16.85	19.59
θ_m°	38.63	37.27	35.797	34.186	32.409	30.422	28.15	25.4
l_m, mm	15.94	16.53	17.21	18.023	19.01	20.25	21.89	24.25
A_m, mm^2	499.0	481.4	462.34	441.529	418.58	392.9	363.5	328.07

Table 4.7 Geometrical variation due to the increase of the distance between the adjacent magnets

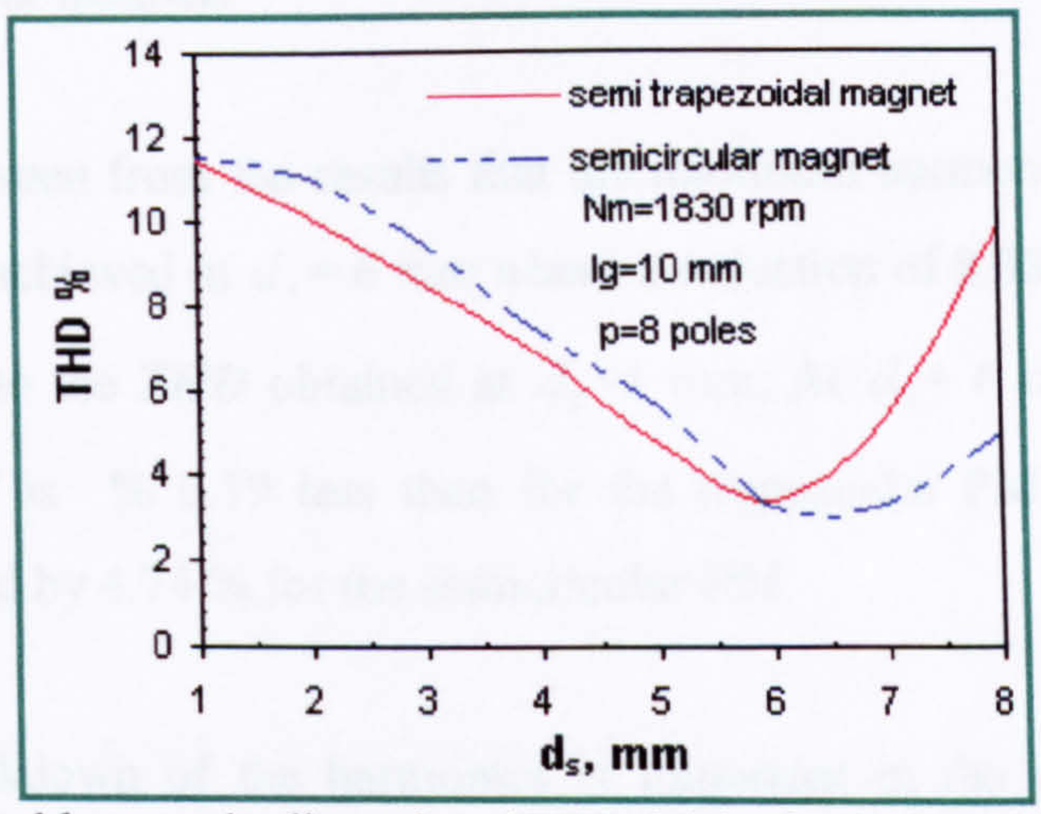

Figure 4.33 Total harmonic distortion (*THD %*) in the induced voltages vs. distance between adjacent magnets for semicircular and semi trapezoidal magnets

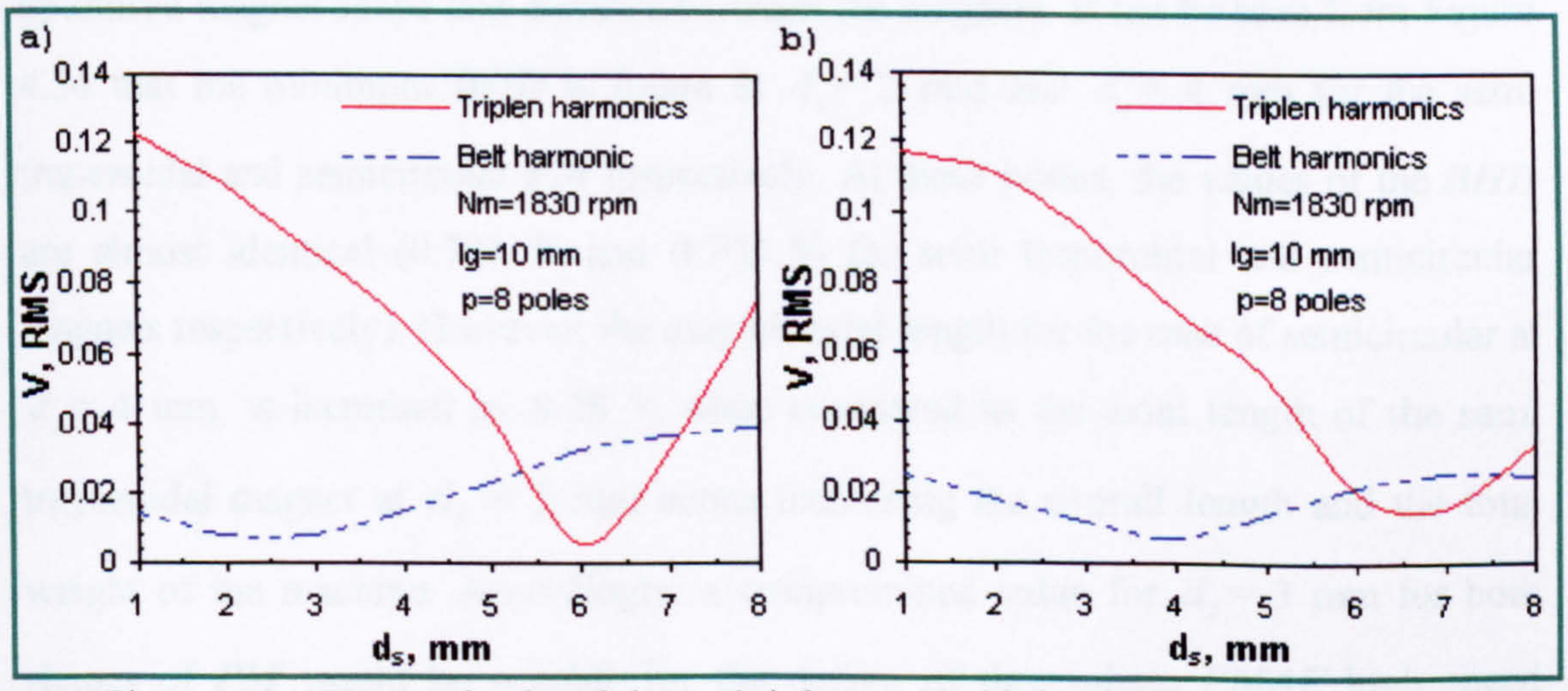

Figure 4.34 Harmonics breakdown (triplen and belt) for the *PMAF* generator a) semi trapezoidal magnets b) semicircular magnets

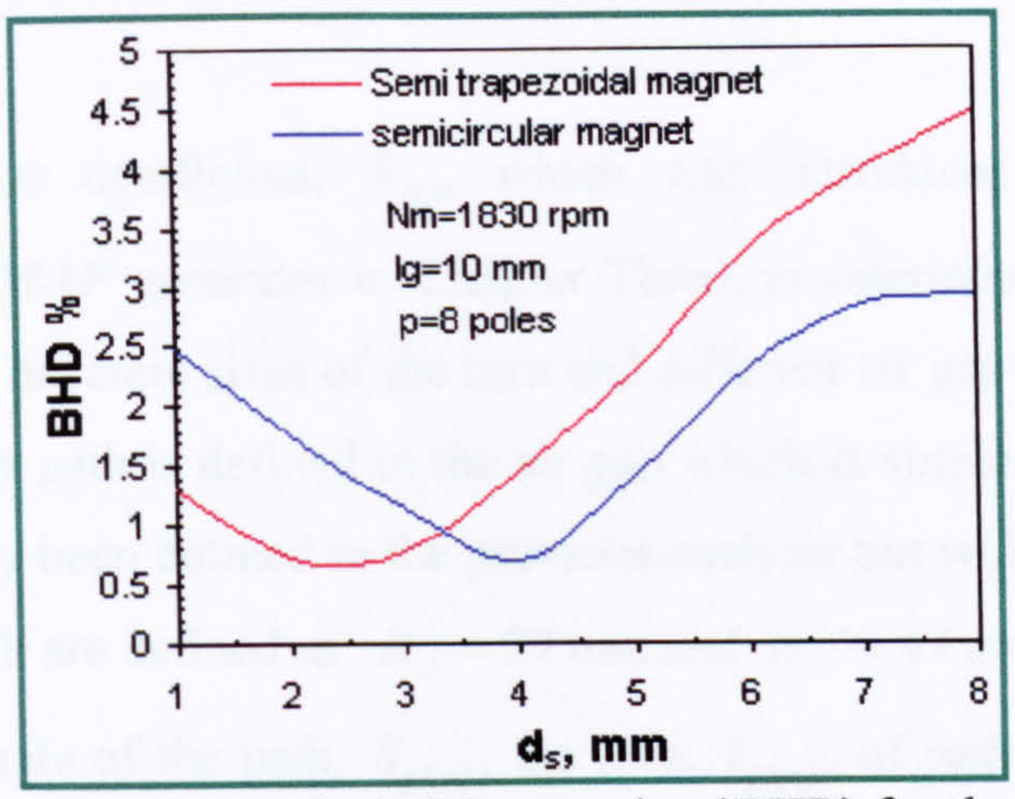

Figure 4.35 Distortion due to the belt harmonics (***BHD***) for the semi trapezoidal and semicircular magnets

It can be seen from the results that the minimum harmonic distortion for both shapes of ***PM*** is achieved at d_s= 6 mm where a reduction of 8.38 % is achieved in the ***THD*** compared to the ***THD*** obtained at d_s=1 mm. At d_s= 6 mm, the ***THD*** for the semicircular ***PM*** is % 0.19 less than for the trapezoidal PM. However, the peak voltage is reduced by 4.74 % for the semicircular ***PM***.

The breakdown of the harmonics is important in the design of the ***AFPM*** generator. If the generator is designed as single phase generator, then ***THD*** should be considered. For three phase generator, the triplen harmonics are all cancelled and only the distortion due to the belt harmonics (***BHD***) should be considered for the purpose of optimised magnet shape and distance between the magnets. It can be seen from Figure 4.34 that the minimum ***BHD*** is found at d_s= 2 mm and d_s= 4 mm for the semi trapezoidal and semicircular ***PM*** respectively. At these points, the values of the ***BHD*** are almost identical (0.721 % and 0.703 % for semi trapezoidal and semicircular magnets respectively). However, the magnet axial length for the case of semicircular at d_s= 4 mm, is increased by 8.28 % when compared to the axial length of the semi trapezoidal magnet at d_s = 2 mm hence increasing the overall length and the total weight of the machine. Accordingly, a compromised value for d_s= 3 mm for both shapes of ***PM*** would be suitable for the design of three-phase ***PMAF*** high speed generator.

4.5.3.3 Determination of the coil size coefficient

The coil size coefficient, k_{size} which was introduced in the theoretical modelling of the *PMAF* generator in Chapter Three, is determined based on the *FE* results obtained for different sizes of the turn and different air gap lengths. To perform the analysis, another path is defined in the air gap which is similar to the shape of the path that has already been defined in the previous analysis but with the inner and outer radii of the new path are defined as $R_{ci} = 27\,\text{mm}$ and $R_{co} = 47\,\text{mm}$ respectively. Thus for a given span angle of the path, $\theta_{p(n)}$, the area, $A_{p(n)}$, of path number (n) can be calculated as:

$$A_{p(n)} = \frac{\pi(R_{co}^2 - R_{ci}^2)\theta_{p(n)}}{360} \tag{4.32}$$

For this analysis, θ_p for each path is equal to the pole pitch i.e. 45°. Hence the area of the path is calculated as $A_{p(1)}$= 15833.3 mm^2 and $A_{p(2)}$= 581.1 mm^2 for the first path and the second path respectively. With the two defined paths are positioned opposite to the *PM* for maximum magnetic flux, the axial air gap length is varied over the range of 8 mm to 16 mm with an increment step of 2 mm to account for the variation in the magnetic circuit. Once the maximum flux crossing each path, $\phi_{\max(n)}$, is found, then the average magnetic flux density, $B_{ave(n)}$ for the n-path can be calculated as:

$$B_{ave(n)} = \frac{\phi_{\max(n)}}{A_{p(n)}} \tag{4.33}$$

Through this variation in the axial air gap length, the air gap magnetic flux density B_g is determined and the ratio of flux density, $C_{B(n)}$, can be given as:

$$C_{B(n)} = \frac{B_{ave(n)}}{B_g} \tag{4.34}$$

To account for the effect of the materials used for the retainment ring, the analysis is performed once with Maraging G125 used as a retainment ring and then a non-magnetic material properties assigned for another simulation. The results obtained from both analyses are presented in Tables 4.8 and 4.9.

l_g mm	$\phi_{max(1)}$ mWeb	$\phi_{max(2)}$ mWeb	$B_{ave(1)}$ T	$B_{ave(2)}$ T	B_g T	$C_{B(1)}$	$C_{B(2)}$
8	35.78	28.59	0.226	0.492	0.761	0.296	0.645
10	30.94	24.58	0.195	0.423	0.677	0.288	0.624
12	27.62	22.14	0.174	0.381	0.595	0.292	0.640
14	24.68	18.36	0.156	0.316	0.524	0.297	0.602
16	22.10	15.91	0.139	0.274	0.461	0.301	0.593

Table 4.8 Results obtained for non magnetic retainment ring

l_g mm	$\phi_{max(1)}$ mWeb	$\phi_{max(2)}$ mWeb	$B_{ave(1)}$ T	$B_{ave(2)}$ T	B_g T	$C_{B(1)}$	$C_{B(2)}$
8	28.41	25.92	0.179	0.446	0.727	0.246	0.613
10	24.51	21.92	0.154	0.377	0.638	0.242	0.591
12	21.26	18.64	0.134	0.321	0.553	0.242	0.579
14	18.50	15.86	0.117	0.273	0.479	0.243	0.571
16	16.19	13.57	0.102	0.233	0.418	0.244	0.557

Table 4.9 Results obtained for Maraging G125 retainment ring

The ratio of the magnetic flux obtained from each analysis is averaged thus, $C_{B(1)} = 0.295$ and $C_{B(2)} = 0.621$ for non-magnetic retainment ring and $C_{B(1)} = 0.243$ and $C_{B(2)} = 0.582$ for Maraging retainment ring. Hence after some manipulation, the size coefficient for any turn in the coil is given as:

- For non magnetic retainment ring

$$k_{size(n)} = -325A_{t(n)} + 0.8098 \tag{4.35}$$

- For Maraging retainment ring

$$k_{size(n)} = -338A_{t(n)} + 0.778 \tag{4.36}$$

where $A_{t(n)}$ is the area of the n^{th} turn in the coil represented by a defined path in the air gap.

4.5.3.4 Determination of the air gap length coefficient, k_g

Although the air gap length physically can be determined by the distance between the two opposite magnet rotors, the actual air gap length is slightly larger due to the fringing effects where the majority of the flux lines travel in lengthened paths in the air gap rather than in a shortcut path.

Hence the air gap length l_g is multiplied by a coefficient which should be greater than 1.0 to make its actual length larger. To determine this coefficient for both cases of retainment reigns, the air gap flux density B_g and the attainable flux density, B_u, at the surface of the permanent magnet are determined for a particular air gap length. Hence the ratio of the attainable flux, k_g, is determined by:

$$k_g = \frac{B_u}{B_g} \tag{4.37}$$

The results obtained from the *FE* model for this particular analysis are given in Table 4.10 and 4.11 for the nonmagnetic and Maraging ring respectively. After some manipulation on these results the air gap length coefficient is presented as a function of the air gap length for each type of material retainment ring, thus:

- For nonmagnetic retainment ring;

$$k_g = 10.33l_g + 1.0283 \tag{4.38}$$

- For Maraging retainment ring;

$$k_g = 17.33 l_g + 0.9903 \tag{4.39}$$

l_g mm	B_g T	B_u T	V_{pk} V	*THD* %	k_g
8	0.761	0.846	1.951	10.369	1.111
10	0.677	0.760	1.783	8.669	1.122
12	0.594	0.686	1.624	7.142	1.154
14	0.524	0.614	1.478	6.019	1.173
16	0.461	0.538	1.351	4.958	1.167

Table 4.10 Results obtained from *FE* model for nonmagnetic retainment ring

l_g mm	B_g T	B_u T	V_{pk} V	*THD* %	k_g
8	0.727	0.821	1.508	11.370	1.129
10	0.6348	0.729	1.339	9.65	1.142
12	0.553	0.654	1.164	8.389	1.182
14	0.479	0.591	1.022	7.397	1.233
16	0.4179	0.513	0.921	5.97	1.220

Table 4.11 Results obtained from *FE* model for Maraging retainment ring

The results found in Tables 4.10 and 4.11 contain useful data where the performance of *PMAF* generator for different axial air gap lengths can be compared for both types of retainment rings. These results are also shown in Figures 4.36 – 4.38.

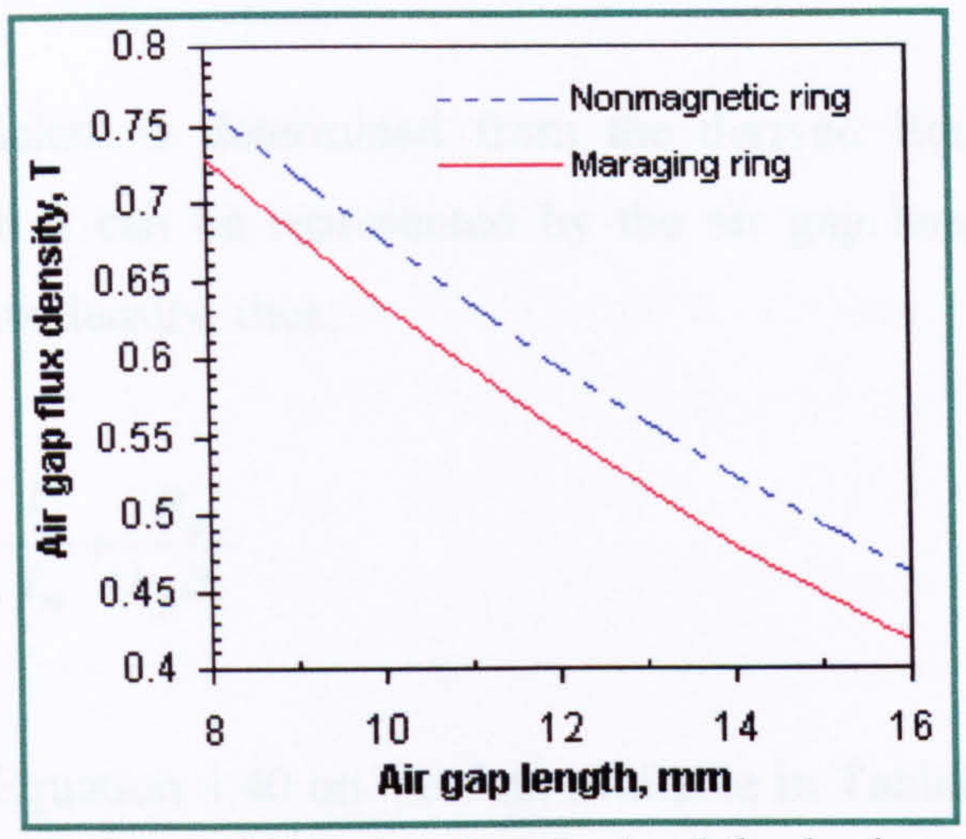

Figure 4.36 Comparison of flux density obtained for both types of retainment rings

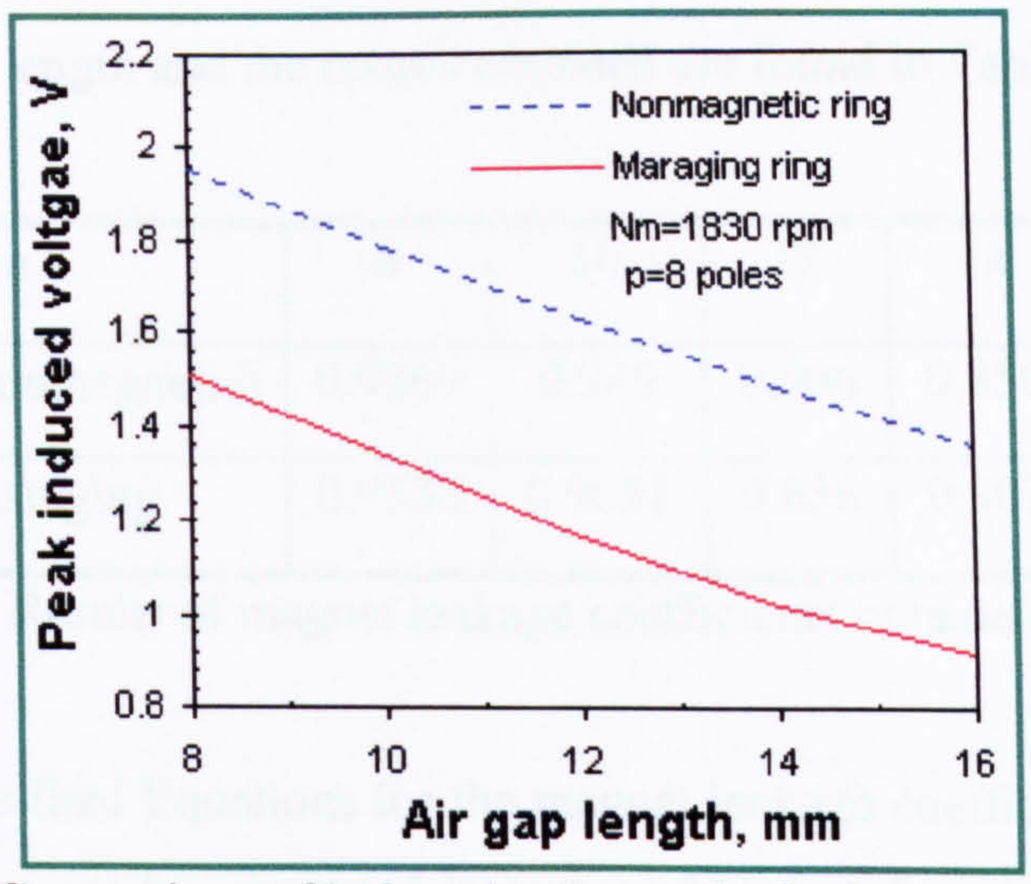

Figure 4.37 Comparison of induced voltages for both types of retainment rings

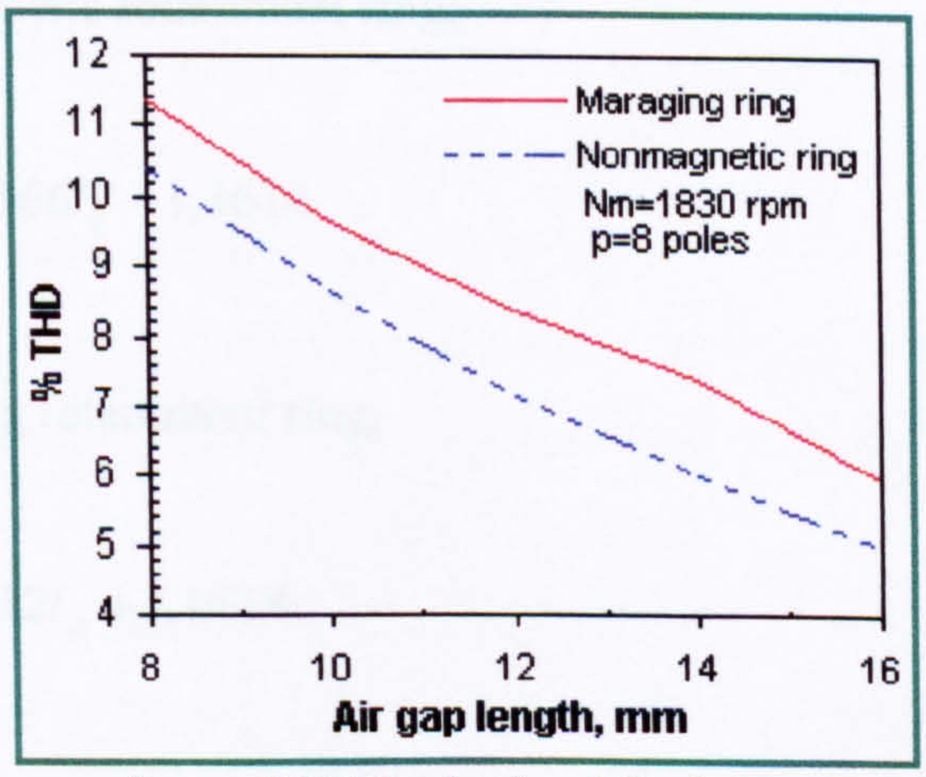

Figure 4.38 Comparison of *THD* obtained for both types of retainment rings

4.5.3.5 Determination of the magnet leakage coefficient, k_{Br}

This coefficient is determined from the derived Equation 3.42 in Chapter Three, from which it can be represented by the air gap length, magnet length and magnet residual flux density, thus;

$$k_{Br} = \frac{B_g}{k_p B_r}\frac{l_g}{l_m} + \frac{B_u}{k_p B_r} \tag{4.40}$$

Applying Equation 4.40 on the data available in Tables 4.10 and 4.11 for both types of rings considering an axial length of the magnet, $l_m = 17\,\text{mm}$ and magnet residual flux density, $B_r = 1.22$ T, the magnet leakage coefficient is determined at each particular air gap length and the results obtained are found in Table 4.12.

l_g, mm	8	10	12	14	16
k_{Br} (nonmagnetic)	0.9869	0.949	0.906	0.856	0.794
k_{Br} Maraging	0.9533	0.9051	0.856	0.807	0.7428

Table 4.12 Results of magnet leakage coefficients obtained from *FE* model

Hence the final Equations for the magnet leakage coefficient for this particular deign of the rotor can be presented in terms of air gap length for the given magnet length and magnet residual flux density as follows:

- For non magnetic retainment ring;

$$k_{Br} = -21.8166 l_g + 1.1614 \tag{4.41}$$

- For Maraging retainment ring;

$$k_{Br} = -26.312 l_g + 1.1638 \tag{4.42}$$

4.5.3.6 Modelling the final coil of the *PMAF* high-speed generator

In this analysis, the final shape of the coil is considered for the prediction of the induced voltage and *THD* of the *PMAF* high-speed generator. Five concentric paths for each layer are defined having their shape and dimensions approximately similar to the shape and dimensions of the coil that was shown in Figure 3.17 in Chapter Three. These paths which are shown in details in Figure 4.39 are rotated about the axis of rotation and the flux change in all coil is determined hence the induced voltage and harmonics are predicted in the same way which was described for a single path.

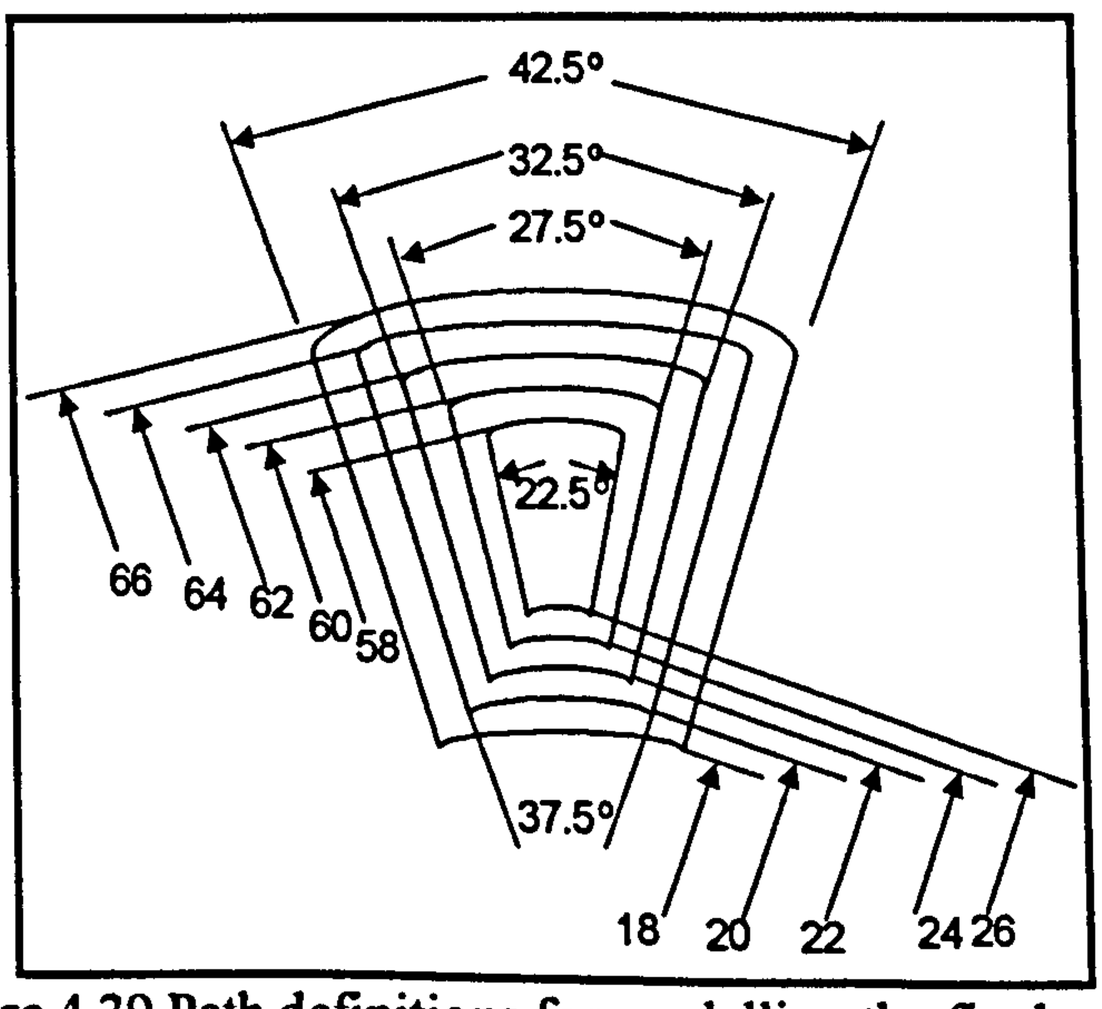

Figure 4.39 Path definitions for modelling the final coil of the *PMAF* high-speed generator

To predict the no-load induced voltage accurately, the above-described paths are placed at a plane at a distance of 2 mm from the centre of the air gap which represents the middle of the thickness of the single layer of the actual constructed coil. Finally the results obtained from these paths are multiplied by two since there are two identical layer for each coil then multiplied by eight which is the total number of coils per stator. Since the no-load voltage is required from this analysis, the results are modelled at a speed of 1830 rpm so that they can be compared with the experimental results obtained at the same speed in Chapter Seven. The induced voltage from each individual turn of the coil for the case of Maraging G125 retainment ring is shown in Figure 4.40. The total induced voltage compared to a pure sinusoidal waveform and

the spectrum analysis of the induced voltage from all turns of the stator coils for the case of Maraging G125 retainment ring and nonmagnetic retainment ring are shown in Figure 4.41 and 4.42 respectively. The comparison between the induced voltages for both types of retainment rings is shown in Figure 4.43.

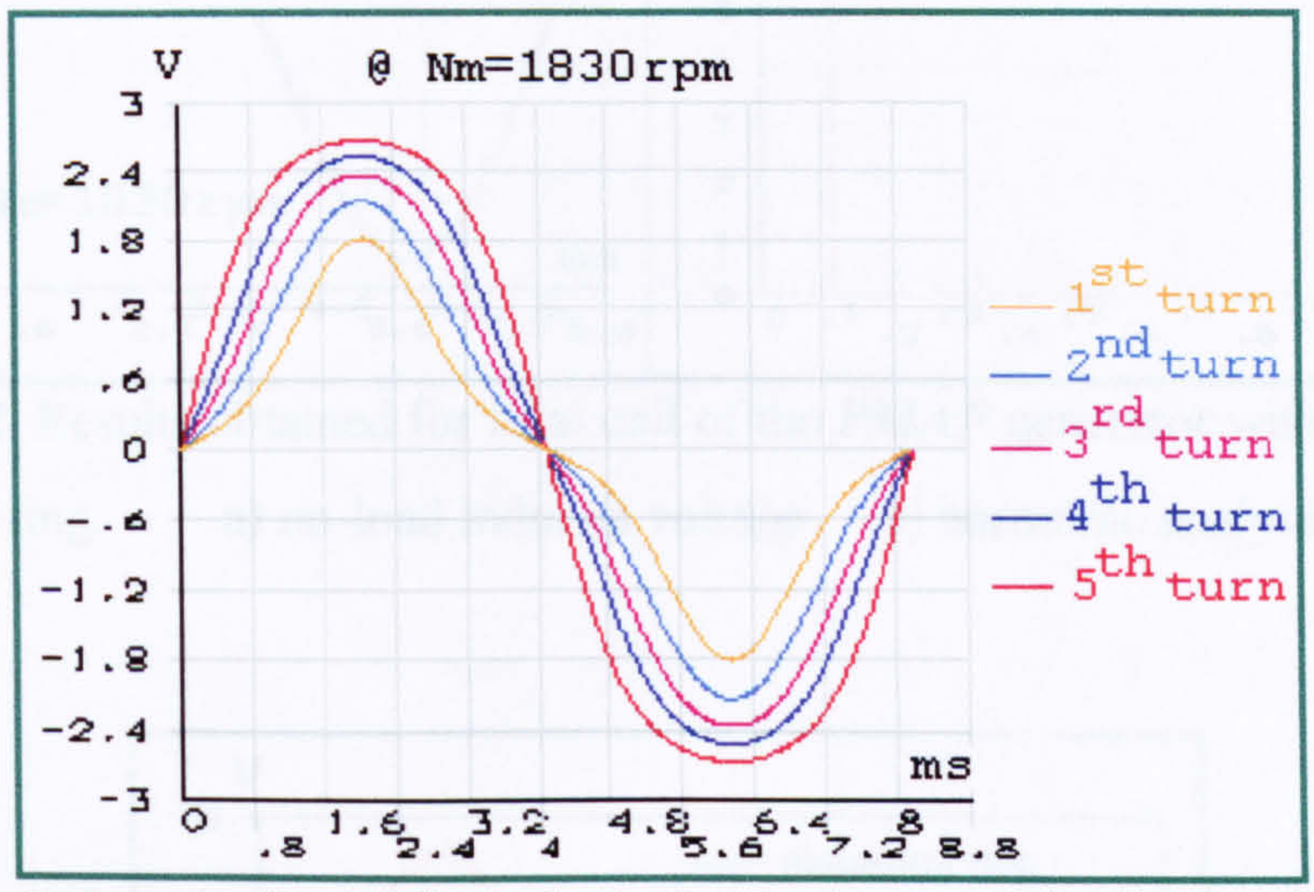

Figure 4.40 Induced voltages from the individual turns of the final coil for the case of Maraging G125 retainment ring rotor

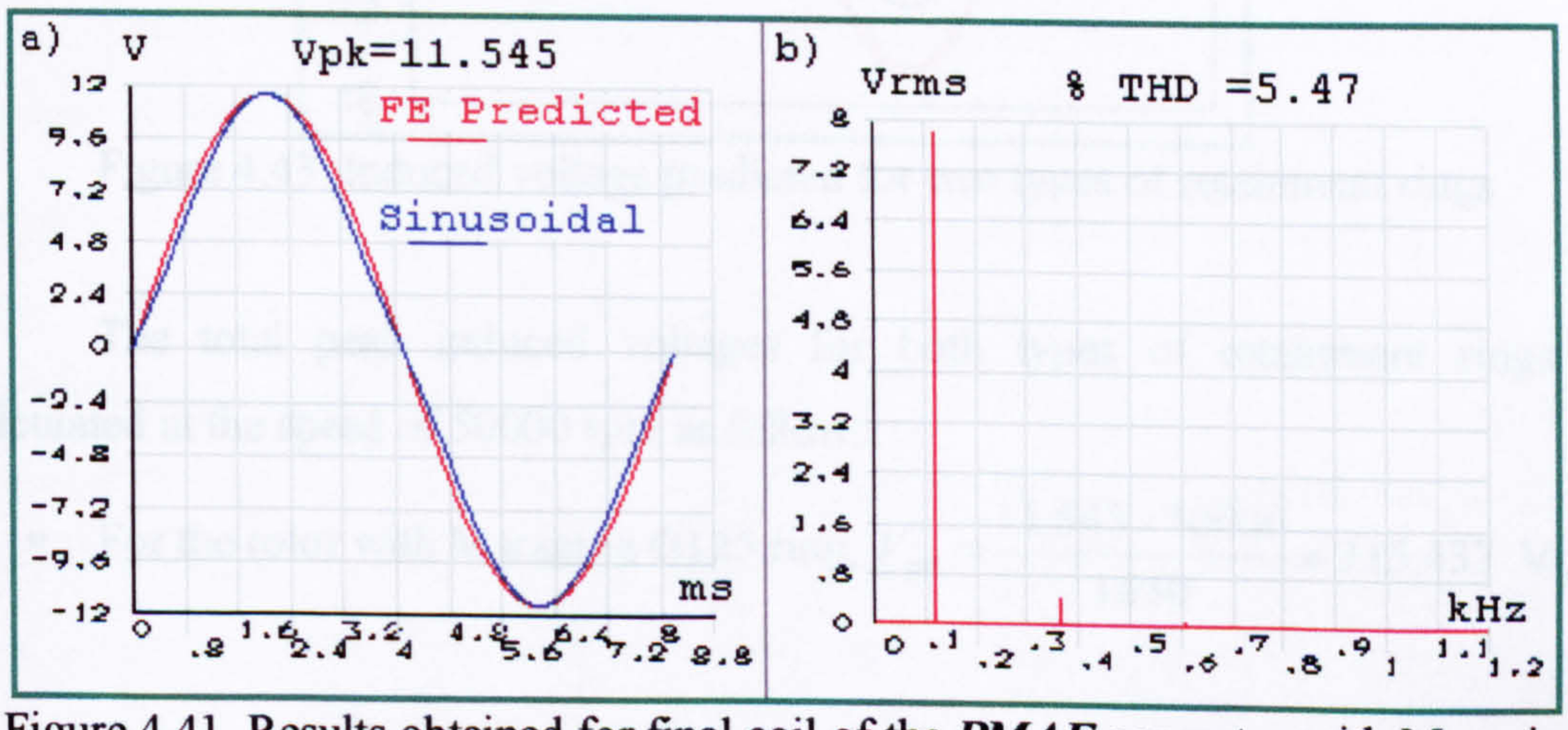

Figure 4.41 Results obtained for final coil of the ***PMAF*** generator with Maraging G125 retainment ring a) no-load induced voltage b) harmonic analysis

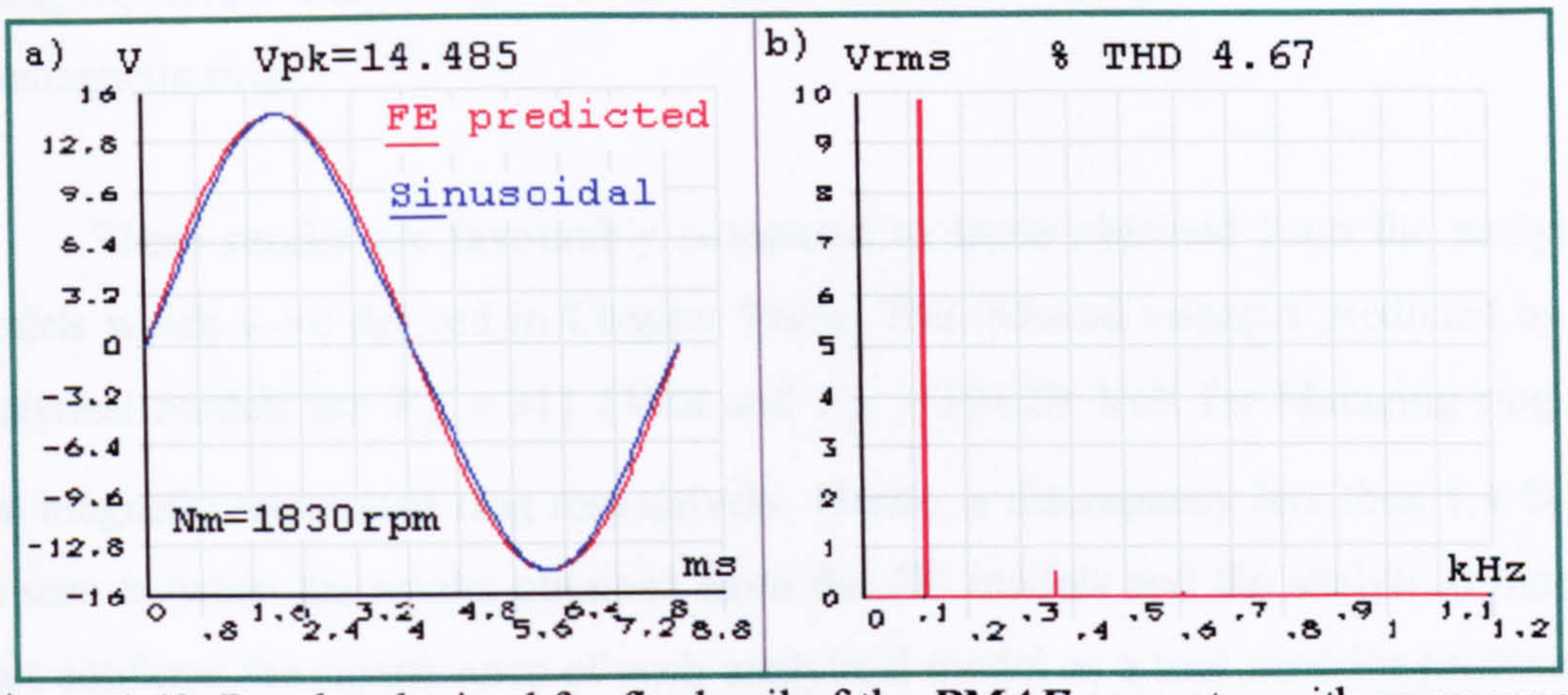

Figure 4.42 Results obtained for final coil of the ***PMAF*** generator with nonmagnetic retainment ring a) no-load induced voltage b) harmonic analysis

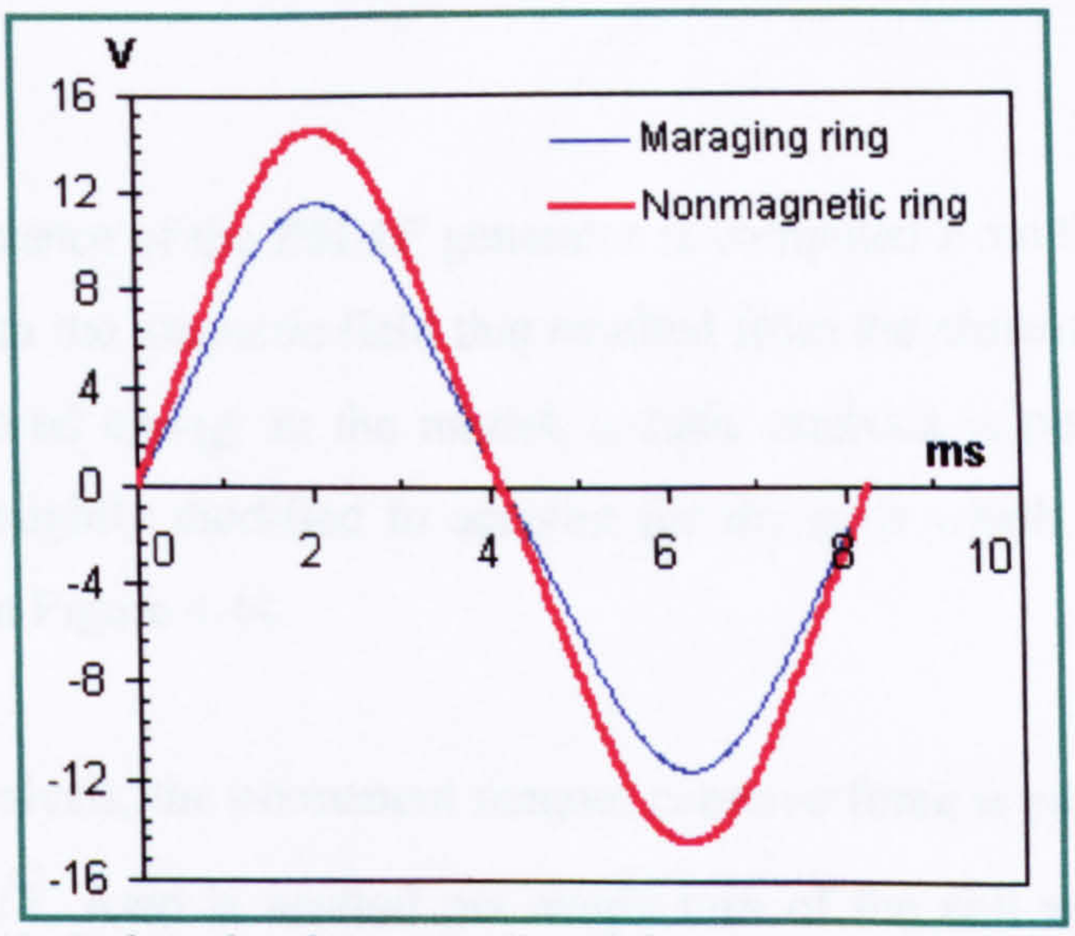

Figure 4.43 Induced voltage predicted for two types of retainment rings

The total peak induced voltages for both types of retainment rings are calculated at the speed of 50000 rpm as follows:

- For the rotor with Maraging G125 ring, $V_{pk} = \frac{11.545 \times 50000}{1830} = 315.437$ Volt

- For the rotor with nonmagnetic ring, $V_{pk} = \frac{14.485 \times 50000}{1830} = 395.76$ Volt

It is shown from the results that the peak no-load induced voltage for the Maraging G125 ring is 21 % less than induced voltage from the rotor with nonmagnetic rings.

These results are favourably compared to these obtained from the analytical models which were derived in Chapter Three. The induced voltages predicted by the analytical models are $V_{pk} = 311.1$ Volt and $V_{pk} = 394.29$ Volt for Maraging ring and non magnetic retainment ring respectively. Hence, a discrepancy less than 1.4 % can be seen between the results obtained from the *FE* models and the analytical models. This confirms the significance of such analytical model as a tool used for preliminary design and assessment of the *PM* generator.

4.5.3.7 Computation of the inductance of the *PMAF* High speed generator

The inductance of the *PMAF* generator is computed from the stored energy in the machine due to the magnetic field that resulted from the armature current [48,69]. To determine the stored energy in the model, a static analysis is performed by the *3D* model which is slightly modified to account for the coils which has its geometrical shape as shown in Figure 4.44.

In this analysis, the permanent magnet coercive force is set to zero and a peak current of $75 \times \sqrt{2}$ Amp is applied per single turn of the coil which has $N_{CT} = 10$ turns. This is done by selecting the elements that represent the coil and a current density of 13.25 Amp/mm^2 is injected into these elements which have a total cross-sectional area of 0.8 mm^2. Since the coil has an oval shape, it was necessary to divide it into four regions from which each region has its elements oriented according to a local coordinate systems that have been created specially for this purpose (Figure 4.44). The flux density distribution in the model as a result from the injected current alone is shown in Figure 4.45.

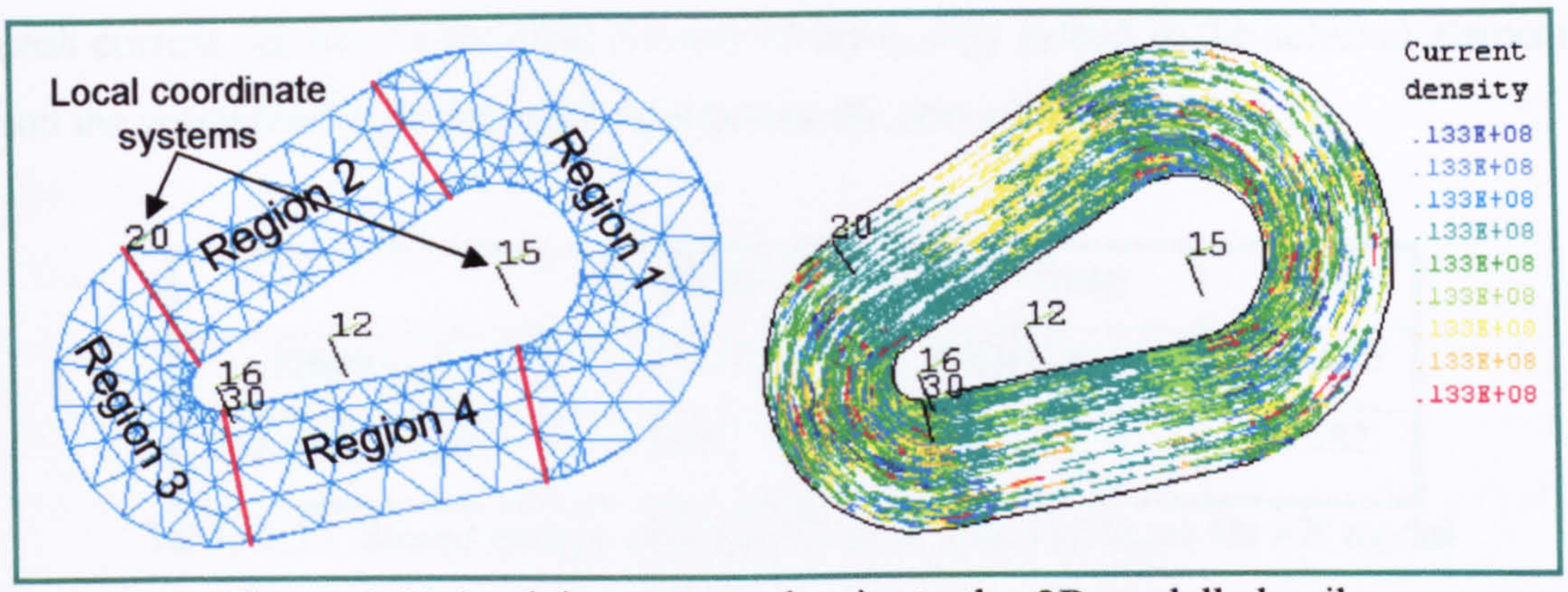

Figure 4.44 Applying current density to the ***3D*** modelled coils

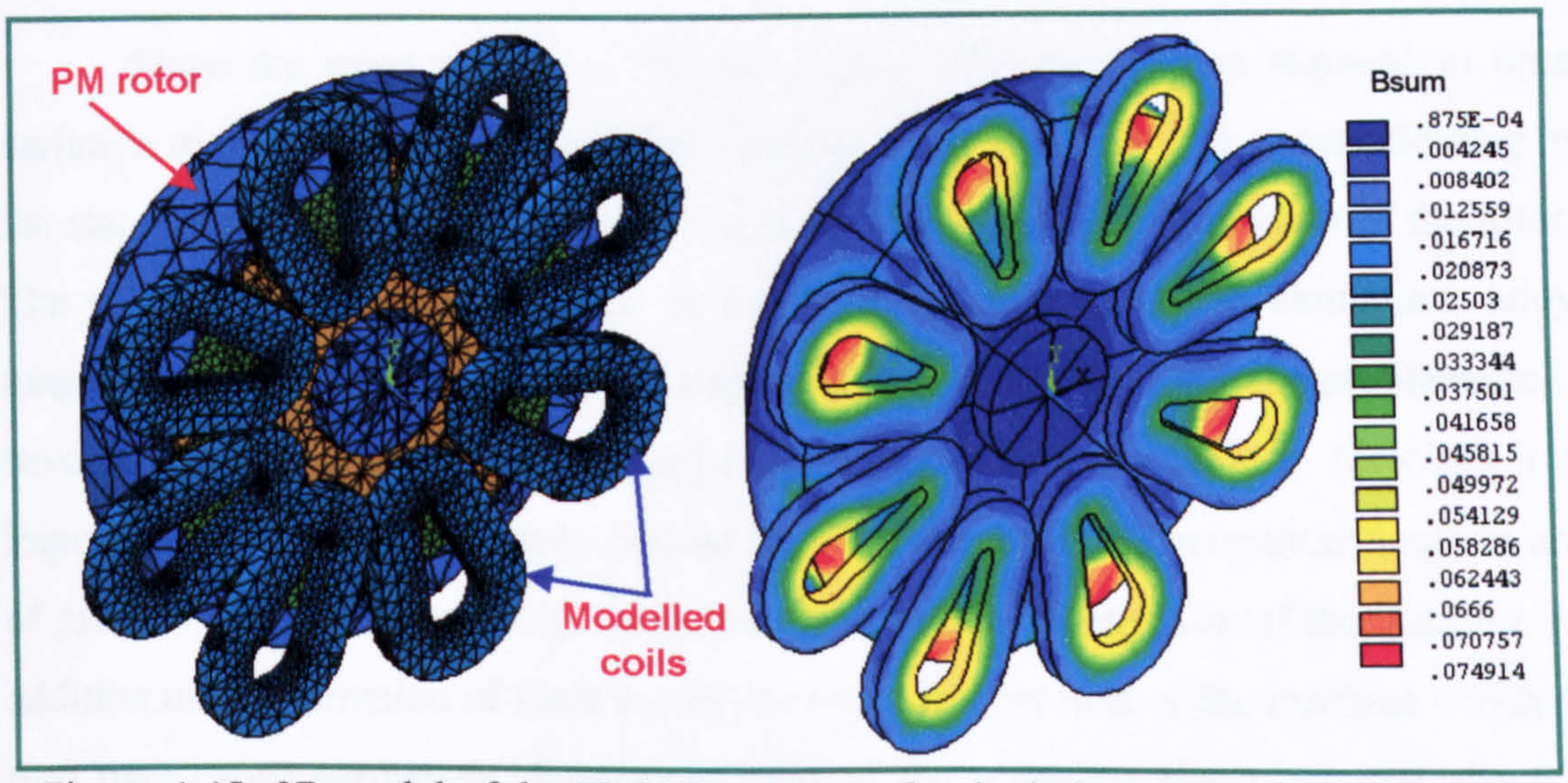

Figure 4.45 ***3D*** model of the ***PMAF*** generator for the inductance calculations; flux shown is due to armature current only

To compute the total inductance of the windings, the total elements in the model are selected then the energy stored in these elements is calculated by invoking the built-in macro provided through the ***ANSYS*** postprocessor. In fact, this macro gives that total stored energy in the whole model as well as the discrete values of the energy stored in each component in the model from which the leakage and magnetising inductances are calculated as follows:

$$L_l = \frac{2W}{i^2} \tag{4.43}$$

where W is the energy stored in the selected elements in the model (Joule) and i is the peak current per turn of the coil. Results of the energy stored in the selected elements and the corresponding computed inductances are presented in Table 4.13.

	Leakage	Magnetising	Total
Energy, J	0.08219	0.14467	0.22686
Inductance, μH	14.630	25.752	40.382

Table 4.13 Stored energy and inductances obtained from ***3D FE*** model

4.5.3.8 Evaluation of rotor eddy current losses

Since the rotor surface of the high-speed ***PM*** generator is exposed to time variation in the flux density due to the magnetic flux created by the current flowing in the stator, eddy current is induced and it is distributed over several parts of the rotor. The eddy current loss may occur in the magnet material, in the aluminium alloy magnet carrier and in the retainment ring over the magnets and may be problematic if several precautions are not considered in the design of such machines. Although it is important to know the total eddy current losses in the rotor, the permanent magnets are of primary concern since a high loss may result in demagnetisation of the magnets. In addition underestimation of these losses me result in over heat of the machine which in turn may cause permanent demagnetisation of the magnets. Hence an accurate and rigor method is required to evaluate the eddy current losses in such machines.

In literature, several methods were presented to calculate the eddy current losses in the rotor of cylindrical machines [45,46,47]. **Polinder et al** [46] have presented a modified model for calculating the losses in the magnets of the surface mount ***PM*** cylindrical high speed machines which is based on the following formula:

$$P_e = \frac{b_m^2}{12\rho}\left(\frac{dB}{dt}\right)^2 \tag{4.44}$$

where b_m is the magnet circumferential width and ρ is the resistivity of the ***PM***. The model has shown a good agreement between the predicted and the measured losses for

a particular machine at locked rotor test and the author finally suggested that the eddy losses in the magnets can be minimised by reducing the magnet width or by using pure sinusoidal stator current. However, this model is based on many simplified assumptions which may be valid for such a particular machine configuration. Moreover, winding end effect and harmonics effect were all neglected in the calculations. **Abu Sharkh etal** [36] have also presented a ***2D FE*** method for calculating the rotor eddy current losses in cylindrical ***PM*** machines under various conditions. Results obtained showed more agreement with the experimental data have been achieved when compared to the results obtained from the simplified analytical models.

Accordingly, and due to the complex nature of the proposed ***PMAF*** high-speed generator, it was decided to compute the eddy current losses in the rotor with the aid of the ***3D FE*** model which has been introduced in the previous sections. In this analysis, the ***PM*** again is set off (deactivated) and AC harmonic analysis is performed instead of the magnetostatic analysis and the procedures of the analysis are summarised as follows:

- All resistivities for the material used in the model are specified.
- The DC current injected in the elements of the coils in the previous analysis is set off.
- Extra degree of freedom (***CURR***) is added for the elements of the coil that have already been defined by ***SOLID97*** element and this is done through the element's options available in the ***ANSYS*** program.
- This additional degree of freedom allows simulating the case of voltage fed stranded coil with the rotor locked at certain position.
- The stranded coil is described through the real constant of the specified ***ANSYS*** element where number of turns, coil cross sectional area, actual volume of the coil and filling factor are all defined.
- The nodes of the coil are coupled in the current degree of freedom (***CURR***) and specified values of voltage drop and phase angle are applied to the coil elements.
- The type of analysis is set to harmonic analysis and the frequency range is defined. All boundary conditions applied in the previous static analysis are valid for this type of analysis.

- The solution is performed and the results are viewed in particular the current density in the coil is checked first to make sure that the full load current is drawn through the coil. This current density can be adjusted by the amount of the voltage drop specified at the beginning of the analysis. If the current density is satisfied then other results of interest can be viewed in details.
- The eddy current losses in any part of the rotor can be calculated by invoking the built in macro in ***ANSYS*** program (***POWERH***) which calculates the RMS power loss in any conducting body in the model represented by the selected elements. The theory for calculating eddy current using this macro is given as follows [69]:

$$P_{Rrms} = \frac{1}{2}\int_{vol} \rho \left|\tilde{J}_t\right|^2 d(vol) \tag{4.45}$$

where:

P_{Rrms} = rotor rms power loss, W

ρ = material resistivity, $\Omega.m$

J_t = total current density, Amp/mm^2

~ = complex quantity

The macro evaluates Equation 4.45 by integrating over the selected element set according to:

$$P_{Rrms} = \frac{1}{2}\mathrm{Re}\left\{\sum_{i=1}^{n}\left(\left([\rho_i]\{\tilde{J}_{ti}\}\right)^* \cdot \{\tilde{J}_{ti}\}\right) vol_i\right\} \tag{4.46}$$

where:

n = number of elements

Re{ } = real component of a complex quantity

$[\rho_i]$ = resistivity matrix

$\{J_{ti}\}$ = total eddy current density vector for element i

vol_i = element volume

* = complex conjugate operator

- The calculations of the eddy current losses are performed on the rotor which has its dimensions and geometry defined in previous sections with the material resistivities are given in Table 4.14. The first set of results is obtained for the load current varied in the range from from 15 – 75 Amp with a step increment of 15 Amp. The calculations are obtained at an operating frequency of 3333 Hz. The total as well as the discrete eddy losses in each component in the rotor is given in Table 4.15 and also presented graphically in Figure 4.46. The Flux density distribution as well as the induced eddy current density distribution in the whole rotor and in each individual part of the rotor are shown in Figures 4.47 – 4.51.

Material	Magnet Carrier (Alumec 89)	PM (NdFeB)	Retainment Ring (Maraging G125)	Back-iron (steel)
Resistivity, $\Omega \cdot m$	3×10^{-8}	70×10^{-8}	20×10^{-8}	20×10^{-8}

Table 4.14 Material resistivities used for rotor eddy current calculations

Load current, Amp	Rotor Eddy losses, W @ frequency =3333 Hz				
	Magnet carrier	PM	Retainment ring	Back-iron	Total
15	7.61	1.178	3.47	0.20	12.46
30	30.49	4.72	13.91	0.79	49.96
45	68.45	10.61	31.23	1.87	112.16
60	121.69	18.86	55.52	3.34	199.41
75	188.46	29.21	85.99	5.04	308.8

Table 4.15 Rotor eddy current losses at different load current

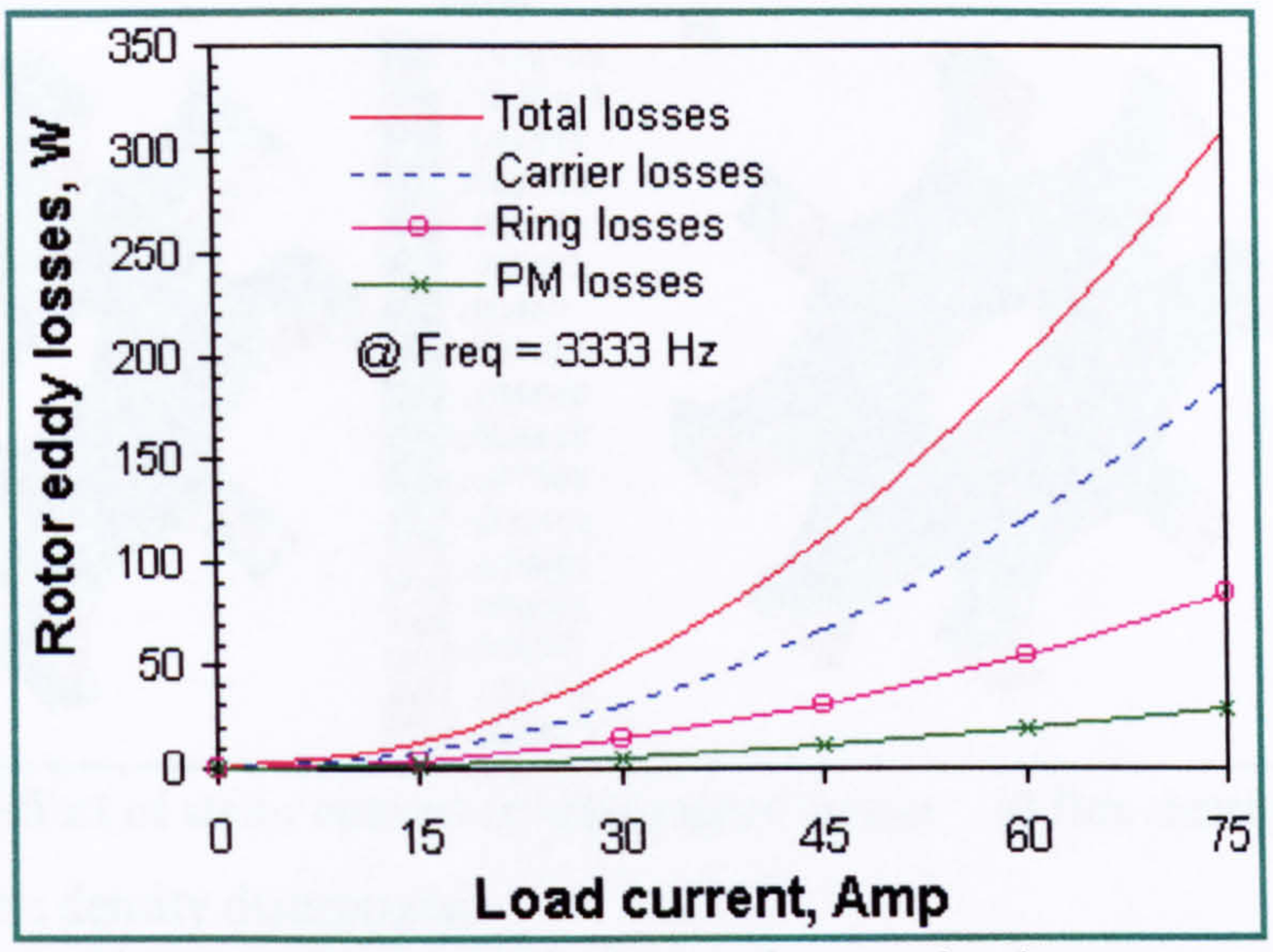

Figure 4.46 Rotor eddy current loss vs. load current

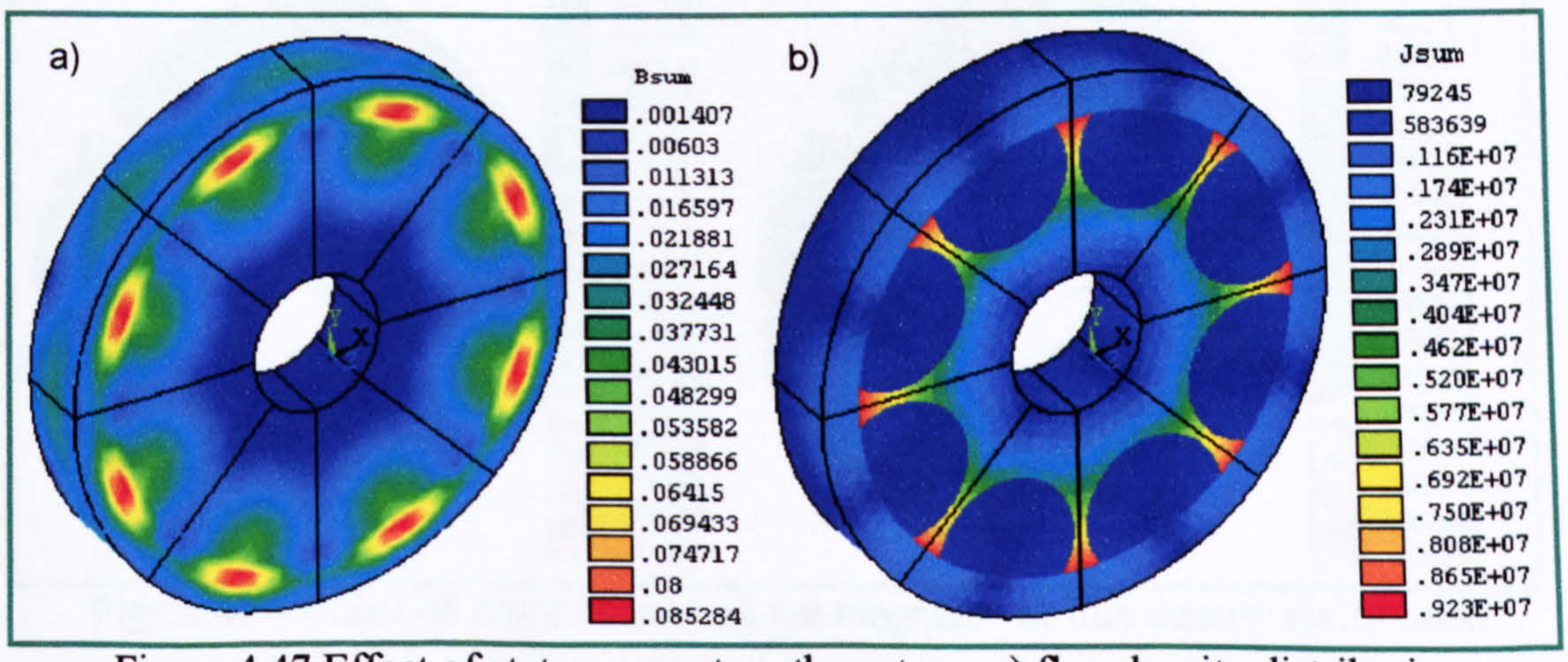

Figure 4.47 Effect of stator current on the rotor a) flux density distribution

b) eddy current density distribution

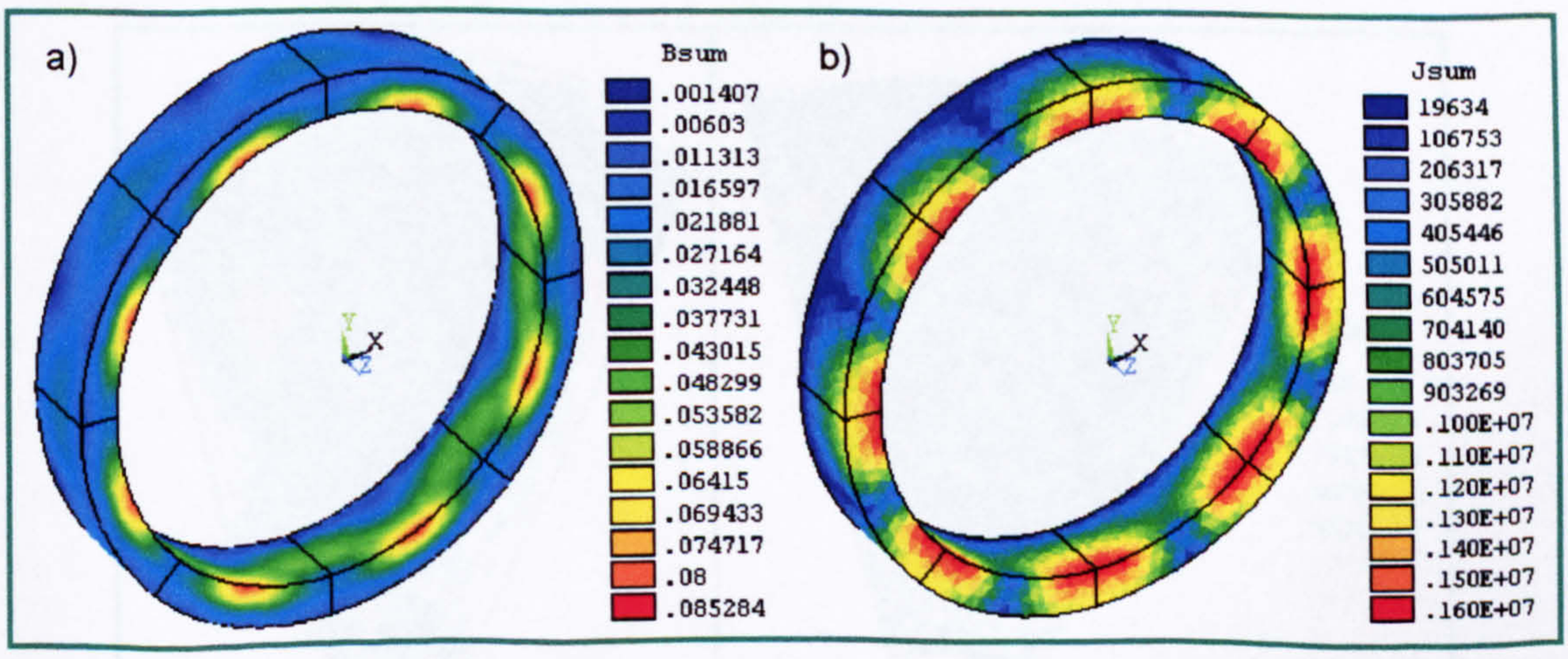

Figure 4.48 Effect of stator current on the retainment ring a) flux density distribution

b) eddy current density distribution

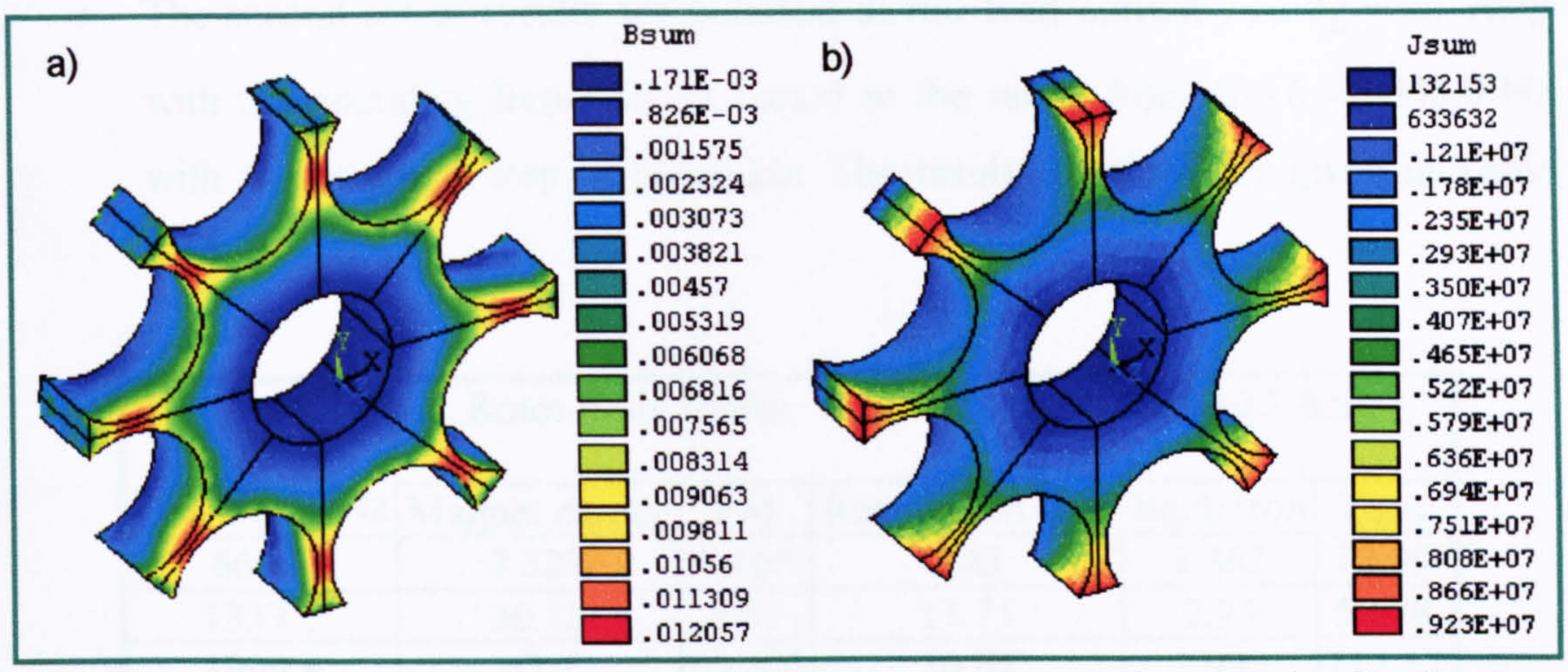

Figure 4.49 Effect of stator current on the magnet a) flux density distribution b) eddy current density distribution

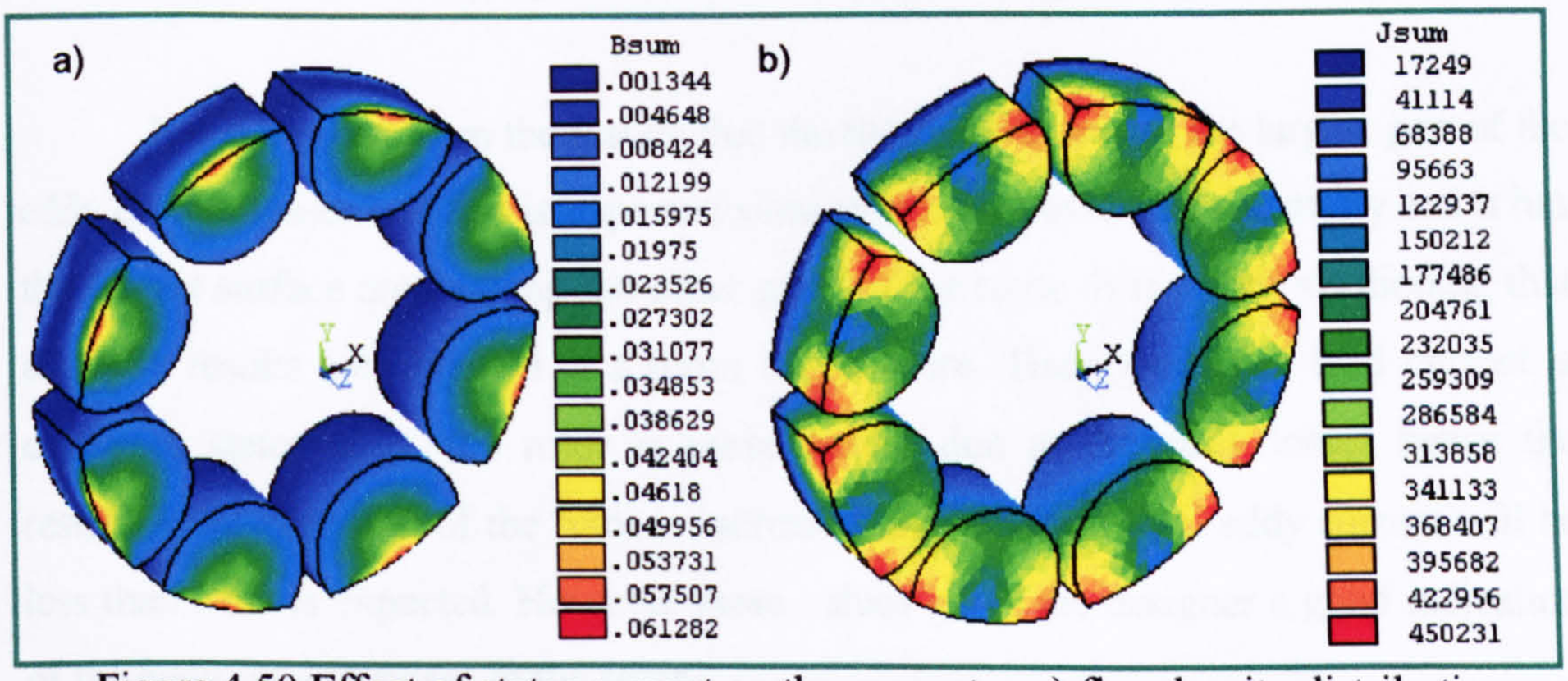

Figure 4.50 Effect of stator current on the magnets a) flux density distribution b) eddy current density distribution

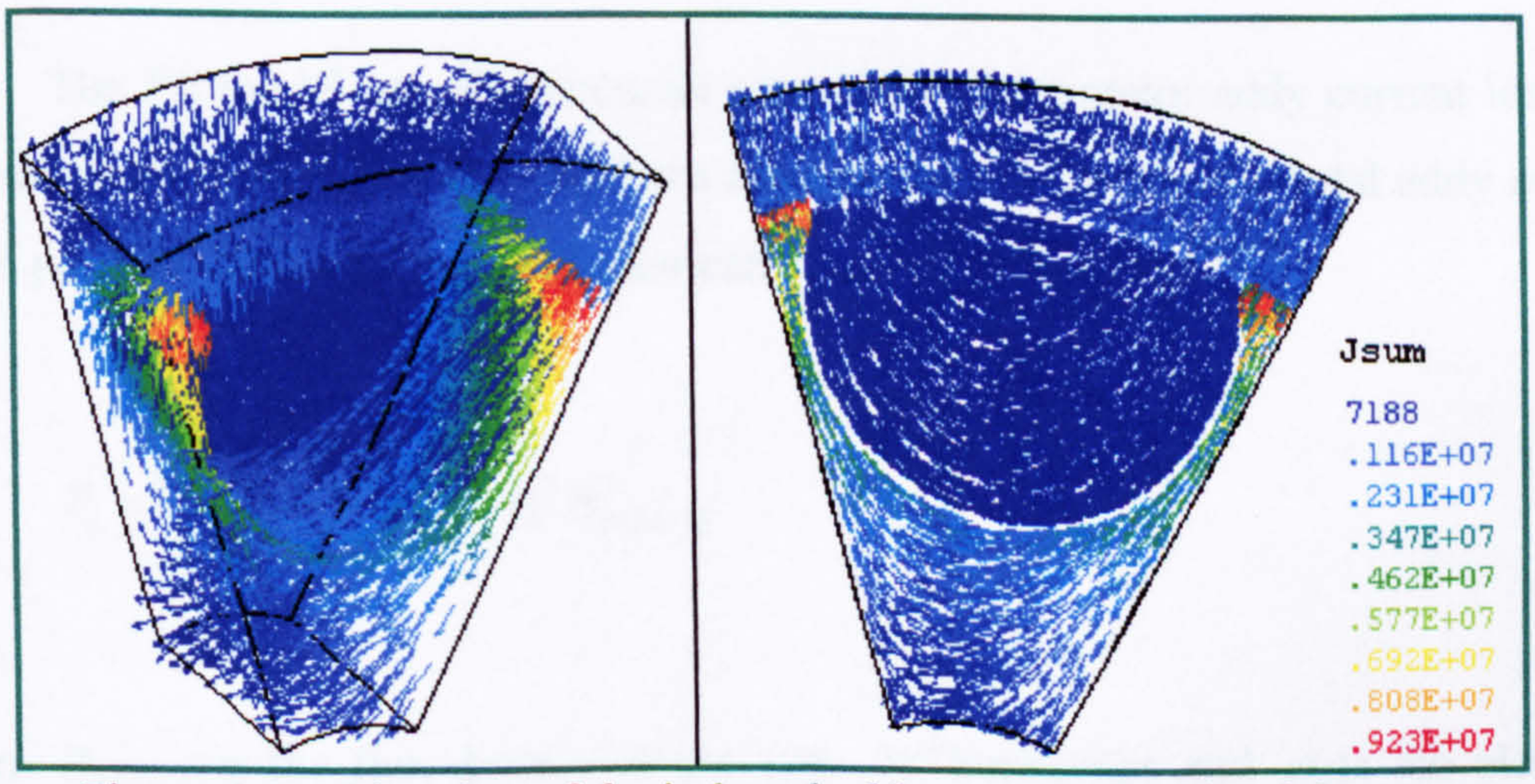

Figure 4.51 Direction of the induced eddy currents in 1/8 of the rotor

- The second set of results are obtained at full load current , i.e. $I_L = 75$ Amp with the operating frequency is varied in the range from 666.6 – 3333.0 Hz with an increment step of 666.6 Hz. The results obtained are given in Table 4.16.

	Rotor Eddy losses, W @ full load current =75 Amp				
Frequency, Hz	Magnet carrier	PM	Retainment ring	Back-iron	Total
666.6	7.527	1.166	3.43	1.867	13.99
1333.2	30.13	4.67	13.75	2.23	50.78
1999.8	67.7	10.505	30.92	2.995	112.12
2666.4	120.62	18.69	55.03	3.91	198.25
3333.0	188.46	29.212	85.99	5.138	308.8

Table 4.16 Rotor eddy current losses at different operating frequency

It can be seen from the results that the magnet carrier has the largest part of the eddy current losses and this is expected since it has got the lowest resistivity and it has the largest surface area among the other parts of the rotor. It is worth mentioning that all these results are obtained at a room temperature. Thus, when full load current is drawn in stator coils, the rotor is more heated due to the eddy losses hence the resistivity of each part of the rotor is increased and the rotor total eddy current will be less than what is expected. However these values gives the designer a good indication of the eddy current losses in the rotor.

4.5.3.9 Evaluation of stator eddy current losses

The *FE* model can give accurate prediction of the stator eddy current losses if the harmonics in flux density waveform are determined. Hence, the total eddy current losses per unit volume of the conductor can be given as follows [16,80]:

$$P_e = \frac{d_{std}^2 \omega_e^2}{32 \rho_c} \sum_{n=1}^{\infty} (2n-1)^2 B_{p(2n-1)}^2 \qquad (4.47)$$

where $B_{p(2n-1)}$ is the flux density at the $(2n-1)^{th}$ harmonics and ω_e is the electrical angular frequency (rad/sec).

The harmonic contents in the flux density waveform can be determined from the ***FE*** model where the flux density at the middle of the air gap is scanned per pole pitch i.e. in the angular coordinates from 22.5° – 67.5° and at a fixed radial coordinate, $R = 36$ where B_g is maximum. The waveform of the air gap flux density which is shown in Figure 4.52-a) is Fourier analysed and its harmonic analysis is shown in Figure 4.52-b). The values of the flux density at their harmonic's order and their corresponding eddy current losses are given in Table 4.17.

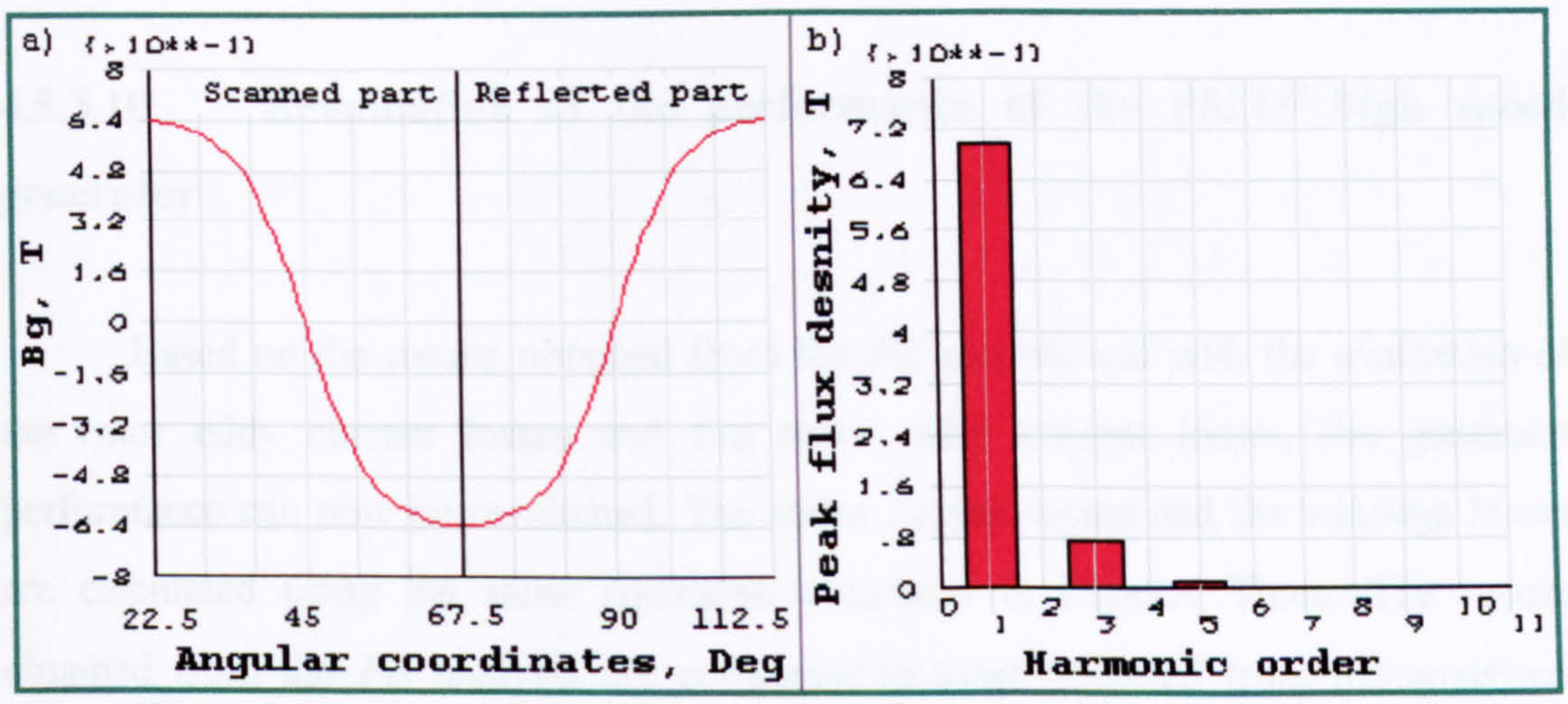

Figure 4.52 Air gap flux density a) waveform b) harmonic analysis

Harmonics	1st	3rd	5th	7th	9th	11th
B_p, T	0.698	0.0737	0.0111	2×10^{-4}	1.59×10^{-3}	3.55×10^{-3}
P_{eu}, W/m	46.6	4.67	0.294	0.000182	0.0174	0.1457

Table 4.17 Waveform harmonic analysis and stator eddy current losses per unit length of the conductor

where P_{eu} in the table is the eddy current losses per unit length of the strands calculated at room temperature i.e. $\rho_c = 1.729\times10^{-8}\,.\Omega\cdot m$. Hence these losses will be reduced when the full load current is drawn and the temperature of the stator coils increases. The sum of all losses is found to be 51.72 W/m which represents an increase of 9.9 %

in the eddy current losses due to the harmonics in the waveform. Accordingly, the total eddy current losses in the stator can be calculated as:

$$P_{Se} = P_{eu} \times L_{edd} \tag{4.48}$$

where L_{edd} is the total conductor length and it is found from Equation 3.89 in Chapter Three. Hence the total eddy current losses in the stator due to the presence of all harmonics of the air gap flux density is found to be 165.5 W for a conductor length of 3.2 m.

4.5.3.10 Revaluation of the performance of the *PMAF* high speed generator

Based on the results obtained from the *FE* models and with the evaluation of the rotor eddy current losses and the stator eddy current losses, the generator performance can now be revaluated. The stator copper losses and the windage losses are calculated using the same equations presented in Chapter Three. The results obtained from the *FE* analysis are compared to these obtained from the analytical solutions and are presented in Table 4.18. It can be seen from the results that the analytical model is a good tool for evaluating the generator performance

Parameter	FE	Analytical
No-load Volt, Vrms	223	220
Resistance, Ω	0.0828	0.0828
Leakage inductance, μH	15	12
Magnetising Inductance, μH	25	26
I^2R loss, W	466	466
Windage loss, W	350	350
Rotor eddy loss, W	309	Not predicted
Stator eddy loss, W	165.5	124.61
Terminal voltage, Vrms	207.75	205.39
Pout, W	15581.25	15403.46
Voltage regulation %	6.83	6.64
Efficiency %	92.35	94.31

Table 4.18 Performance prediction of the *PMAF* high speed generator using *FE* and analytical models

CHAPTER 5

DESIGN & FE ANALYSIS OF THE BACK-IRON DISC

5.1 INTRODUCTION

The "back-iron", normally called the keeper disc, is the part which completes the magnetic circuit in any electric machine. In general, back-iron has been used in laminated forms in generators, motors, transformers and electromagnetic switches to minimise the hysteresis and eddy current losses generated due to the time variation of the flux density in their stator cores. Also, for the same reason, in some applications laminated sheets have been used in the rotor of generators and motors running at low and moderate speed. However, in high-speed applications, laminated sheets are not suitable for the rotor structure since they can be a source of mechanical failure due to the high centrifugal forces exerted on these parts. In addition, epoxy resin and sometimes tie rods and bolts are required for stacking process and mechanical support of the laminated structure and these complicate the design.

Accordingly, an alternative design for the back-iron disc is required for the high-speed generator. In this work, a solid disc form of the back-iron is proposed for the purpose of high speed application, not only because of its rigidity, mechanical integrity and robustness, but also due to the simplicity and cost reduction in manufacturing and assembly. In this chapter, initial mechanical analysis is performed for the simplified circular disc of the back-iron. Then investigation is carried out on different materials in the light of their meeting design requirements in terms of availability, suitability and cost. Finally, further analysis is carried out to obtain the final design data for the back-iron disc with the aid of ***FE*** electromagnetic and structural modelling.

5.2 INITIAL ANALYSIS OF THE BACK-IRON DISC

The proposed ***PMAF*** high-speed generator was described earlier in Chapter Three and was shown in Figures 3.1 and 3.2. The proposed back-iron disc, which is a steel based alloy, is assembled adjacent but at the backside of the magnet rotor disc to endorse a good path for the flux lines that are leaving the permanent magnets of interchanged polarities rather than to leak into the free air space. Thus, the back-iron disc and magnet rotor disc are both fitted at the same shaft and will be rotating together at the same speed.

As was stated earlier in this chapter, making the back-iron in the laminated form was essential in most of conventional electric machines to minimise eddy current in their cores. In the present proposed ***PMAF*** generator arrangement, there will be no relative motion between the magnet rotor disc and the back-iron disc. Hence, the only flux density variation occurs within the back-iron disc will be due to the current drawn in the stator coils that are placed in the air gap between the two opposite magnet rotor discs. Earlier ***FE*** magnetic analysis of the generator was carried out in Chapter Four has shown that the flux density variation within the back-iron disc is marginal, hence negligible eddy current losses will be generated in the back-iron as a result of the current drawn in stator coils.

Because of the high-speed limitations, a solid form of the back-iron disc is proposed for the ***PMAF*** high-speed generator. Preliminary, uniform circular disc is presented for the purpose of initial analysis. Basically, the design of the back iron disc will follow the design of the magnet rotor disc. Hence, the principle dimensions of the back-iron disc have been obtained from the design data for the magnet rotor disc, which was determined earlier in Chapter Three. A sectional view for the simplified magnet rotor assembly and the back-iron disc is shown in Figure 5.1, whereas the principal dimensions of the magnet rotor disc are presented in Table 5.1.

An appropriate material can be selected partly on the basis of stress levels in the rotating disc. In order to perform the initial stress calculations for the back-iron

disc rotating at the design speed, a uniform back-iron disc was selected with axial thickness $l_i = 15$ mm, outer radius $R_{io} = 47$ mm and inner radius $R_{ii} = 7.5$ mm.

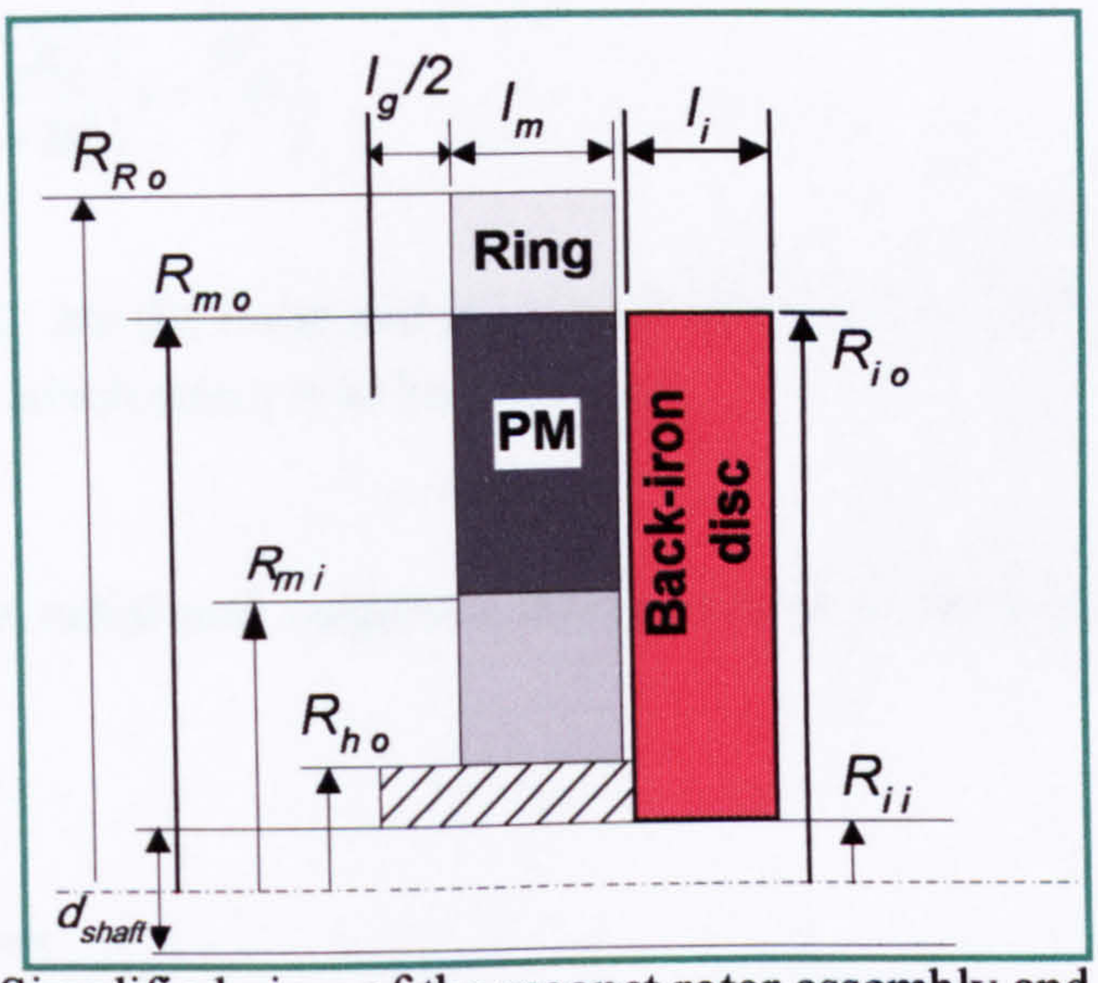

Figure 5.1 Simplified view of the magnet rotor assembly and back-iron disc

$l_g/2$ mm	l_m mm	l_i mm	R_{Ro} mm	R_{mo} mm	R_{io} mm	R_{mi} mm	R_{ho} mm	R_{ii} [mm]
5	17	15	55	47	47	27	15	7.5

Table 5.1 Principal dimensions of the magnet rotor disc

5.2.1 Initial stress analysis for the uniform back-iron disc

The disc is fitted on the shaft via shrink fit to prevent slippage while it is running at the operating speed of 50,000 r.p.m. The required amount of interference fit and the associated stresses can be calculated as follows:

First, when the disc is standstill, a contact pressure P_{cont} is exerted on the disc bore due to the shrink fit on the shaft. Hence, the residual radial and tangential stresses can be calculated using Lame solution for thick-walled cylinder theory [56,57]:

$$\sigma_{r1} = \frac{P_{cont} R_{ii}^2}{R_{io}^2 - R_{ii}^2}\left(1 - \frac{R_{io}^2}{r^2}\right) \tag{5.1}$$

$$\sigma_{\theta 1} = \frac{P_{cont} R_{ii}^2}{R_{io}^2 - R_{ii}^2}\left(1 + \frac{R_{io}^2}{r^2}\right) \tag{5.2}$$

where R_{io} and R_{ii} are the outer and inner radii of the back-iron disc respectively and r is the radius at which stress is to be calculated.

Maximum radial and tangential stresses occur at the bore of the disc, i.e. at $r = R_{ii}$, hence:

$$\sigma_{r1} = -P_{cont} \tag{5.3}$$

$$\sigma_{\theta 1} = P_{cont} \frac{R_{io}^2 + R_{ii}^2}{R_{io}^2 - R_{ii}^2} \tag{5.4}$$

The disc-plus shaft assembly acts as if it were a single solid disc (with initial stresses) until the shrink fit loosens. Thus, the associated stresses at $r = R_{ii}$ for a solid rotating disc are calculated as:

$$\sigma_{r2} = \frac{3+\nu}{8}\rho\omega^2 R_{io}^2\left(1 - \frac{R_{ii}^2}{R_{io}^2}\right) \tag{5.5}$$

$$\sigma_{\theta 2} = \frac{3+\nu}{8}\rho\omega^2 R_{io}^2\left(1 - \frac{1+3\nu}{3+\nu}\frac{R_{ii}^2}{R_{io}^2}\right) \tag{5.6}$$

The disc will be made of some type of steel-based alloy so Poisson's ratio and the mass density of the disc are basically given as $\nu = 0.3$ and $\rho = 7850$ kg/m^3 respectively.

Finally, the net stresses are calculated by combining both cylinder and solid disc solutions. The compressive contact pressure on the disc bore decreases as the rotational speed increases. When the shrink fit loosens, the net radial stress at the bore of the disc becomes zero. Thus, by adding Equation 5.3 to Equation 5.5 and equating it to zero we get:

$$\sigma_{rT} = \sigma_{r1} + \sigma_{r2} = 0 \tag{5.7}$$

$$0 = -P_{cont} + \frac{3+\nu}{8}\rho\omega^2 R_{io}^2\left(1-\frac{R_{ii}^2}{R_{io}^2}\right) \tag{5.8}$$

Hence, the required contact pressure to keep the disc rotating with the shaft is given as:

$$P_{cont} = \frac{3+\nu}{8}\rho\omega^2 R_{io}^2\left(1-\frac{R_{ii}^2}{R_{io}^2}\right) \tag{5.9}$$

By substituting Equation 5.9 into Equation 5.4 we get:

$$\sigma_{\theta 1} = \frac{3+\nu}{8}\rho\omega^2\left(R_{io}^2 + R_{ii}^2\right) \tag{5.10}$$

The net tangential stress at the bore is calculated by adding Equation 5.6 and Equation 5.10:

$$\sigma_{\theta T} = \frac{3+\nu}{8}\rho\omega^2\left[\left(R_{io}^2 + R_{ii}^2\right) + R_{io}^2\left(1-\frac{1+3\nu}{3+\nu}\frac{R_{ii}^2}{R_{io}^2}\right)\right] \tag{5.11}$$

The minimum amount of interference fit required to keep the disc in contact with the shaft is found from:

$$\delta = \frac{p_c \sqrt{R_{io}^2 R_{ii}^2}}{E} \tag{5.12}$$

From the above analysis and using Young 's modulus of elasticity, E, for steel as 210 GPa, results for the uniform back-iron disc are given in Table 5.2.

p_c [MPa]	δ [μm]	$\sigma_{\theta 1}$ [MPa]	$\sigma_{\theta 2}$ [MPa]	$\sigma_{\theta r}$ [MPa]
188.5	16.8	198.35	190.58	389.93

Table 5.2 Results of the mechanical analysis for the uniform back-iron disc

Next, an investigation needs to be carried out on some available soft magnetic materials to select one that can match both magnetic and mechanical requirements for the specific application.

5.2.2 Material requirements for the back-iron disc

It is worth mentioning that system requirements such as high operating speed and high power density imply that the material of the back-iron disc must have both good magnetic and mechanical properties. The initial stress calculations performed assuming the use of normal steel has shown that the disc is not capable of withstanding the high stresses developed due to the high rotational speed. Hence, an alternative material is required which should exhibit high strength capability as well as high magnetic relative permeability and high saturation level. Minimum requirements for the magnetic and mechanical properties are summarised in Table 5.3.

Yield Strength [MPa]	% Elongation	Forms & Dimensions [mm]	Saturation [T]	Relative Permeability
> 500	> 10	Round Bars $100\phi \times 30$ L	> 1.2	1000

Table 5.3 *Minimum requirements for the properties of back-iron material*

An extensive survey was carried out and several worldwide suppliers and manufacturers were contacted in order to find a suitable material that satisfies these demands. Aspects such as cost effectiveness, manufacturing processability, and availability were also considered in the survey.

Information and data sheets for several different types of soft magnetic materials were obtained from Carpenter Technology Corporation which is a leading international manufacturer of specialty alloys and engineered products. A comparison chart for these materials based on magnetic property selector and cost is shown in Figure 5.2.

Among these general types of soft magnetic alloys, four particular materials were found to be suitable as regards meeting the requirements already listed. A brief description of these materials and their properties are shown in Table 5.4. Further details can be obtained from the manufacturers data sheets [82].

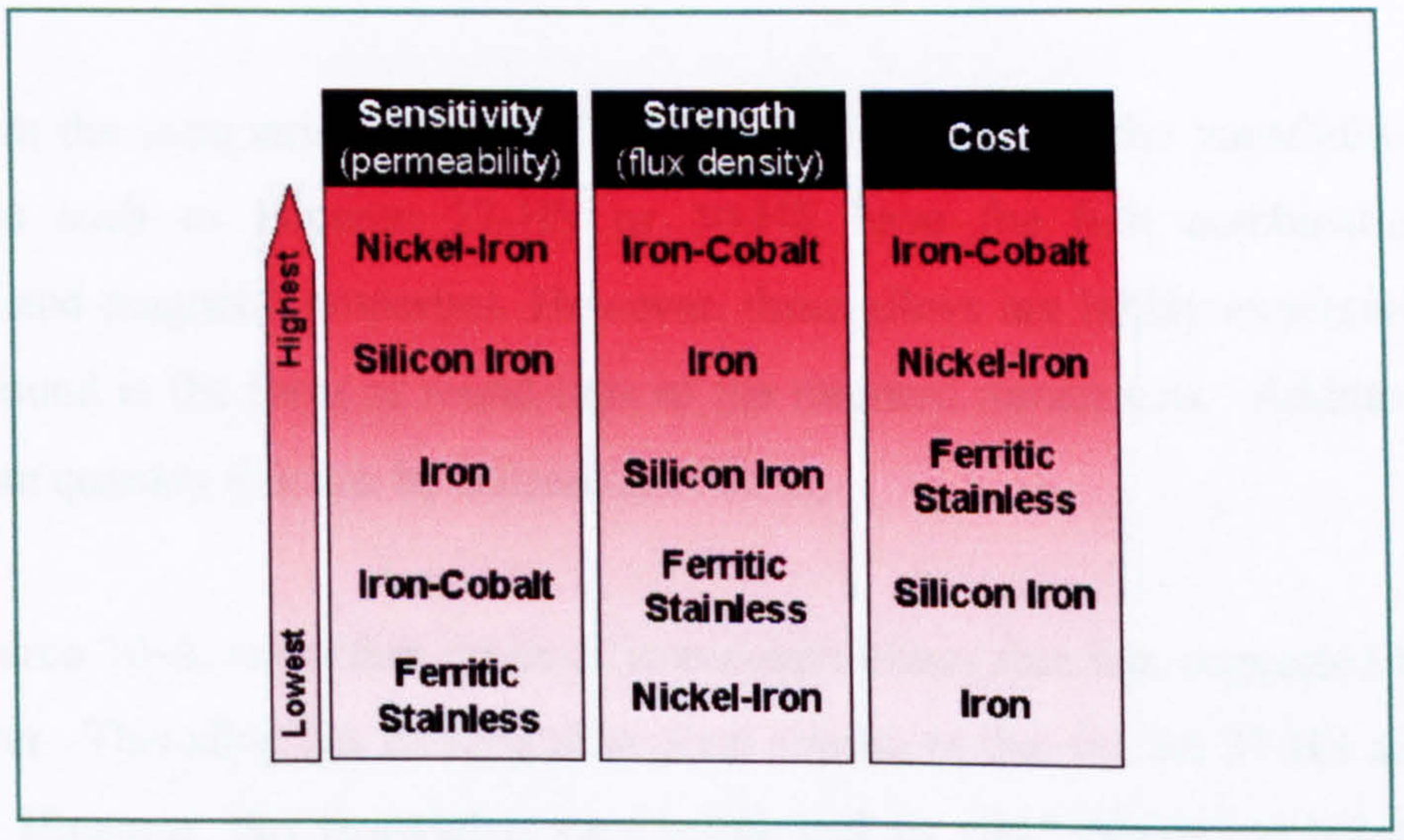

Figure 5.2 Magnetic property selector for soft magnetic materials

It is worth mentioning that, the mild steel or normal iron will not be considered in the evaluation because of its low mechanical strength (yield strength < 200 MPa) despite its high magnetic saturation level (B_s > 2.0 T) and high relative permeability (3000 - 5000).

Material Property	Iron Cobalt (Hiperco 27-HS) or (50-HS)	Silicon Iron (Type-C)	Ferritic Stainless (17/4 PH-1150)	Ferritic Stainless (17/4 PH-A)
0.2 Yield Strength [MPa]	552	517	860	760
Tensile strength [MPa]	896	655	1000	1034
% Elongation	23	30	19	6-15
Heat Treatment after machining	Required	Required	Required	Not Required
Magnetic Saturation [T]	2.4	2.06	1.01	1.38
Magnetic Permeability	2000	4000	-	1000
Cost / kg [£]	265	58	25	16
Source of Material	Scientific Alloys, Inc. USA.	Scientific Alloys, Inc. USA.	West Yorkshire Steel Co Ltd. UK.	West Yorkshire Steel Co Ltd. UK
Round Bars Availability	N.A. Alternative is Hiperco 50 A	Available	Available	Available

Table 5.4 Properties of selected soft magnetic materials

From the summarised data in Table 5.4, it is clear that the vanadium iron-cobalt-alloys such as Hiperco 27-HS or 50-HS have the best combination of mechanical and magnetic properties. However, these alloys are highly expensive and are rarely found in the form of round bars of the required dimensions. Additionally, the minimum quantity that can be ordered is 1000 kg.

Hiperco 50-A, is another grade of iron-cobalt alloys that was suggested by the manufacturer. This alloy has its saturation level similar to that for the 27-HS and 50-HS grades. However, this material is very brittle and its yield strength is below 370 MPa. Hence, this rules out iron-cobalt alloys as an option although their magnetic ***B-H*** curve is considered in the magnetic analysis in the next sections of this Chapter for the sake of comparison with the other soft magnetic materials such as silicon-iron and ferritic stainless steel alloys. It also can be noticed that the mechanical strength of ferritic stainless alloys is higher than that of silicon-iron alloys whereas the latter have a higher magnetic relative permeability and saturation level. In addition, the cost of the

silicon-iron alloys is high relative to the ferritic stainless steel alloys. However, less material is required when silicon-iron is used for the back-iron disc due to its high magnetic saturation level. These property interactions mean that, for the precise determination of the optimum dimensions and shape for the back-iron disc, non-linear solution ***FE*** analysis needs to be undertaken using the magnetic ***B-H*** curve for each of these various materials.

5.3 MAGNETOSTATIC *FEA* OF THE BACK-IRON DISC

This section deals with the ***FE*** magnetic analysis of the back-iron disc using the ***ANSYS 2D*** planer model which was developed earlier in Chapter Four. The objective is to optimise the geometrical parameters for the minimum volume of the back-iron disc that could handle the highest flux without saturation. The analysis is performed taking into account the non-linear behaviour of the proposed soft magnetic material for the back-iron disc. The intention is then to examine the influence of the back-iron dimensions and geometry on the magnetic flux and hence the influence of these parameters on the overall performance and operation of the generator. To accomplish this, a parametric analysis is carried out on the main geometrical parameters such as back-iron axial thickness and tip radius for a selected type of material. Then, the shape of the back-iron disc is modified where a certain cut, basically a quarter circular shape, on the outer edge is carried out. Finally, the magnetic attraction force exerted on the back-iron disc is calculated for the use in the upcoming ***FE*** structural analysis, which will be discussed in the next sections of this Chapter.

5.3.1 Justification of the *2D* model

Before proceeding with the required analysis, the ***2D*** planar model is verified against the ***3D*** model which was presented in Chapter Four. The results of the flux density in the air gap for a particular solution are obtained at two different positions defined by paths similar to those which were found in Chapter Four. These results are presented graphically in Figures 5.3 and 5.4 where both ***2D*** and ***3D*** models are compared to each other.

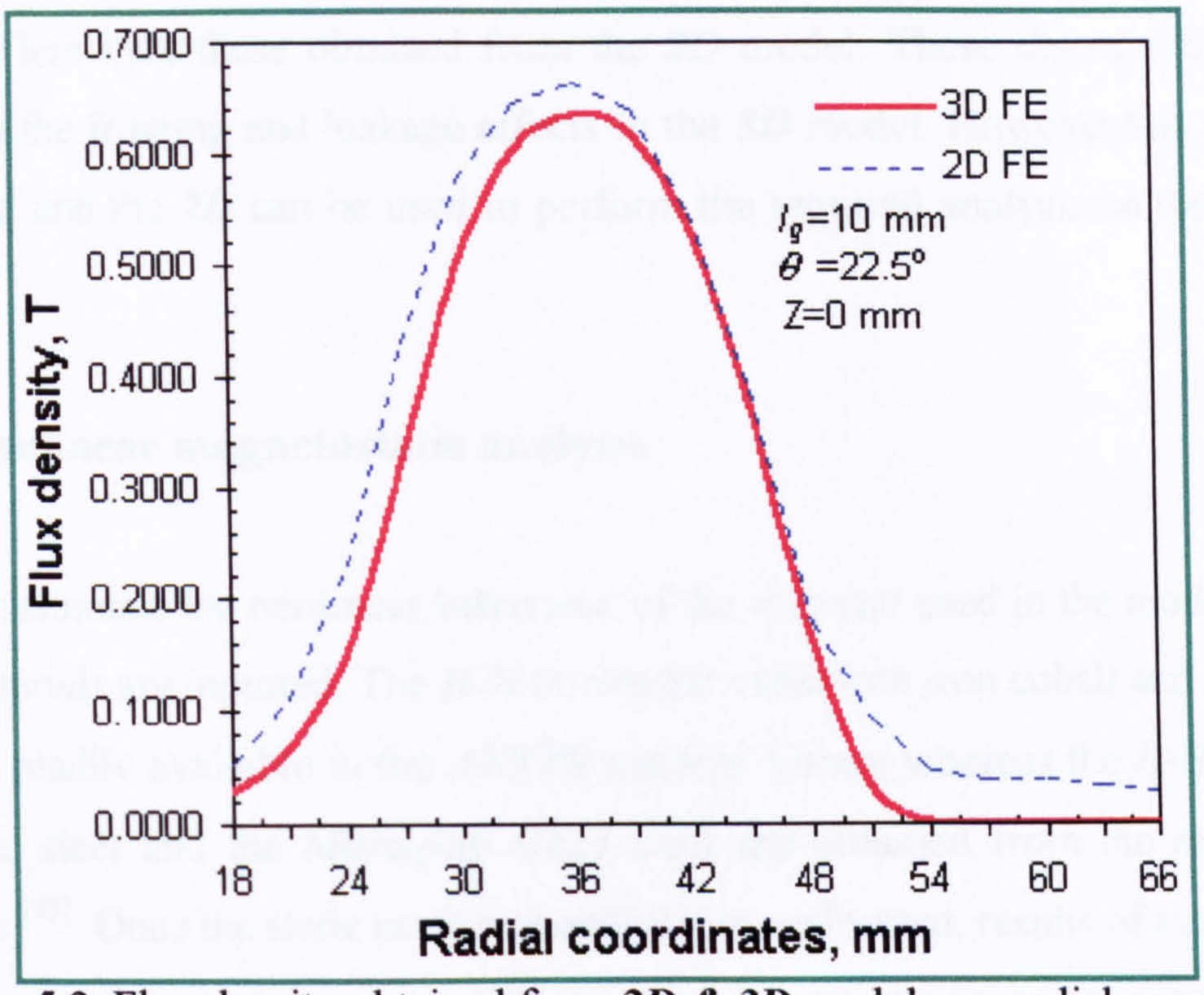

Figure 5.3 Flux density obtained from ***2D & 3D*** models vs. radial coordinates

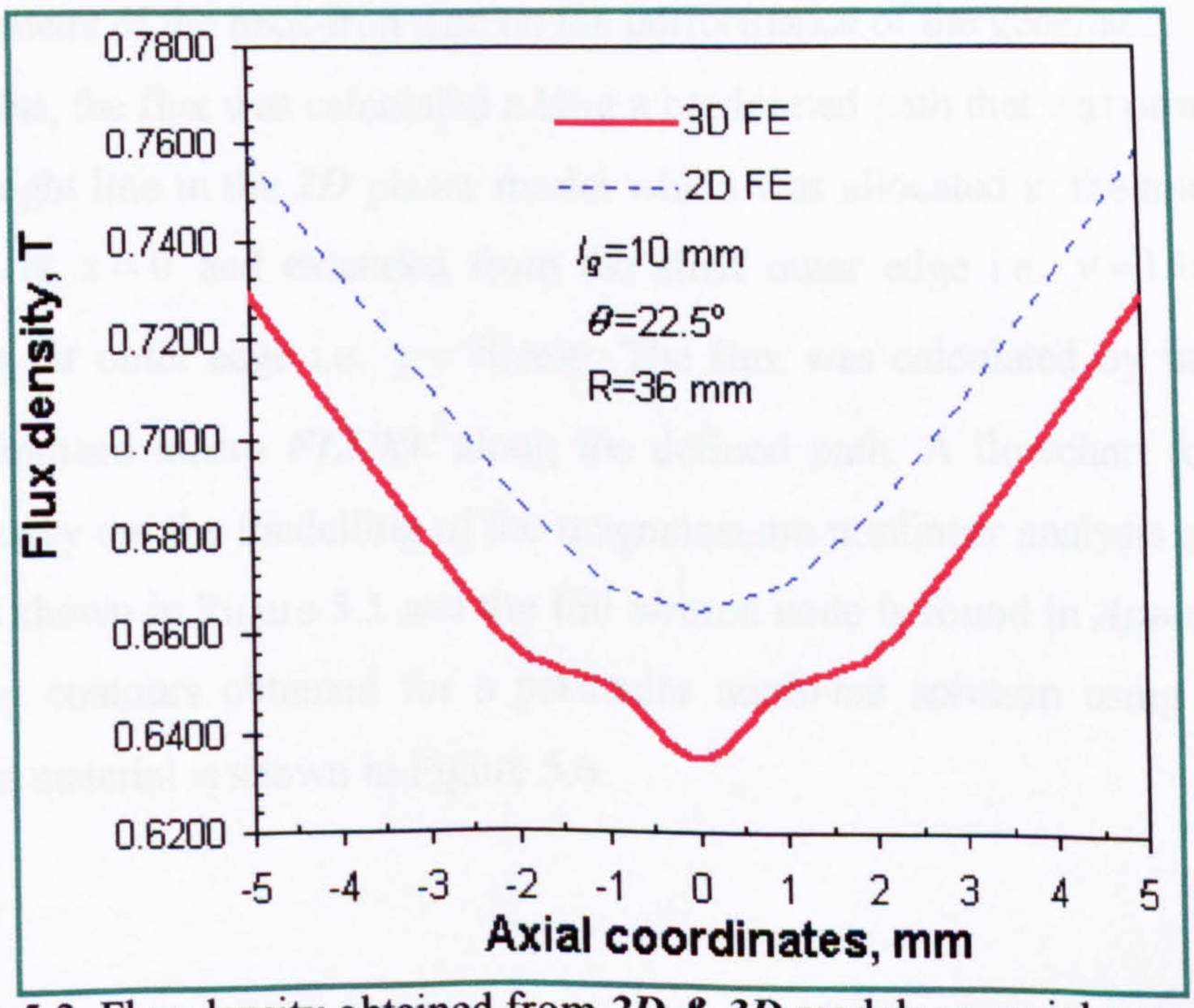

Figure 5.3 Flux density obtained from ***2D & 3D*** models vs. axial coordinates

It is shown from the graphs that the flux density values found in the ***3D*** model are 4.5 % less than these obtained from the ***2D*** model. These discrepancies can be referred to the fringing and leakage effects in the ***3D*** model. However this percentage is accepted and the ***2D*** can be used to perform the required analysis on the back-iron disc.

5.3.2 Nonlinear magnetostatic analysis

To simulate the nonlinear behaviour of the material used in the model, the ***B-H*** for all materials are inputted. The ***B-H*** curves for vanadium iron cobalt and silicon iron alloys are readily available in the ***ANSYS*** material library whereas the ***B-H*** curves for the ferritic steel and the ***Maraging G125*** steel are obtained from the manufacturer datasheets [83]. Once the static nonlinear analysis is performed, results of interest can be viewed.

In studying the results of the magnetostatic analysis, the value of the useful flux crossing the air gap is necessary to evaluate the influence of subsequent changes of the design parameter of the back-iron disc on the performance of the generator. In order to determine this, the flux was calculated a long a predefined path that was presented by a vertical straight line in the ***2D*** planar model which was allocated in the middle of the air gap i.e. at $x = 0$ and extended from the shaft outer edge i.e. $y = 15\,\text{mm}$ to the surrounding air outer edge i.e. $y = 70\,\text{mm}$. The flux was calculated by invoking the ***ANSYS*** command macro ***FLUXV*** along the defined path. A flowchart for the code created to carry out the modelling of the magnetostatic nonlinear analysis of the back-iron disc is shown in Figure 5.5 and the full written code is found in ***Appendix D***. the flux density contours obtained for a particular nonlinear solution using one of the ferritic steel material is shown in Figure 5.6.

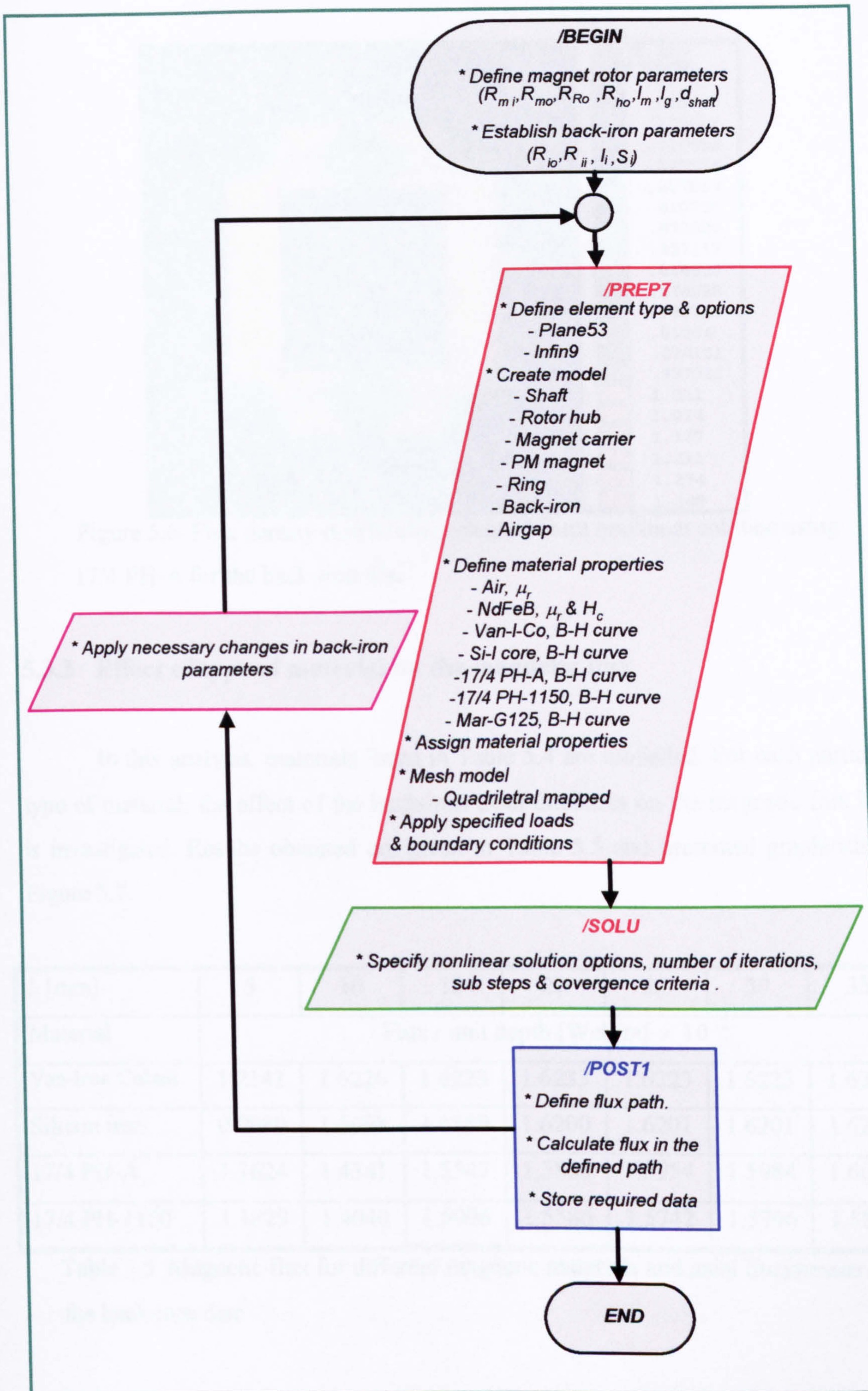

Figure 5.5 Flowchart for ***FE*** modelling of the back-iron disc

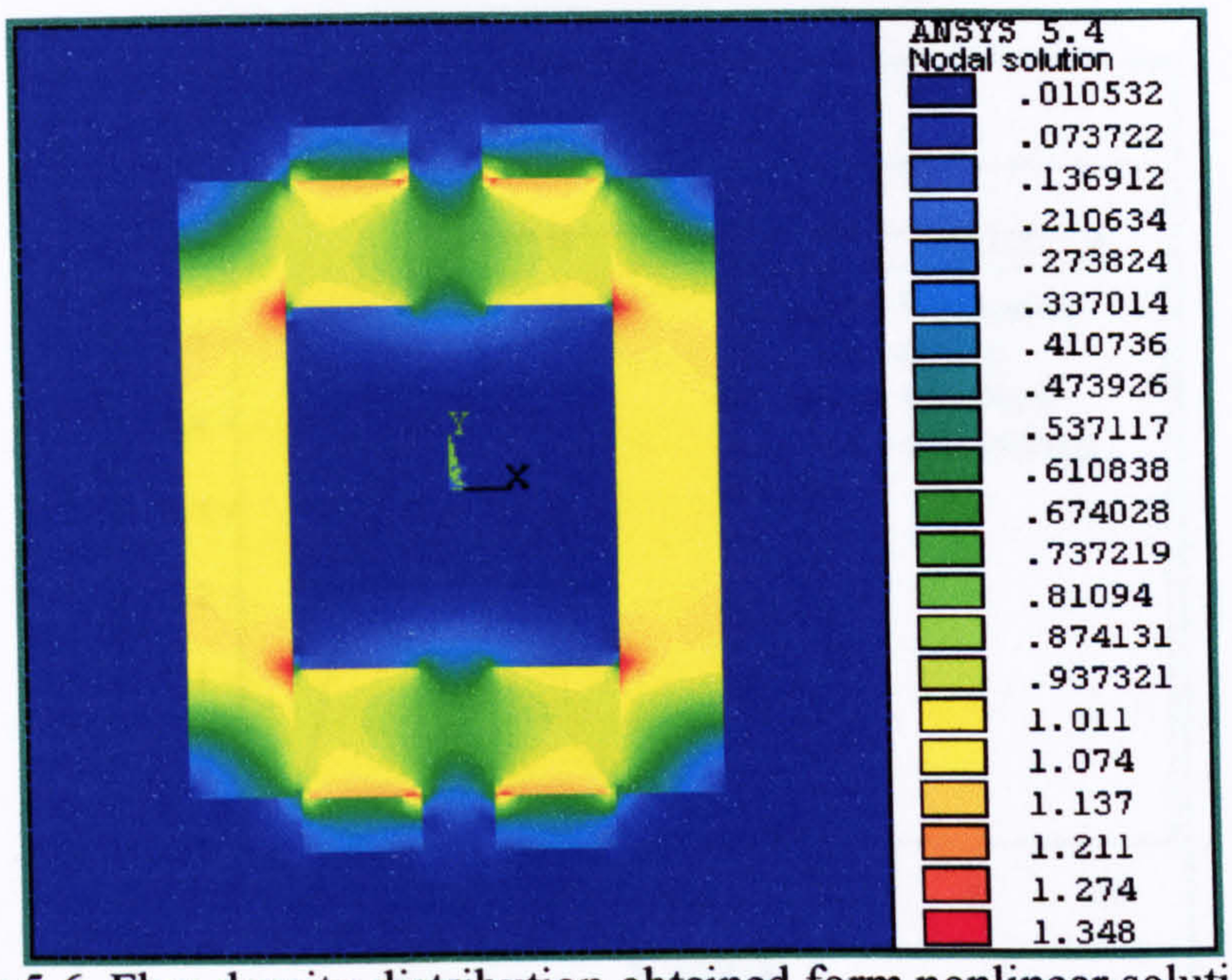

Figure 5.6 Flux density distribution obtained form nonlinear solution using 17/4 PH-A for the back-iron disc

5.3.3 Effect of type of material on the magnetic flux

In this analysis, materials listed in Table 5.4 are modelled. For each particular type of material, the effect of the back-iron axial thickness on the magnetic flux level is investigated. Results obtained are given in Table 5.5 and presented graphically in Figure 5.7.

l_i [mm]	5	10	15	20	25	30	35
Material	Flux / unit depth [Web/m] $\times 10^{-2}$						
Van-Iron Cobalt	1.2141	1.6226	1.6223	1.6233	1.6223	1.6223	1.6225
Silicon iron	0.9980	1.5698	1.6189	1.6200	1.6201	1.6201	1.6202
17/4 PH-A	1.1624	1.4341	1.5547	1.5863	1.5954	1.5984	1.6003
17/4 PH-1150	1.1829	1.4040	1.5096	1.5586	1.5742	1.5796	1.5826

Table 5.5 Magnetic flux for different magnetic materials and axial thicknesses of the back-iron disc

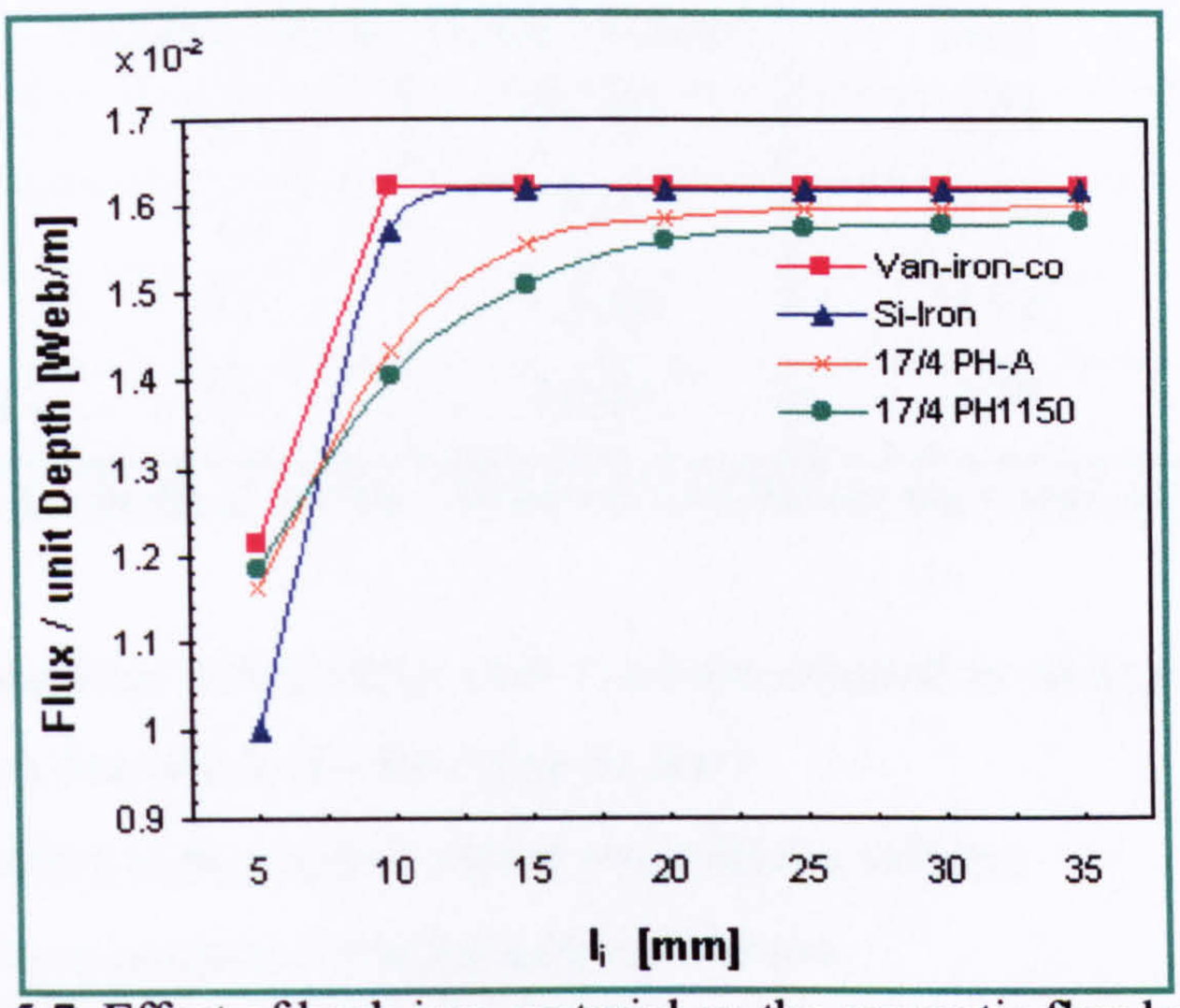

Figure 5.7 Effect of back-iron material on the magnetic flux level with different disc axial thicknesses

It is seen from Figure 5.7 that in terms of useful magnetic flux and minimum material volume the best material for the back-iron disc is the vanadium-iron-cobalt. A high and constant level of magnetic flux level can be achieved at thickness of 10 mm. However, as explained earlier in this Chapter, this material is expensive and is not available on the round bar forms. The next best material is silicon-iron. A flux level similar to that for the previous material can be achieved with a slight increase in the axial thickness (2.5 mm) i.e. 25 % increase on the total volume. Although this material is relatively expensive compared to the 17/4 PH steel, less volume is required with silicon-iron material to produce high magnetic flux. The maximum magnetic flux achieved using 17/4 PH-A and 17/4 PH-11500 are less by 1.3 % and 2.5 % respectively than that achieved with vanadium-iron-cobalt. However, to achieve the highest flux level using 17/4 PH steel, a minimum axial thickness of 30 mm is required. This represents an increase of 200 % of the total back-iron volume. Table 5.6 summarises the results for the purpose of the evaluating the different materials in terms of thickness, magnetic flux, weight and cost for use in the back-iron disc.

Material	Minimum axial thickness [mm]	Flux / unit depth [Web/m]	Weight / disc [kg]	Cost / disc [£]
Van-Iron Cobalt	10	1.6226	0.53	140
Silicon-Iron	12.5	1.6150	0.66	38
17/4 PH-A	30	1.5984	1.58	25
17/4 PH-11500	30	1.5826	1.58	25

Table 5.6 Results obtained for the evaluation of different back-iron disc materials

From this analysis, Silicon-Iron steel has been selected as an appropriate material for the back iron disc due to the following reasons:

- It provides a high magnetic flux at low material volume.
- Low cost as a result of smaller material volume.
- Good mechanical strength capabilities.
- Available in round bar form

5.3.4 Effect of back-iron outer radius on the magnetic flux level

In the previous analysis, the axial thickness of the silicon-iron core back-iron disc has been determined. Further use of the ***ANSYS*** model already described with a silicon-iron steel disc of thickness 12.5 mm allowed the optimisation of disc outer radius, R_{io} for a maximum attainable magnetic flux. The outer radius was varied in the range of 43 to 49 mm. Results obtained from this analysis are shown in Figure 5.8.

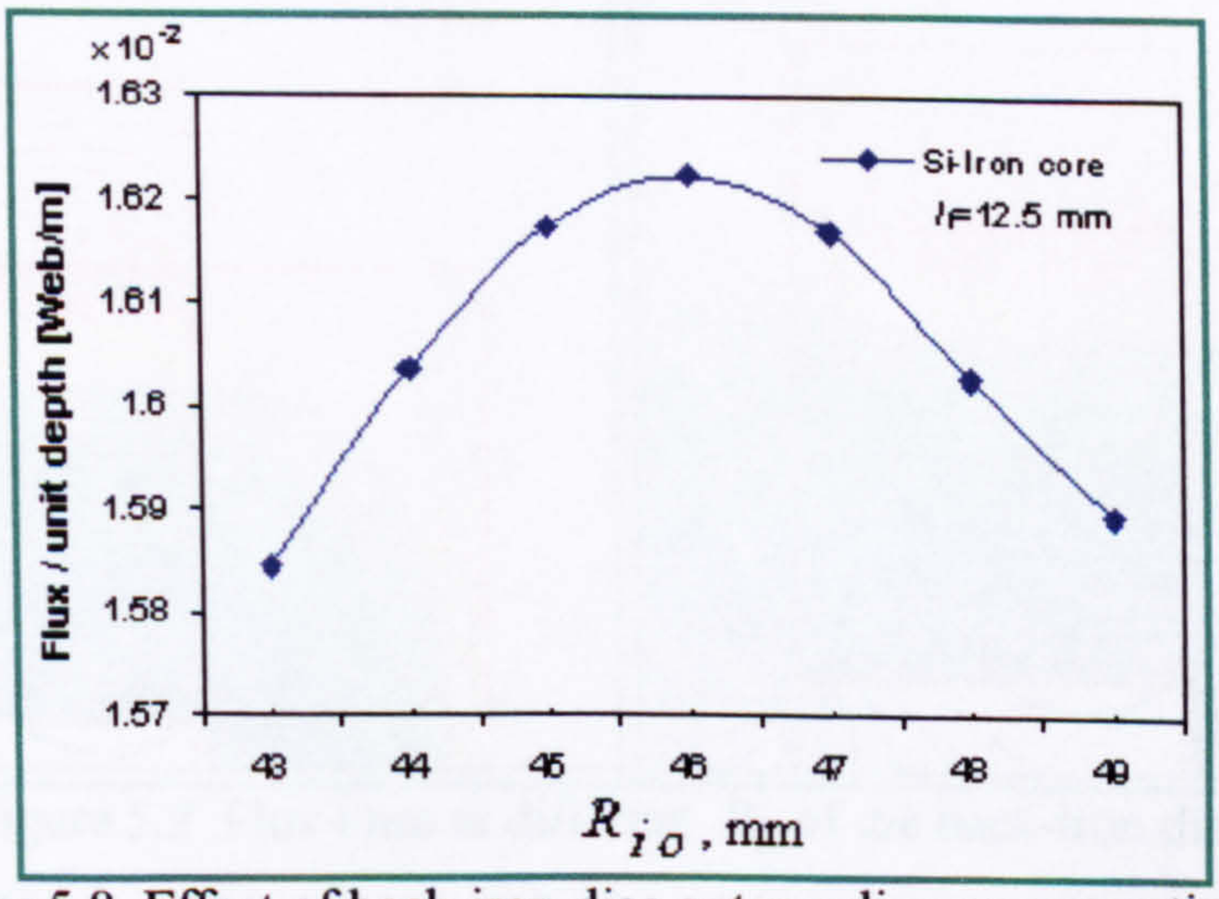

Figure 5.8 Effect of back-iron disc outer radius on magnetic flux

It is seen from this Figure that the maximum magnetic flux is achieved at a disc outer radius, R_{io}, of 46 mm. Lesser or greater radii will force more flux lines to link with the retainment ring thus short-circuiting the flux lines around the ring and reducing the useful magnetic flux in the air gap. Figure 5.9 shows the behaviour of the flux line at selected outer radii of, 43 mm, 46 mm, 47 mm and 49 mm, of the back-iron disc. The Figure is an enlarged sectional view for right upper part of the ***2D*** planar model of the magnet rotor disc with the back-iron disc. It is seen that the minimum number of flux lines that links with the retainment ring occurs when $R_{io} = 46\,\text{mm}$.

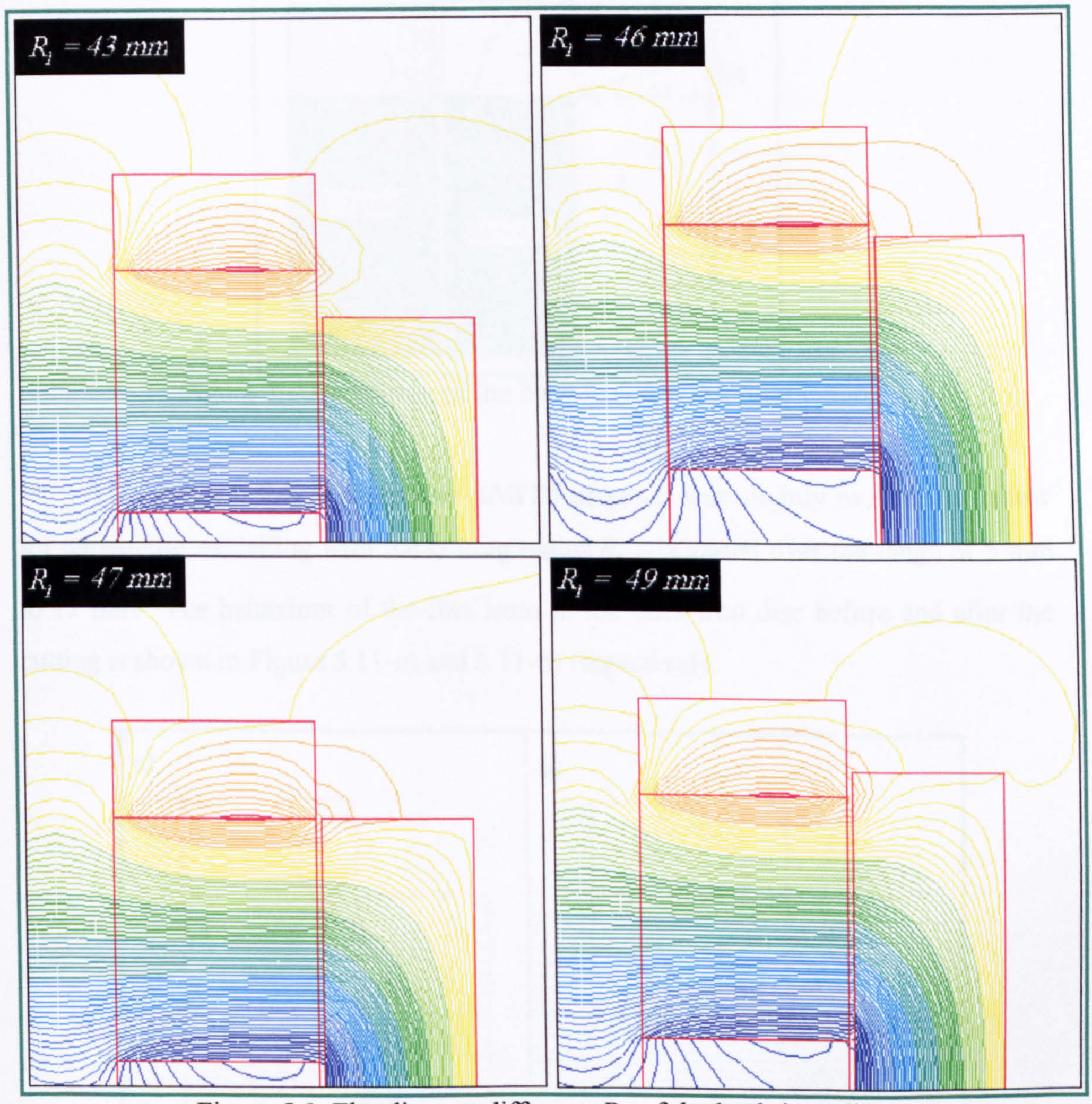

Figure 5.9 Flux lines at different R_{io} of the back-iron disc

5.3.5 Shape optimisation of the back-iron disc

To further reduce the weight, hence mechanical stresses, "profiling" of the back-iron disc was investigated. It was shown in the previous analysis that the flux lines are less concentrated at the outer rear corners of the discs. Hence, to a certain extent, discarding some of the disc's material not used for the flux path at that place, will not deteriorate the flux level. A circular cutting shown in Figure 5.10 was used for manufacture ease and performance comparison.

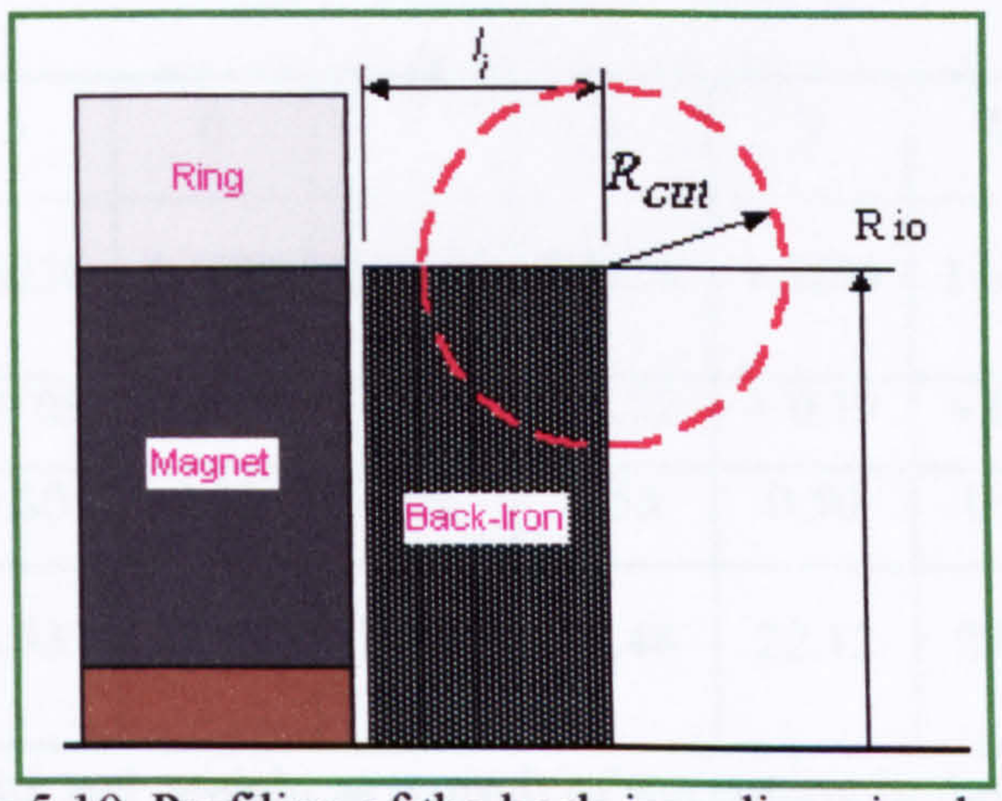

Figure 5.10 Profiling of the back-iron disc, circular cutting

To perform this analysis, the ***ANSYS*** program was slightly modified to allow for parametric modelling with the cutting radius R_{cut} is varied over the range of 5 mm to 12 mm. The behaviour of the flux lines in the back-iron disc before and after the cutting is shown in Figure 5.11-a) and 5.11-b) respectively.

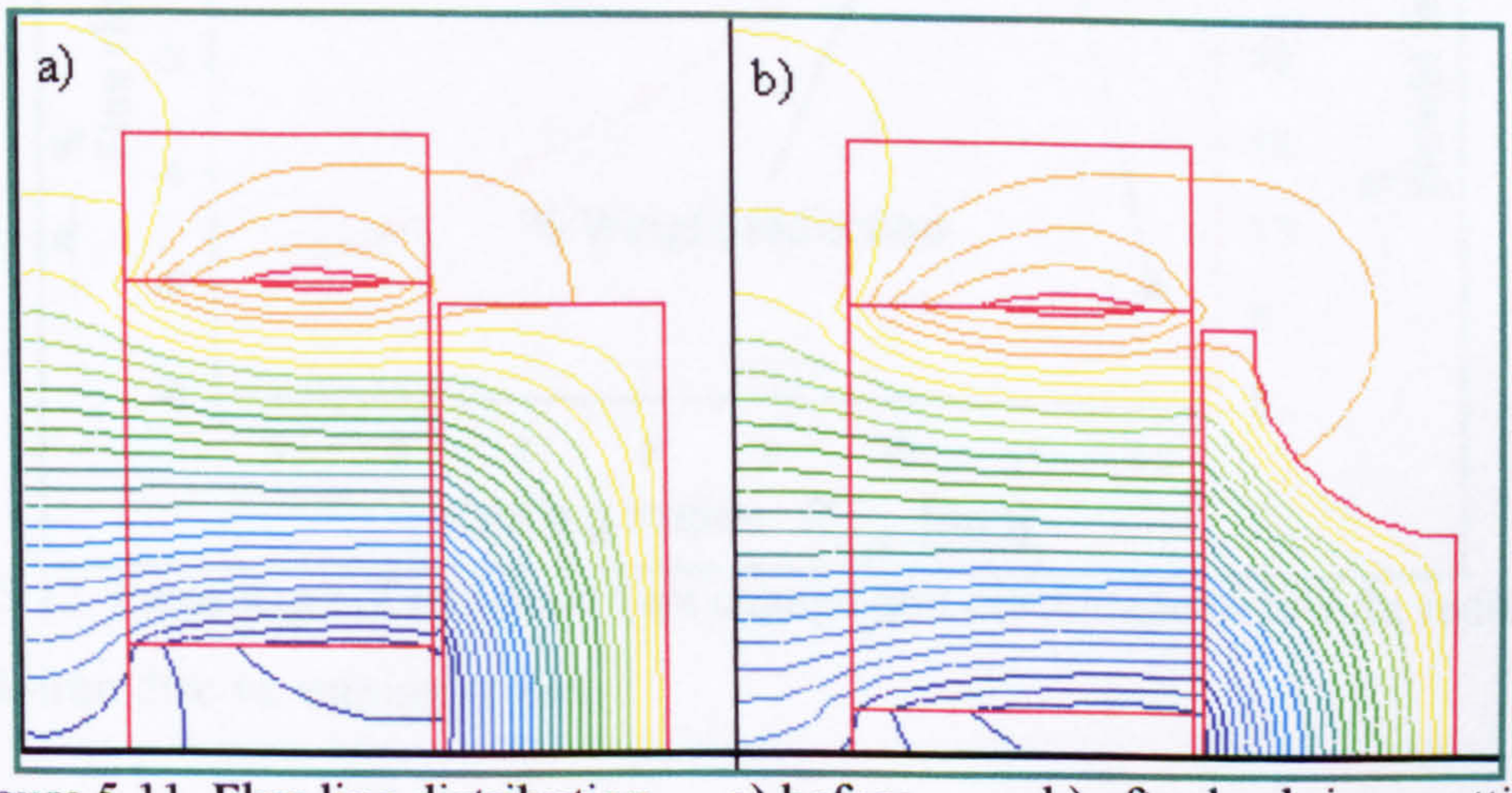

Figure 5.11 Flux line distribution a) before b) after back-iron cutting

Results of the ***FE*** analysis are summarised in Table 5.7. Additionally, percentages of magnetic flux change across the air gap and weight reduction in the back-iron disc are included. These results are also represented graphically in Figure 5.12 which shows that the flux/depth change is just about zero as the cutting radius increases from 5 mm to 10 mm. Then the flux/depth decreases and a reduction of 5% is observed at a radius of 12 mm. The weight of the disc is reduced of course as the cutting radius increases. A design point with a cutting radius of 10 mm was selected since, at this point, the maximum magnetic flux is maintained and a relatively high percentage of weight reduction (27.3 %) is achieved.

R_{cut} [mm]	5	6	7	8	9	10	11	12
Flux / unit depth [Web/m] $\times 10^{-2}$	1.6230	1.6233	1.6260	1.6258	1.6253	1.6264	1.6098	1.5415
% Flux change	+ 0.05	+ 0.07	+ 0.24	+ 0.22	+ 0.19	+ 0.26	- 0.75	- 5.0
Weight [kg]	0.60	0.58	0.56	0.53	0.50	0.47	0.43	0.39
% Weight reduction	6.83	9.83	13.38	17.48	22.12	27.31	33.0	39.33

Table 5.7 Flux and weight as a result of the cutting in the back-iron disc.

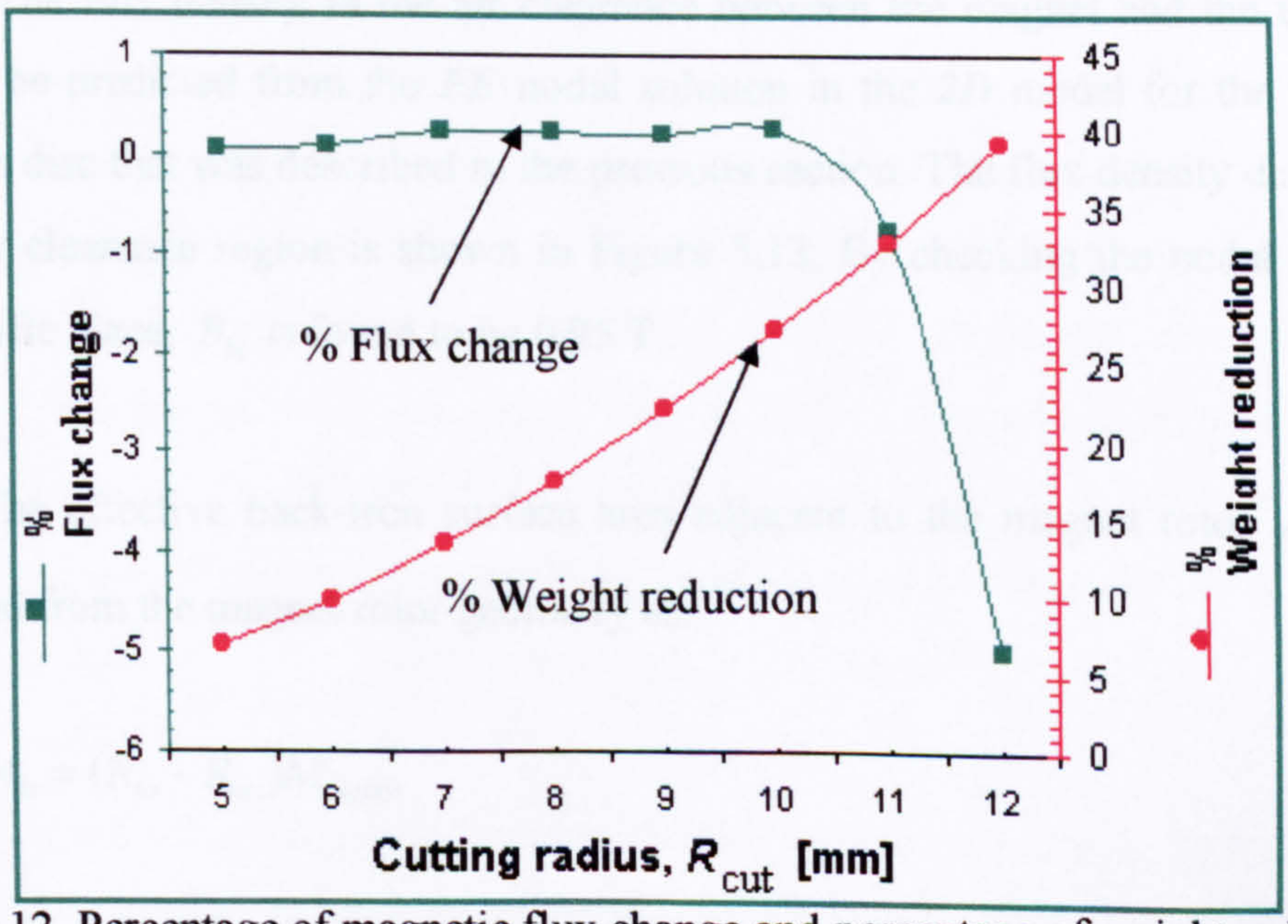

Figure 5.12 Percentage of magnetic flux change and percentage of weight reduction of the back-iron disc vs. cutting radius

5.3.6 Calculation of magnetic attraction force on the back-iron disc

Using the selected type of material, the analysis so far has enabled the three main design parameters for the back-iron disc to be optimised. These are, l_i, R_{io} and R_{cut}. Next, a further analysis is performed to determine the magnetic attraction force on the back-iron disc so that these values can be used for a *FE* stress analysis. For simplicity, we shall name the back-iron disc having the circular profile cutting as "modified" back-iron disc.

When the back-iron disc is assembled on the shaft at the backside of the magnet rotor disc, a clearance gap $S_i = 0.5$ mm is set between the back-iron disc and the magnet rotor disc for the purpose of mechanical isolation while they are running at high rotational speed. If the magnetic flux density, B_{bi}, across this clearance can be predicted then the attraction force can be calculated analytically as:

$$F_x = -\frac{B_{bi}^{\,2} A_{bi}}{2\mu_o} \tag{5.13}$$

The flux density in the air clearance between the magnet and the back-iron disc can be predicted from the *FE* nodal solution in the *2D* model for the modified back-iron disc that was described in the previous section. The flux density distribution in the air clearance region is shown in Figure 5.13. By checking the nodal results at this specific place, B_{bi} is found to be 0.95 T.

The effective back-iron surface area adjacent to the magnet rotor A_{bi} can be calculated from the magnet rotor geometry as:

$$A_{bi} = (R_{io} - R_{mi}) M_{depth} \tag{5.14}$$

where M_{depth} is the unit depth of the magnet in the z-direction, $R_{io} = 0.046$ m and $R_{mi} = 0.027$ m. Hence, the calculated force per unit depth, $F_x = -13645$ N/m.

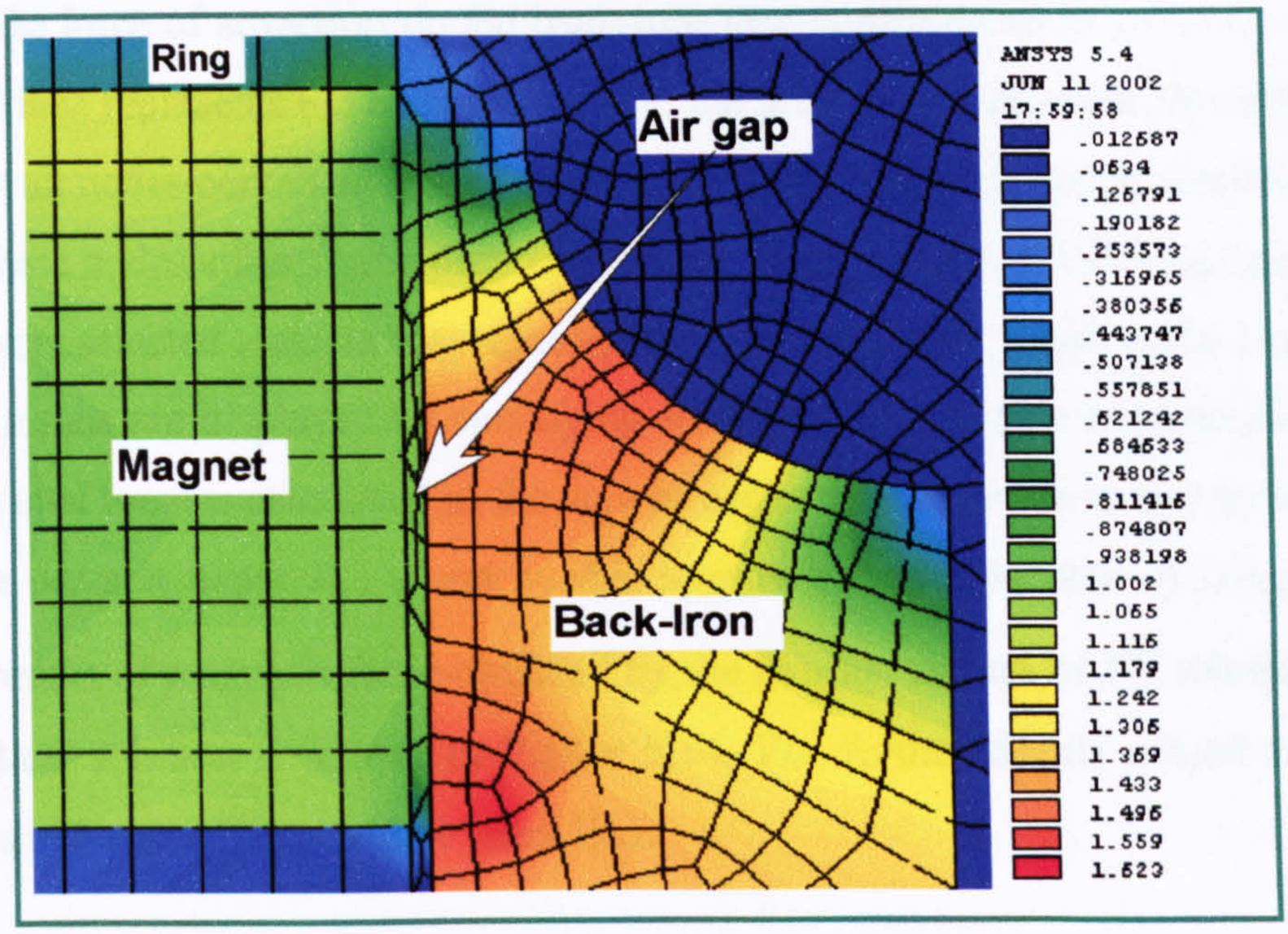

Figure 5.13 Magnetic flux density nodal solution in the air clearance region between the magnet rotor disc and the modified back-iron disc

Alternatively, in ***ANSYS FE*** model, there are two different techniques that can be used to calculate the magnetic forces on ferromagnetic materials surrounded by air. The first approach is done by invoking the ***FOR2D*** macro which calculates the magnetic forces on a body that is completely surrounded by air. A closed path passing through the air elements surrounding the back-iron disc is defined in a counter-clockwise order to give the correct sign on the forces. This macro makes the use of the ***Maxwell*** stress tensor to evaluate the force on a body. It computes the local stress at all points of the bounding surface and then sums the local stresses by means of surface integral to find the net force on a body. Thus, the macro interpolates the values of flux density, B, along the defined path and integrates to obtain the force on the body surrounded by air. The force per unit depth calculated by this approach is F_x = -12941 N/m.

The second approach calculates the magnetic forces using the virtual work method. The force is obtained as the derivative of the energy versus the displacement of the movable part. This calculation is valid for a layer of air elements surrounding the movable part.

The second approach is a simple and quick technique which can be done in ***ANSYS***. The force of attraction on the back-iron disc is calculated by selecting one of the areas which represents the back-iron disc in the previously described ***2D*** model and then select all nodes contained in this specific area then applying virtual displacement loads on these nodes either in the preprocessor or solution stage. ***ANSYS*** calculates the force in every selected element that represents the selected area, which is the back-iron disc. The results are displayed by specifying ***ANSYS*** element table command (nmisc, 3) and the total force is calculated as the sum of each result stored in each element. The total force per unit depth, F_x, found by this approach is -13551 N/m. A comparison between results of magnetic force obtained by the two techniques of ***FE*** solutions and the analytical solution is shown in Figure 5.14. For further details related to these techniques, reference [69] should be consulted.

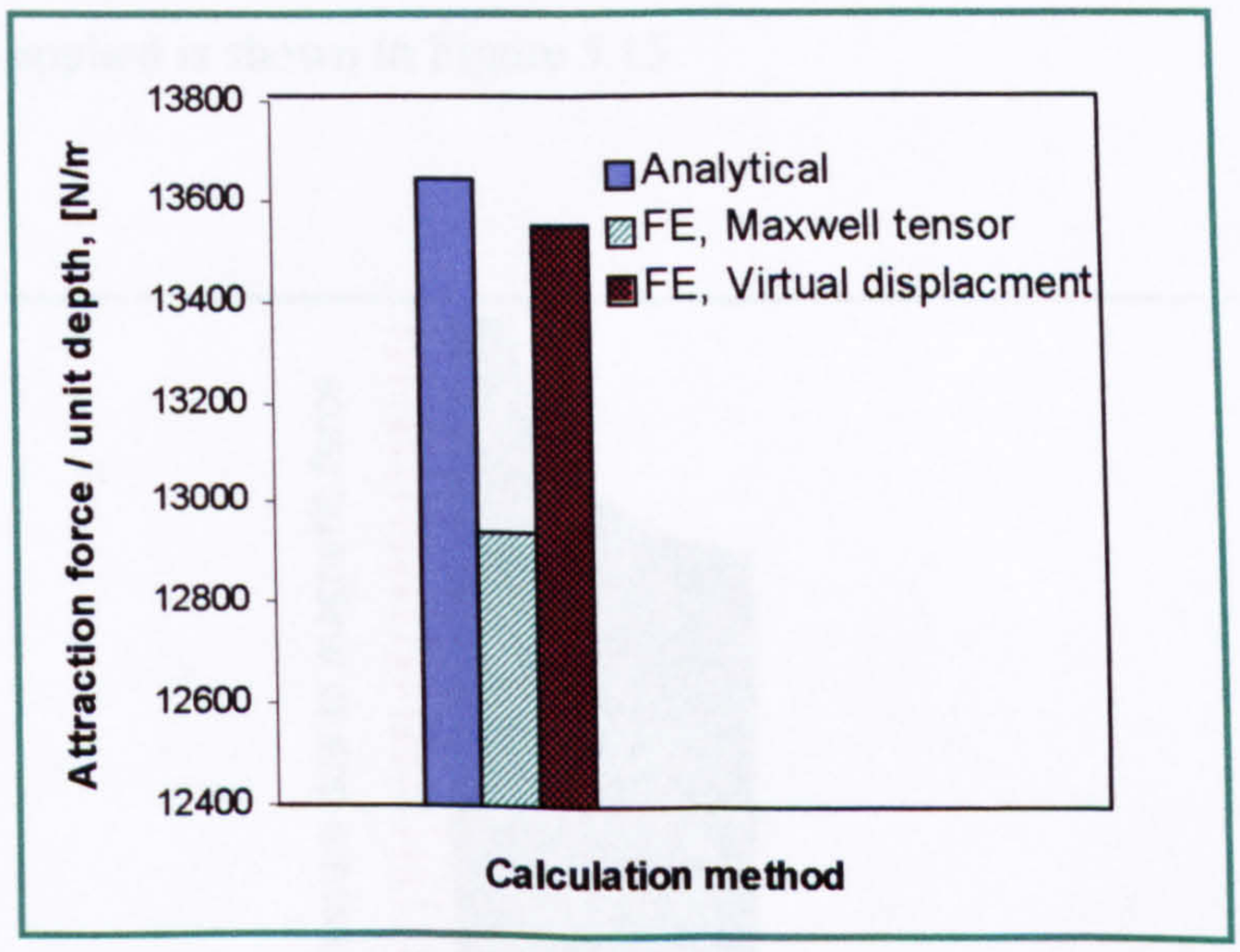

Figure 5.14 Attraction force on the back-iron disc calculated by different approaches

It can be seen from Figure 5.14 that the results obtained by the second approach, which is based on the virtual displacement method are much close to these obtained from analytical solution. Hence this value of magnetic force, F_x = -13551 N/m, will be used for the stress analysis carried out in the following section.

5.4 FE STRUCTURAL ANALYSIS OF THE BACK-IRON DISC

The results obtained from the initial stress analysis for the back-iron disc carried out earlier in this chapter have indicated the stress levels developed in the rotating disc at the design speed. However, in order to finalise the design, a more precise knowledge of these levels, of the lateral deflection and vibration characteristics is required especially for the modified disc. In fact, the axial force of attraction exerted on the back-iron disc from the magnets also should be taken into consideration since there is an air clearance between the disc and the magnet rotor in order that there is mechanical isolation between the two parts. The purpose of this section is to perform ***FE*** structural analysis for the back-iron disc using again the ***ANSYS*** software package. The programme written for this analysis is similar in its nature to that axisymmetric ***2D FE*** code which was used for stress analysis of the magnet rotor disc presented in Chapter Four. The ***FE*** model for the modified disc with all boundary conditions and possible loads applied is shown in Figure 5.15.

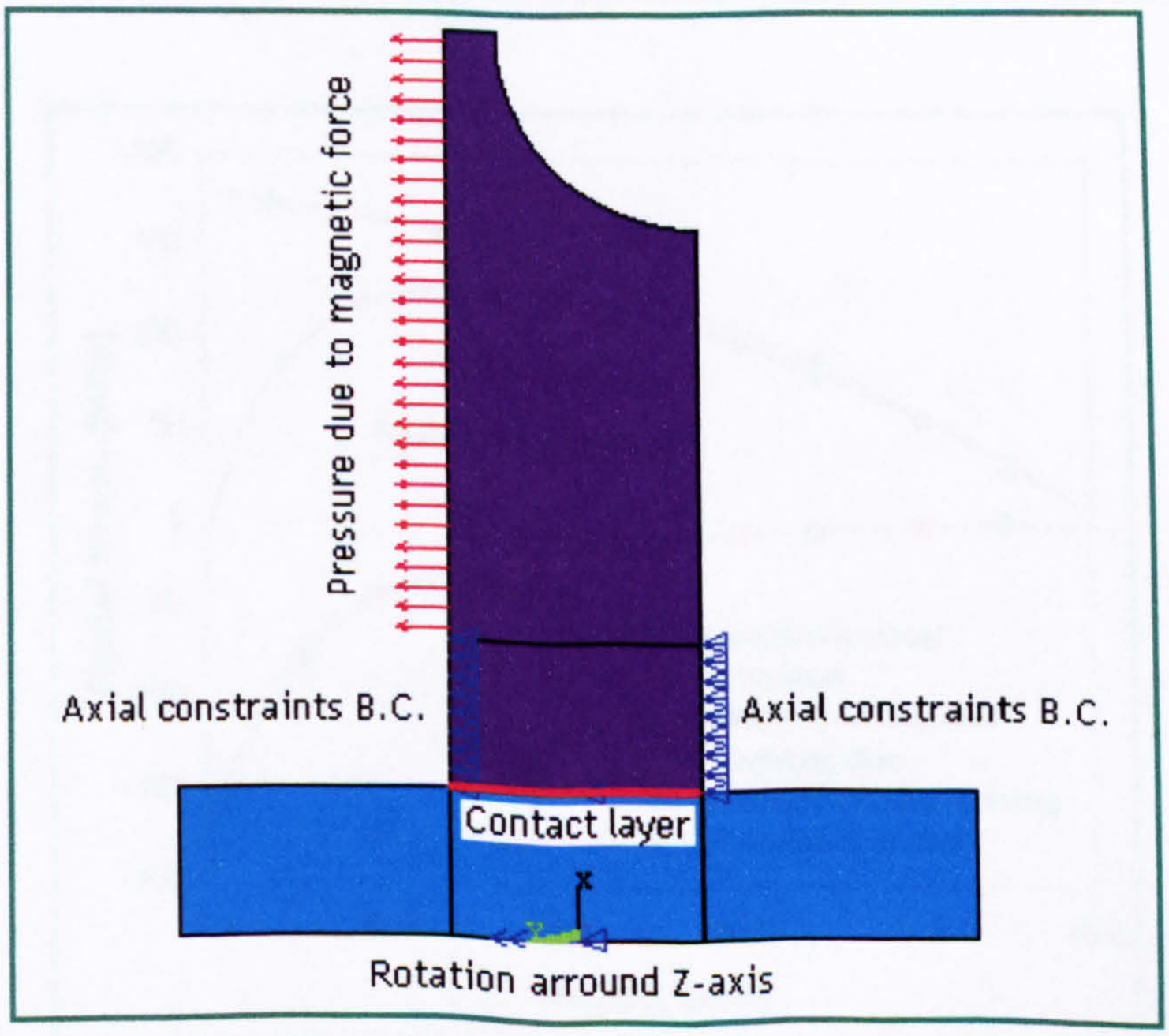

Figure 5.15 ***2D*** axisymmetric ***FE*** model for the modified back-iron disc

5.4.1 Results of the stress analysis

For the purpose of comparison, the ***FE*** stress analysis was performed on both the simple back-iron disc of uniform thickness and the modified disc of the geometrical shape and dimensions that were previously defined and optimised in the magnetic analysis. The details of the geometry for both discs used in the analysis are shown in Table 5.8. The radial and hoop stress results obtained from the ***FE*** solution for the uniform disc are obtained first and compared with the results obtained from the analytical Equations 5.1-5.12 presented earlier in this Chapter. These results are shown in Figures 5.16 and 5.17.

Disc type	d_{shaft} [mm]	R_{io} [mm]	l_i [mm]	R_{cut} [mm]	δ [μm]
Uniform	15	46	12.5	-	16.8
Modified	15	46	12.5	10	16.8

Table 5.8 The geometrical details for both uniform and modified back-iron discs

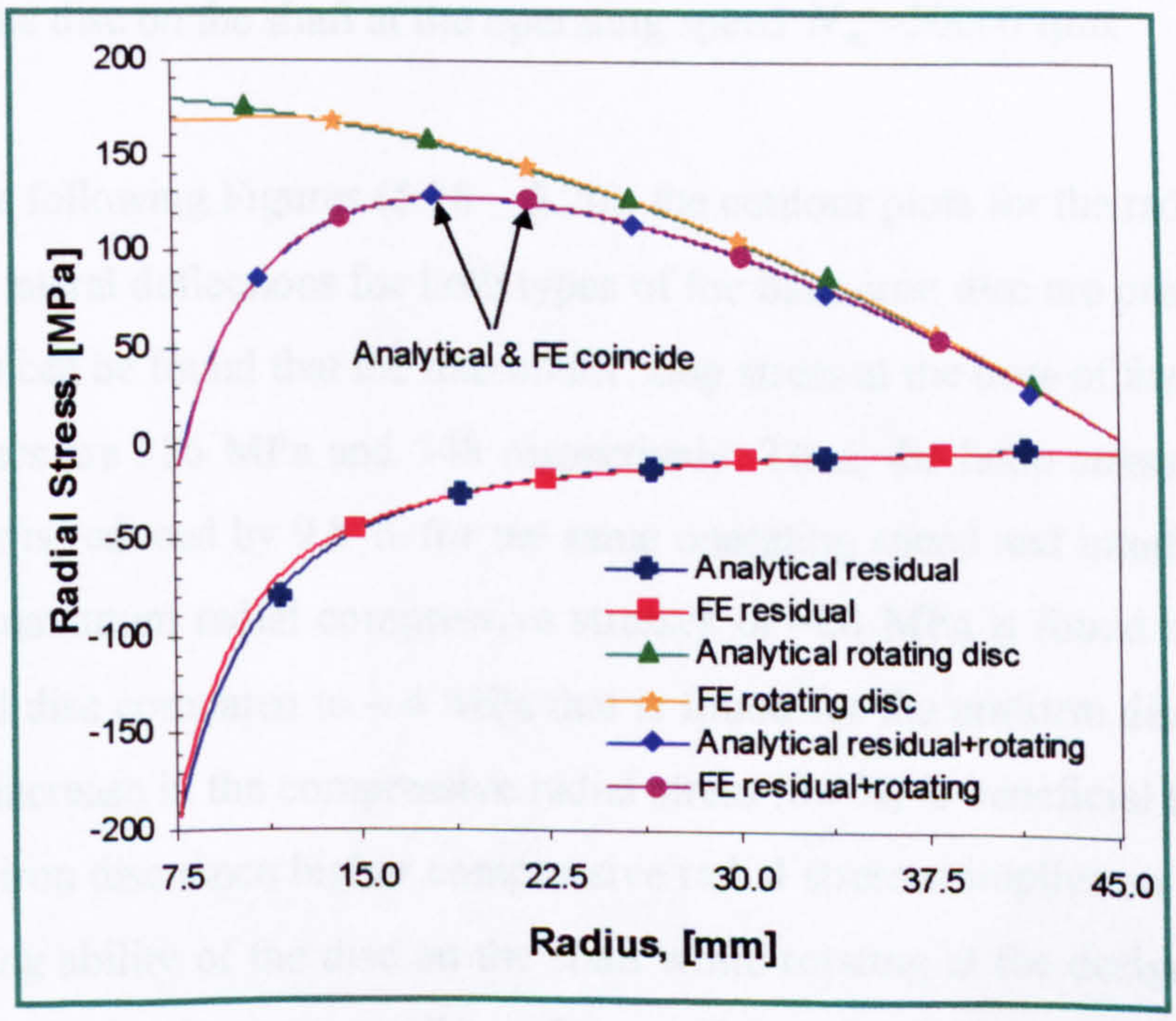

Figure 5.16 Analytical & ***FE*** radial stress results for the uniform disc

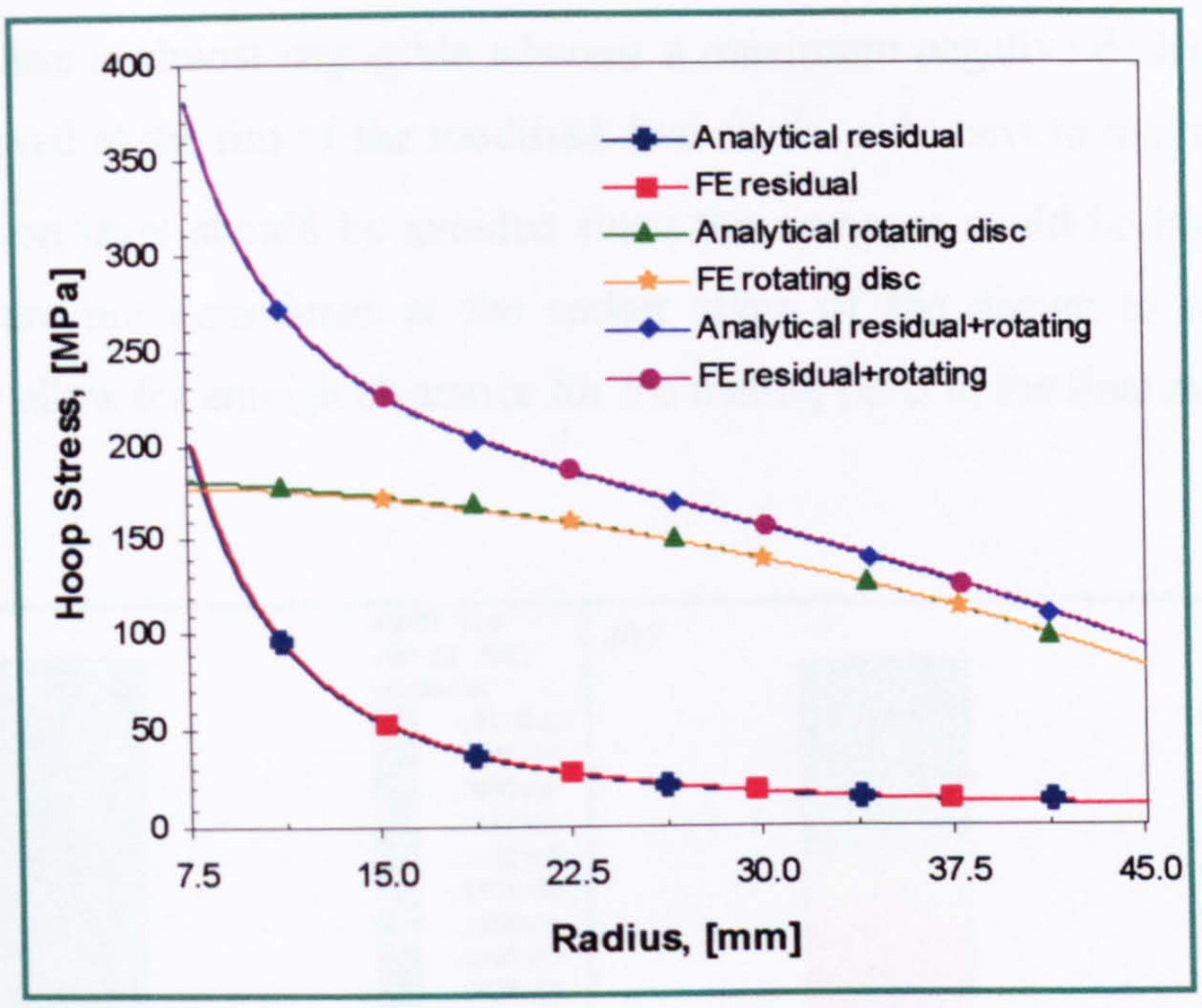

Figure 5.17 Analytical & ***FE*** hoop stress results for the uniform disc

With confidence, the stresses and lateral deflection of the modified back-iron disc could be compared with the corresponding values for the uniform back-iron disc using the minimum value of interference fit of $\delta = 16.8\ \mu$m required to prevent slippage of the disc on the shaft at the operating speed N_m =50000 rpm.

In the following Figures (5.18 – 5.20), the contour plots for the radial and hoop stresses and lateral deflections for both types of the back-iron disc are presented. From these plots it can be found that the maximum hoop stress at the bore of the uniform and modified discs are 386 MPa and 348 respectively. Thus, the hoop stress for the non-uniform disc is reduced by 9.8 % for the same operating speed and interference fit. In addition, a maximum radial compressive stresses of –28 MPa is found at the bore of the modified disc compared to – 4 MPa that is found for the uniform disc at the same place. This increase in the compressive radial stress (86 %) is beneficial for the design of the back-iron disc since higher compressive radial stresses implies an improvement in the sticking ability of the disc on the shaft while rotating at the designed operating speed. Accordingly, the amount of interference fit can be further reduced, thus lower hoop stresses can be maintained as a result of removing some of the material by performing the previously described cut in the geometry of the back-iron disc

It can be also seen from the Figure 5.20 that the lateral deflection at the rim of the uniform disc is almost negligible whereas a maximum negative deflection of 21.3 μm is observed at the rim of the modified disc on the side next to the magnet rotor. High deflection level should be avoided since the damages could be highly sever if precautions are not considered at the earlier stage of the design to minimise the deflection or allow for enough clearance for the mating parts in the final assembly.

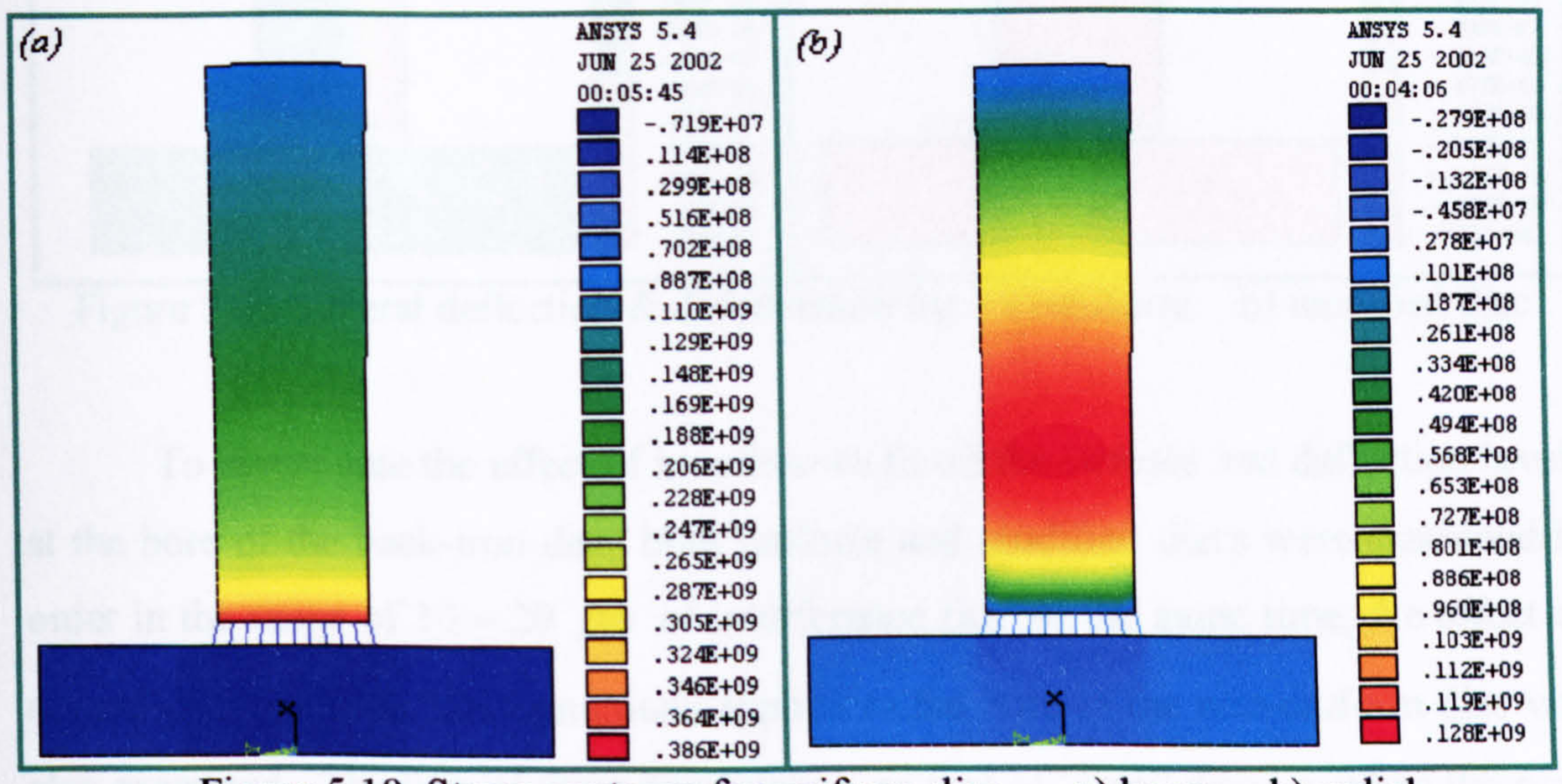

Figure 5.18 Stress contours for uniform disc a) hoop b) radial

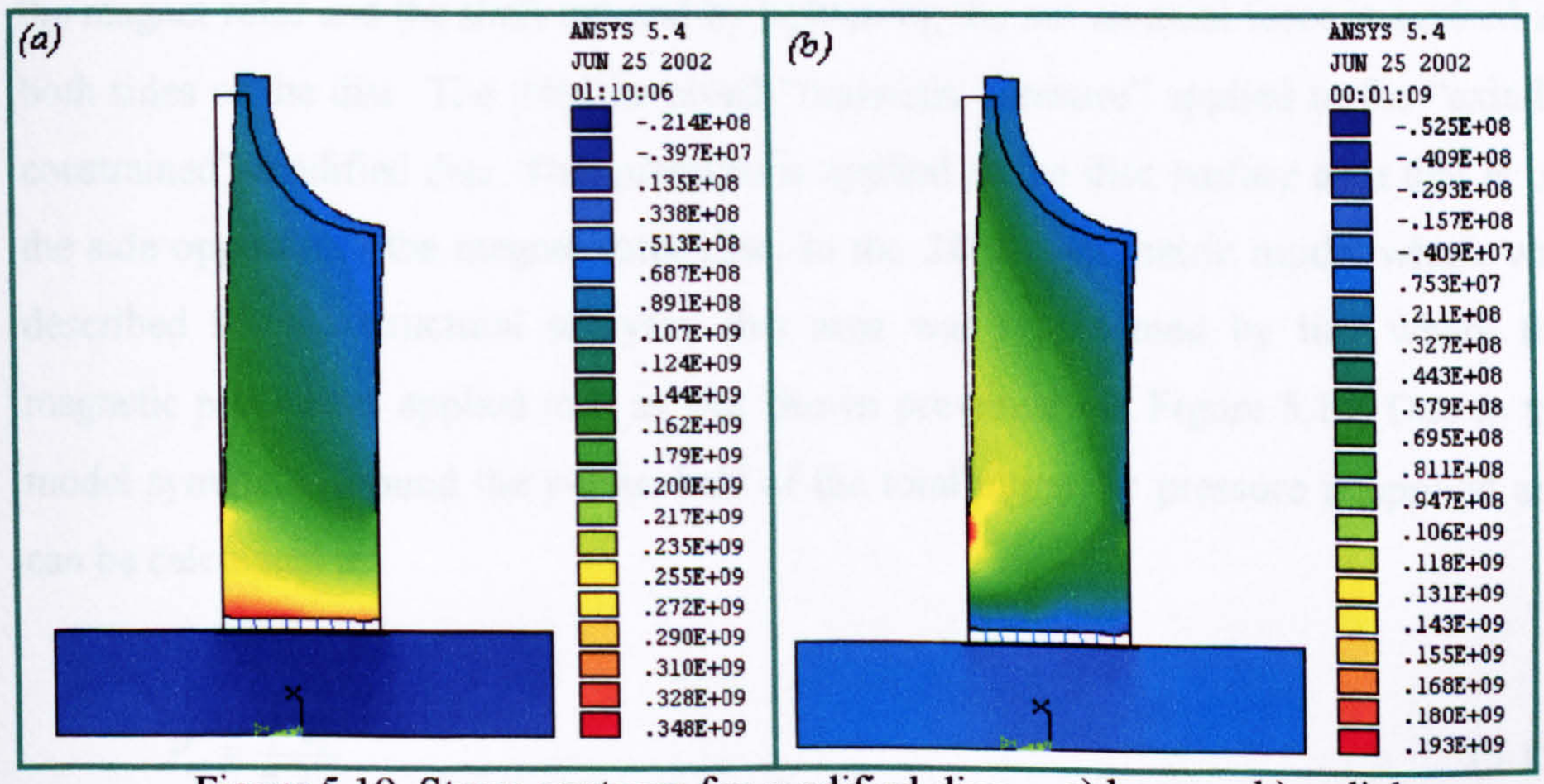

Figure 5.19 Stress contours for modified disc a) hoop b) radial

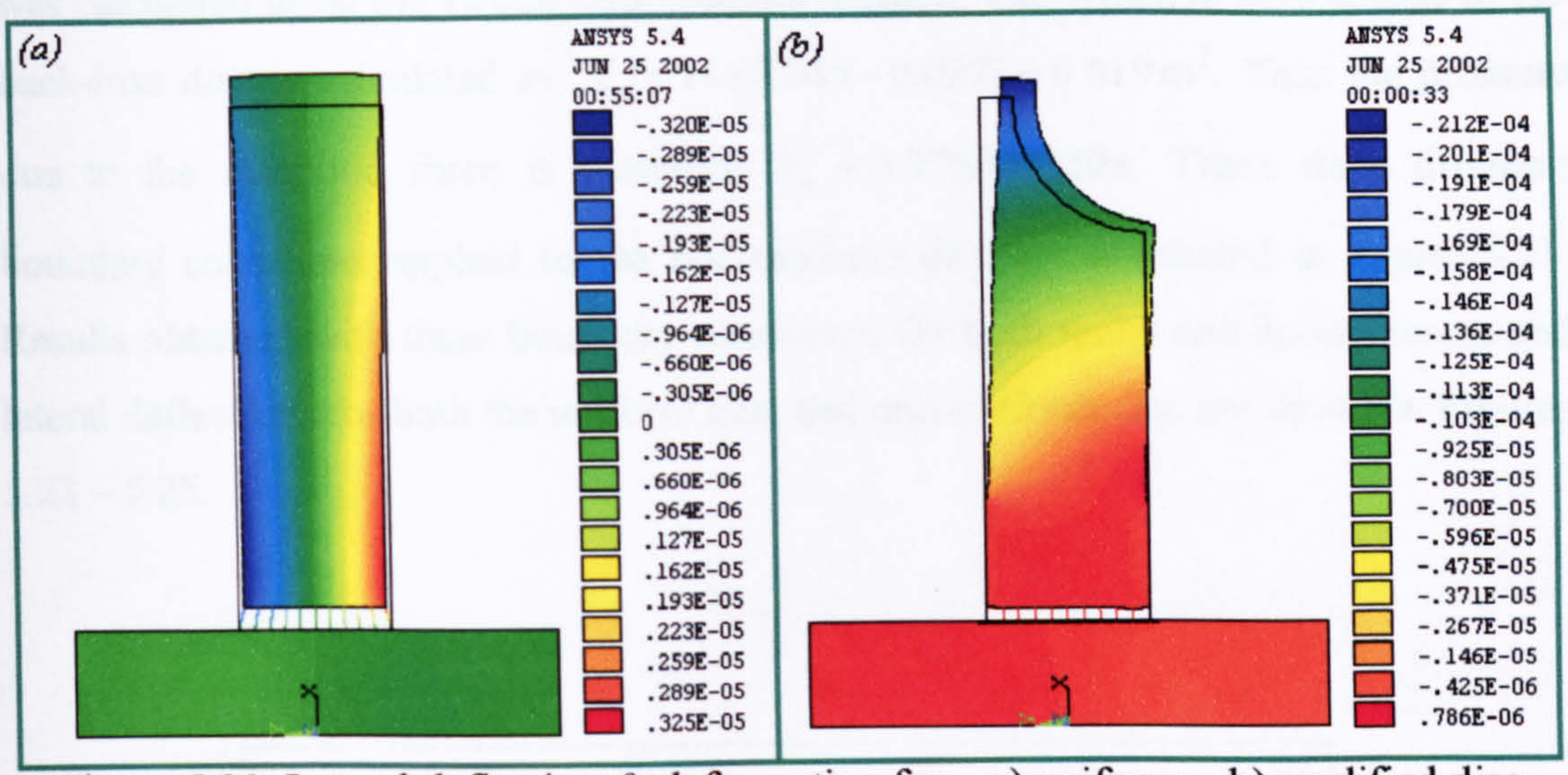

Figure 5.20 Lateral deflection & deformation for a) uniform b) modified disc

To investigate the effect of interference fit on the stresses and deflection levels at the bore of the back-iron disc, both uniform and modified discs were examined in order in the range of $10 - 20$ μm of interference fits. At the same time, the effect of several different boundary conditions applied to the bore of the non-uniform disc was also examined. The first of these conditions was that of "free" disc i.e. when the non-disc is alone shrunk onto the shaft hence there are no axial constraints on both sides of the disc. The second was that of "axial constraint" i.e. when the disc is placed between the magnet rotor and the shaft nut and by tightening the nut an axial force is applied to both sides of the disc. The third involved "magnetic pressure" applied to the "axially constrained" modified disc. This pressure is applied to the disc surface area that is on the side opposite to the magnet rotor disc. In the ***2D*** axisymmetric model which was described for the structural analysis, this area was represented by line where the magnetic pressure is applied to it as was shown previously in Figure 5.15. Due to the model symmetry around the y-axis, half of the total magnetic pressure is applied and can be calculated as:

$$P_m = \frac{|F_x|}{2A_{bi}} \tag{5.15}$$

where $F_x = 13645$ N/m is the magnetic axial force of attraction per unit length which was calculated using the virtual displacement method. The effective surface area of the back-iron disc is calculated as $A_{bi} = 1 \times (0.046 - 0.027) = 0.019\,\text{m}^2$. Thus the pressure due to the magnetic force is therefore $P_m = 0.359079\,\text{MPa}$. These three different boundary conditions applied to the non-uniform disc are illustrated in Figure 5.21. Results obtained with these boundary conditions for both radial and hoop stresses and lateral deflections for both the uniform disc and non-uniform disc are shown in Figures 5.22 – 5.25.

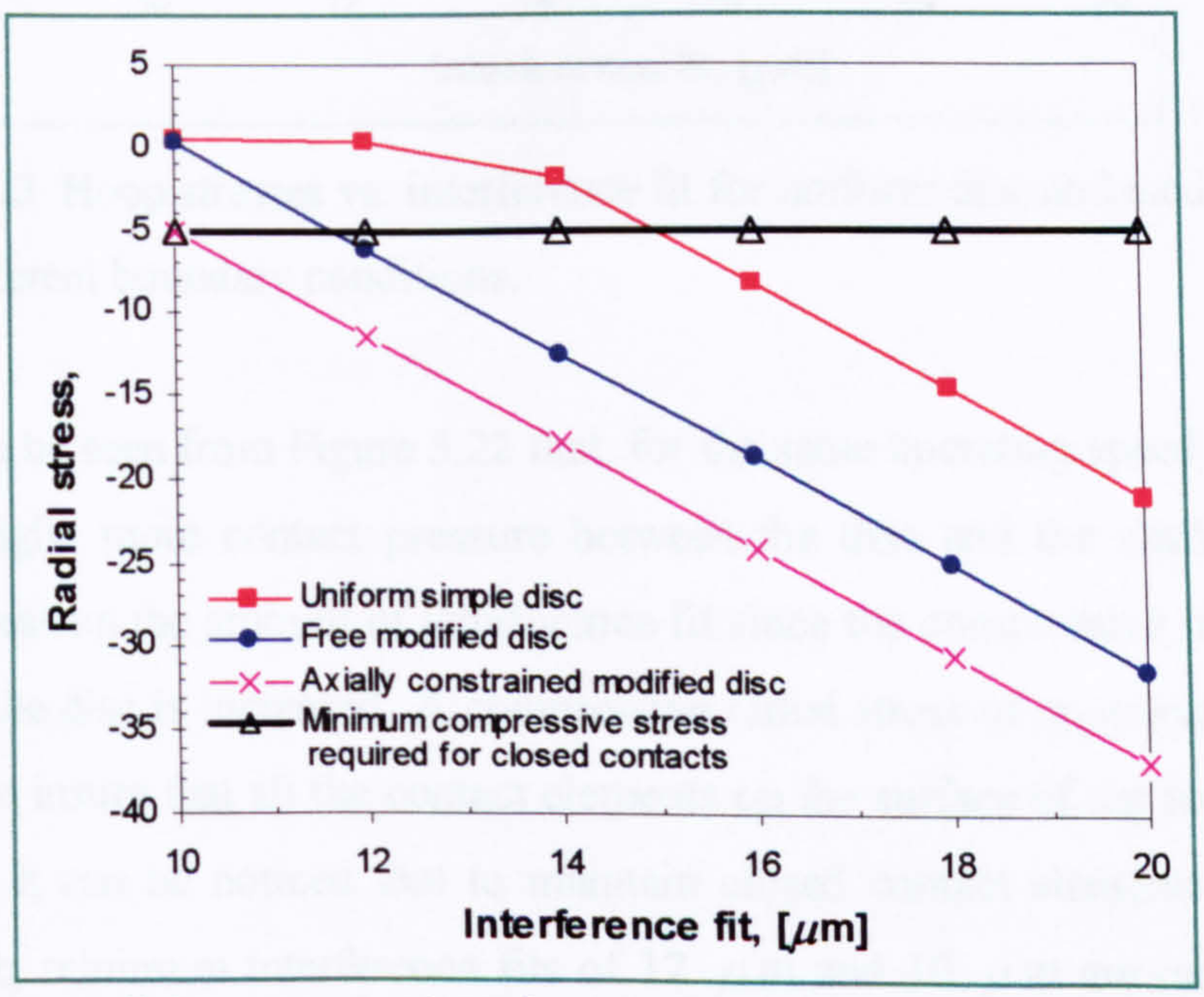

Figure 5.22 Radial stresses vs. interference fit for uniform disc and modified disc with the three different boundary conditions.

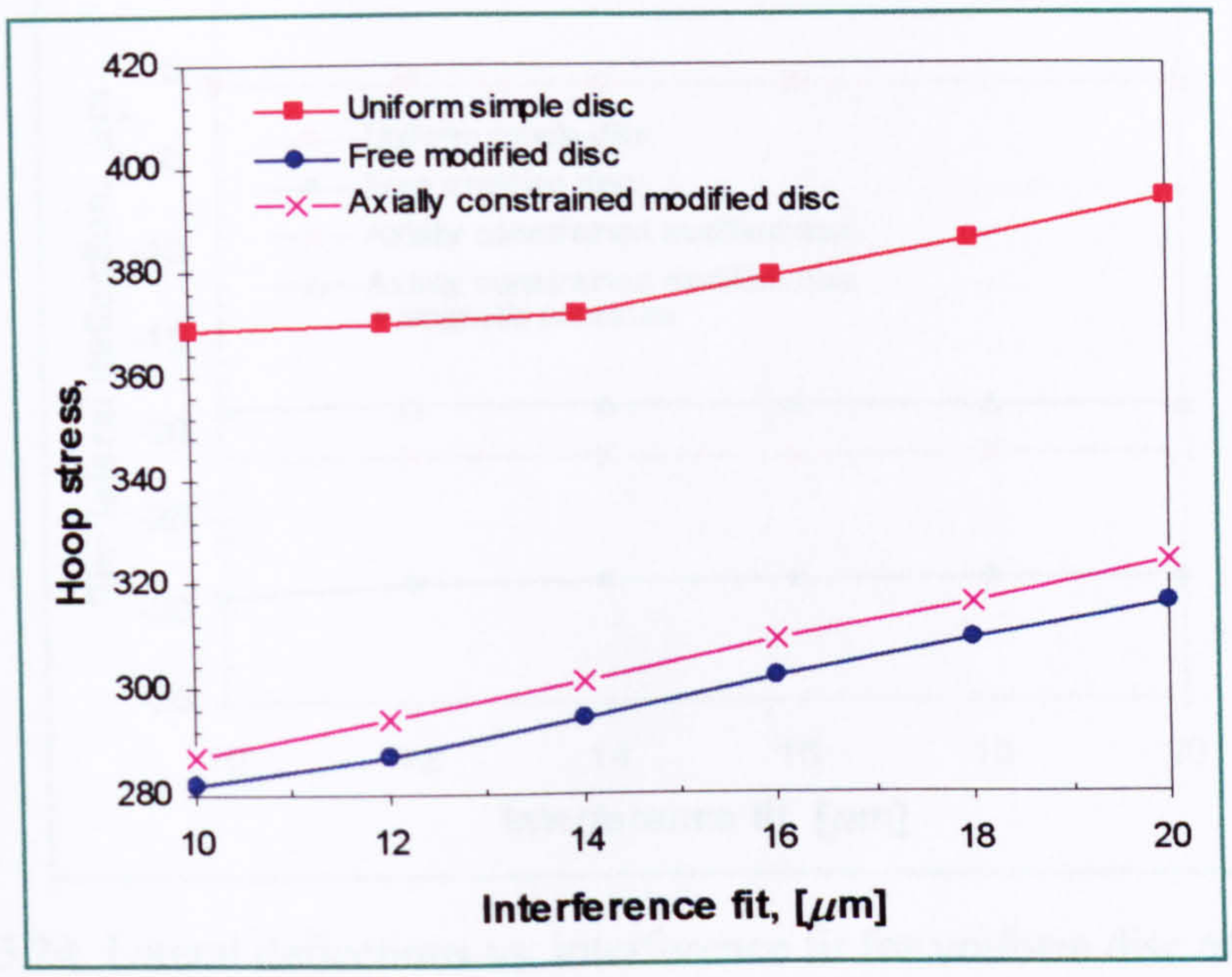

Figure 5.23 Hoop stresses vs. interference fit for uniform disc and modified disc with different boundary conditions.

It can be seen from Figure 5.22 that, for the same operating speed and possibly not surprisingly, more contact pressure between the disc and the shaft is achieved through increasing the amount of interference fit since the compressive radial stress at the bore of the disc is increased. A compressive radial stress of approximately 5 MPa is required to insure that all the contact elements on the surface of the bore of the disc are closed. It can be noticed that to maintain closed contact elements for the non-uniform disc, minimum interference fits of 12 μm and 10 μm are required for the "free" and for the "axially constrained" boundary conditions respectively. Accordingly, these values represent a reduction of 25 % and 37.5 % of the required interference fits compared with the uniform disc. A minimum interference fit of 16 μm is required to maintain closed contacts for the uniform disc.

Compared to the uniform disc, the hoop stresses for the "free" modified disc and the "axially constrained" modified disc are 18.4 % and 20.3 % respectively less when examined at the same interference fit of 16 μm.

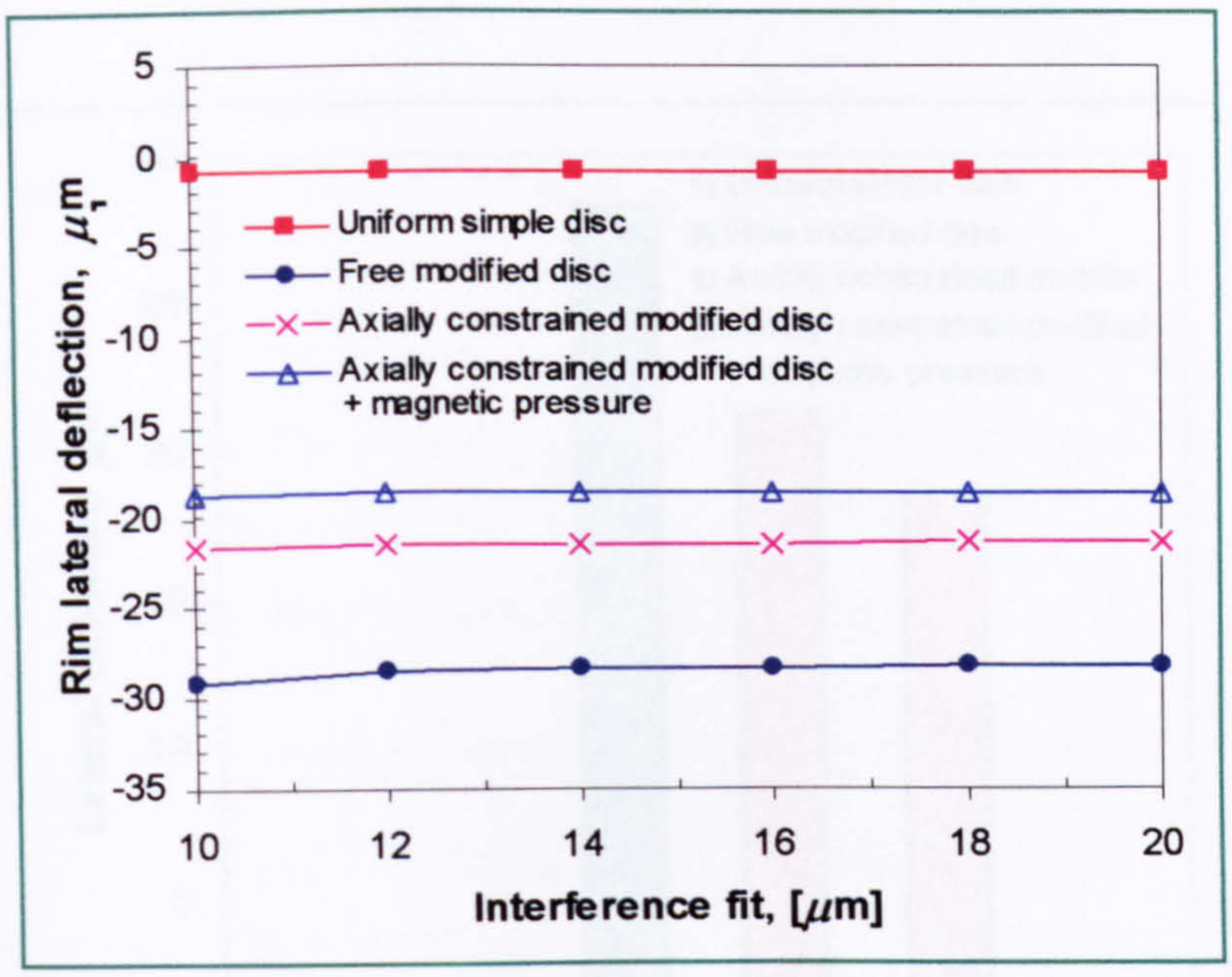

Figure 5.24 Lateral deflections vs. interference fit for uniform disc and modified disc at different applied boundary conditions.

Figure 5.24 shows the effect of change in interference fit on the lateral deflections is minimal. A precise comparison between the deflection of the uniform disc and the deflection of the non-uniform disc at an interference fit of 16 μm at the three different boundary conditions is shown in Figure 5.25. It can be seen that the uniform disc has the minimum deflection (0.825 μm), whereas the 'free" modified disc has the maximum lateral deflection (28.31 μm) compared to the "axially constrained" modified disc (21.36 μm). However, the lateral deflection is slightly decreased (18.54 μm) when "magnetic pressure" is added to the "axially constrained" modified disc. The later value is the minimum deflection that can be achieved for the non-uniform disc. It is considered that this is a safe value since a clearance gap of 0.5 mm is reserved between the back-iron disc and the magnet rotor disc and enough clearance is also kept for the other mating parts such as stator casing and bearing housing.

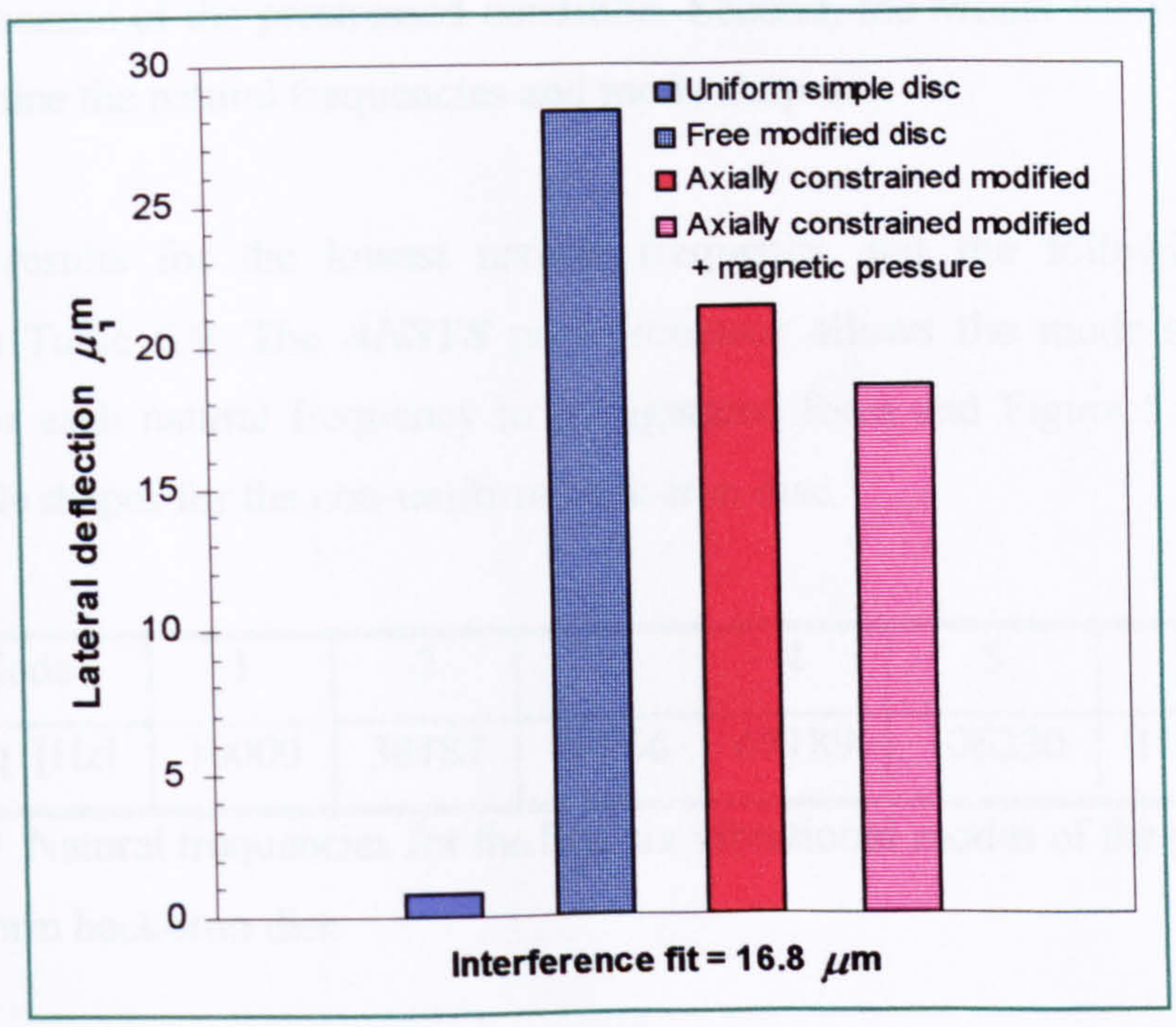

Figure 5.25 Comparison of Lateral deflections for uniform and modified disc with different boundary conditions at interference fit of 16.8 μm

5.4.2 Results of Modal analysis

Every structure has a very large number of natural frequencies at which it can be excited. These natural frequencies and their associated mode shapes are important parameters in the design of a structure that is subjected to dynamic loading condition. For rotating machines, it is essential to avoid any prolonged operation of the machine close to or at any of the natural frequencies otherwise the machine will start vibrating in a potentially violent way under resonant conditions. In order to prevent the destruction of the rotor this situation has to be avoided.

In this Section, Modal analysis is used to determine the natural frequencies and the mode shapes of the back-iron disc. The ***ANSYS*** program structure that used for stress analysis is slightly modified to perform the required analysis on the pre-stressed back-iron disc. The major modification in the program structure was achieved by actually deleting the contact elements between the shaft and the disc by merging the coincident nodes at the mating areas that represent the shaft and the disc.

Modal analysis here is carried out in two steps. First, a static analysis is performed because of the prestressed condition. Second, the Modal analysis is carried out to determine the natural frequencies and mode shapes.

The results for the lowest natural frequency and the following five are presented in Table 5.9. The ***ANSYS*** post-processor allows the mode shapes to be displayed for each natural frequency in exaggerated form and Figure 5.26 show the first six mode shapes for the non-uniform back-iron disc.

Mode	1	2	3	4	5	6
Freq. [Hz]	10000	38187	46866	67189	106230	119760

Table 5.9 Natural frequencies for the first six vibrational modes of the prestressed non-uniform back-iron disc

It can be seen from the results in Table 5.9 that the lowest natural frequency of 10000 Hz is an order of magnitude greater than the (rotational) operating frequency of the modified back-iron disc which is 833 Hz. These relatively high frequencies are expected since the analysis is performed on the back-iron disc alone. Other components such as shafts and assemblies were not included in the analysis. It must be mentioned that different results would be obtained if all the components of the generator were modelled i.e. including the ***PM*** discs of the generator plus accessories such as bearings, tightening nuts and washer springs that are mounted on the shaft. However, the results given in Table 5.9 give an initial indication of the lowest natural frequencies and mode of shapes that might be excited by rotation.

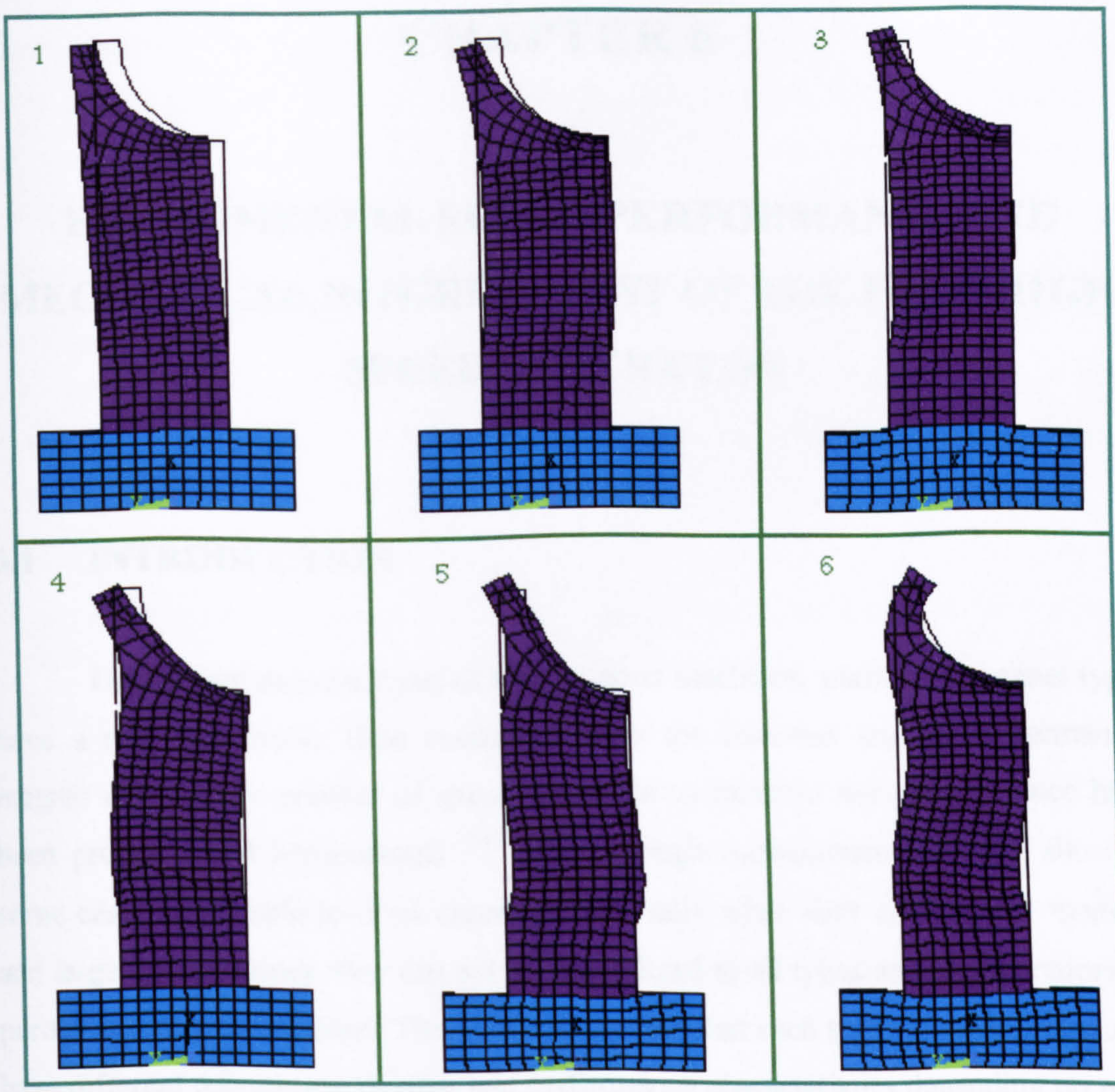

Figure 5.26 Mode shapes for the prestressed, modified back-iron disc for the six lowest natural frequencies

CHAPTER 6

EXPERIMENTAL SETUP, PERFORMANCE AND MECHANICAL INTGRITY TEST OF THE *PMAF* HIGH-SPEED GENERATOR

6.1 INTRODUCTION

Unlike conventional types of synchronous machines, permanent magnet types have a non controllable field excitation. With the renewed interest in permanent magnet machines, a number of special methods to measure their performance have been proposed and implemented [14,32,44]. Although measurement methods show in some cases remarkable level of accuracy, especially when they are used for medium and large size machines, they can not be generalised to all types and configurations of permanent magnet machines. This is due to the fact that such types of machines would have different operating behaviour and performance characteristics depending on rotor configuration and type of application. Furthermore, in the case of high-speed machines some assumptions that are acceptable for large sizes, are not any more valid. Therefore, the suitable alternative to overcome the above mentioned difficulties is to establish a direct measurement and analysis methods.

In this Chapter, a simple but reliable approach is used to measure the steady state synchronous performance of the *PMAF* high-speed generator. The method is based on direct on-line measurements of the equivalent circuit parameters [47]. Other related tests such as no load tests, flux density measurements are also found in this Chapter. Finally, the mechanical integrity test on the rotors of the *PMAF* high-speed generator is also described.

The constructed single phase prototype of the ***PMAF*** high-speed generator, was designed for a minimum output voltage of 220 V AC RMS and a maximum current output of 75 Amp AC RMS at the operating speed of 50000 rpm. However, there was no available engine that could drive the prototype fully loaded at this speed. The development of a special drive mechanism to operate the prototype at its ultimate speed was beyond the aim of this work. Moreover, a separate but simultaneous project was undertaken at the ACME department by another colleague to design and develop an inward flow radial gas turbine engine (***IFRGT***) especially to drive the ***PMAF*** generator at a speed of 50000 rpm. Unfortunately, up to the stage of writing up this thesis, the engine was not ready to operate at its ultimate design objectives. Hence, a simple but reliable alternative drive system was used to test the prototype for the following tests:

- Electromagnetic performance tests which included magnetic flux density measurements, low speed no-load test and low speed load test.
- Mechanical integrity and acceptance tests for the individual magnet rotor discs of the prototype. The specified acceptance test consisted of acceleration to design speed, operation at this speed for a prolonged operation 1-2 hours, and deceleration. This test was performed via cold air test rig using a fractional horsepower turbine. Details regarding this test are given in the following pages.

6.2 ELECTROMAGNETIC TEST

6.2.1 Magnetic flux density measurement

At the start of the experimental work, the flux density values at several points across the air gap of the preliminary prototype and at the magnet surface were required. This preliminary test was necessary to understand the magnetic behaviour of the model. The prediction of the effect of the materials type of the retainment ring in the magnet rotor disc on the flux level and flux distribution in the air gap was also vitally required. Moreover, these measurements were also required for the validation of the ***FE*** results obtained in Chapter Four and also to assist for the calibration of the analytical models that were derived in Chapter Three.

To accomplish this task, the Hirst GM05 handheld gauss meter with RS232 interface was procured from Hirst Magnetic Instruments Ltd. The instrument is capable to measure magnetic flux density of magnets and magnet assembly. The gauss meter can measure DC, DC peak, AC RMS, AC RMS Max and AC peak. It can measure from 0 – to 3 Tesla with a resolution of 1 MicroTesla on most of the available ranges. The gauss meter was pre-calibrated by the manufacturer with an accuracy of $\pm 1\%$ at a temperature of $20°C$. More details about the instrument and its specifications can be found in [84].

A transverse flux probe that was supplied with the gauss meter was used for the measurement of the flux density and it was held in the place of the tool-post of a small lathe that was available in the lab. This arrangement has allowed for precise measurement of the flux density at different locations by fine movement of the probe in radial and axial directions i.e. R and Z respectively. On the other hand, the rotors of the prototype were held through the shaft in a three jaw chuck of the lathe which in turn has allowed the movement of the rotors in the θ direction. Figure 6.1 shows the experimental setup used for the flux density measurements for the preliminary prototype.

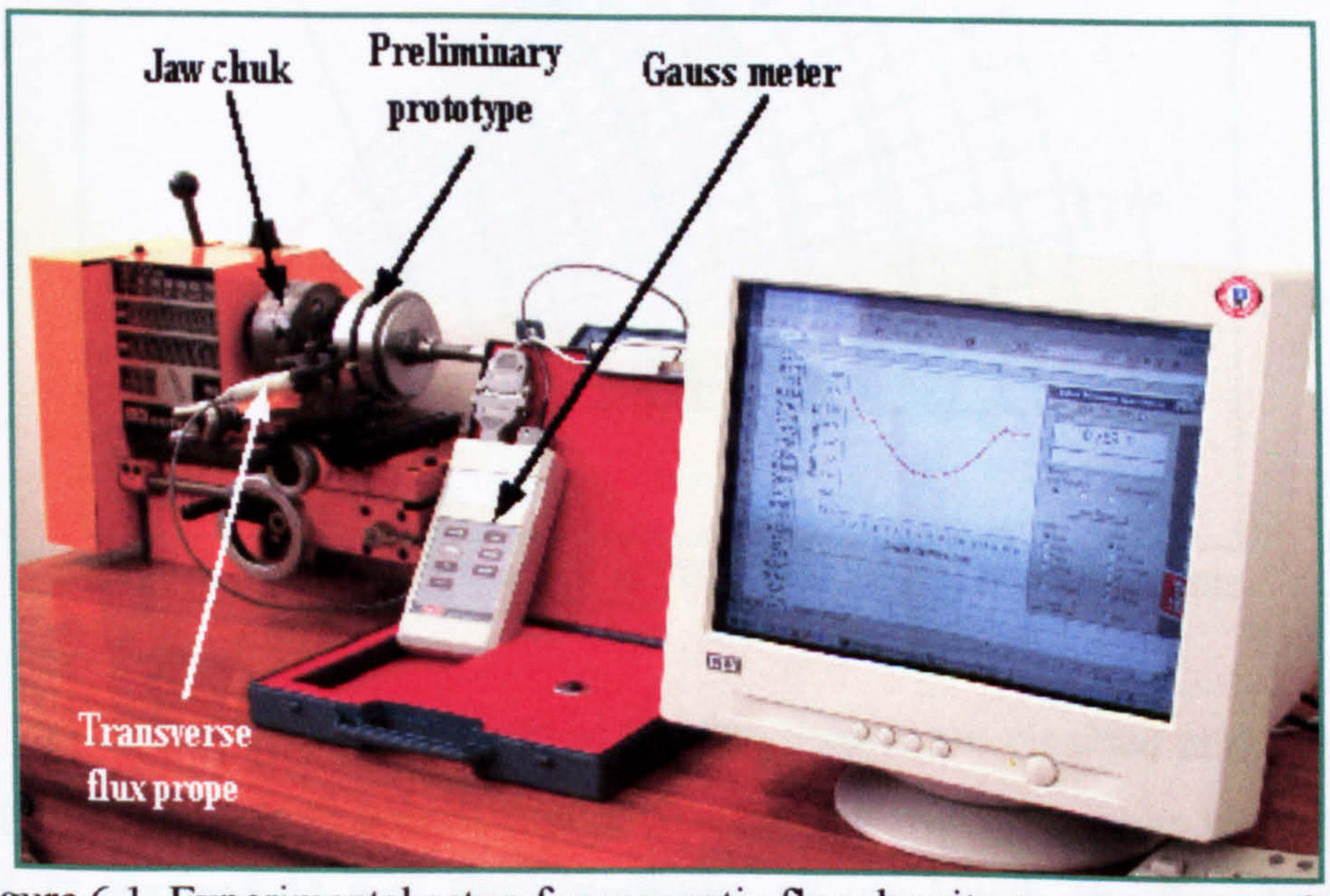

Figure 6.1 Experimental setup for magnetic flux density measurement of the preliminary prototype

The constructed preliminary prototype which is described in ***Appendix A***, is a single module flexible generator which has two of magnet rotor discs and two back-iron discs at the backside of each magnet rotor disc. These discs are mounted on a threaded shaft to allow for adjustment of the air gap length between the magnet rotor discs. The flux density measurements were performed for one sector of the magnet rotor disc which represents 1/8 of the rotor area that was enclosed by a virtual path similar in the shape and dimensions of the path that was presented in the ***FE*** model. In order to get accurate results, the sector was divided into small rectangles similar to the mesh which was generated in the ***FE*** models. This mesh which can be seen in Figure 6.2, was defined from $0°$ to $45°$ in step of $2.5°$ in θ direction and from 18 mm to 66 mm in step of 3 mm in the radial directions. This mesh was placed on a non magnetic sheet and placed at the middle of the air gap for three different cases of air gap lengths these are; 10 mm, 12 mm and 14 mm.

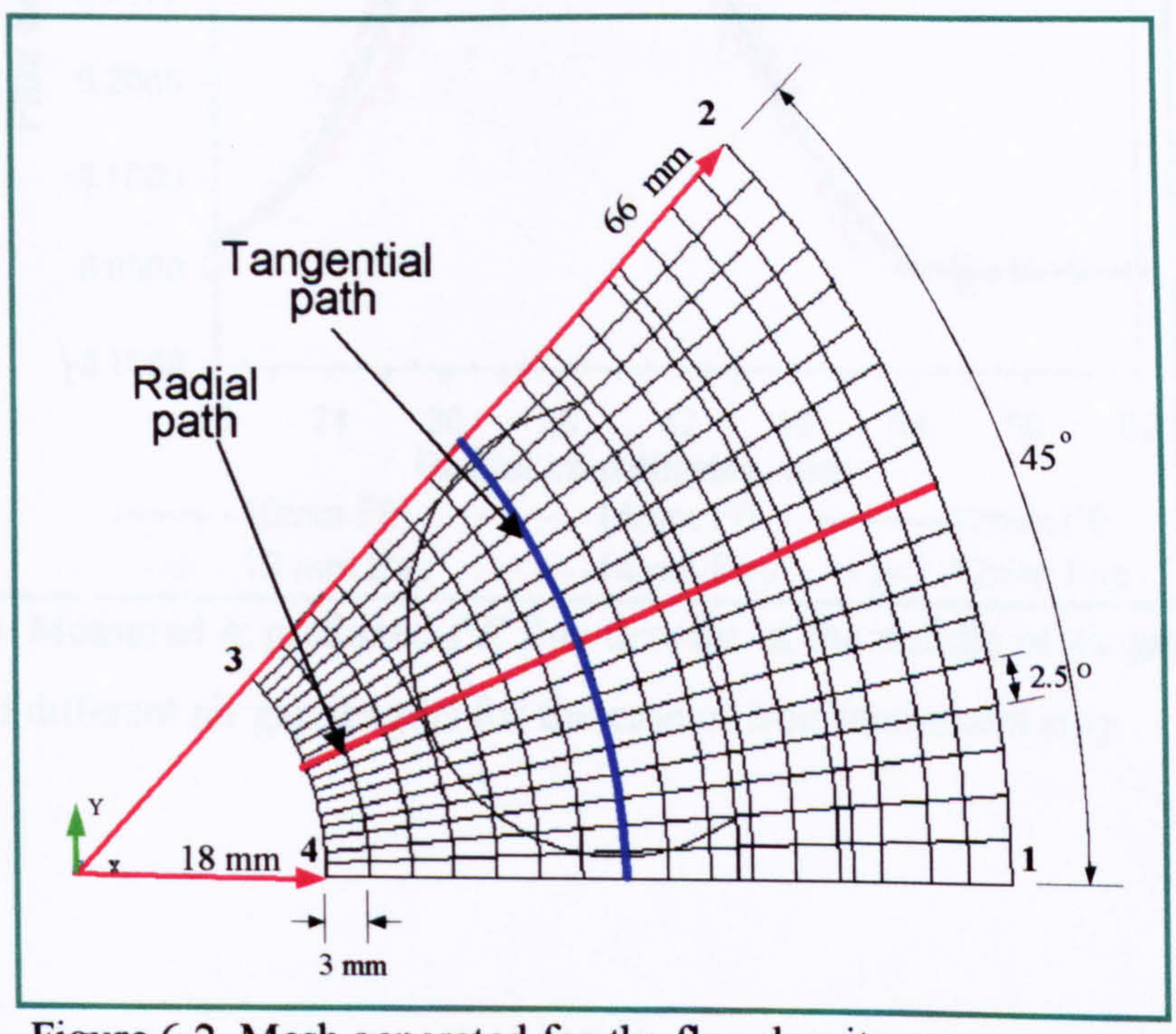

Figure 6.2 Mesh generated for the flux density measurements

The first set of measurements of the flux density are obtained at the middle of the air gap for the case of normal iron retainment ring with the air gap length is set to 10 mm, 12 mm and 14 mm. For a particular air gap length, the flux density was measured at two different paths which were shown in Figure 6.2. The measured values were compared to the ***FE*** results and they can be seen in Figures 6.3 and 6.4. Thus the

results of the ***FE*** model were validated since they were favourably compared to the measured values of the flux density.

Similar tests were performed on the rotors having Aluminium retainment ring. The flux density measured at a particular case of 10 mm air gap length was compared to that obtained from the rotors having iron ring at the same air gap length. Results obtained are presented graphically in Figure 6.5.

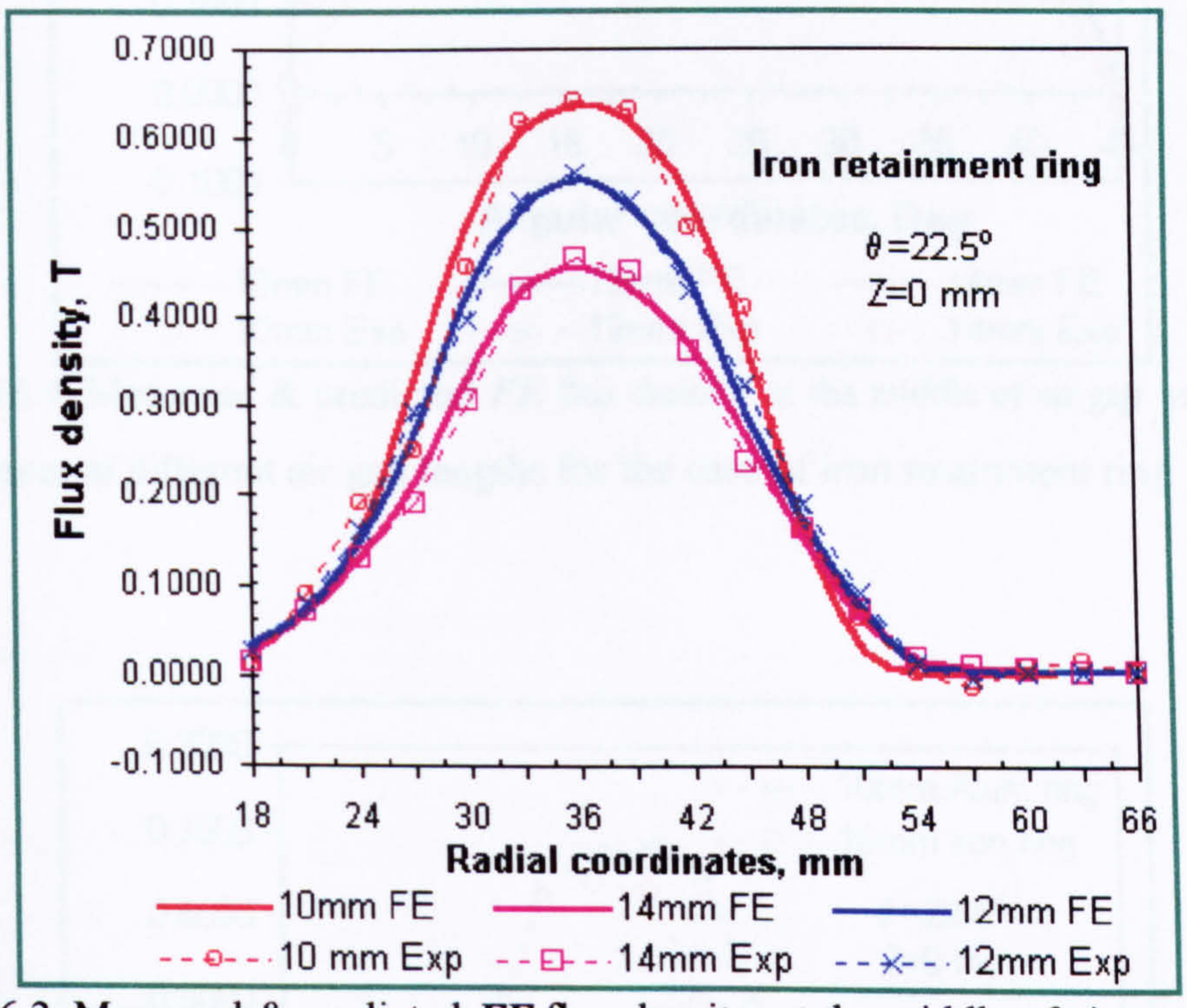

Figure 6.3 Measured & predicted ***FE*** flux density at the middle of air gap vs. radial distance at different air gap lengths for the case of iron retainment ring

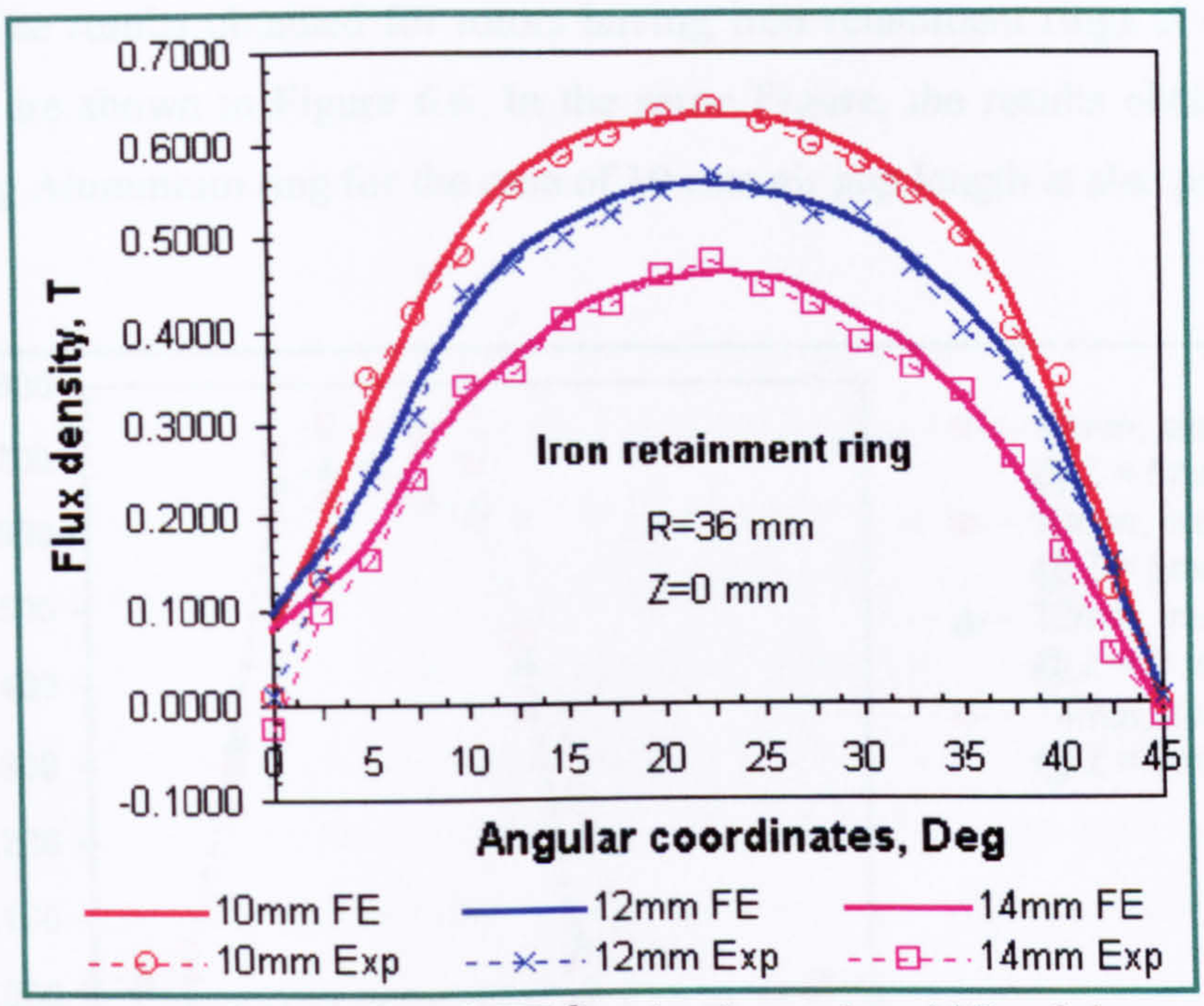

Figure 6.4 Measured & predicted ***FE*** flux density at the middle of air gap vs. angular co-ordinates at different air gap lengths for the case of iron retainment ring

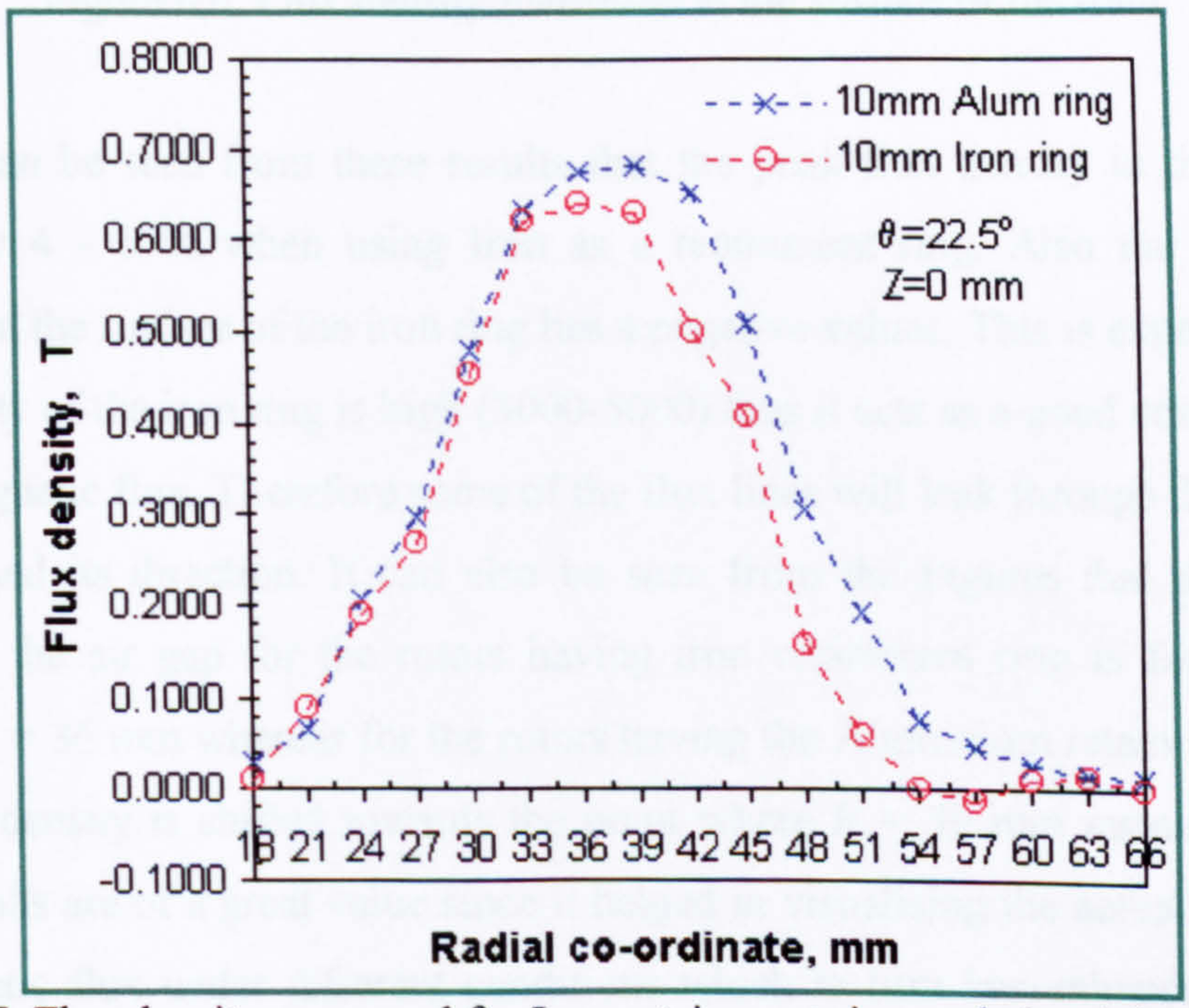

Figure 6.5 Flux density measured for Iron retainment ring and aluminium retainment ring for the case of 10 mm air gap length

The same tests were performed but with the probe was placed at the surface of the rotor. The results obtained for rotors having iron retainment rings at different air gap length are shown in Figure 6.6. In the same Figure, the results obtained for the rotor having Aluminium ring for the case of 10 mm air gap length is also presented.

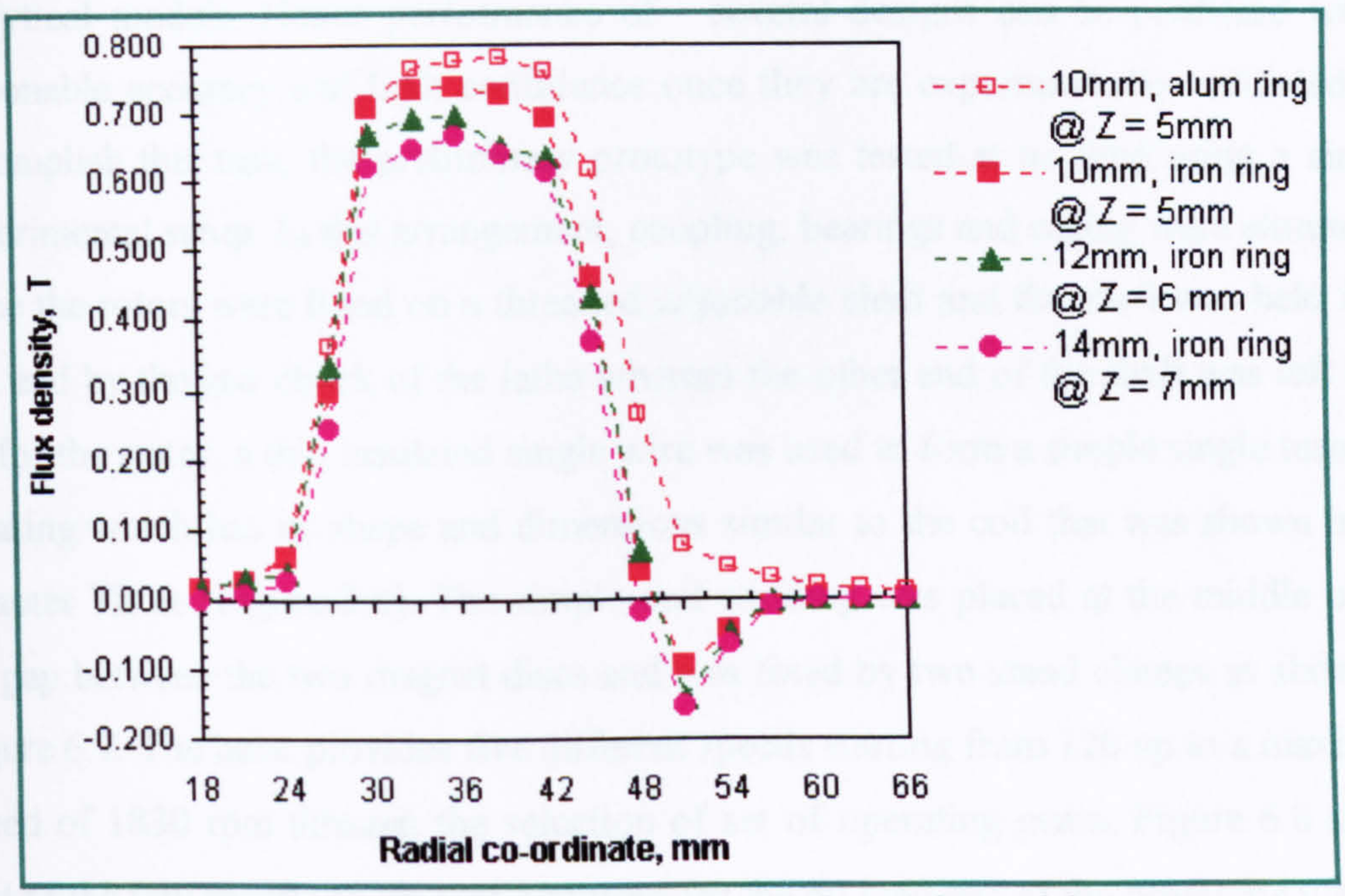

Figure 6.6 Flux density measured at the surface of the rotor

It can be seen from these results that the peak flux density in the air gap is reduced by 4 – 5 % when using Iron as a retainment ring. Also the flux density measured at the surface of the iron ring has a negative values. This is expected sine the permeability of the iron ring is high (3000-5000) thus it acts as a good conduction path for the magnetic flux. Therefore some of the flux lines will leak through the ring and it will reversed its direction. It can also be seen from the Figures that the peak flux density in the air gap for the rotors having iron retainment ring is found at radial distance R = 36 mm whereas for the rotors having the Aluminium retainment ring, the peak flux density is shifted towards the point where R = 39 mm instead of 36 mm. These results are of a great value since it helped in visualising the actual behaviour of the magnetic flux under different conditions which in turn has enhanced the design capabilities for the ***PMAF*** high-speed generator.

6.2.2 Low speed no load test of the prototype with simple coil winding

The objective is to test the preliminary prototype at no load and to obtain preliminary experimental data at the earlier stage of the design so that it can be sued to verify several ***FE*** electromagnetic models which can be used then to calibrate the analytical models. Hence performance of several designs can be predicted with a reasonable accuracy and high confidence once they are experimentally validated. To accomplish this task, the preliminary prototype was tested at no load using a simple experimental setup. In this arrangement, coupling, bearings and casing were eliminated since the rotors were fitted on a threaded adjustable shaft and the shaft was held from one end by the jaw chuck of the lathe whereas the other end of the shaft was left free. As for the stator, a thin insulated single wire was used to form a simple single turn coil winding which has its shape and dimensions similar to the coil that was shown in the Chapter Three (Figure 3.8). The simple coil winding was placed at the middle of the air gap between the two magnet discs and was fixed by two stand clamps as shown in Figure 6.7. The lathe provides five different speeds starting from 120 up to a maximum speed of 1830 rpm through the selection of set of operating gears. Figure 6.8 shows part of the low speed test rig that was used for the no load test of the prototype with the simple coil winding.

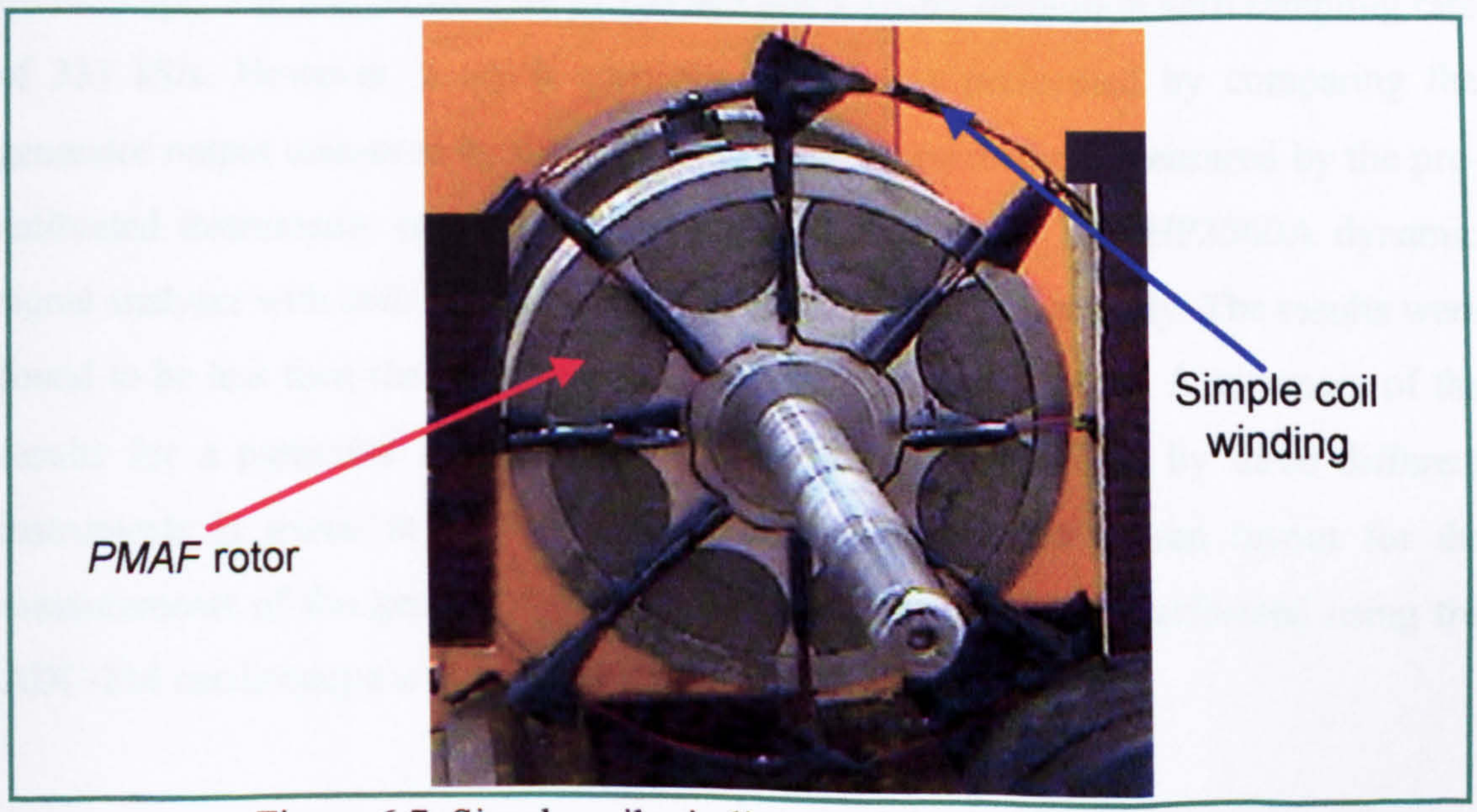

Figure 6.7 Simple coil winding used for the no load test

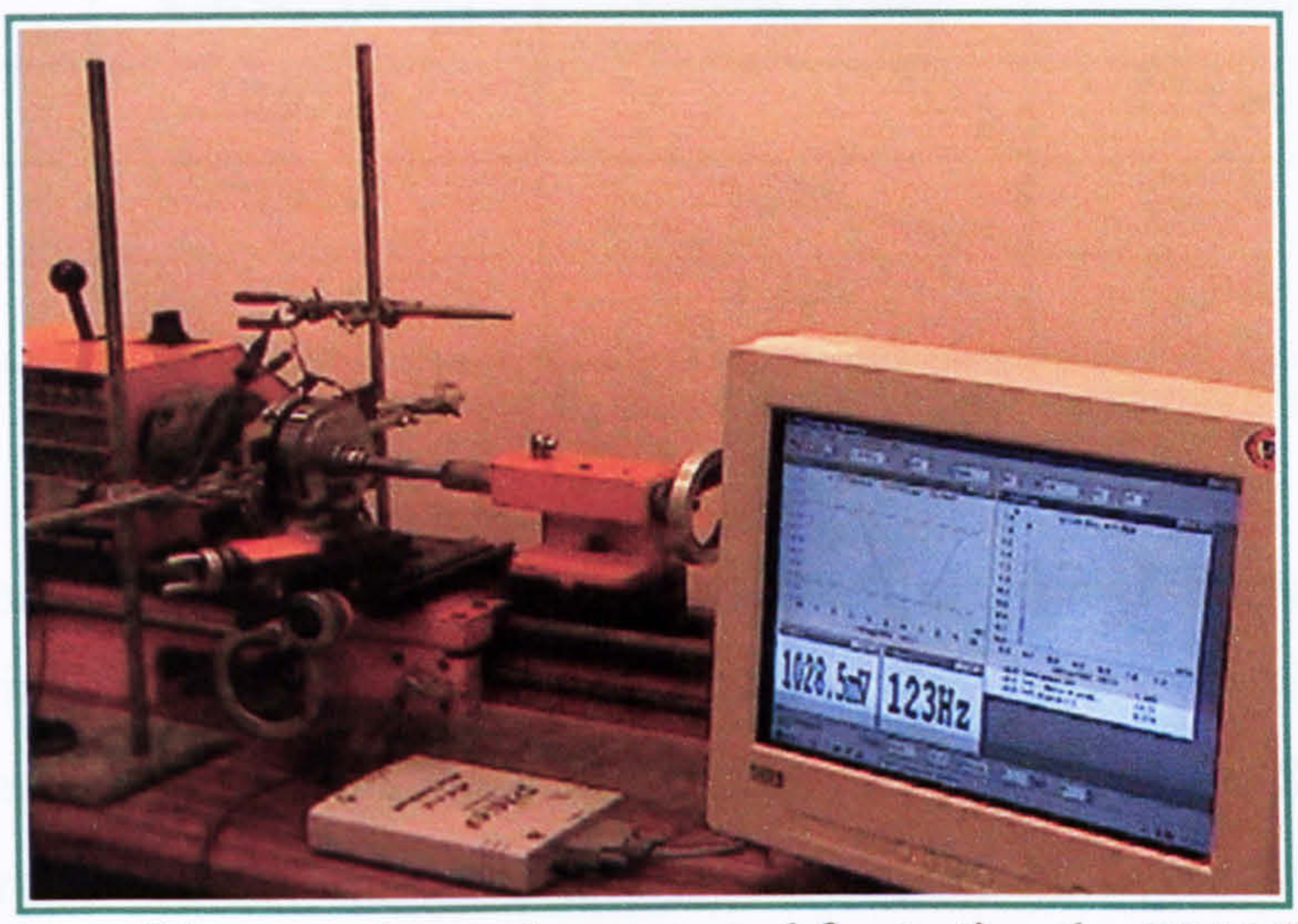

Figure 6.8 Part of the experimental set up used for testing the ***PMAF*** prototype at no-load with simple coil winding

In this test, the no load induced voltage was measured at the speed of 1830 rpm and the harmonics contents were analysed. A PC based oscilloscope, ADC-216, was procured from Pico Technology Ltd. The instrument is supplied with the PicoScope software, which turns a PC into an oscilloscope, spectrum analyser and a meter. Measurements and waveforms can be annotated with notes and printed, saved or exported to other applications. The ADC-216 is a high resolution, high precision oscilloscope. The unit is accurate to 1% and has a 16-bit resolution with sampling rate of 333 kS/s. However, a quick accuracy check was performed by comparing the generator output measured by the ADC-16 oscilloscope to these measured by the pre-calibrated instruments such as Fluke-83 digital multimeter and HP3560A dynamic signal analyser with their accuracy are 0.1 % and 0.08 % respectively. The results were found to be less than the manufacturer specified accuracy of 1 %. A summary of the results for a particular output signal of the prototype obtained by three different instruments is found in Table 6.1. A typical view for the screen layout for the measurements of the generator output voltage and its spectrum performed using the ADC-216 oscilloscope is shown in Figure 6.9.

Instrument	V-RMS [Volt]	V-Peak [Volt]	Freq. [Hz]	THD %
Fluke-83	0.9550	-	122.54	-
HP3560A	0.9548	1.289	122.51	4.151
ADC-216	0.9627	1.300	123.40	4.116

Table 6.1 Measurements obtained by three different pre-calibrated instruments

Two sets of measurements were performed on ***PMAF*** prototype with the simple coil winding. The first set was performed on the prototype having Aluminium retainment ring with the axial air gap length was varied in the range from 8 –16 mm with an increment step of 2 mm. The second test was similar to the first one but with the aluminium ring was replaced by iron rings. These measurements including harmonic analysis of the induced voltages were also compared with the results which were obtained from the ***3D FE*** model in Chapter Four. This comparison can be clearly seen in Figures 6.10 – 6.13 for a particular air gap length of 16 mm. The summary of the results for this particular case is given in Table 6.2.

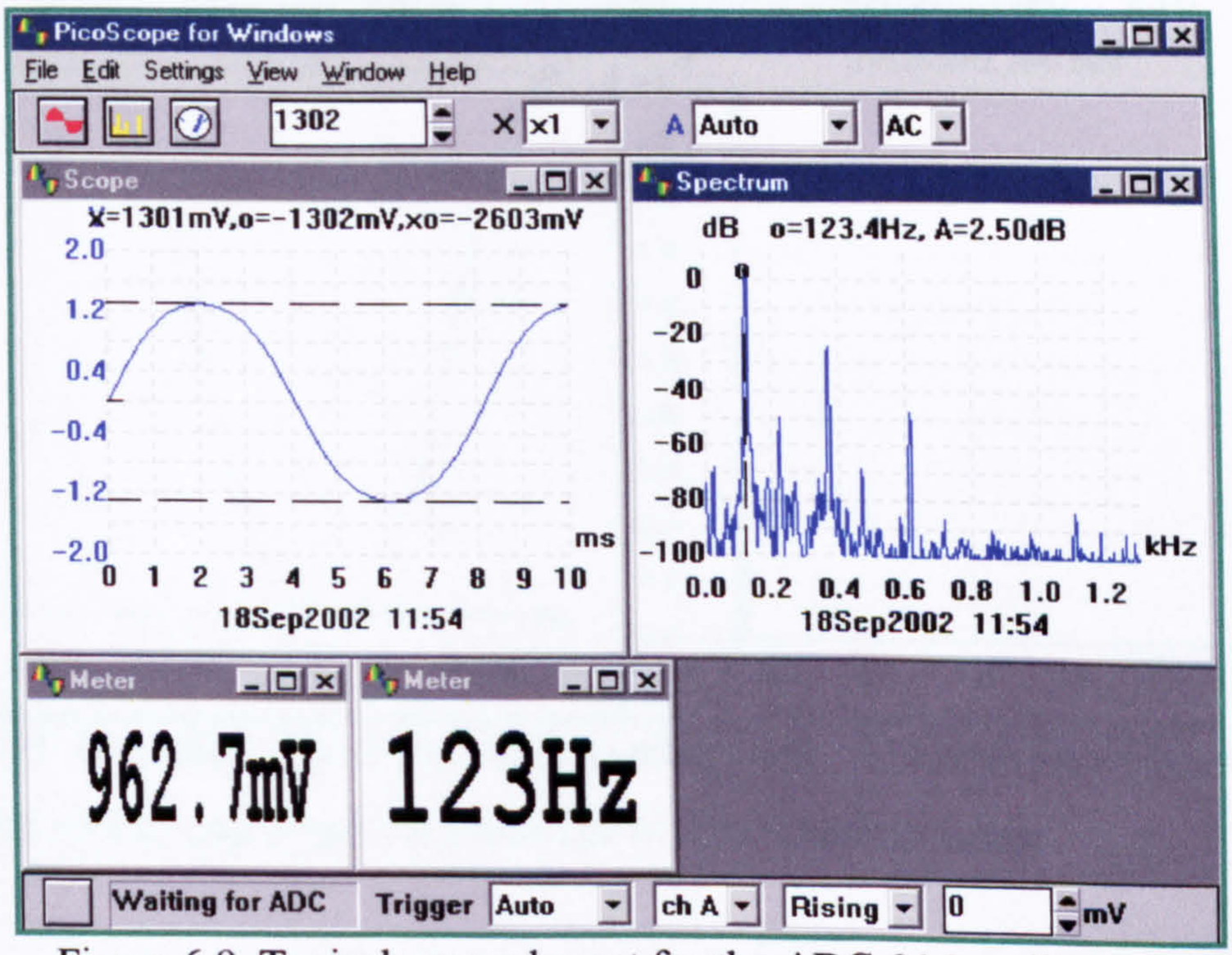

Figure 6.9 Typical screen layout for the ADC-216 oscilloscope

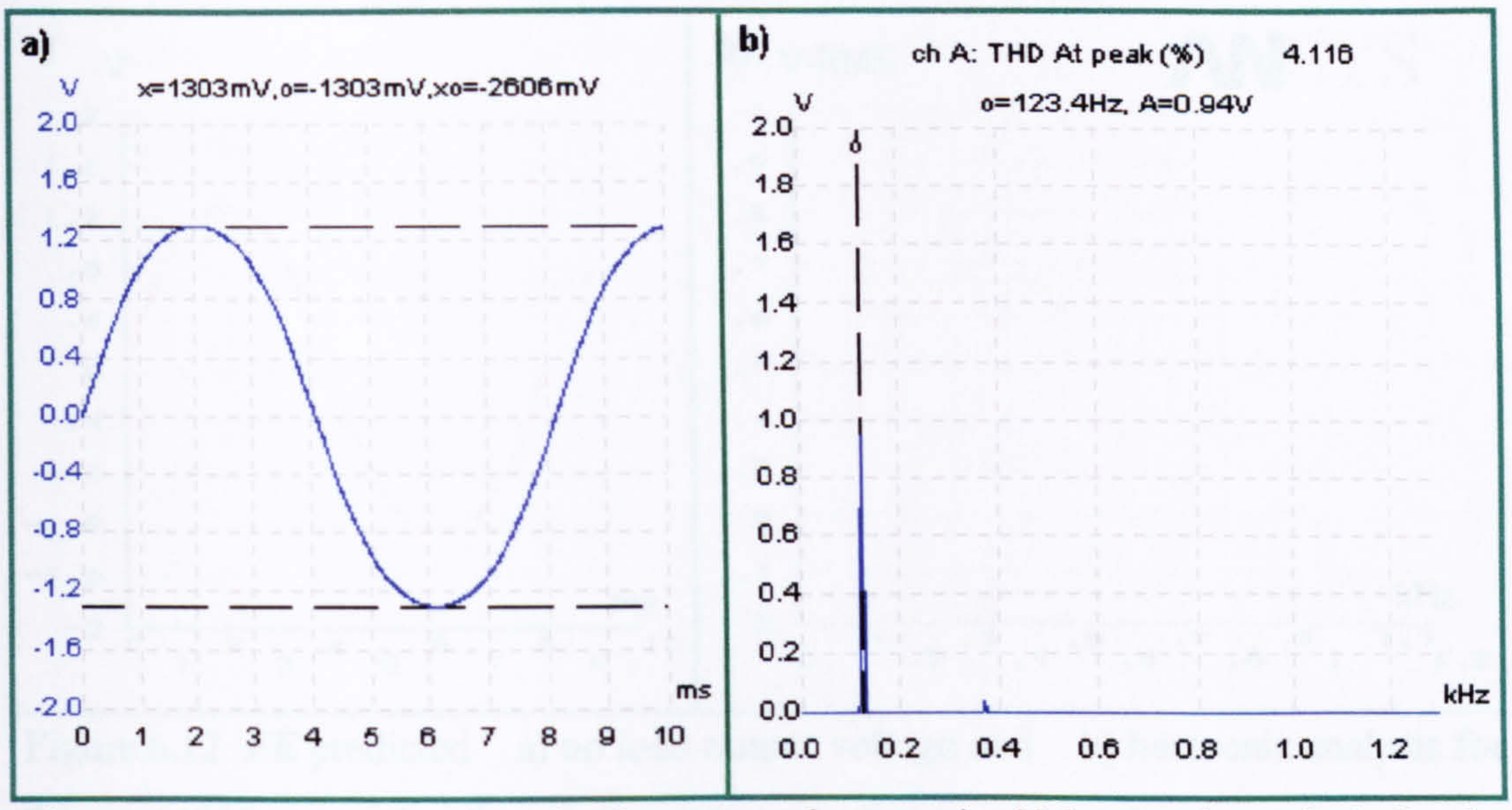

Figure 6.10 Measured a) no load output voltage and b) harmonic analysis for the case of 16 mm air gap length for prototype of aluminium retainment ring

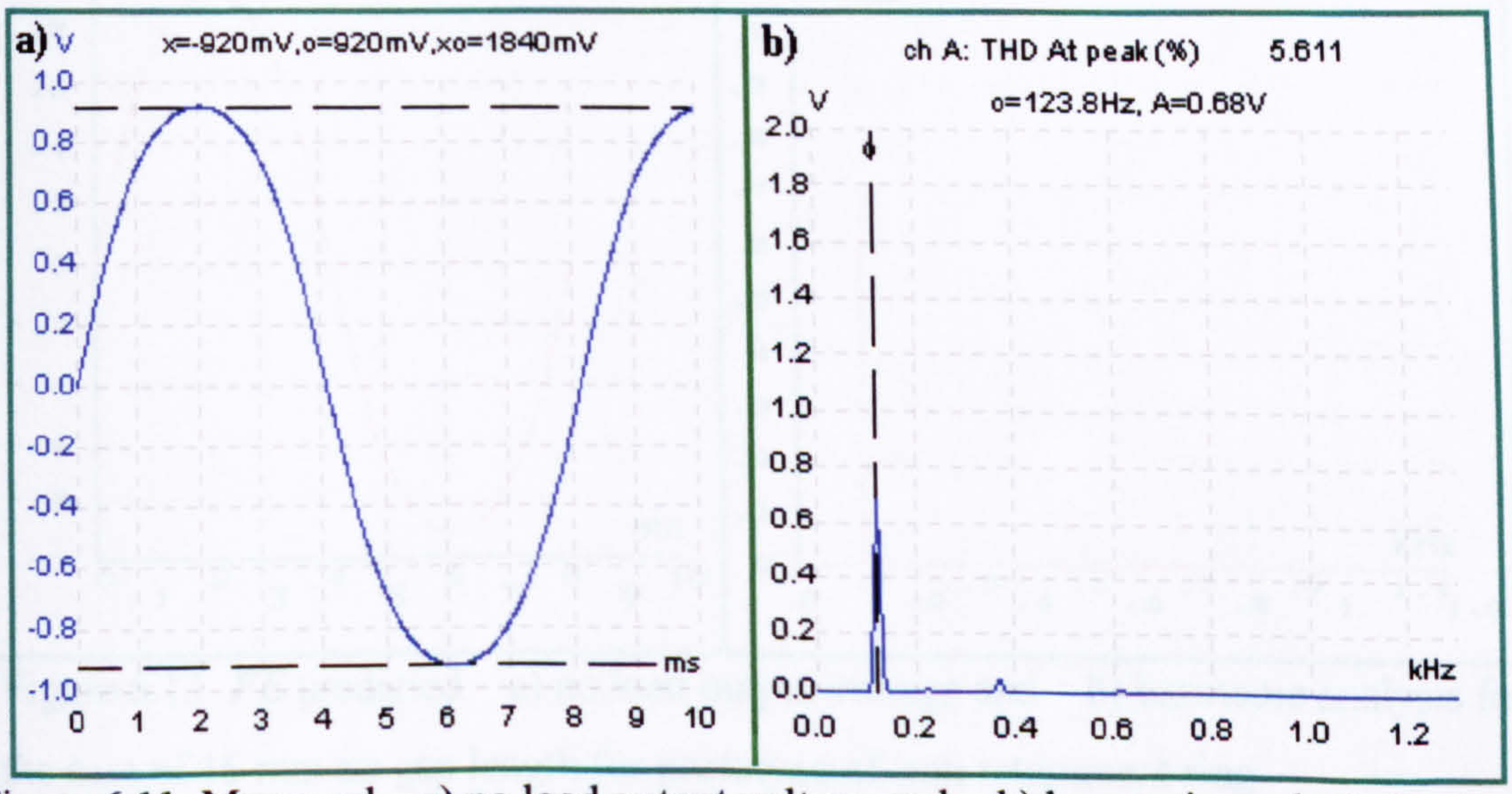

Figure 6.11 Measured a) no load output voltage and b) harmonic analysis for the case of 16 mm air gap length for prototype of iron retainment ring

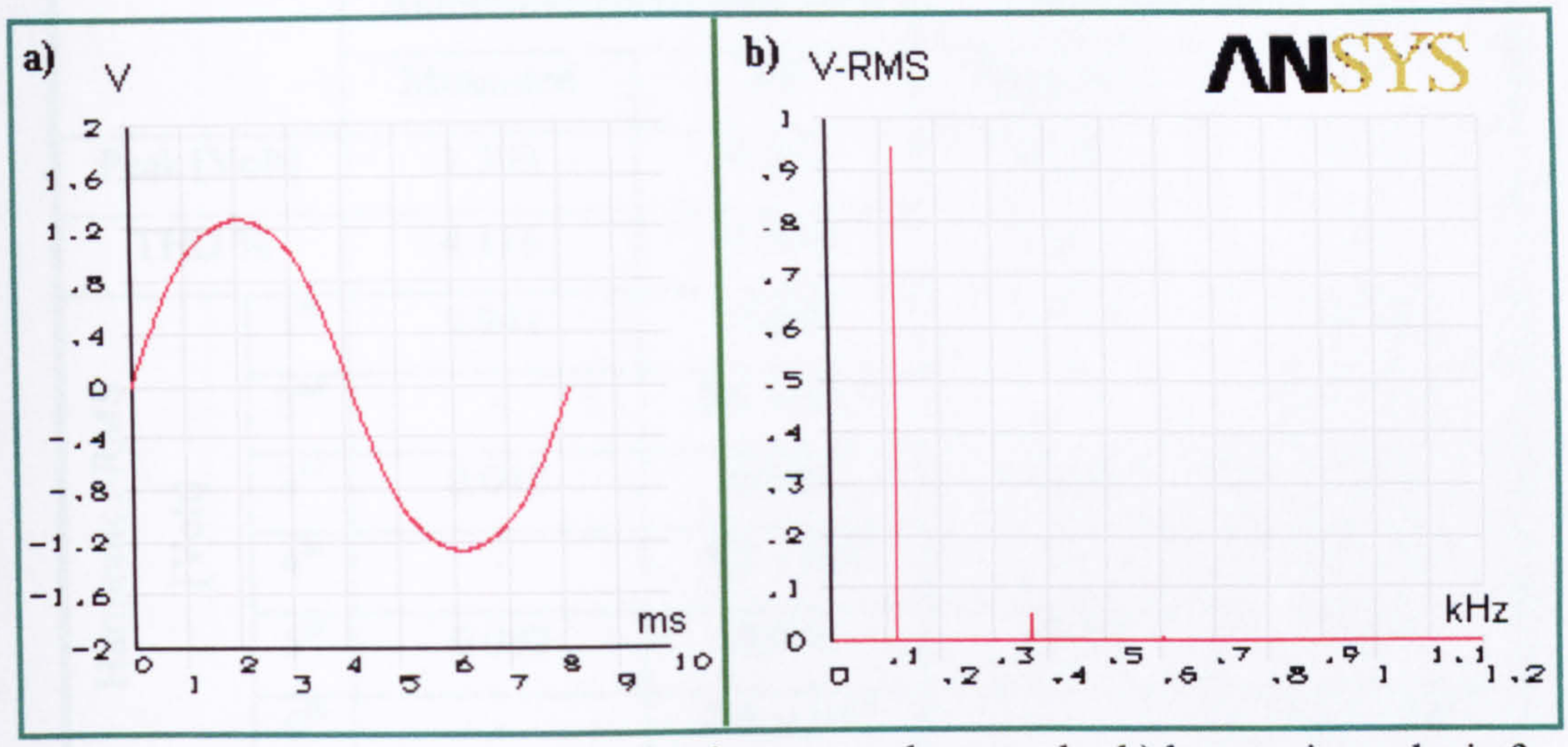

Figure 6.12 ***FE*** predicted a) no load output voltage and b) harmonic analysis for the case of 16 mm air gap length for prototype of aluminium retainment ring

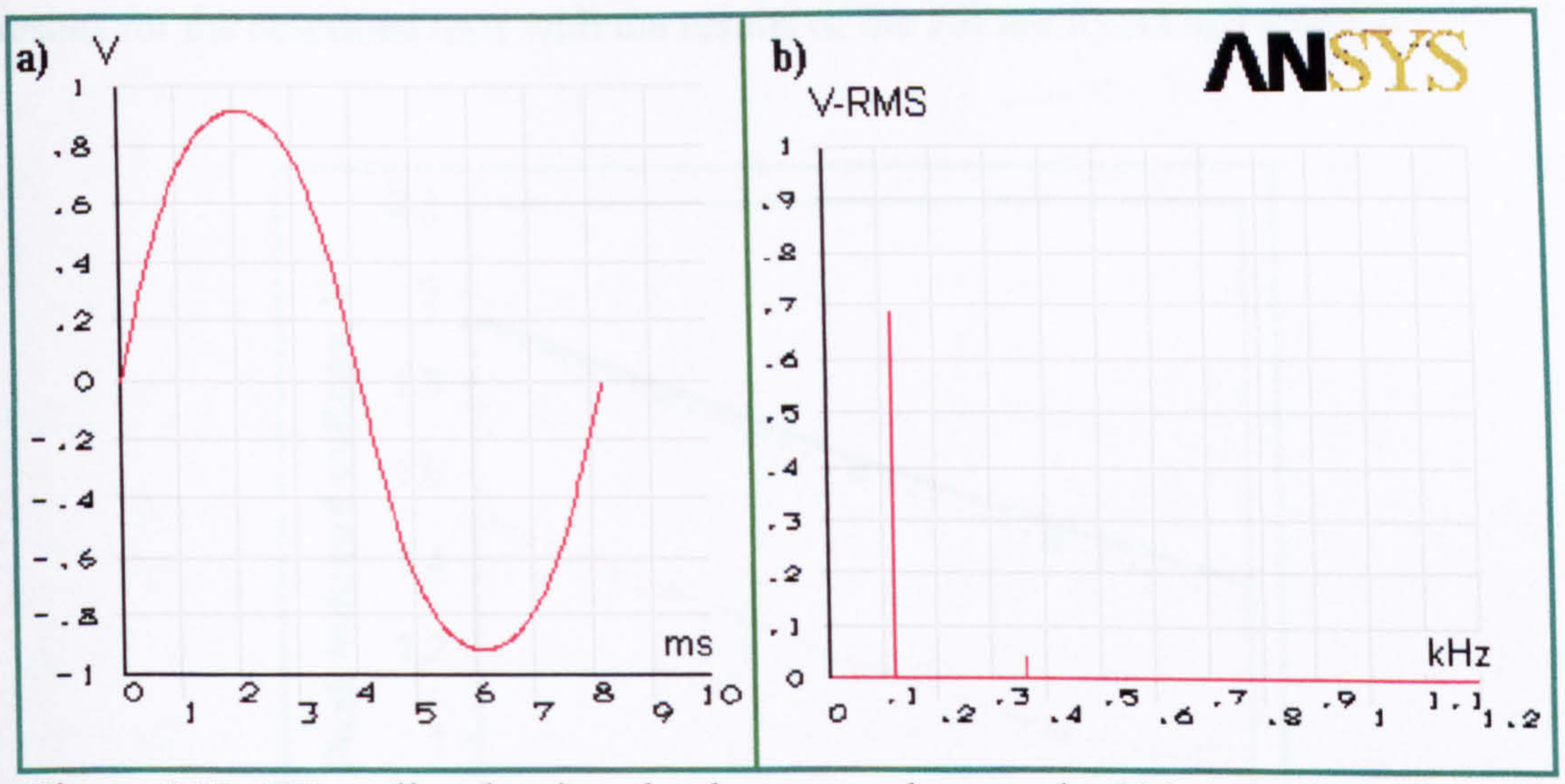

Figure 6.13 ***FE*** predicted a) no load output voltage and b) harmonic analysis for the case of 16 mm air gap length for prototype of iron retainment ring

		Aluminium retainment ring		Iron retainment ring	
		Measured	FE	Measured	FE
Peak [Volt]		1.303	1.351	0.920	0.921
THD %		4.116	4.958	5.611	5.974
Harmonics-RMS [Volt]	1st	0.941	0.939	0.680	0.685
	2nd	-	2.6×10^{-5}	-	2.4×10^{-5}
	3rd	0.042	0.046	0.038	0.041
	4th	-	5.2×10^{-5}	-	4.8×10^{-5}
	5th	0.002	0.004	0.002	0.002
	6th	-	7.8×10^{-5}		7.32×10^{-5}

Table 6.2 Measured and predicted ***FE*** data for the case of 16 mm air gap length for the prototype of both aluminium and iron retainment ring

For the complete two sets of measurements the peak voltages were considered and compared with the corresponding ***FE*** results as shown in Figure 6.14. Complete results for the described tests with the results of the ***FE*** are found in Table 6.3

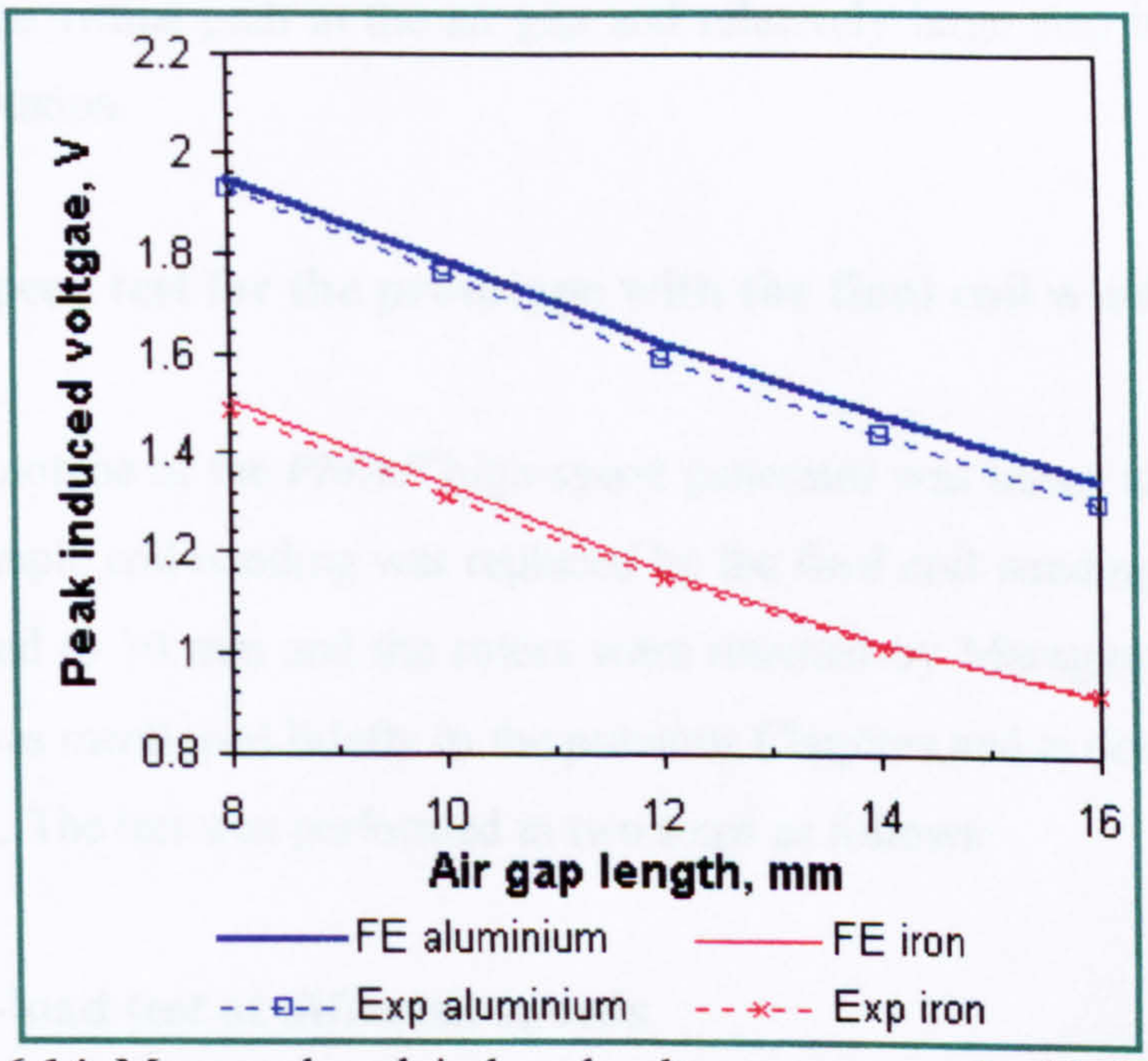

Figure 6.14 Measured peak induced voltages compared with ***FE*** results

Air gap length, mm	Peak voltage, V (Aluminium ring)		Peak voltage, V (Iron ring)	
	FE	Exp	FE	Exp
8	1.95	1.925	1.508	1.487
10	1.783	1.76	1.339	1.313
12	1.6247	1.592	1.164	1.149
14	1.478	1.443	1.022	1.016
16	1.351	1.303	0.921	0.92

Table 6.3 Complete results for induced peak voltages

It can be seen from the results that a good agreement was achieved between the *FE* results and the experimental results. The maximum differences in the induced voltage were 3.5 % and 1.9 % for the rotors of aluminium retainment ring and iron retainment ring respectively. It can be also seen that the induced voltage for the rotors of iron retainment ring is 20 % - 22 % less than that for the rotors of aluminium retainment rings. As for the THD, the increased values in the *FE* results can be referred to one or more of the following reasons; poor meshing, low number of points which define the virtual path in the air gap and relatively large step increment in the path through rotation.

6.2.3 Low speed test for the prototype with the final coil windings

The prototype of the *PMAF* high-speed generator was tested also at low speed but with the simple coil winding was replaced by the final coil winding and the air gap length was fixed to 10 mm and the rotors were retained by Maraging ring. The final coil winding was mentioned briefly in the previous Chapters and is described in details in *Appendix A*. The test was performed in two steps as follows:

6.2.3.1 No-load test at different speeds

The prototype was tested at no load at five different speeds which were attainable by the lathe. The measured peak induced voltages were again compared to

these obtained from the ***FE*** models as shown in Figure 6.15. The induced voltage waveforms at different speeds are shown in Figures 6.16 and 6.17.

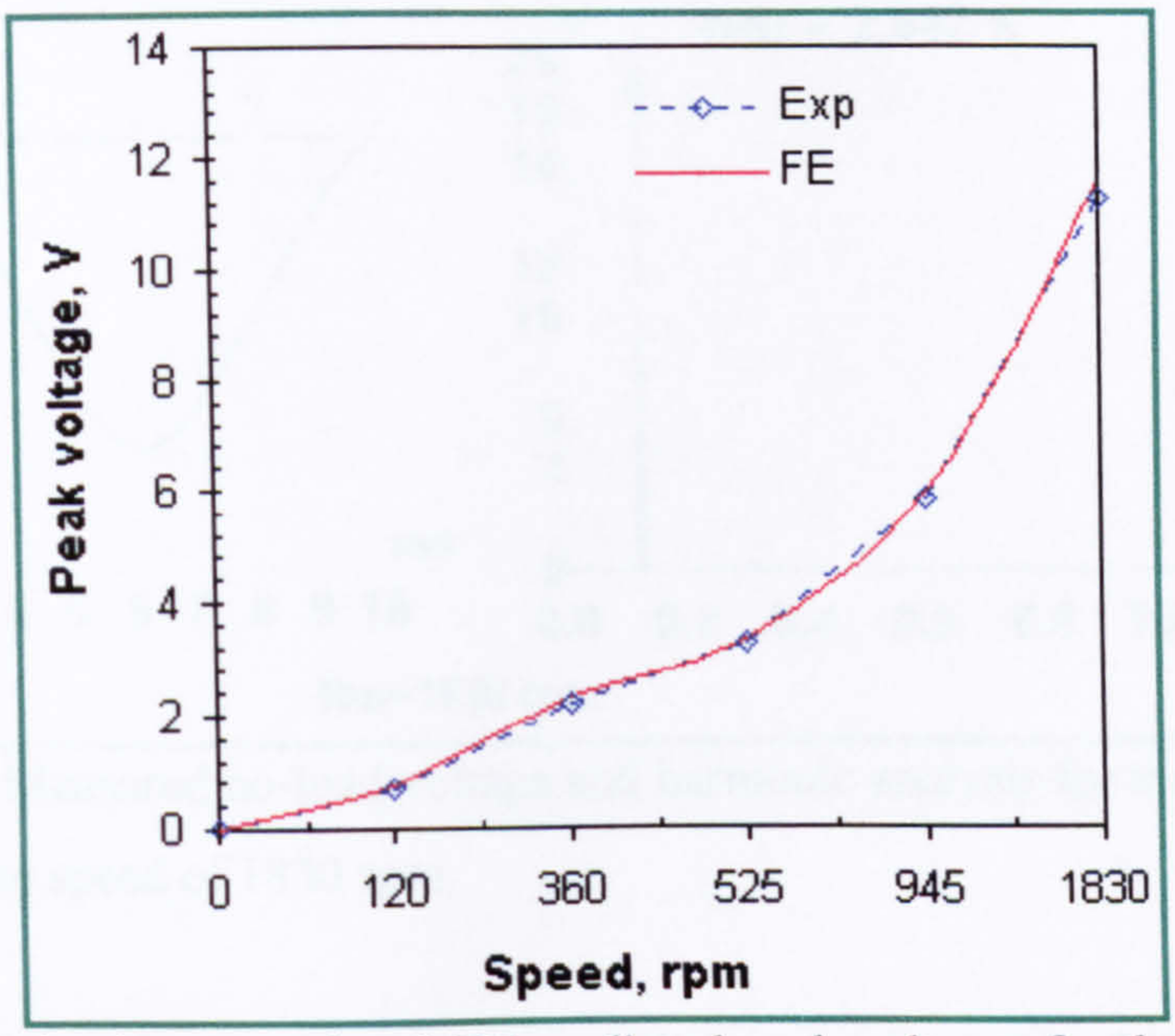

Figure 6.15 No load measured and ***FE*** predicted peak voltages for the final coil of the ***PMAF*** obtained at different speed

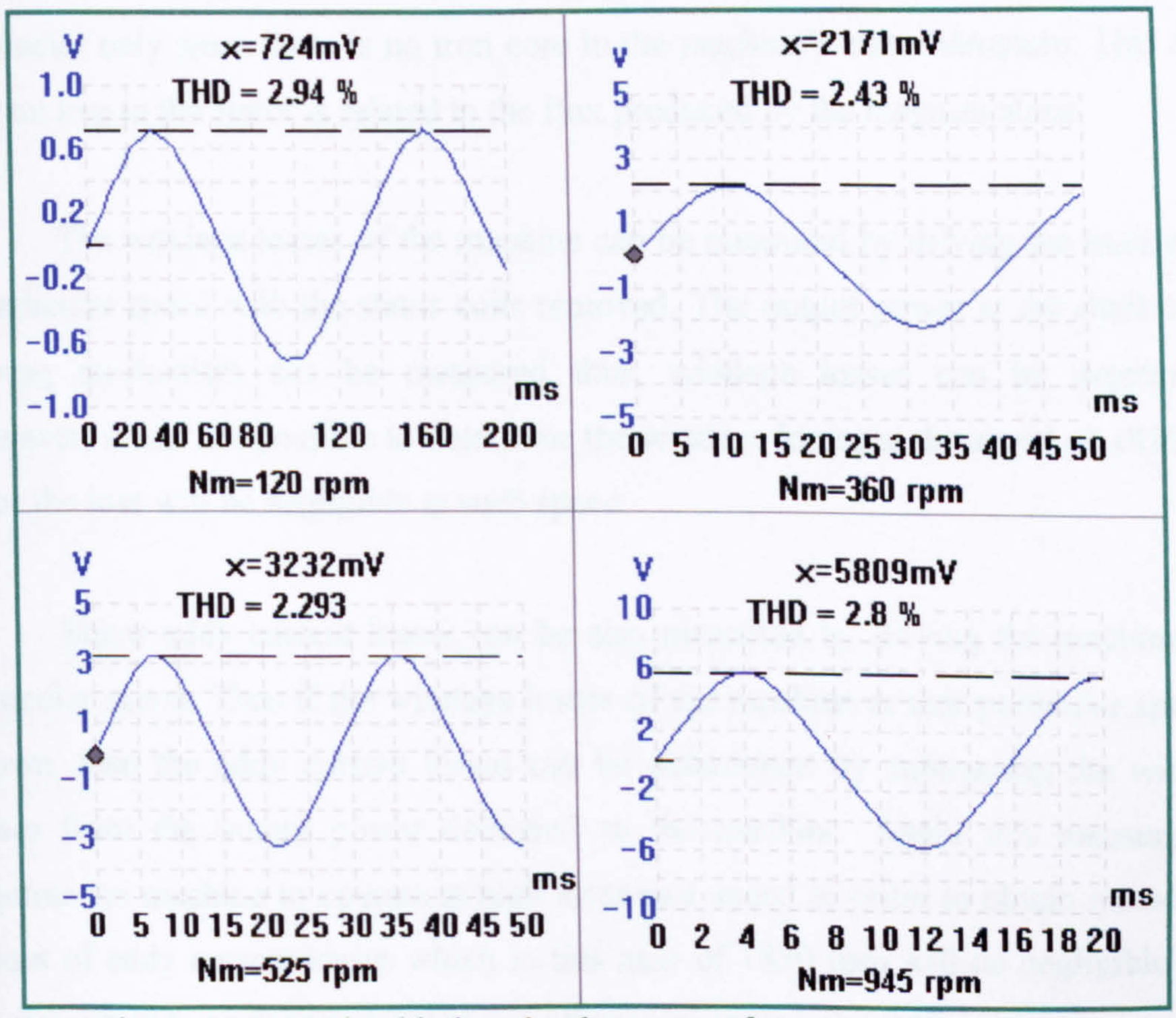

Figure 6.16 No-load induced voltage waveforms at different speeds

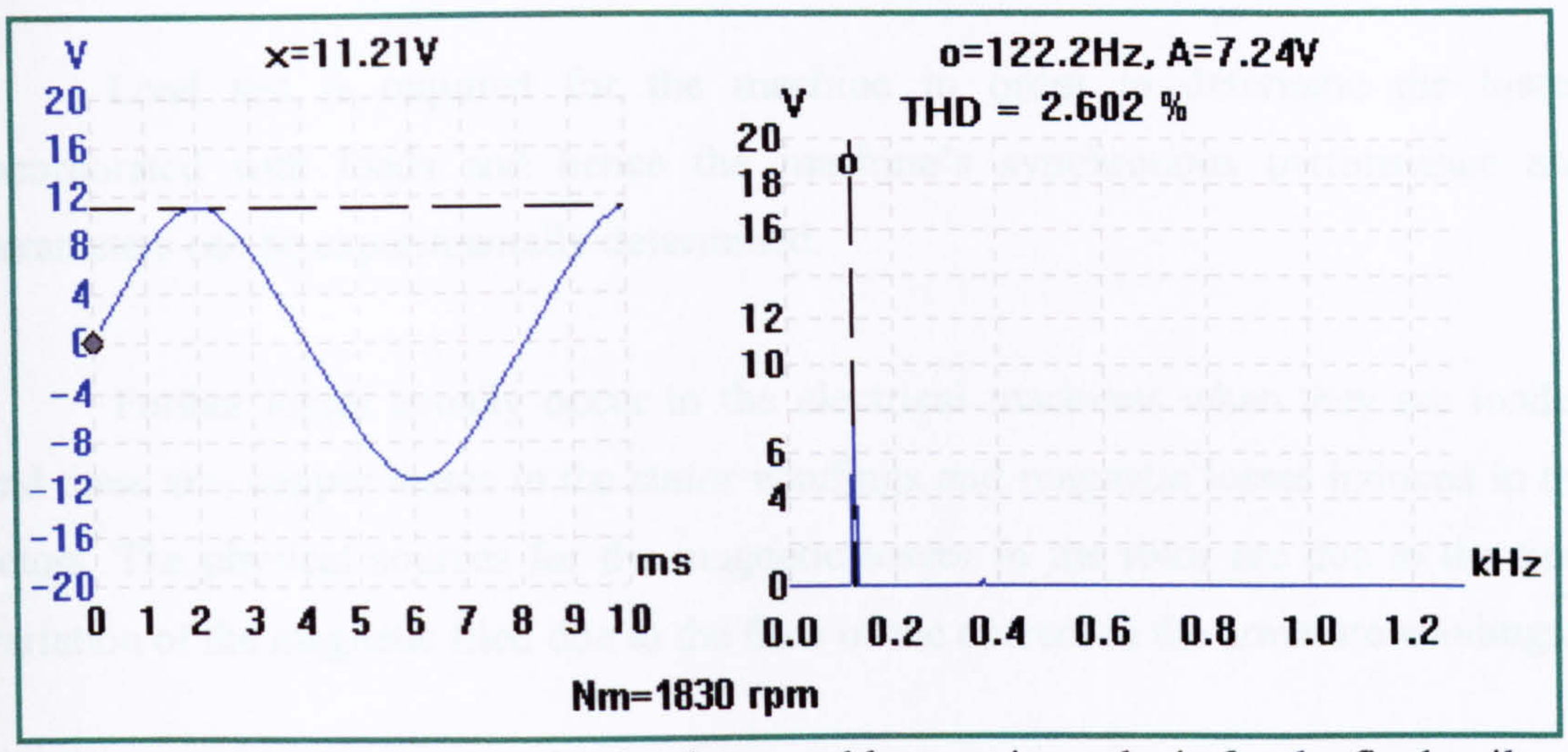

Figure 6.17 Measured no-load voltage and harmonic analysis for the final coil winding at the speed of 1830 rpm

It is worth mentioning that two types of losses can be deduced from the no load test these are; mechanical and stator eddy current losses. The mechanical losses are restricted to windage losses while stator eddy current losses are attributed in the stator conductor only since there is no iron core in the machine's stator structure. This eddy current loss in the stator is related to the flux produced by the magnets alone.

The windage losses of the machine can be measured by driving the machine at a particular speed with the stator coils removed. The output power at the shaft of the driving mechanism can be measured thus, windage losses can be determined. However, it was not possible to determine the windage losses at the speed of 1830 rpm since the loss will be negligible at such speed.

Stator eddy current losses can be also measured by driving the machine at a particular speed. Thus if the windage losses of the machine at that particular speed is known, then the eddy current losses can be determined by subtracting the windage losses from the output power delivered to the machine. Again this measurement requires the machine to operate at high rotational speed in order to obtain measurable values of eddy current losses which in this case of 1830 rpm will be negligible since the stator windings are constructed from thin stranded wires.

6.2.3.2 Load test

Load test is required for the machine in order to determine the losses incorporated with loads and hence the machine's synchronous performance and parameters can be experimentally determined.

Further losses usually occur in the electrical machines when they are loaded and these are; copper losses in the stator windings and magnetic losses induced in the rotors. The physical sources for the magnetic losses in the rotor are due to the time variation of the magnetic filed due to the flow of the current in the armature windings.

In small machines, the major part of the losses is attributed to the copper losses in the stator winding resistance. Therefore the value of the effective resistance is very important to be determined with reasonable accuracy in order to predict the machine performance, since this resistor is the dominant parameter. At high operating speed, a high frequency current will flow in the stator windings. In addition the stator windings will be subjected to high frequency flux and high temperature. Therefore the AC value of the resistance would be higher than its DC value since it is affected by the skin effect, proximity effect, and temperature rise.

In many investigations the effective values of the winding resistance is assumed to be constant and it is equal to the value that can be directly obtained from its DC value. However, in the current research, the winding resistance was obtained directly from the load test by using the on line measurement of the phasor angle from the phasor diagram.

Recalling the phasor diagram which was shown in Figure 3.16. There are four parameters should be measured in order to determine the effective resistance of the windings these are;

- No load induced voltage, E_{NL}
- Terminal voltage, V_t, at a particular load current, I_L.
- Air gap induced voltage, E_1 at the same load current.

- The phase shift between E_1 and I_L. In case of pure resistive load, this phase shift is equal to the angle between E_1 and V_t. We shall call this angle as the internal power factor, ψ_i.

The first parameter can be measured directly across the resistive load whereas the other two parameters require special arrangements for the coil winding and measurement techniques. To accomplish this task, a "dummy coil" winding was constructed simultaneously with the final coil winding having the same shape and approximately the same dimensions. This was done at the earlier stage of construing the stranded wire where 3 strands out of the 96 strands were marked and left especially for making an embedded but separate coil. No current will be flowing in this "dummy" coil since it will not be connected to a load. The load will only be connected across the terminals of the major coil which is formed by the remaining strands. Hence measuring the voltage across the dummy coil will give E_1 and measuring the phase shift between E_1 and V_t will give ψ_i.

The *PMAF* generator was tested at the speed of 1830 rpm. Part of the experimental setup used for load test is shown in Figure 6.18. Summary of the measurements obtained are given in Table 6.4. Terminal voltage measured across the resistive load vs. load current is compared with that predicted by *FE* models as shown in Figure 6.19. Also, winding temperature was measured using K-type thermocouples and plotted vs. load current as shown in Figure 6.19. Since no forced cooling was used in this particular test the maximum current drawn was limited to 40 Amp where maximum winding temperature measured at this current was $100°C$. All instruments used for current, volt and temperature measurements are pre-calibrated at RS Calibration Laboratories.

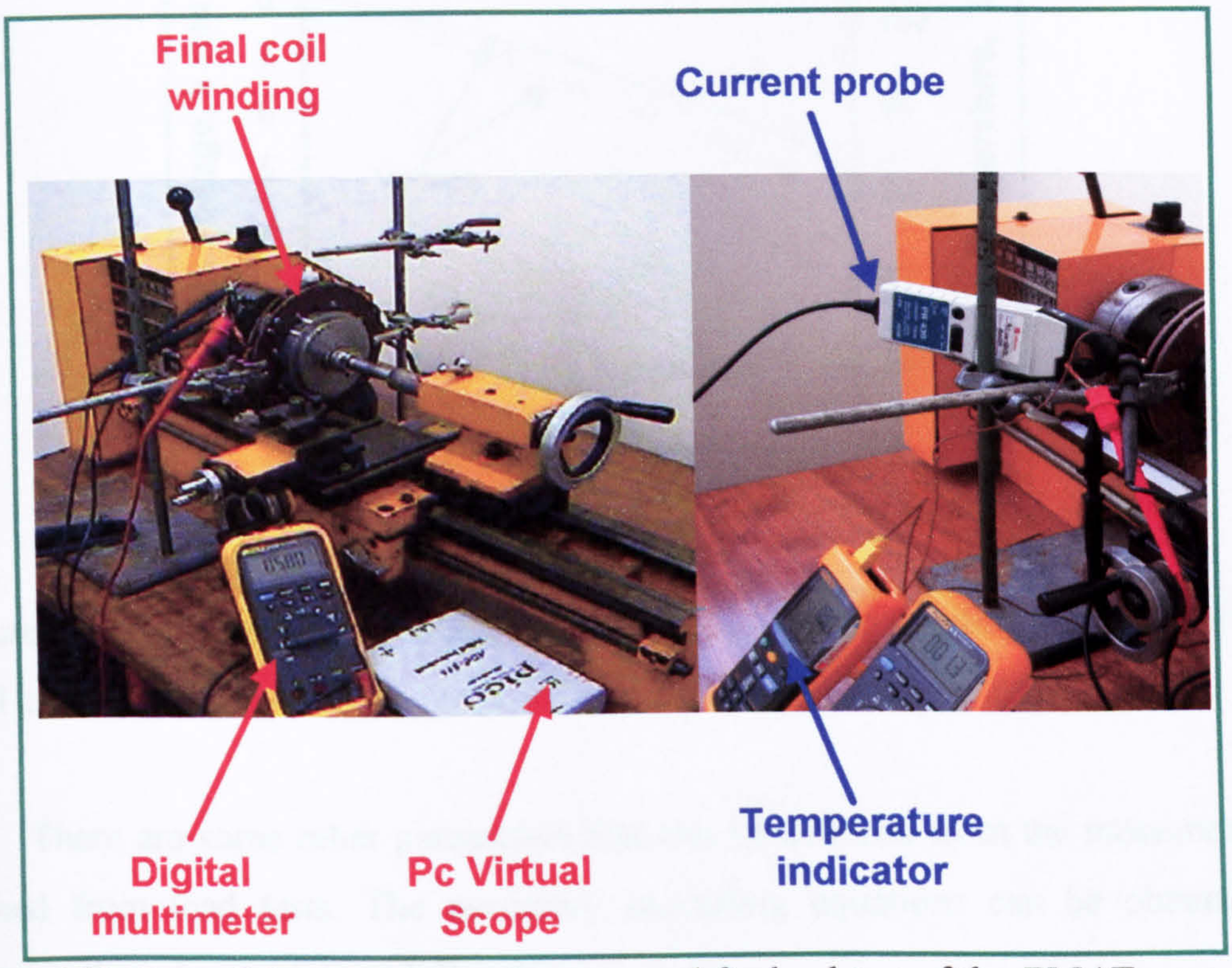

Figure 6.18 Part of the experimental setup used for load test of the ***PMAF*** generator

I_L Amp	Temperature °C	V_t V rms	E_1 V rms	ψ_i Deg
0	25	7.926	7.925	0
5	25	7.592	7.924	0.51
10	26	7.25	7.913	1.1
15	29	6.89	7.903	1.7
20	39	6.48	7.88	2.24
25	50	6.033	7.859	2.95
30	61	5.551	7.823	3.58
35	75	5.01	7.76	4.02
40	100	4.307	7.71	4.62

Table 6.4 Measured parameters obtained from load test

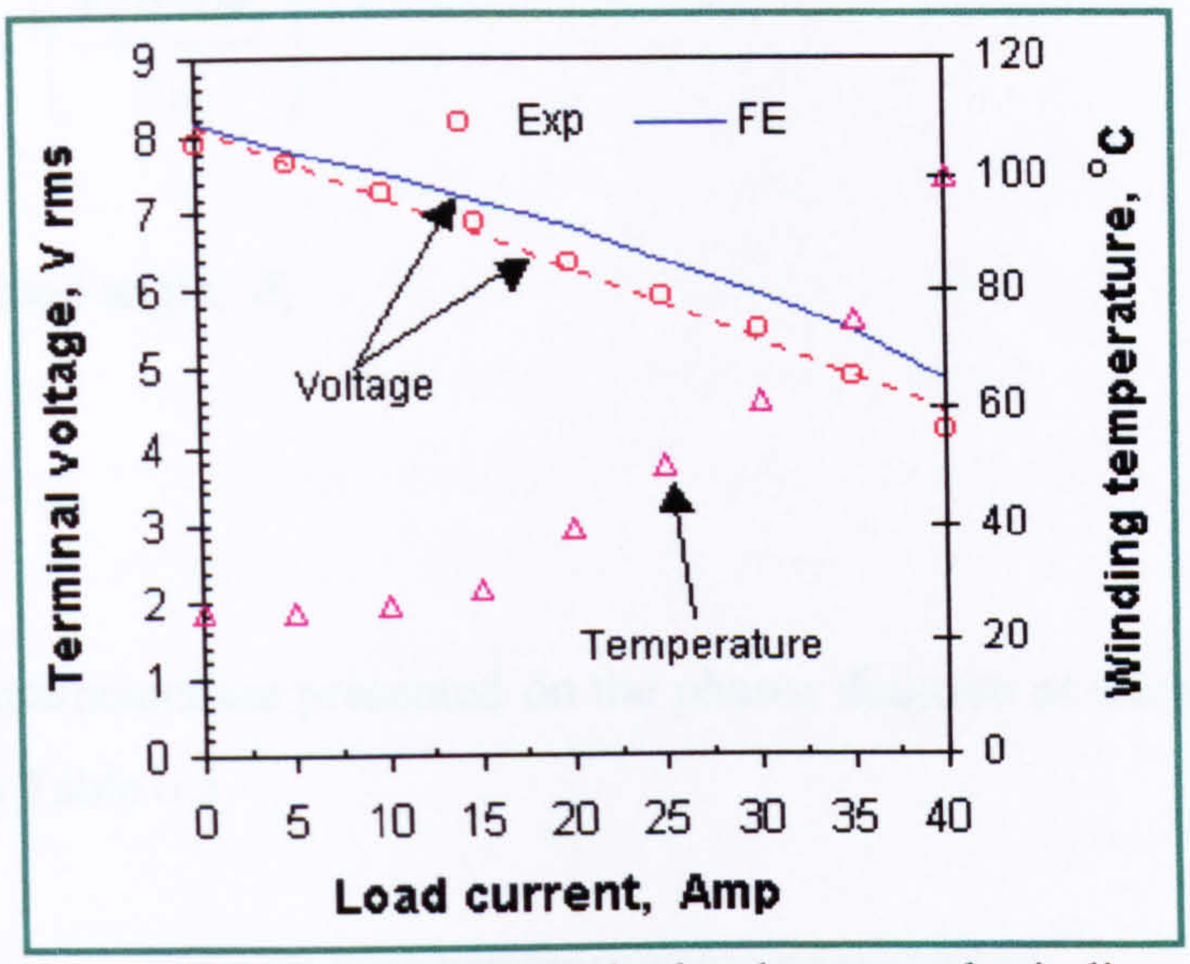

Figure 6.19 Measured and predicted terminal voltages and winding temperature vs. load current

There are some other parameters that can be deduced from the measurements obtained from load tests. The necessary modelling equations can be obtained to determine these parameters as follows:

- Leakage reactance

$$X_L = \frac{E_1 \sin \psi_i}{I_L} \tag{6.1}$$

- Magnetising reactance

$$X_M = \frac{\left[E_{NL}^2 - (E_1 \cos \psi_i)^2\right]^{1/2}}{I_L} - X_L \tag{6.2}$$

- Effective resistance

$$R_{AC} = \frac{E_1 \cos \psi_i - V_t}{I_L} \tag{6.3}$$

- External load angle, δ_L

$$\delta_L = \cos^{-1}\left[\frac{E_1 \cos\psi_i}{E_{NL}}\right] \tag{6.4}$$

- Internal load angle, δ_i

$$\delta_i = \delta_L - \psi_i \tag{6.5}$$

These parameters are presented on the phasor diagram as shown in Figure 6.20 and are given in Table 6.5.

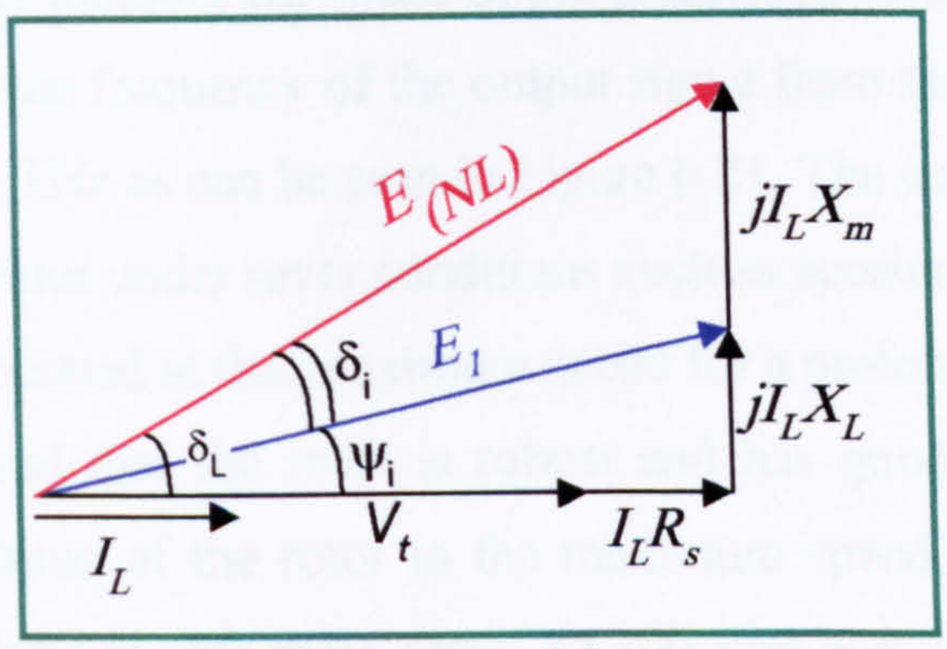

Figure 6.20 Phasor diagram used for parameters calculations

I_L Amp	X_L Ω	X_M Ω	R_{AC} Ω	δ_L Deg	δ_i Deg
5	0.0141	0.0242	0.0663	1.38	0.87
10	0.0152	0.0326	0.0661	3.46	2.36
15	0.0156	0.0275	0.0673	4.68	2.98
20	0.0154	0.0299	0.0696	6.56	4.33
25	0.0161	0.0280	0.0726	8.01	5.06
30	0.0163	0.0291	0.0752	9.91	6.33
35	0.0155	0.0331	0.0783	12.40	8.38
40	0.0155	0.0329	0.0844	14.16	9.54

Table 6.5 Other parameters deduced from the measured parameters at load test

It can be seen from the results that effective resistance of the machine is 40 – 50 % higher than the synchronous reactance. The average leakage and magnetising reactances are found as $0.0154\ \Omega$ and $0.0297\,\Omega$ respectively. The synchronous reactance was calculated as $0.0451\,\Omega$ from the load tests whereas the predicted one was found by ***FE*** as $0.0306\,\Omega$.

6.3 MECHANICAL INTEGRITY TEST

An acceptance test of the individual rotors to demonstrate the mechanical integrity of the ***PMAF*** high-speed generator at the design speed was required. To accomplish this task, a simple cold test rig comprising a small radial turbine rotor was constructed as shown in the Figure 6.21. The magnet rotor was mounted (at the non-magnetised stage) on the same shaft of the turbine rotor and a pressurised air controlled by a pressure regulator was used to run the turbine at different speeds. Although the rotor was required to run safely at a speed of 50000 rpm, the maximum speed obtained by the turbine was 47000 rpm. A pre-calibrated magnetic pickup transducer was used to measure the speed of the prescribed rotor. A digital multimeter was used to measure the frequency of the output signal from the magnetic pickup and it was found as 6.251 kHz as can be seen in Figure 6.21. The test was repeated several times to operate the rotor under sever conditions such as acceleration and deceleration. Also the rotor was operated at that maximum speed for a prolonged time (1 – 2 hours). The tests have showed that the rotor is robust and has good mechanical structure. Through the acceleration of the rotor to the maximum speed, the rotor was slightly vibrated at two different speeds these were; 22,300 rpm and 39,000 rpm. Apart from these two speeds, the rotor was running smoothly without suffering any problems.

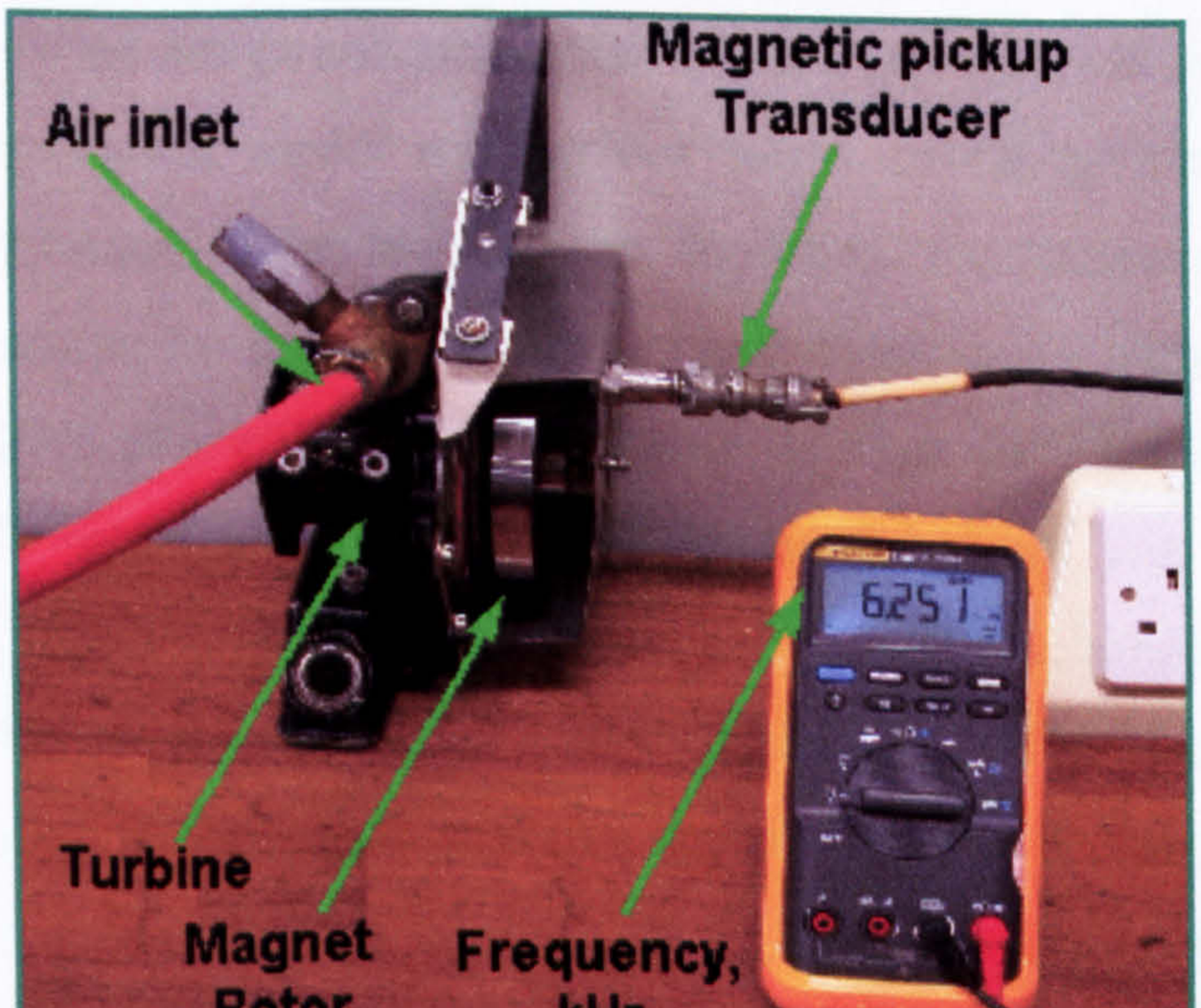

Figure 6.21 Part of the cold test rig used for testing the magnet rotor discs for its mechanical integrity at the speed of 47,000 rpm

CHAPTER 7

CONCLUSIONS AND FUTURE WORK

7.1 CONCLUSIONS

A design methodology was presented for the permanent magnet axial flux high-speed generators to be incorporated in a lightweight and compact electrical generating set for use in emergency situations. The design of such generator involves conflicting mechanical and electromagnetic requirements. Attention was given to design the generator with high power/weight ratio, and providing an adequate mechanical strength to the rotor, reasonable high efficiency and minimum cost of manufacturing. This was demonstrated by designing a single-stage (single phase) 16.7 kW generator and can be applied for designing higher output power generator. The significance of the design that it is based on a modular design basis, thus for a particular rotor design, higher output generators can be designed by increasing the number of modules i.e. stator and rotor stages on the shaft.

To assist in the design and assessment of such generators at their earlier stages of deign, a mathematical model was derived based on the generator main design geometrical parameters. This model was modified by incorporating empirical coefficients to account for the magnet leakage and losses in the magnet circuit of the model. These empirical coefficients were determined from the ***FE*** results with the aid of experimentally validated data for several proposed designs. This model was then used to evaluate several proposed designs obtained through the variation of number of turns and number of poles as major design parameters. The design process was accomplished by implementing two different approaches. The first approach was based on setting a fixed numerical value for the ratio, $k_{mr} = 0.577$, of the magnet inner radius to its outer radius as a determinant factor in the rotor geometry. The flux density in the air gap required to produce a certain output voltage for a given number of turns and number of poles was then calculated and the magnet axial length was determined. The

second approach was based on selecting a value of the air gap flux density where at this point maximum energy product for a particular permanent magnet material can be achieved in a certain magnetic circuit. Hence the rotor dimensions were determined to satisfy this value of flux density for a given number of turns and number of poles to produce a certain output voltage.

Through the design calculations in both approaches, the successful rotors, in terms of electromagnetic design, was always checked vs. its mechanical integrity. A high strength steel alloy (Maraging G125) was used as an alternative to the Carbon Fibre sleeve which has been used in the design of some of the radial flux *PM* high speed machines and more recently in axial flux machines. The radial thickness of this retainment ring was optimised based on the minimum required thickness to achieve a safe design and the amount of interference fit required to assemble the ring onto the rotor was also calculated. The outcome of the two approaches was a set of several successful possible designs with their performance data and geometrical characteristics were all determined. By screening these data and based on the design objectives it was possible to select the best design among the successful designs.

It appeared by using the second approach that more successful designs can be achieved. This is because in the first approach the rotor was bounded by the magnet ratio k_{mr}. When evaluating the generator performance, the theoretical analysis provided results within 5 % of the *FE* and experimental results. This demonstrated the usefulness of the theoretical analysis method.

A particular design of configuration, 8 poles, 5 turns/coil/layer, was selected from the first approach based on the maximum achieved power density. For that particular design, a power density of 6.21 kW/kg, based on the electromagnetic components, was achieved and an efficiency of 94.31 % was quoted. The selected design was then analysed using *FEM*. The stress in the rotor was accurately predicted using *3D FE* with interference effect included in the model. Results have shown that the proposed rotor is capable to operate safely at the design speed in excess of 50000 rpm. A *3D FE* electromagnetic analysis was also performed on the selected design. The model was capable to evaluate induced voltages, harmonics, synchronous

parameters, rotor and stator eddy current losses and performance of the machine. Results obtained were favourably compared to the experimental results. By performing parametric analysis with the aid of ***FE*** modelling, it was possible to predict the effect of some influential design parameters such as permanent magnet topology and type of material used for the retainment ring on the performance and characteristics of the machine. With the appropriate design of magnet topology it was possible to reduce the total harmonic distortion (THD) in the induced voltage by 8 %. This reduction in the THD was beneficial for minimising rotor eddy current losses which were attributed due to the flow of the current in the stator coils. Pure sinusoidal waveform will produce a minimal eddy current loss in the rotor of the machine. It was found from the electromagnetic analysis, that when a magnetic material was used for the retainment ring such as Maraging G125, the induced voltage was reduced by at least 20 % when compared to that induced from the same design of the rotor but with nonmagnetic material. However, this drawback was offset by advantages such as ease of manufacturing and assembling, low manufacturing cost and availability, offered by using such metallic rings.

More in this research, a novel design of the back-iron disc was proposed for the ***PMAF*** high-speed generator. With careful mechanical design and structural ***FE*** analysis, it was possible to utilise the silicon iron material for the back-iron disc as a replacement for the ferritic stainless steel. With the aid of ***FE*** electromagnetic analysis it was possible to minimise the weight and volume of the disc without detracting from the generator performance. A reduction of 200 % on the volume of the disc was achieved when the silicon iron material was used instead of the ferritic stainless steel materials.

A prototype of the proposed design for the ***PMAF*** high-speed generator was constructed and tested at low speed and the results obtained were favourably compared to the predicted one. A simple but reliable technique was used to determine the synchronous parameters of the machine based on the direct on line measurements of the parameters of the phasor diagram. For the mechanical test, the individual rotors of the machine were tested safely on a cold run test rig at a maximum speed of 47000 rpm without suffering any severe mechanical problems.

7.2 RECOMMENDATIONS FOR FUTURE WORK

The distinctive advantages gained by using ***PMAF*** machines, led them to be very attractive to be used in many applications and in particular for high speed applications. Thus research in this field is still gaining momentum in order to improve their performance and lower their cost. Research in this field needs to be conducted in both computational and experimental aspects.

7.2.1 Computational aspects

- The accurate calculation of eddy losses and the appreciation of their dependence on machine design parameters are of great importance. Thus further analysis on the rotor and stator eddy current losses could be conducted taking into account velocity effect.
- Further analysis could be conducted to evaluate the transient performance of the machine by ***FE*** analysis.
- Heat transfer and cooling aspect is also a major area of further work. In addition, design and construction of an efficient integral fan is required.
- Alternative stators comprising iron powder material in their cores can be designed, built and tested. Thus, further ***FE*** analysis can be performed on the machine having such stators.
- Vibration analysis of the machine taking into account all components on the shaft is needed. For modal analysis, it is worth pointing out that not taking the shaft into account does not seem very useful, for low frequency modes will certainly appear on the shaft. An example for modal analysis on one single components considered in this research was the back-iron disc.
- Further work is required on the evaluation of windage losses.

7.2.2 Experimental aspects

- The prototype of a single phase ***PMAF*** high-speed generator is now ready to be tested at its design speed. Hence a high-speed test is to be carried out by coupling the described generator to the gas turbine engine which was designed

and developed especially for this purpose as a separate but parallel part to this project.

- A data acquisition unit for the on line measurement can be built to be a part of computer aided testing system. This system can be modified to measure the transient performance for the machine. Moreover, such measurement can be of a great help in building a computer controlled drive system.
- Constructing and testing a three-phase version of the generator is required and this can be done by incorporating another two stator and two rotor discs on a new longer shaft.

REFERENCES

[1]. **Whitfield A. and Baines N. C.,** "Design of radial turbo-machines". *Longman*, 1st Edition, 44-45, 1990.

[2]. **Mackay R., Noe J. C.,** "High efficiency, low cost, small, gas turbines". *ASME COGEN-TURBO IGTI*-Vol. 6, 1991.

[3]. **Bhinder, F. S.,** "A contribution to designing a radial flow gas turbine stage". *ASME Paper*, No. 90-GT-187, 1990.

[4]. **Liebenberg L., Nel A. L. and Pullen K. R.,** "Computer simulation of electric-, gas turbine-and gas turbine hybrid electric vehicles". *SAE technical paper series*, International off-highway & powerplant congress & exposition, pp. 1-13, Milwakee, Wisconsin, U.S.A. 12-14 September 1994.

[5]. **Cohen R., Gilroy W. K. and Spencer W. B.,** "High performance turboalternator and associated hardware, I- Design of turboalternator". *NASA CR-1290 technical report*, prepared by Pratt & Whitney aircraft, East Hartford, USA. 1969.

[6]. **NASA,** "Potassium turboalternator (KTA) preliminary design study, II-Alternator performance design". *NASA technical report CR-1499*. 1970.

[7]. **Rodger C.,** "Performance development history – 10 kW Turboalternator". *S.A.E*, Paper No. 740849, pp. 1-12, 1974.

[8]. **Ferreira C. A., Jones S. R., Heglund W. S. and Jones W. D.,** "Detailed design of a 30-kW switched reluctance starter/generator system for a gas turbine engine application". *IEEE transaction on industry application*, vol. 31, No. 3, pp. 553-561, May/June 1995.

[9]. **Malmquist A., Aglen O., Keller E., Suter M. and Wickstrom J.,** "Microturbines: speeding the shift to distributed heat and power". *ABB review 3/2000*, pp. 22-30, 2000.

[10]. **James B. P. and Al Zahawi B. A. T.,** "A high speed alternator for a small scale gas turbine CHP unit". *Electrical machines and drives*, IEE conference publication No. 412, pp. 281-285, 11-13 September 1995.

[11]. **Bowman Power Ltd,** "Turbo Alternators'. *Literature taken from the website*: www.bowmanpower.com, July 2001.

[12]. **Najim Al-Din M.,** "Computer aided analysis, and design optimization of high speed permanent magnet synchronous motors". *PhD thesis*, Department of electrical and electronic engineering, University of Technology, Baghdad, Iraq 1997.

[13]. **Pullen K. R.,** "The design and development of a small gas turbine and high speed generator". *PhD thesis*, Imperial college of science, technology and medicine, department of mechanical engineering, University of London, UK. 1991

[14]. **Sahin F., Tuckey A. M. and Vandenput A. J A.,** "Design, development and testing of a high-speed axial-flux permanent-magnet machine". *IEEE publications*, pp. 1640-1647, 2001.

[15]. **Chalmers B. J., Spooner E., Honorati O., Crescimbini F. and Caricchi F.,** "Compact permanent-magnet machines". *Electric machines and power systems*, No. 25, pp. 635-648, 1997.

[16]. **Spooner E., Chalmers B. J.,** "Torus: A slotless, toroidal-stator, permanent-magnet generator". *IEE proc.-B in electrical power applications*, vol. 139, No. 6, pp. 497-506, 1992.

[17]. **Chalmers B. J.,** "Developments in electrical machines using permanent magnets". *Journal of magnetism and magnetic materials 157/158*, pp. 131-132, 1996.

[18]. **Slemon G. R.,** "Electric machines and drives". *Addison-Wesley publishing company Inc.*, New York, USA 1992.

[19]. **Faiz J., Dadgari A. A., Horning S. and Keyhani A.,** "Design of a three-phase self-excited induction generator". *IEEE transactions on energy conversion*, Vol. 10, No. 3, pp. 516-523, 1995.

[20]. **Demerdash N. A., Wang R. and Secunde R.,** "Three dimensional magnetic fields in extra high speed modified Lundell alternators computed by a combined vector-scalar magnetic potential finite element method". *IEEE transaction on energy conversion*, Vol. 7, No. 2, pp. 353- 366, June 1992.

[21]. **Chen J.,** "Nonlinear transient and steady state analysis for self excited single-phase synchronous reluctance generator". *PhD Dissertation*, College of engineering and mineral resources, West Virginia University, USA 2001.

[22]. **Gould J. E.,** "Permanent magnets applications". *IEEE Transaction on magnetics*, Vol. Mag-5, No. 4, pp. 812-821, 1969.

[23]. **Parker M. A. and Studders G. R.,** "Permanent magnets and their application". *John Wiley and Sons Inc.* First edition, New York, 1962.

[24]. **Moskowitz L. R.,** "Permanent magnet design and application handbook". *Krieger publishing company*, Malabar, Florida, Second edition 1995.

[25]. **Jardao R. G.,** "A contribution to the analysis of magnetic circuit excited by permanent-magnets". *IEEE Transaction on education*, Vol. 38, No. 3, August 1995.

[26]. **Spooner E. and Williamson A. C.,** "Direct coupled, permanent magnet generators for wind turbine applications". *IEE proc.-electr. Power appl.*, Vol. 143, No. 1, pp. 1-8, 1996.

[27]. **Basak A.,** "Permanent-magnet DC linear Motors". *Clarendon press*, Oxford, 1996.

[28]. **Boldea I., Nasar S. A.,** "Permanent-magnet linear alternators, Part I: Fundamental equations". *IEEE transaction on aerospace and electronic systems*, Vol. AES-23, No. 1, pp. 73-82, 1987.

[29]. **Hanitsch R., Belmans R. and Stephan R.,** "Small axial flux motor with permanent magnet excitation and etched airgap winding". *IEEE transaction on magnetics*, Vol. 30, No. 2, pp. 592-594, 1994.

[30]. **Al-Badi A., Gastli A., Bourdoucen H. and Jervase J.,** "Evolution of axial-field electrical machines". *Science and technology, special review*, pp. 227-245, Sultan Qaboos University, Oman 2000.

[31]. **Tan. G. H., Birch T. S., Howe D. and Brown R.,** "Design calculations for a small permanent magnet generator". *Report for department of electronic and electrical engineering*, University of Sheffield, 1980.

[32]. **Chalmers B. J.,** "Performance of interior-type permanent-magnet alternator". *IEE Proceedings in electric power applications*, Vol. 141, No. 4, pp. 186-190, July 1994.

[33]. **Longya Xu, Lurong Ye, Zhen Li and El-Antably A.,** "A new design concept of permanent magnet machine for flux weakening operation". *IEEE Transaction on industry applications*, Vol. 31, No. 2, pp. 373-378, March/April 1995.

[34]. **Spooner E., Williamson A. C. and Catto G.,** "Modular design of permanent-magnet generators for wind turbines". *IEE Proceedings in electric power applications*, Vol. 143, No. 5, pp. 388-395, September 1996.

[35]. **Mackay R.,** "Gas turbine generator sets for hybrid vehicles". *Report for NoMac Energy systems , Inc.*, No. 920441.

[36]. **Abu Sharkh S. M., Harris M. R. and Irenji N. T.,** "Calculation of rotor eddy-current loss in high-speed PM alternators". *Electric machines and derives*, IEE conf. publication No. 444, pp. 170-174, 1997.

[37]. **Van der Veen J. L. F., Offringa, L. J. J. and Vandenput A. J. A.,** "Minimising rotor losses in high-speed high power permanent magnet synchronous generators with rectifier load. *IEE proc.-electr. power appl.*, Vol. 144, No. 5, pp. 331-337,1997.

[38]. **Denger M. W., Van Maaren R., Fahim A., Novotny D. W., Lorenz E. D. and Syverson C. D.,** "A rotor lamination design for surface permanent magnet retention at high speeds". *IEEE transactions on industry applications*, Vol. 32, No. 2, pp. 380-385, 1996.

[39]. **Muljadi E., Butterfield C. P. and Wan Y.,** "Axial-flux modular permanent-magnet generator with a toridal winding for wind-turbine application". *IEEE transactions on industry applications*, Vol. 35, No. 4, pp. 831-836, 1999.

[40]. **Pullen K. R., Etemad M. R. and Fenocchi A.,** "The high speed axial flux disc generator-unlocking the potential of the automotive gas turbine". *The IEE colloquium on machines and drives for electric and hybrid vehicles*, 152 P. Var paging, 1996.

[41]. **El-Hasan T. S., Luk P. C. K., Bhinder F. S. and Ebaid M. S.,** "Modular design of high-speed permanent-magnet axial-flux generators". *IEEE transactions on magnetics*, Vol. 36, No. 5, pp. 3558-3561, 2000.

[42]. **Huang S., Luo J., Leonardi F. and Lipo T. A.,** "A comparison of power density for axial flux machines based on general purpose sizing equations". *IEEE transactions on energy conversion*, Vol. 14, No. 2, pp. 185-191, 1999.

[43]. **Wu W., Spooner E. and Chalmers B. J.,** "Design of slotless torus generators with reduced voltage regulation". *IEE Proceedings in electric power Applications*, Vol. 142, No. 5, pp. 337-343, September 1995.

[44]. **Caricchi F., Crescimbini F., Honorati O., Bianco G. L. and Santini E.,** "Performance of coreless-winding axial-flux permanent-magnet generator with power output at 400 Hz, 3000 r/min". *IEEE Transaction on industry applications*, Vol. 34, No. 6, pp. 1263-1269, November/December 1998.

[45]. **Irenji N. T.,** "Calculation of electromagnetic rotor losses in High-speed permanent magnet machines". *PhD thesis*, Faculty of Engineering and applied sciences, Department of electrical engineering, University of Southampton, March 1998.

[46]. **Polinder H. Hoeijmakers M. J.,** "Eddy-current losses in the permanent magnets of a PM machine". *Electric machines and drives conference publication,* No. 444, pp. 138-142, September 1997.

[47]. **Najim Al-Din M. S. N, Kader A. F. Al-Samarai J.,** "A new method to compute eddy current losses by the finite elements method". *IEEE Industry applications society*, Paper ref. 97301, pp. 3-9, 1997.

[48]. **Liuchen Chang,** "An improved FE inductance calculation for electrical machines". *IEEE Transactions on magnetics*, Vol. 32, No. 4, pp. 3237-3245, July 1996.

[49]. **Arkadan A. A., Vyas R, Vaidya, J. G. and Shah M. J.,** "Effect of toothless stator design on core and stator conductors eddy current losses in permanent magnet generators". *IEEE Transaction on energy conversion, conversion*, Vol. 7, No. 1, pp. 231-237, March 1992.

[50]. **Wei Y. T.,** "Design & manufacture (assembly) of high speed alternator rotor". *MSc thesis*, Imperial college of science, technology & medicine, Department of mechanical engineering, University of London UK, 1993.

[51]. **Kulkarni S. S.,** "Design of permanent magnet axial flux alternators". *PhD thesis*, Imperial college of science, technology and medicine, Department of mechanical engineering, University of London UK, February 1997.

[52]. **Hall A. S., Holowenko A. R. and Laughlin H. G.,** "Schaum's outline of theory and problems of machine design". SI (Metric) edition, *McGraw-Hill company*, 1980.

[53]. **FAG / Barden Corporation,** "super precision bearing catalogue". Pub l. No. AC41130/3 EA, June 1998.

[54]. **Wire Tronic Inc.,** "A literature taken from the website". www.wiretron.com. October 2001.

[55]. **Laurijssen D.,** "Carbon fibre containment rings for a high speed alternator". *MSc thesis*, Imperial college of science, technology and medicine, Department of mechanical engineering, University of London UK, 1994.

[56]. **Roark R. J.,** "Formula for stress & strain". *McGraw Hill*, 1990.

[57]. **Jonathan Bach-Price,** "Stress analysis for the rotor of a high speed alternator". *MSc thesis*, Imperial college of science, technology and medicine, Department of mechanical engineering, University of London UK, 1995.

[58]. **Magnet Sales Company,** "Magnet sales catalogue". www.magnetsales.co.uk, November 1999.

[59]. **Say M. G.,** "Alternating current machines". 5th edition, *Pitman publishing Ltd*, 1983.

[60]. **Tan G. H.,** "Design of a permanent magnet air-turbo generator and oscillation studies in miniature synchronous motors". *PhD thesis*, Department of electronic and electrical engineering, University of Sheffield, UK 1980.

[61]. **Etemad M. R., Pullen K., Besant C. B. and Baines N.,** "Evaluation of windage losses for high-speed disc machinery". *Proceedings of the institution of mechanical engineers, Part A: Jornal of power and energy*, pp 149-157, 1992.

[62]. **Durkin E. B. and Schauer J. J.,** "Windage power loss of high-speed generator". *Proceedings of the ASME, Advanced energy systems division*, AES-Vol. 37, pp. 35-43, 1997.

[63]. **Burghardt M. D. and Harbach J. A.,** "Engineering thermodynamics", 1995.

[64]. **Dean L. Taylor**: "Computer Aided design", *Addison-Wesley Publishing Company*, 1992.

[65]. **Veinott C.G.** "Computer aided design of electrical machines", *The MIT press*, First edition 1972.

[66]. **Tai-Ran Hus and Dipendra K. Sinha,** "Computer aided design. An integrated approach", *West Publishing Company*, 1992.

[67]. **Eliahu Zahavi,** "The finite element method in machine Design", *Prentice Hal Inc.* First edition 1992.

[68]. **Chari M. V. K. and Silvister P. P.,** "Finite elements in electrical and magnetic field problems", *John Wiley & Sons Inc.* First edition, New York1980.

[69]. **ANSYS Manual** release 5.4, *ANSYS Inc*, 1997.

[70]. **Chalmers B. J., Green A. M, Reece A. B. J, Badi A. H.,** "Modelling and simulation of the Torus generator". *IEE Proc.-Electr. Power Appl.*, Vol.144, No. 6, November 1997.

[71]. **Lavers J. D.,** "Electromagnetic field computation in power engineering". *IEEE Transactions on magnetics*, Vol. 29, No. 6, November 1993.

[72]. **Al-Din M. S. N, Kader A. F and Al-Samarai J.,** "Computer aided analysis of high speed permanent magnets synchronous motors". *CATAEE-97, second international conference*. July, 22-23, Amman-Jordan 1997.

[73]. **Nady Boules,** "Two-dimensional field analysis of cylindrical machines with permanent magnet excitation". *IEEE Transaction in industry applications*, Vol. IA-20, No.5, September/October 1984.

[74]. **Rabinovici R.,** "Magnetic field analysis of permanent magnet motors". *IEEE Transactions on magnetics*, Vol. 32, No. 1, January 1996.

[75]. **Furlani, E. P.,** "Computing the field in Permanent-magnet axial-field motors". *IEEE Transactions on magnetics*, Vol. 30, No. 5, September 1994.

[76]. **Gu C. L, Wu W. and Shao K. R.,** "Magnetic field analysis and optimal design of DC permanent magnet coreless disc machine". *IEEE Transactions on magnetics*, Vol. 30, No. 5, September 1994.

[77]. **Williamson S. and Volschenk A. F.,** "Time-stepping finite element analysis for a synchronous generator feeding a rectifier load". *IEE Proc.-Electr. Power Appl.*, Vol.142, No. 1, pp. 50-56, January 1995.

[78]. **Mavio Ikuyo Nabeta and Albert Foggia,** "Time-stepped finite-element simulation of a symmetrical short-circuit in a synchronous machine". *IEEE Transaction on magnetics*, Vol. 30, No. 5, pp. 3683-3686, September 1994.

[79]. **Andrzej Demenko,** "Movement simulation in finite element analysis of electric machine dynamics". *IEEE Transactions on magnetics*, Vol. 32, No. 3, pp. 1553-1556, May 1996.

[80]. **Jaime De La Ree and Nady Boules,** "Induced voltage harmonic reduction of PM cylindrical machines". *IEEE Transactions on industry applications*, Vol. 28, No. 3, pp. 619-624, May/June 1992.

[81]. **Atallah K., Zhu Z. Q., Mitchell J. K. and Howe D.,** "Curvature effects in radial-field permanent magnet machines". *Electric machines and power systems*, Vo, 22, pp. 511-520, 1994.

[82]. **Carpenter alloys,** "Literature taken from the website".carpenter.idesinc.com. March 2002.

[83]. **Advanced metals international Ltd.,** www.advancedmetals.com. January 2001.

[84]. **Hirst magnetics instruments Ltd.,** www.hirst-magnetics.com. May 2001.

[85]. **Chapman S. J.,** "Electric machinery fundamentals", McGraw-Hill book company, International edition, Singapore 1985.

APPENDIX A

MANUFACTURING & ASSEMBLING OF THE *PMAF* HIGH-SPEED GENERATOR

APPENDIX A

MANUFACTURING & ASSEMBLING OF THE *PMAF* HIGH-SPEED GENERATOR

A.1 INTRODUCTION

The construction and development of the *PMAF* high-speed generator involves many challenging technical tasks such as high precision machining, heat treatment and in some cases assembling via a shrink fit technique. In addition, manufacturing of the stator comprises procedural methods for building the winding such as magnet wire braiding, coil forming and winding encapsulation.

The *PMAF* generator was totally built from the scratch. At the start of the project, there were no older versions or similar prototypes available to the author on which preliminary tests could be carried out. Moreover, as far as the author was aware, detailed technical information and design data especially that concerning the electromagnetic analysis for such a machine was inadequate. Therefore, there was a need to develop and construct a preliminary prototype in order to make an assessment of the design and an evaluation of the electromagnetic *FE* model before the final design of the *PMAF* generator could be created with confidence. In this Appendix, the manufacturing, assembling and technical development of the *PMAF* generator is covered. First, the development of the preliminary prototype is described. Second, the construction of the final design of the *PMAF* generator is presented. A description of the geometrical construction and the development of various components and accessories are included. Finally, detailed work on the manufacturing and assembling processes is also covered in this Appendix.

A.2 DEVELOPMENT OF THE PRELIMINARY PROTOTYPE

A.2.1 Objectives in constructing the preliminary prototype

The main objective of constructing the preliminary prototype was to facilitate and speed up the design procedure by investigating the capability of the model to generate results that met the design requirements. Moreover, there was the necessity to build confidence in the ***FE*** electromagnetic results by experimental validation so that results obtained from ***FE*** analysis during the whole design process could be relied upon since there was not much data published regarding the design and development of such machines.

Among the prototype parts, the magnet rotor disc is the most complicated and relatively the most expensive part because it contains the rare earth ***NdFeB*** permanent magnets and high quality alloys such as Alumec 79 and requires high precision machining. Hence, considerable attention was given during the earlier stages of the project to the design of the magnet rotor disc to ensure that the design was sound and, in its final form, met both the electromagnetic and mechanical requirements. Any alteration in the design parameters of the magnet rotor disc once it had been produced would boost the cost of the construction and would be time consuming. Thus, it was planned that, once the magnet rotor disc was manufactured, any modification in the dimensions and shape of the magnet rotor disc would be as far as possible avoided unless test results showed that a major conceptual modification in the design of the magnet rotor disc was required in order to meet the electromagnetic and mechanical requirements.

Satisfaction of the electromagnetic requirements could be achieved alternatively through the adjustment in one or more of the design parameters of components other than the magnet rotor disc and this could be investigated using the preliminary prototype. With a suitable flexibility in the prototype design, components such as the rotor hub, stator winding, shaft, back–iron disc could be amended in a more or less trouble-free way. Hence, parameters such as air gap axial length, conductor

cross-section, number of winding turns, shape of coils and type of stator winding encapsulation could be easily modified.

The flexibility in the preliminary prototype will make it possible to avoid major costs that would be involved if the ***PMAF*** generator failed in some way and, moreover, some parts of the preliminary prototype could be incorporated into the final design of the ***PMAF*** high-speed generator.

A.2.2 Description of the preliminary prototype

The preliminary prototype was developed for testing at low speeds in the range 1500 – 3000 rpm. The key feature of this prototype is its simplicity and flexibility. It can be easily constructed; assembled, adjusted, modified and easily tested within the available resources and facilities. The preliminary prototype is a single phase, single module generator i.e. it has two magnet rotor discs, two circular back-iron thin discs with one single stator coil in-between. The ***PMAF*** generator preliminary prototype is depicted in Figure A.1

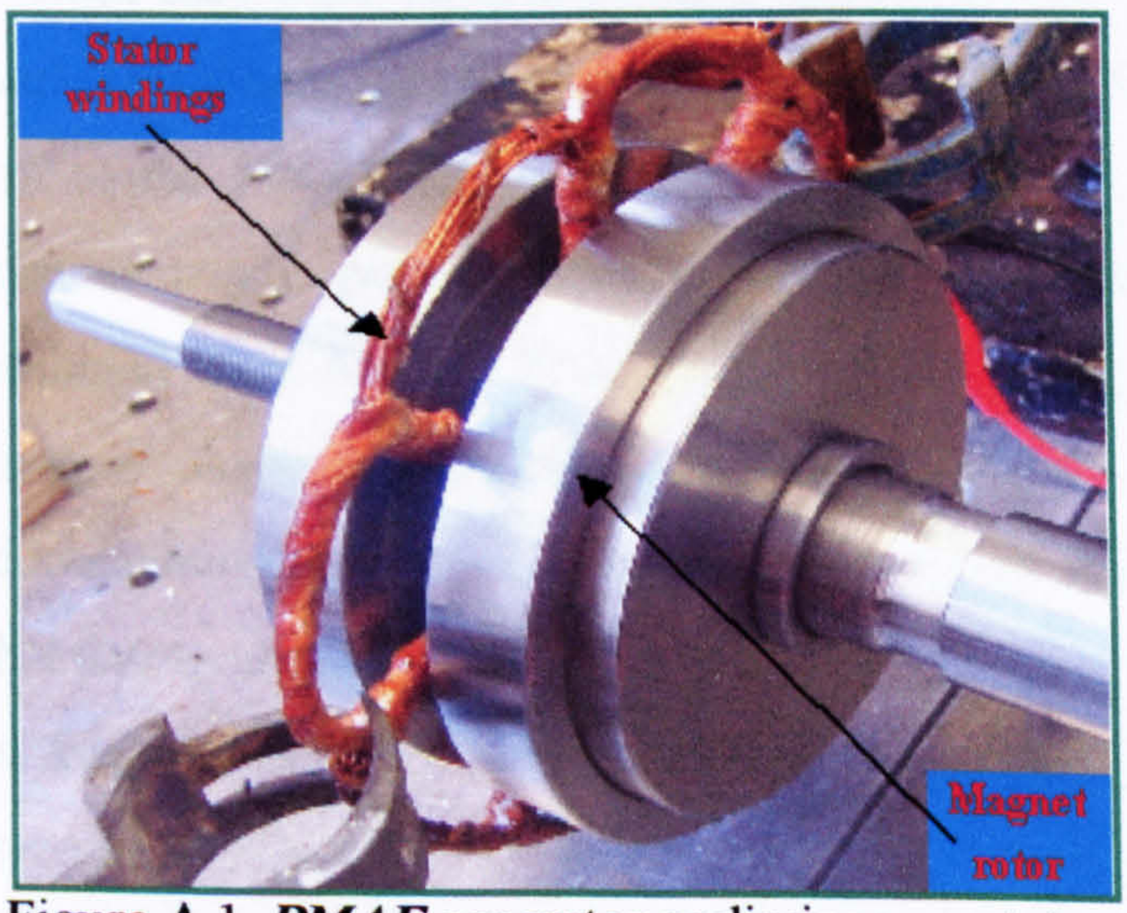

Figure A.1 ***PMAF*** generator preliminary prototype

The magnet disc and back-iron disc are fitted by sliding them onto the rotor hub and fixing via tightening nut at the back of the back-iron disc to prevent the discs from slipping on the hub while they are running at the prescribed speed. The rotor hub and the shaft are both threaded so that the axial distance between the two magnet rotor

discs can be adjusted. The major parts of the preliminary prototype are shown in Figure A.2. The detailed dimensions of these parts can be found in ***Appendix B***.

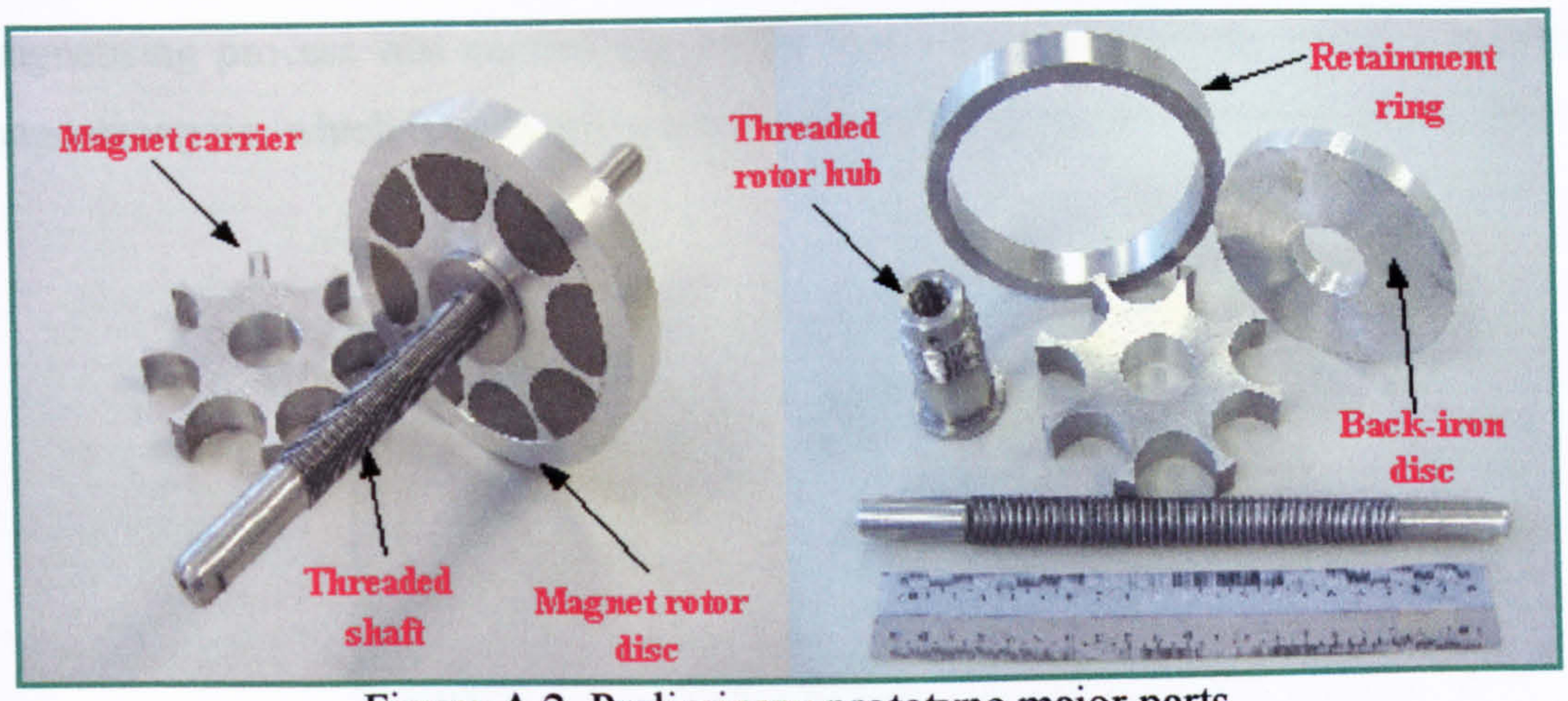

Figure A.2 Preliminary prototype major parts

A.2.3 Manufacturing the magnet rotor disc

The first step in the manufacture of the preliminary prototype was the manufacturing of the magnet rotor disc, i.e. magnets plus magnet carrier without the retainment ring or the rotor hub. This task was given to a UK company, Magnet Sales & Service Ltd [58] since they were capable of carry out the high precision machining required for this part. This disc is the component common to the preliminary prototype and the final form of the ***PMAF*** high-speed generator. This disc comprises eight semicircular permanent magnet pieces made of sintered ***NdFeB,*** grade ***N38H*** and a magnet carrier machined from Alumec 79 aluminium alloy. Although this particular shape of the permanent magnet was considered based on the ease of manufacturing, cost reduction and availability, it was shown in the electromagnetic analysis performed in Chapter Four that that an appropriate magnet topology can improve the performance of such machines. Figure A.3 shows the magnet rotor disc whereas the ***AutoCAD*** drawings can be seen in ***Appendix B***.

The magnet carrier disc was ***CNC*** machined to obtain the tight tolerances on the dimensions especially those on the bore and on the rim of the disc due to shrink-fit requirements. The sintered permanent magnets were machined to the required size before coating and magnetising. Coating is required to prevent corrosion in the

permanent magnets due to the high iron content. For the preliminary prototype, the magnets were magnetised individually and glued into the magnet carrier using high strength Permabond F246 adhesive recommended by the magnet manufacturer. The magnetising process was carried out at the manufacturer premises using a standard magnetising jig, which is normally used for magnetising standard individual magnets.

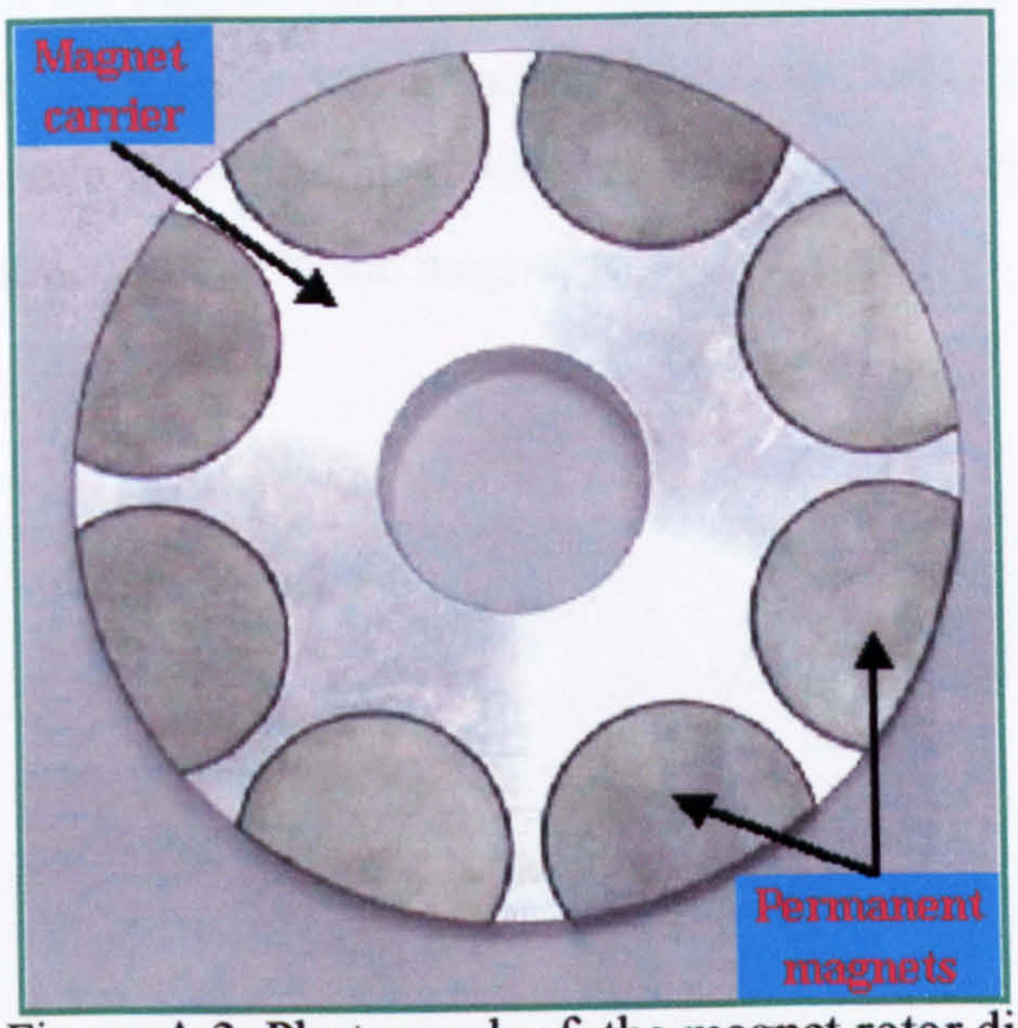

Figure A.3 Photograph of the magnet rotor disc

A.2.4 Manufacturing and assembling of retainment rings for low speed test

Although permanent magnets pieces are glued to the carrier, retainment ring is needed to insure that the magnets are securely located in their positions in the carrier during rotation. Two types of rings; one made from aluminium and the other made from mild steel were manufactured. The intention was to test the preliminary prototype using materials of completely different magnetic permeabilities and to observe the influence of each type of ring on the performance of the prototype. Figure A.4 shows the retainment rings of aluminium and mild steel, which were used in the preliminary prototype. Detailed drawings can be found in ***Appendix B***.

The retainment ring was machined using horizontal boring machine and enough clearance was given to the ring inner diameter to prevent damage of the magnets or magnet carrier during assembly or dismantling processes. A machine shop

press was accessible and some tools were machined specially for this purpose. Great care was needed especially when fitting the mild steel ring because of the high attractive forces generated by the magnet disc. Figure A.5 shows the assembling of the retainment ring into the magnet rotor disc of the preliminary prototype. The same arrangement is used for the dismantling process but with the base plate is removed this time. It should be noted that the base ring inner diameter was made slightly bigger than the outer diameter of the magnet rotor disc so that none of the discs could stick in the base ring during the assembly and dismantling processes. All tools and discs used for this purpose were made from non magnetic materials to avoid hazards that could be caused by sudden attraction due to the magnet rotor disc.

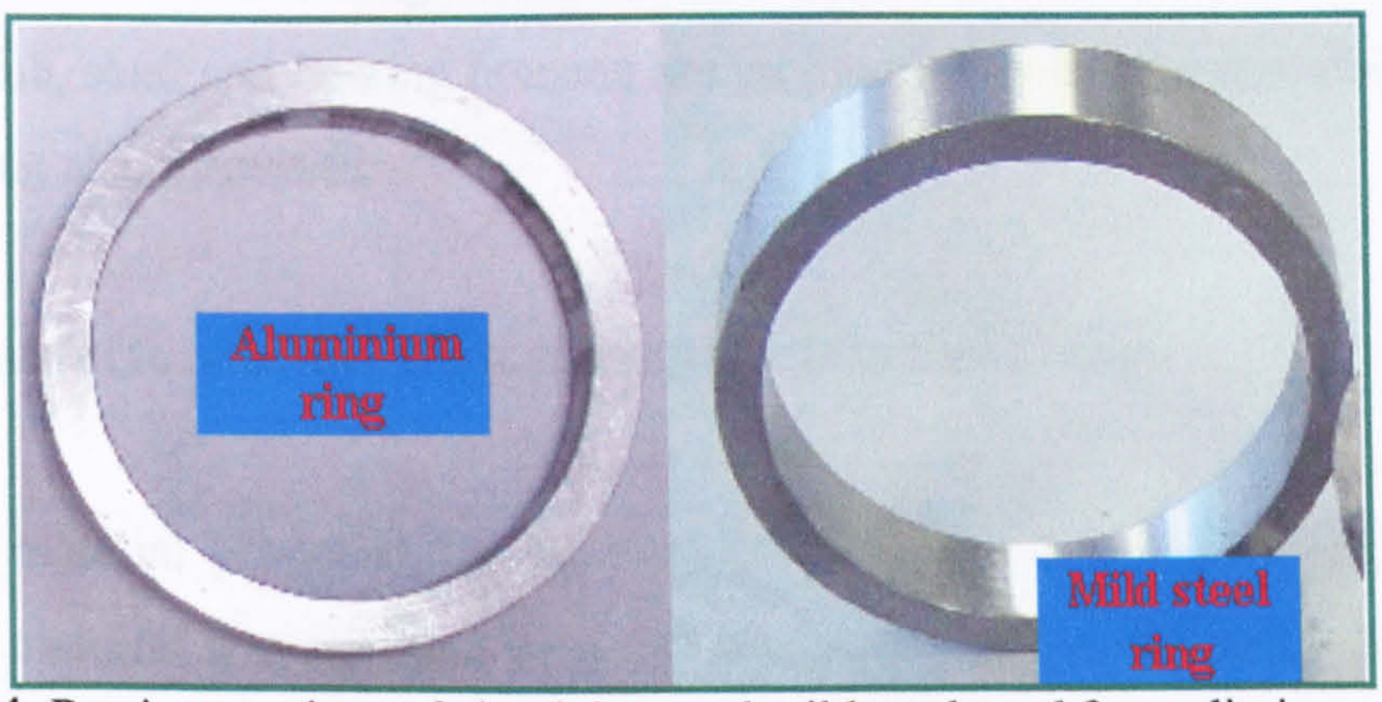

Figure A.4 Retainment rings of aluminium and mild steel used for preliminary prototype

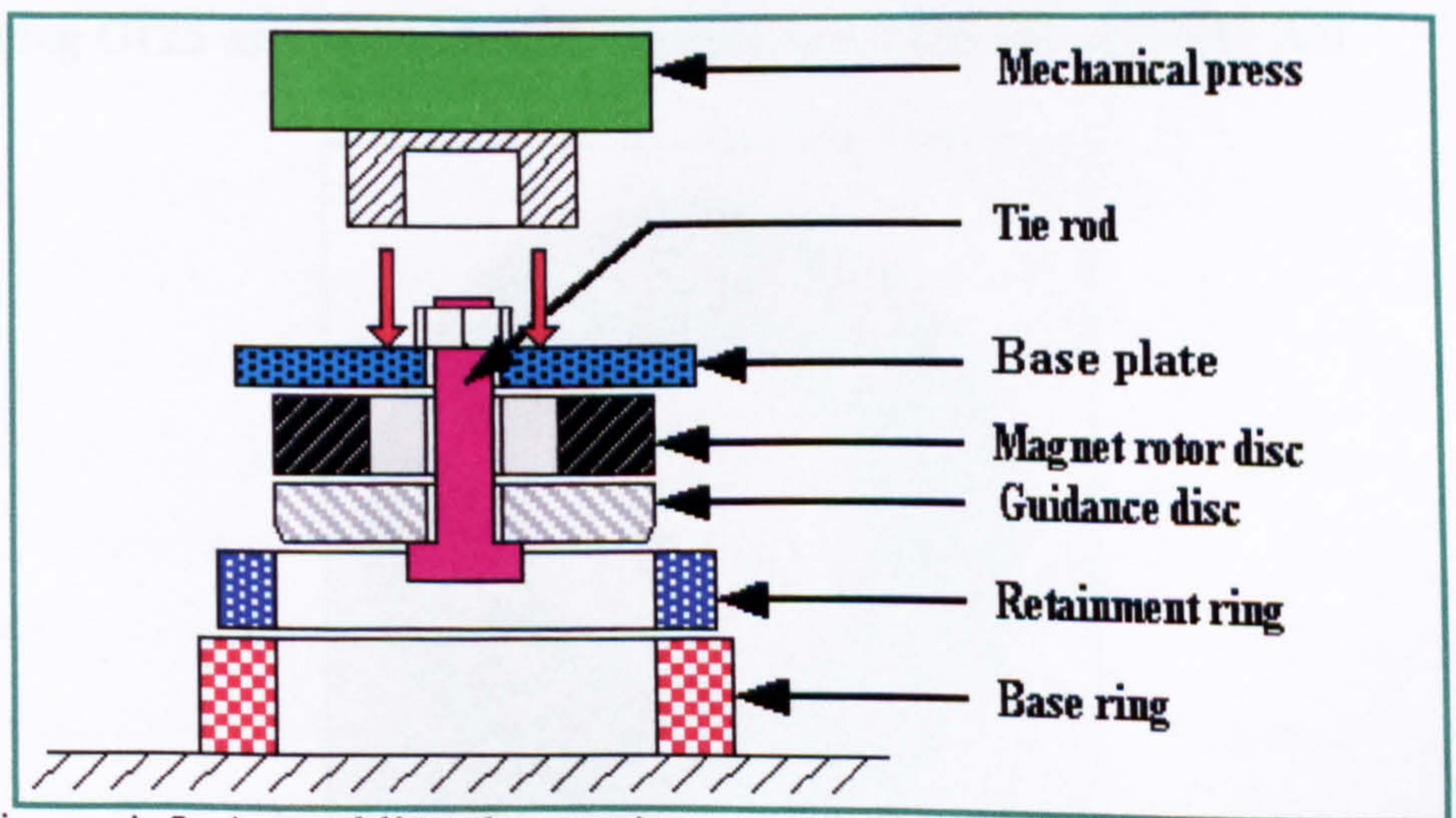

Figure A.5 Assembling the retainment ring for the preliminary prototype

A.3 DEVELOPMENT OF THE FINAL DESIGN OF THE *PMAF* HIGH-SPEED GENERATOR

The manufacturing and development of the final design of the ***PMAF*** high-speed generator requires high precision machining to satisfy the mechanical design aspects. The same design and construction of the magnet rotor disc, which was covered in the previous section, will be incorporated for the final design of ***PMAF*** generator except that the magnets will not be magnetised individually. Instead, they will be magnetised after assembling using a special magnetising fixture built specially for this purpose in a way that will be described in this section. Also in this section technical details for manufacturing and assembling of the high strength steel retainment ring for the magnet rotor disc will be given. The manufacture and assembly of the back-iron disc, rotor hub, shaft and bearing housing are included. Finally, the manufacture of the stator winding also discussed.

A.3.1 Manufacture of the high strength retainment ring

The material proposed for the ring is a high strength steel alloy, Maraging G125. This material was supplied by a UK company, Advanced Metals International Ltd. [83]. Maraging G125 is supplied as forged rings with roughly the following dimensions; 117 mm OD x 75 mm ID x 25 mm thickness that can be machined to the following dimensions: 110 mm OD x 94 mm ID x 17. mm thickness. The forged ring of Maraging G125 as supplied by the manufacturer is shown in Figure A.6.

Figure A.6 Forged ring of Maraging G125

The forged ring is supplied in the solution-annealed condition, which is the best condition for machining where the most of the machining is performed on a lathe. After machining, heat treatment was carried out to give the alloy its full mechanical properties. Simple aging treatment at a temperature of 482 $^{\circ}C$ for 5 hours was performed followed by air cooling. It should be noted that 0.5 – 1 mm clearance was left on each side of the ring to account for distortion due to aging process. After aging, the ring was machine-finished to the specified tight tolerances of the required dimensions. The inner diameter was the most critical part and cylindrical grinding was carried out on this surface to insure good quality and smooth surface finish. Dimensions for the ring are given in ***AutoCAD*** drawing in ***Appendix B***.

It can be seen from this drawing that the inner diameter of the ring was finished at 0.520 mm less than the outer diameter of the magnet rotor disc with the tolerance of ± 0.005 mm was specified on this dimension. This difference in diameter is the amount of interference fit required between the magnet disc and the retainment ring to keep the magnets under compressive stresses while rotating at the design speed. On the other hand, the non-magnetised magnet rotor disc was fine ground at the outer diameter to insure good surface contact with ring during the assembly procedure.

A.3.2 Assemble of the high strength retainment ring

The assembling of the high strength retainment ring involved a shrink-fit process. Normally, heating or cooling one of the parts is sufficient to permit assembly. However, in this case the amount of interference fit is relatively large and so both heating and cooling is required simultaneously to accomplish the task. The process is not easy and any underestimation to any of the requirements could cause the loss of the most important and expensive part of the generator. Therefore, it was decided not to jeopardise the real magnet disc and a dummy rotor disc was constructed to carry out the first testing of the assembly procedure using the shrink-fit technique. The expensive materials in the real magnet disc were replaced by low cost materials with thermal expansion coefficients similar to those of the real disc. The permanent magnets were replaced by mild steel and the Alumec magnet carrier was replaced by aluminium. The Maraging G125 retainment ring was replaced by ring made of

stainless steel. All parts in the dummy rotor were machined to the same dimensions and tolerances of the real disc. Finally, a reliable process of assembly process was evolved as follows:

- Calculate the amount of temperature difference required to fit the ring into the disc. As was found in Table 4.3, the temperatures required for the retainment ring and the disc were calculated as $+363°C$ and $-190°C$ for the retainment ring and the magnet disc respectively.
- Manufacturing of the assembly fixture, which contains the following parts: shrink fit base plate, shrink fit guidance plate, assembly vessel, centring rod and shrink fit pressing cap (***Appendix B***).
- Expansion by heating of the retainment ring using an air-circulating electric furnace. The ring should be inserted into the furnace while it is at room temperature and the furnace switched on to allow a slow warm-up to a temperature of 363 $°C$ over 40 – 50 minutes. Figure C.7 show the electric furnace used for the ring expansion.
- Freezing the magnet disc. A sufficient quantity of liquid nitrogen and a suitable container that allows the magnet rotor disc to be submerged totally in the liquid nitrogen are required. It was found that at least two to three litres of liquid nitrogen is required to cool the magnet disc down to –190 $°C$ within 10 – 15 minutes. Great care should be taken when taking the magnet rotor disc out of the container to avoid damaging the disc since it will be very brittle at this temperature.

Figure B.7 Electric furnace used for the expansion of retainment ring

- Removing the magnet disc from the furnace and the retainment ring from the liquid nitrogen. Clearly, these and subsequent operations need to be carried out quickly. All equipment and accessories required in the assembly process must be to hand so that the time required for the process is minimised. Any delay in handling and assembling might result in fitting failure.
- Positioning the magnet disc and the retainment ring in their specified locations in the assembling fixture.
- Pressing the arrangement using hydraulic press (Figure A.8) in the assembling fixture (Figure A.9).
- Removing the assembled disc from the assembling fixture. The colour of the retainment ring will have changed to a brassy colour due to the heating process. Surface grinding is now carried out to finish the disc to the required dimensions. Figure A.10 shows the assembled disc before and after surface grinding.

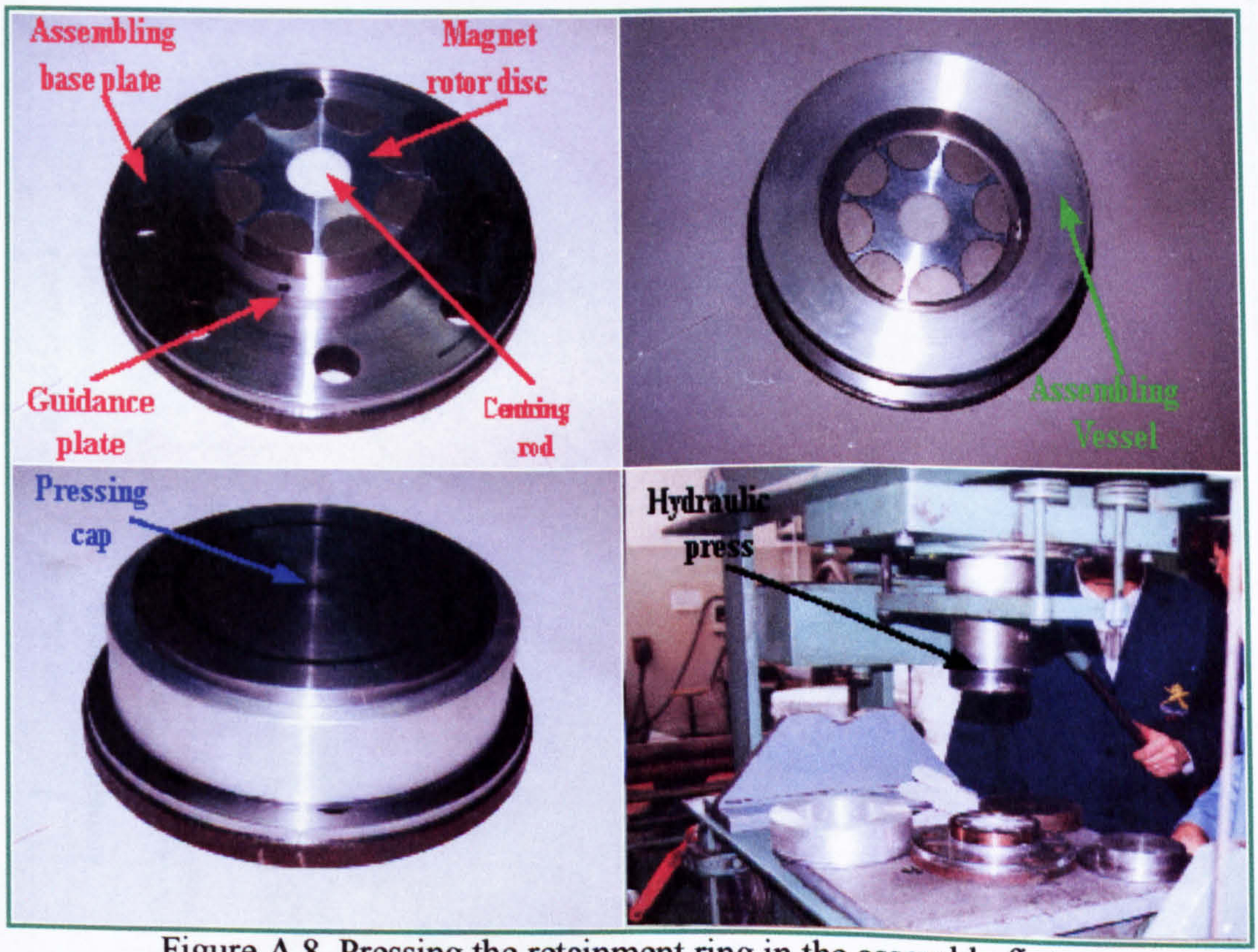

Figure A.8 Pressing the retainment ring in the assembly fixture

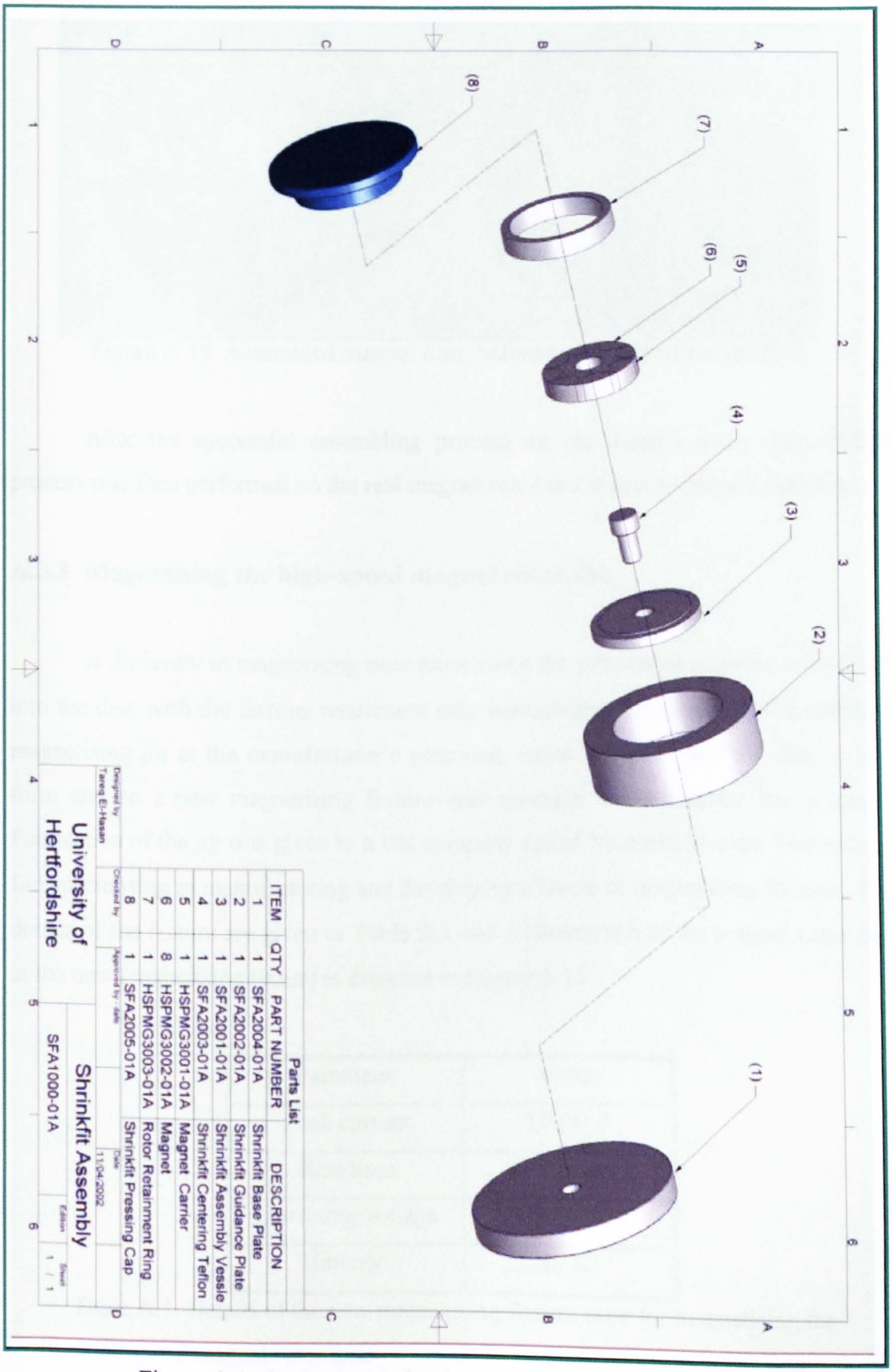

Figure A.9 Arrangement for the shrink fit assembling fixture

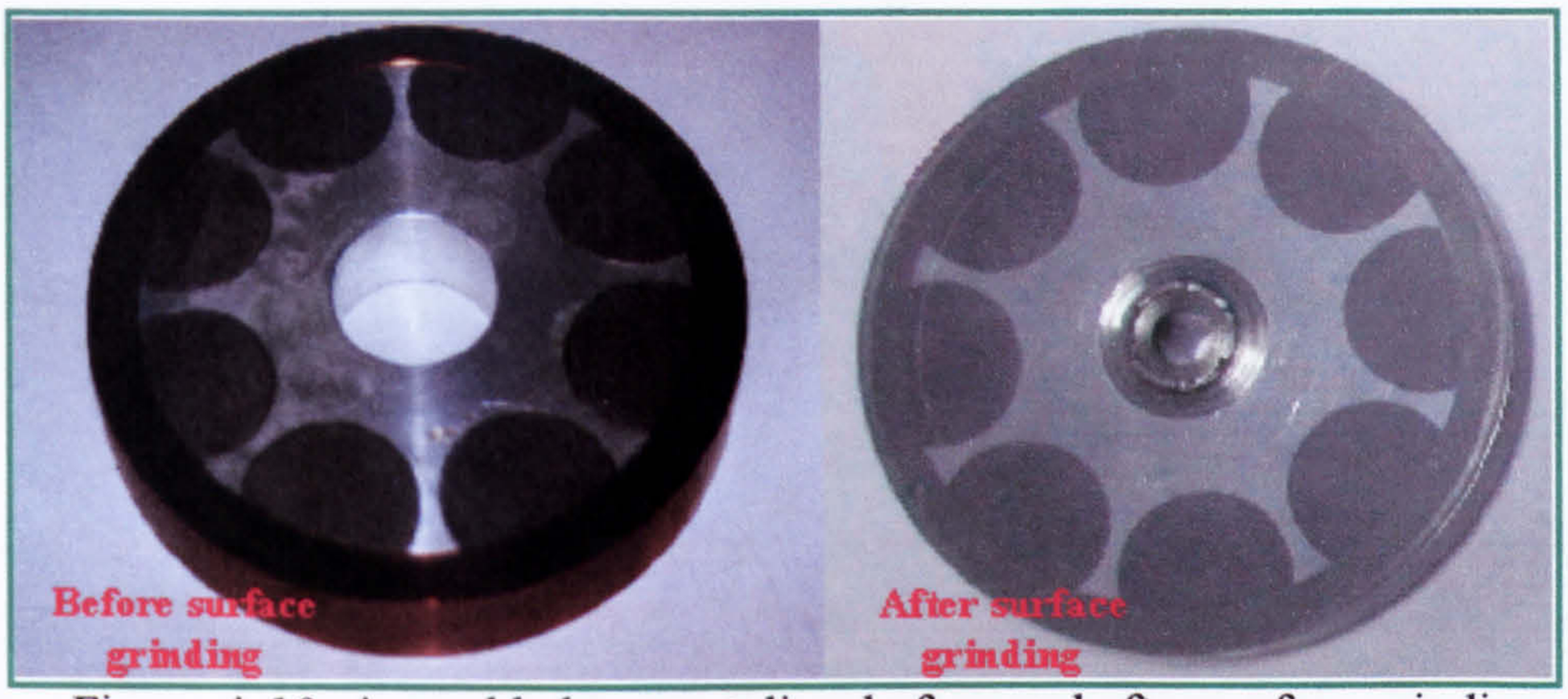

Figure A.10 Assembled magnet disc; before and after surface grinding

After the successful assembling process on the dummy rotor, this reliable process was then performed on the real magnet rotor and it was a successful process.

A.3.3 Magnetising the high-speed magnet rotor disc

A difficulty in magnetising now arose since the permanent magnets were fitted into the disc with the ferrous retainment ring surrounding the magnets. The standard magnetising jig at the manufacturer's premises, could not deal with the disc in this form and so a new magnetising fixture was specially developed for this purpose. Fabrication of the jig was given to a UK company called Magnetic System Technology Ltd specialising in manufacturing and developing all sorts of magnetising fixtures. The details of the fixture are given in Table A.1 and a photograph of the magnet rotor disc in the new magnetising fixture is depicted in Figure A.11.

Parameter	Value
Peak current	13000 A
Rise time	0.7 ms
Operating voltage	2000 V
Energy	10 KJ

Table A.1 Details of the new magnetising fixture used for magnetising the high speed magnet rotor disc

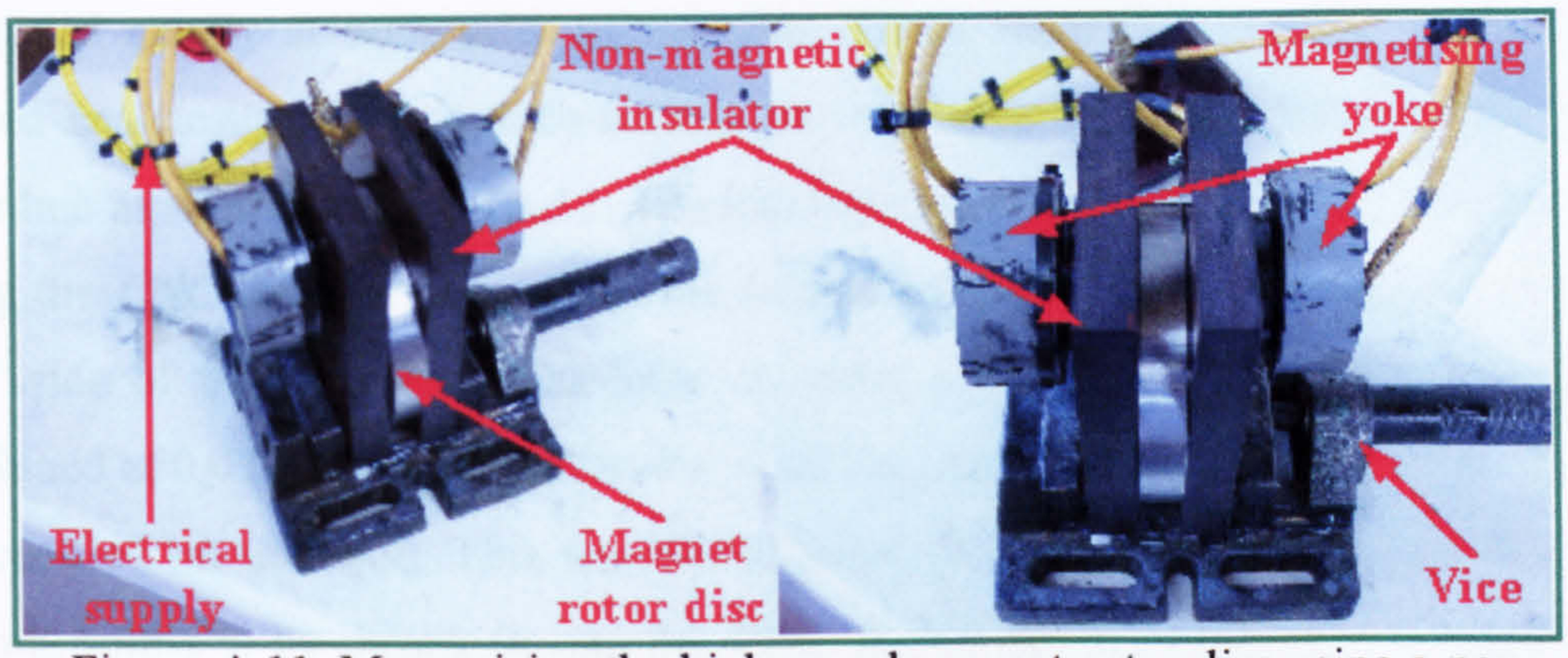

Figure A.11 Magnetising the high speed magnet rotor disc using a new magnetising fixture

A.3.4 Manufacturing the back-iron disc

The design of the back-iron disc was covered in Chapter five. Silicon iron core material of grade B-FM was selected and it was supplied by a US company, Scientific Alloys, Inc. The raw material was supplied on the form of uniform solid discs in the solution-annealed condition with the following dimensions: 100 mm OD x 20 mm thickness. Major machining process was carried out on the disc while it was in the solution-annealed condition. Heat treatment task was given to a UK company, Kepston Limited since a special wet hydrogen-atmosphere heat treatment was required. The discs were heated at temperature of $850°C$ for three hours and cooled at a rate of $50°C$ per hour to $538°C$ and then at rate of $100°C$ per hour to room temperature. For further details regarding the heat treatment of this material, reference [82] can be consulted. After heat treatment, the disc was finished by high precision machining to the tight tolerances required for the shrink fit process.

A.3.5 Manufacturing the rotor hub, locking spline and shaft

The ***PMAF*** high-speed generator was developed based on a modular design basis and intended for easy assembling and dismantling. Accordingly, the rotor hub was designed and manufactured to meet these requirements. The material selected was the same material as used for the shaft, which was EN24T. This material has good mechanical strength, good workability and it does not require heat treatment.

The rotor hub was machined using a ***CNC*** machine. The rotor has three splines protruded axially at both sides of the hub. These splines were 120 degree equally spaced and designed to fit male-female into the locking spline and into the second rotor hub as shown in Figure A.12. The locking spline was also machined from EN24T using the ***CNC*** machine to perform the female cut into the side that mates the "open end" side of the rotor hub. The bore diameter of the locking spline was precisely machined at 0.030 mm smaller than the shaft diameter with a tolerance of ± 0.005 mm is specified on this side. This was the amount of interference fit calculated for the locking spline to be shrunk fit into the shaft. As for the bore diameter of rotor hub, it was designed to allow for sliding fit of the rotor hub on the shaft. Thus, once the magnet rotor and the back-iron discs are shrunk fit into the rotor hub, the assembly can be easily assembled and dismantled on the shaft on demand.

The solid shaft was precisely machined to a diameter of 15.000 mm and a tolerance value of ± 0.003 mm was assigned to meet the high precision bearing manufacturer's specification and recommendation.

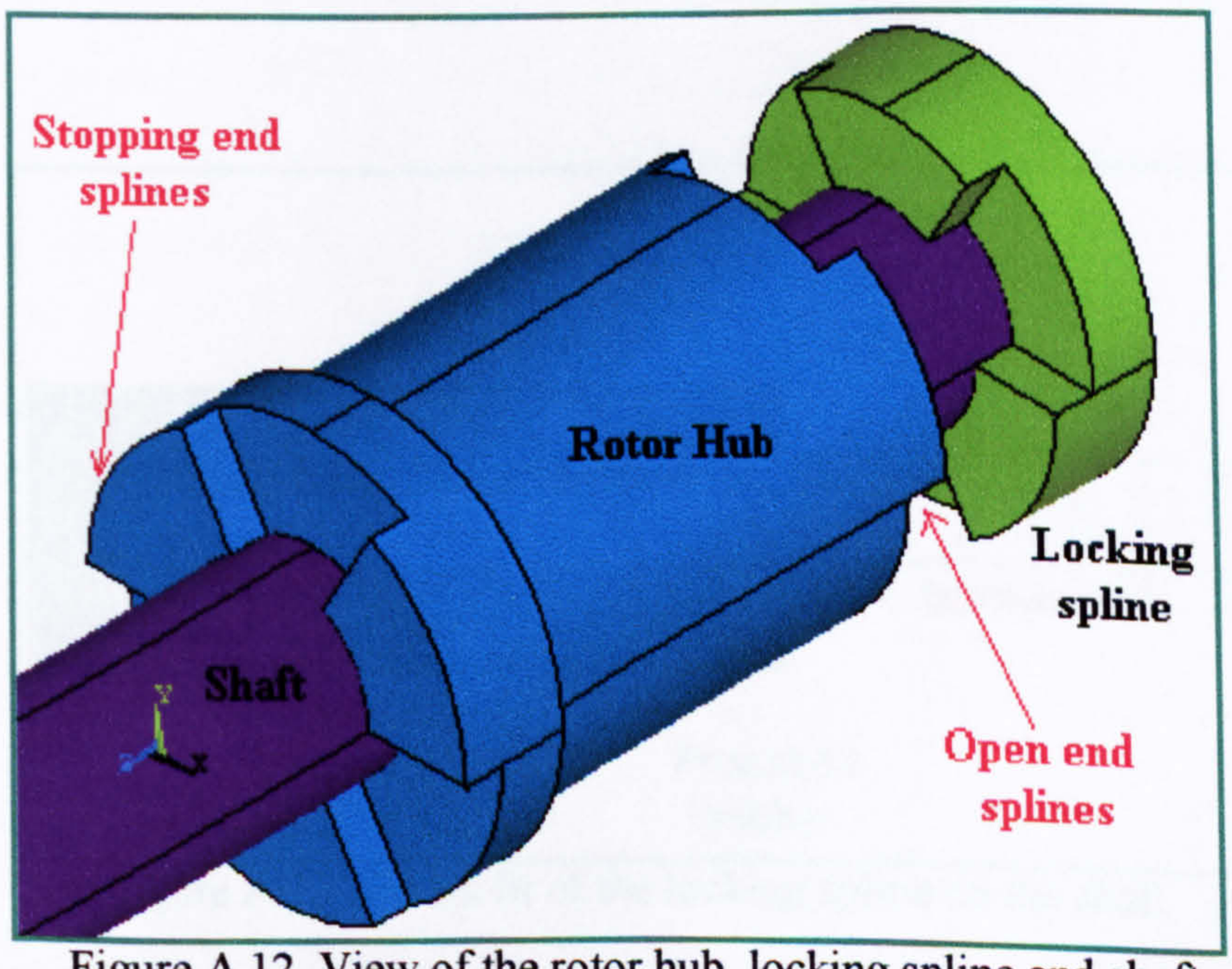

Figure A.12 View of the rotor hub, locking spline and shaft

A.3.6 Assembling of the high-speed rotor assembly on the shaft

In this section, the process of assembling of the high-speed rotor is illustrated with the aid of diagrams. Only the assembling of one module is presented, i.e. two magnet rotor discs for a single-phase stator. The three-phase machine is outside the scope of this thesis. The procedure of assembling was carried as follows:

A.3.6.1 Shrink- fit of the locking spline

The first step in the assembly process was fitting the locking spline into the shaft by shrink fitting. The minimum temperature difference required for the shrink-fit was calculated using Equation 3.62 as 182 C. To achieve this difference, the shaft was cooled down to –190 C and the locking spline warmed up to + 50 C. The shaft was removed from the liquid nitrogen and clamped inside a steel can coated by rubber on its inside to prevent damaging or scratching the shaft during the assembly process. The steel can has a predetermined length, which acted as a stop while the locking spline was advanced along the shaft (Figure A.13). Once the locking spline was fitted onto the shaft the components were left to attain room temperature.

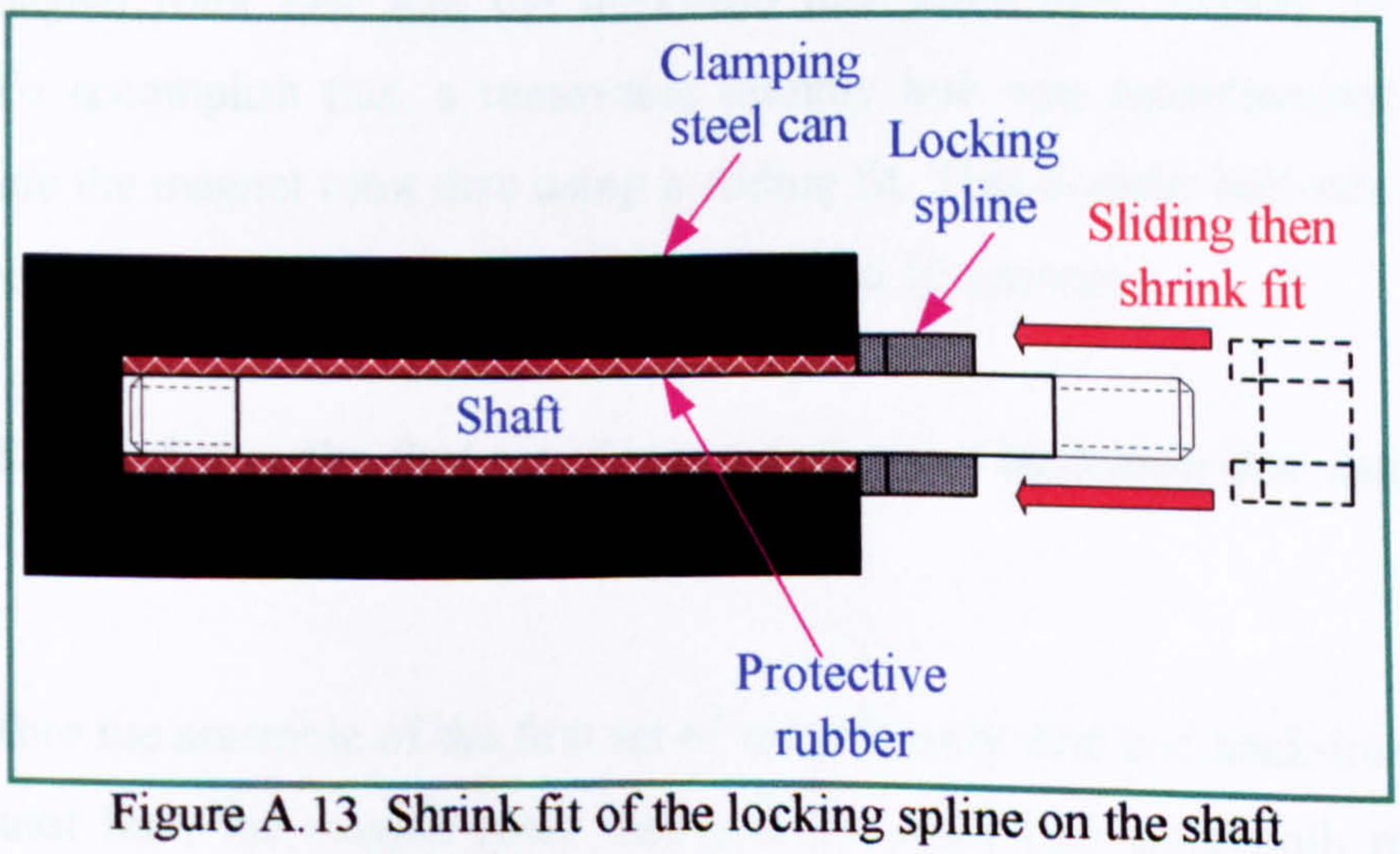

Figure A.13 Shrink fit of the locking spline on the shaft

A.3.6.2 Fitting the first rotor hub

The first rotor hub was then fitted by sliding it towards the "open end" of the shaft with the "open end" side of the rotor hub facing the locking spline. The rotor hub then locked with the locking spline (Figure A.14).

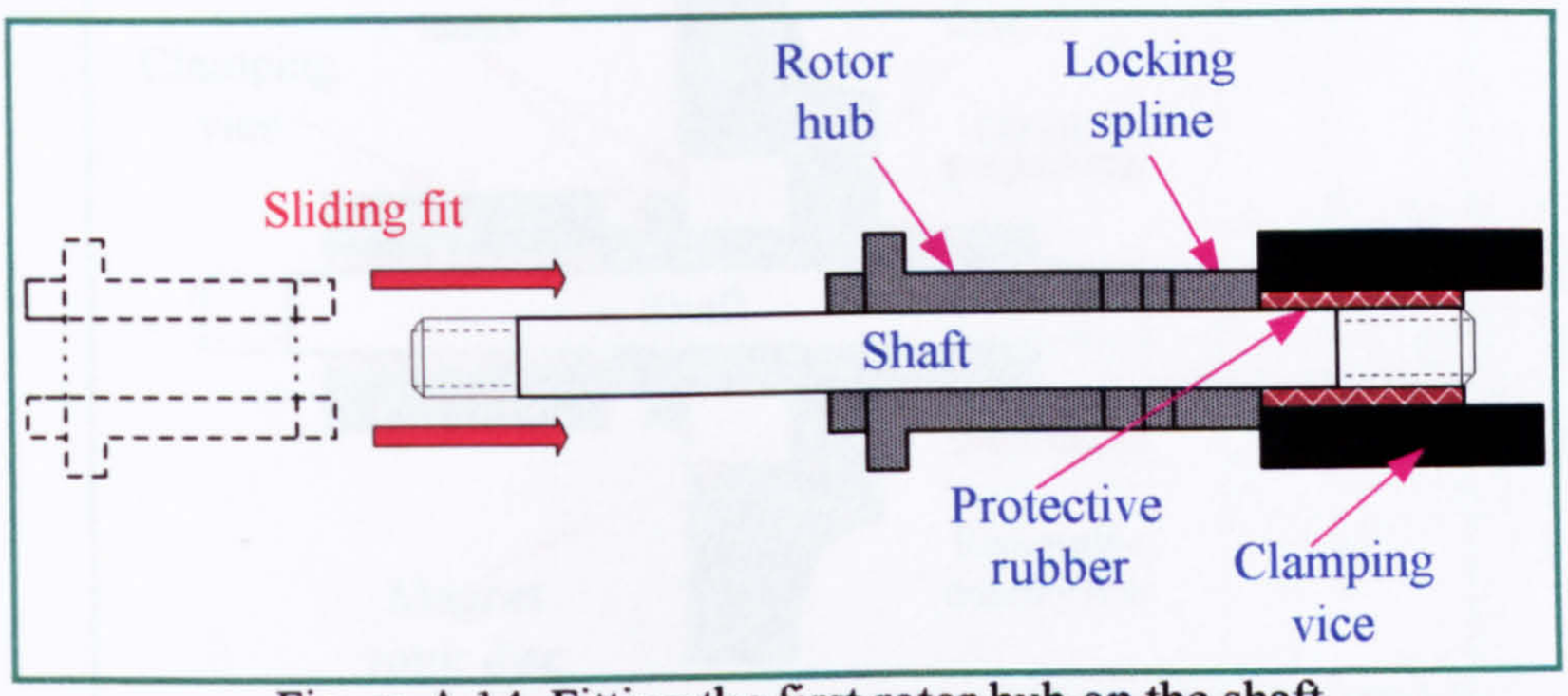

Figure A.14 Fitting the first rotor hub on the shaft

A.3.6.3 Sliding the magnet disc and the back-iron disc onto the dummy rotor hub

Before assembling the magnet rotor disc into the rotor hub, the magnet rotor disc and the back-iron disc were temporarily assembled next to each other to ensure that the magnet rotor disc and the back-iron disc were both aligned in the right position. To accomplish this, a removable dummy hub was manufactured and was placed inside the magnet rotor disc using a sliding fit. This dummy hub was also used as guidance for the magnet rotor set during the shrink fit process.

A.3.6.4 Shrink-fitting the first set of magnet disc and back-iron disc into the first rotor hub

Before the assemble of the first set of magnet rotor disc and back-iron disc into the first rotor hub, the magnet rotor disc and the rotor hub were both rotationally aligned and marked to ensure proper alignment of the magnet poles when the magnet rotor discs are assembled opposite to each other. The set of magnet rotor disc and the back-iron disc were then shrink-fitted onto the rotor hub. The shaft, rotor hub and locking spline assembly were clamped in a vice while the set of the magnet disc and

back-iron disc was advanced along the fitted rotor passing through the locking spline. The dummy hub was pushed away by the locking spline during the insertion thus leaving just the magnet disc and the back iron disc assembly on rotor hub. This process is shown in Figure A.15.

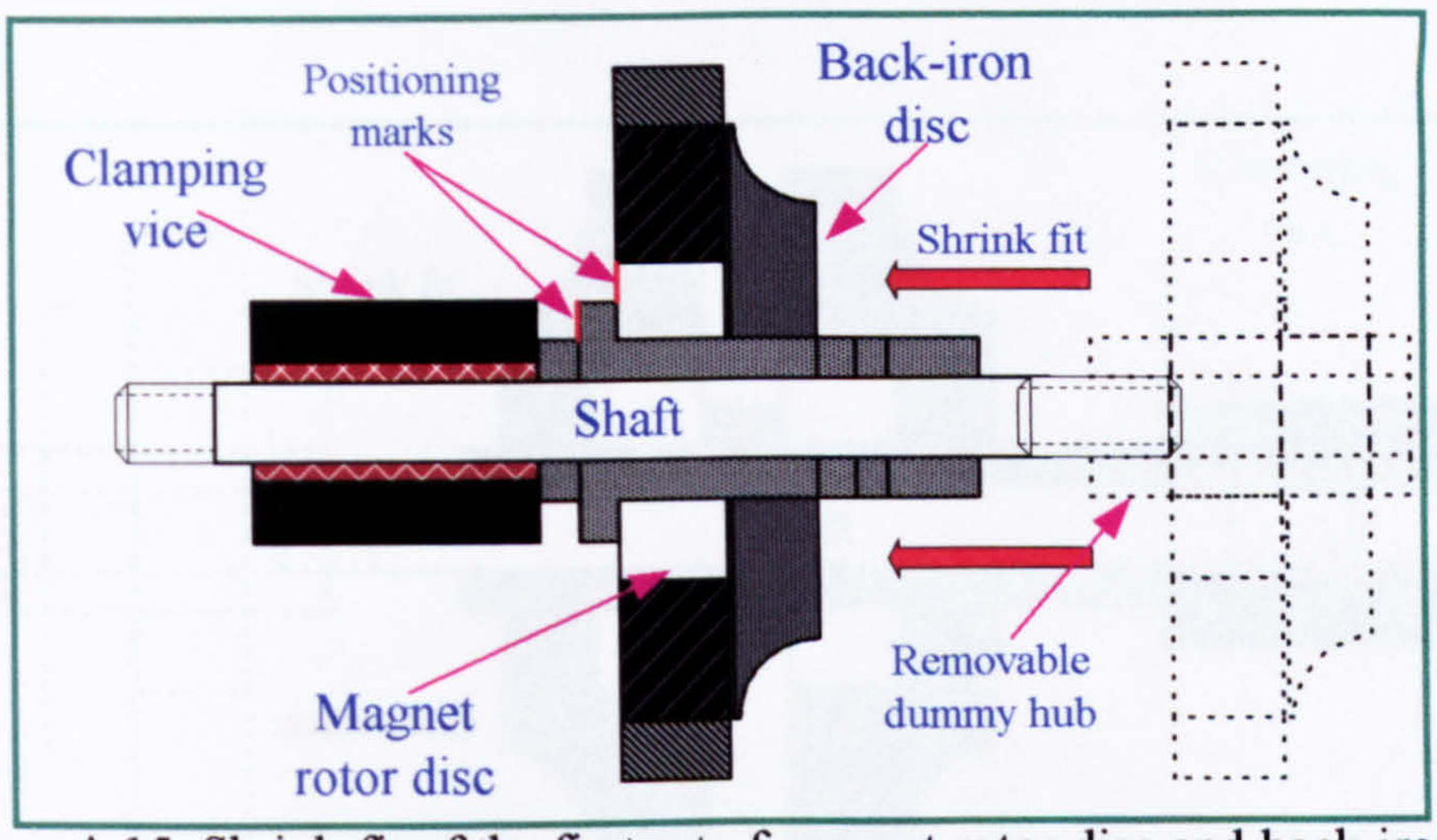

Figure A.15 Shrink-fit of the first set of magnet rotor disc and back-iron disc onto the rotor hub

A.3.6.5 Sliding the second rotor hub onto the shaft

Once the first set of magnet rotor disc and the back-iron disc were assembled onto the first rotor hub, the second rotor hub was inserted by sliding onto the shaft and locked with the first rotor hub with the "stopping end" of the second rotor hub facing the similar "stopping end" of the first hub (Figure A.16).

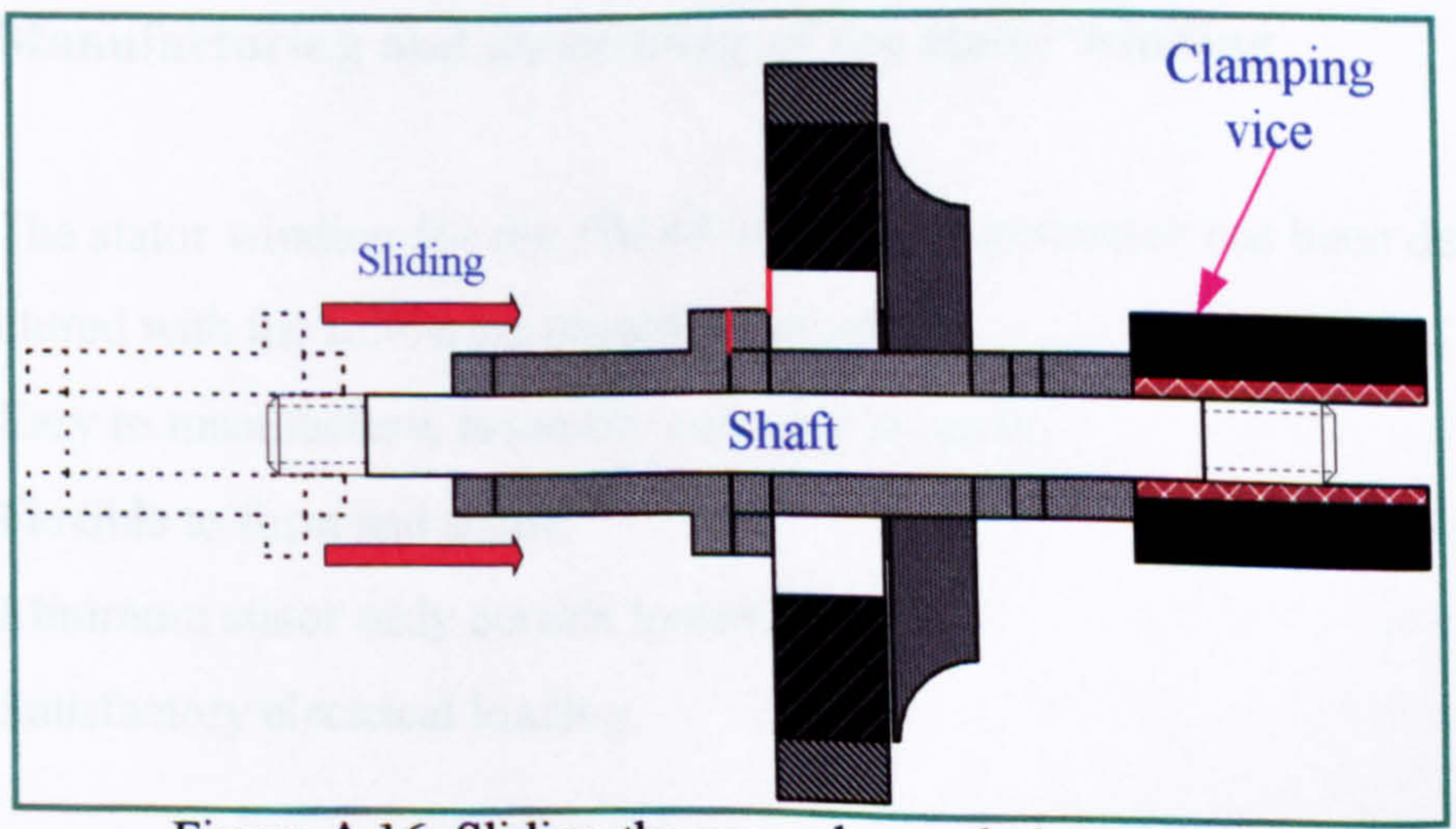

Figure A.16 Sliding the second rotor hub onto the shaft

A.3.6.6 Shrink-fitting the second set of magnet disc and back-iron disc onto the second rotor hub

Procedures similar to those described earlier for assembling the first set of magnet rotor disc and back-iron disc were followed (Figure A.17).

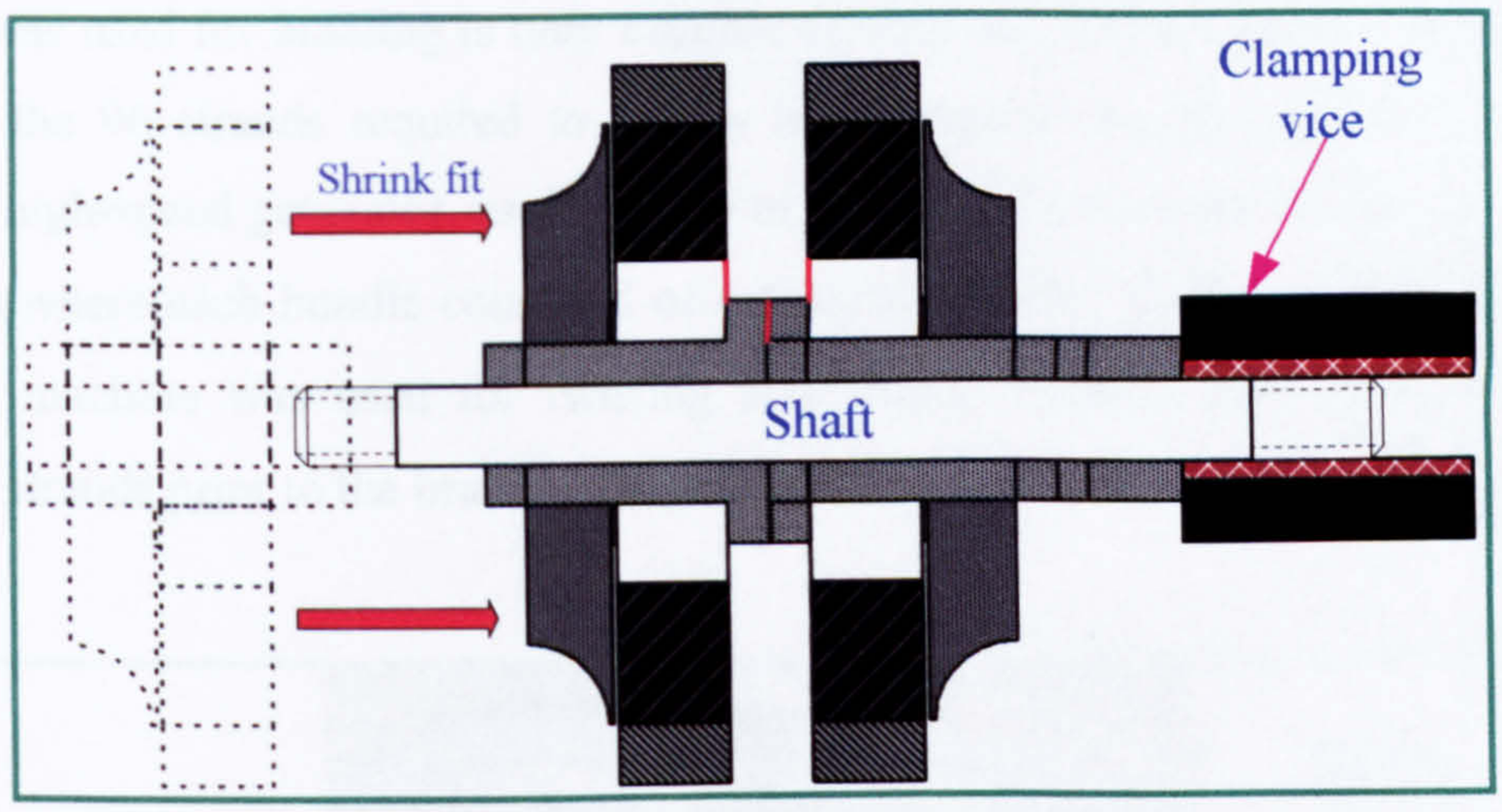

Figure A.17 Shrink-fitting the second set of magnet disc and back-iron disc onto the second rotor hub

The high-speed rotor is now assembled and is ready for the fitting of the bearings and bearing housings, spacers, washer springs and tightening nuts onto the shaft. The stator could be easily assembled between the two magnet rotor discs since it was manufactured in two separate halves. The manufacturing and assembling of the stator winding designed for the ***PMAF-HSG*** is described in the following section.

A.3.7 Manufacturing and assembling of the stator winding

The stator winding for the ***PMAF*** high-speed generator has been designed and manufactured with the following objectives in mind:

- Easy to manufacture, assembly and easy to repair.
- Flexible to form and shape.
- Minimum stator eddy current losses.
- Satisfactory electrical loading.

Manufacture of the stator windings were performed as follows:

A.3.7.1 Manufacture of the braided conductor

The conductor used in the stator is similar in its shape and construction to Litz wire. Each bundle contains twisted stranded wires called magnet wire. The machine which was used for braiding is only capable of handling sixteen pulleys at maximum. Hence, the 96 strands required to satisfy the electrical design requirement for the ***PMAF*** high-speed generator, as described in Chapter Three, were divided into sixteen bundles where each bundle consisted of 6 twisted strands. To accomplish this task, a feeding machine was used for twisting and filling sixteen small pulleys with six twisted strands prior to the braiding (Figure A.18).

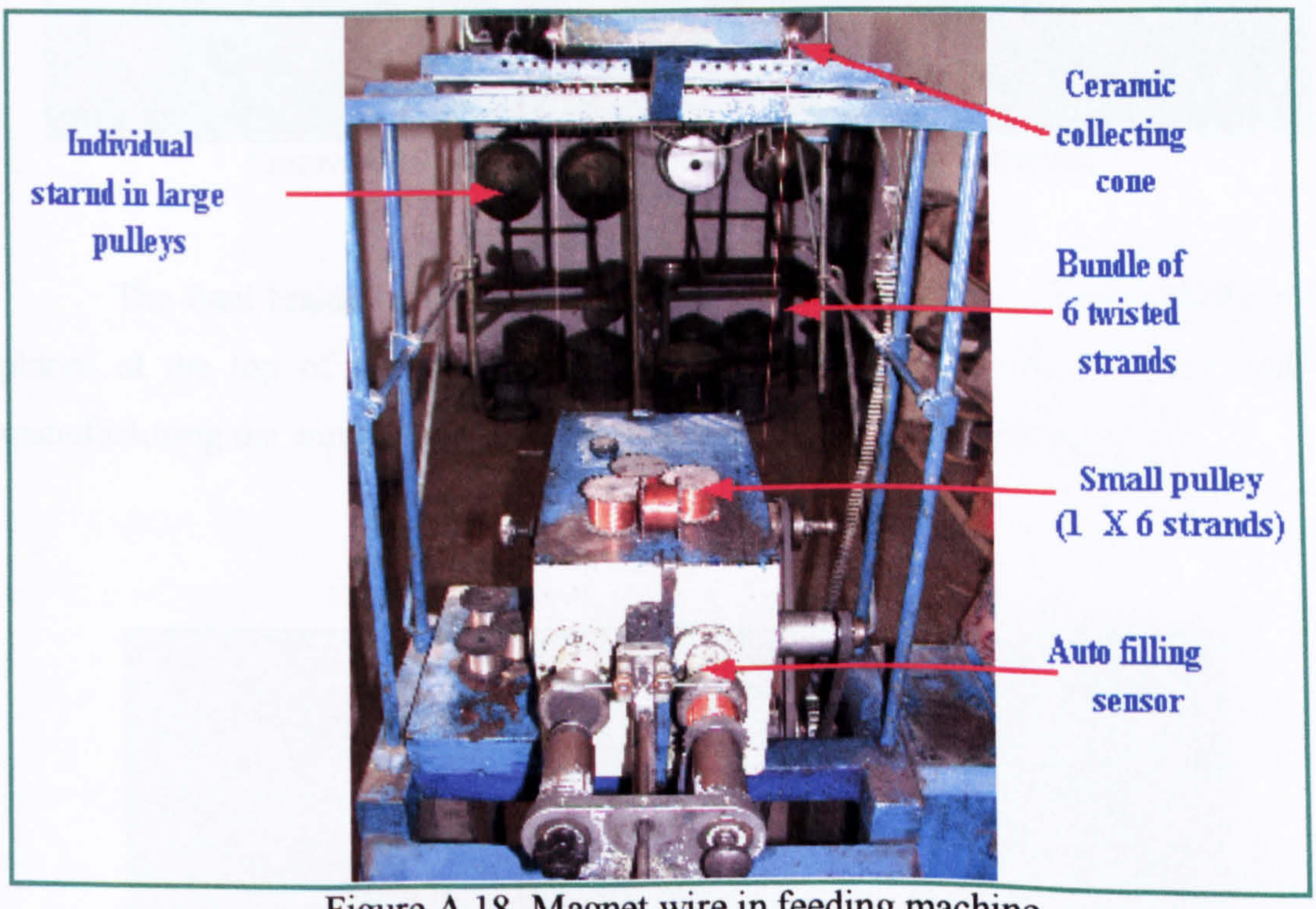

Figure A.18 Magnet wire in feeding machine

These small sixteen pulleys were then placed into their positions in the braiding machine. The barding machine which is shown in Figure A.19, was originally used for braiding the shielding wires for coaxial antenna cables. Hence some modification on the machine was carried out since the wires used in the shield were bare copper wires

i.e. not insulated wires. A protection technique was developed to prevent scratching or damaging the wire insulation by the feeding or braiding processes.

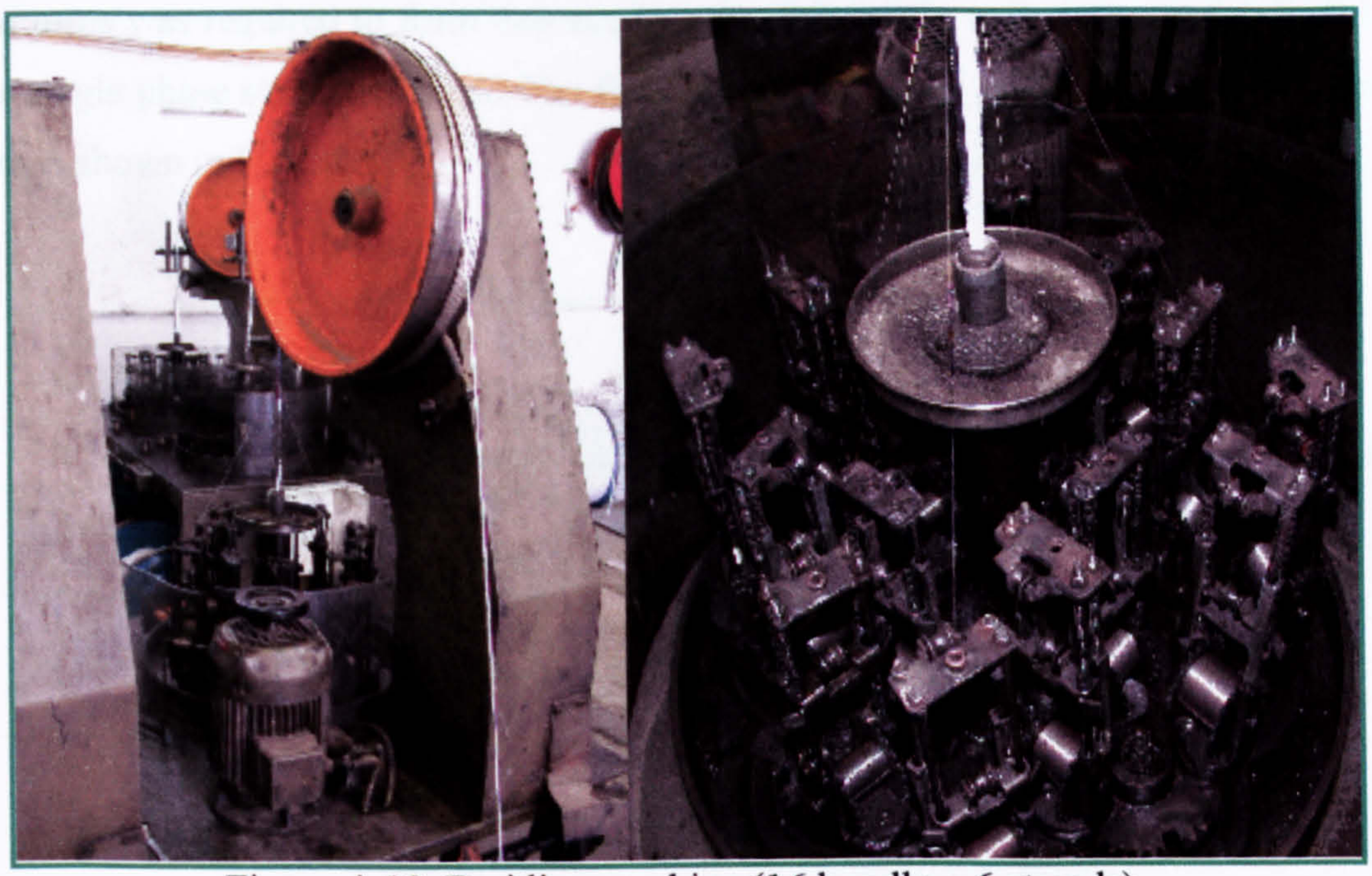

Figure A.19 Braiding machine (16 bundle x 6 strands)

The final braided wires were then automatically fed into a large rotating drum placed at the top of the braiding machine. The constructed braided wire used in manufacturing the windings of the ***PMAF*** generator is shown in Figure A.20.

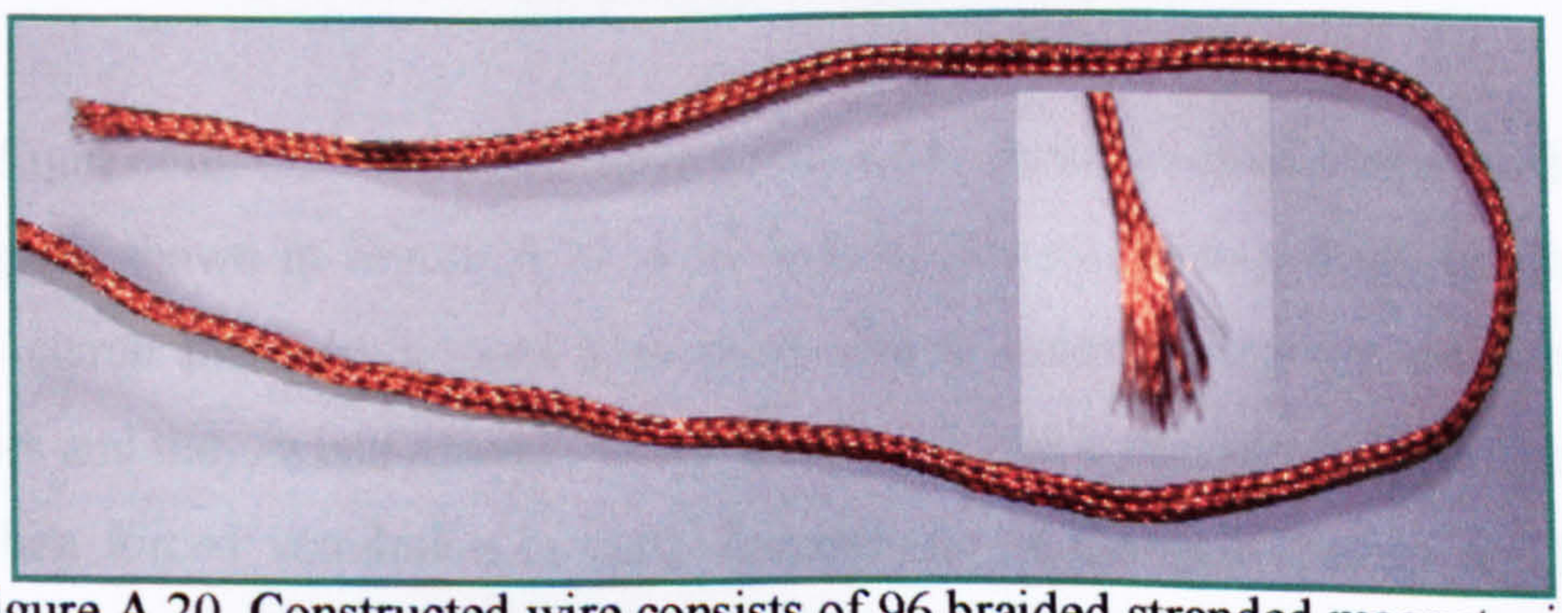

Figure A.20 Constructed wire consists of 96 braided stranded magnet wires for use in ***PMAF*** high-speed generator windings

A.3.7.2 Manufacturing and assembling of the coils

The thickness of the braided wire was measured and was found to be 2.3 mm. Ten turns was required to form one single coil of the eight coils that are required for one single phase stator windings. The final shape of the coil constructed from braided wire is shown in Figure A.21.

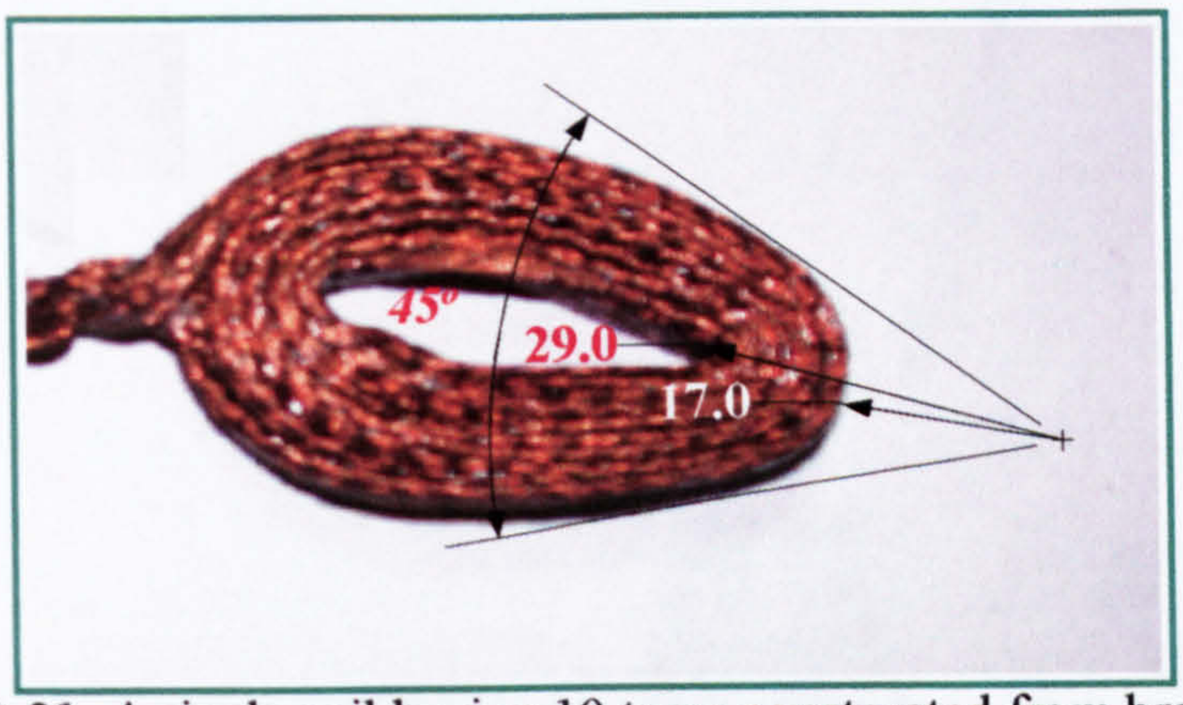

Figure A.21 A single coil having 10 turns constructed from braided wires

It can be seen from this photograph that the coil spans an angle of 45 degrees, which is equal to the pole pitch. This coil was formed into this particular shape using a special mould that was manufactured especially for this purpose. Also, a special winding fixture was manufactured to assist in pressing the coil and in encapsulating it with a special epoxy resin (Figure A.22). Detailed ***AutoCAD*** drawings for both the moulds and winding fixture parts are found in ***Appendix B***.

Eight coils were held into their positions to form the final shape of the stator windings as shown in Figure A.23. Four halves of stator casing made of fiber were used to clamp these coils from both sides. These stator casing are good electrical insulators and they, when assembled together, work like a passage duct for cooling the coils when forced ventilation is used. Dimensions of the coil casings are found in ***Appendix B***. The method of fixing the coils in the stator casing can be shown in Figure A.24.

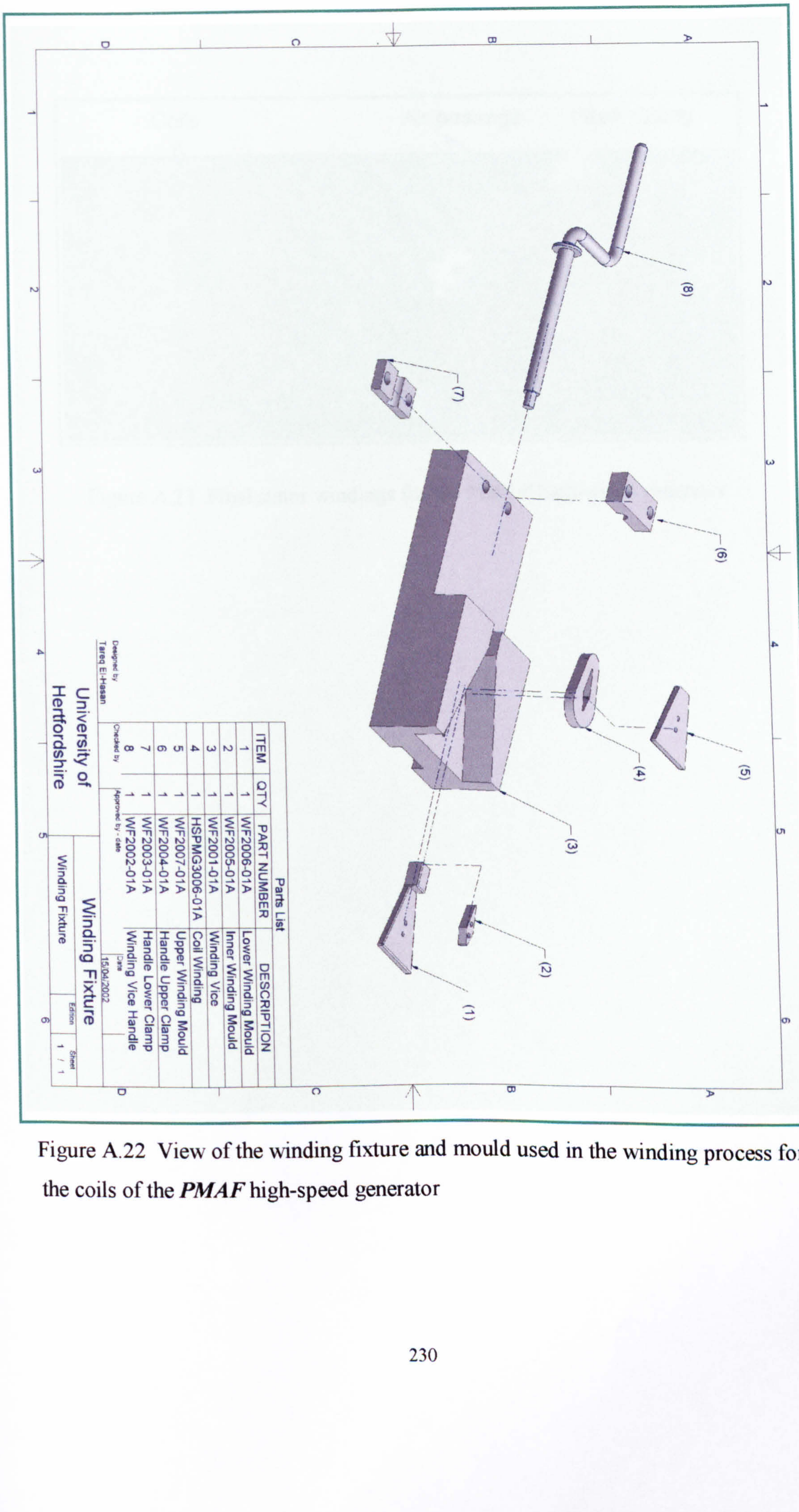

Figure A.22 View of the winding fixture and mould used in the winding process for the coils of the ***PMAF*** high-speed generator

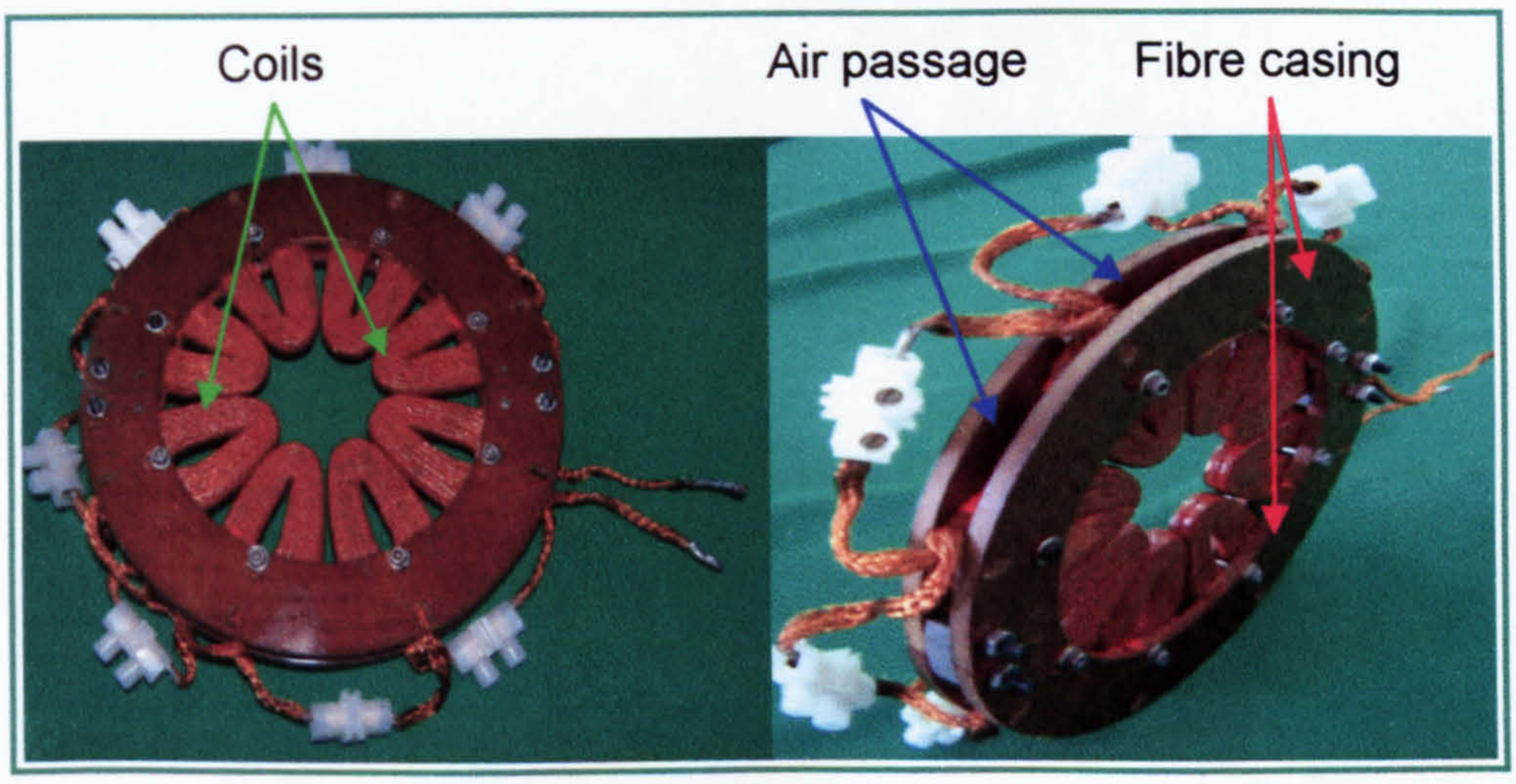

Figure A.23 Final stator windings for the ***PMAF*** high-speed generator

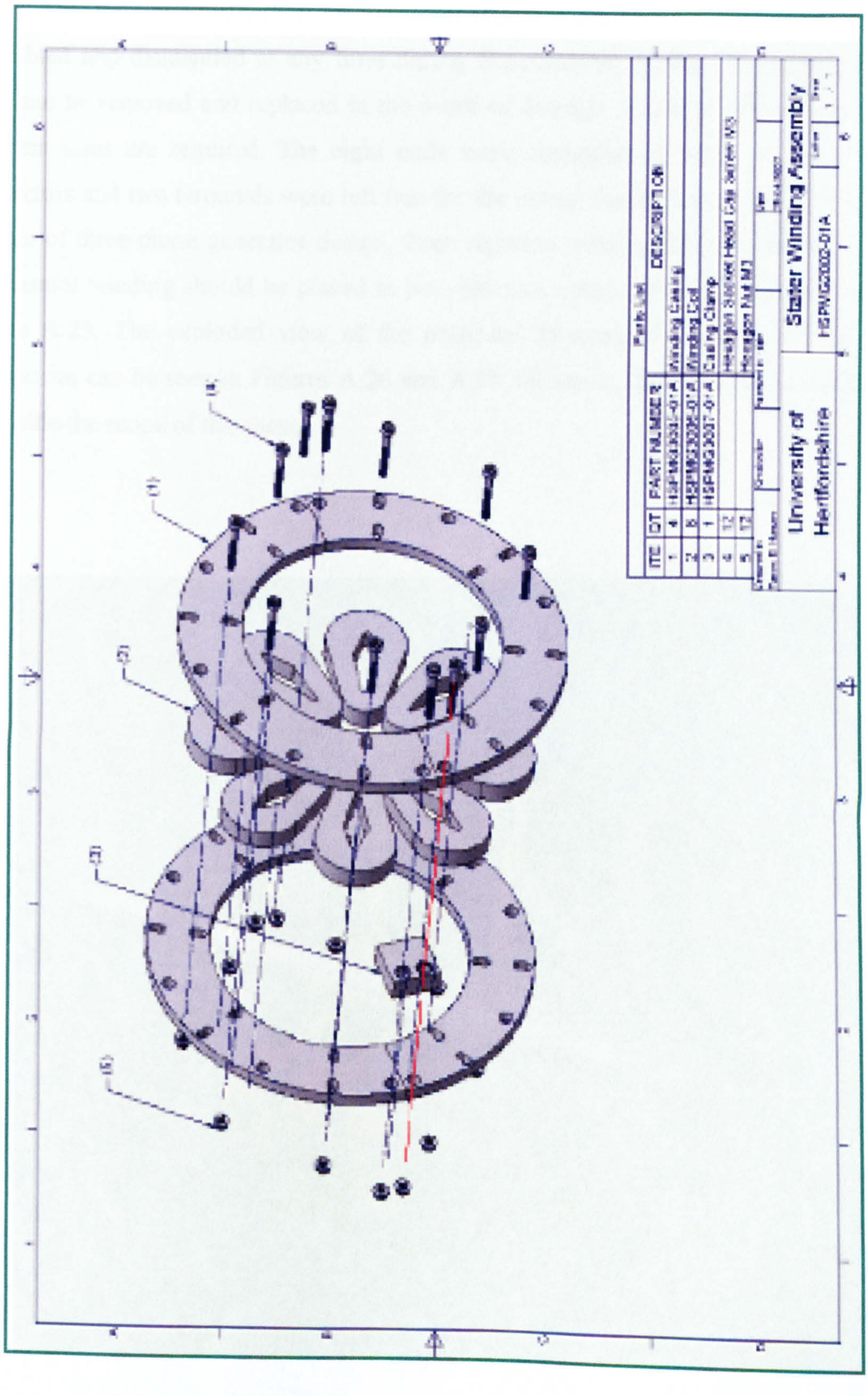

Figure A.24 Fixing the coils in the stator casing

This type of construction for the stator makes it easy for the stator coils to be assembled and dismantled at any time during experimental testing. In addition, any coils can be removed and replaced in the event of damage or when different coils of different sizes are required. The eight coils were connected in series via electrical connectors and two terminals were left free for the output connection of the generator. In case of three-phase generator design, three separate winding discs should be used. Each stator winding should be placed in between two magnet rotor discs as shown in Figure A.25. The exploded view of the proposed three-phase machine and its all accessories can be seen in Figures A.26 and A.27. However, the three-phase machine is outside the scope of this thesis.

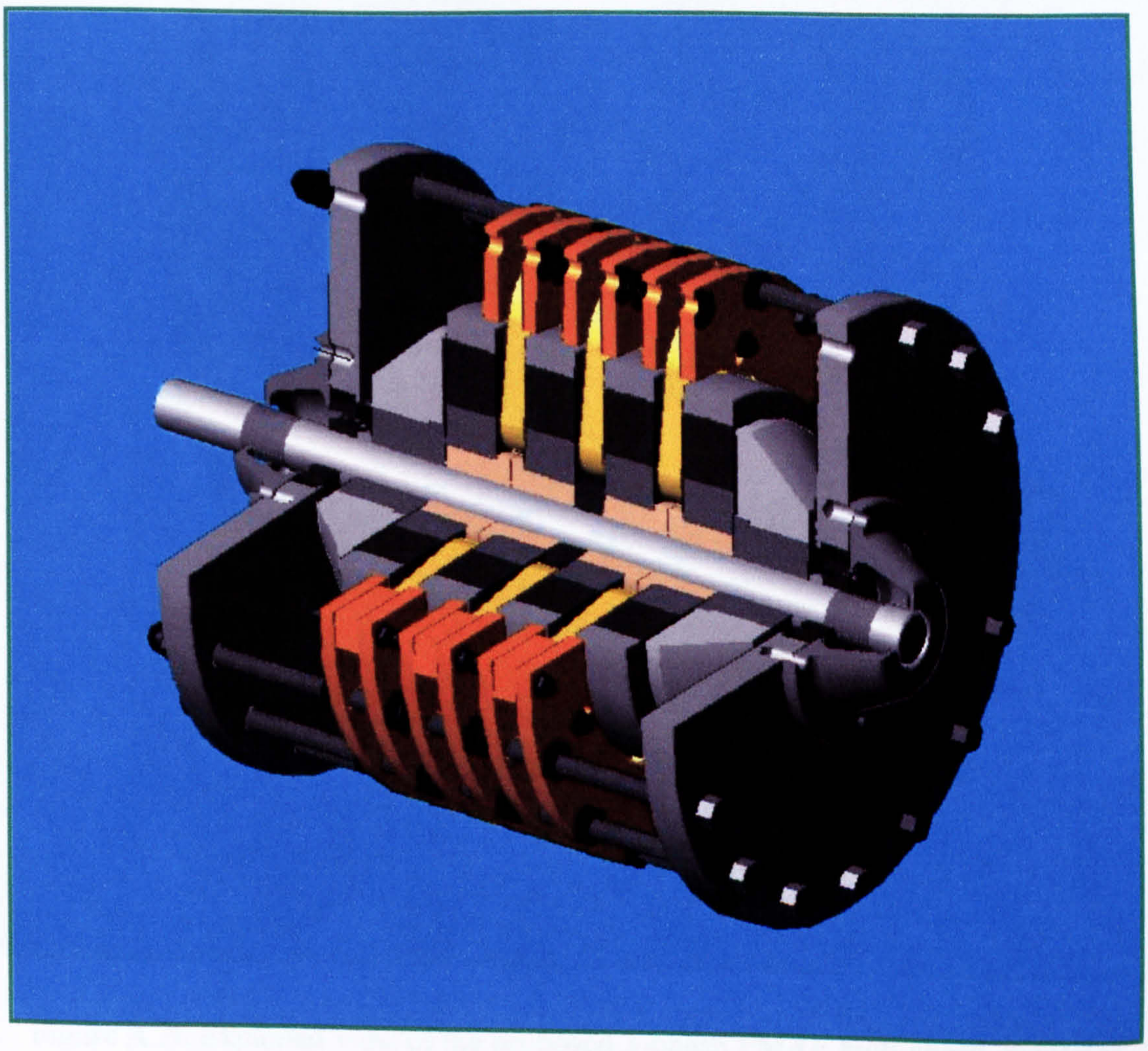

Figure A.25 Exploded view for a three-phase ***PMAF*** high-speed generator

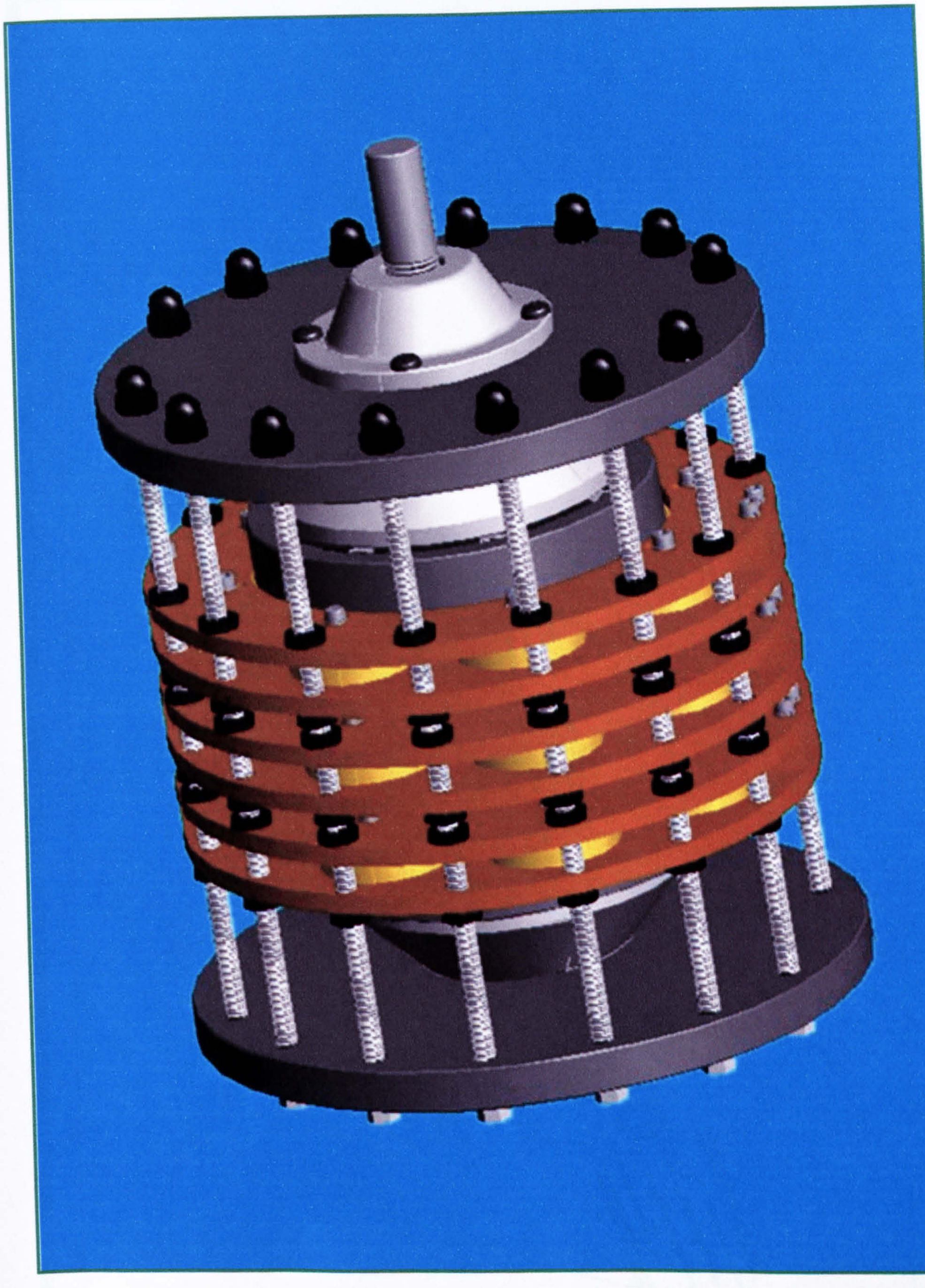

Figure A.26 Exploded view of the proposed 3-phase ***PMAF*** high-speed generator

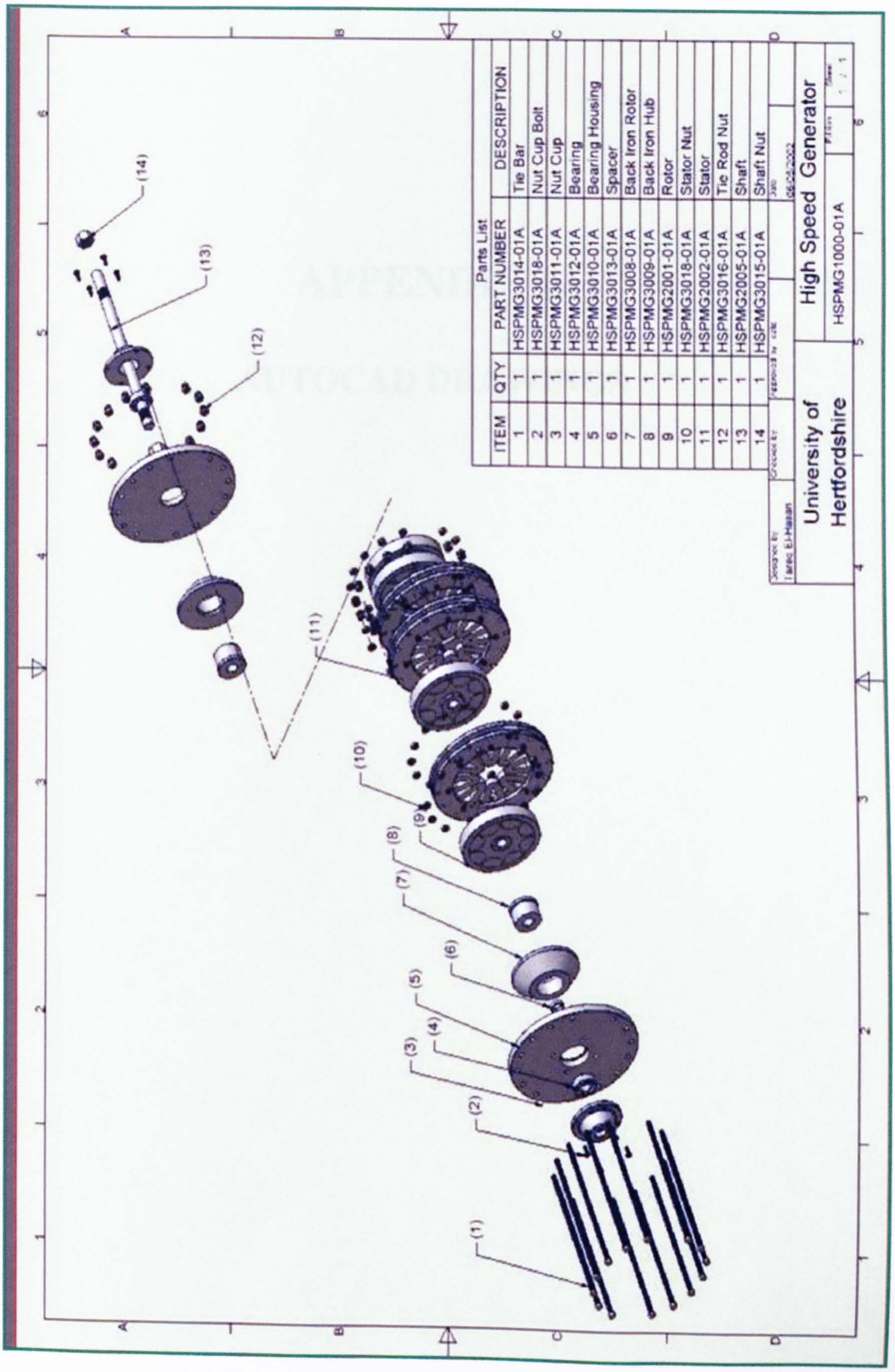

Figure A.27 ***3D*** view of the disassembled ***PMAF*** generator

APPENDIX B

AUTOCAD DRAWINGS

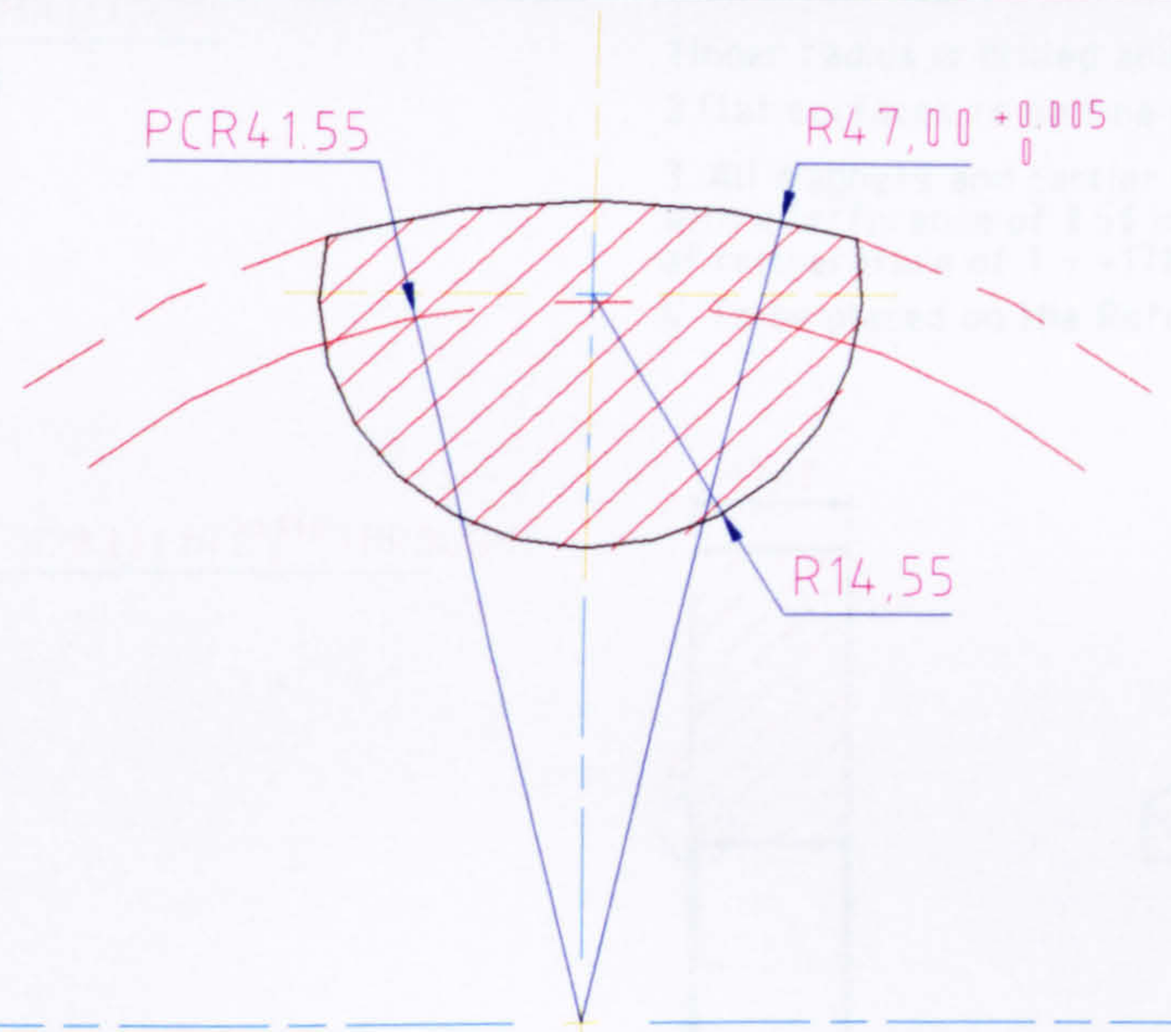

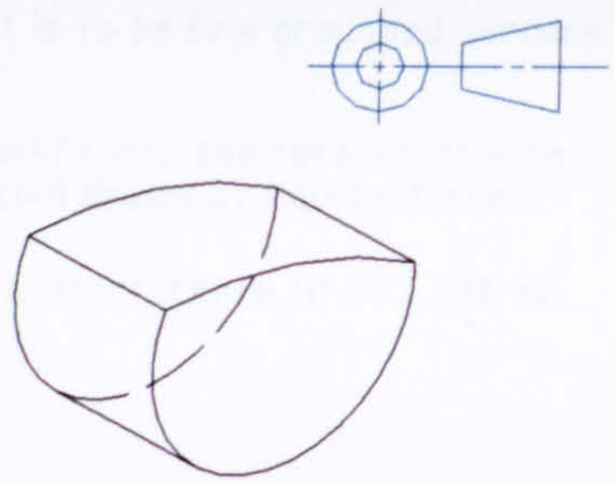

University of Hertfordshire

Faculty of Engineering & Information Sciences

Dept.	Aerospace Civil & Mechanical Engineering Dept.			Title	Permanent Magnet
Designed By	Tareq El-Hasan	Scale	N.T.S.		
Drawn By	Moh Momani	Material	Sintered NdFeB Grade N38H	Drawing /Part Number	HSPMG3002-01a
Date	18/4/2002	Qty.	32	Sheet 1	Of 1

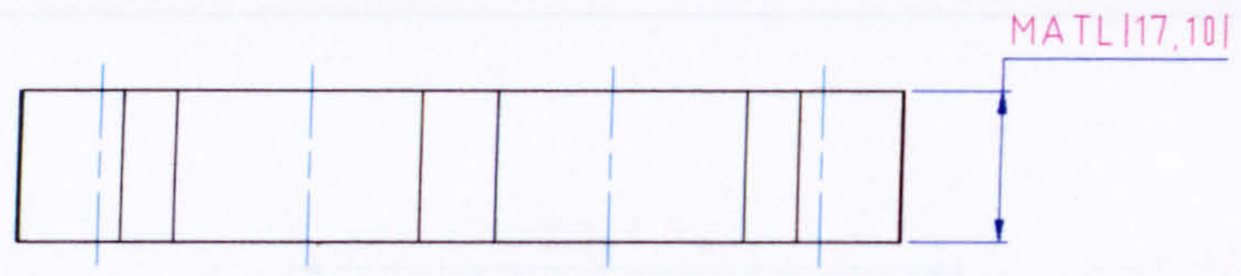

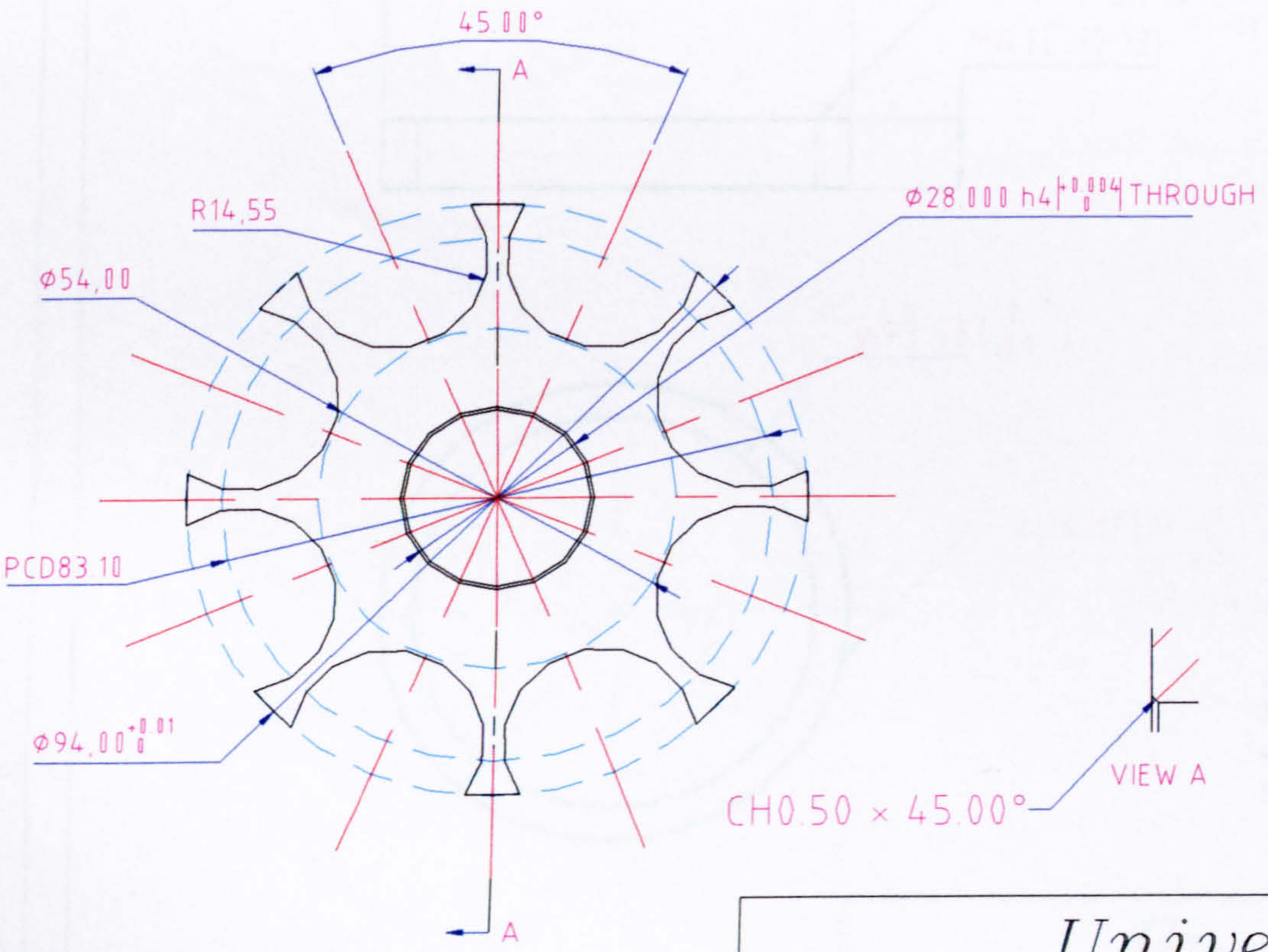

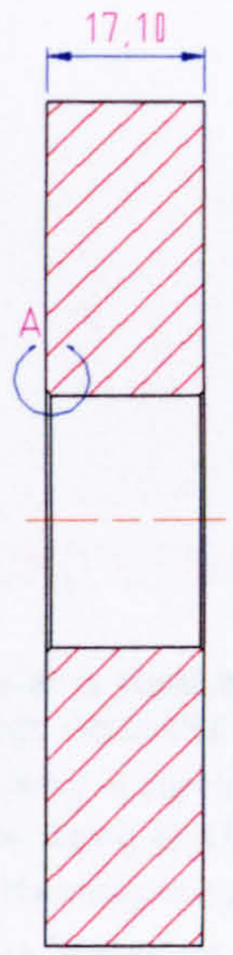

SECTION A-A

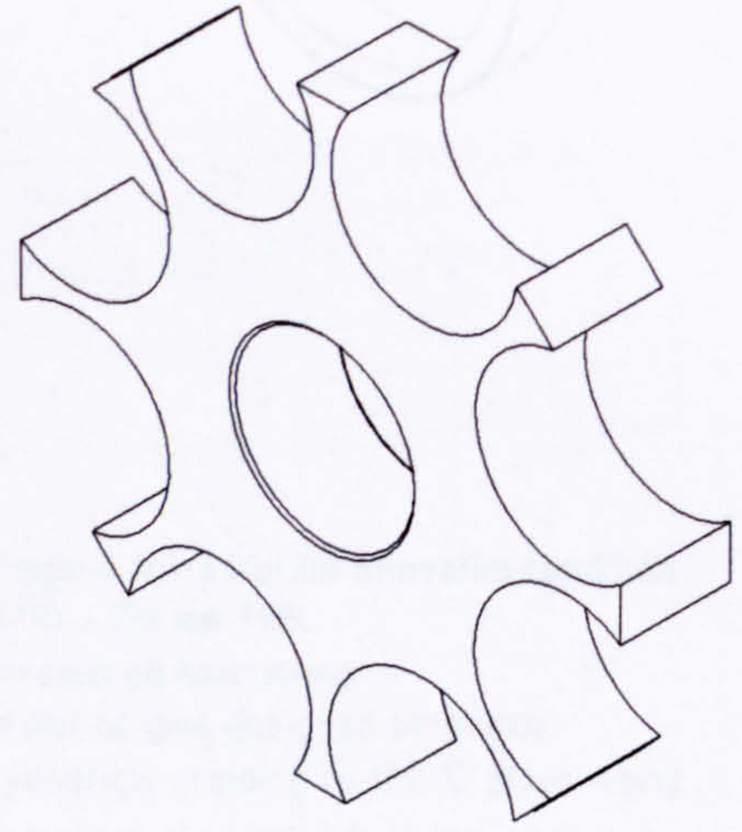

NOTES:-

1. Inner radius is drilled and reamed. It is to be fine grounded surface.
2. Flat surfaces to be fine grounded.
3. All magnets and carrier to be shrinkfit into the retainment Ring with interference of 0.50 mm, to be cold drawn by liquid nitrogen at temperature of T = -170 C .
4. To be placed on the Rotor hub with interference fit of 0.030 mm

All Dimensions are in mm Unless Otherwised Stated
All Tolerances are ±0.01mm Unless Otherwised Stated

University of Hertfordshire
Faculty of Engineering & Information Sciences

Dept.	Aerospace Civil & Mechanical Engineering Dept.			Title	Magnet Carrier
Designed By	Tareq El-Hasan	Scale	N.T.S.		
Drawn By	Moh Momani	Material	Alumec 79	Drawing /Part Number	HSPMG3001-01A
Date	18/4/2002	Qty.	4	Sheet 1	Of 1

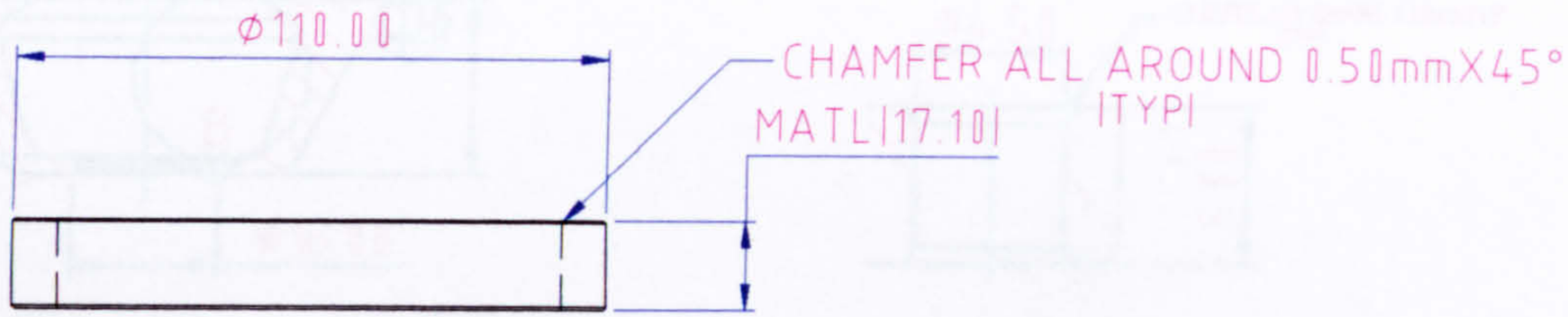

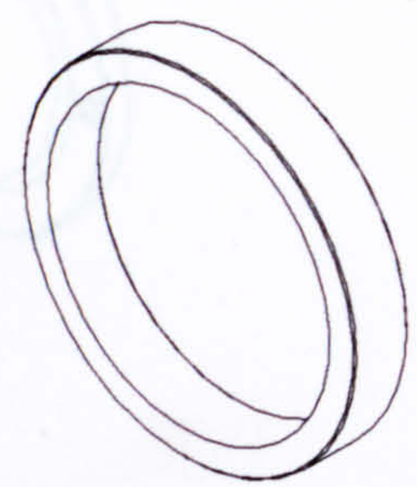

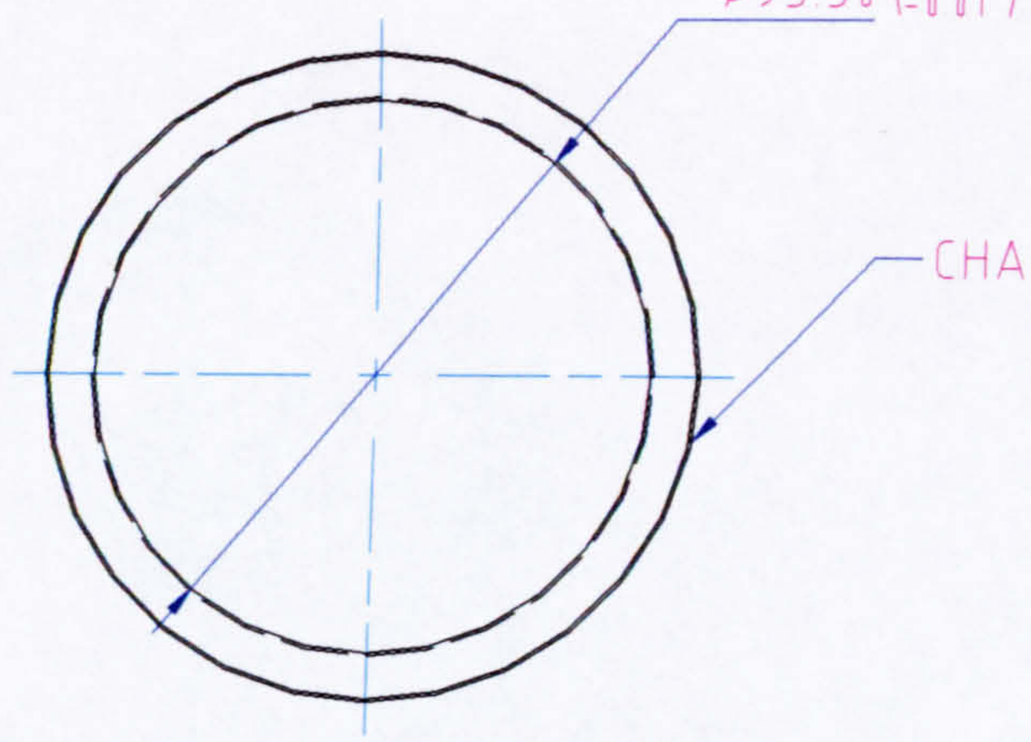

1. Material is supplied as forged rings in the solution Annealed condition at rough dimension of 175 ID × 117 OD × 251 mm THK.
2. Machining is carried out to meet reqiured dimensions .
3. Simple Aging at 450 c° is carried out to give designed strength.
4. Fine Machinig is carried out by cylindrical grinding to the ID after Aging .
5. Ring is heated up to 250 C° & to be placed shrink fit on the magnet carrier with interference fit of 0.5 mm.

All Dimensions are in mm Unless Otherwised Stated

All Tolerances are ±0.01mm Unless Otherwised Stated

University of Hertfordshire

Faculty of Engineering & Information Sciences

Dept.	Aerospace Civil & Mechanical Engineering Dept.			Title	Retainment Ring
Designed By	Tareq El-Hasan	Scale	N.T.S.		
Drawn By	Moh Momani	Material	Maraging G125	Drawing /Part Number	HSPMG3003-01A
Date	14/4/2002	Qty.	4	Sheet 1	Of 1

9

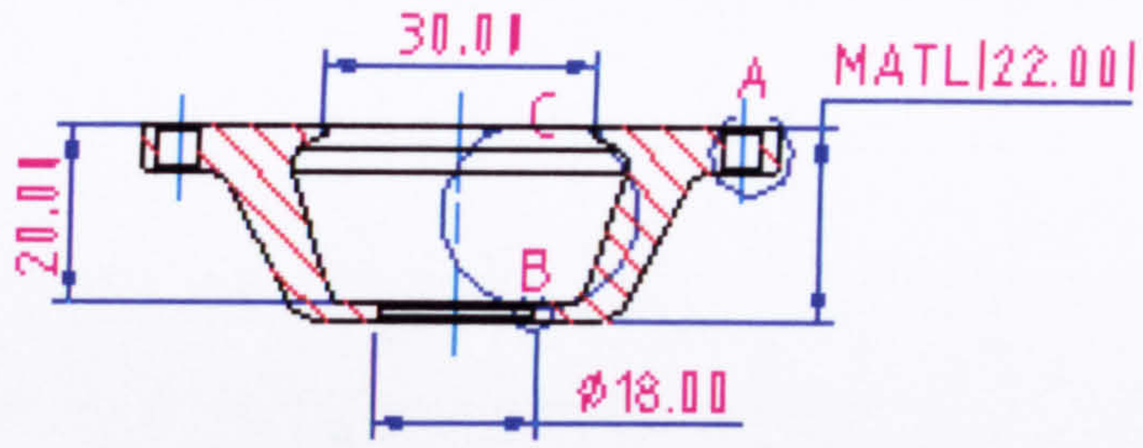

SECTION A-A

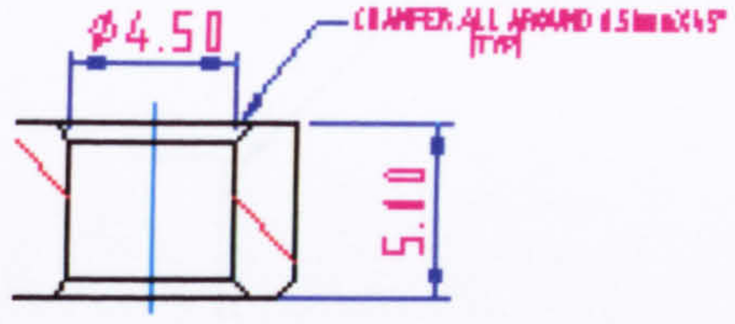

Detail A

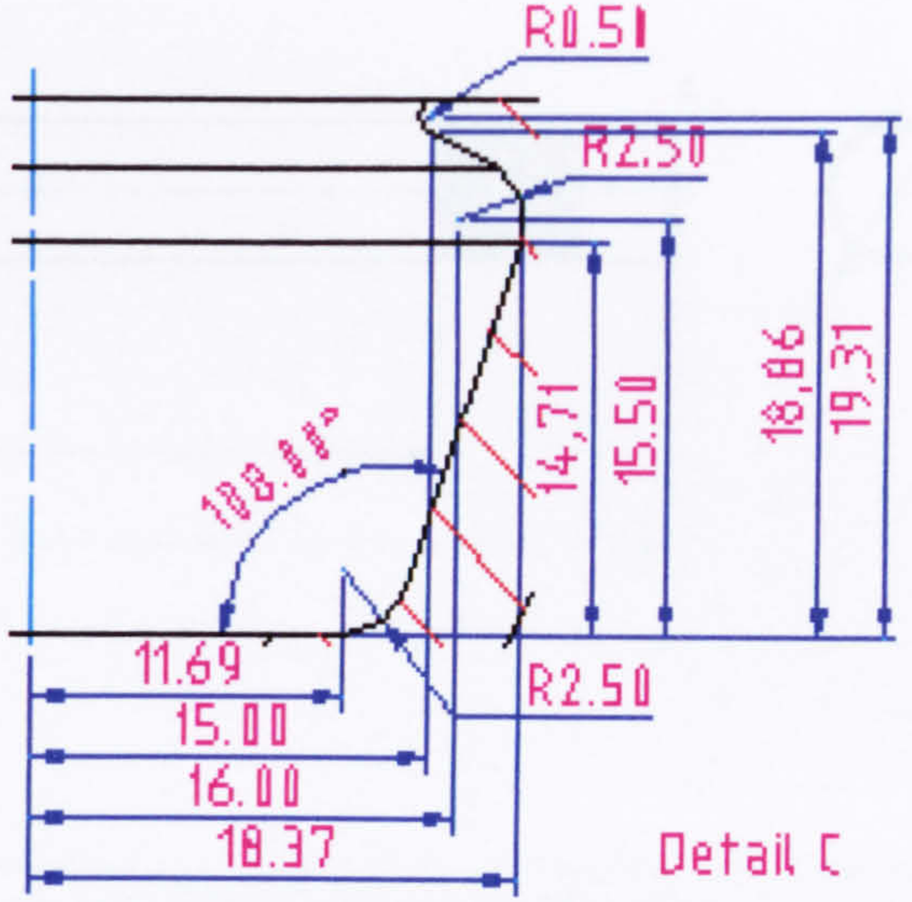

Detail C

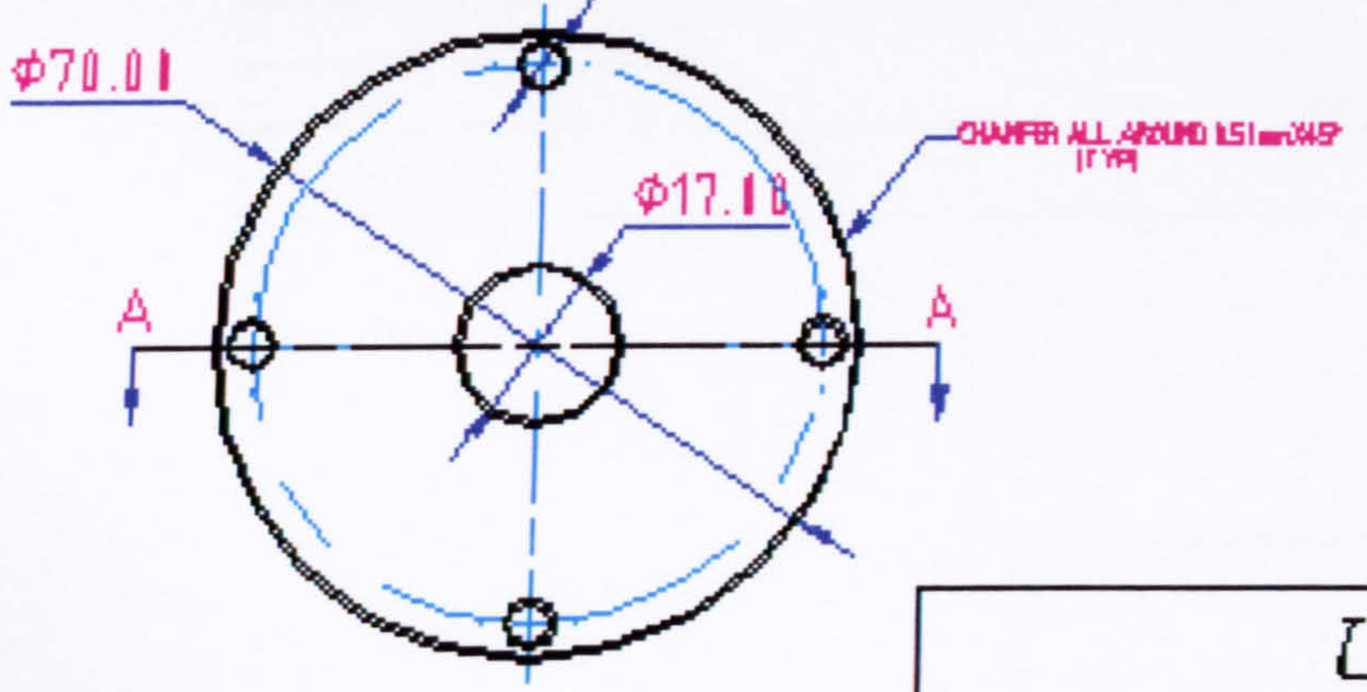

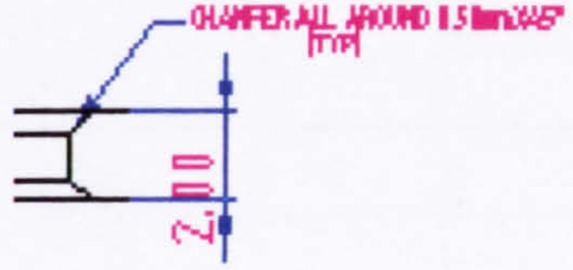

Detail B

All Dimensions are in mm Unless Otherwised Stated
All Tolerances are ±0.11mm Unless Otherwised Stated

University of Hertfordshire
Faculty of Engineering & Information Sciences

Dept.	Aerospace Civil & Mechanical Engineering Dept.			Title	Nut Cup
Designed By	Tareq El-Hasan	Scale	N.T.S.		
Drawn By	Moh Momani	Material	Steel	Drawing / Part Number	HSPMG3011-11A
Date	22/4/2012	Qty.	2	Sheet 1	Of 1

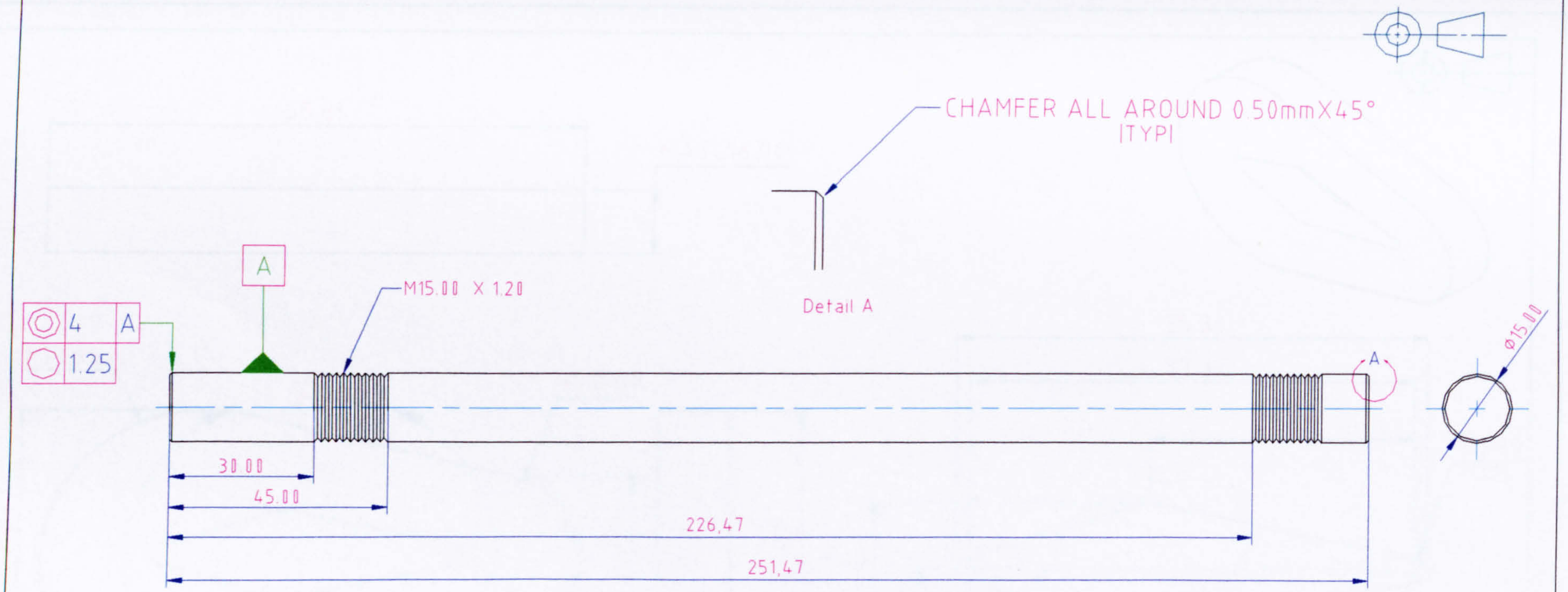

All Dimensions are in mm Unless Otherwised Stated

All Tolerances are ±0.01mm Unless Otherwised Stated

University of Hertfordshire

Faculty of Engineering & Information Sciences

Dept.	Aerospace Civil & Mechanical Engineering Dept.			Title	Shaft
Designed By	Tareq El-Hasan	Scale	N.T.S.		
Drawn By	Moh Momani	Material	Steel	Drawing /Part Number	HSPMG2005-01A
Date	25/4/2002	Qty.	1	Sheet 1	Of 1

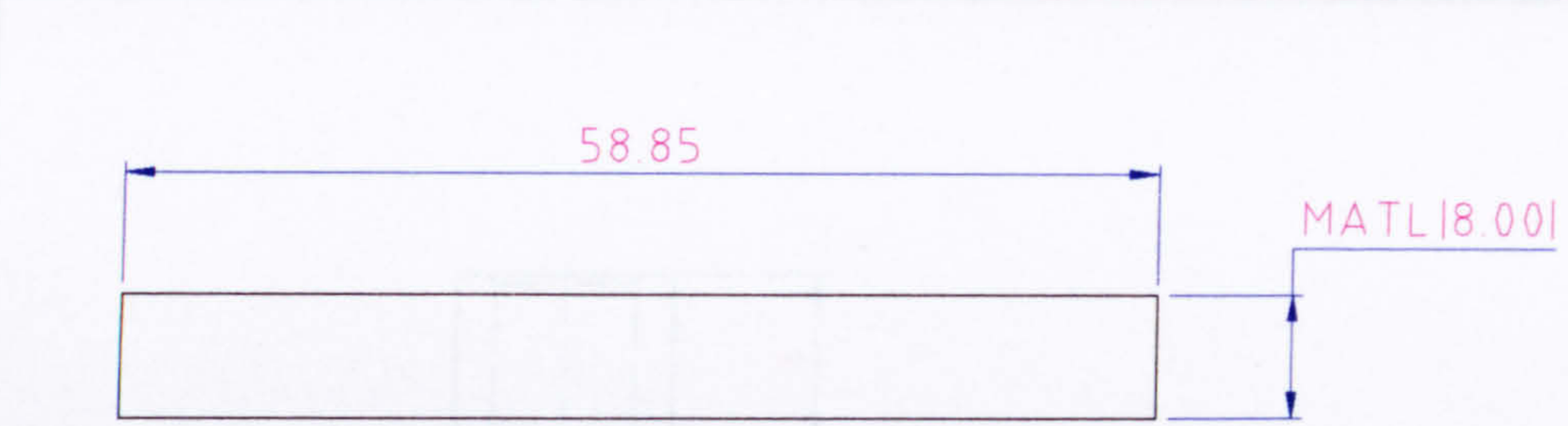

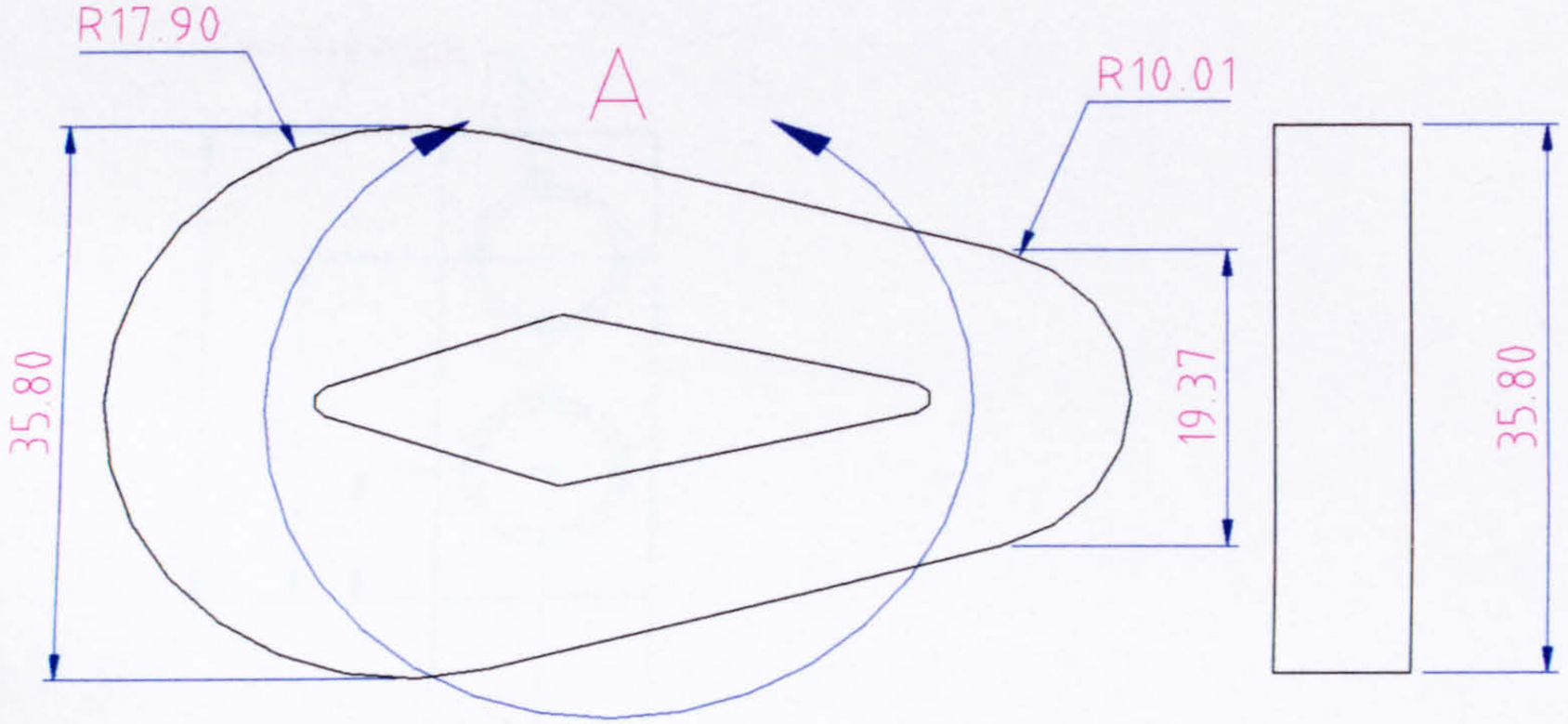

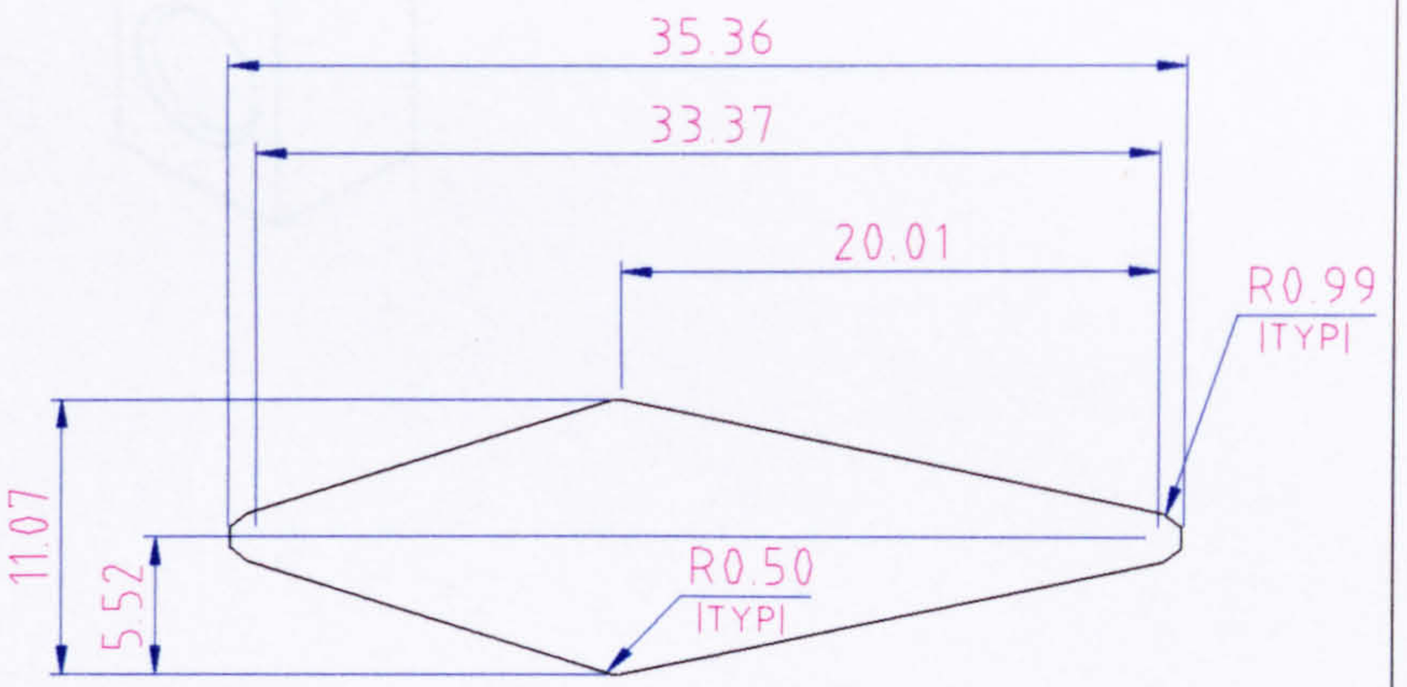

Detail A

All Dimensions are in mm Unless Otherwised Stated
All Tolerances are ±0.01mm Unless Otherwised Stated

University of Hertfordshire
Faculty of Engineering & Information Sciences

Dept.	Aerospace Civil & Mechanical Engineering Dept.			Title	Coil Winding
Designed By	Tareq El-Hasan	Scale	N.T.S.		
Drawn By	Moh Momani	Material	Braded Magnet Wire Class F Grade 2	Drawing /Part Number	HSPMG3006-01A
Date	14/4/2002	Qty.	24	Sheet 1	Of 1

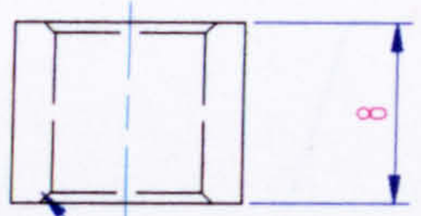

CHAMFER ALL AROUND 0.50mmX45°
(TYP)

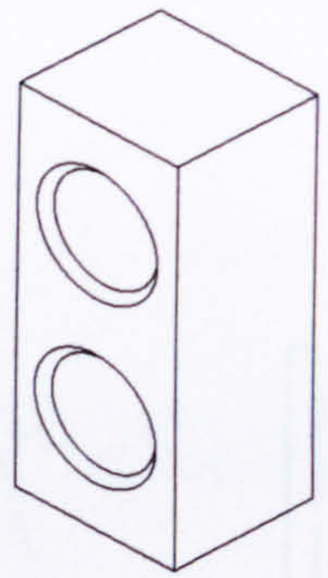

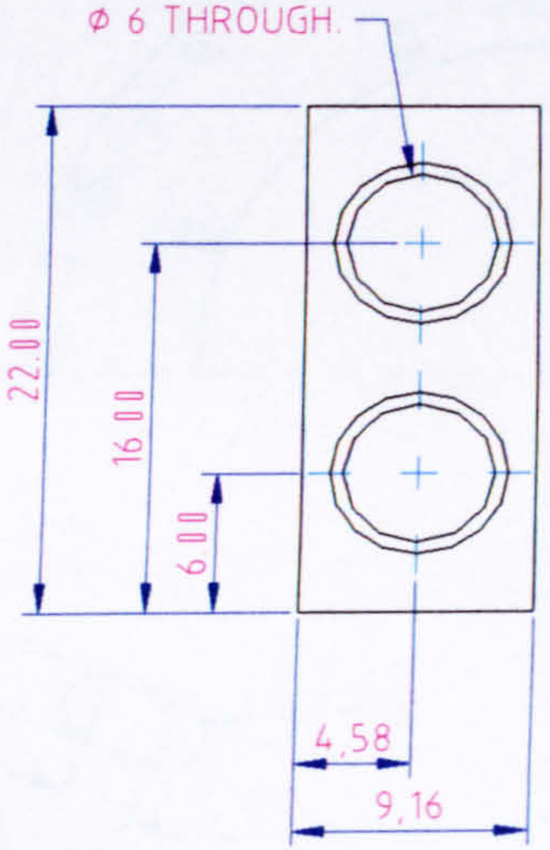

All Dimensions are in mm Unless Otherwised Stated
All Tolerances are ±0.01mm Unless Otherwised Stated

University of Hertfordshire

Faculty of Engineering & Information Sciences

Dept.	Aerospace Civil & Mechanical Engineering Dept.			Title	Casing Clamp
Designed By	Tareq El-Hasan	Scale	N.T.S.		
Drawn By	Moh Momani	Material	Fiber	Drawing /Part Number	HSPMG3007-01A
Date	18/4/2002	Qty.	12	Sheet 1	Of 1

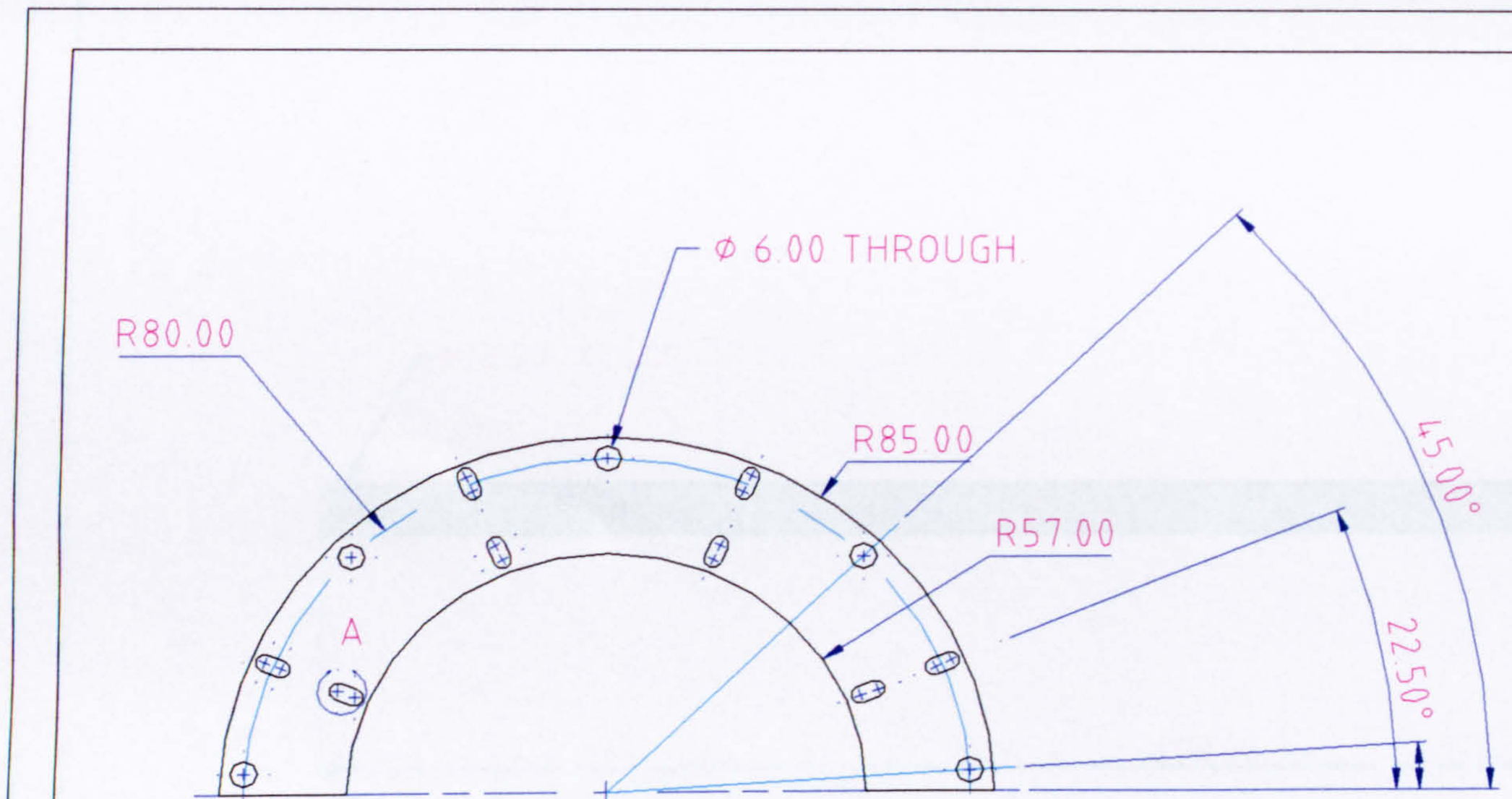

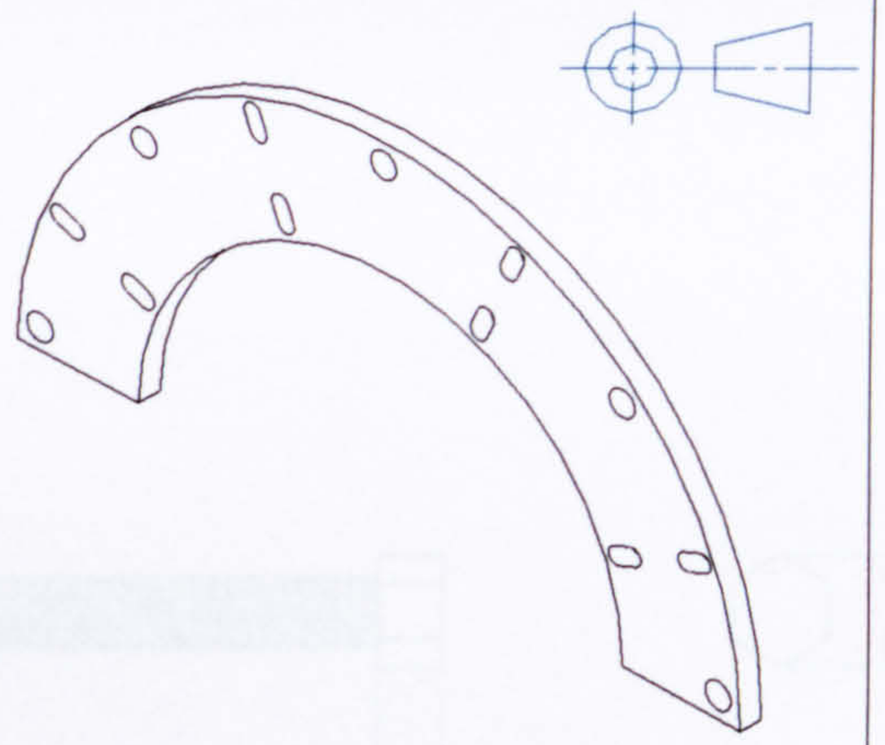

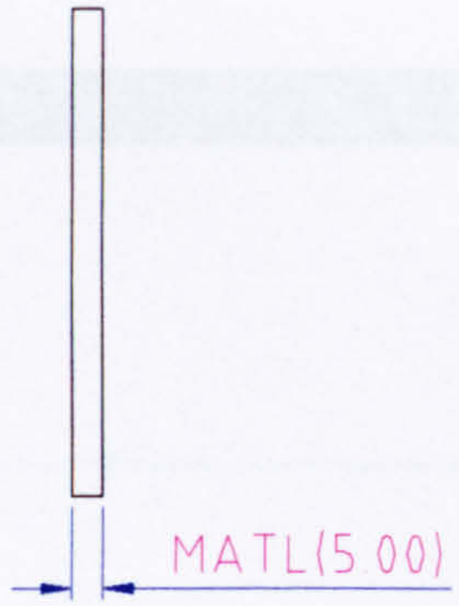

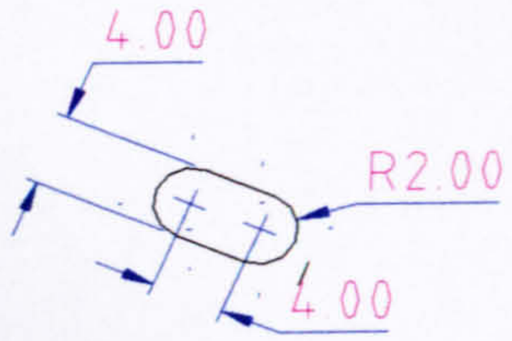

Detail A

All Dimensions are in mm Unless Otherwised Stated
All Tolerances are ±0.01mm Unless Otherwised Stated

University of Hertfordshire
Faculty of Engineering & Information Sciences

Dept.	Aerospace Civil & Mechanical Engineering Dept.			Title	Winding Casing
Designed By	Tareq El-Hasan	Scale	N.T.S.		
Drawn By	Moh Momani	Material	Fiber	Drawing /Part Number	HSPMG3005-01A
Date	14/4/2002	Qty.	12	Sheet 1	Of 1

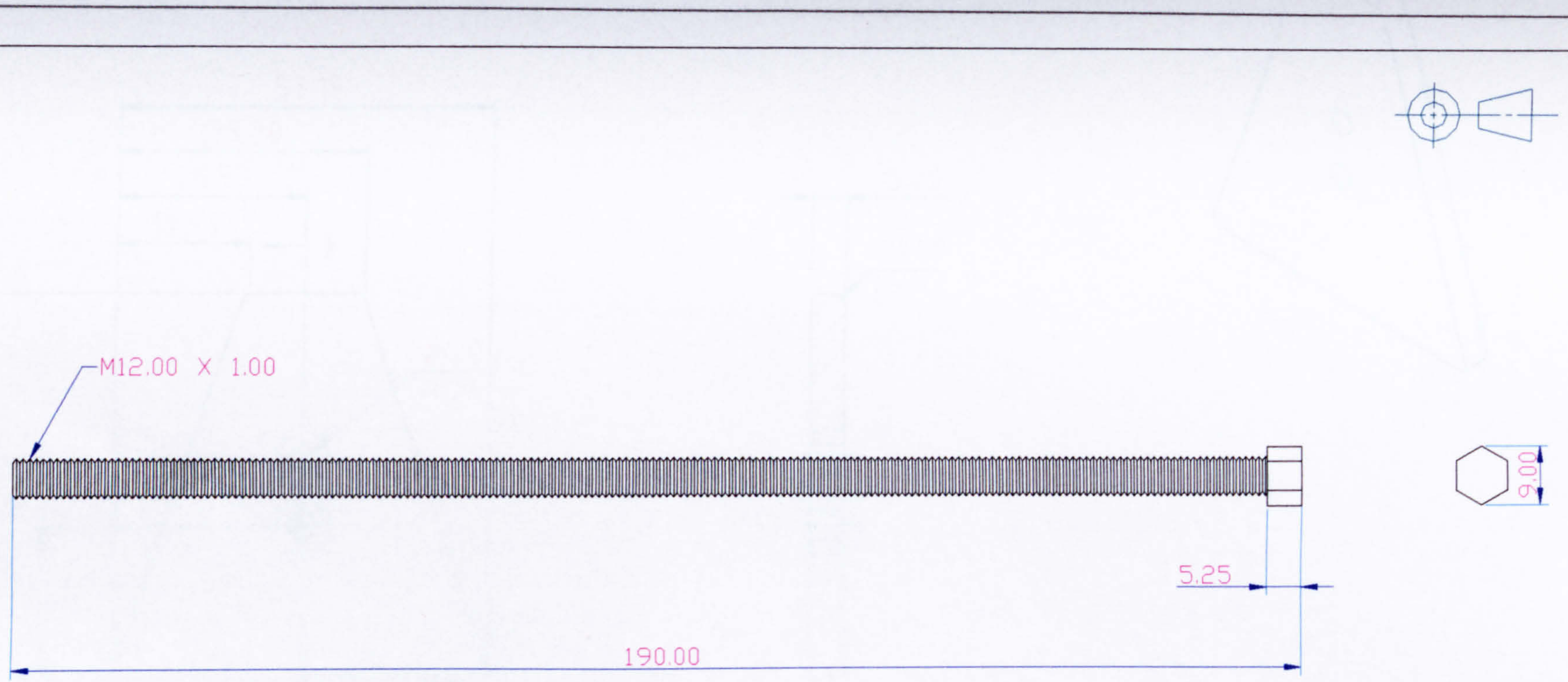

All Dimensions are in mm Unless Otherwised Stated

All Tolerances are ±0.01mm Unless Otherwised Stated

University of Hertfordshire

Faculty of Engineering & Information Sciences

Dept.	Aerospace Civel & Mechanical Engineering Dept.				
Designed By	Tareq El-Hasan	Scale	N.T.S.	Title	Tie Bar
Drawn By	Moh Momani	Material	Steel	Drawing /Part Number	HSPMG3014-01A
Date	25/4/2002	Qty.	14	Sheet	of 1

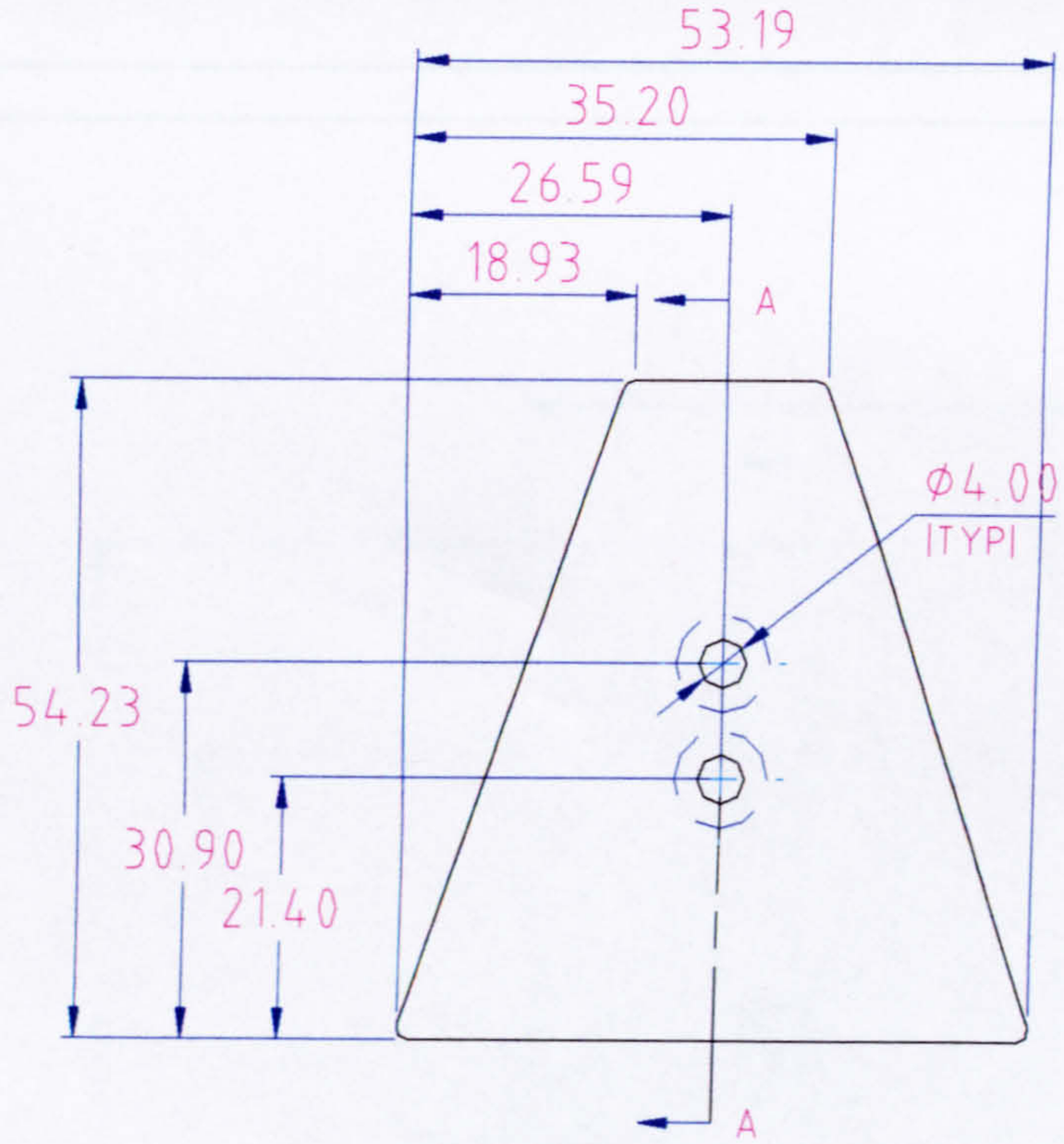

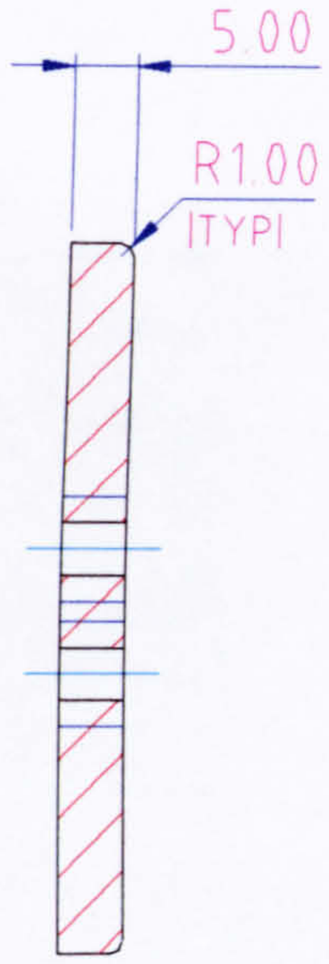

SECTION A-A

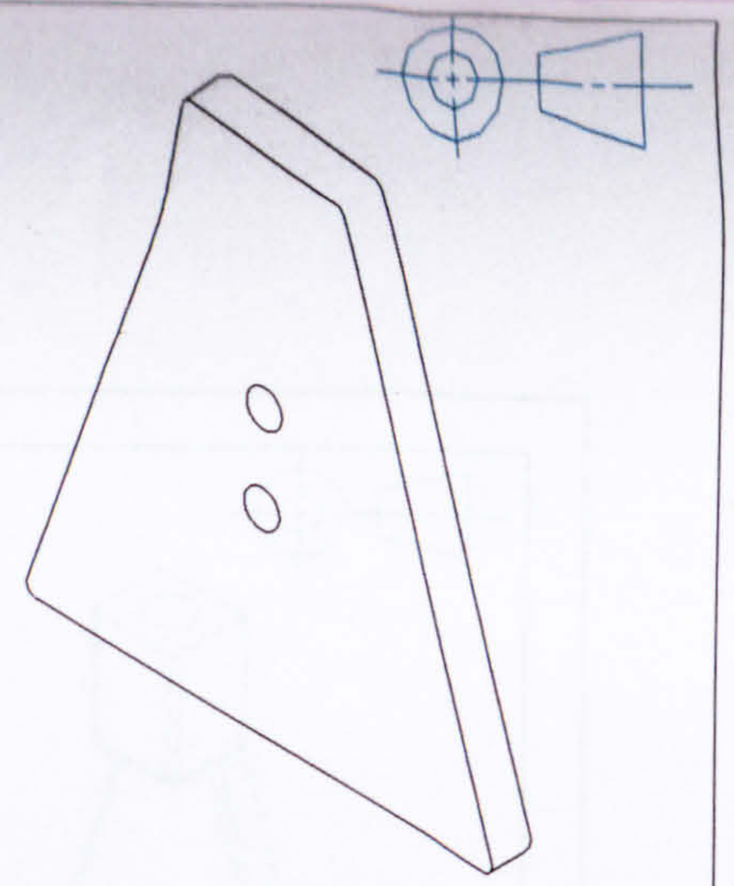

All Dimensions are in mm Unless Otherwised Stated

All Tolerances are ±0.01mm Unless Otherwised Stated

University of Hertfordshire

Faculty of Engineering & Information Sciences

Dept.	Aerospace Civil & Mechanical Engineering Dept.			Title	Upper Winding Mould
Designed By	Tareq El-Hasan	Scale	N.T.S.		
Drawn By	Moh Momani	Material	Steel	Drawing /Part Number	WF2007-01A
Date	14/4/2002	Qty.	1	Sheet SHEETNO	Of 1

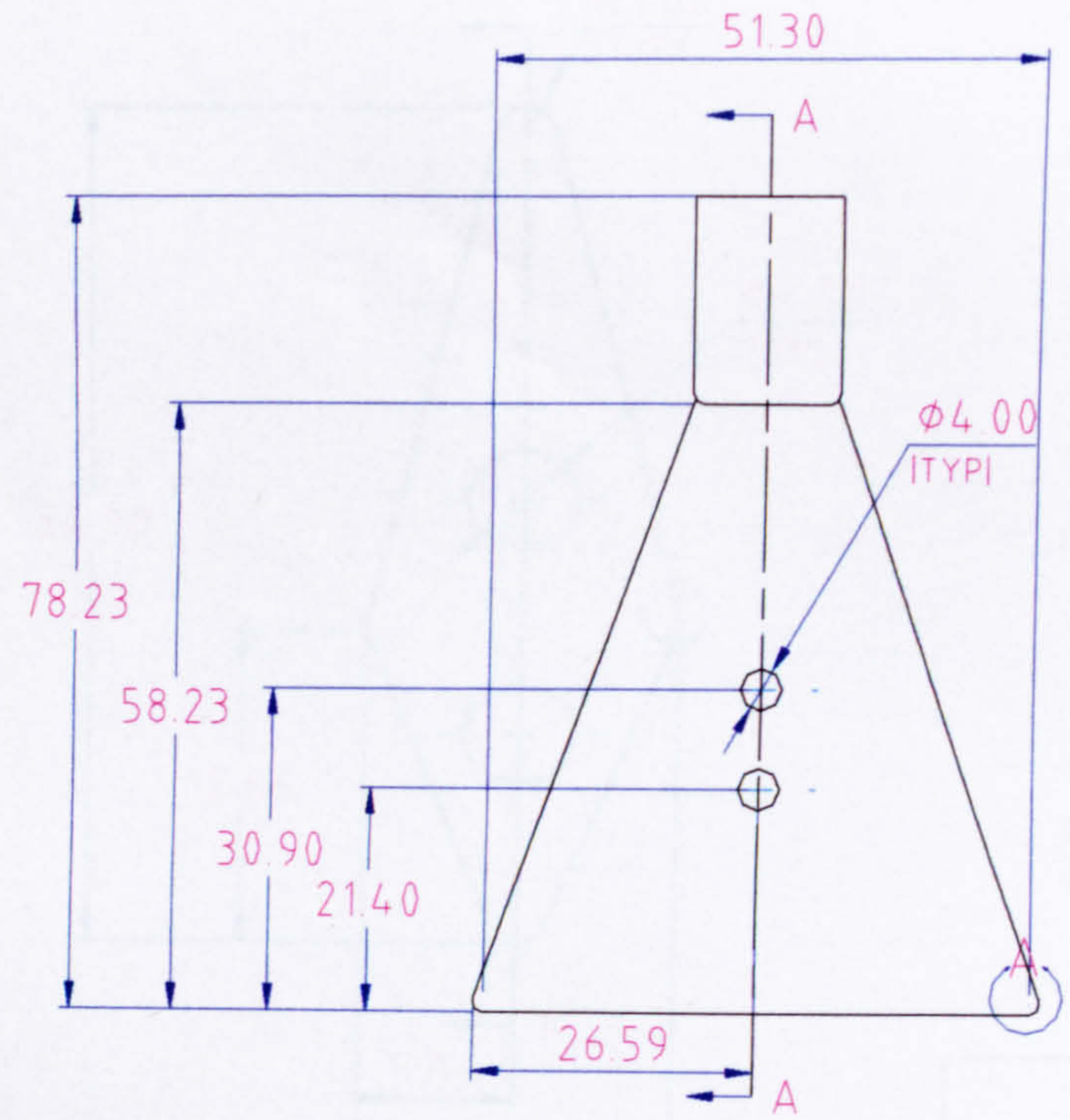

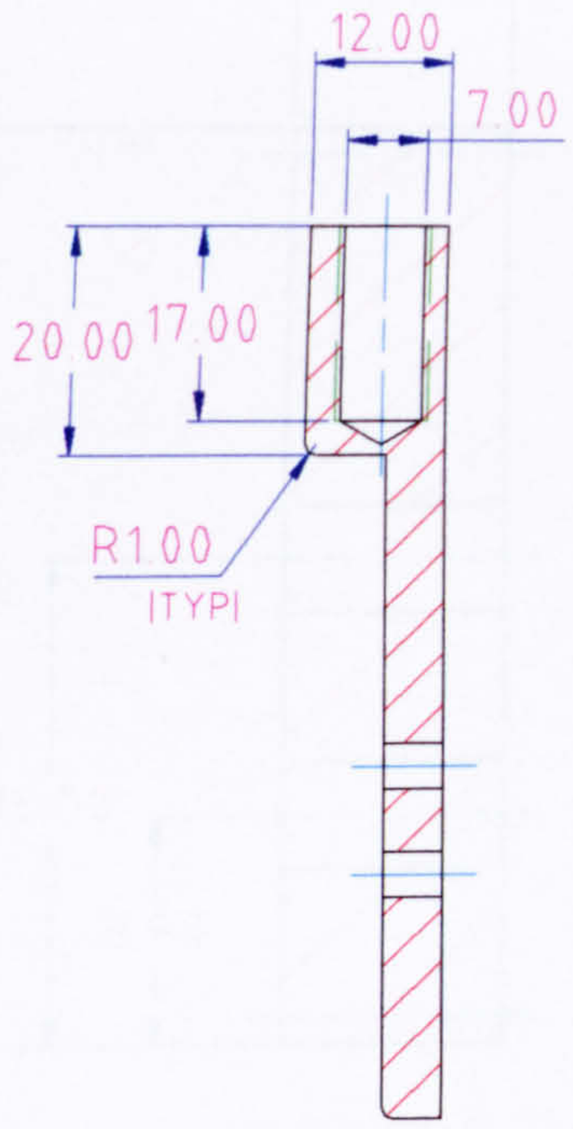

SECTION A-A

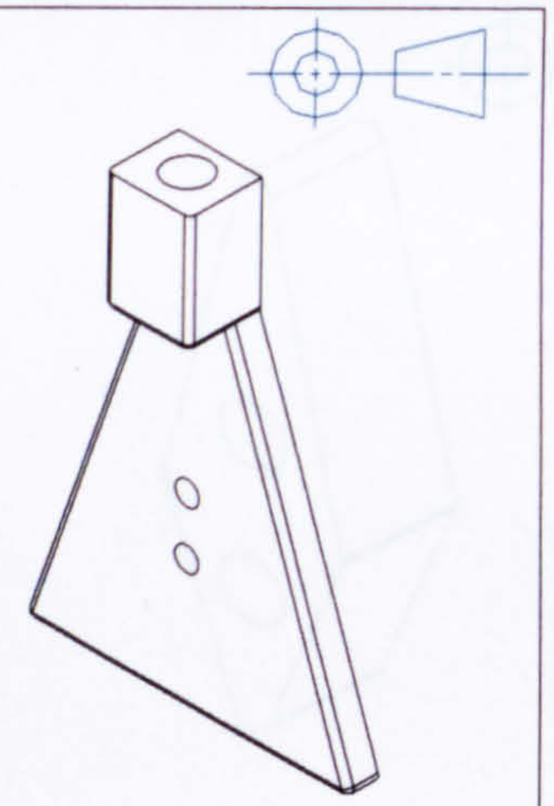

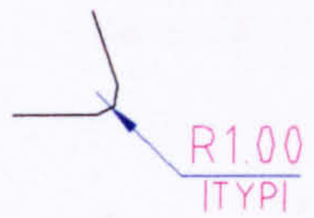

Detail A

All Dimensions are in mm Unless Otherwised Stated

All Tolerances are ±0.01mm Unless Otherwised Stated

University of Hertfordshire

Faculty of Engineering & Information Sciences

Dept.	Aerospace Civil & Mechanical Engineering Dept.			Title	Lower Winding Mould
Designed By	Tareq El-Hasan	Scale	N.T.S.		
Drawn By	Moh Momani	Material	Steel	Drawing /Part Number	WF2006-01A
Date	14/4/2002	Qty.	1	Sheet 1	Of 1

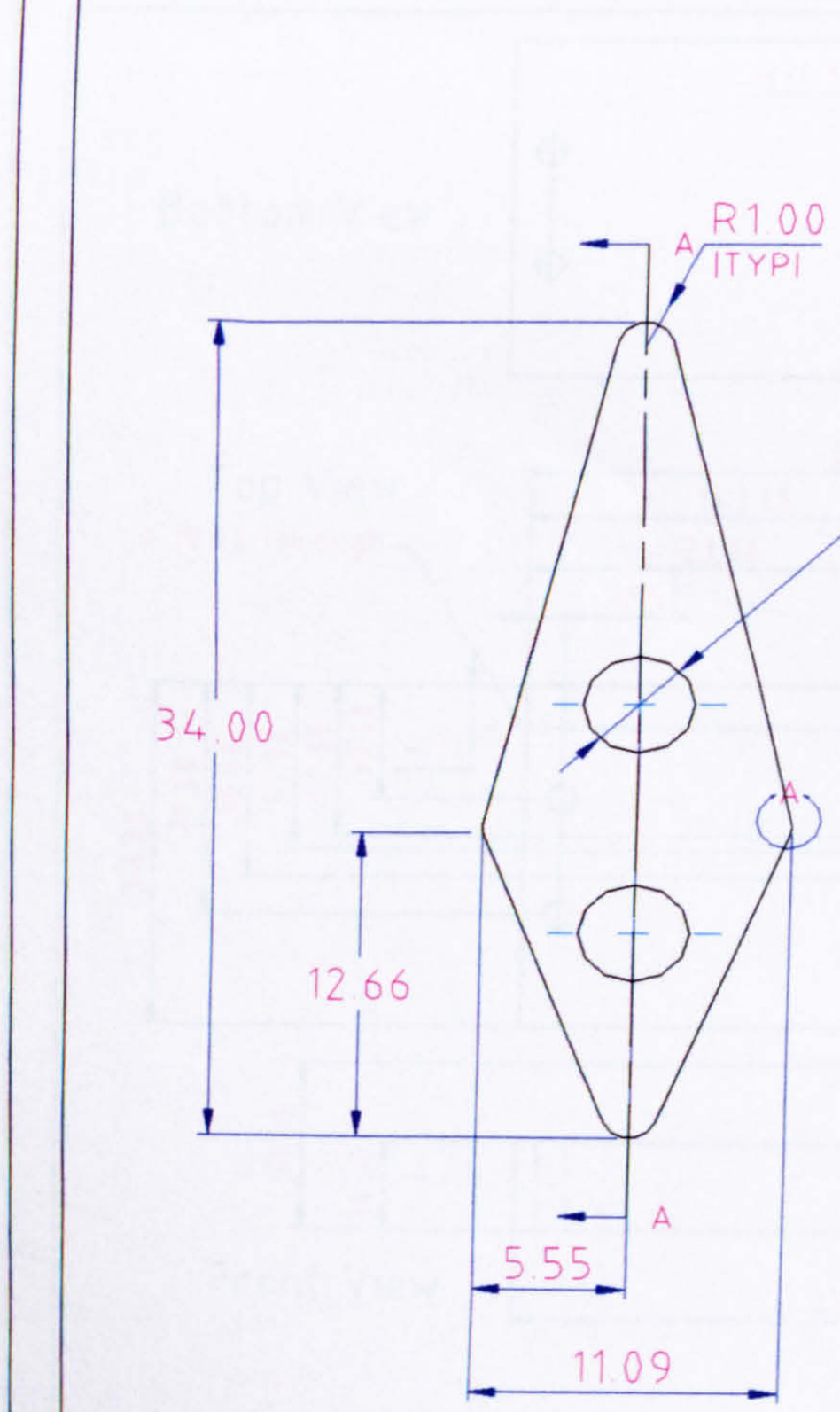

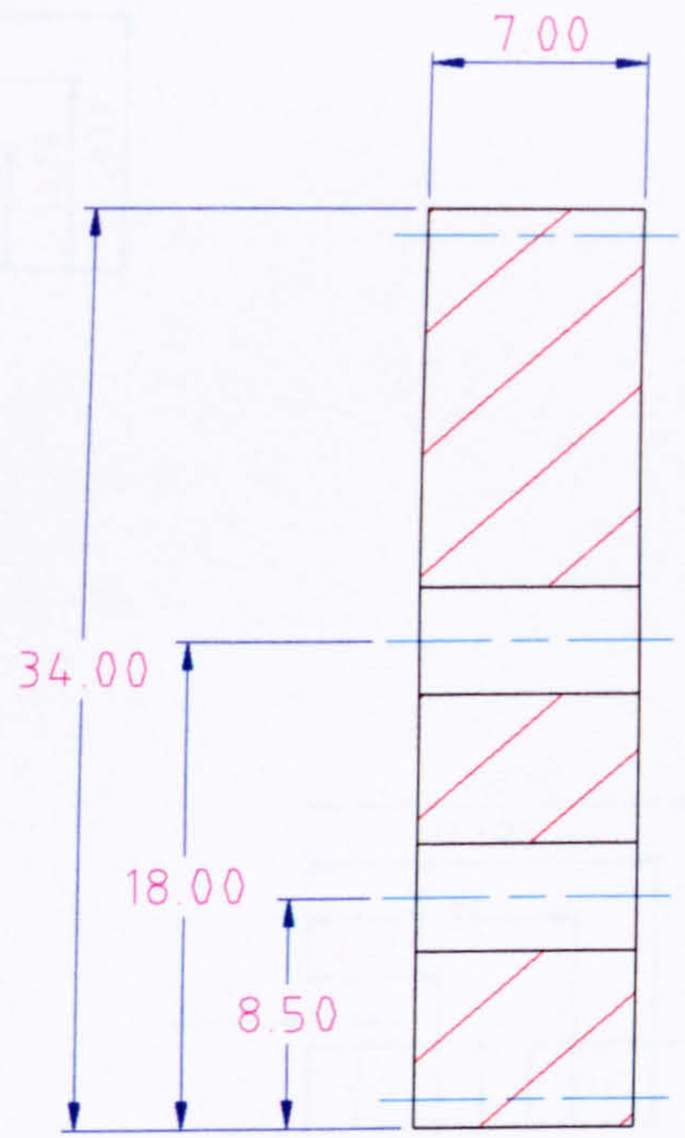

SECTION A-A

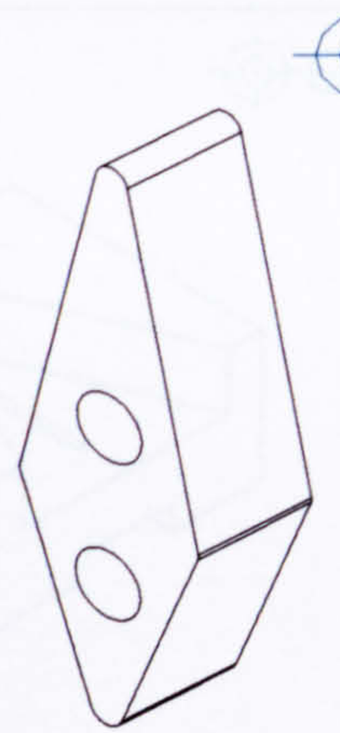

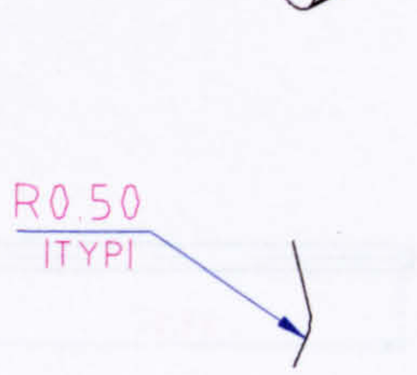

Detail A

All Dimensions are in mm Unless Otherwised Stated
All Tolerances are ±0.01mm Unless Otherwised Stated

University of Hertfordshire

Faculty of Engineering & Information Sciences

Dept.	Aerospace Civil & Mechanical Engineering Dept.			Title	Inner Winding Mould
Designed By	Tareq El-Hasan	Scale	N.T.S.		
Drawn By	Moh Momani	Material	Fiber	Drawing /Part Number	WF2005-01A
Date	14/4/2002	Qty.	1	Sheet 1	Of 1

Bottom View

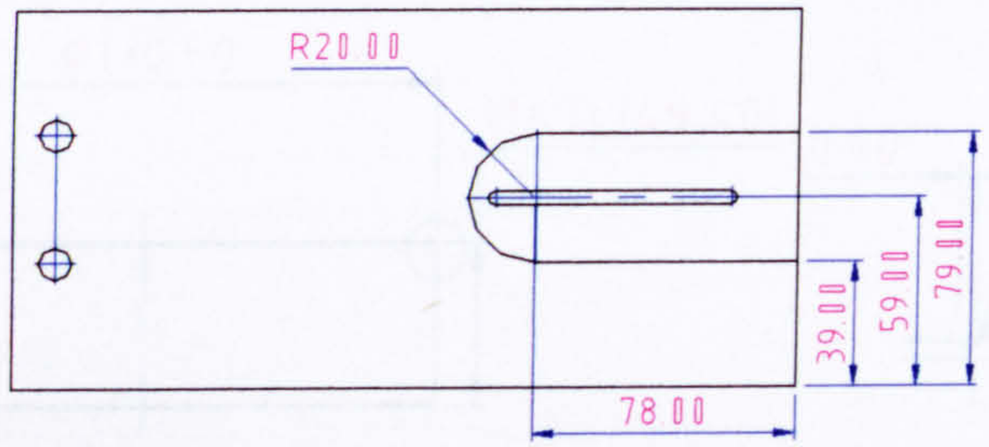

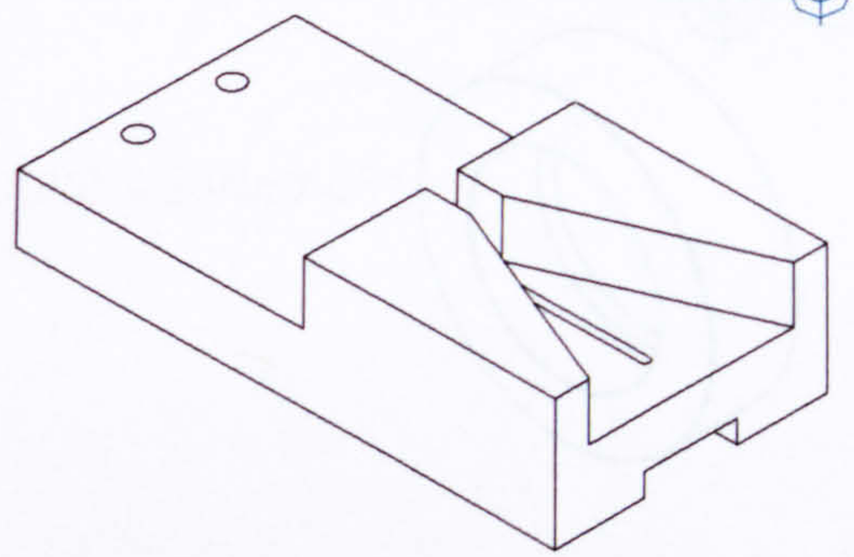

Top View

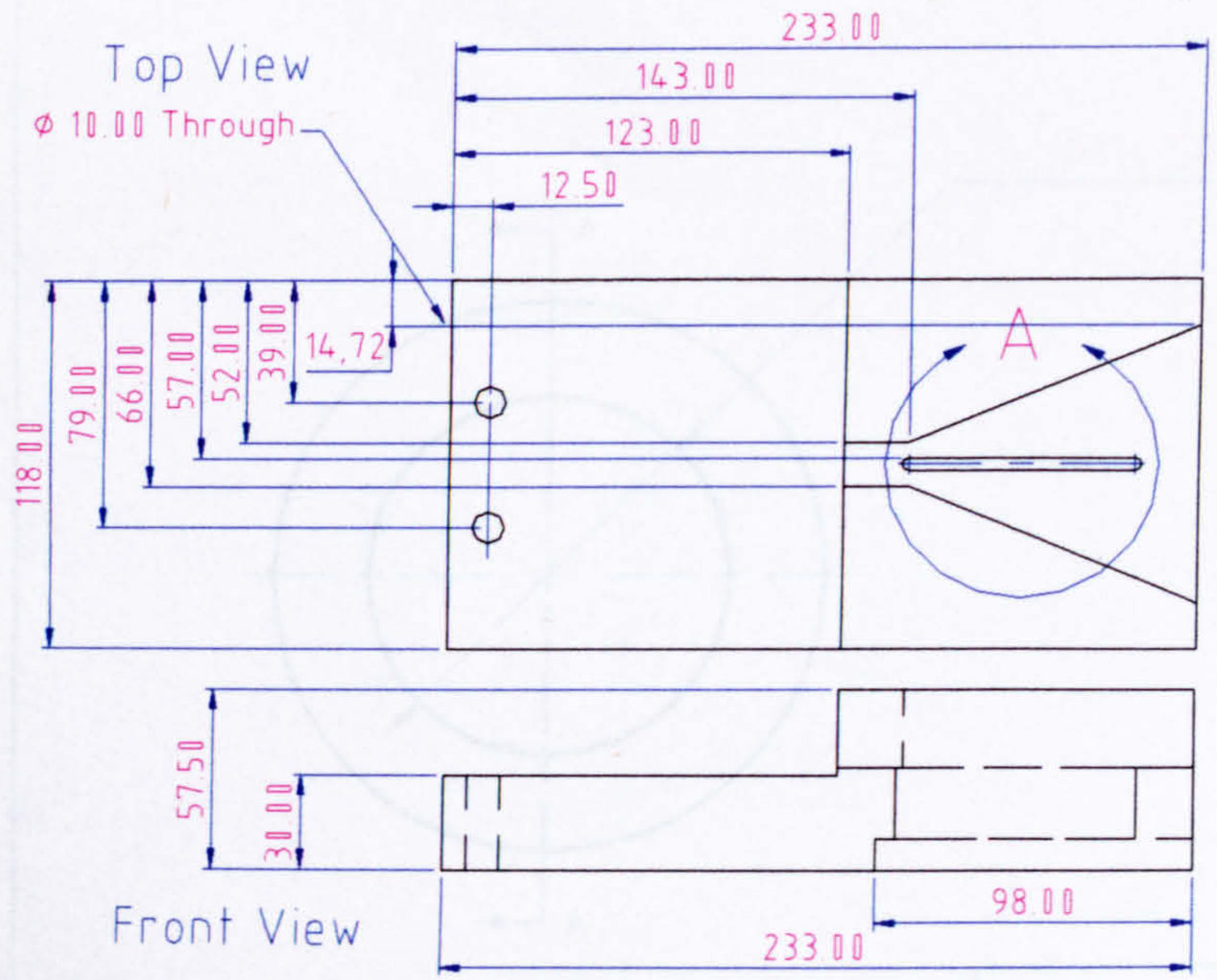

Front View

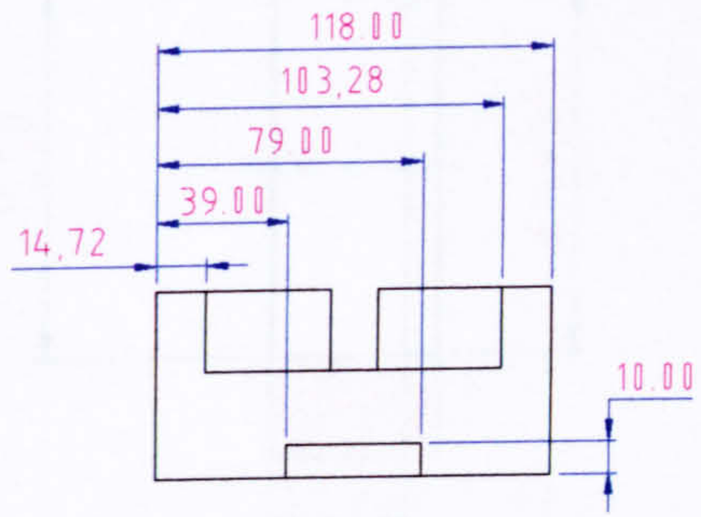

Left View

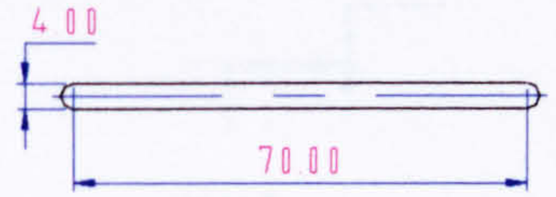

Detail A

All Dimensions are in mm Unless Otherwised Stated
All Tolerances are ±0.1mm Unless Otherwised Stated

University of Hertfordshire

Faculty of Engineering & Information Sciences

Dept.	Aerospace Civel & Mechanical Engineering Dept.			Title	Winding Vice
Designed By	Tareq El-Hasan	Scale	N.T.S.		
Drawn By	Moh Momani	Material	Fiber	Drawing /Part Number	WF2001-01A
Date	14/4/2002	Qty.	1	Sheet 1	Of 1

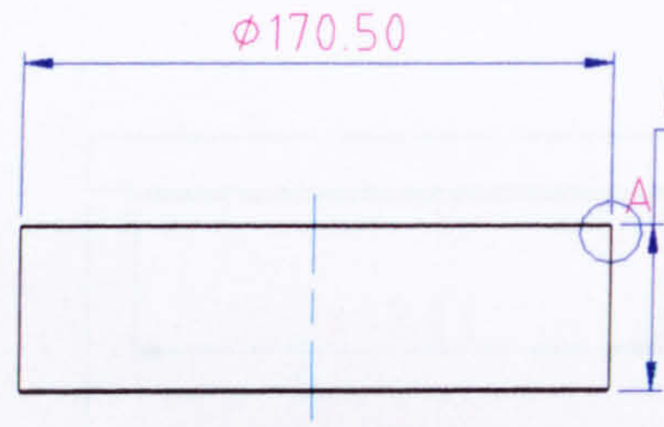

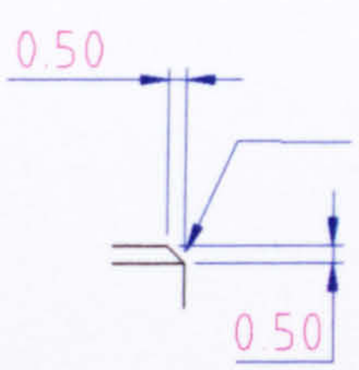

Detail A

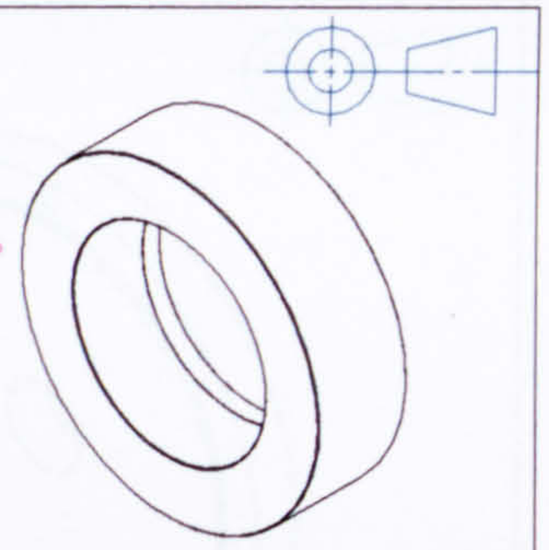

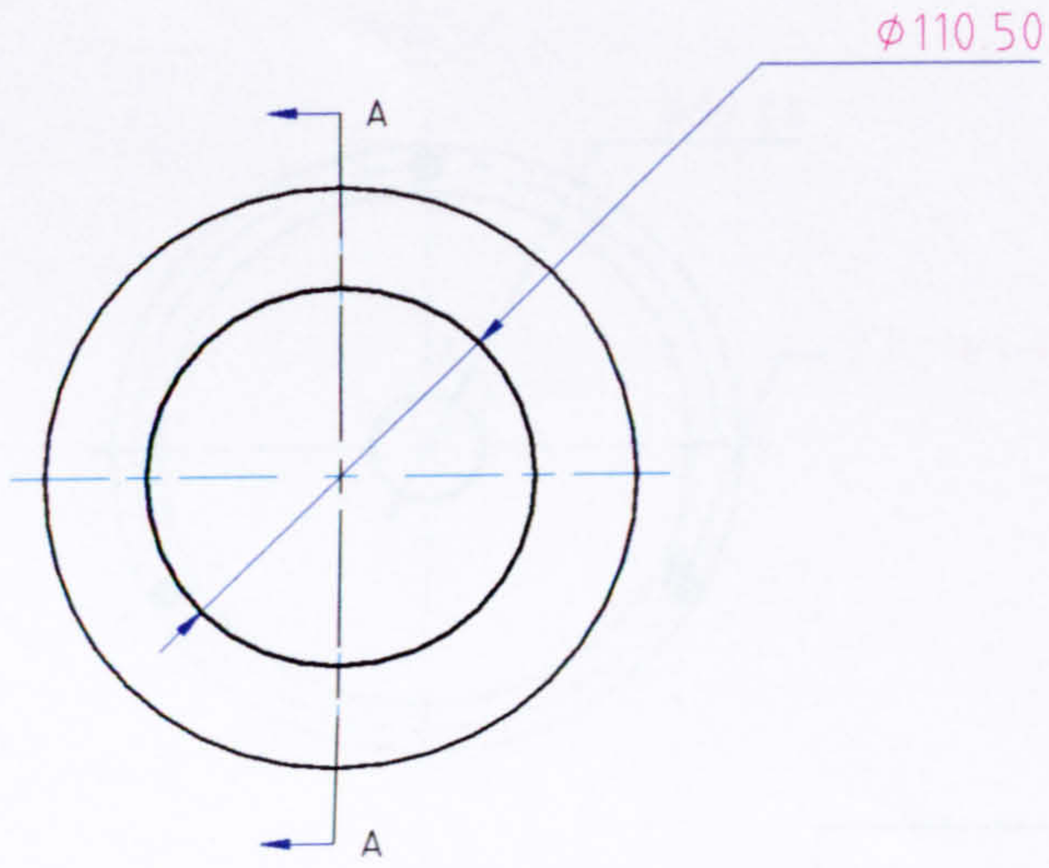

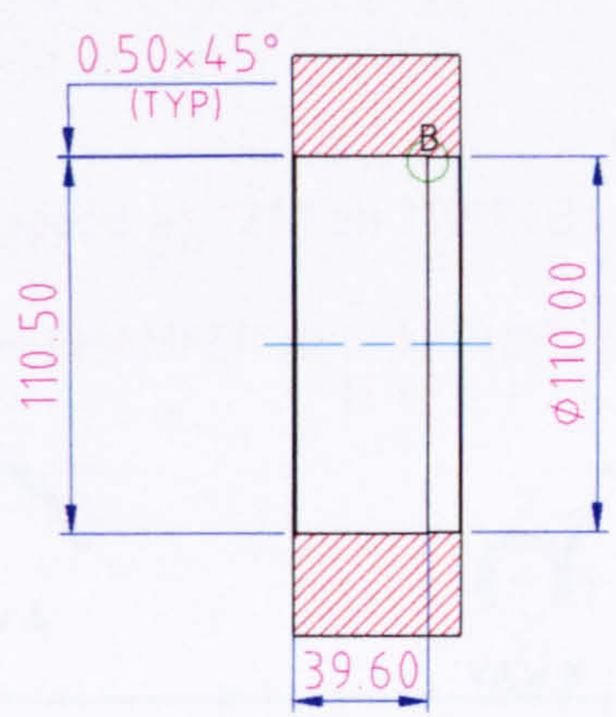

SECTION A-A

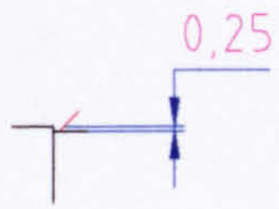

VIEW B

All Dimensions are in mm Unless Otherwised Stated
All Tolerances are ±0.01mm Unless Otherwised Stated

University of Hertfordshire
Faculty of Engineering & Information Sciences

Dept.	Aerospace Civil & Mechanical Engineering Dept.			Title	Shrinkfit Assembly Vessel
Designed By	Tareq ElHasan	Scale	N.T.S.		
Drawn By	Moh Momani	Material	Aluminum	Drawing /Part Number	SFA2001-01A
Date	10/4/2002	Qty.	1	Sheet 1	Of 1

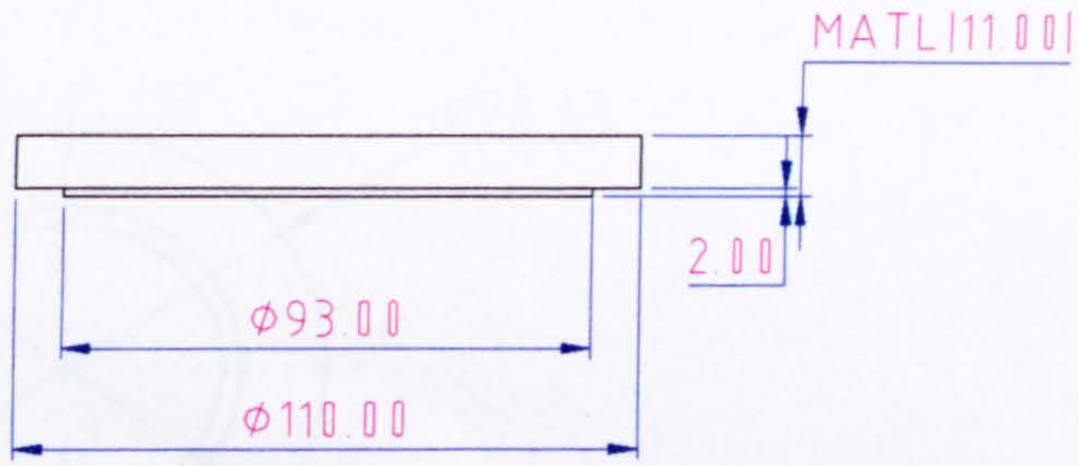

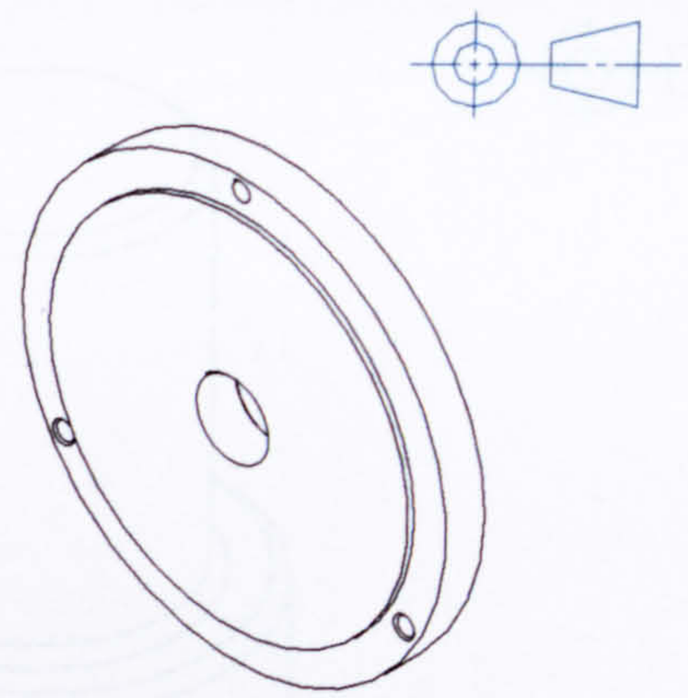

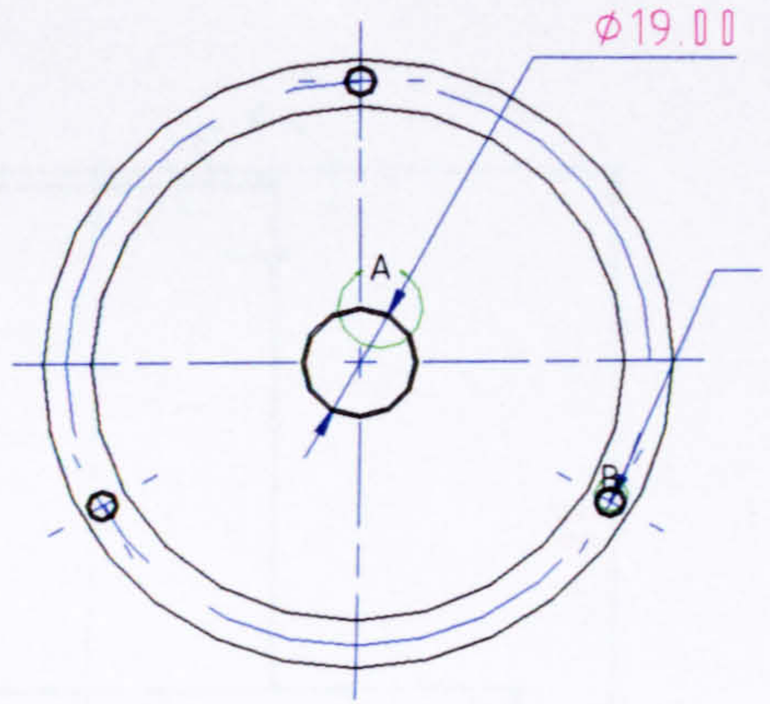

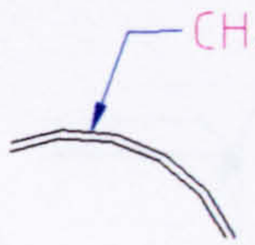

VIEW A

VIEW B

All Dimensions are in mm Unless Otherwised Stated

All Tolerances are ±0.01mm Unless Otherwised Stated

University of Hertfordshire

Faculty of Engineering & Information Sciences

Dept.	Aerospace Civil & Mechanical Engineering Dept.			Title	Shrinkfit Guidance Plate
Designed By	Tareq El-Hasan	Scale	N.T.S.		
Drawn By	Moh Momani	Material	Steel	Drawing /Part Number	SFA2002-01A
Date	10/4/2002	Qty.	1	Sheet 1	Of 1

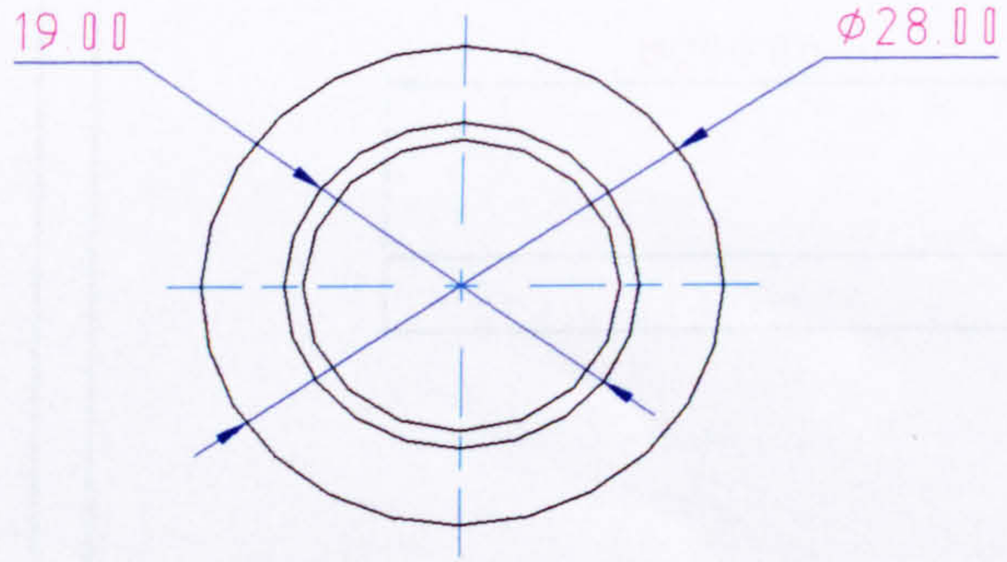

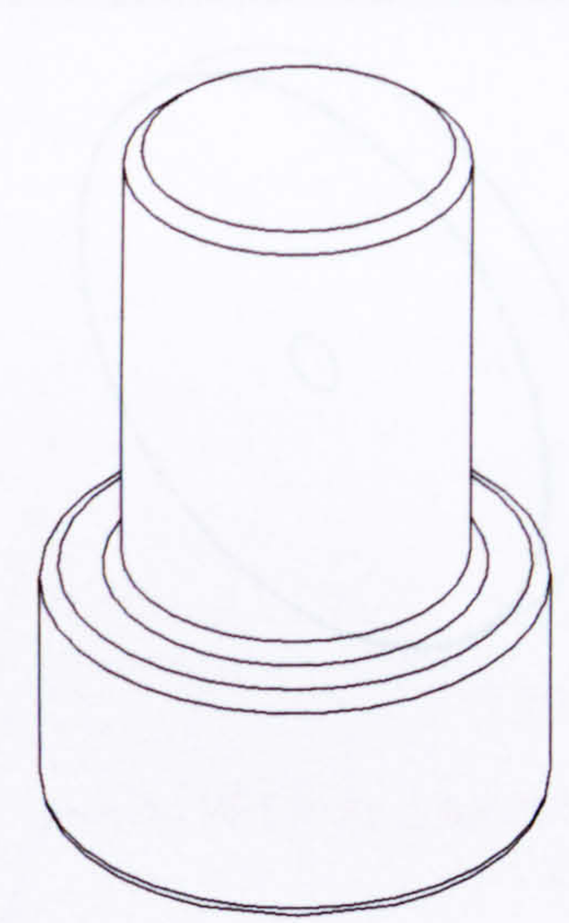

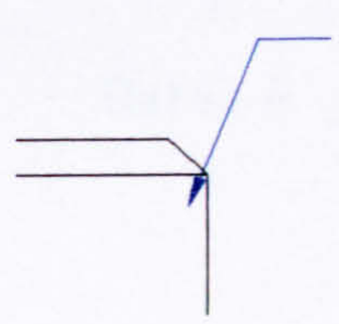

VIEW A

All Dimensions are in mm Unless Otherwised Stated
All Tolerances are ±0.01mm Unless Otherwised Stated

University of Hertfordshire
Faculty of Engineering & Information Sciences

Dept.	Aerospace Civil & Mechanical Engineering Dept.			Title	Shrinkfit Centering Rod
Designed By	Tareq El-Hasan	Scale	N.T.S.		
Drawn By	Moh Momani	Material	Teflon	Drawing /Part Number	SFA2003-01A
Date	10/4/2002	Qty.	1	Sheet 1	Of 1

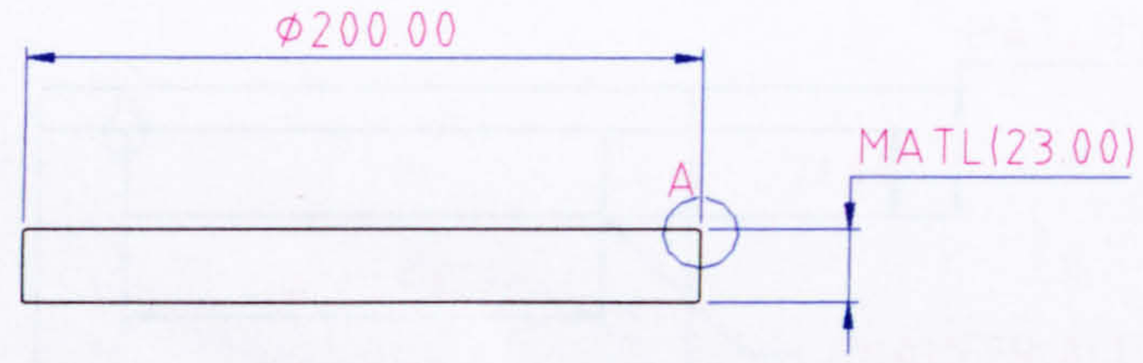

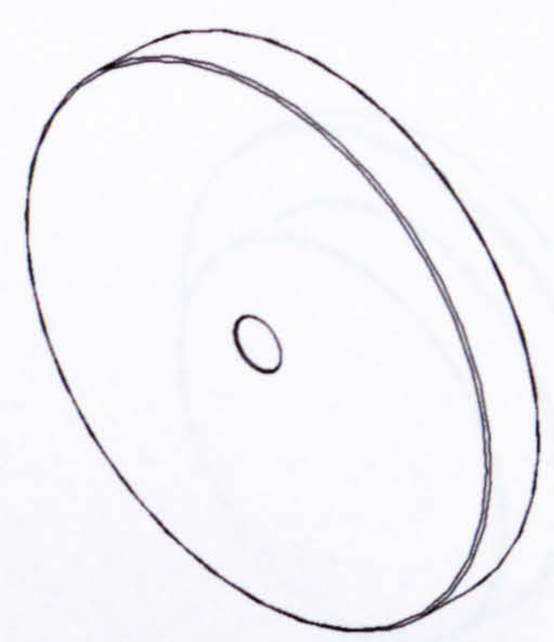

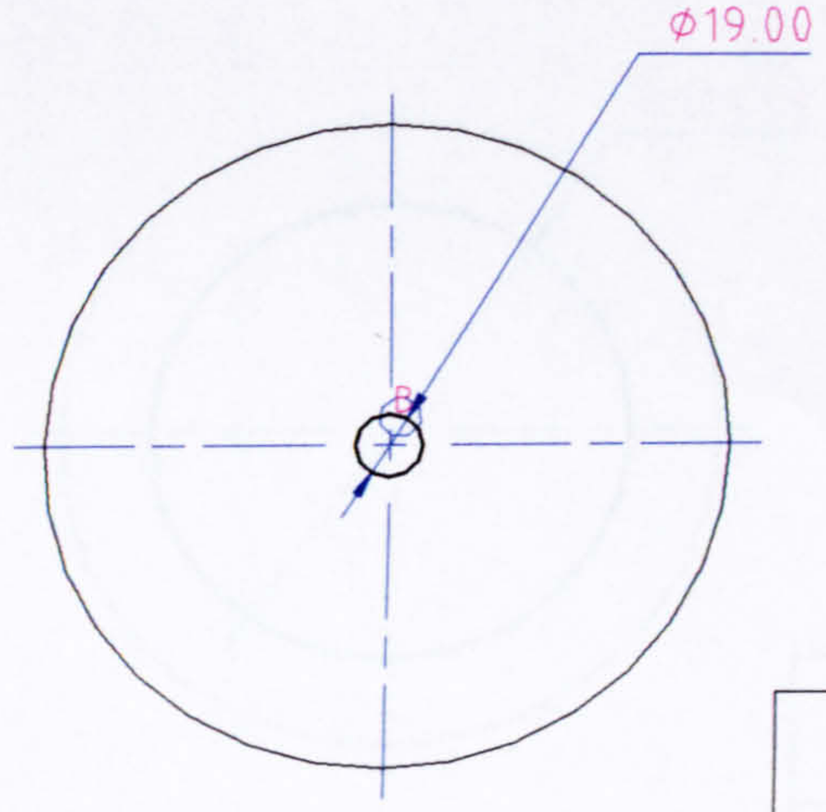

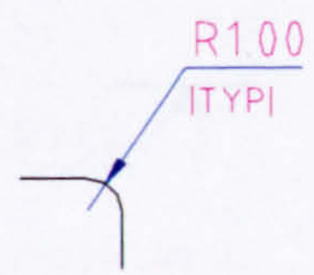

Detail A

VIEW B

All Dimensions are in mm Unless Otherwised Stated

All Tolerances are ±0.01mm Unless Otherwised Stated

University of Hertfordshire

Faculty of Engineering & Information Sciences

Dept.	Aerospace Civil & Mechanical Engineering Dept.			Title	Shrinkfit Base Plate
Designed By	Tareq EL-Hasan	Scale	N.T.S.		
Drawn By	Moh Momani	Material	Steel	Drawing /Part Number	SFA2004-01A
Date	10/4/2002	Qty.	1	Sheet 1	Of 1

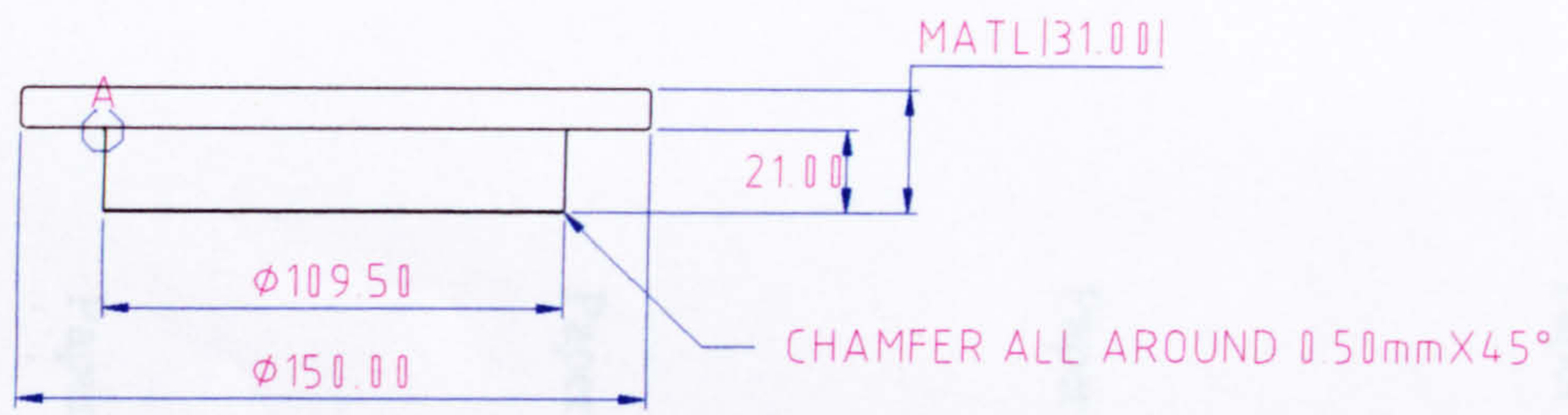

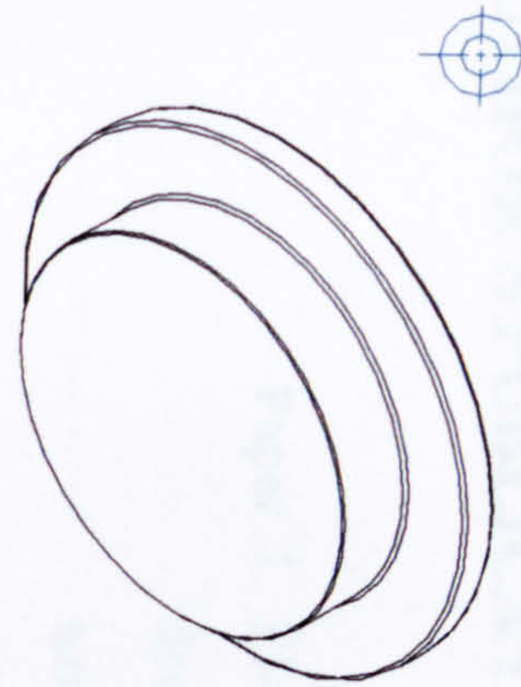

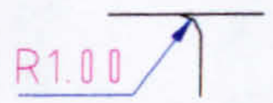

Detail A

All Dimensions are in mm Unless Otherwised Stated
All Tolerances are ±0.01mm Unless Otherwised Stated

University of Hertfordshire
Faculty of Engineering & Information Sciences

Dept.	Aerospace Civil & Mechanical Engineering Dept.			Title	Shrinkfit Pressing Cap
Designed By	Tareq El-Hasan	Scale	N.T.S.		
Drawn By	Moh Momani	Material	Steel	Drawing /Part Number	SFA2005-01A
Date	10/4/2002	Qty.	1	Sheet 1	Of 1

APPENDIX C

AUTHOR'S PUBLICATIONS RELATING TO THE STUDY

Paper 1. El-Hasan T. S., P. C. Luk et al. "Modular design of high-speed permanent-magnet axial-flux generators". *IEEE transactions on magnetics*, Vol. 36, No. 5, pp. 3558-3561, 2000.

Paper 2. Ebiad M., El-Hasan T. S. et al. "A unified approach for designing a radial flow gas turbine" *ASME* conference proceedings. Paper No: GT-2002-30578, Amsterdam, June 2002.

Paper 3. P. C. Luk and El-Hasan T. S. "Back iron design for high speed PM axial flux generators". *INTERMAG2003 Conference proceedings*. Digest No. 201, Boston, USA. April 2003.

Paper 4. El-Hasan T. S. and P. C. Luk "Magnet topology optimisation to reduce harmonics in high-speed axial flux generators". *INTERMAG2003 Conference proceedings*. Digest No. 886, Boston, USA. April 2003.

Paper 5. El-Hasan T. S. and P. C. Luk "Three-Dimensional FE analysis of disc type high-speed PM generators". *INTERMAG2003 Conference proceedings*. Digest No. 1235, Boston, USA. April 2003.

TEXT BOUND INTO

THE SPINE

Modular Design of High-Speed Permanent-Magnet Axial-Flux Generators

Tareq S. El-Hasan, Patrick C. K. Luk, *Member, IEEE*, F. S. Bhinder, and M. S. Ebaid

***Abstract*—A modular design methodology for high-speed permanent magnet (PM) axial flux generators is proposed. Based on first principles and therefore applicable to a wide range of generators, this analytical design method is illustrated with a case study on a 50 kVA, 420 V, 3-phase, 50 000 rpm PM generator. Results on the efficiency with a number of critical design parameters, including magnet size, number of modular stator stages and poles, are presented.**

***Index Terms*—Axial flux generators, high-speed generators, modular design, permanent magnet machines.**

Nomenclature

$e_{11'}$	induced voltage in winding segment $1-1'$ (V)
B_g	airgap magnetic flux density (Wb/m^2)
$R_{1,2}$	magnet inner and outer radius (m)
k_r	$= R_1/R_2$, the magnet (rotor) ratio
R_m	magnet mean radius (m)
R_b	rotor bore radius (m)
R	radial distance (m)
v	tangential speed at radius r (m/s)
ϕ	angle between conductor dr and vector $v \times B_g$ (rad)
ψ	angle between B_g and v vectors (rad)
d_b	windings bundle diameter (m)
k_f	winding backing factor (1.2 ~ 1.3%)
t_f	winding former axial thickness (m)
t_r	surface thickness of epoxy resin (m)
c_s	cooling space between the phases layers (m)
c_g	clearance gap between stator and rotor (m)
B_r	magnet remanence flux density (Wb/m^2)
l_g	effective airgap length (m)
P_{out}	power output (W)
$E_{A,rms}$	generator rms armature voltage/phase (V)
I_A	armature current (A)
p	generator number of poles/rotor stage
N_t	number of turns of one phase wave-winding
$\mathcal{R}_{g,m}$	airgap, magnet reluctance (A/Wb)
$A_{g,m}$	airgap, magnet surface area (m^2)
ρ	conductor resistivity (Ω.m)
ρ_a	air density (kg/m^3)
μ_a	air vescosity [kg/(m.s)]
$p_{e,w}$	eddy current, windage losses (W)
d	strand or conductor diameter (m)
B_p	peak flux density (T)
ω_m	mechanical rotational speed (rad/s)
ω_e	electrical angular frequency (rad/s)

I. Introduction

SMALL scale generating sets of high power densities, previously used predominately in military applications, are attracting growing attention for a wide variety of civil and industrial applications. One salient feature of these sets is the use of a high-speed generator directly coupled to a small gas turbine, resulting in significant reduction of weight and size due to the elimination of the gearbox [1], [2]. The use of rare-earth permanent magnets such as Ne–Fe–B for field excitation further reduces the size and weight. As higher compactness can be achieved at higher rotational speed, research opportunities exist for overall design methodology for these high speed systems where inter-relationships between the electrical and mechanical limits must be critically investigated.

Although such high speed systems in the form of turbo-alternators have been developed for aerospace applications [3], they are expensive and commercially rare, and have relatively low efficiencies. Due to commercial confidentiality, their design method is not available in the literature. However, design methods in permanent magnet generators have been discussed [4]–[6], albeit mainly on either lower output power or lower speed ranges.

In this paper, a design method based on a mathematical model derived from first principles is proposed. The generator model is a function of a number of dependent and interdependent variables. A parametric study is carried out to investigate the influence of each main variable on the geometry and performance. The design procedure uses an analytical and systematic approach aimed at optimizing a number of design parameters as well as ensuring the overall mechanical integrity and maximum power output. The first design parameter to be optimized in the procedure is magnet size i.e. rotor inner to outer diameter. Then at certain given speeds, the main design variables such as number of poles, number of turns per phase, number of modules, winding bundle diameter, number of strands per bundle and strand diameter are varied over a wide range.

Manuscript received February 9, 2000. This work was supported by the Royal Jordanian Armed forces (RJAF).

T. S. El-Hasan is with the Faculty of Engineering and Information Sciences, Department of Aerospace, Civil and Mechanical Engineering (ACME), University of Hertfordshire, Hatfield, UK, and the Royal Jordanian Armed Forces (RJAF) Amman, Jordan (e-mail: elhassan@hotmail.com).

P. C. K. Luk is with the Department of Electronic, Communication, and Electrical Engineering, University of Hertfordshire, Hatfield, UK (e-mail: pluk@ieee.org).

F. S. Bhinder is with the Royal Scientific Society, Amman Jordan. He was with the Department of Aerospace, Civil and Mechanical Engineering (ACME), University of Hertfordshire, Hatfield, UK (e-mail: bhinder@mars.rss.gov.jo).

M. S. Ebaid is with ACME, University of Hertfordshire, Hatfield, UK, and RJAF, Amman, Jordan (e-mail: ebaid@hotmail.com).

Publisher Item Identifier S 0018-9464(00)07961-9.

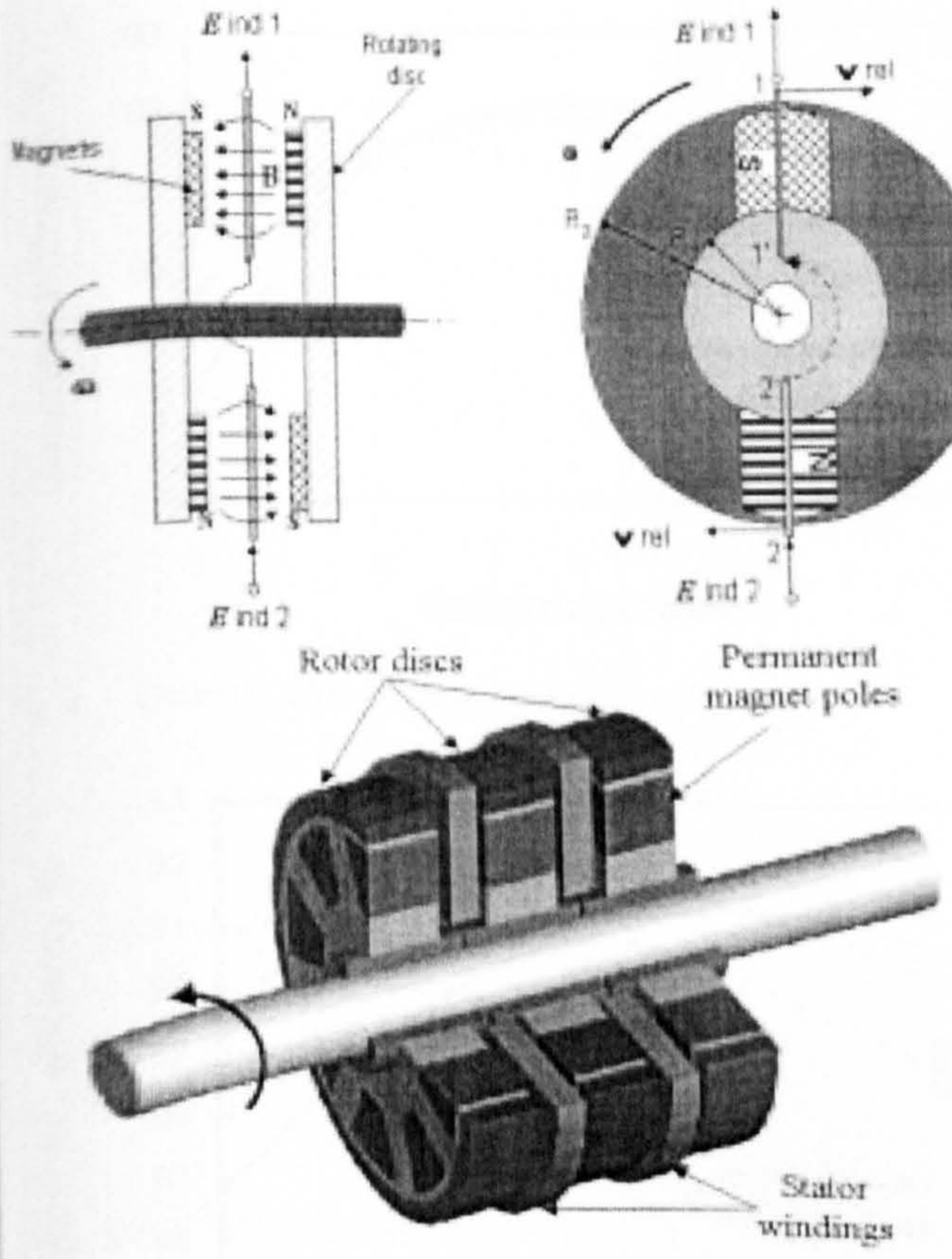

Fig. 1. Axial flux PM generator.

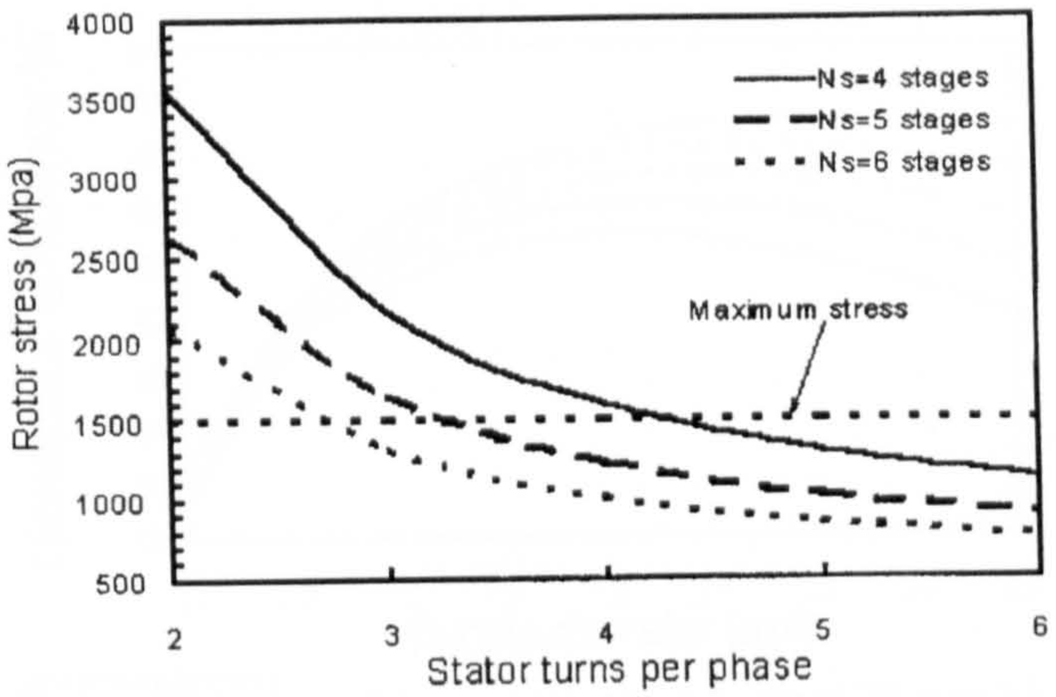

Fig. 2. Rotor hoop stresses versus number of turns/phase for different stator stages Ns (with $p = 8$).

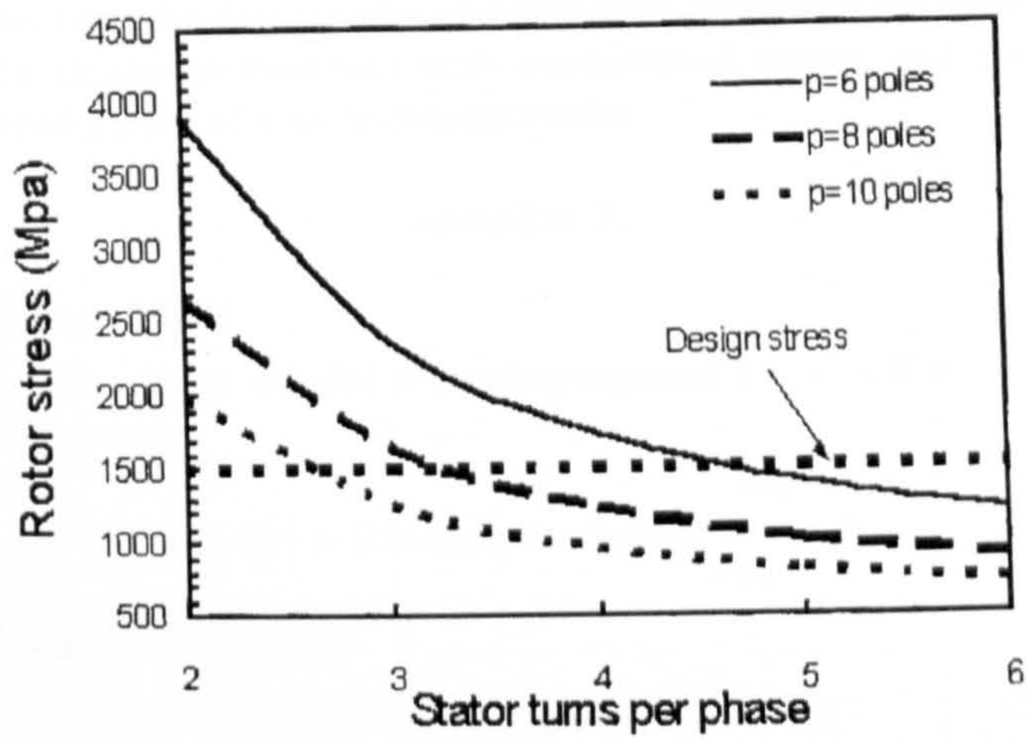

Fig. 3. Rotor hoop stresses versus no. of turns/phase for different pole number p (with $Ns = 5$).

The paper is organized as follows. In Section II, the structure of an axial flux PM generator is reviewed, and a mathematical model for the design modules is established. Section III presents and discusses the analytical results on the case study of a 50 kVA, 420 V, 3-phase, 50 000 rpm PM generator. Concluding remarks are in Section IV.

II. Modeling and Optimization of Modular Design

A. Review of Design on Axial Flux PM Generators

Fig. 1 shows a typical modular axial flux PM generator [4]. In Fig. 1(a), the magnets are bonded to the surface of the rotating disc, and stator windings are arranged normal to the axis of rotation between the two opposite discs. Alternative disc types with embedded magnets inside a "spider" retainment shell to reduce centrifugal forces at very high speed have been reported [1]. Fig. 1(b) is an exploded view showing a two-rotor configuration with the ferrous keeper discs and a single stator stage. For higher power ratings, N_s number of stator stages and $(N_s + 1)$ number of rotors are assembled. The terminals of the windings are connected either in series or in parallel.

B. Mathematical Model

The power output per unit volume at a given speed, the most important design parameter for these high speed generator sets, is related to the concept of *electric loading* and the *magnetic loading*. For the model depicted in Fig. 1, the determination of the electric loading necessitates the use of a voltage model based on the structure. The determination of magnetic loading concerns the optimization of magnet size, shape and orientation. The derivations of the associated formulae from first principles, including detailed design parameters, are given in the Appendix.

III. Analysis and Analytical Results

The performance analysis is based on the design study of a 50 000 rpm, 50 kVA, 3-phase, 420 V generator model at full load and at a power factor of 0.9. The variation of efficiency versus the design parameters (p, Nt, Ns) are studied over specified ranges. Magnetic loading of 0.56 Wb/m^2 is used. Stress calculations based on the pessimistic formulae developed in [7], [8], with a safety margin of 20% of the operating speed, are first used to establish the mechanical integrity of the system. The effects on rotor stress by the number of stator turns per phase for different stator stages and pole number are shown in Figs. 2 and 3 respectively. A design value of 1500 Mpa based on the use of a 6 mm of carbon fiber shell and 15 mm of rotor bore radius, is chosen in the case study. The efficiency variations with stator turns per phase at different stator stages and pole number are shown in Figs. 4 and 5. It is noted that a maximum efficiency of 92% is achievable with this modular axial flux design. In high-speed generators, maintaining low values for rotor

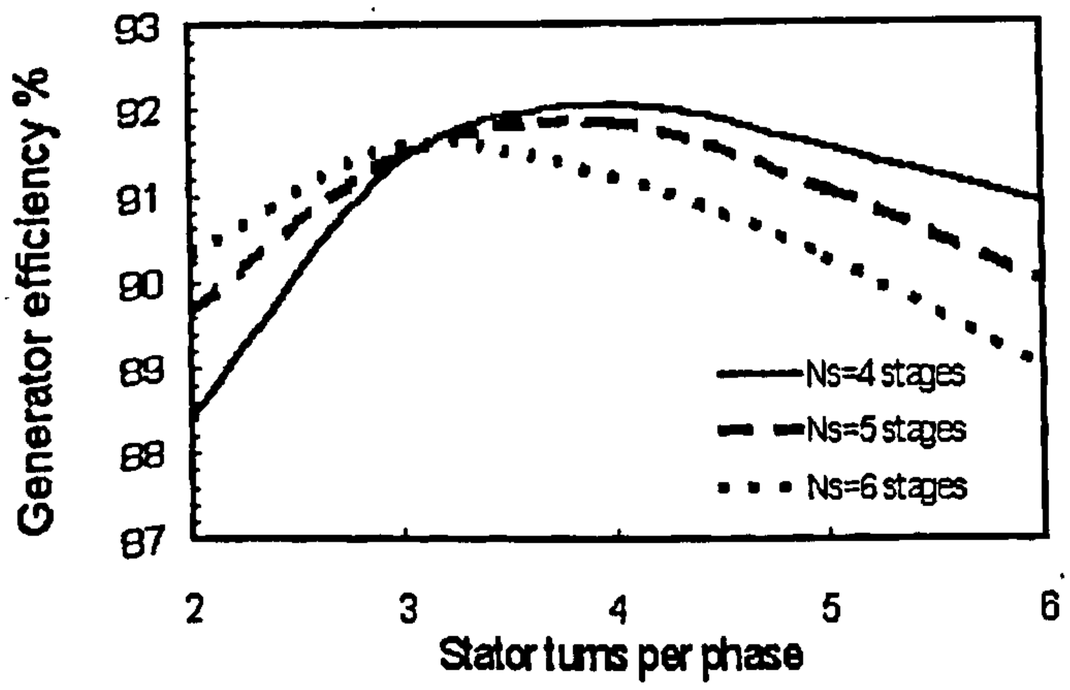

Fig. 4. Generator efficiency versus number of turns for different Ns.

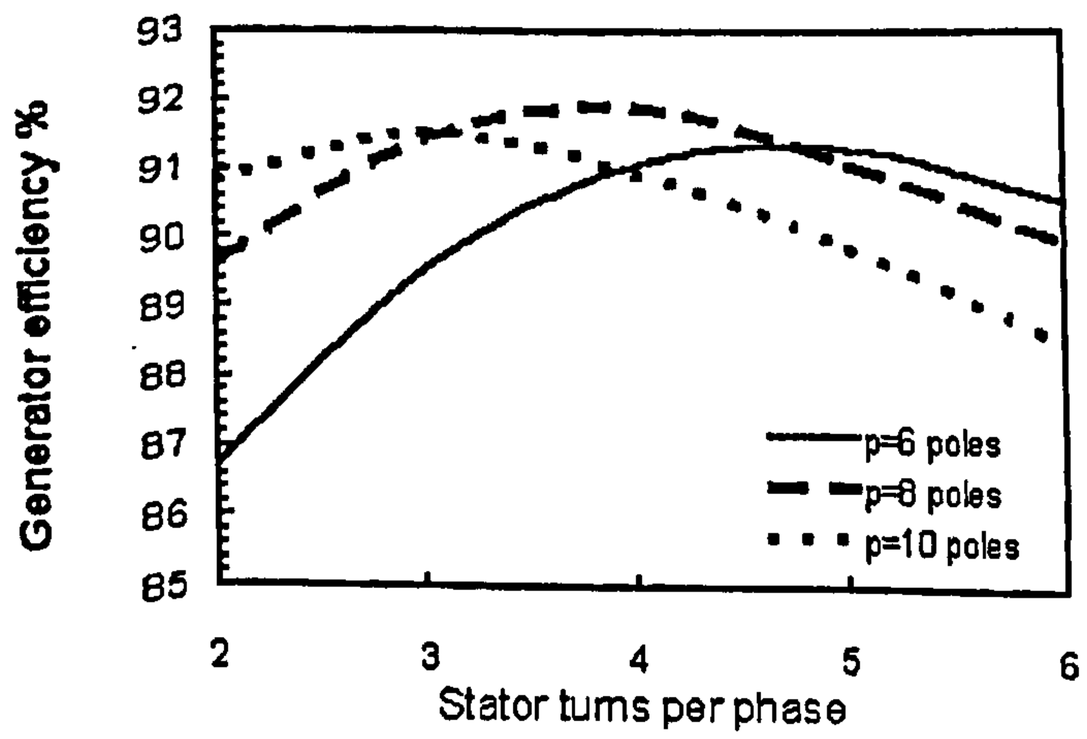

Fig. 5. Generator efficiency versus no. of turns for different no. of poles p.

outer radius is important to minimize windage losses which can be calculated based on the formula [8] shown in Appendix. The optimization of rotor radius involves the study of the bundle diameter d_b, strand diameter d_s and number of strands per bundle, and how they affect eddy current and stator copper losses. Results of calculated filling factor f_f for measured values of d_b and d_s are found in the range of (0.73 ~ 0.76) for different strand and bundle diameters. Eddy current losses are calculated using the formulae [6] in the Appendix. Optimized values of d_b and d_s shown in Fig. 6 illustrate how the method of windings affects the efficiency at very high speeds.

IV. Conclusion

A design methodology for a modular high-speed PM axial-flux generator from first principles has been proposed. Optimization of the design parameters is shown to be is very complex due to the multi-variable nature of the system. Here a good first degree of approximation is achieved by examining the variations of efficiency with different parameters. An efficiency of 92% in this proposed design, considerably superior to conventional low speed generators, has been achieved where iron losses have been eliminated, and others have been minimized by proper selection of design parameters. These initially promising results will be followed up by further work

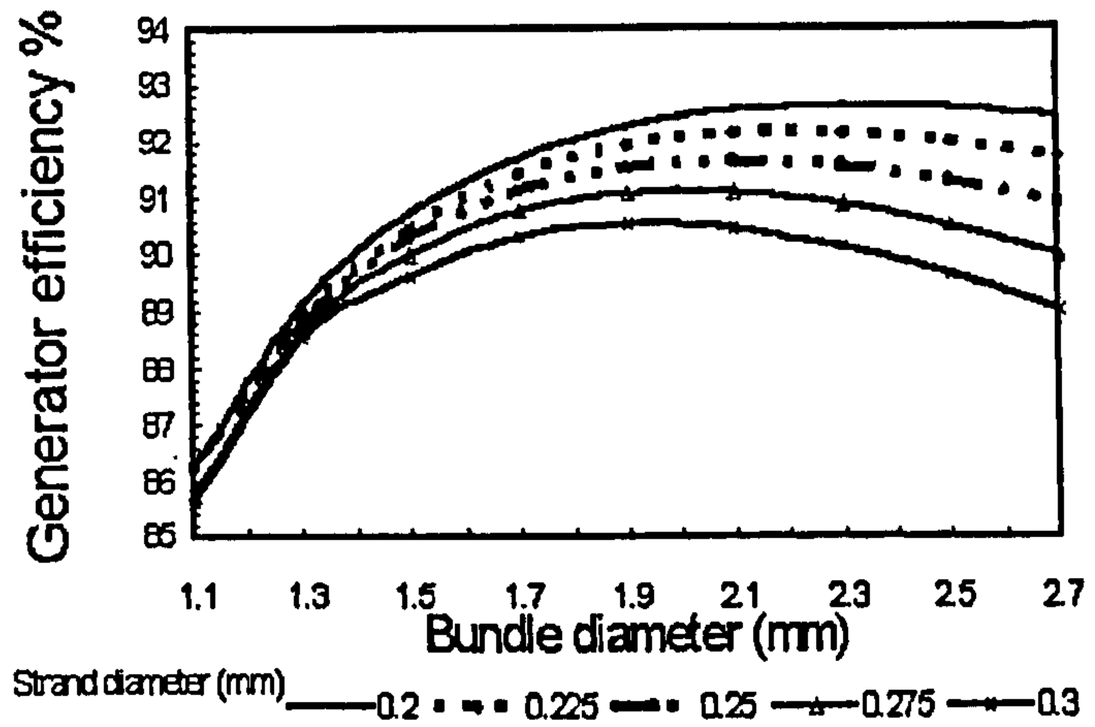

Fig. 6. Efficiency versus bundle diameter for different strands.

involving the development of a prototype generator to validate the design methodology with experimental results, and the development of a finite element model.

Appendix I

Voltage Model

The voltage induced in winding segment $1 - 1'$ in Fig. 1(a) is given by

$$e_{11'}(\psi) = 0.5\omega_m B_g \cos\phi \sin\psi \int_{R_1}^{R_2} r\,dr \qquad (1)$$

Integrating (1) gives

$$e_{11'}(\psi) = 0.5\omega_m B_g \sin\psi (R_2^2 - R_1^2) \qquad (2)$$

Induced voltage in the segment $2 - 2'$ is

$$e_{22'}(\psi) = 0.5\omega_m B_g (R_2^2 - R_1^2) \sin(180 - \psi) \qquad (3)$$

Hence, the total voltage $e(\psi)$ in the two segments is

$$e(\psi) = e_{11'}(\psi) + e_{22'}(\psi) \qquad (4)$$

Thus, for pN_t conductors in a single-phase coil, the total rms induced armature voltage of N_s stator stages is given by

$$E_{A,\text{rms}} = 0.353 p N_t N_s \omega_m B_g (R_2^2 - R_1^2) \qquad (5)$$

Electric Loading and Magnet Size Optimization

From (5), assuming a unity power factor and neglecting any drop voltage across the three-phase windings, the output power P_{out} is given by

$$P_{\text{out}} = 3 \times \left[0.353 p N_t N_s \omega_m B_g (R_2^2 - R_1^2)\right] I_A \qquad (6)$$

The electric loading q at the inner radius of the stator is:

$$q = 3 I_A p N_t / (2\pi R_1) \qquad (7)$$

Substituting (7) into (6) and rearranging yields

$$P_{\text{out}} = 0.707\pi q N_s \omega_m B_g R_2^3 k_r (1 - k_r^2) \qquad (8)$$

Rearranging (8) gives

$$P_{\text{out}} = C k_r (1 - k_r^2) \qquad (9)$$

where

$$C = 0.707\pi q B_g \omega_m N_s R_2^3 \tag{10}$$

From (9), $dP_{\text{out}}/dk_r = 0$ gives conditions for maximum P_{out}, which is $k_r = 0.577$. Once R_1 and R_2 are found, the magnet axial length l_m is calculated as

$$l_m = B_g l_g/(B_r - B_g) \tag{11}$$

$$l_g = 3(b_f d_b + t_f + t_r + c_s) + 2c_g \tag{12}$$

The magnet inner radius R_1 is calculated as

$$R_1 = R_b + N_t d_b b_f + c_g \tag{13}$$

Self L_{ss} and armature L_{sr} inductances are derived based in stator and magnet geometry and calculated respectively as

$$L_{ss} = N_t^2 p^2 \mu_0 (R_2 - R_1)(t_f + d_b)/(8\pi R_m) \tag{14}$$

$$L_{sr} = p N_t^2 [1/(\Re_g + \Re_m)] \tag{15}$$

where:

$$\Re_g = l_g/(\mu_0 A_g) \quad \text{and} \quad \Re_m = l_m/(\mu_0 A_m)$$

Windage and eddy current losses are found by (16) and (17) respectively:

$$P_w = 0.0311(s/R)^{-0.25} \mu^{0.25} \rho_a^{0.75} \omega_m^{2.75} R^{4.5} \tag{16}$$

$$P_e = B_p^2 \omega_e^2 d^2/(32\rho) \tag{17}$$

REFERENCES

[1] K. R. Pullen *et al.*, "The high speed axial flux disc generator-unlocking the potential of the automotive gas turbine," in *Proceedings of IEE Colloquium Machines and Drives for Electric and Hybrid Vehicles*, 1996.

[2] C. Rodgers, "Performance development history—10 kW turboalternator," Solar div., International Harvester Co.

[3] "Potassium turboalternator (KTA) preliminary design study,", NASSA contractor report CR-1499, vol. II, Alternator Parametric Design, March 1970.

[4] B. J. Chalmers and E. Spooner *et al.*, "Compact permanent-magnet machines," *Electric Machines and Power Systems*, vol. 25, pp. 635–648, 1997.

[5] B. P. James and B. A. T. Al Zahawi, "A high speed alternator for a small scale gas turbine CHP unit," *Electrical Machines and Drives, Conference Publication*, no. 412, September 11–13, 1995.

[6] E. Spooner and B. J. Chalmers, "Torus: A slotless, toroidal-stator, permanent-magnet generator," *IEE Proceedings—B. Electric Power Applications*, vol. 139, no. 6, November 1992.

[7] A. S. Hall and A. R. Holowenko, *Schaum's Outline of Theory and Problems of Machine Design*, SI Metric ed: McGraw Hill, 1980.

[8] K. R. Pullen, "The design and development of a small gas turbine and high speed generator," Ph.D. dissertation, Imperial Collage, University of London, 1991.

ASME Conference paper No: GT-2003-30578
Amsterdam, June 2003.

A UNIFIED APPROACH FOR DESIGNING A RADIAL FLOW GAS TURBINE

M. S. Y Ebaid, F. S Bhinder, G. H. Khdairi and T. S. El-Hasan

ABSTRACT

Radial flow turbo machines have been used for a long time in a variety of applications such as turbochargers for reciprocating internal combustion engines, cryogenics, auxiliary power units, and air conditioning of aircraft cabins. Hence numerous papers have been written on the design and performance of these machines. The only justification for yet another paper is that it would describe a unified approach for designing a single stage inward flow radial turbine comprising a rotor and the casing. The turbine is designed to drive a direct-coupled permanent magnet high- speed alternator running at 60000 rev/min. and developing 60 kW electrical power.

The freedom of choice of the tip diameter and the tip width of the rotor that would be necessary for optimum isentropic efficiency of the turbine stage was restricted by the specified rotational speed and power output. Hence, an optimisation procedure was developed for determining the principal dimension of the rotor.

The mean relative velocity in the direction of the flow would be accelerated but flow velocity on the blade surfaces experiences a significant space rate of deceleration. The rate of deceleration can be controlled by means of a proper choice of the axial length of the rotor. A prescribed mean stream velocity distribution procedure was used to spread the rate of deceleration the mean flow velocity along the meridianal length of the flow passages.

The nozzle-less volute casing was designed to satisfy the mass flow rate, energy and angular momentum equations simultaneously.

The paper describes the design procedure for both the rotor and the casing. As interest in developing gas turbine based hybrid road vehicles is growing, the authors believe that the paper would lead to a stimulating discussion.

NOTATION

A	Area normal to mean flow direction (m^2)
b	Blade width (m)
B_f	Blockage factor
C	Absolute flow velocity of gas (m/s)
C_p	Specific heat capacity at constant pressure for gas (kJ/kgK)
d	Diameter (m)
f_c	Friction factor
J	Polar second moment of area (m^4)
M	Absolute Mach number
M_r	Relative Mach number
$\dot{m}$	Mass flow rate (kg/s)
N	Rotational speed (rpm)
N_s	Specific speed
n_b	Number of blades
P	Stagnation pressure (N/m^2, bar)
R	Degree of reaction
R_e	Reynolds number
r_c	Radius of curvature (m)
S_p	Speed parameter
S_T	Specific Torque
T	Stagnation temperature (K)
t	Blade thickness (m)
u	Rotor tip velocity (m/s)
v	Relative velocity (m/s)
W	Work output (kJ)
z	Axial length (m)

Greek symbols

α	Absolute flow angle relative to axial direction (degree), angle between meridional streamline and axis
β	Relative flow angle relative to axial direction (degree), angle between relative velocity vector and meridional plane
β_b	Blade angle
θ	Relative angular co-ordinate
γ	Ratio of specific heats
η	Efficiency of a process
ρ	Gas density (kg/m^3)
ψ	Blade loading
ϕ	Pressure loss coefficient

φ	Centriod
σ_{shear}	Shear stress (N/m^2)
τ	Torque (Nm)
ω	Angular velocity (rad/s)
Δ	Small increment of

Subscripts

0	Stagnation conditions
3	Inlet turbine station
2	Inlet rotor station
1	Outlet rotor station at mean
a	Air
av	Average
c	Compressor
e	Exit condition , exducer
h	Hub
i	Inlet condition
m	Mean
s	Spouting velocity, shroud
SFL	Skin friction loss
t	Turbine
tt	Total to total
w	Tangential direction
rms	Root mean square
r	Radial direction
x	Any station inside the rotor passage

INTRODUCTION

Inward radial turbines have established their place in industry, especially in the field of small turbo-machinery because of their simplicity, reliability, lower pollutant emissions, multi-fuel capabilities and fast response. These attractive features have made them ideal prime movers for many applications and in particular, producing small electrical power generation in the range 10-100 kW.

Research programms regarding the design of these machines (the rotor and the casing) have been cited in the open literature. For the rotor design, **Von der Nuell [1] and Balje [2,3]** both suggested that the choice of the principal dimensions might be based on specific speed and specific diameter. **Rohlik [4]** developed a relationship between specific speed and a number of important design ratio. He argued that for the same specific speed, it was possible to produce a large number of rotor shapes by choosing different combination of these ratios. Therefore, the problem was to find specific speed that would result in maximum efficiency.

Wallace *et al.* **[5]**, used one-dimensional analysis together with empirical loss models to determine the principal dimensions of the rotor. Further studies on one-dimensional design analysis procedures for radial flow turbines have been described by other authors, **Rodgers [6], Whitfield and Baines [7] and Wasserbauer and Glassman [8].** The common features of these are that the user has to specify the geometry of the turbine, together with any assumptions about losses from which to calculate an efficiency values. Since most of the turbine geometry is likely to be undefined and many different assumptions about losses are possible, then a large combinations are possible and must be investigated. This is time consuming and there is very incentive to reduce the time taken and the number of cases to be investigated. **Whitfield [9]** proposed a method based on maximizing efficiency by minimizing the energy losses of the fluid which are considered to be a function of the square of the velocity and expressed at inlet and outlet conditions in terms of Mach numbers. The procedures is largely non –dimensional and is based on an initial power ratio and an estimate of the of the total to static efficiency. The later in particular can cause problems, because the designer has still to decide on the likely magnitude of the efficiency can be achieved.

In recent years, a number of computer aided design procedures have been developed for turbine rotors. **Benson and Fisher [10] and Baines *et al.* [11]** in their work assumed a preliminary shape, which would be improved progressively through analysis. This work is an indirect mode and the main draw back of this approach is that a decision on whether or not a particular step produces a satisfactory result tends to be made quite arbitrarily. Furthermore, it is not a simple matter to know what changes in the geometry would produce the desired results.

For the turbine casing design, it is often based on the assumptions of an adiabatic incompressible flow, together with a free vortex distribution about the rotor. The passage design is specified in terms of area to radius ratio at the centriod as described by **Bhinder [12], Chapple *et al* [13], Hussian *et al* [14]. Whitfield and Noor [15]** extended the work further by considering the flow to be viscous and compressible.

From the foregoing, several limitations to these procedures can be identified which deserve attentions:

1. Most of the design methodology was based on iterative procedure involving successive modifications to the hub, shroud and blade profiles to arrive at an acceptable and efficient design.

2. For a given set of performance requirements such as power output, pressure ratio and rotational speed or mass flow parameter, several rotor shapes may be drawn which would appear to meet the specifications. The choice of optimum shape is by no means simple.

3. The choice of number of rotor blades was based on empirical formulae given in the open literature and the choice of axial length was chosen arbitrarily based on engineering practice.

4. Papers described the whole design of the rotor and the casing was scarce for a specific rotational speed and power.

This paper provides a unified approach for designing radial flow gas turbines, which does not suffer from the above limitations.

PROPOSED DESIGN PROCEDURE

The design procedure of an inward flow radial turbine IFR may be divided into stages, namely:

1. The design of the turbine rotor at which the design methodology consists of two main programmes: Firstly, the determination of the optimum principal dimensions of the turbine rotor and number of blades. Secondly, the choice of axial length and optimisation of passage geometry for a prescribed mean stream velocity distribution.

2. The design of the nozzle-less volute casing where the mass flow rate, energy and angular momentum equations must be satisfied simultaneously.

ROTOR DESIGN

The choice of the principal dimensions of the IFR turbine rotor.

The geometrical shape of a typical IFR turbine rotor is shown in Fig.1. The inlet and outlet velocity triangles diagramms and the thermodynamics of the expansion process are illustrated in Figs. 2 and 3, respectively.

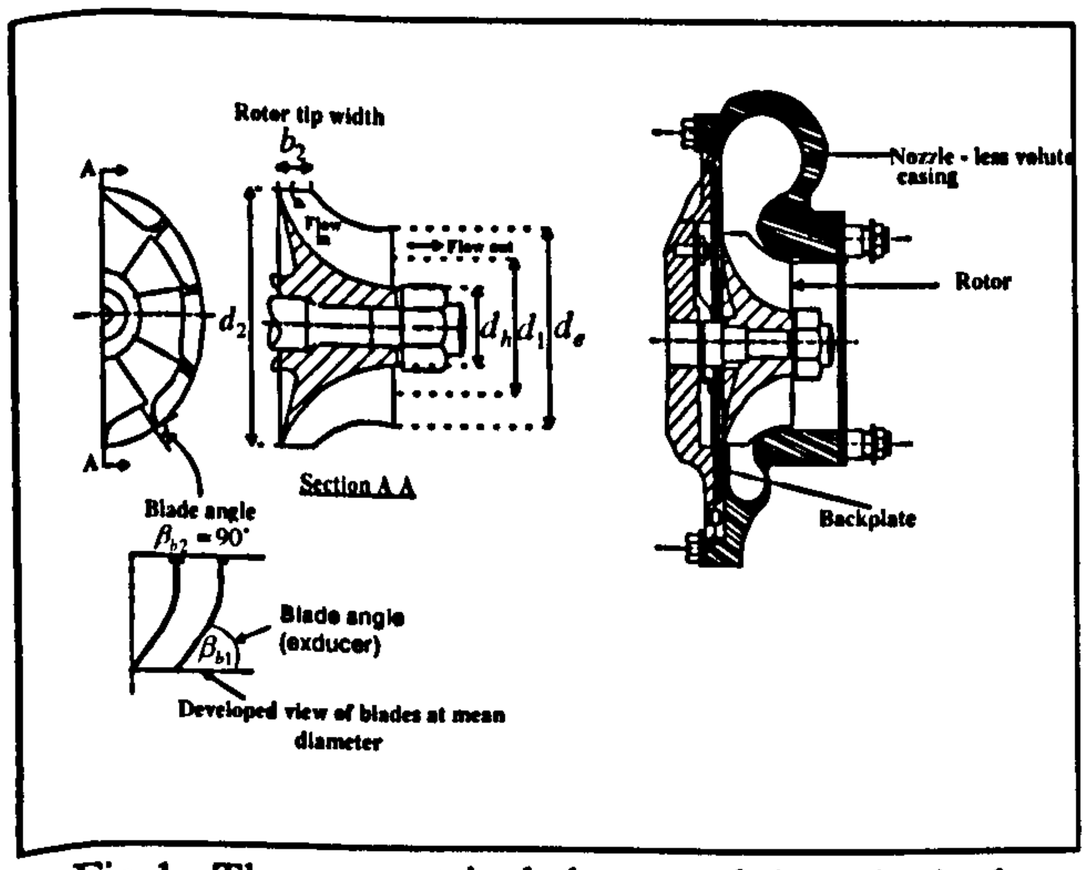

Fig.1 The geometrical shape and the principal dimensions of the IFR gas turbine

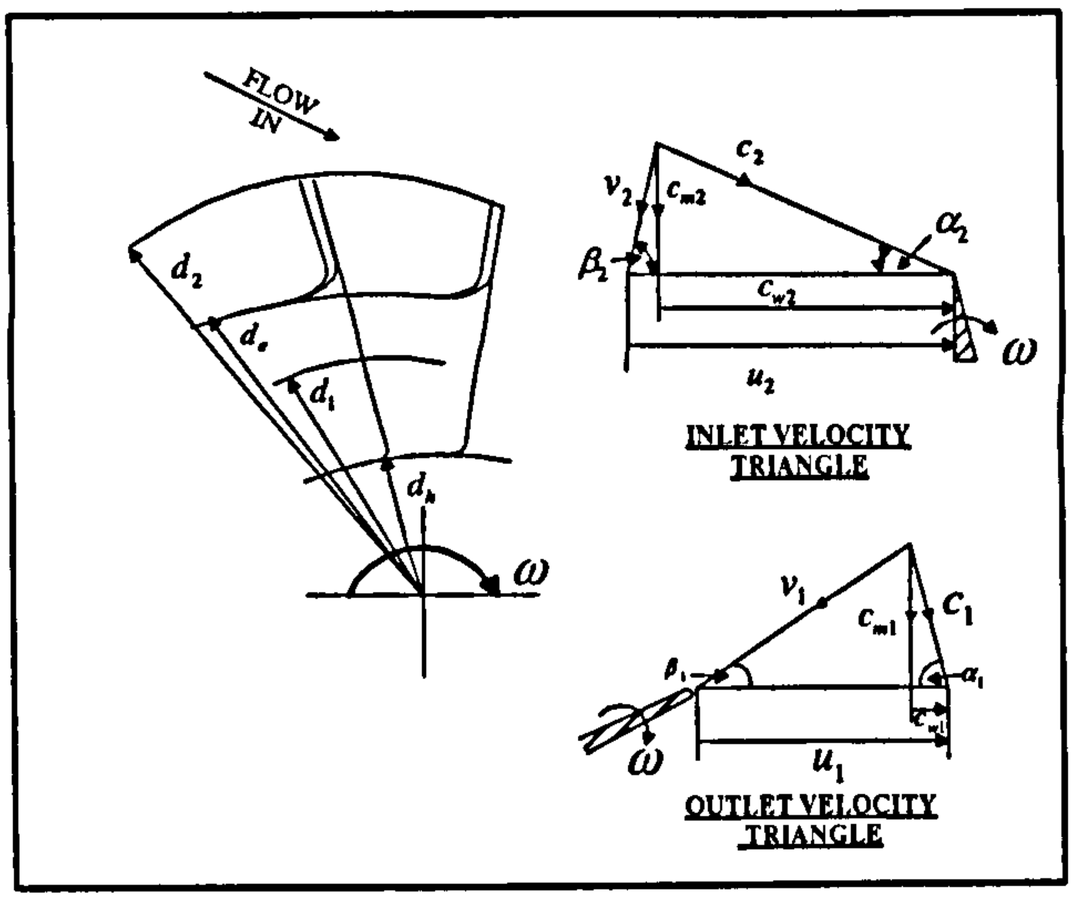

Fig.2 Velocity triangles of an inward flow radial gas turbine

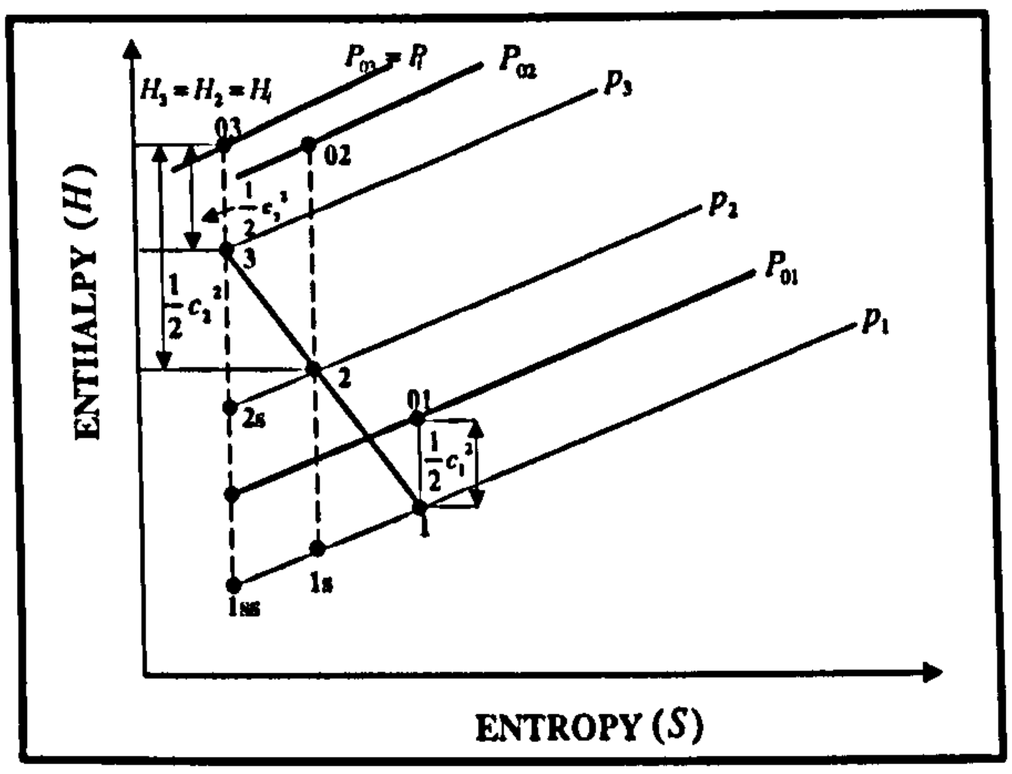

Fig. 3 Enthalpy – entropy diagram for a turbine stage

The momentum, continuity and energy equations can be combined to produce the following principal equations listed hereafter:

1. Speed parameter

$$\frac{d_2 N}{\sqrt{C_p T_i}} = \left(\frac{60\sqrt{2}}{\pi}\right)\left(\frac{u_2}{c_s}\right)\left[\sqrt{1-\left(\frac{P_e}{P_i}\right)^{\gamma-1/\gamma}}\right] \qquad (1)$$

2. Absoluter flow angle at rotor inlet

$$\cos\alpha_2 = \left(\frac{c_{w2}}{u_2}\right)\left(\frac{\pi}{60}\right)\left(\frac{d_2 N}{\sqrt{C_p T_i}}\right)\left(\sqrt{\frac{1+\frac{\gamma-1}{2}M_2^2}{(\gamma-1)M_2^2}}\right) \qquad (2)$$

3. Blade width to tip diameter ratio

$$\left(\frac{b_2}{d_2}\right)=\frac{\dot{m}\sqrt{C_pT_i}}{d_2^{\,2}P_i}\left[\frac{1}{\pi B_{f_2}}\left(\frac{\sqrt{\gamma-1}}{\gamma}\right)\right]\left[\frac{\left(1+\frac{\gamma-1}{2}M_2^{\,2}\right)^{\gamma+1/2(\gamma-1)}}{M_2\sin\alpha_2}\right] \quad (3)$$

4. Mass flow parameter

$$\frac{\dot{m}\sqrt{C_pT_i}}{d_2^{\,2}P_i}=\left(\frac{P_e}{P_i}\right)\left[\frac{1}{\left\{1-\eta_{tt}\left(1-(\frac{P_e}{P_i})^{\gamma-1/\gamma}\right)\right\}}\right]^{1/2}\left[B_{f_1}\left(\frac{\pi}{4}\right)\left(\frac{\gamma}{\sqrt{\gamma-1}}\right)\left((\frac{d_e}{d_2})^2-(\frac{d_h}{d_2})^2\right)\right]$$

$$\times\left[\frac{M_{er}\sin\beta_e}{\left(1+(\frac{\gamma-1}{2})(M_{er}\sin\beta_e)^2\right)^{\gamma+1/2(\gamma-1)}}\right] \quad (4)$$

$$B_{f_2}=1-\frac{1}{\pi}\left[n\left(\frac{\bar{t}_2}{d_2}\right)\right] \quad (5)$$

$$B_{f_1}=\frac{2}{\pi}\frac{n(\bar{t}_1/d_2)}{\left[(d_e/d_2)+(d_h/d_2)\right]} \quad (6)$$

DESIGN SPECIFICATION	DESIGN VALUE
Mass flow, $\dot{m}$	0.572
Pressure ratio, P_i/P_e	3.6
Inlet stagnation temperature, T_i	$1000^\circ K$
Rotational speed, N	60,000 $r.p.m$
Total to total efficiency, η_{tt}	0.87
Average blade thickness at rotor inlet, $\bar{t}_2$	2.5 mm
Average blade thickness at rotor outlet, $\bar{t}_1$	1.5 mm

Table 1 Input data at design point

For a given set of design specifications as shown in Table 1, the optimum principal dimensions of the rotor can be found by solving equations (1) to (6) within the specified ranges of the constraints variables. The solution can be obtained by using a suitable optimisation algorithm. The authors used the algorthims OPRQP developed by **Biggs [16,17]**. The general mathematical representation of the algorithm can be stated as:

Minimise $F(\bar{x})$, where $\bar{x}=[x_1,.....x_n]^t$

Subject to: $g_i(\bar{x})=0 \qquad i=1,.....q$

$g_j(\bar{x})\geq 0 \qquad j=q+1,.....m$

Where $F(\bar{x})$ represents the objective function, in our case is the inlet tip diameter d_2 and the functions and $g_i(\bar{x})$ and $g_j(\bar{x})$ are sets of equality and inequality constraints, respectively. The detailes of the optimisation programme which have been used are beyond the scope of this paper, but may be found in **Refs. [16,17]**.

OPTIMIZATION RESULTS

The optimization programme was run for several numbers of blades ranging from 12 to 20 blades. Number of blades specified within this range in accordance with the assumed efficiency η_{tt}, blockage B_f and blade loading factor c_{w2}/u_2.

The optimization results reveal that the optimum number of blades lies in the range between 12 and 20. Consequently, any blade number in this range is quite satisfactory provided it satisfies the other design criteria and specifications set by the designer. The design velocity diagrams based on optimization technique and the complete design data are shown in Fig. 8 and Table 2, respectively.

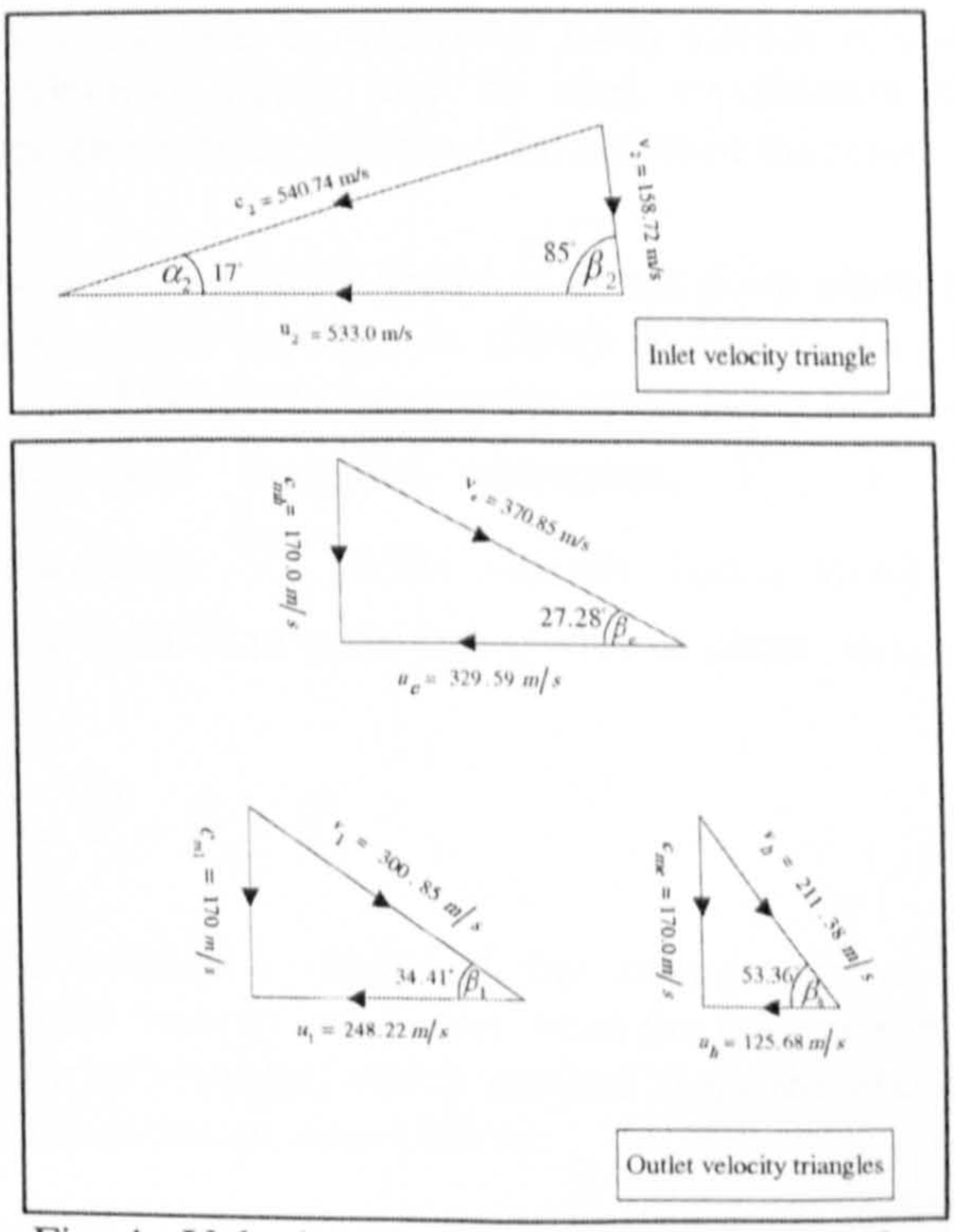

Fig. 4 Velocity triangle based on numerical optimization programme

FLOW VELOCTIES AT ROTOR INLET	FLOW VELOCTIES AT ROTOR EXIT
$c_2 = 538.82 m/s$	$c_1 = 186.77 m/s$
$v_2 = 158.13 m/s$	$c_{w2} = 0.0 m/s$
$c_{m2} = 157.34 m/s$	$c_h = 186.77 m/s$
$c_{w2} = 515.11 m/s$	$c_e = 186.77 m/s$
	$v_1 = 346.77 m/s$
	$v_h = 267.32 m/s$
	$v_e = 411.39 m/s$
ROTOR SPEED AT ROTOR INLET AND EXIT	**PERFORMANCE PARAMETERS**
$u_2 = 531.24 m/s$	$\dot{m} = 0.574$
$u_1 = 292.18 m/s$	$S_P = 0.157$
$u_h = 191.25 m/s$	$S_T = 0.24$
$u_e = 366.55 m/s$	$\eta_{tt} = 0.87$
	$R = 0.56$
	$c_{m1}/u_2 = 0.32$
	$N_s = 0.56$

TABLE 2 Design data (1) for an IFR turbine rotor based on numerical optimization

DESIGN SPECIFICATIONS	GEOMETRICAL DIMENSIONS
$W_{net} = 60 kW$	$d_2 = 16.91 cm$
$N = 60000 r.p.m$	$b_2 = 0.87 cm$
$P_i/P_e = 4.0$	$\bar{t}_2 = 0.25 cm$
$T_i = 1000 K$	$d_1 = 9.30 cm$
$u_2/c_s = 0.67$	$d_h = 6.09 cm$
	$d_e = 11.67 cm$
	$\bar{t}_1 = 0.15 cm$
FLOW ANGLES AT ROTOR INLET AND EXIT	**MACH NUMBERS AT ROTOR INLET AND EXIT**
$\alpha_2 = 17.0^\circ$	$M_2 = 0.93$
$\beta_2 = 84.2^\circ$	$M_1 = 0.35$
$\alpha_1 = 90^\circ$	$M_{hr} = 0.50$
$\alpha_h = 90^\circ$	$M_{1r} = 0.65$
$\alpha_e = 90^\circ$	$M_{er} = 0.8$
$\beta_h = 44.32^\circ$	
$\beta_1 = 32.59^\circ$	
$\beta_e = 27.0^\circ$	

TABLE 3 Design data (2) for an IFR turbine rotor based on numerical optimization

Optimization of passage geometry and the choice of axial length

The choice of a suitable axial length is almost a pre-requisite for completely defining the passage geometry. The effect of the axial length on velocity distribution is shown qualitatively in Fig. 5. It can be seen that the shortest channel length of rotor A should produce minimum friction loss, but the flow would probably separate due to high deceleration rate in the exducer section. In contrast, rotor C, which has the longest channel, would be expected to produce highest friction loss, but flow separation might be delayed due to the gradual deceleration rate in the exducer.

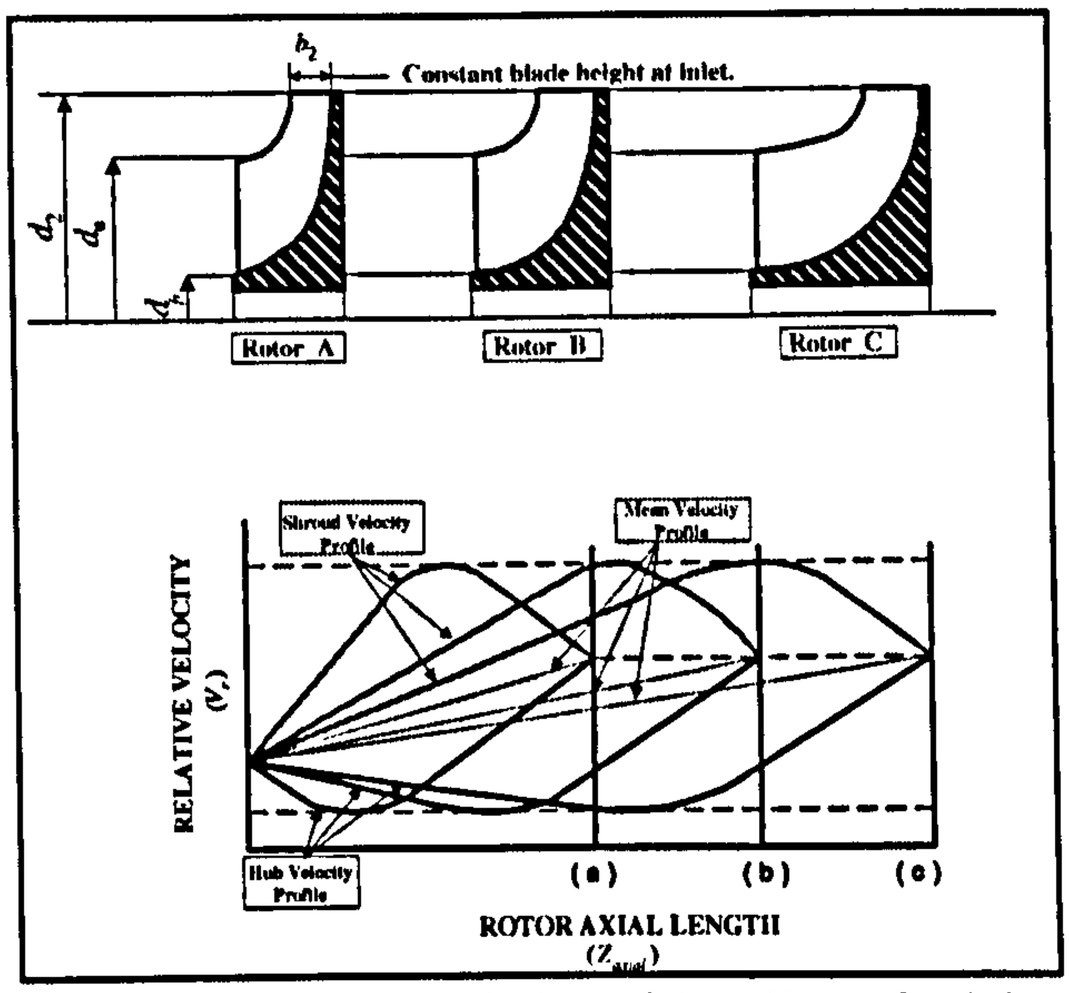

Fig 5 Qualitative description of the effect of axial length on velocity distribution

Following this, a prescribed mean stream velocity distribution theory may be used to optimize the passage geometry and the axial length of the rotor.

The relative velocity vector $\overline{V}$ at any point inside the turbine rotor passage, as shown in Fig. 6, may be resolved into three basic components along the axial, radial and tangential directions, $\overline{V}_z$, $\overline{V}_r$ $\overline{V}_w$, respectively. $\overline{V}_m$ is the velocity vector along the mean streamline in the hub-to-shroud plane , hence:

$$\overline{V} = \overline{V}_z + \overline{V}_r + \overline{V}_w \qquad (7)$$

The boundary values of the components of the relative velocity are known from the inlet and outlet velocity triangles, which resulted from the previous optimisation as shown below:

At rotor inlet: $V_z = 0$, $V_r = (V_r)_{\max}$ and $V_w = (1-\psi)U_2$

At rotor outlet: $V_z = (V_z)_{\max}$, $V_r = 0$ and $V_w = V_2 \sin\beta_1$

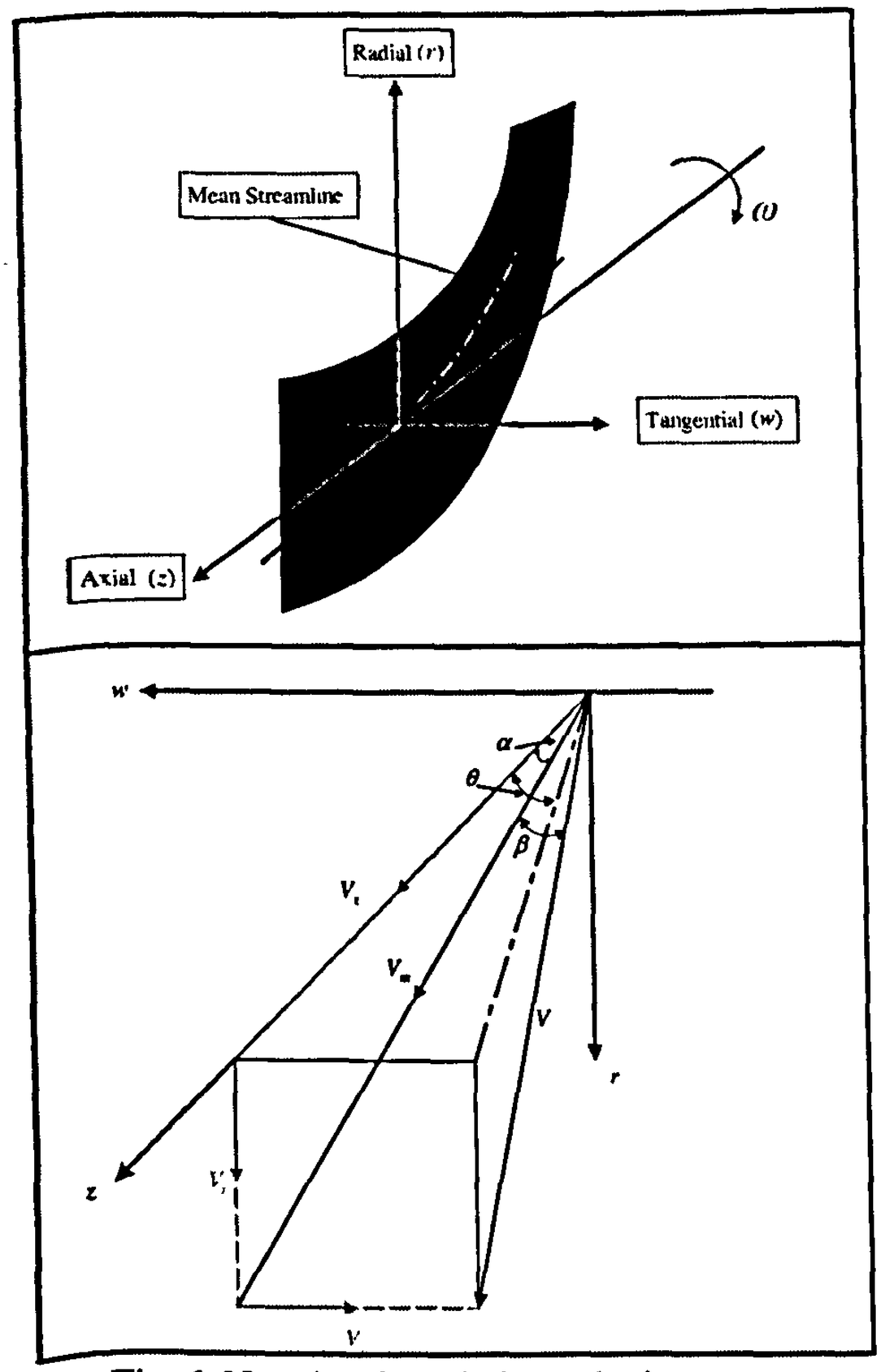

Fig. 6 Notation for relative velocity vector and its components

The angles shown in Fig. 6 can be expressed in terms of the velocities as shown below:

$$\beta = \sin^{-1}\sqrt{1-V_m^2/V}\ ,\ \tan\theta = \frac{V_z}{V_w} \text{ and } \cos\alpha = \frac{V_z}{V_w}$$

By combining the above relationships, the angles (α, β and θ) are related to each other by the following relationship:

$$\tan\beta = \tan\theta\cos\alpha \qquad (8)$$

The spatial description of the mean streamline can be found iteratively by assuming a starting value for the meridional length z_m, and the distributions of the relative velocity vector. **Fig. 7** shows three meridional lengths $0.02, 0.04, 0.06$ of a turbine rotor. **Fig. 8** describes the velocity components V_r, V_z and V_w for one assumed value of Z. At the start, all these figures are based on the assumption that the relative velocity vector V variation is linear.

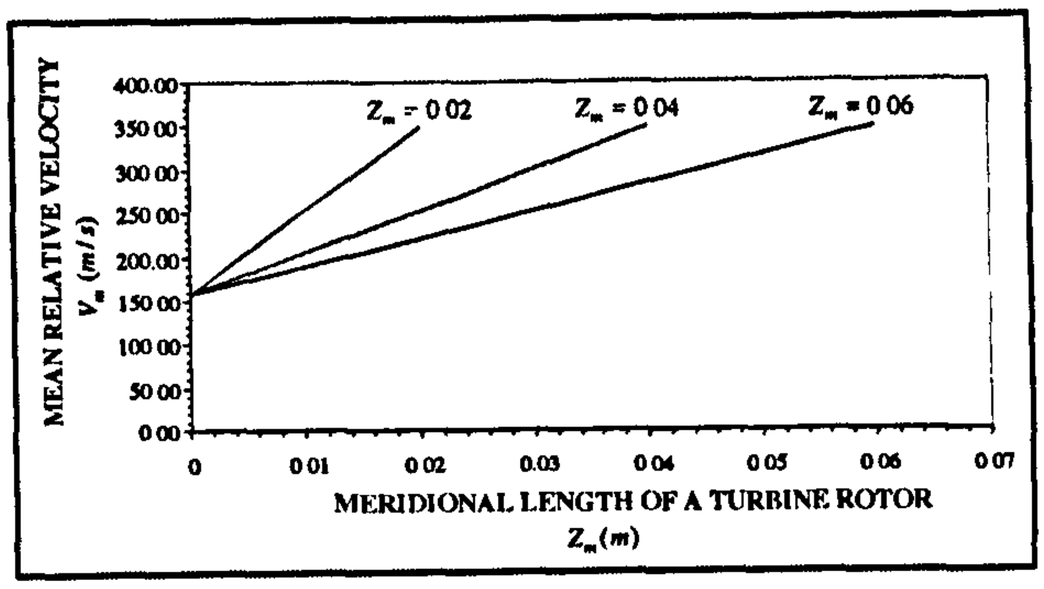

Fig. 7 Assumed variation of the relative velocity vector at various meridional lengths for the same boundary conditions

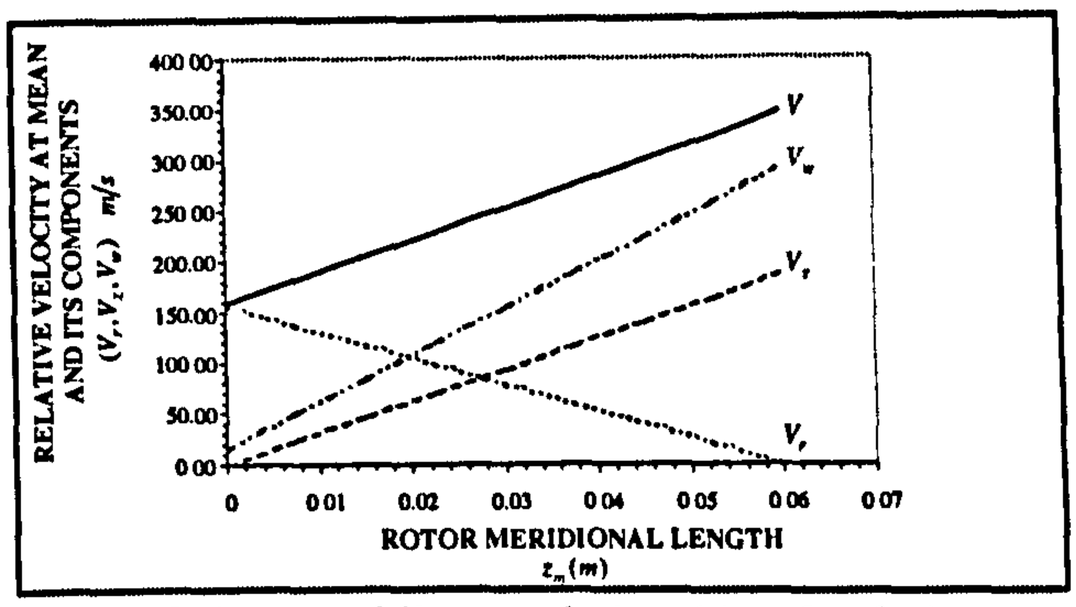

Fig. 8 Assumed linear relationship of relative velocity vector and its components for an assumed $Z = 0.06m$

A computer programme was written to perform the iterative calculations to check this linear relationship variation of relative velocity vector along the mean streamline. The output results are plotted in **Fig. 9** and a flow chart based on this programme is shown in **Fig. 10**

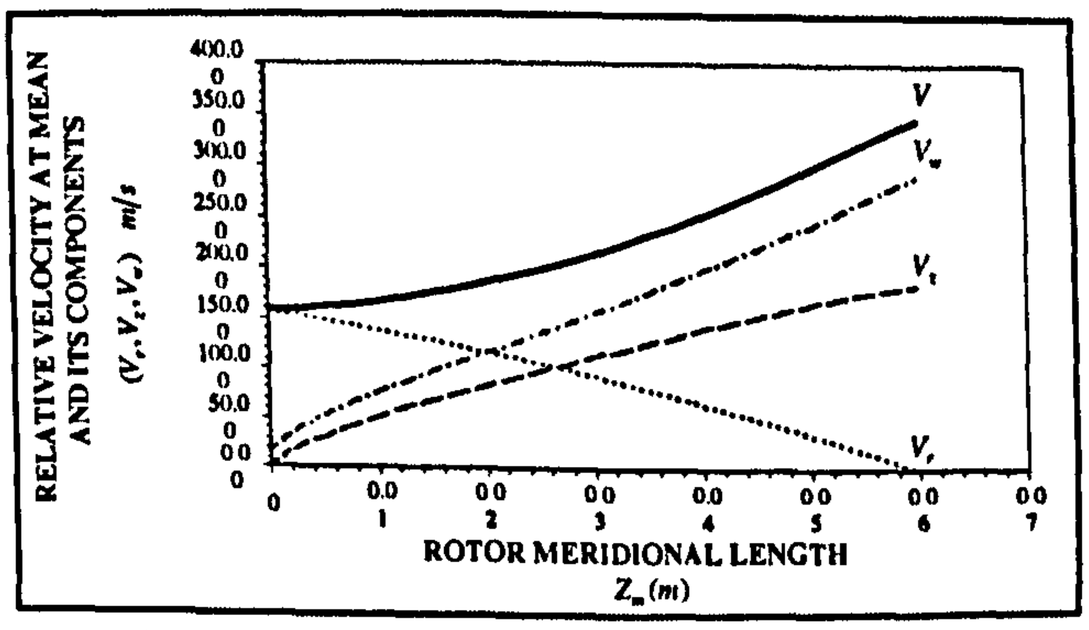

Fig. 9 Prescribed relative velocity distribution along mean streamline for an assumed meridional length of $0.06m$

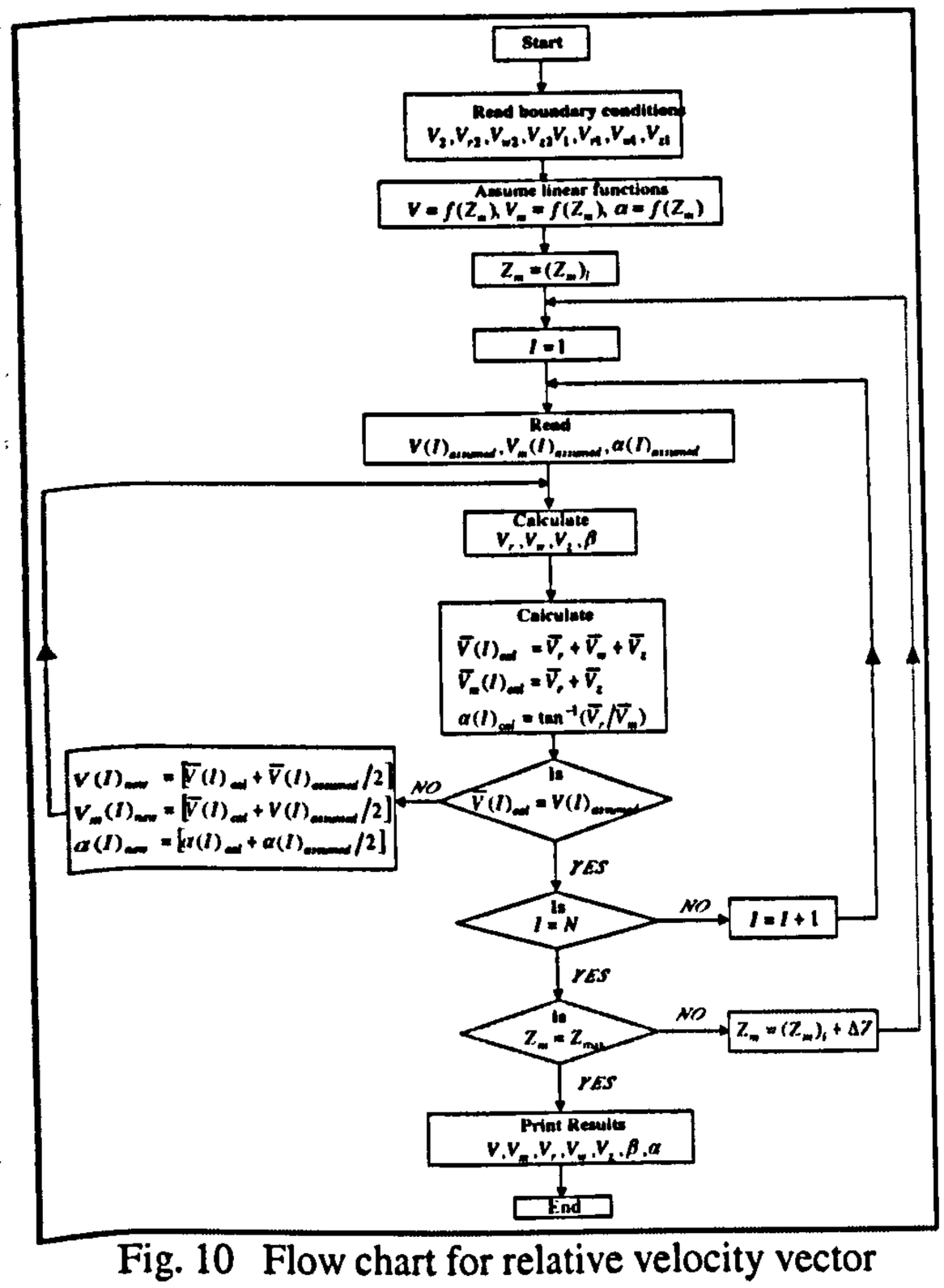

Fig. 10 Flow chart for relative velocity vector variation along mean streamline

The next step is to optimize the axial length, Z by minimizing the loss of stagnation pressure in the flow channels. For this purpose, the losses must be expressed as functions of the resultant velocity V and the length of the channel and the radius of curvature r_c. Several models are available in the published literature **Dallenbach [18] and Rodgers [19]** which take account of the losses. These losses are adapted to be used for the turbine rotor. A detailed review of these losses is outside the scope of this paper, but it should suffice to say that any loss models could be integrated into the programme as sub-routine. A computer programme was written to optimize the axial length and the flow passage based on the relations listed below:

The radius r of the mean streamline in the meridional plane can be represented using Lame' ovals relationship as:

$$r = (r - r_2)\left[1 - \left(\frac{z_m - z_{m1}}{z_{m2} - z_{m1}}\right)^3\right]^{1/2} + r_2 \tag{9}$$

The first and second derivatives of dr/dz are given in equations 10 and 11, respectively:

$$\frac{dr}{dz} = -\left[\frac{3}{2}\right]\left(\frac{r_1 - r_2}{z_{m2} - z_{m1}}\right)\frac{l}{j}\left(\frac{z_m - z_{m1}}{z_{m2} - z_{m1}}\right)^2\left(\frac{r - r_2}{r_1 - r_2}\right)^{-1} \tag{10}$$

$$\frac{d^2 r}{dz_m^{\,2}} = \left[\frac{dr}{dz_m}\right]\left[\left(\frac{2}{z_m - z_{m1}}\right) + \left(\frac{-1}{r - r_2}\right)\left(\frac{dr}{dz_m}\right)\right] \tag{11}$$

The length of the streamline is given by:

$$L = \int_{z_{m1}}^{z_{m2}} \left(1 + \frac{dr}{dz_m}\right) dz_m \tag{12}$$

Temperature at any section inside the passage

$$\frac{T_x}{T_i} = 1 + \frac{1}{2}\left(\frac{u_x^{\,2} - 2c_{wi}u_i}{C_p T_i}\right) \tag{13}$$

Pressure at any section inside the passage

$$\frac{P_x}{\phi P_i} = \left(\frac{T_x}{T_i}\right)_s^{\gamma/\gamma-1} \tag{14}$$

Density at any section inside the passage

$$\rho_x = \left(1 - \frac{v_x^{\,2}}{2C_p T_x}\right)^{1/\gamma-1}\left(\frac{P_x}{RT_x}\right) \tag{15}$$

Shroud contours at any section inside the passage

$$r_{sx} = \sqrt{(r_{rms}^{\,2})_x + \frac{1}{2}\frac{\dot{m}\cos\alpha_x}{\pi\rho_x v_{mx} B_{fx}}} \tag{16}$$

Hub contours at any section inside the passage

$$r_{hx} = \sqrt{(2r_{rms}^{\,2})_x - r_{sx}^{\,2}} \tag{17}$$

It can be seen from Equations 16 and 17 that they can be used to calculate the shroud and the hub contours at any section inside the blade passage, hence the final shape of the blade of the blade passage can be defined.

A flow diagram for optimizing the axial length of the turbine rotor and the optimized design of the flow passage are shown in Fig. 11. The output results are plotted as shown in Fig. 12. This plot of the stagnation pressure loss vs. the meridional indicates that the minimum losses of stagnation pressure occurs at a meridional length equal to $40.0\,mm$.

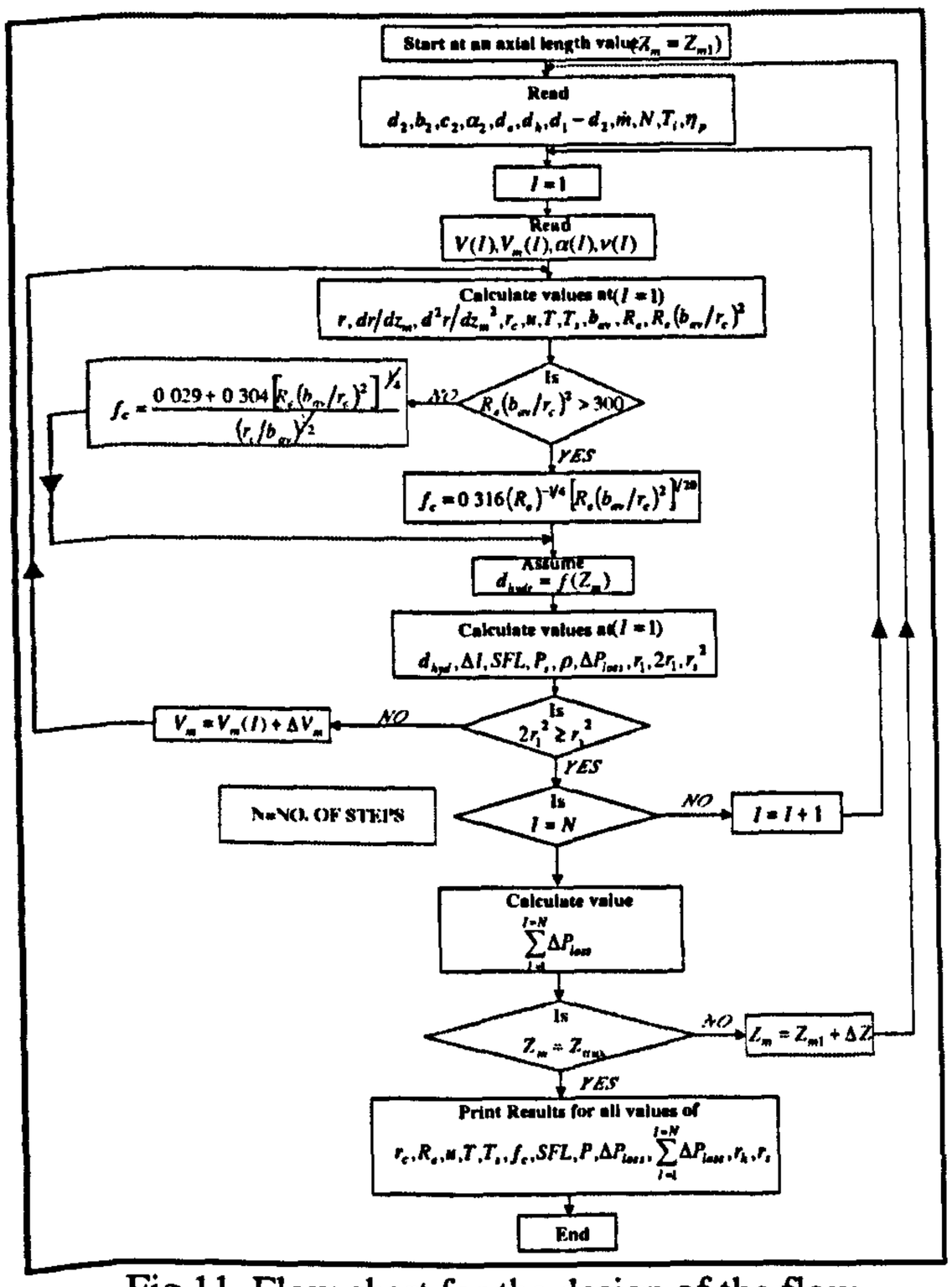

Fig.11 Flow chart for the design of the flow passage and the optimization of the meridional length

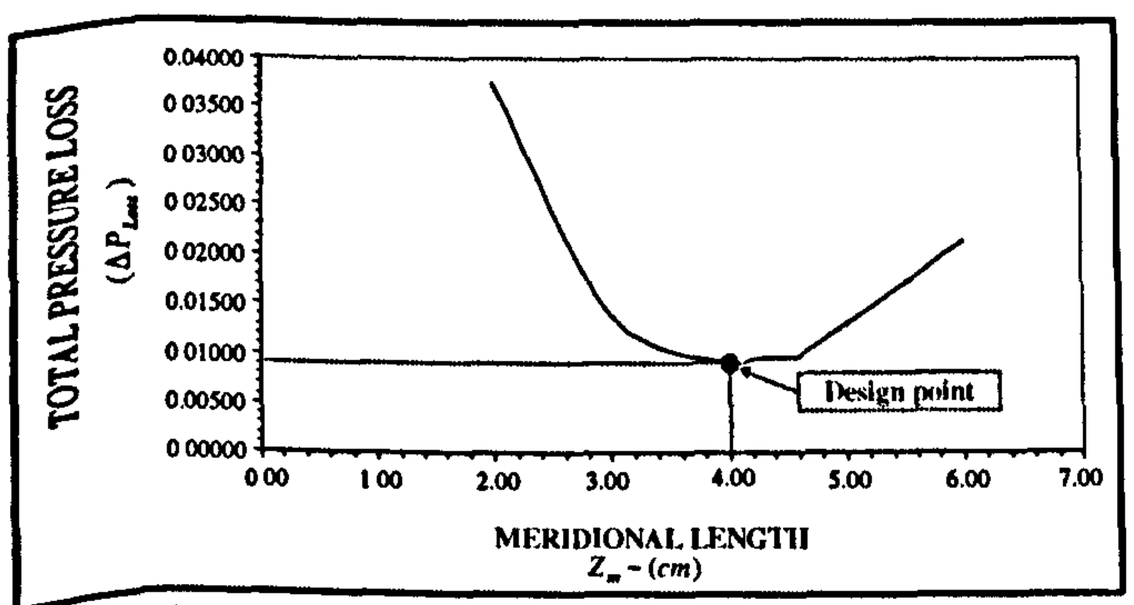

Fig.12 Total pressure loss vs. meridional length

The final drawings of the turbine rotor are shown in Fig. 13, 14 and Fig. 15, respectively.

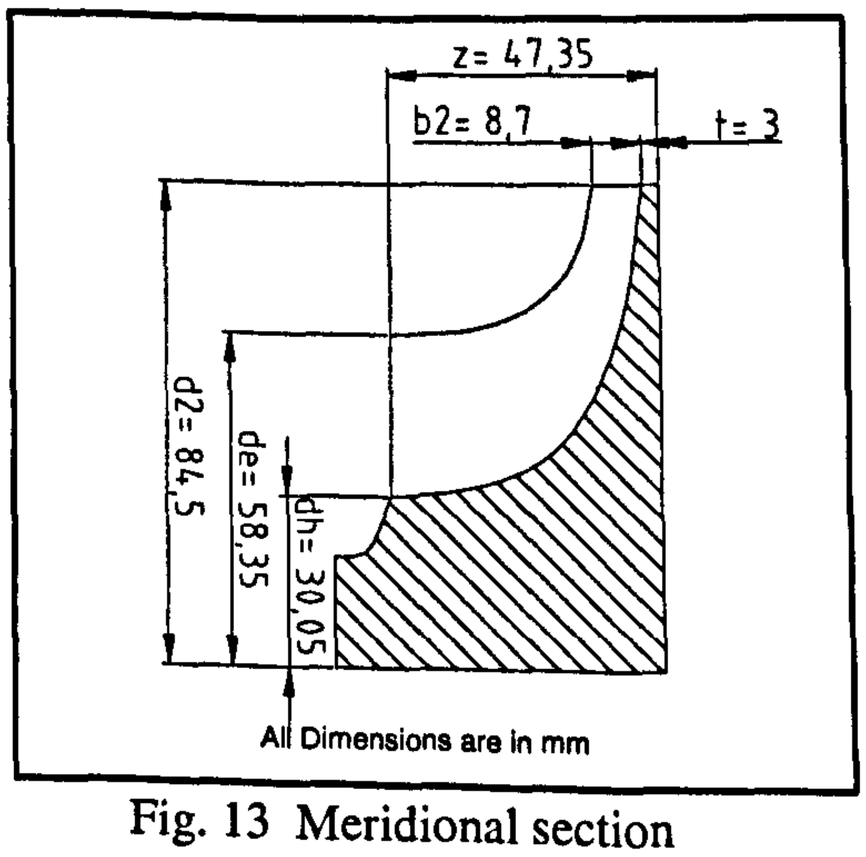

Fig. 13 Meridional section

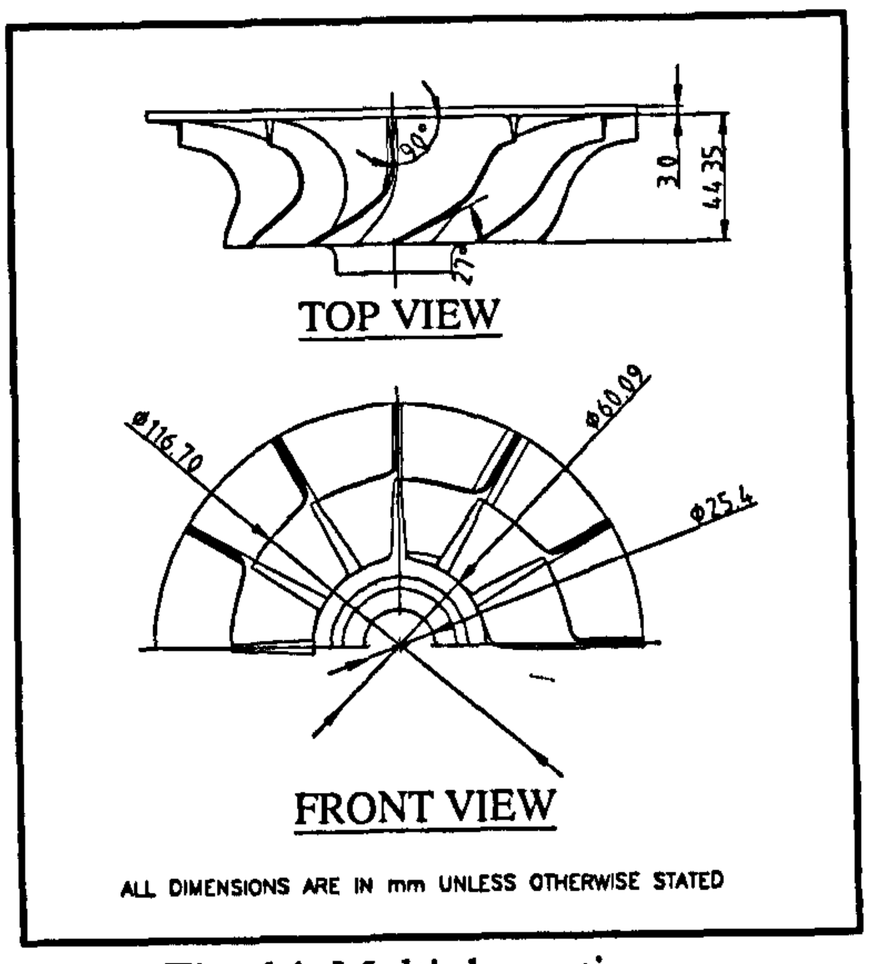

Fig. 14 Multiple sections

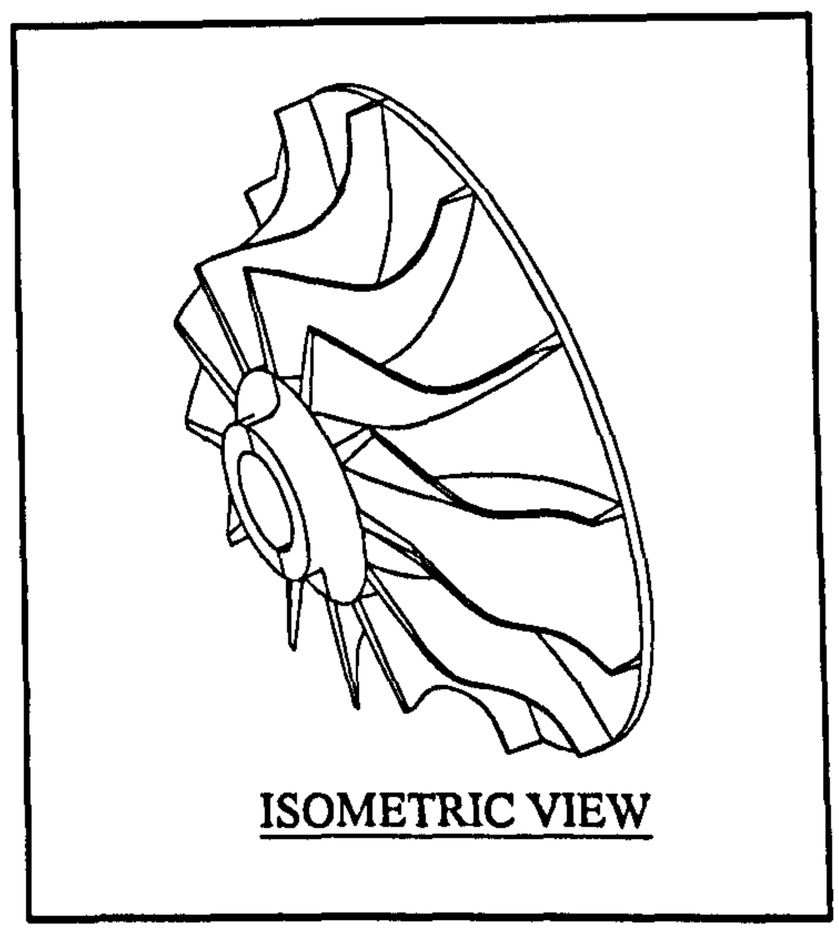

Fig. 15 3-Dimensional view of the rotor

NOZZLE-LESS CASING DESIGN

The design objectives of the casing are:

i. Accelerate the working fluid to the leading edge of the rotor and generate the desired rotor inlet conditions in terms of the magnitude and direction of the absolute velocity vector.

ii. Distribute the working fluid uniformly around the rotor periphery.

iii. Achieve these requirements as efficiently as possible that is with minimum loss in stagnation pressure.

The required inlet conditions must be derived from the desired turbine performance, e.g. the desired power output.

The nozzle-less volute must be designed to provide these rotor inlet conditions. The preliminary design of the volute is often based on the assumptions of an adiabatic flow, together with a free vortex distribution about the rotor.

The passage design is often specified in the form of the variation, with azimuth angle, of cross-sectional area, casing width or parameter A_φ / r_φ . The desired rotor inlet condition is one of a uniform distribution of angular momentum about the rotor periphery, whilst the volute inlet conditions at the tongue are those of a fully developed turbulent pipe flow

VOLUTE DESIGN PROCEDURE DESIGN

1. Assumptions

i. Steady, one-dimensional, isentropic flow, constant angular momentum, energy and conservation of mass along the volute length.

ii. Vortex motion is fully established before the commencement of any outer low from the volute in the radial direction. This is a necessary condition for the flow angles α_2 and β_2 to be independent of the azimuth angle and the flow into the rotor to be uniform.

iii. The flow near the outer wall profile is assumed to follow the same contour as the outer profile of the casing, the boundary layer thickness being negligible.

A diagrammatic sketch of a centripetal turbine fitted with a nozzle-less casing is shown in **Fig. 16**.

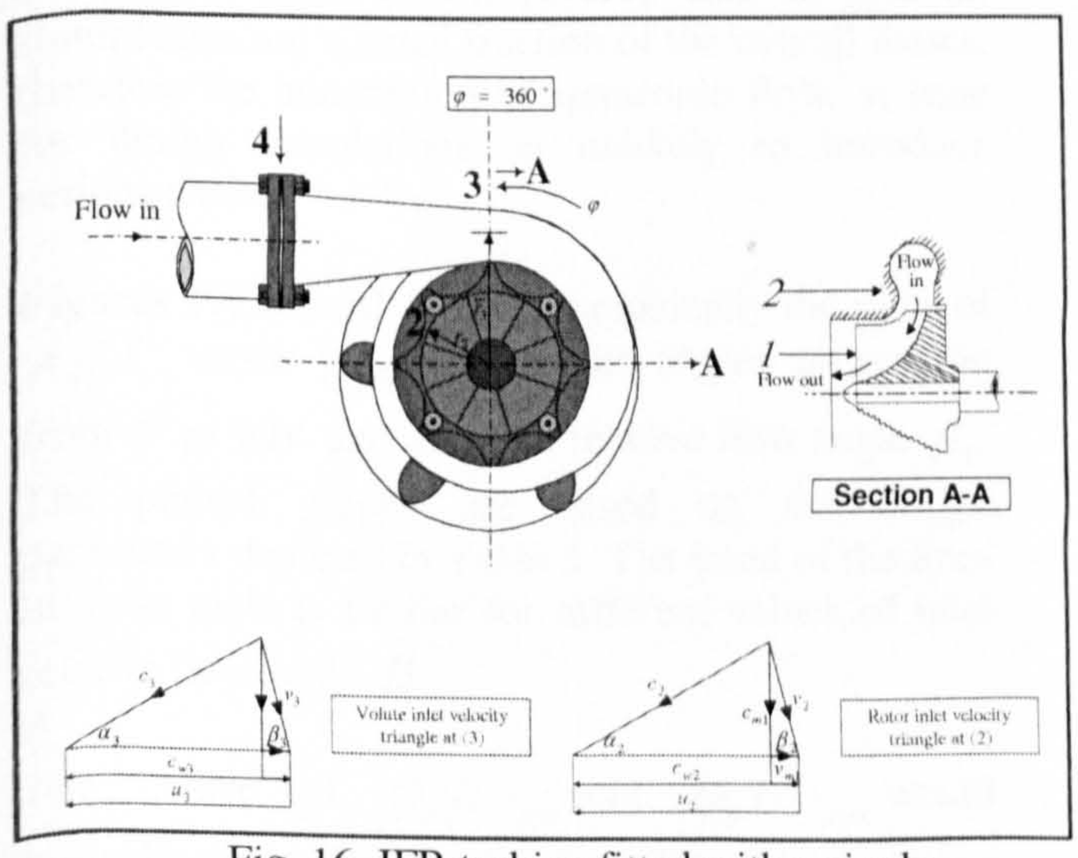

Fig. 16 IFR turbine fitted with a single nozzle-less volute casing

2. principal design variables of the nozzle- less volute casing

A. Volute parameters

i. The cross-sectional area A_φ of the volute and the variation of this area as a function of the azimuth angle φ .

ii. The radial distance of the centriod $\bar{r}_\varphi$ of the cross-sectional area from the axis of rotation.

iii. The shape of the volute cross-section.

B. Rotor parameters

i. Rotor tip diameter d_2 and blade width b_2 .

ii. Effective peripheral flow area A_2 or the number of blades and blade thickness at d_2 .

C. Operating conditions

i. Rotational speed, N

ii. Mass flow rate, $\dot{m}$

iii. Stagnation temperature, T_i and stagnation pressure P_i of the working gas at the entry flange of the turbine.

3. Design method

The frame size and weight of the turbine is often an important design consideration and it is essential that the overall size be minimized. The design procedure first assesses the overall size in terms of the volute radius ratio $\bar{r}_3 / r_2$, and area ratio A_3 / A_2 and consider the parameters, which must be varied in order to adjust the overall size.

Using the equations of mass flow, energy and angular momentum and based on the assumption of free vortex relationship, the following expression defining the interconnection of the design parameters of the casing is shown below:

$$\frac{A_\varphi}{\bar{r}_\varphi} = (B_{f_2})(\tan\alpha_2)\left(\frac{\varphi}{360}\right)\left(\frac{A_2}{r_2}\right)\left[\frac{1-\left(\frac{\pi}{\sqrt{2}}\cdot\frac{d_2 N}{\sqrt{C_p T_i}}\cdot\frac{\sin\beta_2}{\sin(\alpha_2+\beta_2)}\right)^2}{1-\left(\frac{\pi}{\sqrt{2}}\cdot\frac{r_2}{\bar{r}_\varphi}\cdot\frac{d_2 N}{\sqrt{C_p T_i}}\cdot\frac{\sin\beta_2\cos\alpha_2}{\sin(\alpha_2+\beta_2)}\right)^2}\right] \quad (18)$$

Where B_{f_2} is the blockage factor corresponding to rotor entry and is given as:

$$B_{f_2} = \frac{Total\ \ flow\ area\ of\ the\ passage}{Peripheral\ area}$$

$$B_{f_2} = \frac{Peripheral\ \ flow\ area - Blockage\ due\ to\ blades}{Peripheral\ area}$$

$$B_{f_2} = 1 - \left(\frac{n_b t_2 b_2}{\pi d_2 b_2} \right) \qquad (19)$$

Where n_b : Number of blades

t_2 : Thickness of inlet rotor blades

Equation 18 represents a fundamental design equation linking the main design parameter $A_\varphi / \bar{r}_\varphi$ of the volute with relevant principal dimensions of the rotor and the operating conditions as shown below

$$\frac{A_\varphi}{\bar{r}_\varphi} = f\left[\left(\frac{\dot{m}\sqrt{T_i}}{A_2 P_i} \right), \left(\frac{b_2}{d_2} \right), (\alpha_2), (\varphi), (N) \right]$$

i.e. $\frac{A_\varphi}{\bar{r}_\varphi} = f\left(A_2, d_2, b_2, \alpha_2\right)$ - these variables represent rotor parameters.

And $\frac{A_\varphi}{\bar{r}_\varphi} = f\left(\dot{m}, P_i, T_i, N, \alpha_2\right)$- these variables represent operating conditions.

The losses may be included in equation 18. However experiments have shown **[20,21]** that, in general, stator losses are a small fraction of the overall losses, therefore the assumption of isentropic flow, at least for design calculations, is unlikely to introduce serious errors.

Figures 17, 18 and 19 show graphically the plots of A_φ / A_2 versus $\bar{r}_\varphi / r_2$ for azimuth angles φ ranging from 0° *to* 360° and different relative flow angle β_2. The plotted graphs are based on the design parameters depicted in Table 3. The trend of the lines in these plots is similar for different values of inlet relative flow angle β_2.

The choice of $(\bar{r}_\varphi / r_2)_{\min}$ and $(\bar{r}_\varphi / r_2)_{\max}$ would normally dictated by the tip diameter of the rotor and the allowable overall dimensions of the volute casing. The initial design values were chosen to be 1.06 and 2.5, respectively.

DESIGN PARAMETER	VALUES
Speed parameter, $d_2 N / \sqrt{C_p T_i}$	0.157
Inlet absolute flow angle, α_2	17°
Inlet relative flow angle, β_2	73° , 85° , 90°
Blockage factor, B_{f_2}	0.93

Table 3 Constant design parameters

Therefore, The corresponding pairs of values of the dimensionless parameters A_φ / A_2 and $\bar{r}_\varphi / r_2$ can be directly read from such a plot by joining $(\bar{r}_\varphi / r_2)_{\min}$ and $(\bar{r}_\varphi / r_2)_{\max}$ by a straight line as shown in **Figs. 17, 18 and 19**

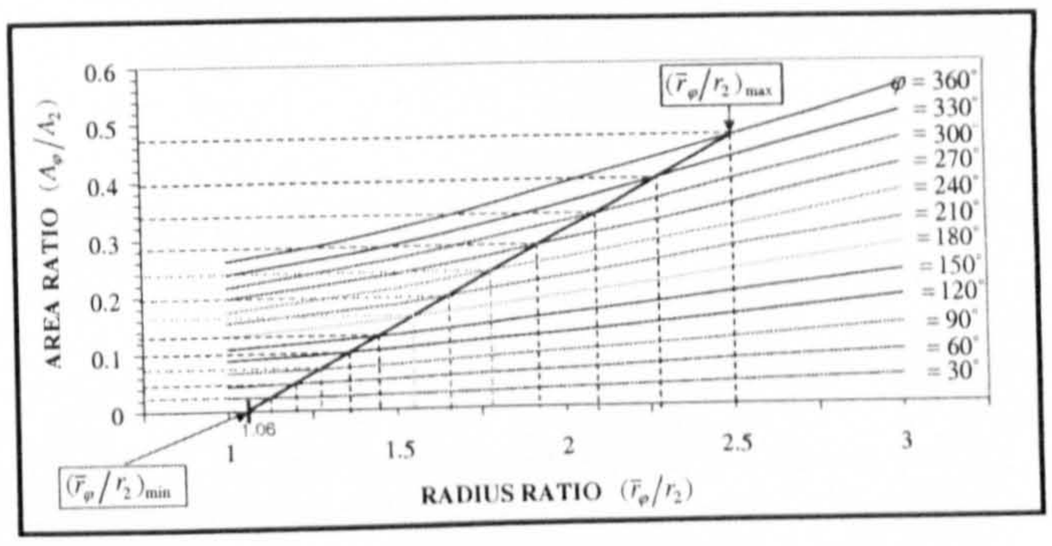

Fig. 17 Relationship between area ratio, radius ratio and azimuth angle $\beta_2 = 85^\circ$

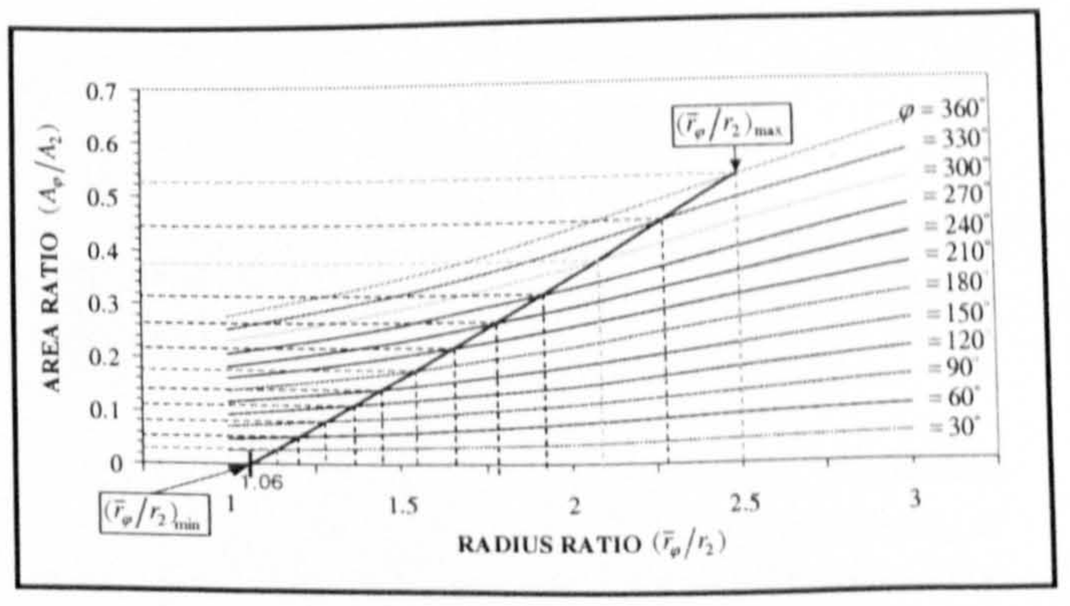

Fig. 18 Relationship between area ratio, radius ratio and azimuth angle for $\beta_2 = 73^\circ$

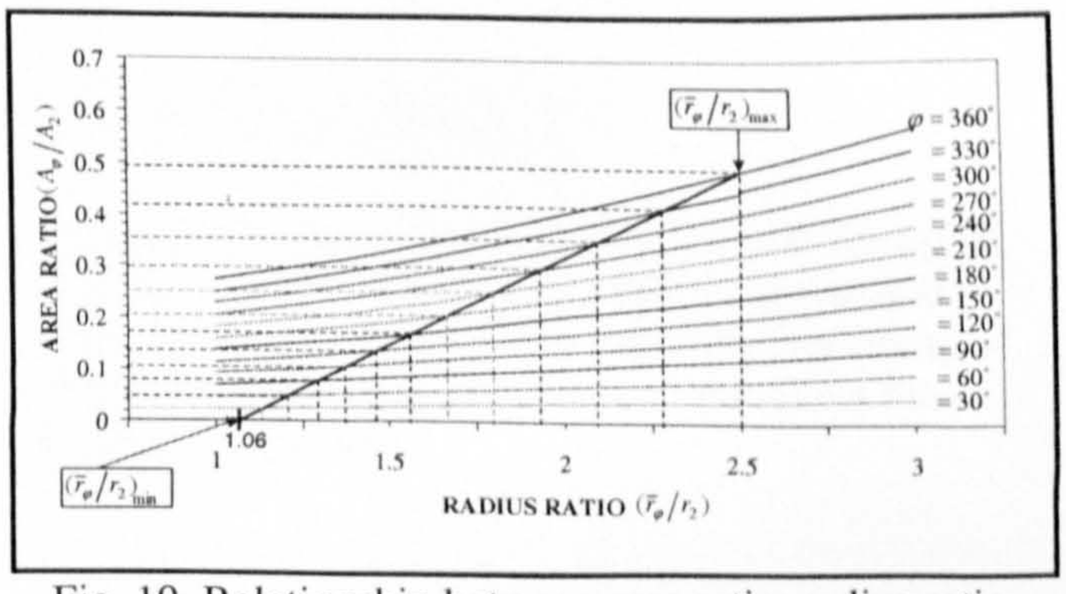

Fig. 19 Relationship between area ratio, radius ratio and azimuth angle for $\beta_2 = 90^\circ$

Since $(A_\varphi/\bar{r}_\varphi) \propto \left[(A_\varphi/A_2) \div (\bar{r}_\varphi/r_2)\right]$, Then

$$\left(\frac{A_\varphi}{\bar{r}_\varphi}\right) = K\left(\frac{A_\varphi}{A_2}\right)\left(\frac{r_2}{\bar{r}_\varphi}\right)$$

Where $K = A_2/r_2$ to satisfy the expression above. The final design graph of $A_\varphi/\bar{r}_\varphi$ versus φ can be obtained from the corresponding values of A_φ/A_2, $\bar{r}_\varphi/r_2$ and φ which can be read either from **Figs. 17 to 19**. Such a graph is shown in **Fig. 20**.

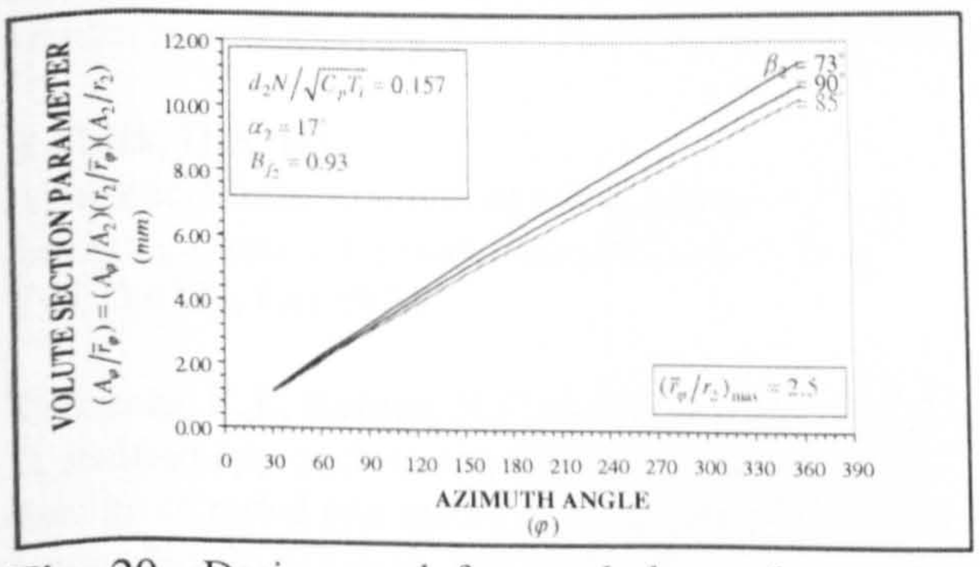

Fig. 20 Design graph for nozzle-less volute casing for different incidence angles for $(\bar{r}_\varphi/r_2)_{max} = 2.5$

It should be noted that the shape of the graph above depends on the shape of the line joining the minimum and maximum values of on the value of $(\bar{r}_\varphi/r_2)$ chosen by the designer. Once the shape of cross-section, i.e $b = f(r)$ has been decided, in our case, a circular cross-section was chosen, its dimensions can be found from the following equation

$$\left(\frac{A_\varphi}{r_\varphi}\right) = \int_{r_2}^{r_1}\left(\frac{b}{r}\right)_x . dr \qquad (20)$$

The final design dimensions and drawing for the nozzle-less casing is shown in Fig. 20 and Table 4.

Position of Points	Azimuth angle (Degree)	Radius of Centroid (mm)	Elevation - z - (mm)	Radius of Casing Cross Section (mm)
1	0	85.65	-53	3.00
2	30	90.26	-51.53	4.47
3	60	94.87	-50.93	5.07
4	90	99.49	-48.23	7.77
5	120	104.10	-44.62	11.38
6	150	108.71	-40.6	15.40
7	180	113.32	-36.27	19.73
8	210	117.94	-31.67	24.29
9	240	122.55	-26.91	29.09
10	270	127.16	-21.89	34.11
11	300	131.77	-16.64	39.36
12	330	136.39	-11.16	44.84
13	360	141.00	-5.43	50.57
14	383	144.54	-5.43	50.57

Table 4 Design values of turbine nozzle-less casing

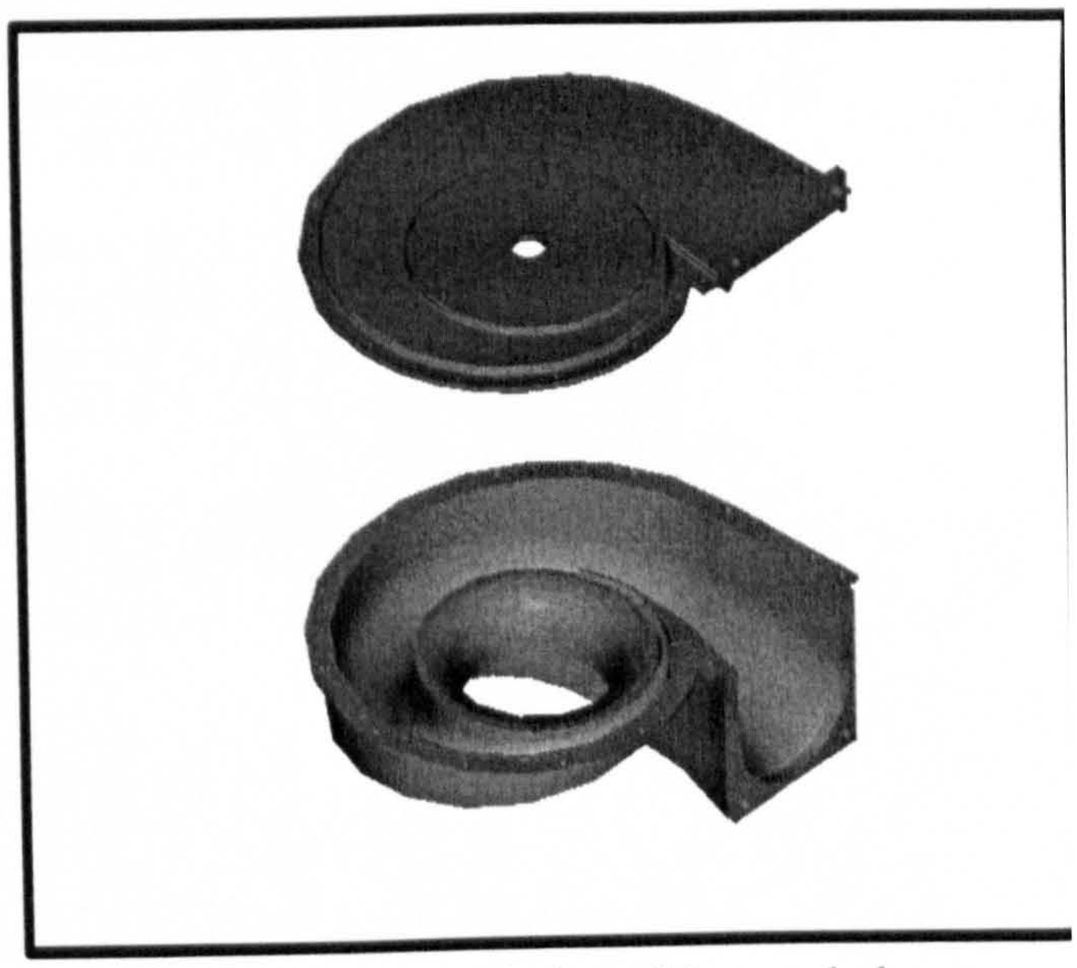

Fig. 21 3-Dimensional view of the nozzle-less casing

CONCLUSIONS

1. A unified approach for designing a single stage inward flow radial turbine comprising a rotor and a nozzle-less casing to drive a direct-coupled permanent magnet high speed alternator running at $60000\,rpm$ and developing $60\,kW$ electrical power has been described

2. A computer programme was developed to find the optimum choice of the principal dimensions of the rotor and the number of blades.

3. The theory of the prescribed mean stream velocity distribution was used to find the optimum axial length and optimizing the blade passage.

4. A procedure for designing the nozzle-less casing was given based on using the equations of mass flow rate, energy and angular momentum. The flow is assumed to be isentropic and satisfies the free vortex relationship.

ACKNLODGEMENTS

The authors wish to thank king Abdullah II Design & Development Bureau for their endless support and encouragements. Also wish to thank the University of Hertfordshire for their cooperation throughout this research programme.

REFERENCES

Single stage radial turbines for gaseous substances with high rotative and low specific speed ASME paper 51-f-16, Fall meeting. Minneapolis, Sept 1951.

Balje, O.E. [2]
A contribution to the problem of designing radial turbomachines. ASME paper 51-F-12, Fall meeting, Minneapolis, Sept.1951

Balje, O.E. [3]
A study of design criteria and matching of turbomachines. Part A-similarity relations and design criteria of turbines. ASME paper No. 60-Wa-230 winter annual meeting. New York, Nov-Dec, 1960.

Rohlik, H.E. [4]
Analytical determination of radial inflow turbine design geometry for maximum efficiency. NASA-TN D 4384, Oct 1970.

Wallace, F.J., Baines, N.C and Whitfield, A. [5]
A unified approach to one dimensional analysis and design of radial and mixed flow turbines. ASME paper No. 76-GT-100, March, 1976.

Rodgers, C.[6]
Small high pressure ratio radial turbine technology. VKI lectures series 1987-07,1987.

Whitfield, A. and Baines, N.C. [7]
Design of radial turbomachines, 1990 (Longman Scientific and Technical)

Wasserbauer, C.A. and Glassman, A.J. [8]
Fortran programme for predicting of-design performance of radial inflow turbines. NASA report TND-8063, 1975.

Whitfield, A. [9]
The preliminary design of radial inflow turbines. Trans. ASME, pp 50-57, Jan. 1990

Benson, R.S. and Fisher, U. [10]
A proposal scheme for computer aiaded design and manufacture of radial turbine rotors. ASME paper No. 78-GT-156, April, 1978.

Baines, N.C, Wallace, F.J. and Whitfield, A. [11]
Computer aided design of mixed flow turbines for turbochargers. ASME paper No. 78-GT-191, April 1978.

Bhinder F.S. [12]
Investigation of flow in the nozzle-less spiral casing of a radial inward flow gas turbine, Proc. Instn. Mech. Engns, Vol.184 pt. 3G(II), pp 66-77, 1969.

ASME Conference paper No: GT-2003-30578
Amsterdam, June 2003.

Chapple, P.M., Flynn, P.F. and Mulloy, J.M. [13]
Aerodynamic design of fixed and variable geometry nozzle-less casings. Trans ASME J engng power, Vol. 102, pp 141-147, 1980.

Hussian, M., Ilyas, M. and Bhinder, F.S. [14]
A contribution to designing a nozzle-less volute casing for the inward flow radial turbine. Instn. Mech. Engns. London Paper No. C35/82, 1982.

Whitfield, A. and Noor, A.B. [15]
A non-dimensional conceptual design procedure for the vaneless volute of radial inflow turbines. ASME, 1991.

Biggs, M. C. [16]
Recursive quadratic programming methods for non-linear constraints. In Powel, M.J.C., ed., " Nonlinear optimization ". 1981 (Academic press, London, 1982), pp. 213-221.

Biggs, M.C. [17]
Further methods for nonlinear optimization ". Mathematics division, University of Hertford shire, 1999.

Dallenbach, Coppage *et al.* [18]
Study of supersonic radial compressors for refrigeration and pressurization. WADC Technical Report 55-257, A.S.T.I.A document No. AD110467, Dec 1956.

Rodgers.C [19]
A diffusion factor correlation for centrifugal impeller stalling, Trans. ASME. Jr. of Eng. For Power, Vol. 100.Oct,1978

Iliett, G. F. and Johnston, I. H. [20]
Experiments concerning the aerodynamic performance of inward radial flow turbine ". Proc. Instn. Mech. Engrs. London, 178, Pt 3I (II), 1964.

Benson, R. S. [21]
An analysis to the losses in a radial gas turbine. Paper No. 16, I.Mech.E. Thermodynamics and Fluid Mechanics Convention, April 1966.

TEXT BOUND INTO THE SPINE

Back Iron Design for High Speed PM Axial Flux Generators

Patrick C. K. Luk, *Member, IEEE,* Tareq S. El-Hasan

Abstract **– For high speed permanent magnet (PM) generators, the back iron on the rotor magnetic circuit is not laminated to minimize vibration and risks of mechanical breakdown. The design of back iron is no longer trivial for mechanical, magnetic and thermal reasons. The scarcity of published work for design study on back iron in these machines has not help to reflect this. This paper reports an integrated design approach for the back iron based on vigorous magnetic and stress analysis using efficient finite element (FE) modeling. By considering both the optimization of the back iron geometry and economy of design, the study seeks to highlight the inherent complex design issues virtually ignored by the literature.**

Index Terms**-- Back iron design, flux generators, disc type generators, high PM generators.**

I. Introduction

Although high-speed permanent magnet (PM) generators generally benefit from superior power-to-weight ratios and compact structures to their lower speed counterparts, the main design challenge in these machines lies in preventing overheating rather than achieving optimum performance. Axial flux design with its disc type geometry is conducive to better cooling because of higher stator surface area and lower electrical losses when compared with other designs [1]. Typically the design takes two forms, a multi-pole PM rotor disc rotating between two stator windings, or a disc-shape stator winding being inserted between two PM rotor discs. The latter form facilitates better heat extraction due to the natural cooling action of two rotating discs. However, the accurate predictions of the heat losses due to eddy currents and hysteresis are extremely difficult to achieve, partly due to the fact that non-ideal sinusoidal stator currents generate harmonics which induce flux to surrounding components with magnitudes which are likely to be unknown. In particular, the back-iron on each of the rotor discs, which provides a high permanence path to complete the magnetic circuit formed by the rotor PMs, will critically affect the flux formation. Furthermore, in order to minimize vibration and more importantly the risk of mechanical failure due to extreme centrifugal force at high speed, the back-iron is not laminated. The thickness of the solid back-iron must therefore be kept to minimum to avoid potentially excessive induced eddy currents, while ensuring designed magnetic flux levels to be maintained and undue flux leakage paths to be minimized. Thus, the design of the back-iron for the high speed rotor discs is non-trivial, for magnetic, mechanical and thermal reasons.

However, the literature suggests very few published work in back-iron design, and mainly on linear machines [2]. This paper reports an integrated design approach for high speed PM generators based on vigorous magnetic and stress analysis using efficient finite element method (FEM), and focuses on the optimization of the back-iron to meet the magnetic and mechanical requirements. Aspects on the economy of the design are also considered. Sufficient FEM simulation results underline the significance of the proposed back-iron design.

II. Initial Design Stages

A. Disc-Type Generator

Fig.1 shows the disc-type generator under investigation. It has an output of 18kVA at 50krpm. The modular structure however facilatates multistage and multiphase arrangement, making it easy to extent to a 3-phase generator with three times the power, for instance [1]. The back-iron disc is mounted on the same shaft and fixed at the outer end of each of the rotor magnet assembly (only one rotor disc is shown for clarity).

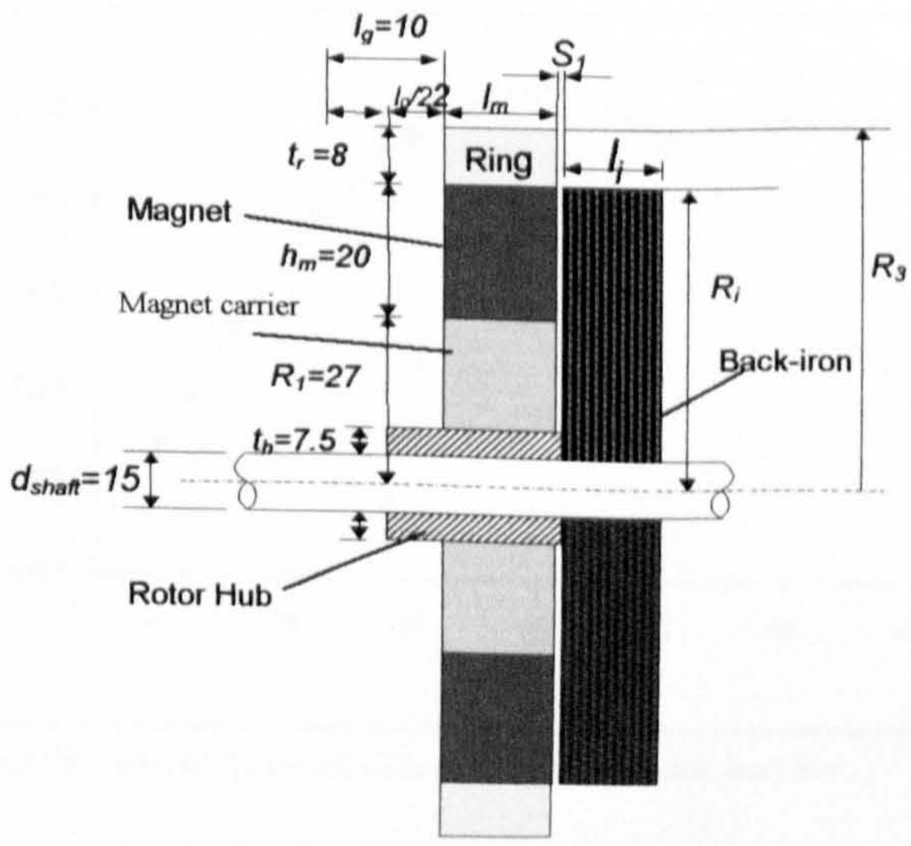

Fig.1 Disc-type generator with key dimensions

Manuscript received January 4, 2003. This work was part supported by the Jordanian Armed Forces and King Abdullah Design and Development Bureau (KADDB) under the designation number *AB15*.

P.C.K.Luk is with Department of Aerospace, Power and Sensors, Cranfield University, Shrivenham, Oxfordshire, SN6 8LA UK. Tel: 0044 1793-785528 (e-mail: p.c.k.luk@rmcs.cranfield.ac.uk).

T.S.El-Hasan is with the Jordanian Armed Forces and currently is a PhD student in the Aerospace, Automotive and Mechanical Engineering Department, University of Hertfordshire, Hatfield, AL10 9AB, UK. Tel: 0044 1707- 286083. (e-mail:T.S.El-Hasan@herts.ac.uk).

B. Initial Stress Analysis for Uniform Disc

An initial stress analysis is carried to estimate the mechanical properties required for the back iron disc. The disc is designed to be mounted on the shaft via shrink fit to prevent slippage at the operating speed of 50,000 rpm. The required amount of interference fit is determined by the contact pressure exerted on the disc bore due to the shrink fit at standstill. Then, the Hoop stresses can be calculated using Lame solution for thick-walled cylinder theory [3]. Table 1 shows the results.

TABLE I
MECHANICAL ANALYSIS FOR UNIFORM BACK-IRON DISC

Quantity	Value /Units
Interference fit	16.8 μm
Contact pressure due to interference fit	188.5 MPa
Hoop stress due to rotation	198.35 MPa
Hoop stress due to pressure	190.58 MPa
Total Hoop stress	389.93 Mpa

C. Choice of Back Iron Material

The system requirements at high operating speed and high power density imply that the material of the back-iron disc must have both good magnetic and mechanical properties. The initial stress calculations performed above uses normal steel (density) and has been shown that normal steel disc is not capable of withstanding the high stresses. An alternative material must be sourced to satisfy the high strength capability, high relative permeability and saturation level. Minimum requirements for the magnetic and mechanical properties are summarised in Table 2. An extensive survey was carried out worldwide and four particular materials were found to meet the requirements, with cost effectiveness and manufacturing processability taken into consideration. The variation of flux level with axial thickness of the back iron for these different materials is shown in Fig.2, in which vanadium-iron-cobalt is best in terms of magnetic flux and minimum volume, with a high constant level of magnetic flux level achieved at thickness of 10 mm. Si-iron is however chosen for a marginally lower flux level but a huge cost advantage. The possibility exists that the cost advantage may be used to compensate the flux level lost. A flux level similar to that for the previous material can be achieved at 12.5 mm, that is, a slight increase of an axial thickness of 2.5 mm, which represents a 25 % increase on the total volume.

TABLE 2
MINIMUM REQUIREMENTS FOR BACK-IRON MATERIAL

Yield Strength [MPa]	Elongation %	Forms & Dimensions [mm]	Saturation [T]	Relative Permeability
> 500	> 10	Round Bars 100∅ × 30 L	> 1.2	1000

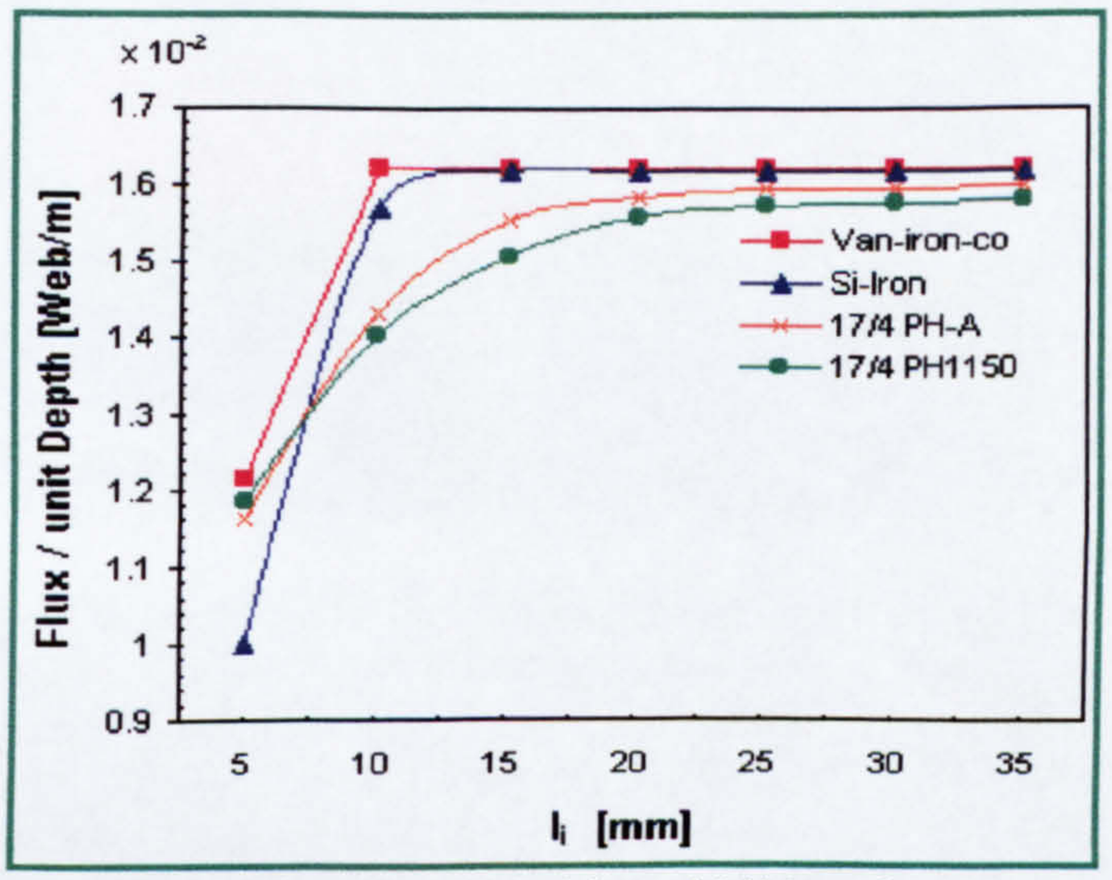

Fig.2 Variation of flux with back-iron axial thickness for different materials

III. BACK IRON OPTIMIZATION DESIGN

A. Effect of Outer Radius on flux level

In the previous analysis, the axial thickness of the silicon-iron core back-iron disc at 12.5 mm has been determined. This allows for the optimization of the outer radius, R_{io} for a maximum attainable magnetic flux, using an efficient FE model for the rotor system. FE analysis gives the variation of flux level over an outer radius range of 43 to 49 mm is shown in Fig.3, in which maximum flux is achieved at R_{io} = 46 mm. Apparently, smaller or greater radii force more flux lines to link with the retainment ring thus short-circuiting the flux lines around the ring, resulting in the reduction of useful magnetic flux in the air gap. Fig.4 is an enlarged sectional view for right upper part of the ***2D*** planar FE model of the magnet rotor disc with the back-iron disc at four selected outer radii (43mm, 46mm, 47mm and 49mm). A detailed study on the behavior of the flux lines explains how the pattern of flux leakage affects the optimum flux level, which occurs when minimum number of flux lines are linked with the retainment ring.

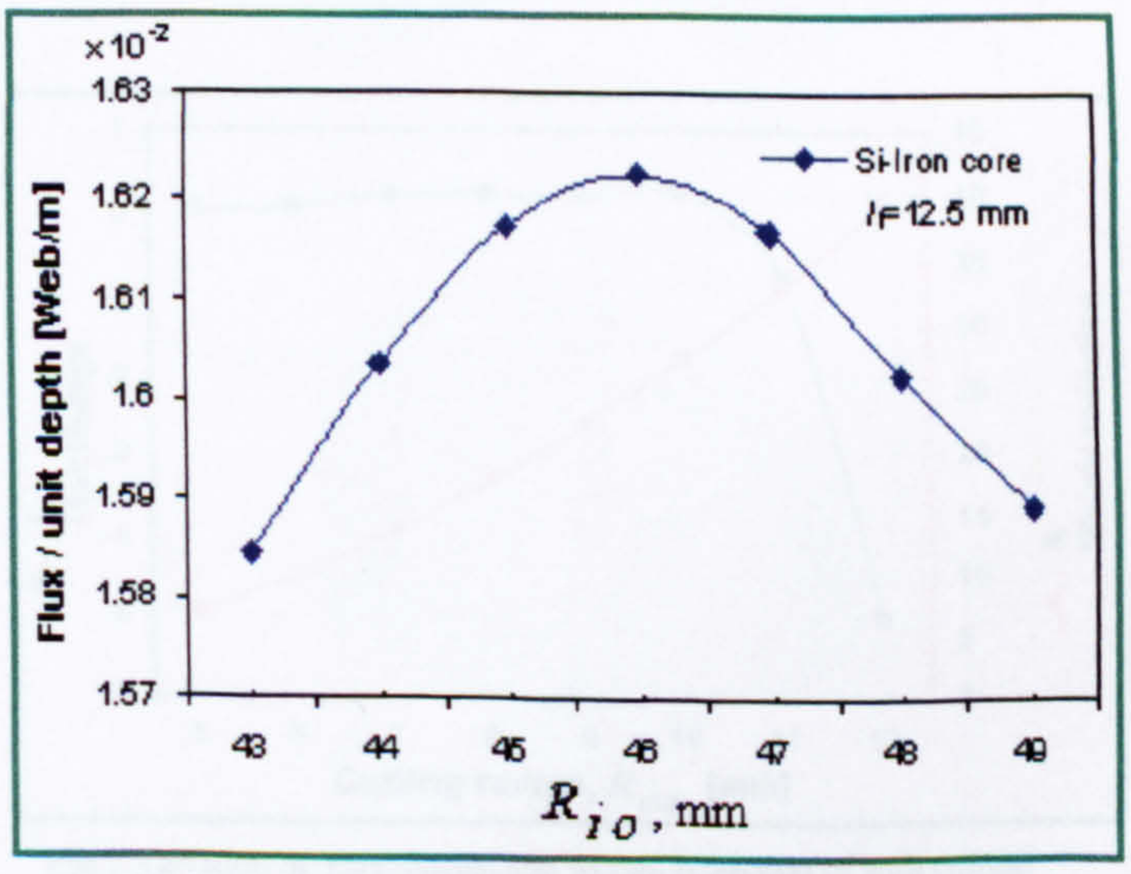

Fig.3 Variation of flux level with outer radius of back-iron disc

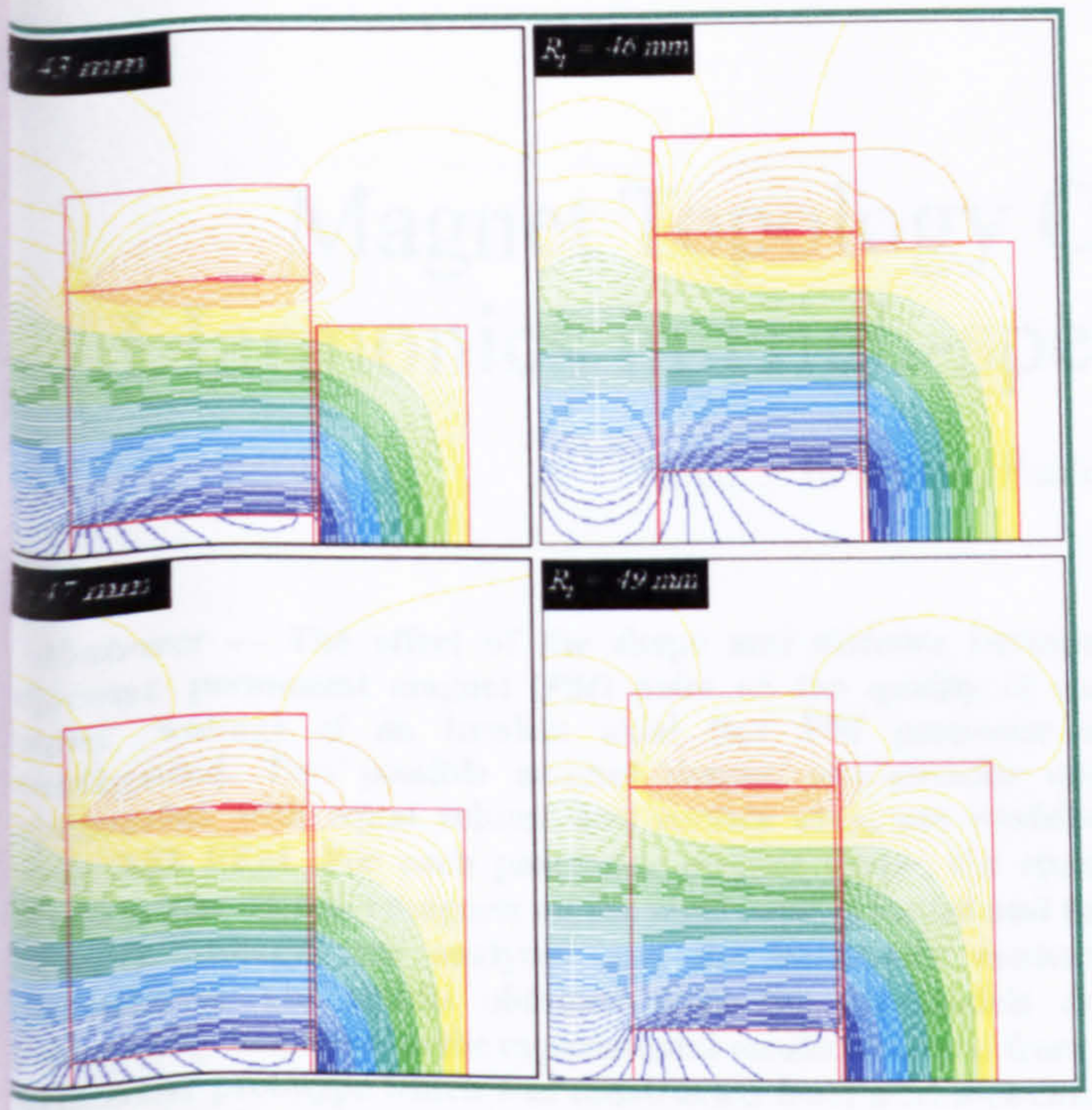

Fig.4 Pattern of flux lines at different outer radii of the back-iron discs

B. *Shape Optimisation*

To further reduce the weight, hence mechanical stresses, "profiling" of the back-iron disc was investigated. It was shown in the previous analysis that the flux lines are less concentrated at the outer rear corners of the discs. Hence, to a certain extent, discarding disc's material at these regions may not deteriorate the flux level, while significant weight advantage can be gained. A circular cutting shown in Fig.5 was used for manufacture ease and performance comparison. To perform this analysis, the FE program was slightly modified to allow for parametric modelling with the cutting radius R_{cut} varied over the range of 5 to 12 mm. The behaviour of the flux lines in the back-iron disc before and after the cutting is shown in Fig. 5. The variation of flux level and weight reduction with cutting radius is shown in Fig. 6. Interestingly, there is no apparent degrade of flux level up to a cutting radius of 10mm. Allowing for simulation tolerance,it appears that the removal of some iron alters the flux line distribution but enhances flux density.

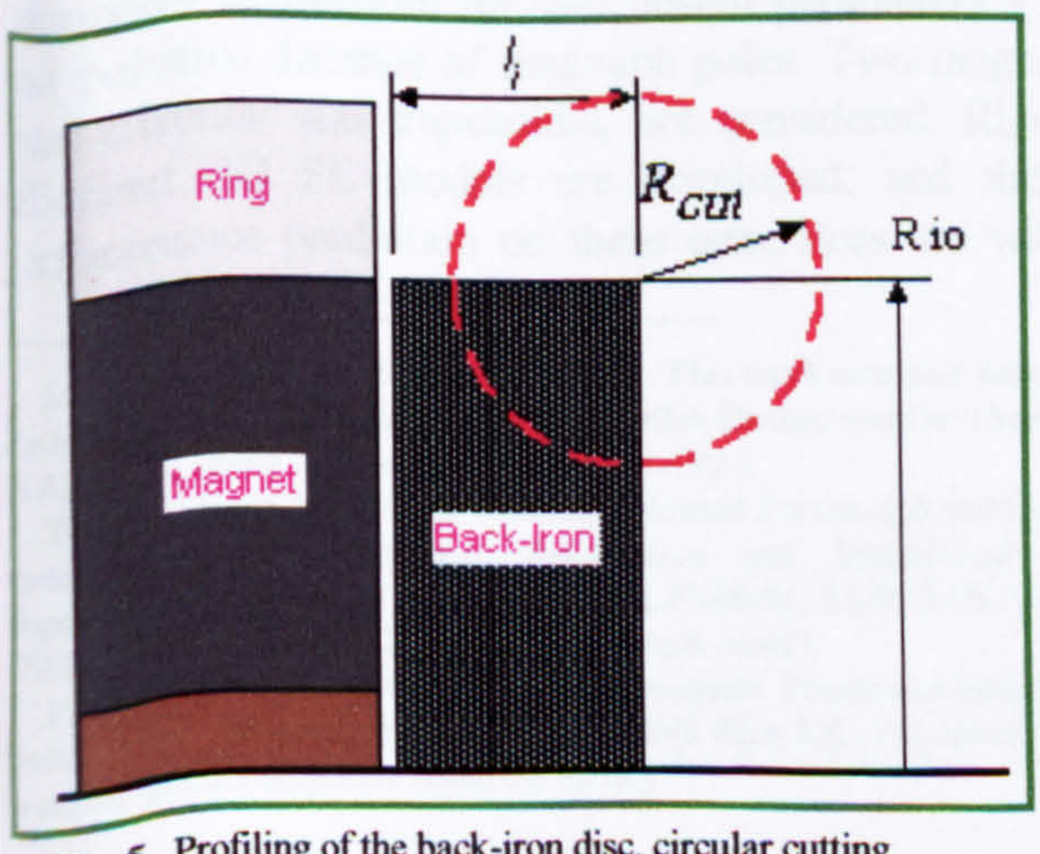

Fig.5 Profiling of the back-iron disc, circular cutting

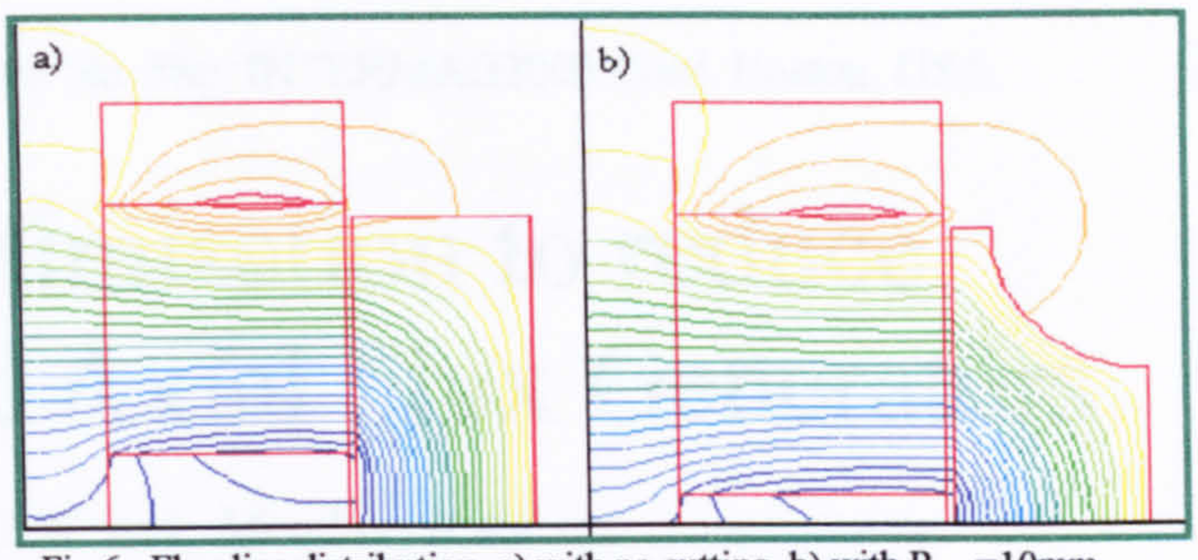

Fig.6 Flux line distribution a) with no cutting b) with R_{cut} =10mm

An 'optimum' value of cutting radius of 10mm was found, which represents a 27% weight reduction at no apparent flux loss in the air gap. From R_{cut}=10mm to 12mm, the flux level experiences a -5% drop but a further weight reduction to 40%. Thus, the part of the curves from R_{cut}=10 to 12mm represents a trade-off region between mechanical and magnetic properties of the system. Depending on the application, optimum design values could be at found at this region.

IV. Conclusion

Back iron design for high speed PM generators has proven to be much more complex than their low speed counterparts, primarily due to the more stringent mechanical requirement, and the usual demand for high power-to-weight ratio expected from them. Although the design study focuses on a particular topology of a disc-type PM generator, the results presented in this investigation serve to highlight some key design parameters that can be considered for back-iron design in other high speed generators.

References

[1] *El-Hasan, T.S.; Luk, P.C.K. et al* "Modular design of high-speed permanent-magnet axial-flux generators", IEEE Transactions on Magnetics, Volume: 36 Part: 1, Sept 2000 pp.3558 –3561.

[2] *Liu,C; Chen.J; Su.K,* "Characteristics of a disc permanent magnet linear synchronous machine with back iron" IEEE INTERMAG 2000, Digest of Technical Papers. pp. 254 –254.

[3] Roark R. J., "Formula for stress & strain". *McGraw Hill*, 1990.

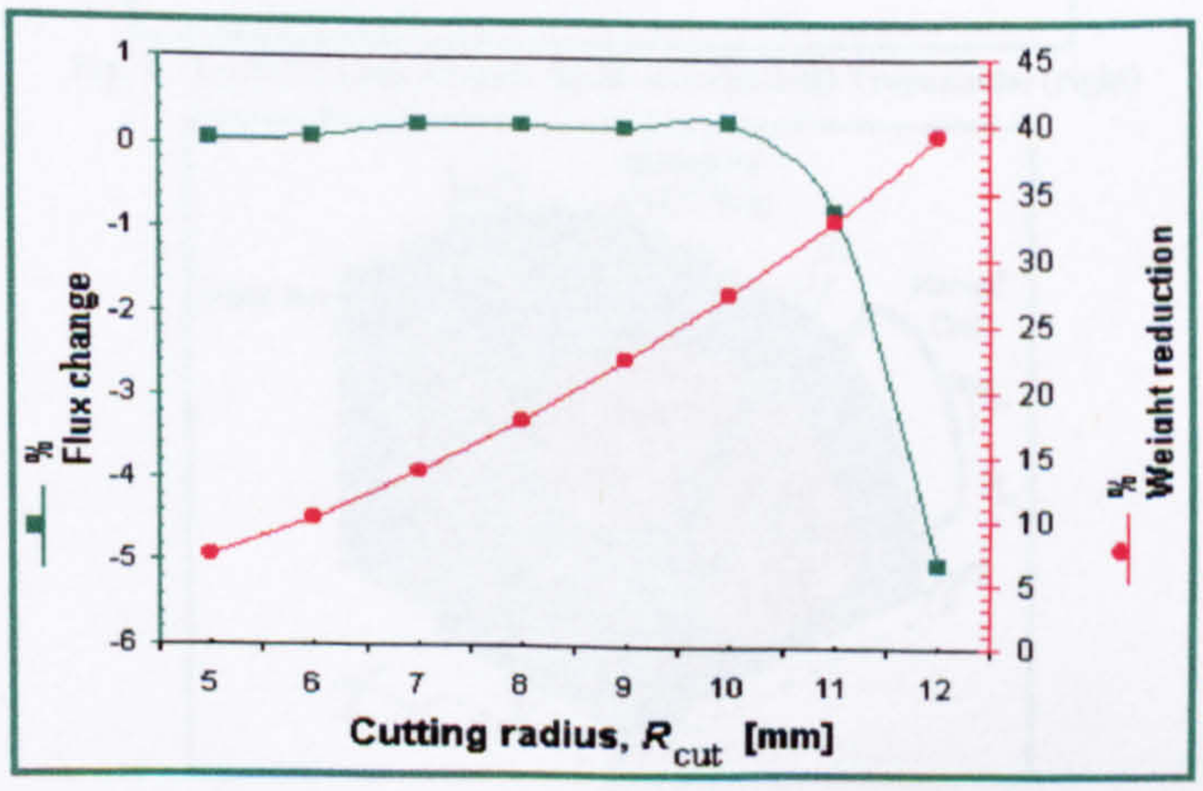

Fig.7 Variation of flux change and weight reduction of with cutting radius on back-iron disc

Magnet Topology Optimisation to reduce Harmonics in High-speed Axial Flux Generators

Tareq S. El-Hasan, Patrick C. K. Luk, *Member*, *IEEE*

Abstract **— The effect of the shape and distance between adjacent permanent magnet (*PM*) poles on the quality of the output voltage of an ironless axial flux PM generator is investigated. Two possible magnet shapes, *semi-circular* and *trapezoidal*, with equal volume and surface area, are modeled using 3D FEM. For each particular magnet shape, the space between the adjacent magnets on the same rotor is varied and the induced voltages are analyzed and the harmonics contents determined. The results obtained from the FE models are favourably compared to the experimental results obtained from a particular prototype which was constructed from a *semi-circular* magnet shape.**

Index Terms **– PM generators, Axial flux generators.**

I. Introduction

Axial flux permanent magnet generators (AFPM), in which air gaps lie across the cross-section of the rotor rather than its periphery, lend themselves mechanically suitable for high speed operations, which has widespread applications in aerospace, mobile power and the like. However, eddy currents induced in the rotors of the AFPM generator could become dominate if several precautions are not considered in the design of such machines. These losses arise because the rotor is exposed to a time varying magnetic fields from the spatial harmonics of the stator current. Eddy current losses are proportional to the square of the magnetic field amplitude, the square of the frequency and inversely proportional to the rotor materials resistivity. As a result, ensuring low levels of rotor losses amounts to producing sinusoidal stator current and making the rotor surface has relatively low surface conductivity.

This paper examines how sinusoidal signals can be established by a design case study on a high speed single phase AFPM generator, and in particular investigates the boundary of freedom for two design parameters - the shape and relative distance of magnetic poles. Two magnet shapes, semi-circular and trapezoidal, are considered. Rigorous and efficient 3D FE models are developed, and their use in performance prediction on these generators are validated by experimental results.

Manuscript received January 4, 2003. This work was part supported by the Jordanian Armed Forces and King Abdullah Design and Development Bureau (KADDB) under the designation number *AB15*.

T.S.El-Hasan is with the Jordanian Armed Forces and currently is a PhD student in the Aerospace, Automotive and Mechanical Engineering Department, University of Hertfordshire, Hatfield, AL10 9AB, UK. Tel: 0044 1707- 286083. (e-mail:T.S.El-Hasan@ herts.ac.uk).

P.C.K.Luk is with Department of Aerospace, Power and Sensors, Cranfield University, Shrivenham, Oxfordshire, SN6 8LA UK. Tel: 0044 1793-785528 (e-mail: p.c.k.luk@rmcs.cranfield.ac.uk).

II. Finite Element Model

Design issues of the *AFPM* generator are well documented [1,2]. Here, two different rotors with two different PM topologies are proposed, as shown in Fig. 1. The machine has a three-dimensional (3D) pattern and the magnetic flux path and its corresponding spatial flux distribution are truly 3D in their nature and as such represents a distinct departure from the conventional radial flux PM machines. This unusual 3D flux pattern in the AFPM generator is largely due to the magnetic circuit of the rotor, and the location and the shape of the stator winding coils. A finite element (FE) design tool was used to develop an efficient 3D FE model. A quarter of the rotor with half of the air gap (Fig. 2) was modeled to reduce computational time. The results for a particular magnet shape and topology were found from one common solution (Fig. 3). The coils in this analysis are replaced by a virtual path of the same shape and presented opposite to the magnets in the middle of the air gap. This virtual path is incrementally stepped in electrical degree where the flux linkage at each position for a particular solution is determined and the induced voltage is found by the derivative of the flux linkage with respect to time at a mechanical speed of 1830 rpm.

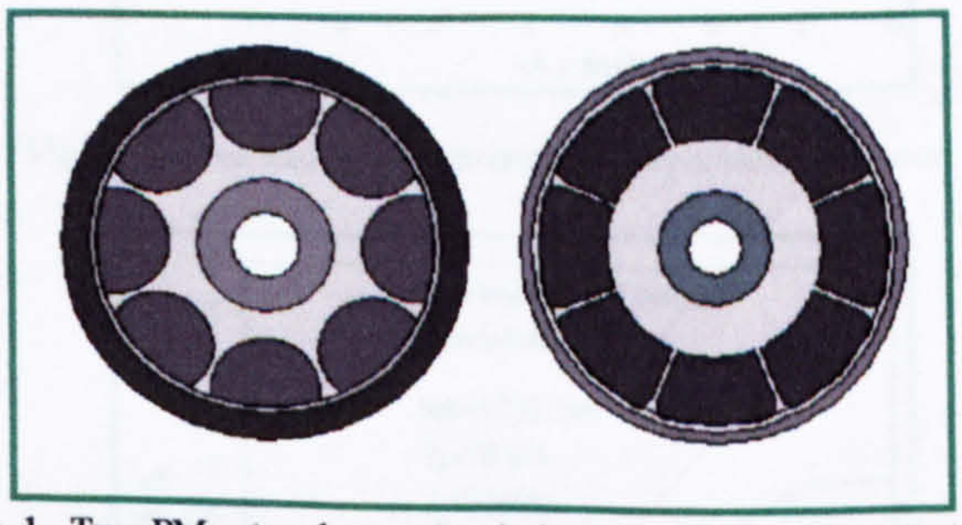

Fig. 1. Two PM rotor shapes. Semi-circular(left) Trapezoidal (right)

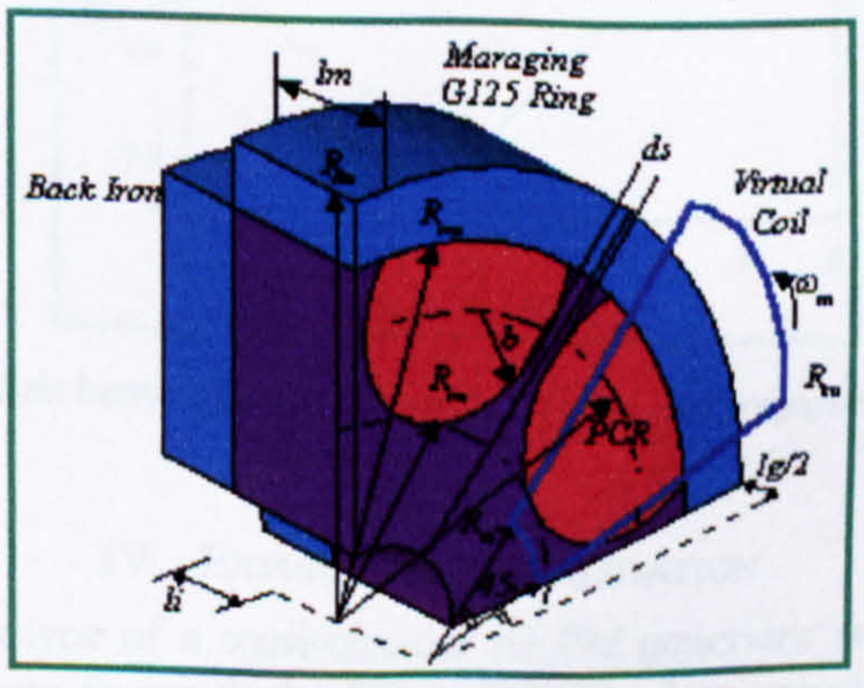

Fig. 2. Modeled part of the AFPM generator

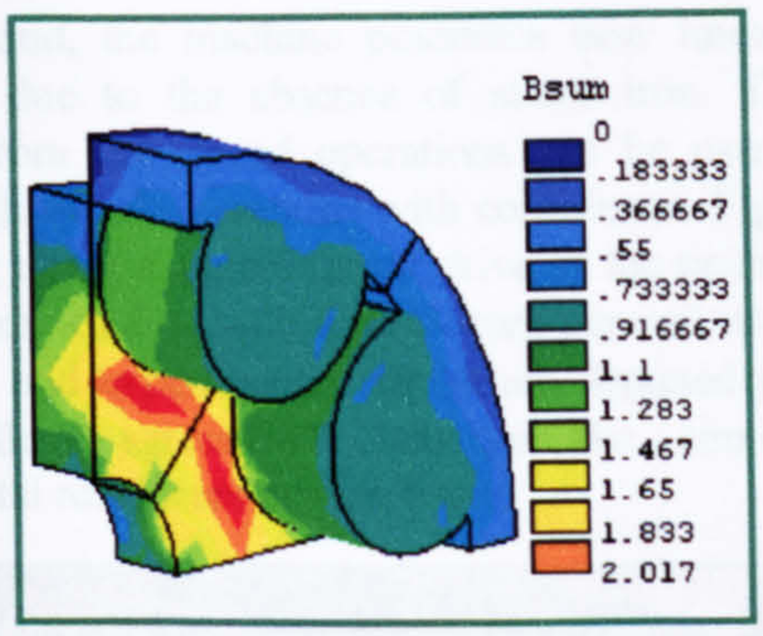

Fig. 3. Magnetic flux density distribution for a semi-circular PM

III. Harmonic Analysis

To investigate the effect of magnet topology on the harmonics of the induced voltages, the distance between the adjacent magnets, d_s, on the rotor of a particular magnet shape (Fig. 4 and 5) is varied in the range of 1 mm to 8 mm with a step increment of 1 mm. For each step, the reduction in the surface area due to the increased distance between the magnets is compensated by increasing the axial length of the magnet to keep the volume of the magnet constant. The induced voltage obtained for each particular case is analyzed and the total harmonic distortion (THD %) in the induced voltage is determined (Fig. 6). Furthermore, the harmonic contents obtained from each case are broken down into triplen and belt harmonics (Fig. 7 – 9).

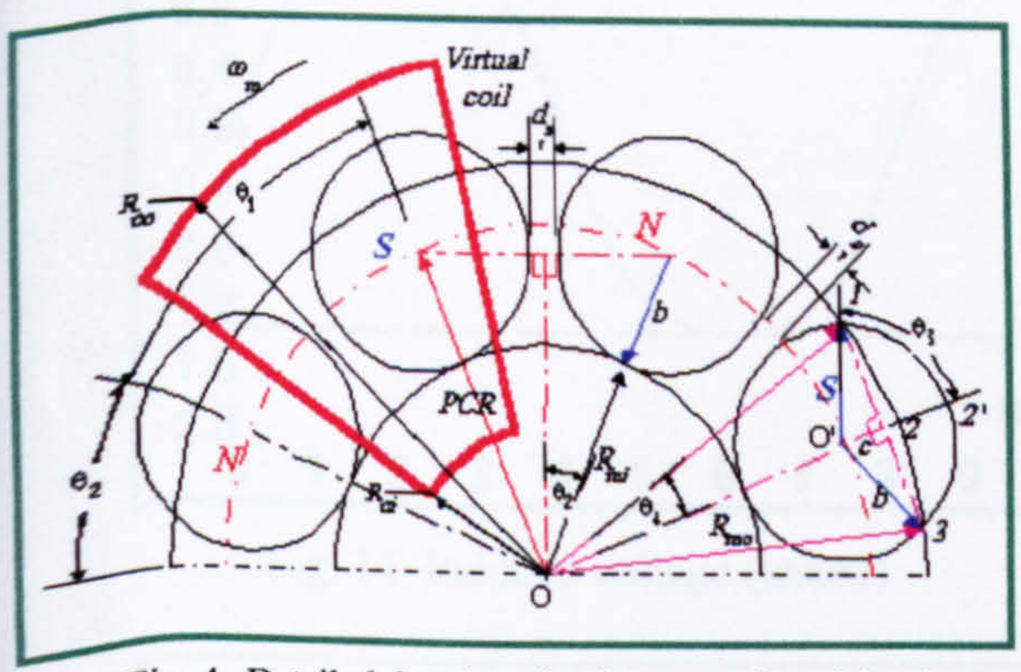

Fig. 4. Detailed drawings for the rotor of semicircular PM

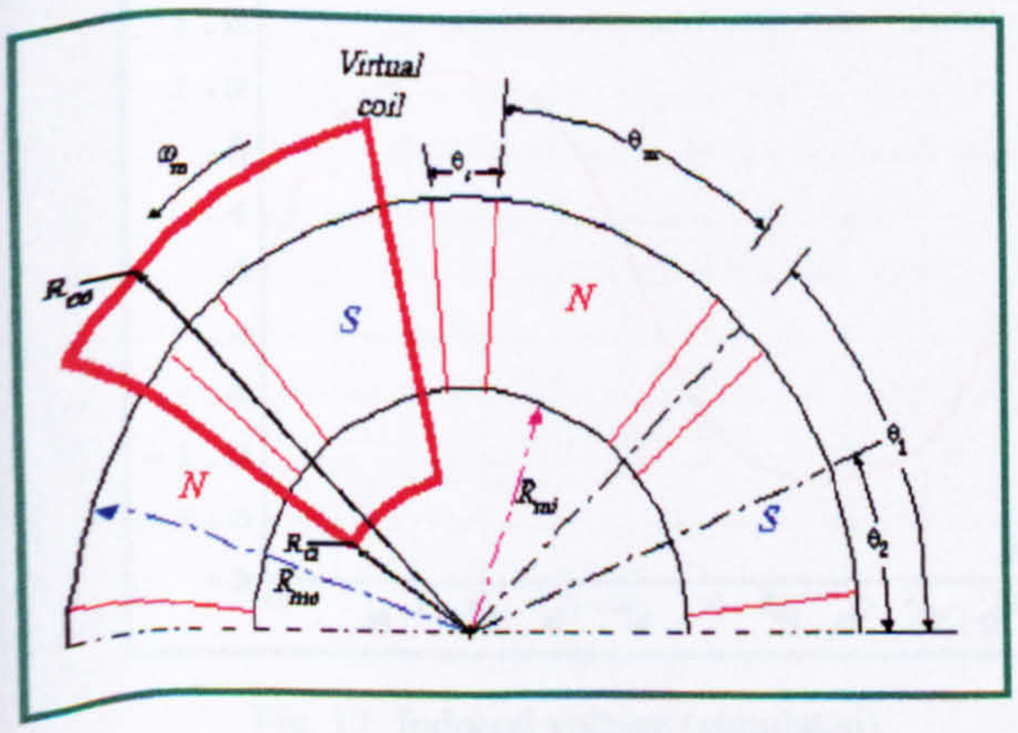

Fig. 5. Detailed drawings for the rotor of trapezoidal PM

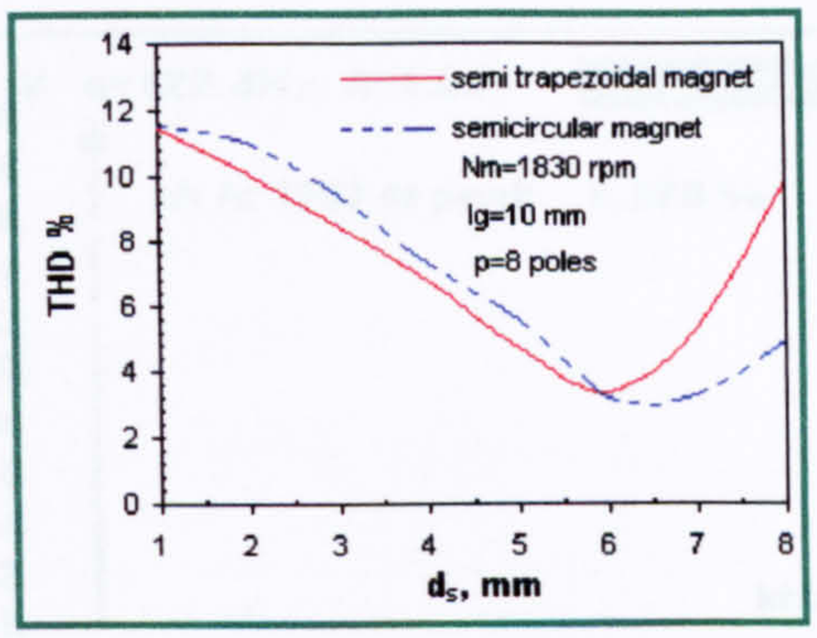

Fig. 6. THD vs. d_s for both magnet shapes

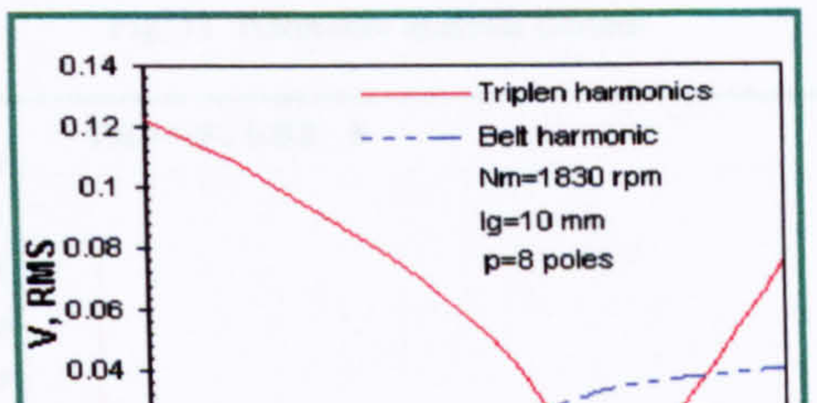

Fig. 7 Triplen and belt harmonics for semicircular PM rotor

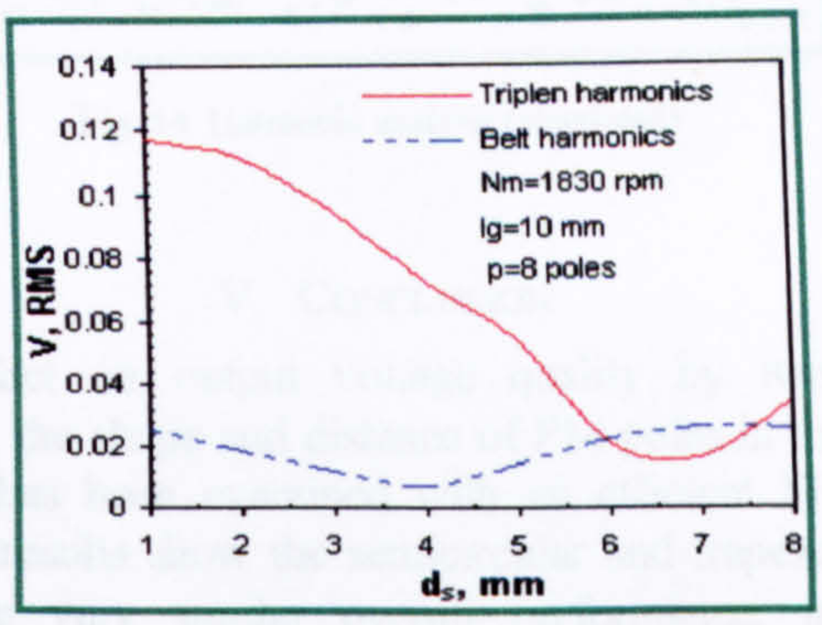

Fig. 8 Triplen and belt harmonics for trapezoidal PM rotor

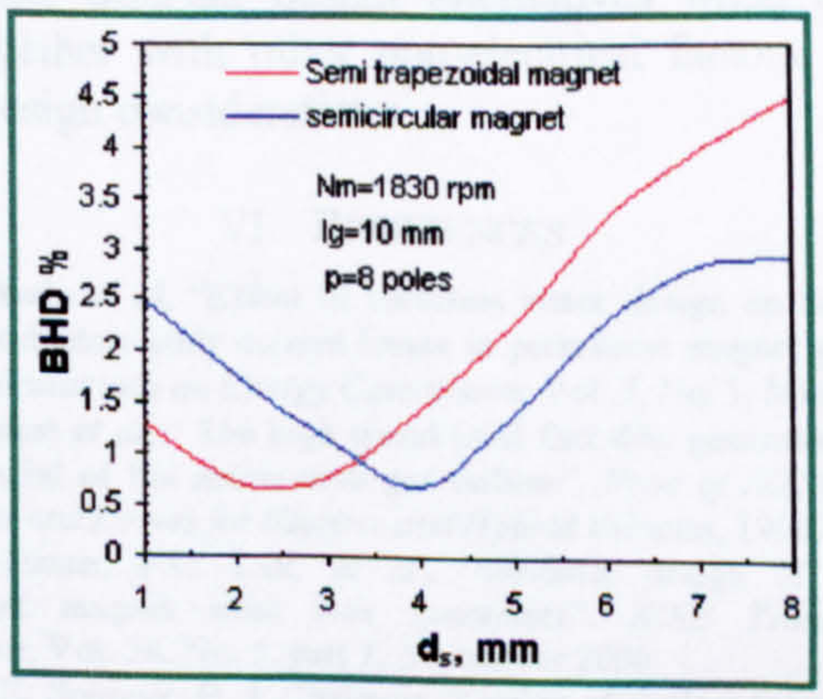

Fig. 9 Belt harmonics for both semicircular and trapezoidal PM

IV. Experimental Validation

A prototype of a semi-circular *AFPM* generator was tested at 1830 rpm to verify the FE model. The low speed test was used for two main reasons. First, it allows easy mechanical

setup. Second, the machine possesses near linear magnetic properties due to the absence of stator iron. Thus results obtained from low speed operations can be extrapolated to predict high speed operations with confidence. Fig. 10 shows the test rig using a simple motor drive as the prime mover. A simple stator winding with a single turn per coil was used. The simulation and experimental results are depicted in Fig. 11 – 14. Excellent agreements between the simulation and experimental results are demonstrated.

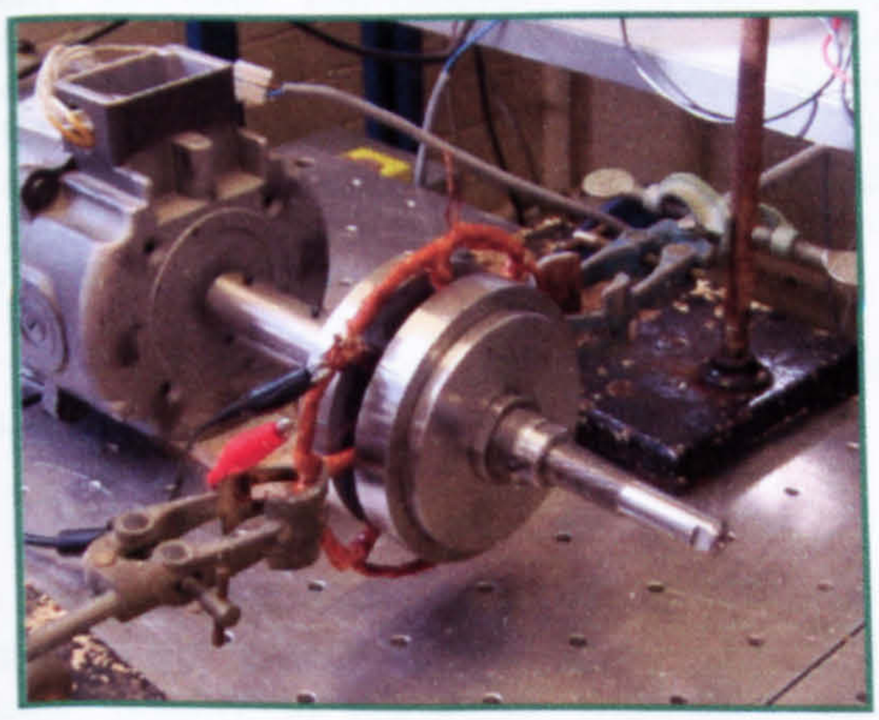

Fig. 10 Snapshot for the prototype test rig

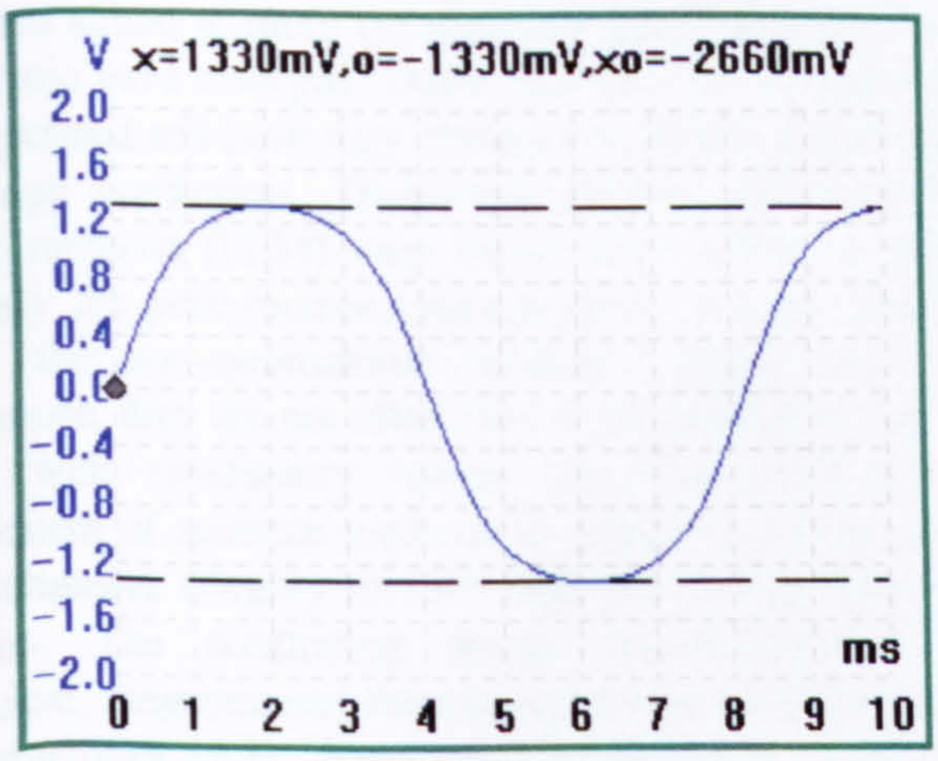

Fig. 11 Induced voltage (tested)

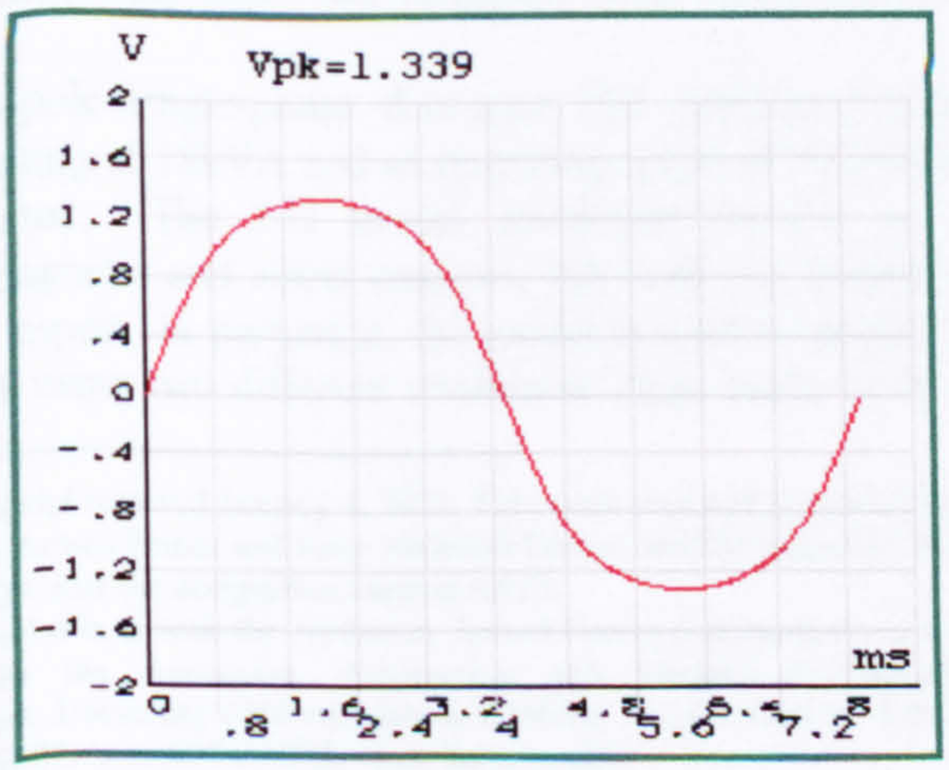

Fig. 12 Induced voltage (simulated)

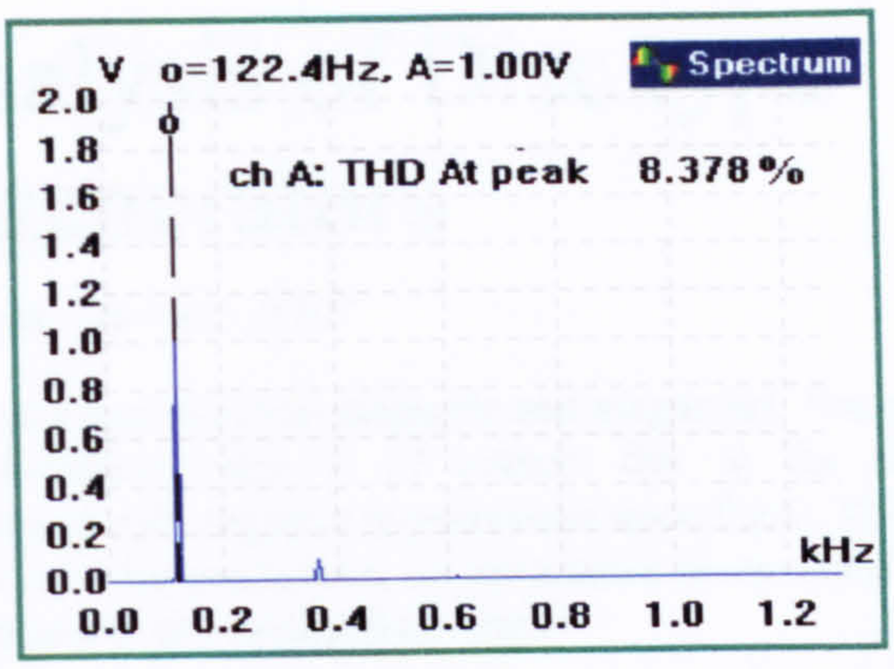

Fig. 13 Harmonic analysis (tested)

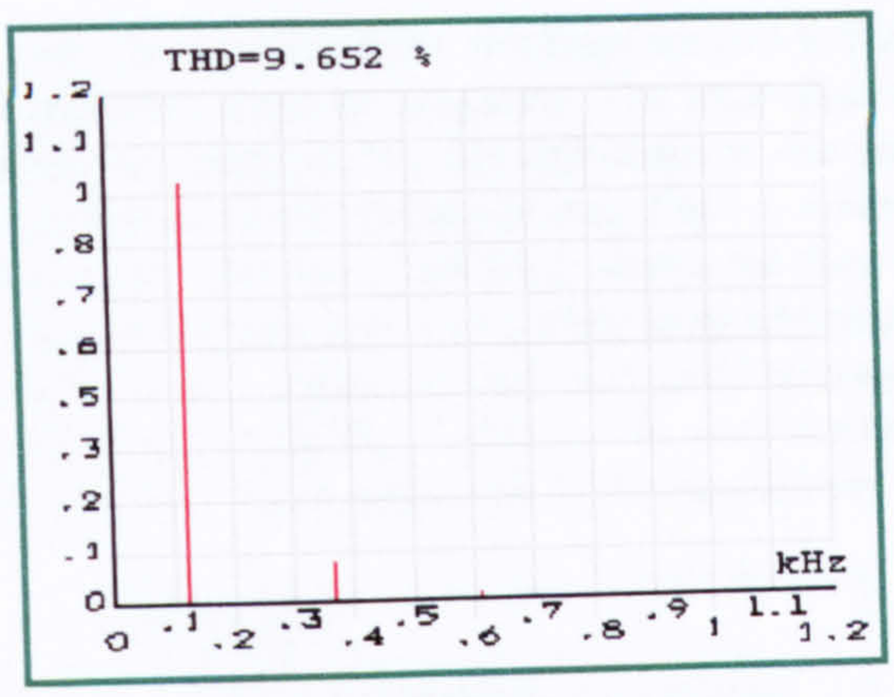

Fig. 14 Harmonic analysis (simulated)

V. Conclusion

The effect on output voltage quality by two design parameters, the shape and distance of PM poles in the *AFPM* generator, has been examined with an efficient FE model. Whilst the results show the semicircular and trapezoidal PM rotors have very similar overall performance, individual harmonic contents appear to vary differently with adjacent pole distance, offering design alternatives when harmonic content, together with other non-electrical factors, are also important design considerations.

VI. References

[1] A. A.Arkadn *et al*, "Effect of toothless stator design on the core and stator conductors eddy current losses in permanent magnet generators". *IEEE Transactions on Energy Conversion*, Vol. 7, No. 1, March 1992.

[2] K. R. Pullen *et al*, " The high speed axial flux disc generator-unlocking the potential of the automotive gas turbine", *Proc of IEE Colloquium Machines and Drives for Electric and Hybrid Vehicles*, 1996.

[3] T.S. El-Hasan, P.C. Luk, *et al.*, "Modular design of high-speed permanent magnet axial flux generators". *IEEE Transaction on Magnetics*, Vol. 36, No. 5, part 1, September 2000.

[4] W. Wu, E. Spooner, B. J. Chalmers "Design of slotless torus generators with reduced voltage regulation". *IEE Proceedings of Electric Power Applications*, Vol. 142, No. 5, Sept. 1995.

[5] Remy Perrin-Bit, Jean Louis Coulomb, " A three dimensional finite element mesh connection for problems involving movement". *IEEE Transactions on Magnetics*, Vol. 31, No. 5, May 1995.

[6] M. Azizur Rahman, Ping Zhou, "Field-Based analysis for permanent magnet motors". *IEEE Transactions on Magnetics*, Vol. 30, No. 5, September 1994.

Three-Dimensional FE Analysis of Disc type High-Speed PM generators

Tareq S. El-Hasan, Patrick C.K. Luk, *Member, IEEE*

Abstract **— An efficient 3-D finite element model for a permanent magnet slot-less high-speed generator is developed. The model addresses non-symmetry problems commonly associated with 2-D modeling, and avoids computational inefficiency and complexity typical of 3-D modeling. Based on a commercial FE tool, the 3-D model can predict both the machine's electromagnetic performance and mechanical integrity accurately. Simulation results from the 3-D model compare very favorably with experimental results.**

Index Terms **– PM generators, axial flux generators, slot-less machines, high-speed generators.**

I. Introduction

There are increasing interests and demands for permanent magnet (PM) generator sets in a wide range of applications, notably in distributed generation where the generators are located closed to the user as micro power plants. More recently advanced configurations of PM generators aimed at more compactness and higher power-to-weight ratio have emerged. These machines are typically high speed operated and have very stringent operation requirements and design constraints. Traditional analysis and 2-D finite element methods (FEM) were found not suitable to predict accurately the performance characteristics of such machines due to the non-symmetrical geometry along their axis. Furthermore, they are not often easy to be simplified into 2-D models with satisfactory results [1]. This calls for the development of accurate methods to predict the performance and mechanical integrity of such high power and high speed machines. The conflicting design requirements in the mechanical, magnetic and thermal aspects are well known for these machines [2,3]. Successful development of accurate prediction methods will thus allow alleviate the complex design task with improved reliability and shortened design cycle.

An 8-pole single-phase disc-type PM generator with a power rating of 18kVA and an operating speed of 50,00rpm is investigated. The 3-D model developed focuses on the electromagnetic and stress analysis, but does not include the thermal aspect. In particular, the model is used to predict the effect of using two different retainment rings made from two different materials (non-magnetic and magnetic). The study of the retainment rings is of interest due to the stringent mechanical and magnetic requirements upon them. The model is also used for predictions on inductance measurement, eddy current losses and mechanical stress.

Manuscript received January 4, 2003. This work was part supported by the Jordanian Armed Forces and King Abdullah Design and Development Bureau (KADDB) under the designation number *AB15*.

T.S.El-Hasan is with the Jordanian Armed Forces and currently is a PhD student in the Aerospace, Automotive and Mechanical Engineering Department, University of Hertfordshire, Hatfield, AL10 9AB, UK. Tel: 0044 1707- 286083. (e-mail:T.S.El-Hasan@ herts.ac.uk).

P.C.K.Luk is with Department of Aerospace, Power and Sensors, Cranfield University, Shrivenham, Oxfordshire, SN6 8LA UK. Tel: 0044 1793-785528 (e-mail: p.c.k.luk@rmcs.cranfield.ac.uk).

II. FE Electromagnetic Analysis

The rotor disc and the stator windings are two key parts of the PM generator under investigation. The rotor disc consists of 8 permanent magnets (8-pole) embedded in the magnetic carrier and locked by the retainment ring. Fig.1 is a meshed 3-D model of the rotor disc, and Fig.2 shows the flux density distribution of the rotor disc, using a non-magnetic retainment ring. with a. levels magnet carrier was analysed using a 3D FE model as shown in Fig. 1 and 2. The results interpreted from the model are discussed in the following sections.

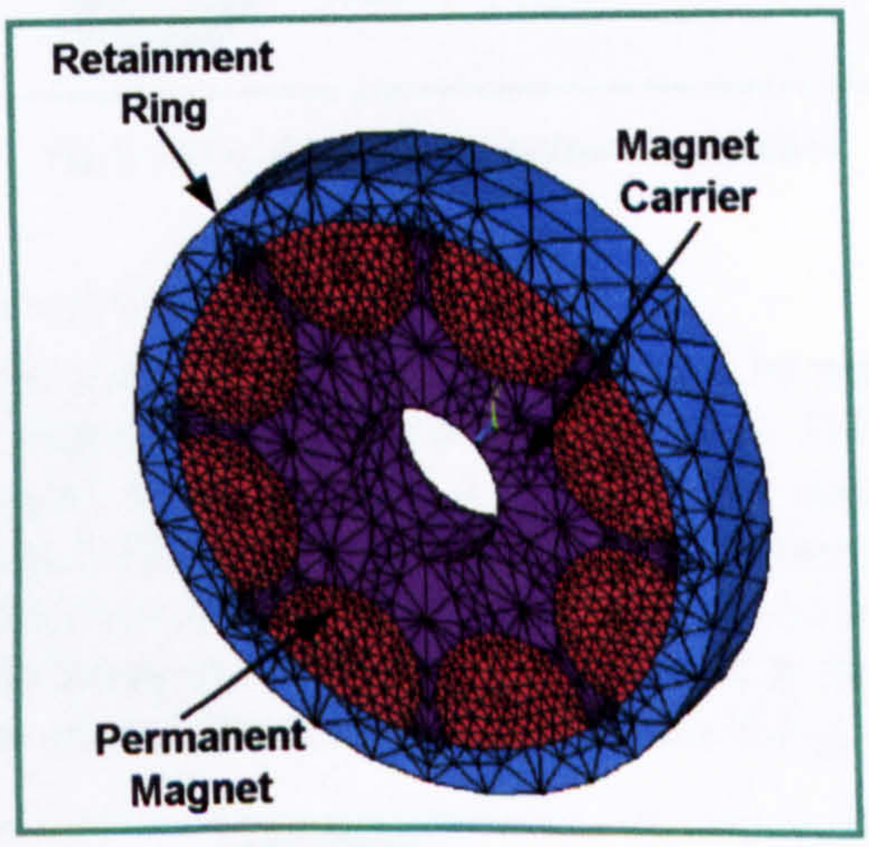

Fig.1 Meshed 3-D model of the disc type generator

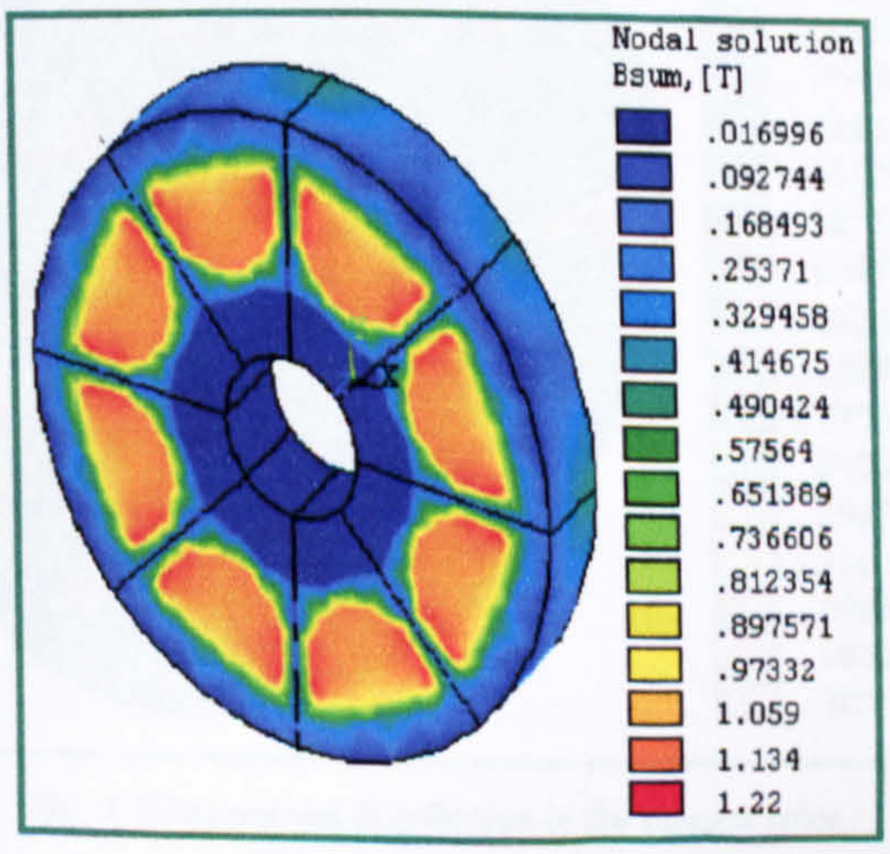

Fig. 2 Flux density distribution

A. Air gap induced voltage

Eight stator coils are positioned between the rotating rotor c to obtain the induced voltage. Fig.3(a) shows a stator coil ten out from the its fibred stator casing. To model the air p induced voltage, the actual stator coils were replaced by ncentric virtual paths, shown in Fig. 3(b), that are identical shape and dimensions to the actual coils. The induced tage was found for two different types of retainment rings, e of Maraging and the other of non-magnetic material, at the ed of 1830 rpm, as shown in Fig. 4. Moreover, the influence air gap length between the magnet rotors on the induced tage for both retainment rings was studied and the results tained were shown to be in good agreement to the perimental results, as shown in Fig. 5.

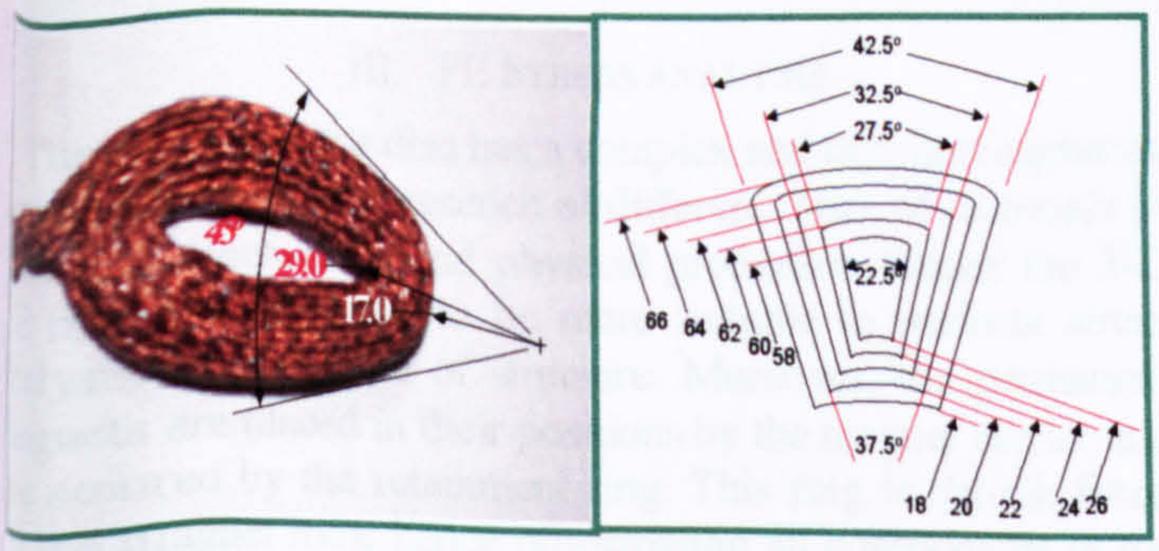

Fig. 3 (a) Actual stator coil (b) Modeled virtual paths

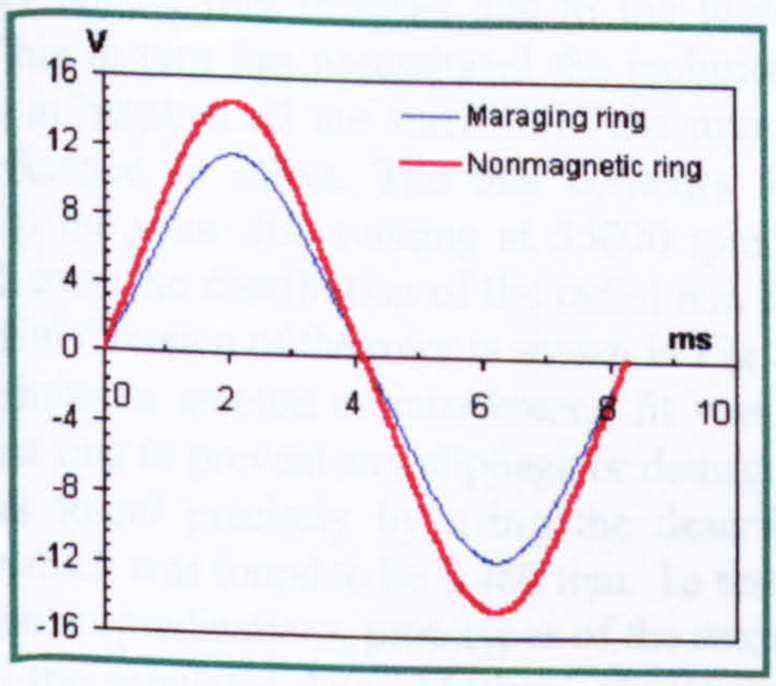

Fig. 4 FE Induced voltages for rotors with magnetic and nonmagnetic retainment rings

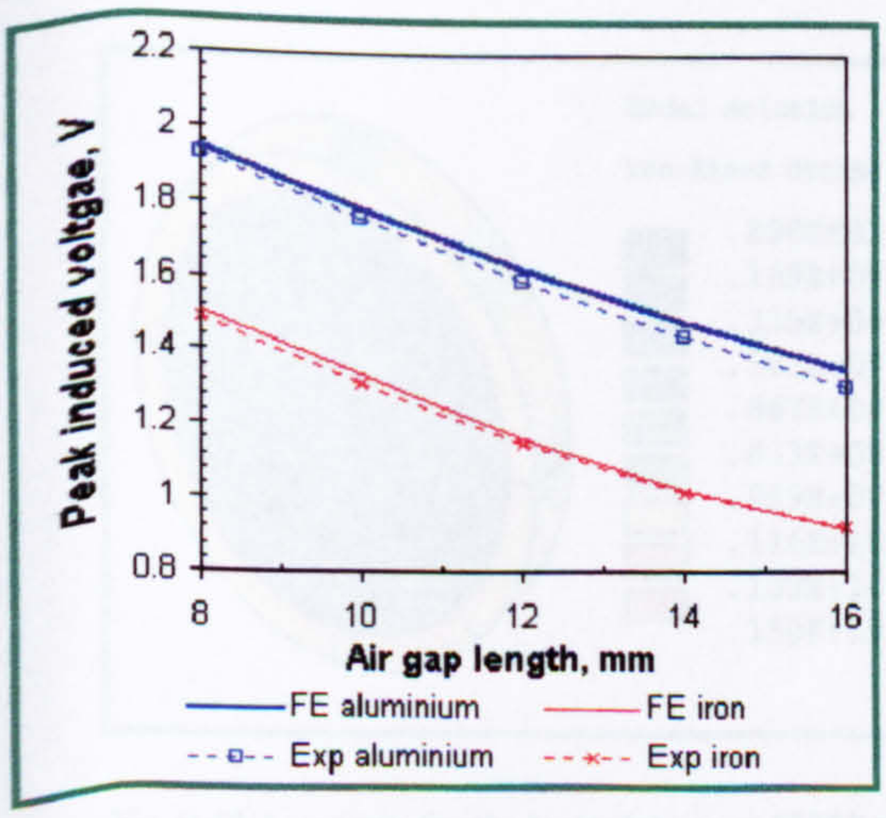

Fig. 5 Induced voltages vs. air gap length

B. Inductance computation

Inductance measurement for the machine was obtained using the energy storage method. In this case the actual coils were modeled (Fig. 6) with the PM coercivity set to zero and a certain dc current level injected in the coil. The leakage and magnetizing inductances were found to be 14.63 MH and 25.75 MH respectively compared to these obtained from experimental results as 20.1 MH and 38.74 MH respectively.

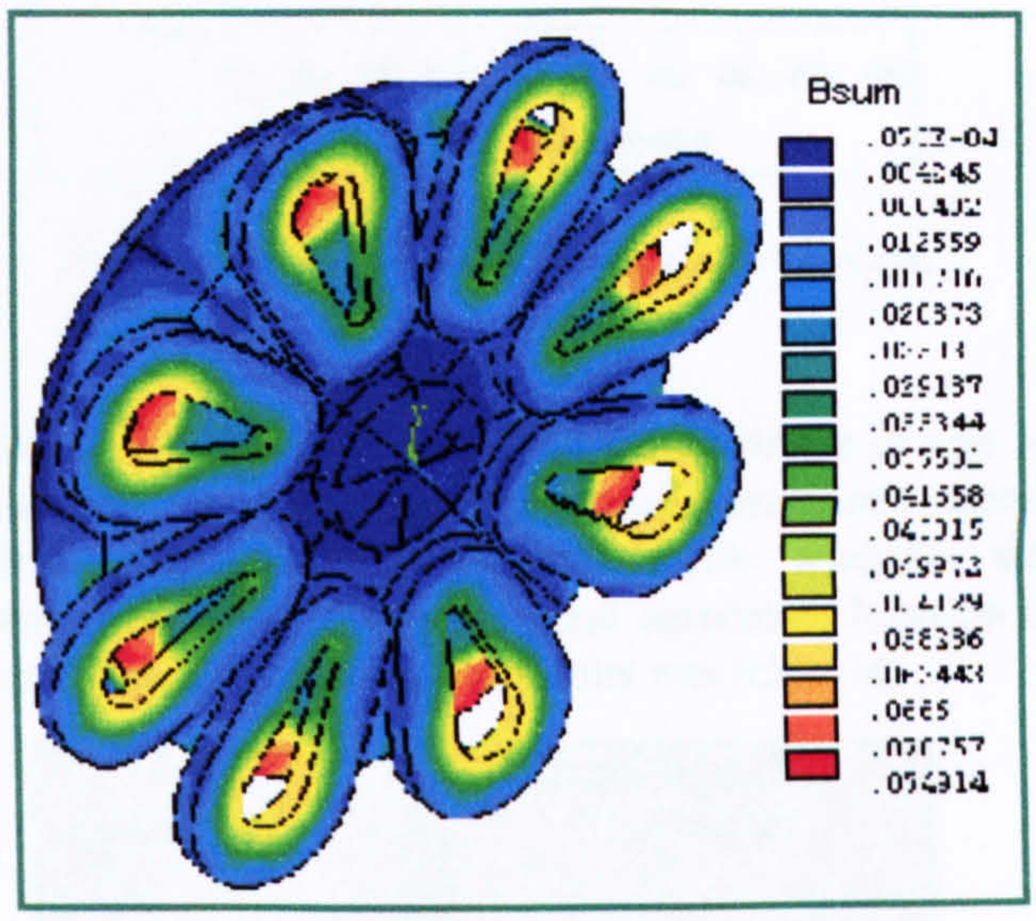

Fig. 6 3-D model used for inductance computation

C. Rotor eddy current losses

The rotor eddy current loss was determined by performing harmonic analysis with the frequency was set to 3333 Hz. In the 3-D model shown in Fig.7, it is possible to visualize the eddy current distribution and to gain insightful observation on effective heat loss for the system. It also allows the evaluation of the eddy losses in the individual component in the magnet rotor as the current drawn increases, as shown in Fig. 8.

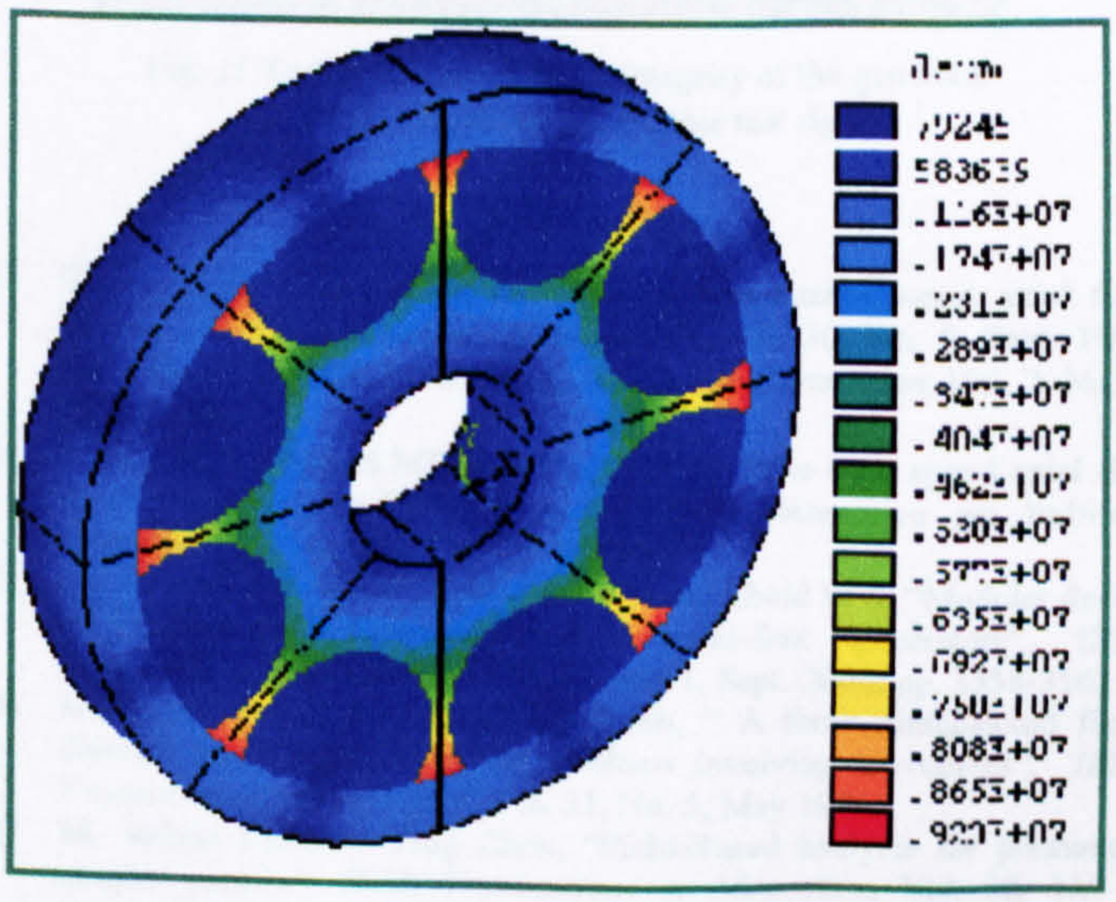

Fig. 7 Eddy current distribution in the magnet rotor

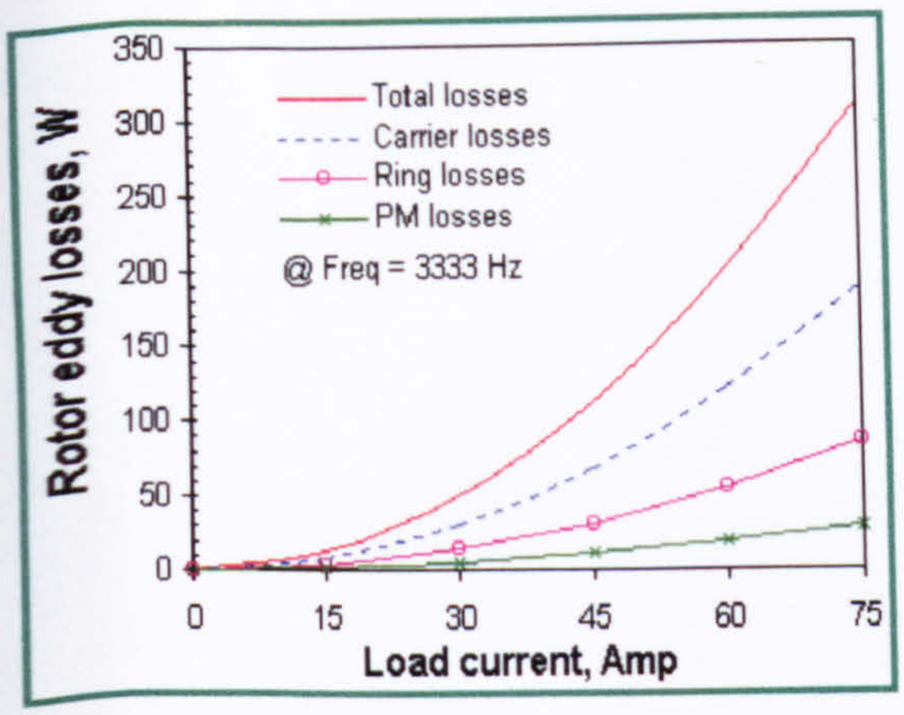

Fig. 8 Eddy current losses vs. current drawn

III. FE Stress analysis

The magnet rotor disc has a complex and non-homogeneous ructure due to the presence of different types of materials of fferent mechanical and physical properties. Hence the 3-D E model was found to be more suitable to perform stress alysis for this type of structure. Moreover, the permanent agnets are placed in their positions by the magnet carrier and e secured by the retainment ring. This ring is shrunk fitted n the magnet rotor hence pre-stressing all components in the ructure. Once the rotor starts to rotate, additional stresses are eveloped on the ring surfaces due to the high centrifugal rces. This in turn has necessitated the inclusion of contact ements in between all the surfaces of the rotor to simulate e interference fit effect. The blot contours for the hoop esses in the rotor disc running at 55000 rpm is shown in Fig.9, whereas the distribution of the radial and hoop stresses n the radial direction of the rotor is shown in Fig. 10.

The minimum amount of interference fit was required for tainment ring to prevent any slippage or damage of the rotor rts was found precisely by using the described 3-D FE alysis which was found to be 0.480 mm. To test the validaty these stress predications, prototypes of the rotor constructed sed on the simulated data.. Mechanical integrity tests were tisfactorily done individually, by using a gas turbine running 55000rpm no load, as shown in Fig. 11.

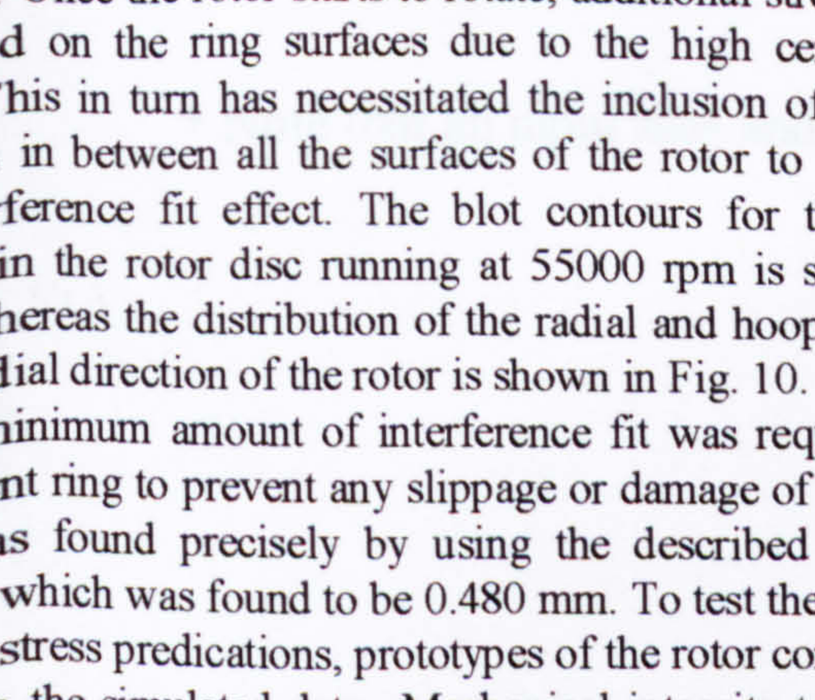

Fig. 9 Plot contours for the hoop stresses at 55000 rpm

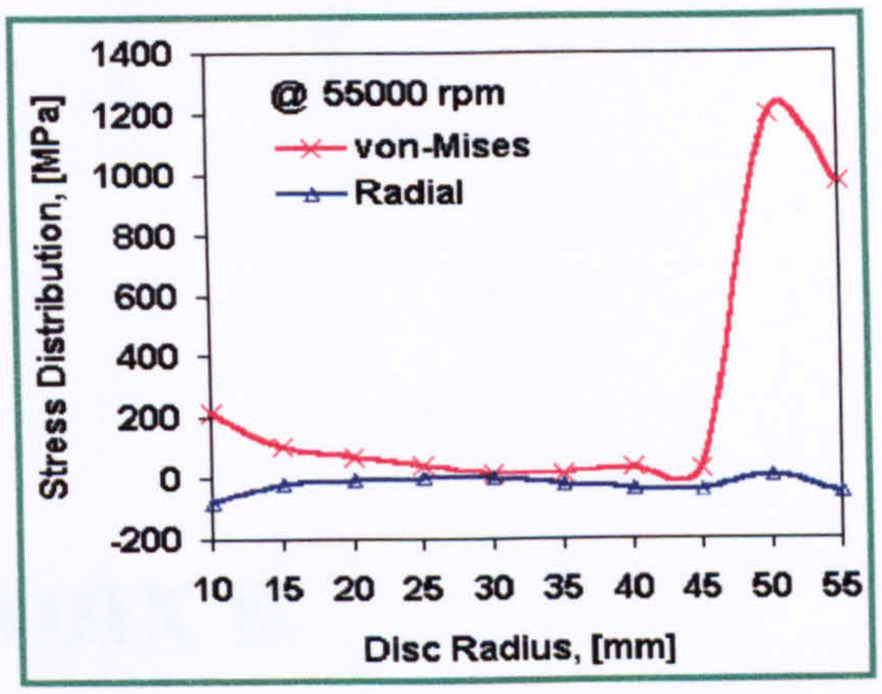

Fig. 10 Radial and hoop stresses distribution at 55000 rpm

IV. Conclusion

The 3D FE model is an efficient tool for the design and analysis of the disc type high-speed generators. Results obtained from the FE electromagnetic analysis were experimentally validated and a good agreement between the FE results and the experimental results was achieved.

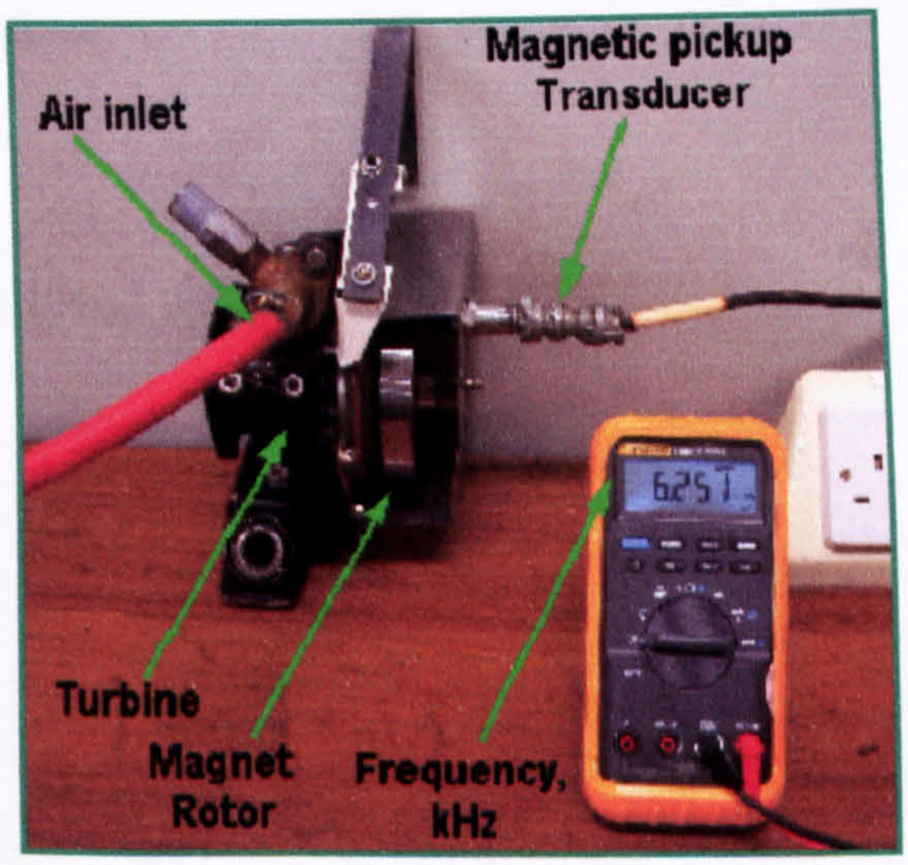

Fig. 11 Testing the mechanical integrity of the generator using a cold run gas turbine test rig

V. References

[1] Furlani E P. "Computing the field in permanent-magnet axial field motors". IEEE transaction on magnetics, Vol. 30, No. 5, Sept. 1994, pp.3660-3663.*IEEE Transactions on Energy Conversion*, Vol. 7, No. 1, March 1992.

[2] Pullen K R, Etemad MR and Fenocchi A. "The high speed axial flux disc generator-unlocking the potential of automotive gas turbine". Coloquium digest-IEE 1996;(152):8-8.

[3] El-Hasan T S, Luk P C K, Bhinder F S and Ebaid M S. "Modular design of high-speed permanent-magnet axial-flux generators", IEEE Transactions on magnetics, Vol. 36, part 1, Sept. 2000, pp. 3558-3561.

[4] Remy Perrin-Bit, Jean Louis Coulomb, " A three dimensional finite element mesh connection for problems involving movement". *IEEE Transactions on Magnetics*, Vol. 31, No. 5, May 1995.

[5] M. Azizur Rahman, Ping Zhou, "Field-Based analysis for permanent magnet motors". *IEEE Transactions on Magnetics*, Vol. 30, No. 5, September 1994.

APPENDIX D

ANSYS FILES & SIMULATION RESULTS ON CD-ROM

- 2D STRESS ANALYSIS OF THE ***PMAF*** ROTOR
- 2D ELECTROMAGNETIC ANALYSIS
- 3D STRESS ANALYSIS OF THE ***PMAF*** ROTOR
- 3D MAGNETOSTATIC ANALYSIS
- 3D HARMONIC ANALYSIS

*** Note that all input files and results are produced using *ANSYS5.4***